Title: Characteristics of Aerosol Assisted and Conventional Chemical Vapour Deposition of Metal Oxide Thin Films on Glass, with or without Metal Dopants

Author: **Gillian Walters**

Institution: **UCL**

Degree: EngD: **Materials Simulation and Molecular Modelling**

Abstract

This thesis describes the characteristics and properties of aerosol assisted chemical vapour deposition (AACVD) and conventional atmospheric chemical vapour deposition (CVD) metal oxide thin films on glass substrates with or without metal, Au, Ag, Cu or Al dopants. Host metal oxide matrices including, ZnO and TiO_2 with various dopants are known to give specific physical and optical properties desired by many industries and have various potential properties *e.g.* thermochromic, photochromic and are known as 'intelligent coatings'. The AACVD synthesis technique was used singularly or in combination with APCVD to achieve thin films on glass substrates either in static or dynamic situations with a range of temperatures (300-600 ºC). Computational fluid dynamics (CFD), Fluent™ software, was used in a 2-equation, numerical study of fluid flow, velocity, particle trajectory, evaporation and thermophoretic effects on six combined AACVD/APCVD vertical reactor head designs; two designs were then selected as experimental prototypes and tested on a pilot rig chosen to more accurately simulate commercial Float glass production. Various functionalities of the thin films were analysed using transmittance/reflectance spectroscopy, RZ ink and stearic acid photocatalysis tests, resistivity and a variety of analytical techniques including SEM, XRD and XPS were used. The main findings include the effect of noble metal dopants (particularly Au and Ag), substrate synthesis temperature, fluid flow and droplet size have on the physical and chemical properties such as the morphology, crystallinity, water surface contact angle of the host metal oxide matrices. The nebulised AACVD droplet size, for solvent systems, are critical for deposition of the precursor chemicals onto the surface of the substrate, CFD particle trajectory of nebulised AACVD methanol droplets were calculated to be 1 order of magnitude too small to overcome the main forces of influence aerodynamic drag and at higher synthesis temperature evaporation.

Declaration

I, Gillian Walters confirm that the work presented in this thesis is my own. Where information has been derived from other sources, I confirm that this has been indicated in the thesis.

Signature:

Gillian Walters

Date: 2nd August 2012

Table of Contents

Table of Figures

Table of Tables

Chapter 1

Properties and CVD Synthesis of Metal Oxide Thin Films

Chapter 1: Properties and CVD Synthesis of Metal Oxide Thin Films

Introduction to the Synthesis and Properties of Metal Oxide Thin Films via CVD Techniques with and without Dopants

1.0.0 Introduction

This thesis describes the incorporation of metal nanoparticles dopants into metal host matrices thin films using atmospheric chemical vapour deposition (CVD) and aerosol assisted chemical vapour deposition (AACVD) synthesis, their characteristic's, physical properties, linear and non-linear optical properties and the simulated fluid flow of synthesis using computational fluid dynamic models.

Noble metal nanoparticle thin films are an intensive area of research due to their interesting functional properties including extensive colouration and anti-microbial properties. The unknowing use of noble metal nanoparticles dates back at least to the 4th and 5th century BC in Egypt[1] and China for colouring various materials including glass and ceramics. The Roman soda-lime-silica glass Lycurgus Cup, see fig. 1, is one of the most famous examples believed to have been manufactured in the 4th century A.D; analysis has revealed that the cup contains colloidal alloy of gold (Au - Ag, 40 ppm and 300 ppm respectively). The cup is ruby red in transmitted light and green in reflected light- these colours arise from the small amounts of embedded Au/Ag alloyed nanoparticles which have exceptional ability to colour objects even at very low concentrations. The Romans formed these highly coloured objects by adding "for good luck" coins into the glass forming melt, these coins dissolved in the high temperature of the glass forming process and adventitiously formed alloyed nanoparticles embedded within the host bulk glass matrix to form a composite. The brilliant colours of noble metal nanoparticles (in excess of the colouration efficiency of the best organic dyes) are due to the surface plasmon resonance (SPR) absorption governed by the noble metal nanoparticles morphology, size, shape and the dielectric constant of the surrounding medium[2].

Figure 1: The Lycurgus Cup. Left image viewed in reflected light; right image viewed in transmitted light. Photographs courtesy of the British Museum.

Thin films containing metal nanoparticles are of interest to a range of industries from the electronics, glass, chemical sensing/detectors[3], bio-, catalysis, semi-conducting to computing industries. The main properties of interest are optical, catalytic, sorbents, electrical/thermal conductivity, antibacterial/biological, colour, photocatalysis, photochromic effects, electrochromic, photoluminescence, the plasmon resonance/shift and enhanced reactivity[4, 5, 6]. The goal of synthesis in this area is to produce nanoparticles of a specified size and shape either at or near the surface or embedded within a host matrix or a combination of both that adheres to the substrate. It is the size and to some extent the shape of the noble metal nanoparticle and distance between the nanoparticles within a host matrix that has the greatest influence on the properties displayed. Therefore control over size, dispersion, shape and homogeneity is the key to inventing devices and technologies that have potential uses across several business sectors and possible solutions to technically difficult problems, such as cheap affordable solar panels for the domestic market. This chapter outlines the underpinning science of nanoparticle thin film work and covers areas of commercial interest, basic concepts and research. It starts with industrial applications of thin films that contain noble metal nanoparticles in fields as diverse as catalysis and antimicrobial coatings, it then reviews the methods of making nanoparticles as discrete entities and how these entities can be incorporated in thin films; and it concludes with an analysis of the optical properties engendered by noble metal nanoparticles and new research directions[2].

1.1.0 Industries, applications and potential applications

Of particular commercial interest are ‘smart’ materials that have been engineered to change in a controlled manner under the influence of external stimuli. These stimuli can include temperature, force, moisture, electric charge, magnetic fields and pH. Existing ‘smart’ materials include piezoelectric, thermoresponsive, shape memory alloys, polychromic, chromogenic and halochromic materials. The following section covers some of the many of the applications and potential applications for noble metal nanoparticles in the glass, electronics, micro-biological and chemical industries.

1.1.1 The Glass Industry

The potential applications in the glass industry are the formation of protective and durable thin film coatings with noble metal nanoparticles used to give; colour, reflectivity and solar control (thermochromic) properties which allow the transmission of light but block IR light at a specified temperature. The most common techniques in current use for applying thin film coatings on glass include conventional atmospheric pressure chemical vapour deposition (CVD) and sputtering techniques[7-9]. Noble metal nanoparticles are of great interest to the glass industry for their optical properties, not least of which is the ability to colour glass. Conventional colouring techniques on plate glass float lines are commercially expensive, the required pigment must be temperature stable and fed directly into the glass-forming mix at the furnace (1400 °C), achieving the right tone of colour on the production line takes several tonnes of glass and waiting for the pigment/dye to fade from the glass furnace mix also takes several tonnes of glass, therefore making the whole process very commercially expensive and time consuming.

1.1.2 The Electronics Industry

1.1.2.1 Semiconductors

The semiconducting industry is seeking new ways of improving the speed and miniaturisation of silicon chip technology and noble metal nanoparticles thin

films and/or nanoparticles may well provide some of the answers. Si chip makers use traditional photolithography methods *i.e.* the patterning and etching of chips with light sources shone over a mask to burn patterns into silicon wafers. This approach runs into serious problems as the current technique only achieves the 0.13-0.18 μm range. The following areas of research on noble metal nanoparticles are currently being pursued with a variety of synthesis techniques including sol-gel spin coating method[10], photochemical (UV radiation)[11, 12], sol-gel[13], multilayer electron beam evaporation[14], the double pulse electrochemical deposition method,[15] metalorganic chemical vapour deposition (MOCVD)[16, 17] and radio frequency magnetron sputtering system[18]. Particular areas of interest include the reduction of resistivity, using embedded dopants in thin films providing free connected conductive pathways, with lower electrical resistivity[7-13] of the thin film, for the enhancement of permittivity[14] (dielectric constant) for host matrices *e.g.* Al_2O_3, for the catalysts for thin films,[15] nanowires[16] and nanobridges[17], see fig. 2, and for electrical contact improvers used for controlled growth of epitaxial mismatches between metal oxide host matrix thin films, such as ZnO and Si substrates, leading to an improvement of electrical contact[18].

Figure 2: Au nanoparticle thin films catalyse the formation of epitaxial InP nanobridges. A single InP nanobridge formed between isolated Si electrodes that had a covering of gold nanoparticles, the horizontal surfaces are free of nanowires, marker = 10 μm[17]

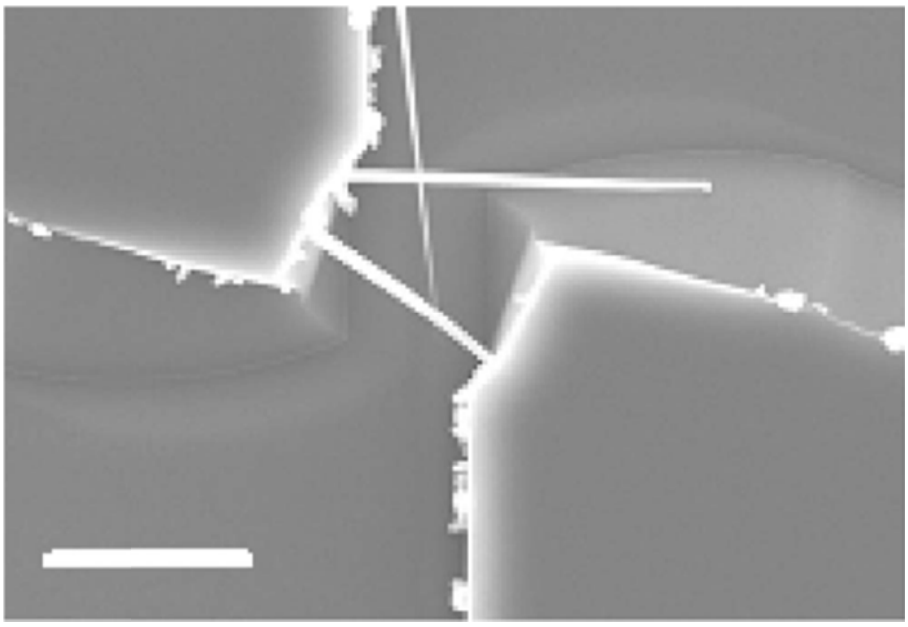

1.1.2.2 Fibre-optics

The telecommunications industry wants to improve the alignment of fibre-optic connections which will improve the efficiency of transmission. A new design for a fibre optic surface plasmon resonance (SPR) sensor was developed by Sharma and Gupta *via* a semiconductor core-shell nano-composite layer (ZnO, PbS, CdSe, CdS)[19], see fig. 3. The three main advantages of using noble metal nanoparticles (Au, Ag) are faster response than conventional fibre optic sensors with better resolution due to the 2-5 μm scale of the surface plasmon wave propagation and simultaneous exhibited localized SPR shifts with surface enhanced Raman Scattering (SERS).

Figure 3: A fibre optic sensor with core-shell metal-semiconductor nanocomposite layer: surface plasmon wave (SPW) exists at the interface of the metal-semiconductor nanocomposite layer and the adjacent sensing layer[19].

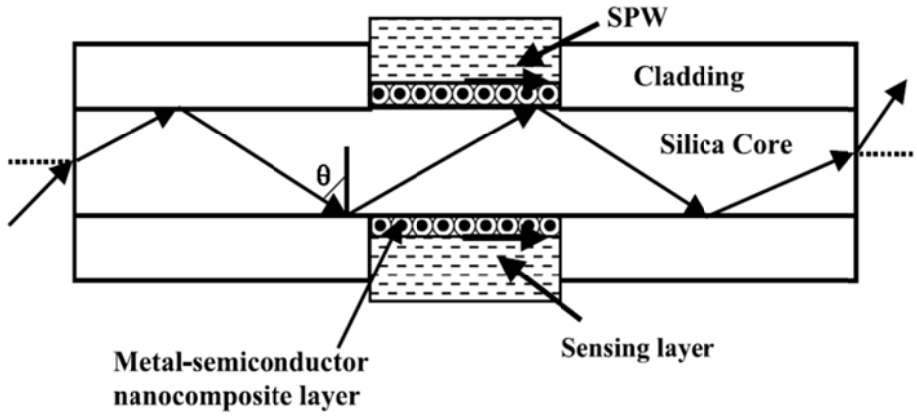

1.1.3 Bio-industries

The main emphases for the Bio-industries are diagnostic tools, sensing and imaging techniques, quantum dots and antimicrobial/antibacterial/antifungal actions of noble metal nanoparticles.

1.1.3.1 Antimicrobial/Antibacterial/Antifungal

The antibacterial properties of silver[20, 21], in particular, are one of the main emphases of research for noble metal nanoparticles. For example the Hyosung Corporation, South Korea, have infused silver nanoparticles into the Mipan Nano-Magic fibre material, preventing infections such as athletes foot, other pneumobacilli infections, colon bacilli infections and fungi infections by at least

99.9%. Copper oxide nanoparticles (mean size 20–50 nm) are currently produced by Nanophase Technologies Corporation for industrial applications including long acting antimicrobial and antifungal agents for incorporation into polymer products for various applications *e.g.* wood preservation, marine antifouling coatings, optical glass polishing agents, ceramics, colours and pigments.

1.1.3.2 Diagnostic Tools

The optical properties of noble metal nanoparticles open up vast opportunities for sensing and imaging techniques, particularly for Au, *in vivo*, as this is essentially non-cytotoxic. Some examples are given below.

1.1.3.2.1 Immunoassay Techniques

The Carter Wallace home pregnancy testing kit product 'First Response' uses a thin film of gold nanoparticles and latex nanoparticles within an external disposable test sheet. Au nanoparticles of different sizes reflect light differently and a specific hormone present during pregnancy causes the nanoparticles to clump together, the bigger gold nanoparticles reflect a distinctive pink colour for a positive test. Gold is also of interest as a possible reagentless electrochemical immunoassay technique[22].

1.1.3.2.2 Quantum dots and noble metal nanodots

Research in this area for new innovative products that enhance biological imaging for medical diagnostics and drug discovery is very active. Quantum dots are semiconductors that emit a vast spectrum of bright colours, when irradiated that can be used to identify cells, locate cells and other biological activities. These nanoparticle QD's offer optical detection up to a thousand times brighter than conventional dyes currently used in the majority of biological tests and render significantly more information and are significantly more resistant to photobleaching. Recent research, by Zheng *et al.* has produced nearly spectrally pure highly fluorescent water soluble gold nanoparticles termed as 'nanodots', with discrete size tunable electronic transitions from the visible to near infrared region, opening the way for new biological labels, energy transfer pairs and light emitting sources in optoelectronics[23], see fig. 4. The

researchers produced size-tunable gold nanodots through a slow reduction of gold salts ($HAuCl_4$ or $AuBr_3$) within aqueous polyamidoamine (PAMAM) solutions, followed by centrifugation to remove large nanoparticles. The fluorescence is comparable to semiconductor quantum dots but with a narrower range excitation spectra. The gold nanodots showed discrete excitation spectra from the ultraviolet to the infrared, dependent upon the number of Au atoms present in the nanocluster, increasing size increases wavelength. The Au nanoclusters behave as multielectron artificial atoms in line with the Jellium model of free electrons rather than single electron artificial atoms like semiconductor QD's. The Jellium model is essentially the Drude free electron model and contains the same assumptions. The plasmon oscillations are thought to be responsible for this behaviour and current research is being carried out to functionalize the Au QD's to cross cell membranes and label specific proteins particularly cancerous cells.

Figure 4: Excitation/emission spectra of different Au nanoparticles: a) Excitation (dashed line) and Emission Spectra (solid line) of different sized Au nanoparticles, b) Emission from the 3 shortest wavelength nanocluster solutions under irradiation with a 366 nm laser.[23]

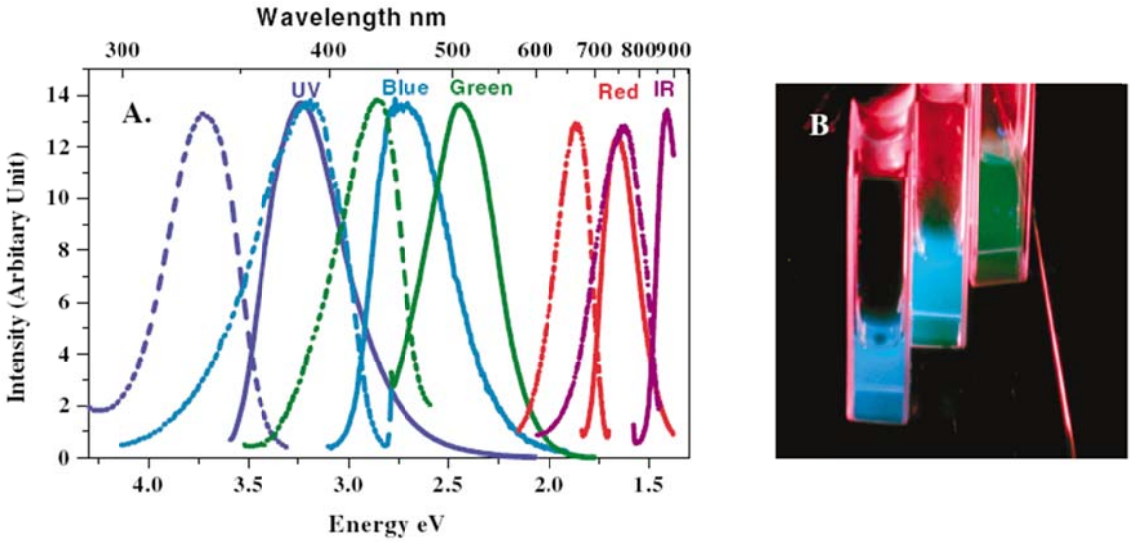

1.1.4 The Chemical Industry

The chemical industries main focus for using noble metal nanoparticles has been in catalysts, gas/vapour sensing detectors, protective equipment and clothing.

1.1.4.1 Catalysis, protective equipment and clothing

Recent research developed by the National Taiwan University transformed CO into CO_2 at 25 °C by using Au-Ag bimetallic nanoparticles supported by mesoporous silica (diameter 2-6 nm) with the potential of incorporating the technology into safety masks and possibly the improvement of fuel cells and photovoltaics[24]. Nanoparticles are used increasingly in catalysis, where the large surface area per unit volume of nanoparticle catalyst may, depending on structure sensitivity, enhance reactions. The enhanced reactivity of these smaller nanoparticles significantly reduces the quantity of catalytic materials required to carry out the necessary reaction. Particular industries interested in his area of research include the oil industry, for refining petroleum and the automobile industry for nanoparticles in catalytic converters. New applications for gold nanoparticle catalysts in particular are being explored in an array of new areas including the removal of smells and poisonous gases, *e.g.* carbon monoxide from rooms and or factories *e.g.* air cleaning[25], also in pollution control in fuel cells[26] , in the production of bulk chemicals[27] and the detection of heavy metals such as mercury in water[28].

Companies such as BASF, Johnson Matthey and 3M have interests in developing commercial applications for gold nanoparticle catalysts. Noble metal nanoparticle catalysts have been investigated for both homogeneous and heterogeneous catalysis. Recent research has shown that the shape and crystal structure of the nanoparticle leads to different catalytic rates for homogeneous catalysis with nanoparticles with more corners and edges having higher catalytic rates[29]. Mixed composites of Cu and ZnO are widely used as a catalyst for the large scale industrial production of methanol and oxidation of carbon monoxide; recent work by M. Shahid *et al.* on the use of single molecular precursors for the deposition of Cu–ZnO composite thin films at different temperatures, using aerosol assisted vapour deposition (AACVD), showed uniform distribution of cubic metallic Cu and hexagonal ZnO phases and could be used for nanocatalysis on a structured surface[30].

1.1.4.2 Gas/vapour sensing detectors

Yang *et al.* have developed an ordered thin monolayer of silver nanowire explosives detector[31]. The tightly packed layer of ordered silver needles make an ideal chemical binding site and a very sensitive substrate for detecting such chemicals as 2, 4-dinitrotoluene (2, 4-DNT), commonly used in land mines and given off as vapour and detected by surface-enhanced Raman spectroscopy. The thin ordered flexible monolayer of silver nanowires could also be applied to surfaces such as glass, flexible plastic polymers and silicon for incorporation into various applications including flexible solar cells and light emitting diodes. Further research by this group includes using the Langmuir-Blodgett[32-36] assembly technique of floating nanowires on top of a liquid, followed by alignment and clumping together through tight compression; monolayers up to 20 cm^2 were formed with individual diameters up to 50 nm across, pentagonal cross-section with pyramidal tips.

1.1.4.3 Summary of industries, applications and potential applications

The applications and potential applications of noble metal nanoparticle thin films or monolayers are enormous from detecting cancerous cells with new non-toxic Au nanoparticles to highly reflective coatings for the glass industry and potential solar control through 'smart' domestic windows. Many industries are focussed on overcoming the technical difficulties ahead, especially synthetic control of morphology, size, shape, distribution and new products from noble metal thin film nanotechnology will likely become commonplace. One particularly noteworthy new direction is the ability to use gold and Fe-doped gold nanoparticles for use in magnetic hyperthermia and localised laser heating[36]. These methods are being investigated for the destruction of bacteria and cancer cells. The process uses the fact that small gold and Fe-doped gold nanoparticles are magnetic and can be heated by an external alternating field or that the gold particle acts as a hot spot for localised laser heating. Such particles and films offer new hope of a new method to fight cancer or septicaemia.

1.2.0 Synthetic routes and techniques

There are two main methods for depositing nanoparticle thin films: the 'top down' method and the 'bottom up' method. The first suffers from the disadvantage of requiring large amounts of material to be removed from a bulk material to leave the nanostructures *e.g.* photolithography, electron beam lithography and the second requires assembly of nanoparticles from the production of reduced ions *e.g.* nanosphere lithography, which suffers from poor monodispersity, due to the need to arrest growth to control the size and distribution of nanoparticles. The synthesis of thin films incorporating noble metal nanoparticles thin film can be split into two parts, the synthesis of the nanoparticles and the synthesis of the thin film. The first part of this section, 1.2.1, addresses the methods of nanoparticle synthesis with some recent developments. The second part of the synthesis section, 1.3.2, examines seven thin film synthetic routes and includes examples of each type of route, some well known techniques such as dip coating, aerosol assisted chemical vapour deposition, sol-gel, magnetron sputtering and some newer types of film synthesis including a two-step laser assisted deposition process onto plastics.

1.2.1 Synthesis of noble metal nanoparticles

The difficulty in synthesising the desired morphology, shape, size, monodispersion and distribution size of noble metal nanoparticles for use in thin films has created many and varied routes, some of which are discussed below. Various mechanisms exist for trying to arrest growth of the nanoparticles for selective size distribution and shape, the main ones being the use of surfactants/ionic salts to solvate, the use of capping agents *e.g.* thiols and altering the alkyl chain lengths on both metal precursors and surfactants/capping agents. The main synthesis routes to nanoparticles for thin film synthesis include the citrate reduction method and the Brust-Schriffin two-phase redox method; both methods have had recent improvements and variations investigated. Other methods include sonolysis, ultrasound, microwave, laser ablation method, micelles and a future possibly environmentally friendly alternative of microbial synthesis of nanoparticles.

1.2.1.1 Citrate reduction method

A standard conventional method of producing Au nanoparticles is the citrate reduction of $HAuCl_4$ in water, which was introduced by Turkevitch *et al.* in 1951 for forming Au nanoparticle size of *ca.* 20 nm size[37]. A more controlled and refined synthesis by Frens in 1973 who varied the ratio of reducing/stabilizing agents (trisodium citrate to gold ratio) to obtain some control of nanoparticle size (15 to 150 nm)[38]. Both methods produce almost spherical particles over a tunable range of sizes. Recent work has demonstrated the strong influence of reactant concentrations, temperature and pH on the morphology of the nanoparticles and that the reduction can be initiated at room temperature by UV exposure and the use of variant reductants such as amino acids, ascorbic acid and sodium ascorbate[39]. Reduction in the thermal citrate reaction temperature tends to increase the size and quality of the nanoparticles creating larger particles. Passivation of the nanoparticles, in particular gold particles, by a high citrate concentration appears to keep particle size small whilst lower citrate concentrations leads to incomplete coverage of the particles allowing aggregation and larger entities to form.

1.2.1.2 The Brust or Brust-Schiffrin method

The Brust method offers a simple two-phase redox synthesis route to thermally and air stable gold nanoparticles with controlled size (1.5-5.2 nm), reduced dispersion and easy repeatable synthesis[40]. This method has the advantage of isolation and extraction into common organic solvents with no increase in decomposition or aggregation. In a typical example $AuCl_4^-$ was phase transferred using tetraoctylammonium bromide phase reagent from aqueous solvent to an organic solvent and reduced with sodium borohydride (aq) the source of electrons.

1.2.1.3 The sonolysis method

The advantages of the sonolysis method are rapid reaction rate and the ability to form very small nanoparticles; however the disadvantages are that metal nanoparticles generally have a wide distribution size. The ultrasound irradiation method has been used to produce colloidal suspensions of Au nanoparticles with different sizes and shapes[41]. The morphology and size distribution were

found to be dependent upon the molar concentration of hydrogen tetrachloroaurate and the anionic surfactant, sodium dodecylsulfate, [$HauCl_4$/[SDS]. Higher concentrations of the anionic surfactant, (2.5 mmol dm^{-3}) and high ultrasonic irradiation power (90 W) lead to uniform spherical nanoparticles, size 10-20 nm. Lower concentrations of the anionic surfactant and irradiation power lead to nanoparticles with different shapes and forms *e.g.* rod, triangle and disk, with greater coagulation/agglomeration[41].

1.2.1.4 The laser ablation method

Laser ablation is a simple and rapid technique in that it allows some control over concentration, size and aggregation of nanoparticles. The advantages of this method are that there is no necessity for removal of excess reagents, *e.g.* surfactants, ions, also of interest and use is the possibility of Au nanoparticle synthesis in both aqueous/organic solvents and the possibility of obtaining nanoparticle polymer/ sol-gel matrices inclusions[42]. Recent work by Amendola *et al.* has shown that it is possible to obtain stable and free Au nanoparticles in a one step process with solvents such as dimethylsulfoxide (DMSO), tetrahydrofuran (THF) and acetonitrile (CH_3CN)[42]. The laser ablation was obtained with Nd: YAG (Quantel YG981E) laser pulses (1064 nm, 9 ns) on a gold plate on the bottom of a solvent/solution containing cell. Laser ablation produced a reduction in particle size and change in morphology due to what is believed to be photothermal effects. The second harmonic of the Nd.YAG laser (532 nm, fluences 1-5 Jcm^{-2}, 1Hz, 5-10 mins) produced a reduction in size and morphological changes of the nanoparticles in DMSO, THF and CH_3CN[42]. Therefore rapid synthesis of Au nanoparticles in organic solvents was achieved in minutes and the solutions were found to be stable (hours-weeks) with the size distribution influenced by the laser irradiation.

1.2.1.5 The microwave method

The microwave (MW) technique normally involves one pot synthesis of nanoparticles in solution with metal salts and polymer surfactants using MW irradiation. Various MW techniques have been used including continuous wave (CW) pulsed and variable frequency (VF). MW dielectric heating leads to two types of effects thermal and non-thermal. For thermal effects the heating is uniform, rapid and homogeneous, therefore leading to uniform growth,

nucleation, crystallinity and small size of nanoparticles. The advantages of the MW method are quick, easy manufacture of nanoparticles with high selectivity of size and shape with narrower distributions and less aggregation than conventional methods. Au, Ag, Cu, Pt, Pd and AuPd nanoparticles have been produced using MW irradiation[43-47]. The morphology, size and shape *e.g.* spherical, triangular plates, sheets, rods, wires, tubes and dendrites of nanoparticles have been controlled by altering the parameters of concentration of the precursors and reagents usually including metal salts, solvents, ionic salts, surfactants and/or capping agents. The length of carbon chain for both surfactants and precursors has been found to have a significant effect on morphology of nanoparticles[43-47].

Table 1: Typical reagents used in Au MW nanoparticle synthesis

Metal Salts	$HAuCl_4$
Solvents	Water
	Alcohols- ethanol, methanol
	N,N-Dimethylformamide (DMF)
	Ethylene glycol (EG)
	N-methyl pyrrolidone (NMP)
Surfactants	Polyvinylpyrrolidone (PVP)
	Tetradecylammoniumbromide (TDAB)
Capping agents	PVP
	Vitamin B_2
	Sugars – α-D glucose, maltose, sucrose
Ionic Salts	TOAB
Reducing Agents	Sugars – α-D glucose, maltose, sucrose
	Vitamin B_2

Table 2: Typical reagents used in Ag MW nanoparticle synthesis

Metal Salts	$AgNO_3$
Solvents	Alcohols- ethanol, pentanol, hexanol, heptanol, octanol
	N,N-Dimethylformamide (DMF)
	Ethylene glycol (EG)
	N-methyl pyrrolidone (NMP)
	Pyridine
Surfactants	Polyvinylpyrrolidone (PVP)
Capping agents	PVP

	Vitamin B_2
	Sodium citrate, $Na_3C_6H_5O_7$
	Dodecylthiol (thiol)
Ionic Salts	$Na_3C_6H_5O_7$
Reducing Agents	Sugars – α-D glucose, maltose, sucrose
	Vitamin B2
	$Na_3C_6H_5O_7$

Table 3: Typical reagents used in Cu MW nanoparticle synthesis

Metal Salts	Copper (II) octanoate
	Copper (II) myristate
	$Cu(NO_3)_2$
Solvents	Alcohols- ethanol, pentanol, hexanol, heptanol, octanol
	N,N-Dimethylformamide (DMF)
	Ethylene glycol (EG)
	N-methyl pyrrolidone (NMP)
	Pyridine
Surfactants	Polyvinylpyrrolidone (PVP)
Capping agents	PVP
Ionic Salts	Cetrytrimethylammonium bromide (CTAB)
Reducing Agents	Carbon

The influence of the size of the alkyl chain on Ag precursor fatty acid salts has been shown to increase nanoparticle size with increasing alkyl chain length[48], this general trend appears to breakdown slightly once the length of chain reaches a critical size ($CH_3(CH_2)_nCOOAg$, ≥ n =16)[48]. The influence of the length of alkyl chain on the copper metal precursor has been shown to alter the size of the nanoparticle in alcohol solvents, the alcohol reduction process ($Cu^{2+} \rightarrow Cu^0$) and therefore the surface plasmon absorption: the longer the alkyl chain on the nanoparticle precursor the smaller the nanoparticle[46]. The length of alkyl chain on the solvent was found to have no effect on nanoparticle morphology[46], see table 4:

Table 4: Comparison of Alkyl Chain Length on Precursors with Plasmon Band Absorption.

Particle Size/nm	**Chain length on Metal Precursor/ no. of atoms**	**Chain length on Ionic Salt**	**Plasmon band Absorption/nm**
2-3	13 atoms	-	400
5-6	7 atoms	-	596

Continuous wave, (CW), MW heating (400 W) have been found to generate Au polygonal plates from a solution of $HAuCl_4$, polyvinyl pyrrolidinone, (PVP) and ethylene glycol (EG)[43] , see fig. 5. For microwave synthesis of Au, Ag and Cu (tables 1-3) nanoparticle morphology, size, shape and distribution of size depend upon molar ratio/concentration of the precursors and the length of alkyl chains attached to the metal precursor or the surfactant/ionic salt/capping agent[43-48].

Figure 5: TEM Au nanoparticles: Obtained by continuous wave microwave heating for 2 min of an auric acid, polyvinyl pyrrolidone and ethylene glycol solution. Right: percentage distribution from the microwave synthesis (2 min)[43].

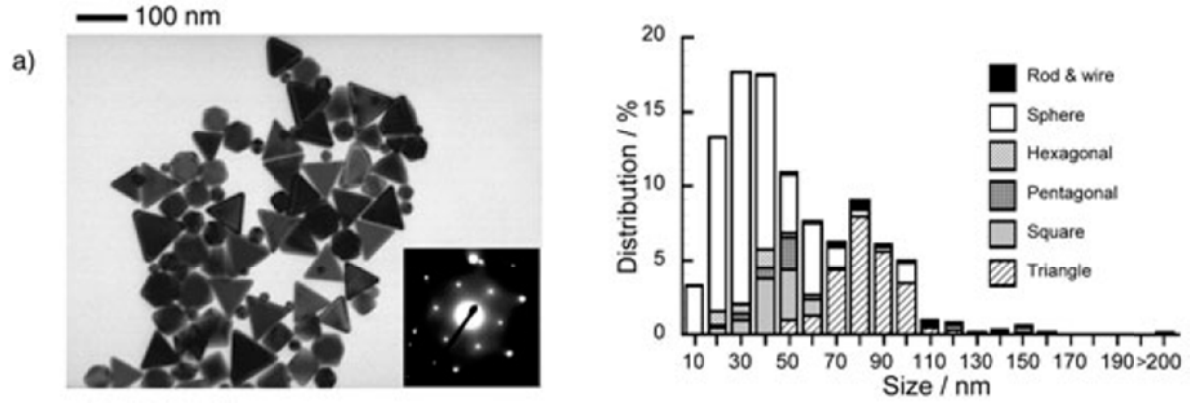

1.2.1.6 Micelle synthesis

Micelle synthesis involves an aggregate of surfactant molecules dispersed in a colloidal liquid usually with a hydrophilic head in contact with the polar solvent and the hydrophobic tail sequestered by the micelle centre[49]. Micelles are generally spherical although ellipsoids, cylinders and bilayers are known. The molecular geometry of the surfactant and solution conditions *e.g.* surfactant concentration, temperature, pH, ionic strength influences the morphology, size, shape, size distribution and monodispersity of the synthesised micelles. Surfactants in excess, *i.e.* at critical micelle concentration, can act as

emulsifiers *e.g.* detergents[50]. Inverse micelle synthesis involves the use of surfactants with a polar group at one end and an organic group at the other to generate small pockets of a water phase in an organic solvent, in which the respective groups face the appropriate water/organic phase[50-52]. Addition of different water volumes linearly affects the size of the micelle generated. Prior to the addition of the reducing agent the metal salt precursor must be added to the surfactant, this ensures a good monodispersity is achieved. Reverse micelle synthesis occurs in non-polar solvents where exposure of the hydrophilic heads to the solvent is energetically unfavourable. The hydrophilic groups therefore surround the micelle core and the hydrophobic heads remain in contact with the non-polar solvent. Recent research includes the synthesis Au nanoparticles using sodium *bis*-(2-ethylhexyl) sulfoccinate (AOT), isooctane as the templating system for producing Au nanoparticles using sulfite as the reducing agent[53]. Good correlation of the surface plasmon peak was found between Mie theory and Au size (commercial gold colloids: 5-10 nm/aq) for the reverse micelles[53].

1.2.1.7 The microbial method

The advantages of a microbial synthesis are a reduction in costs for the reducing agents and energy for forming Au nanoparticles. The main drawback to the use of intracellular or extracellular synthesis is the very slow reduction of aqueous $AuCl_4$ taking typically between 2 and 30 days[54, 55]. Metal reducing bacterial agents have a much faster rate of gold nanoparticle precipitation, typically 30 mins at pH 7 from 1 mM $HAuCl_4$ (aq)[56]. Recent work by Konishi *et al.* has used metal reducing bacteria *S. algae* to precipitate gold nanoparticles within 30 mins at pH 1 extracellularly and pH 7 intracellularly[57], see fig. 6. The pH of the solution had a major influence on the size of the Au nanoparticle: the lower the pH the bigger the particle size. The Au nanoparticles at pH 1 were typically 50-500 nm, some were polyhedral in shape and crystalline; gold particles prepared at pH 7 were typically smaller (5-15 nm) than those prepared at pH 1[57]. The microbial technique is still very much in a development stage but could offer a possible unique industrial method with interesting nanoparticle properties including size and shape.

Figure 6: TEM of Au nanoparticles: incorporated both intra- and extra-cellular from S. algae at a) pH 7, b) pH 2, c) pH 1[57].

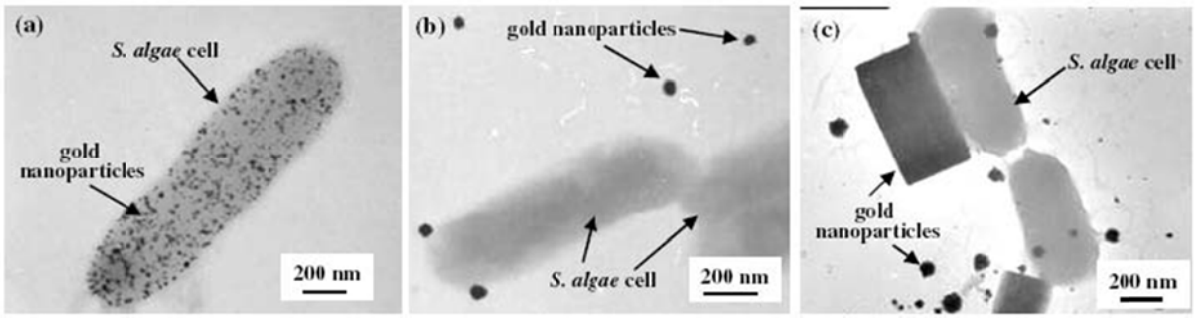

1.2.1.8 Summary of nanoparticle synthesis

The synthesis of Noble metal particles as precursors/reagents for thin film deposition has traditionally evolved from either the citrate method or the two step redox method; if the shape of noble metal nanoparticles becomes an important factor for determining the property of a thin film then synthesis by other methods may well replace traditional methods enabling the mass production of nanoparticles of homogenous shape and size.

1.2.2 Synthesis of thin films incorporating nanoparticles

The synthesis of thin films onto various matrices, e.g. SiO_2, TiO_2, Al_3O_2, ZnO, ITO, ZrO_2 and base substrates such as silica glass, metals and plastics are many and varied. Five main deposition routes are known as summarised in fig. 7, scheme 1.

Figure 7: Scheme 1: Methods of making thin films with embedded nanoparticles.

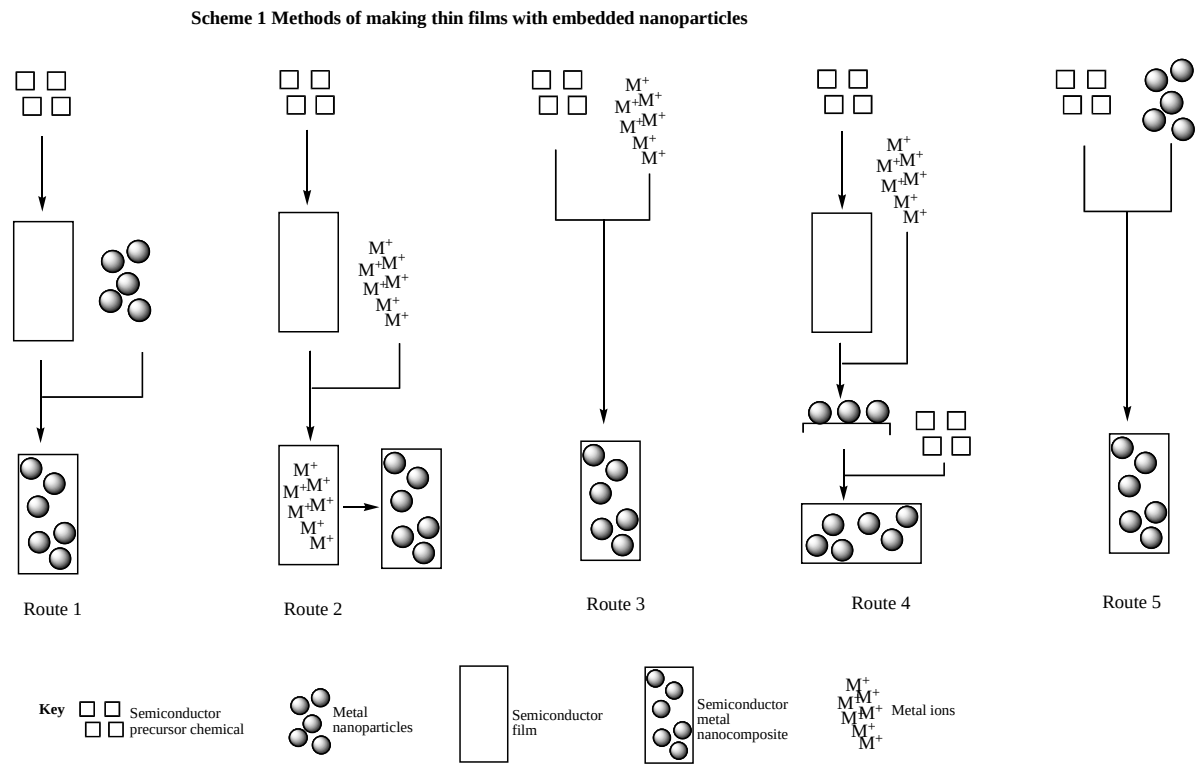

The *first route* involves synthesis of a host matrix with the addition of nanoparticles in a second step. Example techniques include spin coating and dip coating a semiconductor film combined with a nanoparticle solution. Work by Yang *et al.* demonstrated the typical use of the spin-coating (500-3000 rpm, in air, 10-20% relative humidity at 25 °C) method to form highly ordered silica host matrix thin films (30-300 nm) with adorned gold nanoparticles from precursor solutions and silica wafers in conjunction with post treatment curing (vacuum, 180 °C, 5 hrs) or UV irradiation (2 hrs)[58].

The synthesis of a host matrix followed by the application of metal ions in a second step, forming metal particles within the film is a *second route* to nanoparticle host matrix thin films. Example techniques include high-energy ion implantation and spin coating with a metal solution followed by either photocatalytic reduction or heat treatment[59]. Recent work by Kao *et al*. used the spin coat method, (500 rpm for 10 s, 2000 rpm for 15 s) to apply Au nanoparticles suspended in toluene to Cu, Ni and Al foil substrates and then cured (IR) in a protected atmosphere (90 % N_2 - 10 % H_2)[60]. Surface coverage on Cu substrate was continuous but coverage on Ni and Al substrates was intermittent and particularly pronounced with the Al substrate, at lower curing temperatures (200-250 °C). Coverage on the Cu and Ni substrate improved at

higher curing temperatures (300 °C). The fractal like structure of the Au layer on the Al substrate was indicative of oxidation demonstrating aluminium's unsuitability as a substrate for Au nanoparticles. The topography of the films was coarser at lower temperatures. Temperature of the curing process affects adhesion, morphology and coating coverage, higher temperatures improve adhesion, coating coverage and tended to flatten the surface topography.

The synthesis of a host matrix and metal nanoparticles in a single step is a *third route* to nanoparticle host matrix thin films. Example techniques include sol-gel using both semiconductor and nanoparticle precursor, liquid-phase deposition (LPD), multitarget magnetron sputtering deposition and other techniques including chemical vapour deposition (CVD) using separate precursors. Recent research has looked at the incorporation of Cu nanoparticles into amorphous silica films and monolithic glasses[61], Ag nanoparticles into Al doped ZnO thin films[62] and Au nanoparticles into ZrO_2 thin films[63]. The incorporation of Ag nanoparticles into aluminium doped ZnO were found to enhance the crystallization of the Al doped ZnO phase, providing an interconnecting pathway for the reduction of electrical resistivity[62]. Au nanoparticles have also been incorporated into ZrO_2 thin films, upon annealing these Au-ZrO_2 thin films display a red shift in SPR due to size increase of Au nanoparticles size and a blue shift in SPR with increased Au content[63]. The liquid phase deposition method can be used to deposit composite nanoparticle thin films at low temperatures (30-50 °C) from an aqueous solution giving the ability to coat sensitive substrates such as plastics. Ko *et al*. used the LPD technique to incorporate Au nanoparticles into layered thin films of SiO_2/TiO_2[64]. Transmission electron microscopy (TEM) revealed that the Au nanoparticles were found in both layers with migration of nanoparticles after annealing (500 °C) to the more crystalline anatase TiO_2 matrix. Magnetron sputtering is a physical process that involves the removal of atomised material from a solid due to energetic bombardment of the surface layers by ions or neutral particles that then deposit onto a substrate[65]. Recent work by Liao *et al*. used the multitarget magnetron sputtering technique (600-700 °C), to embed, sandwich and multilayer Au nanoparticles in different oxide composite films of ZnO, TiO_2 and SiO_2[66]. Upon thermal annealing, the multilayer films for Au: SiO_2, (950 °C for 2

hrs) remained intact, while the microstructure broke down for both Au: ZnO and Au: TiO_2 thin films, (700 °C for 2 hrs).

The synthesis of layer-by-layer deposition of metal nanoparticles and a host matrix material are a *fourth* synthetic route to thin films. Example techniques include laser ablation and pulsed laser deposition (PLD). PLD is a technique that involves hitting a target precursor solid surface, in a vacuum, with a high pulsed laser creating a plume of aerosol particles that are ejected onto an opposing surface with the stoichiometry of the surface material kept intact. Recent work has involved incorporation of Au nanoparticles into SiO_2/TiO_2 host matrices[67, 68] and Ag and Au nanoparticles incorporated into amorphous ZrO_2 host matrix, with XRD and TEM techniques used to analyse distribution patterns, interface with the host matrix and mean size[69]. Serna *et al.* investigated the optical response of Cu nanoparticles embedded in an amorphous Al_2O_3 host matrix for reactive processes. The plasmon resonance band was found to shift with increasing or decreasing laser fluences, increasing laser fluences was found to increase the degree of change from the simple metallic Cu nanoparticle form to the sputtered Cu-Al oxide covered Cu nanoparticles form[70].

The synthesis of the semiconductor matrix and metal nanoparticles concurrently is a *fifth* route. Example techniques include aerosol assisted chemical vapour deposition (AACVD) and injected jet assisted modified chemical vapour deposition. AACVD involves the generation of multi-component particles for deposition from a gaseous plasma of precursors in liquid solution transported by gas, *e.g.* N_2. The main advantages are the capability of depositing a uniform thin film onto a heated substrate with noble metal nanoparticles in a single step. The main problem with AACVD is that deposition also occurs on surfaces above a horizontally laid substrate currently thought to be due to thermophoretic effects[71]. Another advantage of AACVD is the transport of precursors that are not easily volatised by conventional CVD methods. Recent research by Palgrave *et al.* includes AACVD co-deposition of Au nanoparticles and semiconductor host matrices tungsten oxide, WO_3, (precursor: $[W(OPh_6)]$) and titania oxide, TiO_2, (precursor: $[Ti(O^iPr)_4]$) onto silica glass to form nanocomposite thin films[72]. Three properties are of interest for the anatase titania/Au thin films, reflection of IR/near IR, the further red shift in the SPR

upon annealing and the transmission of visible light, making the titania/Au thin film a potential solar control coating on glass. The control of morphology of TiO_2 thin films by AACVD has been investigated to produce various shaped TiO_2 crystals including dendritic crystals for the potential use in optoelectronic devices such as photovoltaic cells[73]. Control of the dendritic crystals, see fig. 8, was achieved through variation of the homogenous gas phase reaction in combination with the aerosol droplet liquid phase reactions[73]. Further modification of this technique has been carried out by Hong *et al*. using an injected jet assisted modified CVD (MCVD) system to apply a thin film to optical fibres[74]. An electrically heated thin tube was placed in a radial direction inside a conventional modified CVD silica tube. The injected gas enhanced deposition efficiency and uniformity of the composition of the multi-component thin film independent of the type of gas used in the jet.

Figure 8: SEM images on TEM grid: a) SEM of nanoparticles on TEM grid, b) SEM of dendritic structure, c) TEM image of dendritic structure, insert SAED pattern[73].

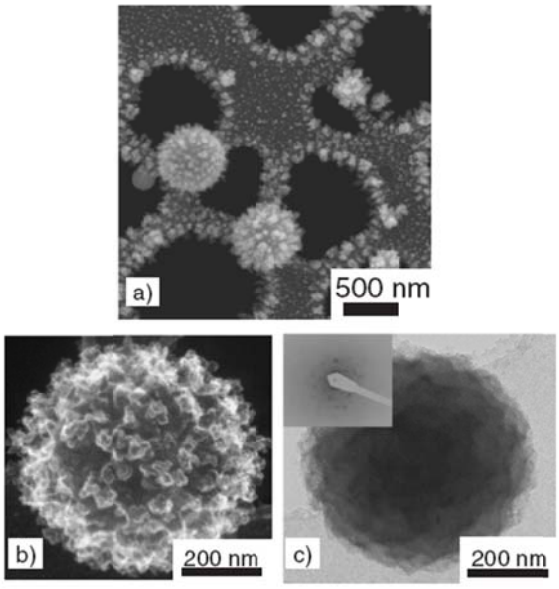

Thin film synthesis onto plastic substrates using a two-step process is a *sixth* example of forming nanoparticle incorporated thin films. The synthesis of a polycrystalline matrix with addition of nanoparticle precursors in the second step using lasers, example techniques include aqueous dispersion of nanoparticles with laser nanoforming. Polycrystalline films were deposited using a Nd: YAG (1064 nm) laser on plastic substrates in air and argon using silicon nanoparticle precursors at ambient temperatures[75]. The main advantage of this technique is the localised heating of nanoparticles without affecting the thermally challenged

substrate, opening up the possibility of high quality flexible microelectronics with Si films on plastic substrates.

1.2.2.1 Summary of thin film deposition routes

Thin film deposition routes onto any substrate follow two main pathways: type one, one pot synthesis where all components are put onto the substrate at the same time *e.g.* host matrix and the nanoparticle precursor; and type two, two step synthesis, host matrix laid on the substrate first followed by the nanoparticle reagent or *vice versa*.

1.3.0 Properties of noble metal nanoparticles incorporated into thin films

The main properties of interest for Au, Ag and Cu nanoparticle composite thin films include linear and non-linear optical, magnetic, conductivity, catalysis, antimicrobial and electrochromic properties. The theoretical principles that describe the nanoparticle matrix interaction are covered by Mie,[76] Maxwell-Garnett[76] and Drude[76, 77] models. The main emphases of this chapter are the optical main properties, such as photoluminescence, photochromic effects and colour. The refractive index and dielectric constant of the host matrix also play a major part in the properties of these thin films. The properties of nanoparticles are either due to the symmetry at the interface or to electron confinement that does not scale linearly with size. Therefore the properties of nanoparticle collections of atoms/molecules are neither those of the bulk properties or the individual atom/molecule properties but new properties that are dependent on size and structure instead of the nature of the element/compound. Nearly all the nanoparticles within a composite thin film are located on the surface or just below the surface, one layer below but are occasionally found deeply embedded in the interior. Au and Ag nanostructures have absorptions across most of the visible region in contrast to semiconductor nanoparticles that have emission spectra across most of the visible region. The new properties exist for noble metal nanoparticles due to electronic confinement of the semi-conducting host matrix and surface effects in the metals.

1.3.1 Optical properties

1.3.1.1 Theoretical principles

Thin films containing small noble metal nanoparticles show absorption due to surface plasmon resonance (SPR) effects resulting in linear and non-linear optical properties. Explanations for the optical properties of small (1 nm) noble metal nanoparticles have been put forward including the following deductions by Doremus *et al*. that the radii of noble metal particles become smaller than the mean free path of electrons the plasma band broadens, for very small particles (<1 nm) the absorption band disappears completely[77]. The reduction in mean free path causes a reduction in effective optical conductivity of a spherical particle increasing ε_2 (complex dielectric constant $\varepsilon^* = \varepsilon_1 - i\varepsilon_2$ of the particles) which is inversely proportional to conductivity in the Drude model for free electrons, see eqn (1).

Equation 1

$$\varepsilon_2 = A\lambda^3 + B$$

Where λ = wavelength of light for free electrons, A = inverse of the mean free path of electrons; B = a correction constant

For noble metal nanoparticles embedded in glass the optical absorption reciprocal λ^4 dependence of absorption, see eqn. 2.

Equation 2

$$\alpha = \frac{18\pi Q n^3 \varepsilon_2/\lambda}{(\varepsilon_1 + 2n^2)^2 + \varepsilon_2^{\,2}}$$

Where α = optical absorption, Q = volume fraction, n = refractive index of the host medium.

Using the Drude model ε_2 is too large when compared to experimental results, the probable explanation being the effect of surface defects of the noble metal nanoparticle skin[77]. Therefore for very small noble metal nanoparticles (1 nm) where the denominator $\varepsilon_2^2 >> (\varepsilon_1 + 2n^2)^2$ then equation (2) becomes, see eqn. 3.

Equation 3

$$D = \frac{18\pi Q n^3}{\varepsilon_2 \lambda}$$

Therefore small noble metal nanoparticles (1 nm) appear to have electronic/characteristic properties of free electrons rather than the atomic band to band/level to level transitions. Quantum size effects do predominant for smaller particles (< 2 nm). The surface plasmon band (SPB) is a property observed in transmission, due to the nanoparticles in either solution or in the solid phase *i.e.* thin films, and has a strong absorbance in the UV-Visible spectrum, *e.g.* one macroscopic property is colour, for metallic noble nanoparticles normally >2 nm, this is referred to as the Mie resonance. The resonance of conducting electrons from the nanoparticles results in the interaction with incident light and the scattering of it. Mie originally solved the Maxwell Garnett equations for small spheres interacting with an electromagnetic field, Gan then extended this to geometries of ellipses[76]. Optical properties like the surface plasmon resonance of noble metal nanoparticles can be related through particle size to Mie theory, see eqn. 4. It should be noted that Mie theory predicts a unique resonance frequency that is not size dependent. The surface plasmon band of alkali metals tend to be red shifted and that of Au and Ag blue shifted based on Mie theory and the relative effective shielding of the valence electrons from the metal nuclei.

Equation 4

$$C_{\text{ext}} = \frac{24\pi^2 R^3 \varepsilon_{\text{m}}^{3/2}}{\lambda} \frac{\varepsilon_2}{(\varepsilon_1 + 2\varepsilon_{\text{m}})^2 + \varepsilon_2^2}$$

Where C_{ext} = Mie extinction cross section, ε_m = the dielectric constant of the surrounding media, $\varepsilon = \varepsilon_1 + \varepsilon_2$ = complex dielectric constant of the particle. The resonance peak occurs whenever the condition of $\varepsilon_1 = -2\varepsilon_m$

Modern methods use the discrete dipole approximation (DDA) which allows arbitrary calculations of the surface plasmon resonance absorption[78-81] *e.g.* for nanorods that have been shown to have two plasmon resonances, one due to the transverse oscillation of the electrons (Au: 520 nm) and one due to the

longitudinal plasmon resonances at longer wavelengths. Longitudinal calculations involve increasing the wavelength and intensity maximum *i.e.* the aspect ratio (increase length/width); the transverse plasmon resonance does not depend on the aspect ratio and behaves very much like the surface plasmon resonance of a sphere. This allows the tuning of the SPR by alteration of the aspect ratio.

1.3.2 Quantum confinement in semiconductor host matrices

Quantum confinement of the electrons in the semi-conducting host matrix is important; as the particle size decreases below the Bohr radius the electron becomes more confined within the particle, leading to an increase in the band gap energy, and the valence and conduction bands become quantized. The band gap emission for CdSe is known to shift from red emission, for large particles, to a blue emission for small particles[82]. Size controls the colour of the nanoparticles, therefore control over nucleation and growth of the semi-conducting nanoparticle is important.

1.3.3 The dielectric constant

The intensity and position of the SPB depends upon the dielectric constant of the surrounding medium and the electronic interaction between nanoparticles and stabilising ligands. The size, morphology, electron density of particles and dispersion of the nanoparticles (*e.g.* the extent of aggregation) depend upon the factors affecting the SPB. The theories of SPB has recently been addressed by Moores *et al.* including the Maxwel-Garnett,[76] Debye[76] and Mie[76] models and determination of the dielectric constant with Drude theory into the motion of electrons in metals[76, 77]. Mie theory is the most used and describes the interactions between light and nanoparticles and as a scattering one it divides the problem into two sections: the solvable electromagnetic part and the material part which requires the determination of the dielectric constant. The problem with Mie theory on its own is that it treats the nanoparticles as simple spheres that are too distant to interact with one another. The dielectric constant of the host medium/matrix influences greatly both the plasmon peak and

intensity. Interparticle distance also influences SPB position and embedded nanoparticles within a host matrix are more complex and require a modification to the dielectric constant known as the medium dielectric constant or the effective medium theory. Maxwell-Garnet replaced the medium dielectric constant with the average dielectric constant and experimental results fit well with theoretical peak positions[76], see fig. 9.

Figure 9: Correlation between interparticle distance and plasmon position[76].

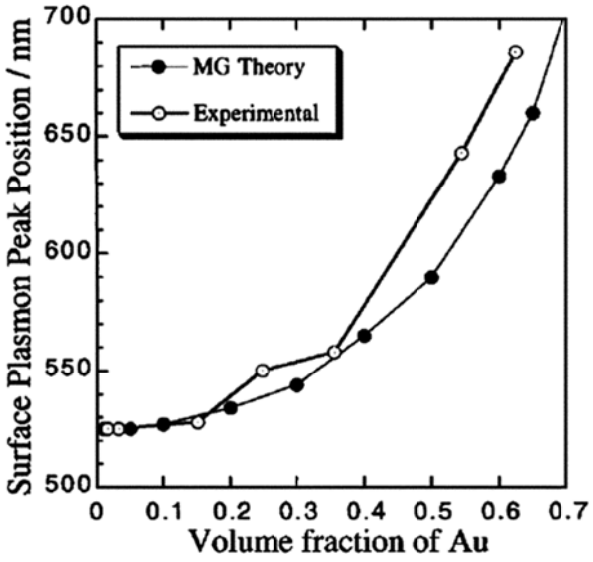

1.3.4 The refractive index of the host matrix/medium

The refractive index (R.I.) is a complimentary property and in some cases a direct function of the dielectric constant of the host matrix/medium; it is a measure of the reduction of the speed of light, the polarization and direction of propagation, within a substrate material. The refractive index (R.I.) of thin films gives information about the variation of the speed of light in the host matrix/medium rather than air, the performance of various optical components, including nanoparticles and the electronic band structure information about the host matrix/medium. The R.I. of the surrounding host matrix or solvent medium can be used to control the surface plasmon resonance of noble metal nanoparticles (Au, Ag, Cu) with great effect as demonstrated by recent research by Medda *et al.* with Ag nanoparticles with a SiO_2 based host matrix (SiO_2: TiO_2, 1:0, n = 1.411): a red shift in the Au SPR (542 - 600 nm) was observed when doped with increasing TiO_2 content[83], see fig. 10.

Figure 10: UV-Vis absorption spectra (Annealed: 500 °C) and R.I. of 5 samples of SiO_2/Au with increasing TiO_2 content[83].

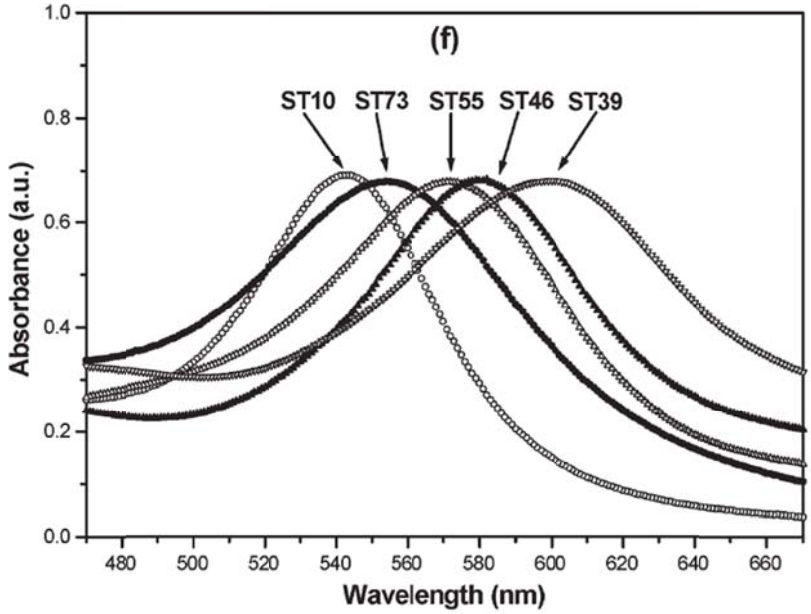

The colours observed with increasing TiO_2 content and increasing Au SPR absorption were pink, magenta, violet and blue, see fig. 11.

Figure 11: Au nanoparticle coloured films (500 °C): SPR tuned using the R.I. of the host matrix[83].

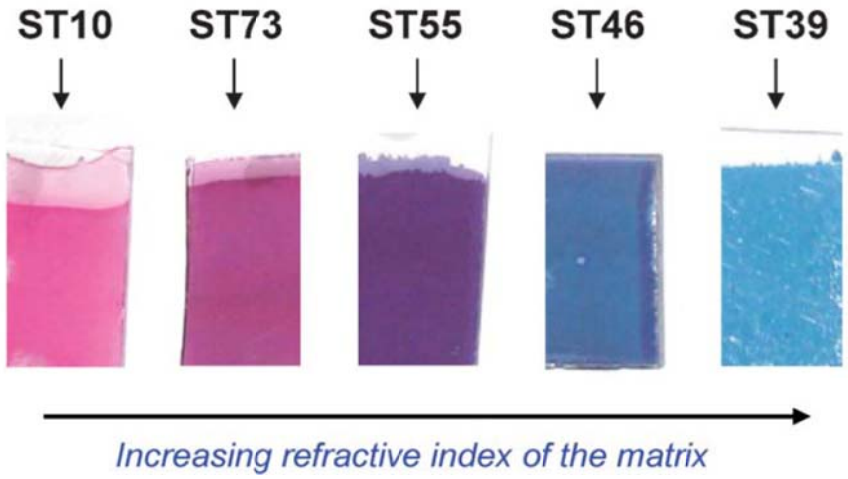

Changing the solvent alters the refractive index of the surrounding medium of a solvent and causes stronger shifts, see fig. 12, but more subtle effects have been observed within host matrices. Size and shape of noble metal nanoparticles influence the SPB intensity and position: it is generally accepted that decreasing nanoparticle diameter results in a blue shift[82].

Figure 12: Absorption of gold nanoparticles of various sizes and shapes[84].

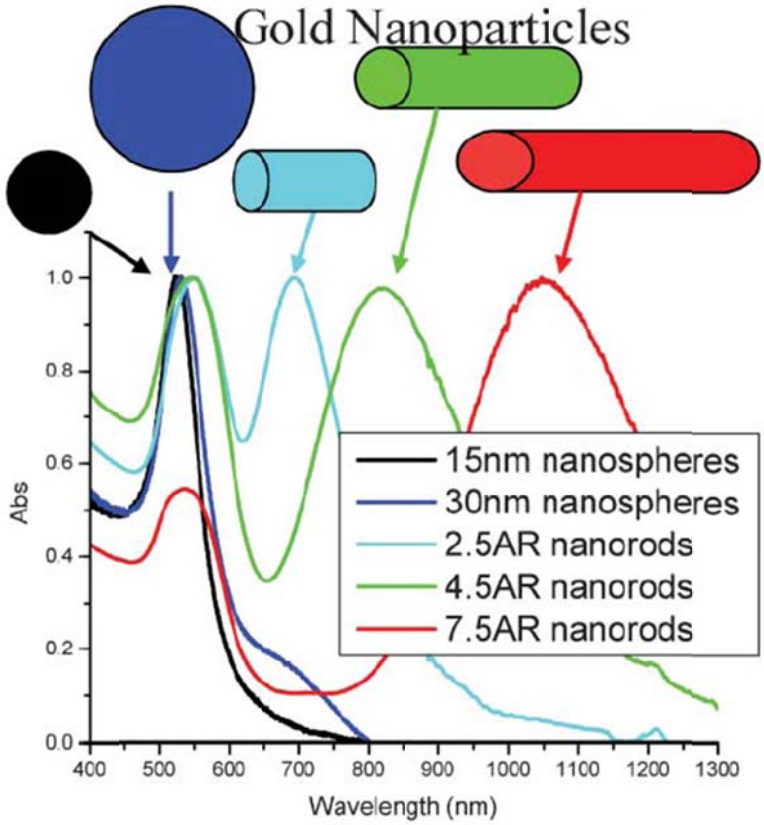

Control of the refractive index of noble metal thin films could be a promising way forward for the control of the SPR and ultimately the capability of causing a SPR shift either to the blue or red end of the spectrum. This will be particularly useful for one pot synthesis techniques where the use of preformed nanoparticles maybe redundant as the synthesis completely changes the original morphology of the nanoparticles.

1.3.5 Noble metal nanoparticles and surface plasmon resonance (SPR)

Gold and silver have been used for centuries to colour glasses and Faraday attributed the colour to finely divided colloidal gold now known as gold nanoparticles[84]. Gold spheres are usually red and silver, copper spheres are usually yellow. The observed colour, in the visible region, changes with size and shape, spherical Au nanoparticles have a characteristic colour change associated with size, where 30-500 nm the colour is crimson to turbid blue, 3 - 30 nm the colour is red, metallic and transparent. The collective oscillations of the electrons in the conduction band produce the colour, known as the surface

plasmon resonance normally the oscillation frequencies of Au and Ag are in the visible region and produce the strong surface resonance absorption. For fundamental reasons the properties of noble metal nanoparticles and semi-conducting nanoparticles (Quantum dots) differ, semiconductor nanoparticle properties are based on the quantum confinement of the electrons and the dielectric constant, and the properties of noble metal nanoparticles are based on the collective oscillations of electrons, the surface plasmon resonance. Therefore a change in size for semi-conducting *e.g.* CdSe nanoparticles alters the optical properties to a greater degree than metal nanoparticles unless the anisotropic shapes occur, *i.e.* different crystal structures, prisms, hexagons, nanorods, nanowires, producing a stronger surface electric field on the surface of the nanoparticle resulting in a stronger plasmon resonance absorption often with multiple "colour modes". The surrounding electromagnetic field is enhanced by anisotropic shapes and their geometry determines the surrounding electric field density and therefore enhances the properties of these noble metal nanoparticles, *e.g.* enhancement of fluorescence, detection sensitivity, Raman signals and light scattering[84]. Chemically bonded molecules can be detected by the effect they have on the electron density on the surface, this shifts the SPR maxima, making noble metal nanoparticles several orders of magnitude better at detecting these molecules than conventional dyes.

1.3.6 The effect of size and shape on the SPR absorption

The shape of very small gold nanocrystals (≤ 20 nm) are naturally disposed thermodynamically to the symmetric face-centred cubic (fcc) types but kinetic factors of growth and nucleation can be used to control or direct shape during synthesis by using different concentrations of surfactants and/or capping agents to obtain larger anisotropic shapes[85]. Spherical nanoparticles tend to have the SPR in the same place just with increasing absorption with increasing size, see fig. 11. Many industries are looking to shift the SPR, particularly Au, into the near infrared for a multitude of promising applications. Therefore control of the shape and size of the nanoparticles, particularly anisotropic crystals, is one way of achieving this shift *e.g.* nanorods display two SPRs (associated with movement of electrons in transverse and longitudinal directions) and experience

a red shift. Many shapes have been synthesized for noble metal nanoparticles including spherical[39, 40, 43-46, 48, 53, 62], triangular[39, 43, 85], prisms[45], hexagons[43, 45], squares[43], cubes[45, 55], octahedron[54, 55], stars (twinning)[84], disks[39], dendritic[72], nanowires[43, 54], nanosheets[43], nanotubes[43] and nanorods[39, 43] by many different synthetic techniques, see fig. 13.

Figure 13: SEM images of non spherical shapes found for Au and Ag nanoparticles: pentagonal cross-section nanowires, decahedrals, cubic, octahedral, tetrahedral, truncated tetrahedral and platelets with different shapes[86].

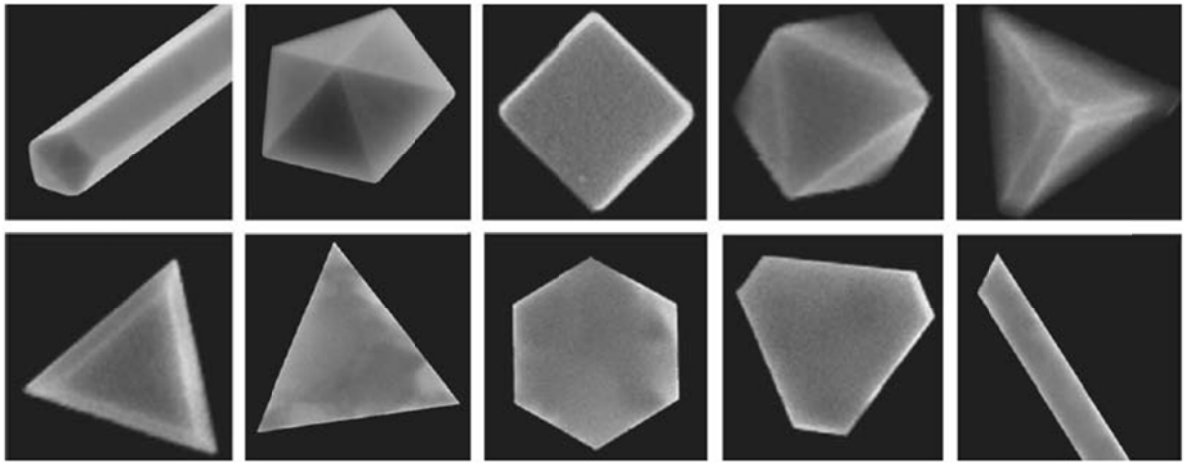

Spherical Au nanoparticles have a transverse SPR absorption around 520 - 580 nm, only the intensity of the absorption increases with an increasing size of the nanoparticle. Spherical Ag nanoparticles are known to absorb in the blue part of the visible spectrum and typical results were obtained by Wada, *et al.* for Ag spherical nanoparticles (4.9-7.4 nm) with a SPR absorption of 418 nm[48]. Although recent work by Lee *et al.* of Ag Nanoparticles in Fluorine doped SnO_2 coated glass substrate, sensitized by a N719 dye solution (0.2 Mm), the peak position of the surface plasmon characteristic absorption increased with the mainly spherical grain size of the nanoparticles in a red-shift[87]. Cu spherical (>5-6 nm) nanoparticles were synthesized by the MW technique and had a transverse SPR absorption of 596 nm, no SPR absorption was observed at particles of size 2-3 nm; increasing size increases the intensity of the absorption[46], see fig. 14.

Figure 14: Time evolution of UV Vis spectra for Cu nanoparticles: a) $Cu(octa)_2$ at 443 K (~160 °C), b) $Cu(myri)_2$ at 443 K (~160 °C)[46].

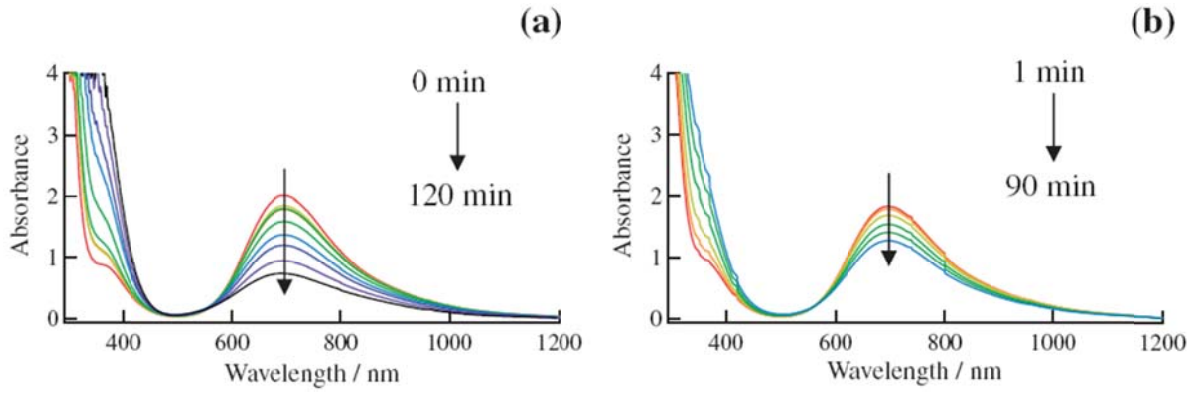

Both Au and Ag nanorods and nanowires are known to have two SPR absorption bands. Anisotropic Au[39, 43, 88], Ag[43, 89, 90] and Cu[91, 92] nanorods have been synthesised by various methods, *e.g.* MW, electro-deposition. One absorption is the high energy transverse SPR corresponding to the oscillation of the electrons perpendicular to the major axis of the nanorod/nanowire and the other absorption is the low energy longitudinal SPR corresponding to the oscillations of the electrons along the major axis of the nanorod/nanowire. An increase in the aspect ratio *i.e.* an increase in size of the Au, Ag and Cu nanorod/nanowire increases the redshift of the longitudinal SPR absorption, *e.g.* Au (2.5 - 7.5AR), see fig. 15.

Figure 15: UV-Vis-NIR absorption spectra and AFM of Ag monolayers: a) UV-Vis-NIR absorption spectra of Ag monolayers with different aspect ratios in unpolarised light; b) 3D Atomic Force Microscopy (AFM) image of Ag monolayers (scale: 100 nm)[90].

a)

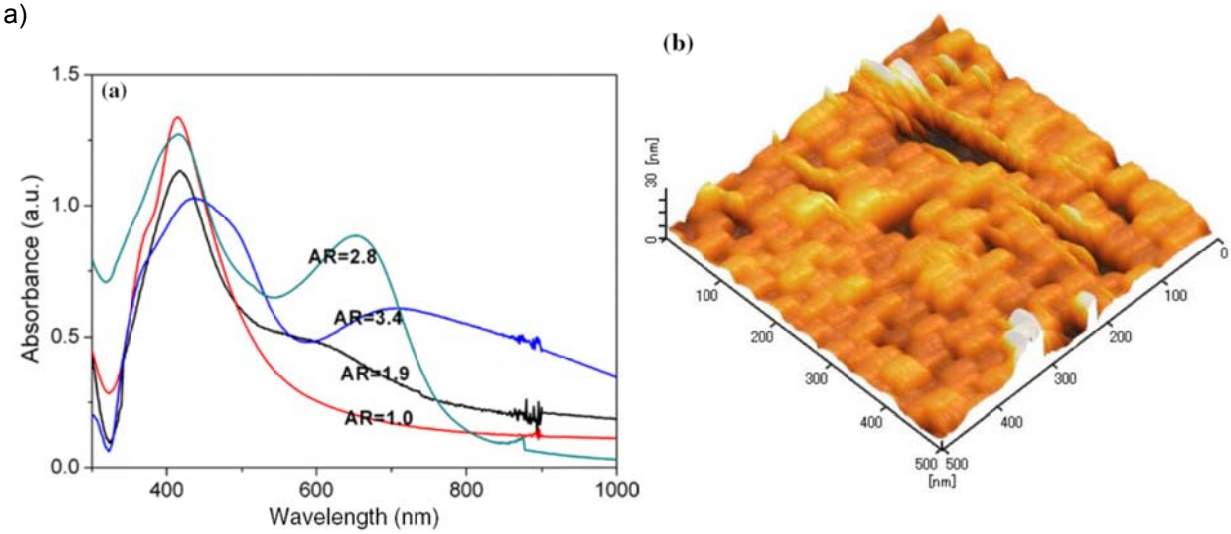

For Ag nanorods transverse (420 nm) and longitudinal (555, 650 and 710 nm, with different aspect ratios) SPR's have been observed[90], see fig. 14. For Cu the typical transverse and longitudinal SPR absorptions were found at about 568 nm and 758 nm (conditions: polarised light, θ: 70°), respectively[92].

Polygonal platelets include disks, triangles, hexagons, squares, octahedra, tetrahedra, truncated tetrahedral, decahedra and other polyhedrals[93]. It has been observed that the number of SPR absorptions for polygonal plates and other more complicated shapes such as prisms appear to increase with increasing number of asymmetric dimensions. This effect is due to SPB breaking/degenerating from one band into two, three or more bands[94]. In recent work by Singh e*t al.* Au triangular nanoparticles have been observed to have two SPR absorptions, one transverse (540 nm) and one longitudinal (≥600 nm)[86], when Au triangular nanoparticles are snipped at the edges *e.g.* truncated this causes a blue shift in the SPR[84]. Au triangles are highly anisotropic with absorption near the infrared part of the spectrum and appear to be blue. For noble metal nanoparticles, particularly Au and Ag, five-fold multiple twinning for fcc nanocrystals also appears to determine the eventual morphology of the noble metal nanoparticle as well as kinetic factors *e.g.* the use of surfactants/capping agents. In recent work by Elechiguerra *et al.* two types of star shaped nanoparticles were identified icosahedra and cuboctahedra[85], see fig. 16.

Figure 16: TEM images of star shaped nanoparticles: a, c) icosahedra, schematic of icosahedra respectively, b, d) cuboctahedra, schematic of cuboctrahedra respectively[85].

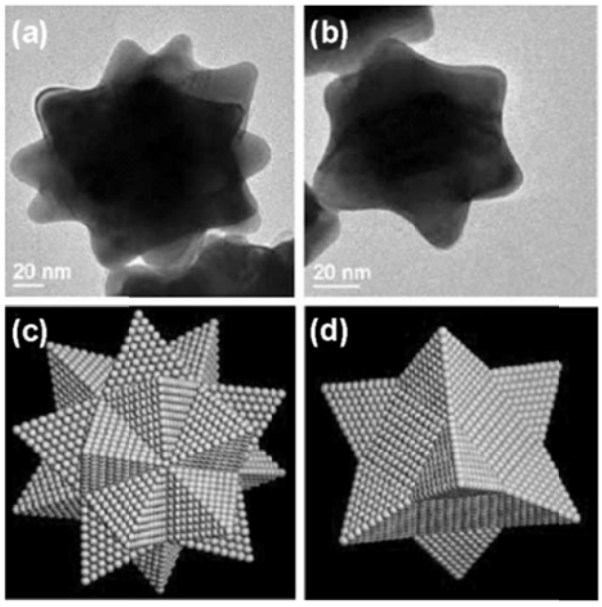

Nehl *et al*. observed Au star shapes exhibited polarization-dependent scattering with multiple spectral peaks that were incredibly sensitive to the dielectric constant of the surrounding host medium, making these nanoparticles ideal for labels for microscopic imaging and localized SPR sensors for low level analytes[95]. Au star shapes were observed to have a possible transverse SPR absorption (586 nm) and a broad longitudinal SPR absorption (773 nm) very similar to the longitudinal SPR absorption of nanorod tips. Single particle spectroscopy using a dark field microscopy with epi-illumination and transmitted light (halogen light source, inverted optical microscope) was used to observe the scattering spectra of the SPR and found to have 3 peaks (647, 700 & 783 nm). The position and strength of these broad near infrared peaks were caused by the variable tip structures and were polarisable at different angles *i.e.* polarization-dependent, opening the possibility for significant biological applications[95]. Spherical nanoparticles have a relatively simple transverse SPR absorption band typically from 520-590 nm the intensity of which is dependent upon on the size of the nanoparticle. For more complicated shapes, *e.g.* anisotropic shapes the SPR absorption degenerates and splits giving new shifted SPR absorptions *e.g.* the longitudinal SPR absorption of nanorods has been observed to have a red shift. These SPR effects are seen both in solution and in thin film form. The colour is also modified by the medium in which the nanoparticle sits and is sensitive to the dielectric constant of the host solvent or thin film. The number of SPR absorption bands appears to be dependent on increasing the anisotropic nature of the nanocrystal with the extreme example of star shapes, which have many SPR peaks due to the twinning nature and number of tips of the nanocrystals. Research into the effects of morphology, size, shape, size distribution and monodispersity have on the SPR absorption for Au, Ag and Cu nanoparticles embedded in a thin film is a very active and an area to be further explored.

1.3.7 Photoluminescence

In 1969 Mooradian first reported the photoluminescence of Au nanoparticles[96]. This work has proved pivotal for the SERS community where enormous enhancements in Raman sensitivities have been observed even down to the single molecule level. When noble metal nanoparticles absorb energy as

photons attain a higher energy state and therefore depending on energy loss pathways can emit photons of equivalent wavelengths; the duration of photoluminescence is usually extremely short, 10 ns or less but can be extended in special circumstances. Work has been carried out using Cu nanoparticles to enhance the photoluminescence of magnesium doped films[97]. Thin films of a CVD-ZnO and magnesium doped ZnO (MZO) incorporating Cu nanoparticles were annealed and irradiated at the surface with an electron beam, 4 keV[97]. The films annealed at 800 °C for 90 min produced the largest emission intensity of the optical emission peaks in the visible region: the ZnO film displayed green and the MZO film displayed a blue colour, fig. 17.

Figure 17: Photographs of CVD ZnO and MZO films irradiated with electron beam: a) photograph of CVD ZnO, b) photograph of MZO thin films irradiated with electron beam (4 keV)[97].

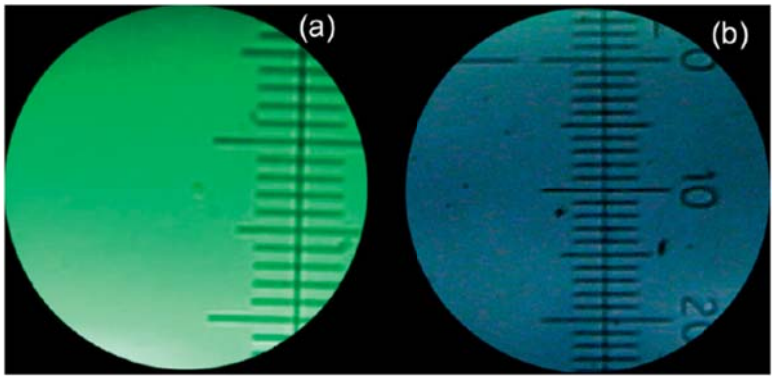

Basak *et al.* has produced poly(methyl methacrylate), (PMMA) thin films doped with Ag nanoparticles and found a shift towards the red in the photoluminescence peak (PL) position towards longer wavelengths, increasing excitation in the range of 350-550 nm in a linear fashion[98]. The change in intensity and PL peak position is associated with change in resonance for the SPR absorption of the Ag nanoparticles and the change in luminescence of the quartz/PMMA film. The red shift in the photoluminescence peak is Ag nanoparticle size dependent[98], see fig. 18. Zhao *et al.* have used the pulsed laser deposition route to synthesis Ag doped ZnO thin films on quartz that have photoluminescence (PL) spectra peak exhibited at 414–420nm for Ag[99]. Recent work by Liao *et al.* have used magnetron sputtering synthesis route to produce composite sandwich layers of Au nanoparticles with various metal oxides (SiO_2, ZnO, TiO_2) with distinct PL peaks located at a wavelength range between 590-680 nm[100].

Figure 18: UV-Vis and photoluminescence spectra of PMMA and Ag nanoparticles: a) UV-Vis spectra of PMMA curve 1 and PMMA plus silver nanoparticles curve 2 cast on quartz plates, b) Photoluminescence spectra, curves 1-7 represent excitation wavelengths 230, 235, 240, 250, 260, 265 and 270 nm respectively, c) curves 1 and 2 represent peak position and full width half at half maximum on the excitations taken from b)[98].

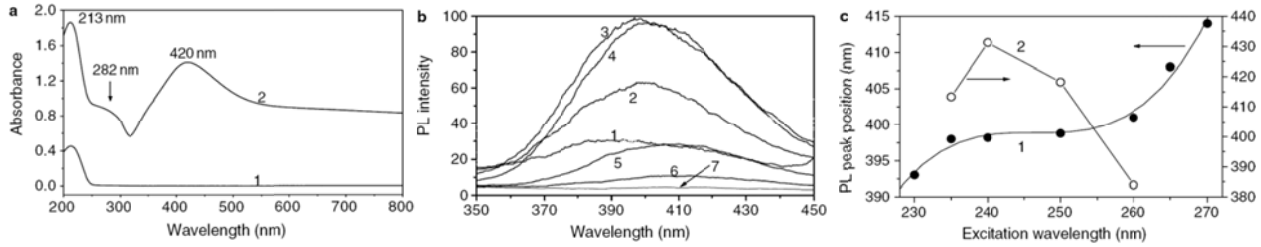

1.3.8 Photochromic effects

Photochromic materials reversibly change colour upon illumination. The novel methods used with nanoparticles include layer by layer electrochromic assemblies, multicolour quantum dots and tunable wavelength reflection from photonic crystals. Ag nanoparticles embedded into a host matrix, TiO_2, near or at the surface on glass were produced by the magnetron sputtering technique and were investigated for the optical and structural changes during the photochromic transition[101]. The Ag nanoparticles plasmon resonance effects gives rise to an adsorption band visible over the entire optical spectrum, due to a spectral hole the transmitted colour is the same as the wavelength used to irradiate the Ag nanoparticles leading to a reduction in the optical extinction peak accompanied by a blue shift in the plasmon resonance for the photoexcited Ag nanoparticles[101]. The effect has been shown using grazing incidence X-ray diffraction (GIXRD) techniques, see fig. 19, to be due to the photoinduced electron emissions decreasing the size of the Ag crystals[101].

Figure 19: GIXRD scans of Ag-TiO_2 composite film: GIXRD scans after successive increasing irradiation time and power density of the Ag-TiO_2 composite showing decreasing peak height and broadening (Ag 111 & Ag 200)[101].

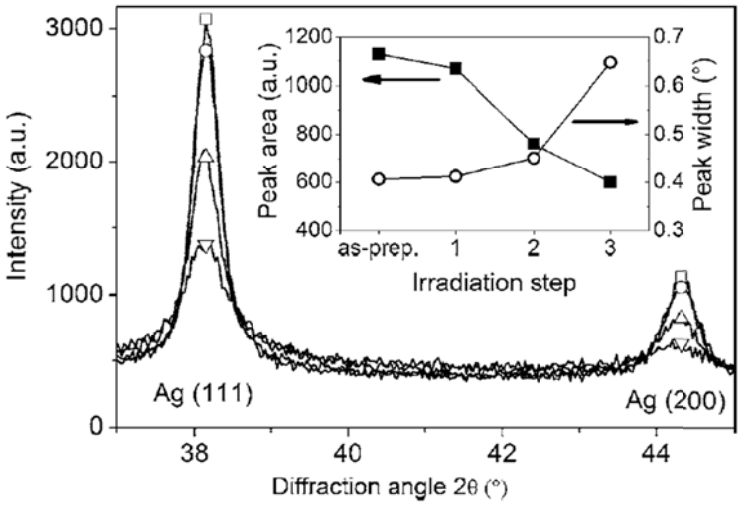

The opportunity of achieving multifunctional active pigments beckons with the possibility of changing the colour of a nanoparticle surface at will. Further interesting work carried out by Speranza *et al*. on Er-Ag silicate glass has shown improvement in photoluminescence of this rare earth metal at 476.5 nm[102], see fig. 20. The mechanism for enhancement is controversial but these results indicate that Ag is present in the non-oxidised form therefore the outer Ag electrons are not strongly bonded chemically to oxygen allowing electron oscillation when excited by laser radiation[102].

Figure 20: Absorption and emission spectra $Er3^+$ with an Ag sample: A) example of an absorption spectrum (plasmon peak ~ 420 nm). B) example of the same sample with an excitation spectrum at 1532 nm, inset: control Er^{3+} emission (indicated by a broken line) compared with enhanced Er^{3+} emission with Ag doped sample[102].

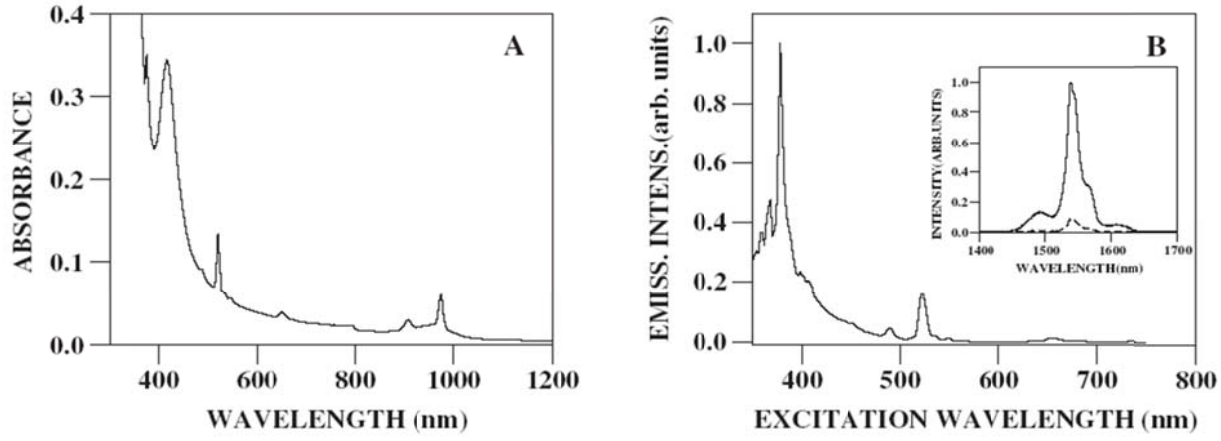

Work by He *et al.* on a MoO_3 composite thin film with Au nanoparticles improves the UV-light coloration performance of the MoO_3 thin film. Both the MoO_3 and the Au doped MoO_3 thin films are almost transparent before UV-light irradiation; these samples turn blue when irradiated with UV light, with broad absorption peaks. The Schottky barrier formed at the MoO_3/Au interface facilitates the separation of photogenerated carriers and therefore the Au nanoparticles enhance absorption of MoO_3 thin film by 2.5 times[103].

1.3.9 Electrochromic effects and micropatterning

Electrochromism is a reversible, visible change in optical absorption under electrochemical oxidation/reduction or when a burst of charge is applied. The energy provided is sufficient to effect the change required. Tungsten oxide (WO_3) is currently used in the production of electrochromic 'smart' windows and rear-view automobile mirrors in various lighting conditions. The amount of light and heat allowed to pass through a 'smart' window can be controlled; the colour persists until a sufficient form of energy has been supplied to effect the change. Au nanoparticles have been investigated by Nah *et al*. on poly[2-methoxy-5-(2-ethylhexyloxy)-1,4-phenylenevinylene] (MEHPPV) thin films deposited on indium tin oxide (ITO) substrate: two types of the film were synthesized (Au/MEH-PPV) by two different deposition conditions of the pulsed-current electrodeposition and spin coating to give two different results for the SPR of the Au spherical nanoparticles[104]. Sample Au1 SPR absorption was 550 nm at -20 m/A cm^{-1} and sample Au2 SPR absorption was 650 nm with a broader absorption band at -30 m/A cm^{-1}, see fig. 21. The colouration of the films was different for both controls. Au1/MEH-PPV was reddish (550 nm) and the Au2/MEH-PPV had two SPRs (550 and 650 nm) that were blue after oxidation probably due to the longer exposure time of the pulsed current. The main reason for the results would probably be the smaller interparticle Au nanoparticle distance in sample Au2 and the effect of red shifting of the SPR absorption. Control of these types of films could be achieved through the density of the Au nanoparticles, *e.g.* increasing density increase the SPR absorption and enhances the electrochromic properties.

Figure 21: Absorption spectra of Au and Au/MEH-PPV samples: Absorption spectra a) Au controls, b) Au1/MEH-PPV with control, c) Au2/MEH-PPV with control[104].

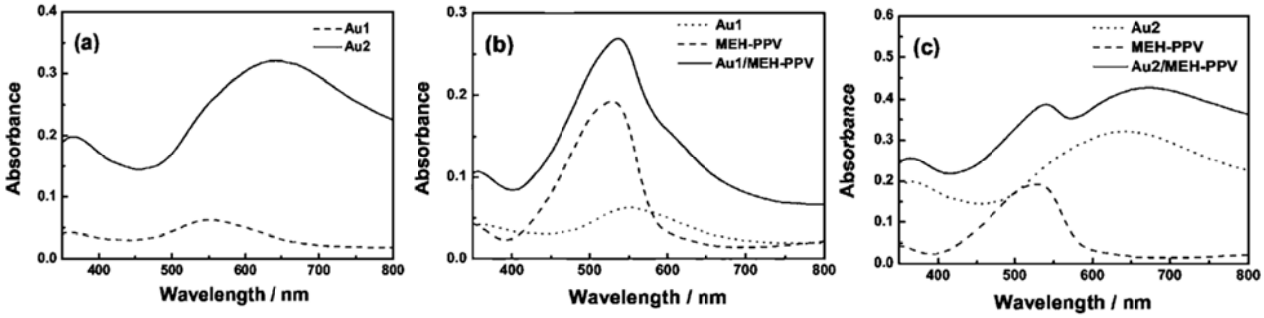

Micropatterened and higher order structures have recently been investigated using noble metal nanoparticles. Eurenius *et al.* have shown how noble metal nanoparticles can be used for the coupling of light in waveguides[105]. Kim *et al.* have shown how porous self-assembled arrays can be synthesised[106] and Kodaira *et al.* have shown how silver nanoparticles can be micropatterened within a thin film[107]. Binions *et al.* have shown how the presence of nanoparticle gold can improve the optical properties of thermochromic coatings on glass[108].

1.3.10 Summary of the properties of noble metal nanoparticles in thin films

The properties of noble metal nanoparticle thin films are dependent upon the morphology, size, shape, size distribution, monodispersity, interparticle distance of noble metal nanoparticles within the film, the refractive index and the dielectric constant of the host matrix. Nanoparticles below a certain size display quantum size effects, electronic effects where oscillating electrons give rise to the phenomenon known as the surface plasmon resonance band described by Mie, Maxwell Garnett and Drude theories and modelled by discrete dipole approximations (DDA). The noble metal nanoparticles Ag and Au precursors are easier to synthesize and use than the Cu nanoparticle precursors, due to the ease of oxidation of Cu in air. Various techniques are used to look at these properties including XRD, TEM, SEM and AFM. It is the surface plasmon resonance band of noble metal nanoparticles that conveys the unusual properties to nanoparticles and the tuning or influencing of this SPR that promises to deliver many new and exciting products to industry.

1.4.0 Modelling fluid flow for *in-situ* synthesis routes

The successful incorporation of noble metal nanoparticles into a metal oxide host matrix is reliant on the characteristics of fluid flow in the synthesis delivery head or reaction chamber. The fluid flow dictates the uniformity of dispersion characteristics and the areas of substrate most likely to grow a thin film and the rate of growth with boundary conditions to be taken into account. One useful way to both qualitatively and quantitatively assess the fluid flow regime in a CVD synthesis is by modelling the fluid flow using computational fluid dynamics (CFD) *e.g.* ANSYS range of CFD software.

1.4.1 Theoretical approach to fluid flow mechanics and CFD

There are two basic types of fluid flow, streamlined, laminar fluid flow and chaotic, turbulent fluid flow with transition points between the two also known as aero-dynamic drag in some industries; particular industries require laminar flow, *e.g.* Formula 1 racing cars, airplanes and CVD reactions for thin films with uniformity of dispersion and growth and some industries require turbulent flow, *e.g.* chemical industries requiring fast reactions of liquids/gases and dishwashers[109].

For laminar flow the motion of the particles of fluid is very orderly with all particles moving in straight lines, layers parallel to the walls or physical boundaries of the system *e.g.* pipe walls, reaction chamber sides or river bank. Putting an obstacle in the path of a laminar fluid flow does not have a significant effect on the pathline taken, the laminar fluid flow will simply follow the curve around the obstacle and carry on streaming away in a smooth straight line, *e.g.* a pebble in a slow flowing river or analogous in chemical terms to a reaction taking the pathline of least resistance and lowest energy[109]. In turbulent flow the motion of the fluid is completely irregular and chaotic with all particles moving in the same direction and destination as the laminar flow pathline but in a chaotic, disorganized way. Increasing the velocity of the fluid flow in the stream to turbulent fluid flow allows chaotic motion to be formed behind the pebble *e.g.* forms swirling eddies[109]. The fluid follows an identical but chaotic pathline to the laminar flow model; analogous in chemical terms to the

molecules becoming more agitated, having more energy, are more excited, move faster and release energy faster by bouncing around *e.g.* a river after a rainstorm, see fig. 22. With sufficient distance turbulent fluid flow will return to laminar fluid flow.

Figure 22**:** a) Turbulent and b) Laminar Fluid Flow

a) b)

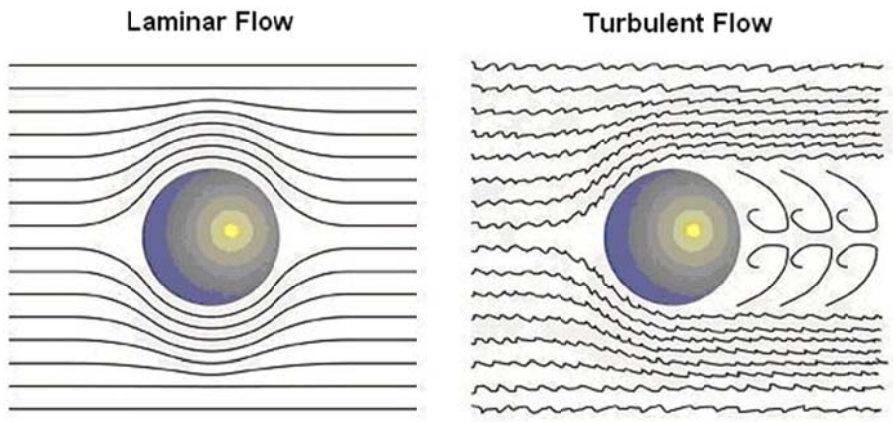

1.4.1.1 Reynold's number

The Reynold's number (Re) is dimensionless and can give a reasonable estimate of the transition point between laminar and turbulent flows: laminar flows are of lower velocity and give a low Re number; turbulent flows are of a higher velocity and give a higher Re number. The transition Re for a given system can be anywhere from 2000 to 4000 and is dependent upon the system under investigation, a normal estimate would be about Re of 3000 for surety of turbulent flow. Laminar flow: Re < 2000; transitional flow: 2000 < Re < 4000; turbulent flow: Re > 4000[109, 110].

Equation 5: Reynold's Number

$$\mathbf{Re = \rho v D/\mu}$$

Where: ρ = fluid density; v = fluid velocity; D = tube diameter; μ = fluid viscosity

1.4.1.2 CFD calculations for fluid flow

Computational fluid dynamic calculations within most software solvers use the default setting for viscous flow with a low velocity value for laminar flow[111]. Turbulent flows are characterized by fluctuating velocity fields, momentum, energy and species concentration, and cause the transported quantities to fluctuate as well[111]. Transport equations modelled for all simulations include momentum, mass and energy. The fluctuations that are small scale with high frequency are too complicated and computationally expensive to simulate directly; therefore the instantaneous governing equations are time-averaged, ensembled-averaged, or otherwise manipulated to remove the small scales[111]. The result is a modified set of equations that are less computationally expensive to solve. Additional unknown variables contained in the modified equations are required to determine the variables in terms of known quantities[111]. There are 7 basic turbulent models with further variations available within some of the models, see table 5[111].

Table 5: List of various CFD turbulent models

Type of CFD Model	Type of Simulation and Equations
Spalart-Allmaras	Solves one transport equation for the kinematic eddy (turbulent) viscosity
κ-ε i) Standard ii) Renormalization-group (RNG) iii) Realizable	Solves two transport equations for turbulent kinetic energy (κ) and dissipation rate (ε). All three models have similar forms. The major differences in the models are the method of calculating turbulent viscosity, the turbulent Prandtl numbers governing the turbulent diffusion of κ and ε and the generation and destruction terms in the ε equation. Calculations common to all models include turbulent production, generation due to buoyancy, accounting for the effects of compressibility, modelling heat and mass transfer.
κ-ω i) Standard ii) Shear-stress transport (SST)	Solves two transport equations for the turbulence kinetic energy (κ) and the specific dissipation rate (ω), which can also be thought of as the ratio of ε to κ
v^2-f	Similar to the standard κ-ε model, but incorporates near-wall turbulence anisotropy and non-local pressure-strain effects. A limitation of the v2-f model is that it cannot be used to solve Eulerian multiphase problems, whereas the κ-ε model is typically used in such applications. The v2-f model is a general low-Reynolds-number turbulence model that is valid all the way up to solid walls, and therefore does not need to make use of wall functions. Although the model was originally developed for attached or mildly

	separated boundary layers it also accurately simulates flows dominated by separation. The distinguishing feature of the v2-f model is its use of the velocity scale, v2, instead of the turbulent kinetic energy, κ, for evaluating the eddy viscosity., v2 which can be thought of as the velocity fluctuation normal to the streamlines, has shown to provide the right scaling in representing the damping of turbulent transport close to the wall, a feature that κ does not provide.
Reynolds stress model (RSM) i) Linear pressure strain ii) Quadratic pressure-strain iii) Low-Re stress-omega	The RSM closes the Reynolds-averaged Navier-Stokes (RANS) equations by solving transport equations for the Reynolds stresses, together with an equation for the dissipation rate. For 2D: 5 additional equations For 3D: 7 additional equations
Detached eddy simulation (DES) i) Spalart-Allmaras (RANS) ii) Realizable κ-ε RANS iii) SST κ-ω RANS	The unsteady RANS models are employed in the near-wall regions, while the filtered versions of the same models are used in the regions away from the near-wall. The LES region is normally associated with the core turbulent region where large turbulence scales play a dominant role. In this region, the DES models recover the respective subgrid models. In the near-wall region, the respective RANS models are recovered. Reynolds-averaged Navier-Stokes equations govern the transport of the averaged flow quantities with the whole range of the scales of turbulence to be modelled
Large eddy simulation (LES) i) Smargorinsky-Lilly subgrid-scale ii) WALE subgrid-scale iii) Kinetic-energy transport subgrid-scale	Filtered time-dependent Navier-Stokes equations in either Fourier (wave-number) space or configuration (physical) space. This filters out the eddies whose scales are smaller than the filter width or grid spacing used in the computations. The resulting equations thus govern the dynamics of large eddies.

Turbulent model choice depends upon the physics of the flow, common practice for type of problem to be solved, accuracy required and computational expense. The most common turbulent models used are the κ- ε models and the κ-ω models, particularly the κ-ε Realizable model which is suitable for most common turbulent fluid flow simulations[112, 113]. At this point in time, time-dependent solutions of the Navier-Stokes equations are unobtainable for high Re number turbulent flows down to the small scale of motion. There are two methods for resolving Navier-Stokes equations so small scale turbulent fluctuations are not directly simulated, one is Reynolds-averaging and the other is filtering. Reynolds-averaged Navier-Stokes (RANS) equations govern the transport of the averaged flow quantities with the whole range of the scales of turbulence being modelled. The RANS based approach reduces the computational effort and is widely used for engineering applications. Models which use RANS

include Spalart-Allmaras, κ-ε, κ-ω and RSM models. The Reynolds stresses are approximately modelled using the Boussinesq hypothesis[114] which relates the Reynolds stresses to the mean velocity gradients; the additional turbulent stresses are given by augmenting the molecular viscosity with an eddy viscosity. The Spalart-Allmaras, κ- ε and the κ-ω models use the Boussinesq hypothesis; the Spalart-Allmaras model resolves one additional transport equation for turbulent viscosity, μ_t; the κ- ε model resolves two additional transport equations for the turbulence kinetic energy, κ, and the turbulence dissipation rate, ε, the κ-ω model also resolves two additional transport equations for κ and the specific dissipation rate, ω and μ_t is computed as a function of κ and ε. One assumption, which is not quite true, of the Boussinesq hypothesis is that μ_t is an isotropic scalar quantity. RSM solves transport equations for all the Reynold stress tensor terms. An additional scale-determining equation (usually for ε) is also required for RSM; therefore five additional transport equations are required in 2D flows and seven additional transport equations are required in 3D flows. Most models based on the Boussinesq hypothesis perform adequately and the extra computational expense of RSM is not justified unless the anisotropy of turbulence is dominant *e.g.* highly swirling flows and/or stress-driven secondary flows.

LES is an alternative approach in which large eddies are resolved in a time-dependent simulation using filtered Navier-Stokes equations *i.e*. models less turbulence but resolves more, errors introduced by turbulence modelling can be therefore reduced. Filtering is a mathematical manipulation of the exact Navier-Stokes equations to remove eddies that are smaller than the size of the filter, *e.g.* the mesh size when spatial filtering is applied. LES requires significant computational effort to accurately resolve the energy containing turbulent eddies in both space and time domains, particularly in near-wall regions where ever decreasing small scale motion requires resolution, this can be reduced by using a coarse mesh but may not be appropriate for the fluid flow problem undergoing simulation; highly accurate spatial and temporal discretizations are also required.

1.4.1.3 Discrete modelling: droplet trajectory

Discrete modelling of the forces, *e.g.* aerodynamic drag, experienced by vapour droplets during AACVD synthesis can give statistical information on solvent droplet trajectory and the size of droplet required to hit the substrate. The discrete second phase simulations are in a Lagrangian frame of reference. The second phase consists of spherical particles (which may be taken to represent droplets or bubbles) dispersed in the continuous phase. The simulation computes the trajectories of these discrete phase entities, as well as heat and mass transfer to/from them. The coupling between the phases and its impact on both the discrete phase trajectories and the continuous phase flow can be included[111].

Various discrete phase modelling options include[111]:

- calculation of the discrete phase trajectory using a Lagrangian formulation that includes the discrete phase inertia, hydrodynamic drag, and the force of gravity, for both steady and unsteady flows
- prediction of the effects of turbulence on the dispersion of particles due to turbulent eddies present in the continuous phase
- heating/cooling of the discrete phase
- vaporization and boiling of liquid droplets
- combusting particles, including volatile evolution and char combustion to simulate coal combustion
- optional coupling of the continuous phase flow field prediction to the discrete phase calculations
- droplet breakup and coalescence

Therefore the evaporation model can give statistical analysis of when the solvent droplet is most likely to evaporate within an AACVD or AACVD/CVD reaction chamber. Other effects that can be simulated and investigated for droplet trajectory, *via* a discrete model, are thermophoretic forces[115].

1.4.2 Summary of CFD modelling simulations

CFD modelling simulations are used in this thesis to investigate fluid flow in AACVD/CVD combined synthesis designs for the incorporation of noble metal nanoparticles into host metal matrices, the effect of thermophoretic force and the characteristics of typical solvent droplet trajectory and evaporation for the AACVD fluid flow are assessed, see chapter 2.

1.5.0 Conclusion of chapter one

The incorporation of noble metal nanoparticles, Au, Ag and Cu into thin film is reviewed. The synthetic routes to gold nanoparticles and the synthesis of thin films on glass/silica, metal and plastic substrates, with a range of various host matrices, including ZnO, TiO_2 and Al_2O_3, are covered with general introductions and examples of current synthesis methods and future applications including anti-microbial coatings. The optical properties of noble metal nanoparticles, numerical theory, including Mie and Maxwell-Garnet equations are explained with particular attention on photoluminescence, photochromic and electrochromic properties. The dielectric effect of the host matrix and the influence on the surface plasmon resonance are explored and various analytical techniques such as AFM and XRD results to illustrate the properties of both the noble metal nanoparticles and the host matrix. Computation fluid dynamics and the various simulation models are reviewed for simulations of fluid flow, particle trajectory using solvents (EtOH, water) and the effect of thermophoresis. The following chapters detail work carried out on CFD simulations, chapter 2, of the combined AACVD/CVD synthesis deposition head; the experimental work using AACVD and combined AACVD/CVD synthesis of metal oxide host matrix thin films (ZnO, TiO_2) with or without doping of noble metal (Au, Ag, Cu) and/or *p*-type metal (Al) nanoparticles onto glass substrates and their characterisation, chapters 3-5, *e.g.* composition, crystal lattice, morphology, resistivity, optical properties, size and shape of nanoparticles.

Chapter 2

Computational Fluid Dynamic Study of Six AACVD/APCVD Reactor Heads

Chapter 2: Computational Fluid Dynamic Study of Six AACVD/APCVD Reactor Head Designs

2.0.0 Introduction

This chapter describes the of use standard numerical computational fluid dynamics (CFD) code to assess the fluid flow characteristics of six AACVD/CVD combined head designs with and without thermophoretic effects. One design was chosen for further evaluation of particle trajectory, droplet size and evaporation of the AACVD fluid flow. This calculational study would provide insight into AACVD reactor design for formation of a coater head for use for forming composite thin films with nanoparticles embedded in a host oxide matrix. Following the calculational study of a new design of AACVD coater was made and evaluated as described in chapter 4 and 5. All numerical computation of fluid transport includes conservation of mass, chemical species concentration, momentum and energy, see appendix 1. Gambit™ software was used as a pre-processor to create the geometry, discretize the fluid domain into small cells to form a volume mesh or grid and to set up the appropriate boundary conditions[116, 117]. The flow properties are then specified and the problems are solved and analysed by the Fluent™ solver[111]. The heat transfer theory was used to solve for energy when required in CFD simulations in Fluent™ software, see appendix 1[118]. The pressure work and kinetic energy terms are often negligible in incompressible flows. For this reason, the pressure-based solver by default does not include the pressure work or kinetic energy when solving incompressible flow[111, 119]. Viscous heating is often negligible when the pressure-based solver is used; therefore Fluent™'s default form of the energy equation does not include them[111]. For the inclusion of the species diffusion term due to enthalpy transport for the pressure based solver see appendix 1. The diffusion component and therefore the net inlet transport at the inlets are not specified. The Reynold's number for turbulence for the combined AACVD/CVD head designs was assumed to be 3000, see appendix 2. There is a lack of research papers that are applicable

for this particular use of CFD in relation to AACVD and CVD fluid flow, droplet trajectory and droplet evaporation simulations, this work represents one of the first such applications.

2.1.0 Turbulent Models

The turbulent models chosen were the two transport two-equation models; κ-ε Realizable model[112] and the κ-ω Shear Stress Transport (SST) model[120, 121] for comparison. The κ-ε realizable model satisfies certain mathematical constraints on the Reynolds stresses for turbulent flows and more accurately predicts the spreading rate of planar and round jets and provides superior performance for rotation, boundary layers under strong adverse pressure gradients, separation and recirculation when compared to other κ-ε models[111]. Limitations of the κ-ε realizable model are the production of non-physical turbulent viscosities where the computational domain contains both rotating and stationary fluid zones *e.g.* rotating sliding parts/meshes due to the inclusion of the effects of mean rotation in the turbulent viscosity *i.e.* extra rotation effect gives superior simulations but multiple rotating and stationary flows being assessed together may cause problems[111]. The κ-ω SST model is a blend of the standard κ-ω model[119] in the near-wall region and the κ-ε free-stream independence in the far field making this more accurate for shear-stress flows such as shockwaves[111, 119]. The turbulent kinetic energy, κ, is solved for both turbulent models and the dissipation rate, ε, is solved for the κ-ε realizable model and the specific dissipation rate, ω, is solved for the κ- ω SST model, for mathematical explanations see appendix 1.

2.1.2 Discrete Models

- The thermophoretic model

The thermophoretic effect was modelled as small particles suspended in a gas that have a temperature gradient and subsequently experience a force in the direction opposite to that of the gradient, see appendix 1[115]. The one assumption made was that the particles were spherical and the fluid behaved like an ideal gas.

- Droplet trajectory model

The droplet trajectory was modelled for 16 droplets, due to the limitations of the diameter of the inlet, at various sizes (0.1-0.0001 mm) using two solvents (water, MeOH) through the AACVD inlet. Fluid flow (including flow from CVD inlets) was assumed to be solved from the previous turbulent modelling and the statistical analysis was repeated until a meaningful set of repeatable results were obtained. The substrate surface was set to trap droplets that hit the surface and the assumption made was that droplets remained and did not then leave the surface.

2.1.3 Geometry construction and mesh generation

Geometry and volume mesh generation for the 2D and 3D fluid areas of the 6 combined AACVD/CVD head designs were generated in the Gambit™ software using the ACIS geometry kernel and hybrids of tetrahedral (tet) and hexagonal (hex) meshes[116, 117]. A hex-dominant mesh usually requires decomposition, and is used primarily for prismatic geometries whilst a tet-dominant mesh is appropriate for complex geometries and a HexCore mesh is used to lower the cell count and improve overall mesh quality, for flow volumes with complexity near the walls and a large core region[116, 117]. A high quality hex-mesh is preferred over a tet-mesh but may not be possible for complex geometries. The discretization error and false numerical diffusion are reduced significantly for a hex-dominant mesh with significantly lower cell counts *e.g.* for a 10 x 10 x 10 cube; hex and tet (cell size of 1), hex-mesh generates 1,000 cells, tet-mesh generates 7,726 cells[116, 117].

Various mesh types with sub schemes are available within Gambit™ and include the following:

- Hex
    - Map, Submap, Tet Primitive, Cooper, Stairstep
- Hex/Wedge
    - Cooper
- Tet/Hybrid
    - TGrid, HexCore

The type of mesh and meshing strategy for the geometry problem depends on considerations of available time, the required mesh quality, the mesh count and physics of the problem[116, 117].

2.2.0 Methods and simulations

Gambit™ software was used to design various AACVD/CVD combination head 2D/3D models with high resolution hybrid meshes (EquiAngle skew ≤ 0.9)[116, 117]. Fluent™ 2 ddp and 3 ddp software was used to model mass, momentum and energy conservation, forces of drag, solvent droplet trajectories (spherical model) and turbulent flow using the κ-ε realizable and the κ-ω SST turbulence model with/without the discrete thermophoretic model and evaporation model for analysis (substrate surface: 600 ºC, solvent droplet: MeOH or water)[111, 112, 115, 118, 120, 121]. The original prototype was assessed using 2D κ-ε realizable modelling simulation for various velocities (CVD 10 l/m, AACVD 10–0.1 l/min) and glass substrate temperatures (450-600 °C)[111]. Five new AACVD/CVD vertical head designs were then assessed, with one AACVD inlet and two CVD inlets simulated in Fluent™ for flow characteristics, with various AACVD (4.32-17.39 m/s) and CVD (8.32-17.39 m/s) velocities, two heads were then assessed for particle trajectory from the AACVD inlet with/without discrete thermophoretic models and evaporation (interaction with continuous phase on various velocities) model, with the previously solved flow and turbulence models turned off (assumption: small changes in droplet size had no significant effect on the solved flow and turbulent solution)[111, 112, 115, 118, 120, 121]. All velocity and turbulent results were taken from either the symmetry or interior plane of the model.

2.2.1 Original AACVD/CVD prototype

The original prototype consisted of three separate AACVD and two CVD synthesis chambers and the initial proposal was the optical layering of TCO material and other nanoparticle layers as stacks to form ‘optical filters’, see fig. 23.

Figure 23: Original combination AACVD/CVD prototype design 1.

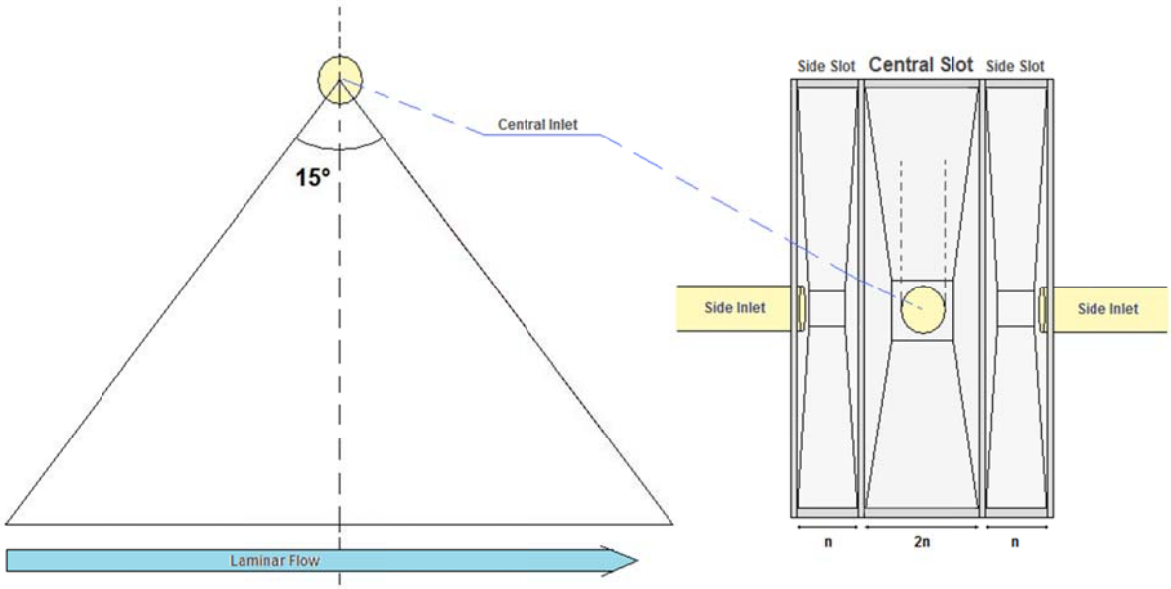

- Central slot: uses the AACVD technique to deliver noble metal or other suitable nanoparticle precursors to the reaction surface. The central slot has a 15° angle that predicts laminar flow rather than turbulent flow; laminar flow would enhance reaction conditions at the surface of the substrate.
- Two side slots: form a curtain stream of conventional CVD delivery method of TCO precursors.

2.2.1.1 Modelling results for the original AACVD/CVD prototype

A 2D hexagonal mesh was used for 2D κ-ε realizable turbulence simulations of MeOH solvent droplets with and without the discrete thermophoretic model gave the following results for various conditions, see table 6. For a description of the 2D representation of the particle flow in the symmetrical plane, in the y direction, of the prototype head with AACVD droplet flow, see fig. 24.

Table 6: Conditions for 2D modelling of original prototype: Droplet size, mm, is varied with substrate temperature (°C) the flow rate for the two CVD inlets (l min^{-1}) which are set at the same value and the flow rate for the AACVD inlet (l min^{-1}).

Droplet Size/mm	Substrate Temperature/ °C	CVD flow rate/ l min^{-1}	AACVD flow rate/ l min^{-1}
2.0	600	10	0.6
1.0	600	10	0.6
0.1	450	10	0.3
			0.6
	600	10	0.6
0.09	600	10	0.6
0.08	600	10	0.6
0.07	600	10	0.6
0.06	600	10	0.6
0.05	600	10	0.6
0.04	600	10	10.0, 5.0, 1.6, 1.5, 1.4, 1.3, 1.2, 1.1, 1.0, 0.9, 0.8, 0.7, 0.3, 0.2, 0.15, 0.1
0.03	600	10	0.6
0.02	600	10	0.6
0.01	450	10	0.3
			0.6
	600	10	0.3
			0.6
0.005	600	10	0.6
0.001	450	10	0.3
			0.6
	600	10	0.3
			0.6

Figure 24: Description of the 2D representation of the symmetrical plane, in the y direction, of the prototype head with AACVD droplet flow. AACVD Droplet Flow: these lines represent the particle traces on moving though the AACVD system.

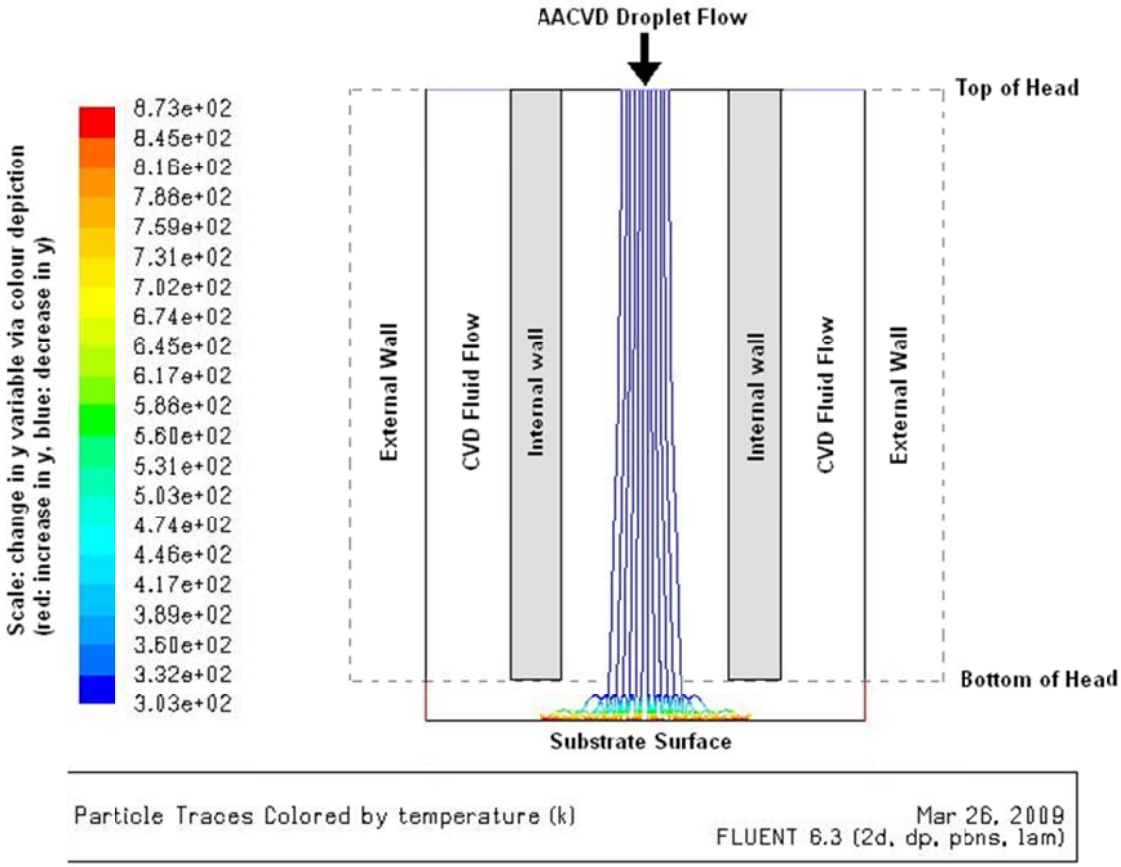

Where CVD fluid flow = air, AACVD droplet flow = MeOH

Dimensions of 2D representation: Head component: height: 70 mm, width: 55 mm, diameter of inlet pipes: 3.5 mm, height to substrate surface: 10 mm.

Results for droplet size comparison from 2 mm to 0.005 mm displayed a preferred solvent droplet size of 0.04 mm to reach the glass substrate at 600 °C, a factor of ten above the average nebulised AACVD droplet size (0.005 mm), changing the velocity of the AACVD flow rate did not affect the size of the solvent droplet required to reach the substrate surface, see fig. 25 a-d). Addition of the discrete thermophoretic model did not affect the result therefore the main force on the 2D simulated system was aerodynamic drag. Reynold's number for turbulence was assumed to be 3000, see appendix 2.

Figure 25: Droplet size comparison of CVD flow rate 10 l min^{-1} and AACVD flow rate 0.6 l min^{-1}: y axis variable; temperature/ k, a) to d) droplet size 0.1 to 0.005 mm

a) Droplet Size: 0.1 mm

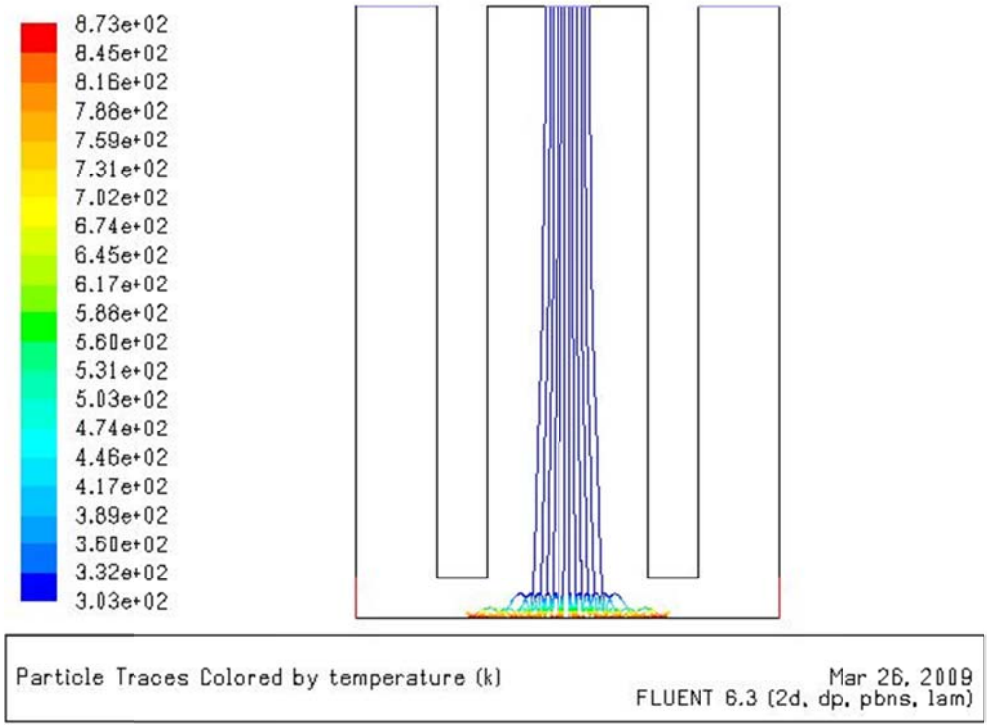

b) Droplet Size: 0.05 mm

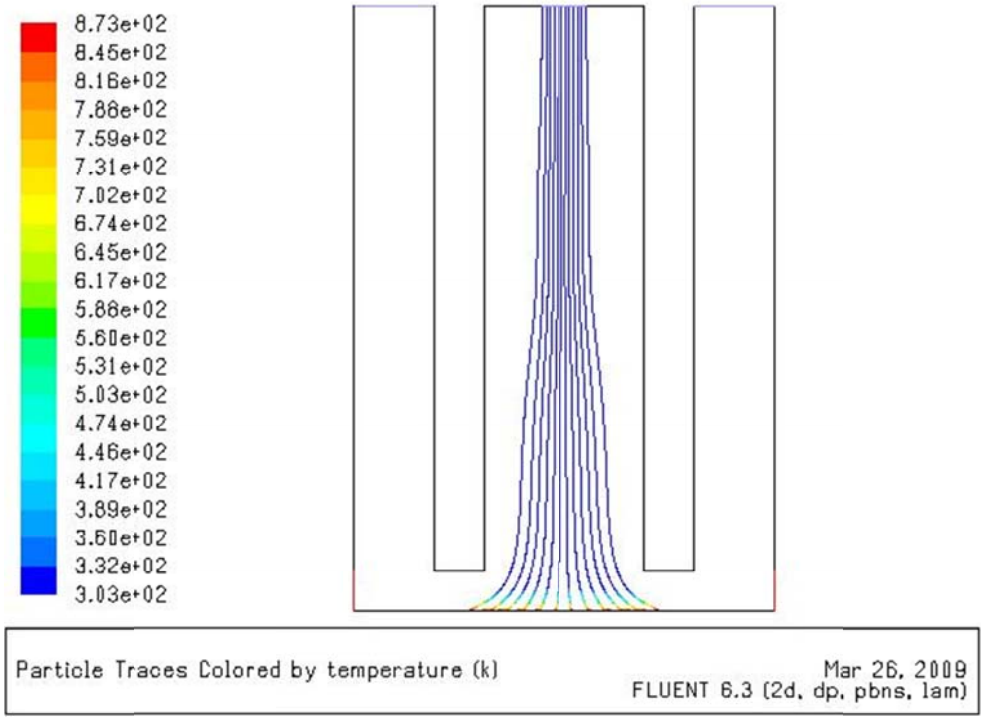

c) Droplet Size: 0.04 mm

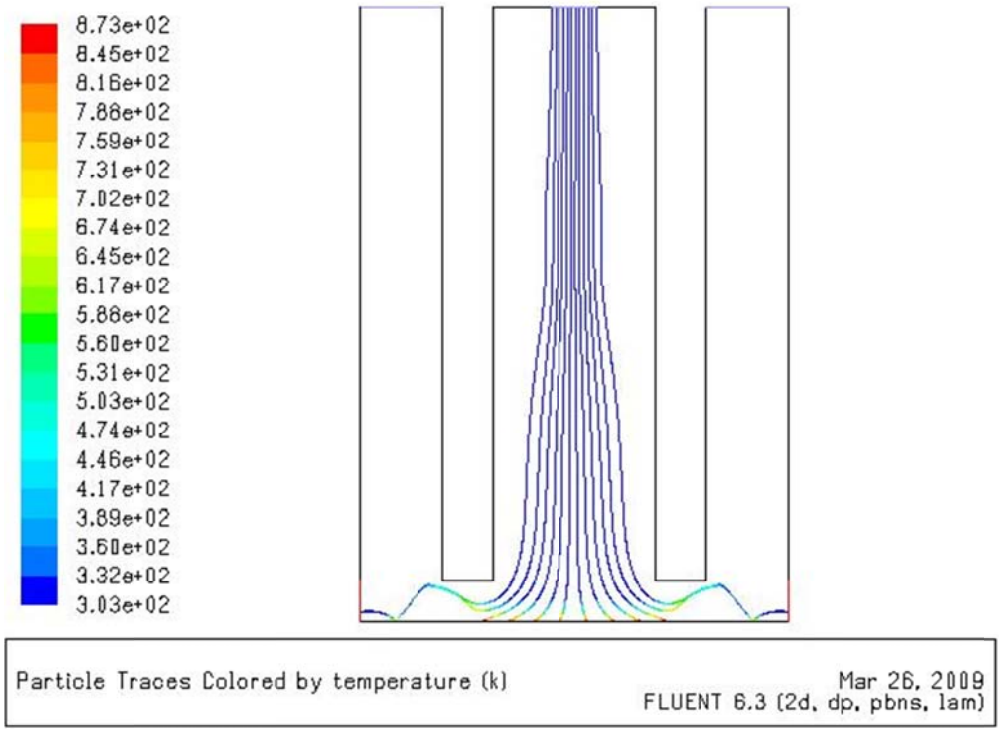

d) Droplet Size 0.005 mm

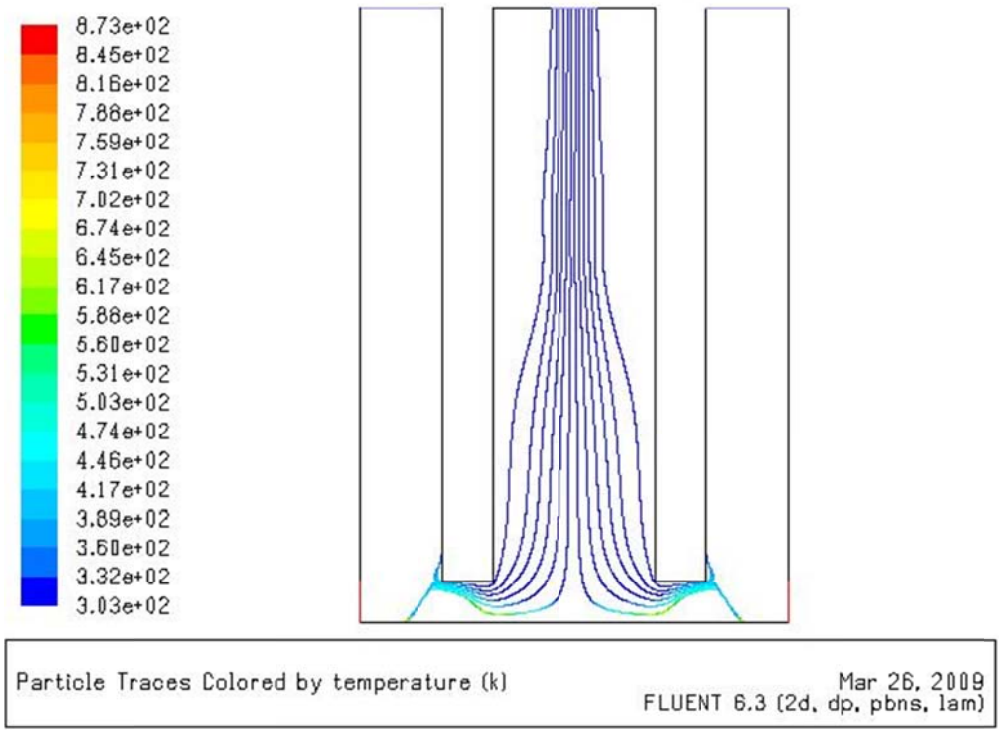

2.2.1.2 Discussion on the original combination AACVD/CVD prototype design

The 2D modelling of the original prototype AACVD/CVD prototype head using the κ-ε realizable turbulence model indicates that the critical droplet size required to reach the surface of the substrate at either 450 or 600 °C was 0.04 mm, an order of ten above the actual nebulised size achievable with the current experimental equipment (0.005 mm) available at the start of the project.

2.3.0 Five combination AACVD/CVD head designs

Common dimensions for the 5 combination AACVD/CVD model designs;

- Head designs 1 and 2: main head component, height: 70 mm, width: 120 mm, depth: 20 mm, pipe components, height: 70 mm, diameter: 3.5 mm. surrounding outlet box to substrate surface: height: 10 mm, depth >99 mm, width >99 mm.
- Head design 3: main head component, height: 70 mm, width: 90 mm, depth at top: 10 mm, depth at the bottom: 120 mm, pipe components, height: 60 mm, diameter: 3.5 mm, surrounding outlet box to substrate surface: height: 10 mm, depth >99 mm, width >99 mm.
- Head design 4 and 5: main head component, height: 70 mm, width: 90 mm, depth top of head: 10 mm, depth bottom of head: 40 mm pipe components, height: 70 mm, diameter: 3.5 mm, surrounding outlet box to substrate surface: height: 10 mm, depth >99 mm, width >99 mm.

Fluid flow type for pipe inlets on all 5 head AACVD/CVD designs: central pipe: AACVD fluid flow, side pipes: CVD fluid flow, see table 7.

Table 7: Model head designs

Head 1	**Head 2**	**Head 3**	**Head 4**	**Head 5**
Inlets parallel to box head chamber	CVD inlets at 90 º angle to box head chamber	Inlets parallel to a 40 º graduated head	CVD inlets at 90 º angle to a 15 º graduated head	Inlets parallel to a 15 º graduated head

Where possible computational effort has been halved by simulating half the model head, on the interior plane of symmetry, for mesh schemes for the five combination AACVD/CVD head designs, see fig. 26 a-e).

Figure 26: Volume mesh schemes for head designs 1 to 5

a) Head Design 1: hex/tet

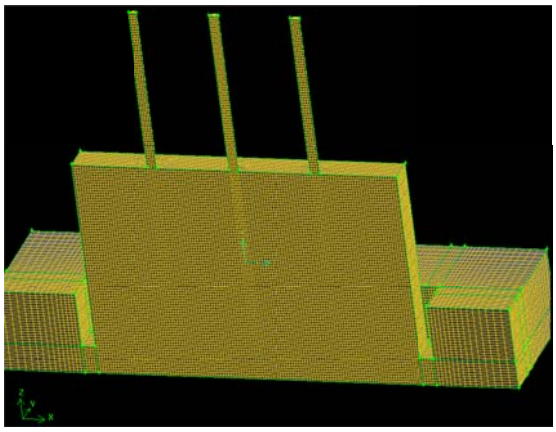

b) Head Design 2: hex/tet

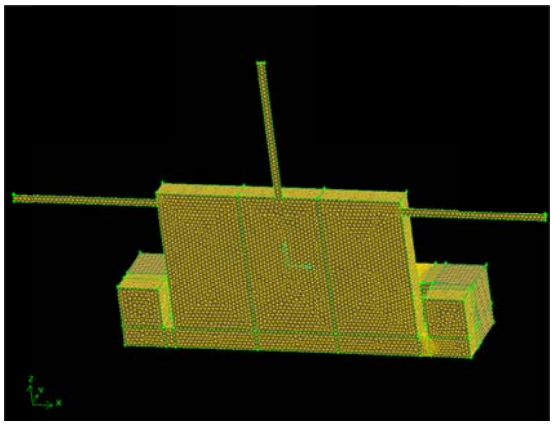

c) Head Design 3: tet/hex core

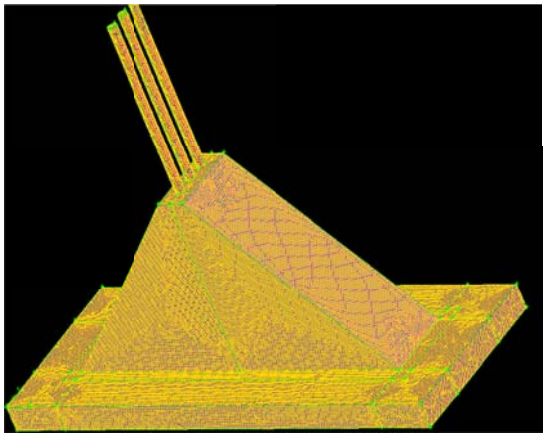

d) Head Design 4: tet/hybdrid

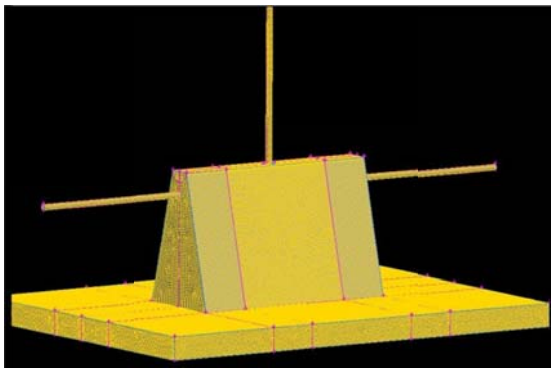

e) Head Design 5: tet/hybrid/hex core

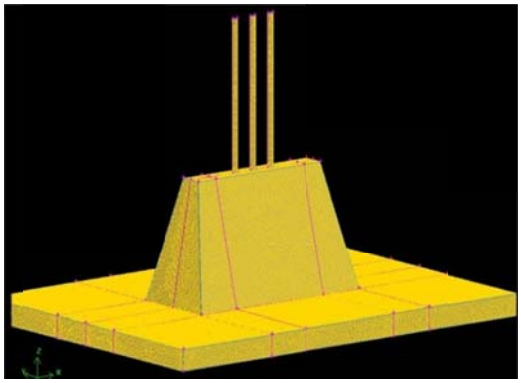

- A hex-dominant mesh usually requires decomposition, and is used primarily for prismatic geometries.
- A tet-dominant mesh is appropriate for complex geometries. Usually, size functions and boundary layers are used to grade the mesh.
- A HexCore mesh is used to lower the cell count and improve overall mesh quality, for flow volumes with complexity near the walls and a large core region.

2.3.1 Methods and simulations for the 5 AACVD/CVD head designs

CFD Parameters: The Fluent™ 3ddp κ-ε realizable model was used with full multigrid (fmg) initialization for 3D modelling. Reynold's number was used as a guide to the point of turbulence at 3000, (14.42 m/s = 8.32 l/min). The default settings were used, (fluid: air, nearest model to reality, wall materials: aluminium), no heat transference models were used for the simulations on fluid flow only; heat transference models were used for the evaporation simulation. First order equations were used for better convergence versus second order equation accuracy, as the resolution of each mesh was very high and therefore second order equations would not bring a significant improvement to accuracy over the computational effort required to achieve a minor improvement. The following fluid flow, m/s, regimes were considered, see table 8 and 9.

Table 8: The main velocity, m/s, scenario's for the AACVD and CVD inlet fluid flows (air) chosen for testing on the 5 head designs, given case numbers 1 to 5.

Case Number	AACVD Flow Rate/ m/s	CVD Flow Rate/ m/s
1	8.32	14.42
2	10.00	17.39
3	17.39	17.39
4	4.32	8.32
5*	14.42	8.00

Key: *Case 5 calculated for head design 4 only.

Table 9: Other velocity, m/s, scenarios for the AACVD and CVD inlet flows tested on a number of the head designs.

Head Design	AACVD Flow Rate/ m/s	CVD Flow Rate/ m/s
1	8.32	8.32
1, 2	8.32	17.39
1	4.32	4.32
1	4.32	8.32
2, 3	8.32	17.39
1, 2	8.32	10.00
3	4.32	10.00

2.3.1.1 Five combination AACVD/CVD head designs results

The fluid flow (air) model for the five reaction head designs was assessed using the κ-ε realizable model and particle trajectory and evaporation model was assessed for head design 4 only; using the κ-ε realizable and κ-ω SST model with spherical solvent droplets (MeOH and water) at various droplet sizes (0.1-0.0001 mm), see figs. 27-31 and figs. 142-153 in appendix 3. The first four fluid flow (air models) cases were calculated for all five head designs and the fluid flow (air models) case 5 was calculated for head design 4 only, see table 8.

2.3.1.1.1 Reaction head design 1

The velocity, turbulent intensity, turbulent kinetic energy and dissipation rate results for fluid flow cases 1, 2, 3 and 4 for head design 1, see table 8, are displayed from the 3D view of the interior plane (plane symmetry of the model) and indicate that the AACVD fluid flow of droplets, from the central inlet, is insufficient and that no substantial mix occurs between the three fluid flows and a drop off in the velocity and turbulent rate for the central AACVD fluid flow occurs; the fig. 27 a-e) and 138 a-d), 139 a-f), 140 a-g), appendix 3 . In particular for fluid flow case 4 there is also an expected significant drop off in both velocity and turbulent energy/viscosity for the central AACVD fluid flow with the contours of turbulent viscosity plot of the AACVD fluid flow 'sat' in the middle of the head space, see fig. 140 g), appendix 3. The velocity and turbulent kinetic energy plots also indicate no significant mixing of the three fluid flows and a slight drop off in the velocity turbulent kinetic energy for

the central AACVD fluid flow, see fig. 27 f-g) and 138 e-f), 139 g-h), 140 h-i), appendix 3. The probable synthesis outcome would be either no inclusion or a very chaotic non-uniform inclusion of nanoparticles within the host metal oxide matrix thin film.

Figure 27: Head 1, fluid flow case 1: 3D view of the interior plane/plane of symmetry of the model, a) contours of velocity, b) velocity vectors/ m/s, c) pathlines of velocity/ m/s, d) contours of turbulent intensity/ %, e) contours of dissipation rate/ m^2/s^3, f) graph velocity magnitude/ m/s, g) graph of turbulent kinetic energy/ m^2/s^2.

a)

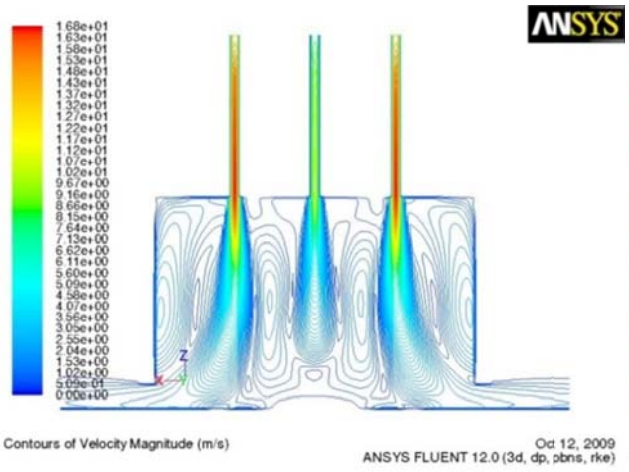

b)

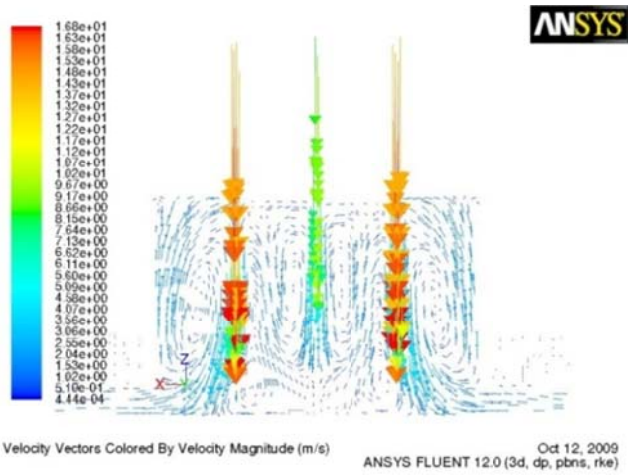

c)

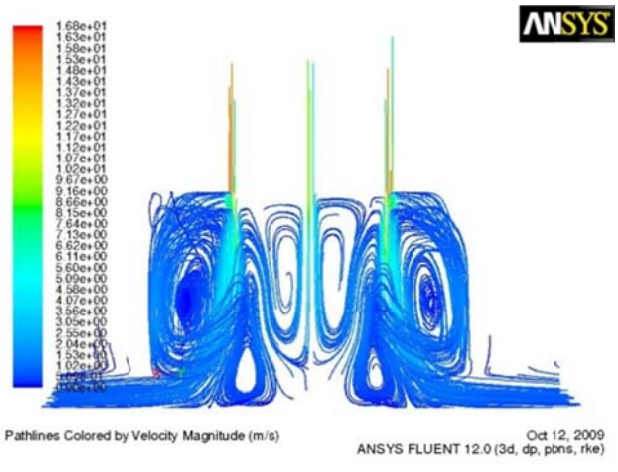

d)

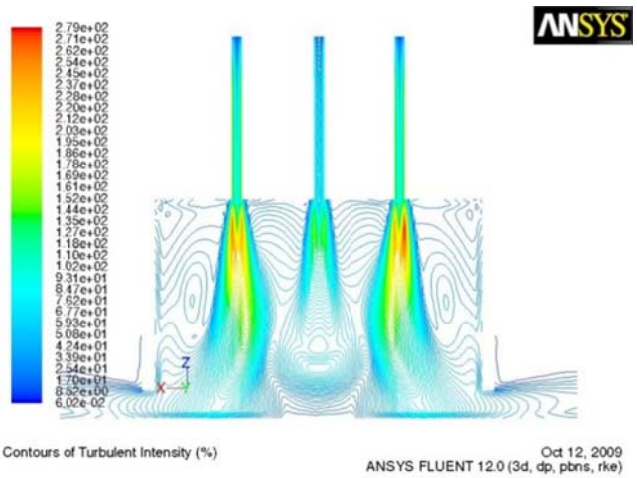

e)

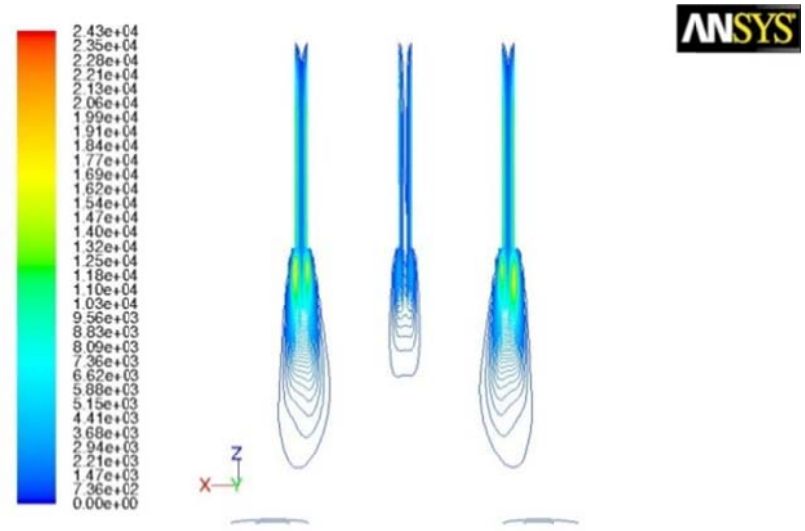

f)

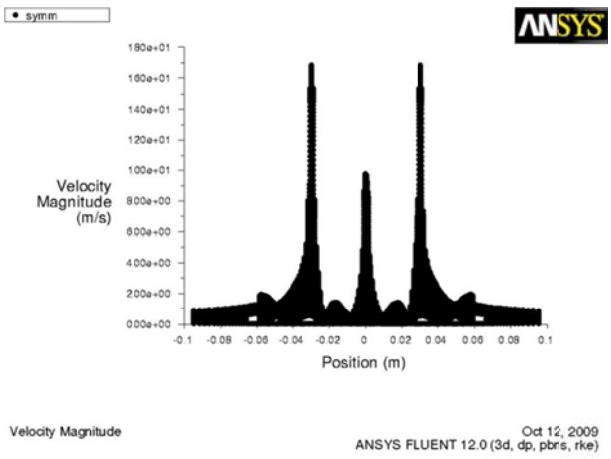

g)

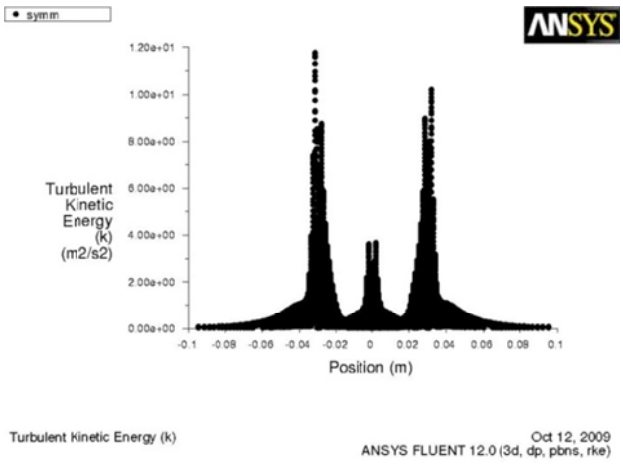

2.3.1.1.2 Reaction head design 2

The velocity, turbulent intensity, turbulent kinetic energy and dissipation rates for fluid flow cases 1, 2, 3 and 4 for head design 2, see table 8, are displayed from the 3D view of the interior plane and indicates no significant mixing of the three fluid flows and a drop off in flow for the central AACVD fluid flow, there is a substantial indication that the flow also veers to one side of the head and would therefore most likely form a non-uniform thin film, see figs. 28 a-f) and 141 a-f), 142 a-f), 143 a-f), appendix 3. The velocity magnitude and kinetic turbulent kinetic energy plots also

indicate the significant decrease in the fluid flow of the central AACVD inlet and the veering of the fluid flow to one side of the head appears to occur as the turbulent kinetic energy of one CVD inlet appears to drop off more rapidly than the other CVD inlet, see figs. 28 g-h) and 141 g-h), 142 g-h), 143 g-h), appendix 3. The probable synthesis outcome would be either no inclusion or a very non-uniform inclusion of nanoparticles within the host metal oxide matrix thin film.

Figure 28: Head 2, fluid flow case 1: 3D view of the interior plane/plane of symmetry of the model, a) contours of velocity/ m/s, b) velocity vectors/ m/s, c) pathlines of velocity/ m/s, d) contours of turbulent intensity/ %, e) contours of dissipation rate/ ms/s^3, f) contours of turbulent kinetic energy/ m^2/s^2, g) graph velocity magnitude/ m/s, h) graph of turbulent kinetic energy/ m^2/s^2.

a)

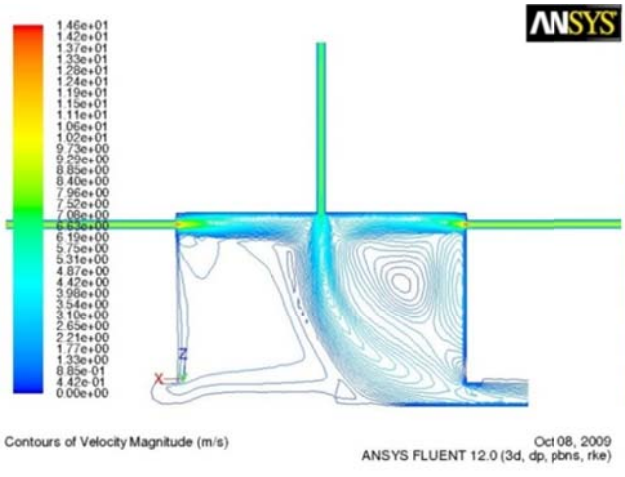

b)

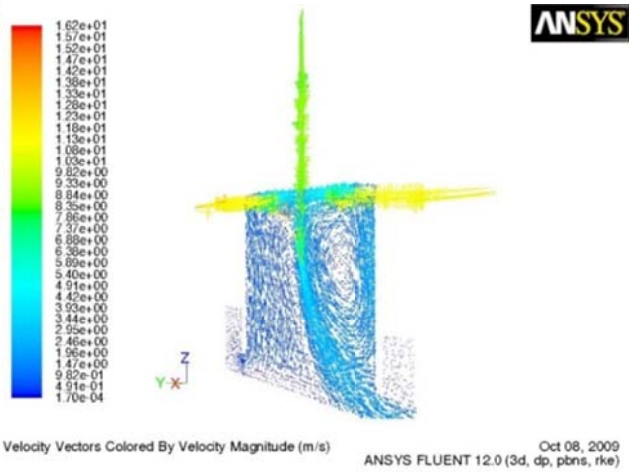

c)

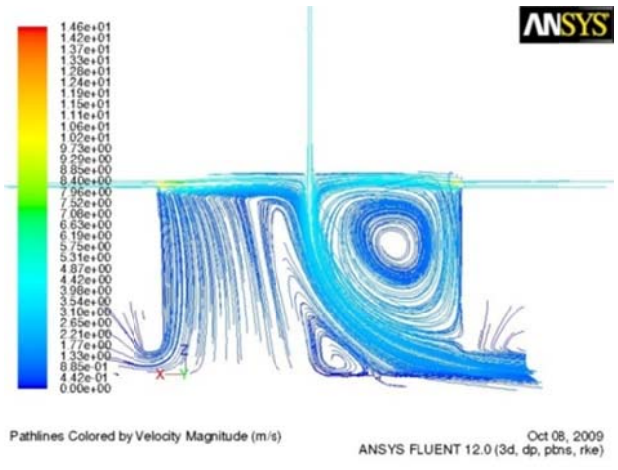

d)

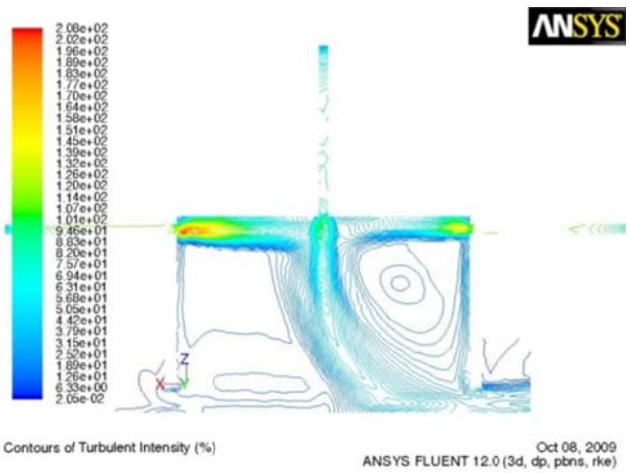

e)

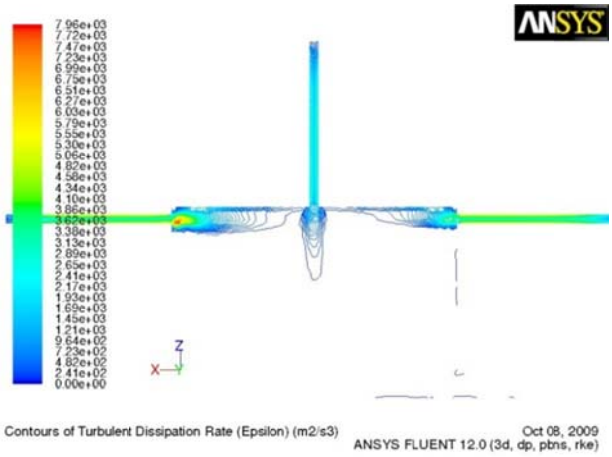

Contours of Turbulent Dissipation Rate (Epsilon) (m2/s3)

Oct 08, 2009
ANSYS FLUENT 12.0 (3d, dp, pbns, rke)

f)

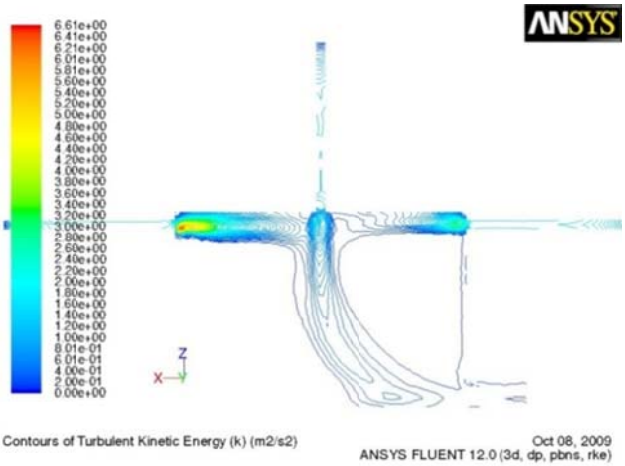

Contours of Turbulent Kinetic Energy (k) (m2/s2)

Oct 08, 2009
ANSYS FLUENT 12.0 (3d, dp, pbns, rke)

g)

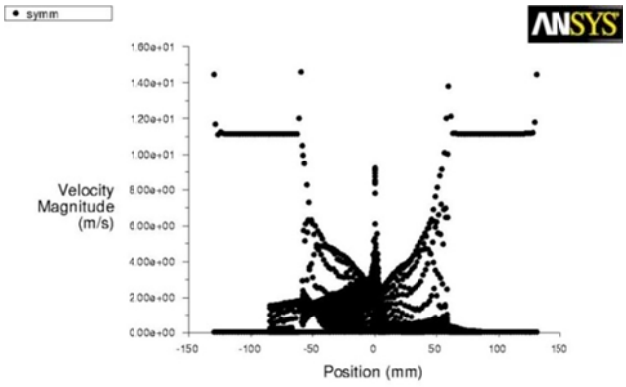

Velocity Magnitude

Oct 08, 2009
ANSYS FLUENT 12.0 (3d, dp, pbns, rke)

h)

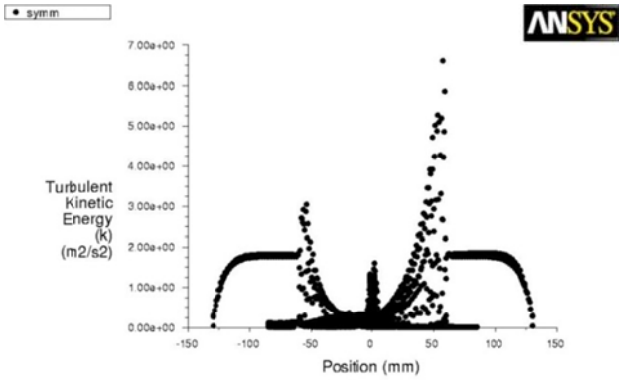

Turbulent Kinetic Energy (k)

Oct 08, 2009
ANSYS FLUENT 12.0 (3d, dp, pbns, rke)

2.3.1.1.3 Reaction head design 3

The velocity, turbulent intensity, turbulent kinetic energy and dissipation rate results for fluid flow cases 1, 2, 3 and 4 for head design 3, see table 8, are displayed from the 3D view of the interior plane and indicate significant fluid flow drop upon entering the reaction chamber head and the pathline results for both velocity and turbulent kinetic energy appear to indicate no significant mixing of the three fluid flows, see fig. 29 a-f) and 144 a-f), 145 a-f), 146 a-f), appendix 3. The velocity magnitude and kinetic turbulent kinetic energy plots also indicate no significant mixing of the three fluid flows and a drop off in velocity and turbulent kinetic energy for the central AACVD fluid flow, see fig. 29 g-h) and 144 g-h), 145 g-h), 146 g-h),

appendix 3. The probable synthesis outcome would either be no inclusion or a uniform inclusion of nanoparticles within the host metal oxide matrix thin film.

Figure 29: Head 3, fluid flow case 1: 3D view of the interior plane/plane of symmetry of the model, a) contours of velocity/ m/s, b) velocity vectors/ m/s, c) pathlines of velocity/ m/s, d) contours of turbulent intensity/ %, e) contours of dissipation rate/ m^2s^3, f) contours of turbulent kinetic energy/ m^2/s^2, g) graph velocity magnitude/ m/s, h) graph of turbulent kinetic energy/ m^2/s^2.

a)

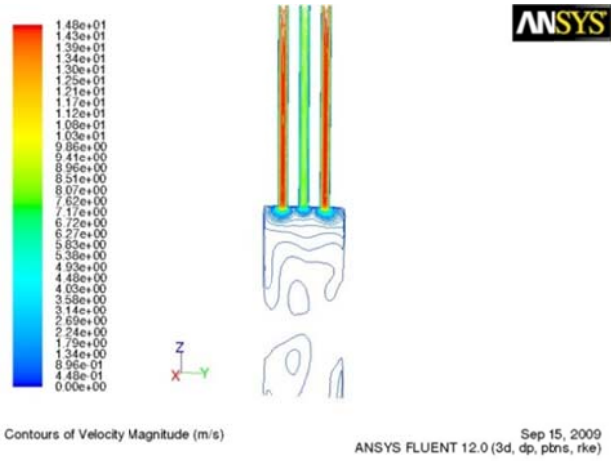

Contours of Velocity Magnitude (m/s)

Sep 15, 2009
ANSYS FLUENT 12.0 (3d, dp, pbns, rke)

b)

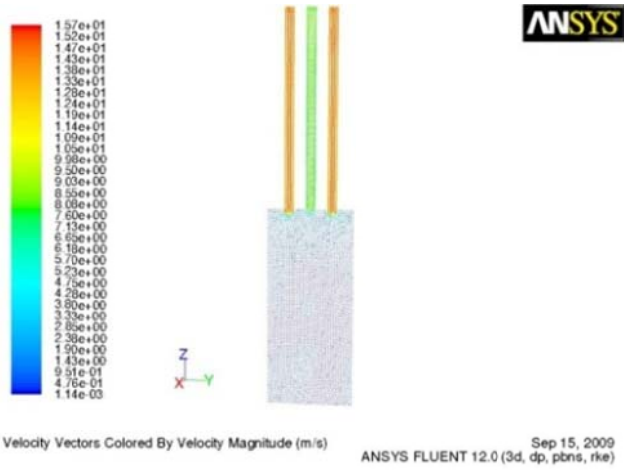

Velocity Vectors Colored By Velocity Magnitude (m/s)

Sep 15, 2009
ANSYS FLUENT 12.0 (3d, dp, pbns, rke)

c)

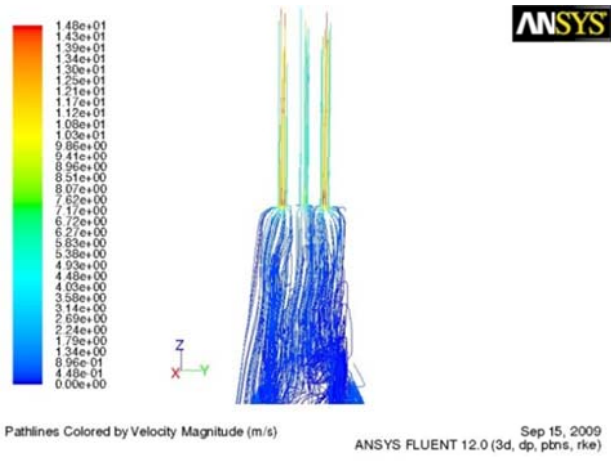

Pathlines Colored by Velocity Magnitude (m/s)

Sep 15, 2009
ANSYS FLUENT 12.0 (3d, dp, pbns, rke)

d)

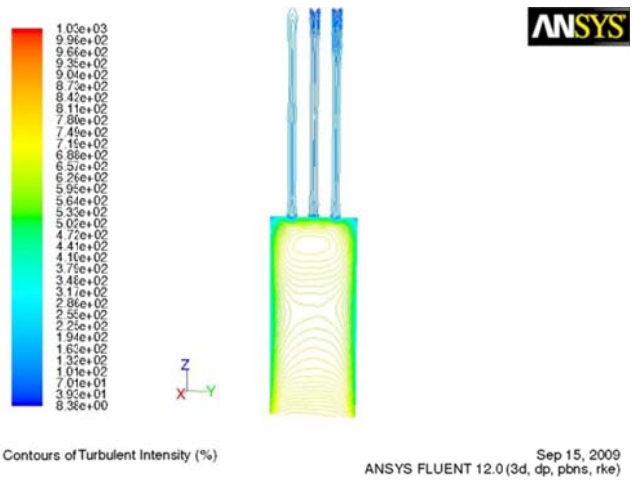

Contours of Turbulent Intensity (%)

Sep 15, 2009
ANSYS FLUENT 12.0 (3d, dp, pbns, rke)

e)

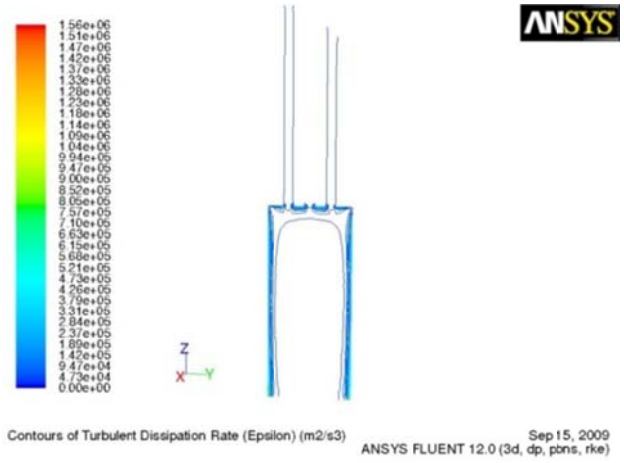

f)

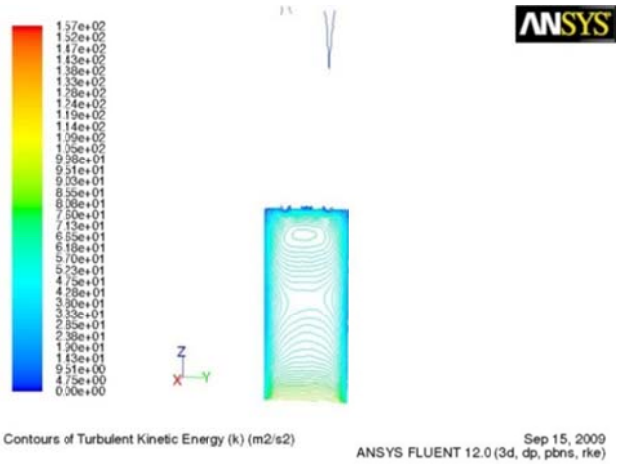

g)

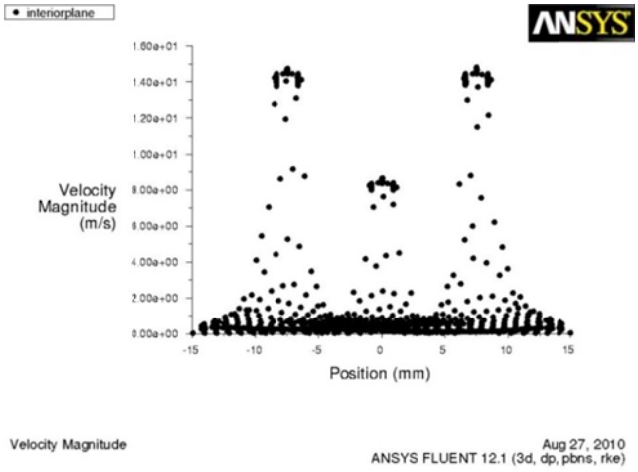

h)

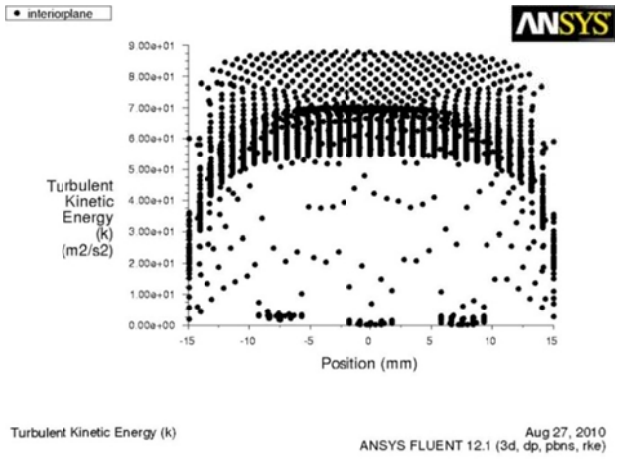

2.3.1.1.4 Reaction head design 4

The velocity, turbulent intensity, turbulent kinetic energy and dissipation rate results for fluid flow cases 1, 2, 3, 4 and 5 for head design 4, see table 8, displayed from the 3D view of the interior plane, indicate that the AACVD fluid flow of droplets, from the central inlet, appear to adequately mix with the two CVD inlet fluid flows and therefore the AACVD fluid flow travels down with the CVD fluid flow in two opposing concentric flows towards the substrate at the bottom of the reaction head, see figs. 30 a-f) and 147 a-f), 148 a-f), 149 a-f), 150 a-f), appendix 3. The velocity magnitude and turbulent kinetic energy plots however indicate that AACVD fluid flow remains in the upper part of reaction head, tending to suggest that the AACVD flow lands on the upper surfaces of the reaction chamber head see fig. 30 g-h) and

147 g-h), 148 g-h), 149 g-h), 150 g-h), appendix 3. In particular fluid flow case 5 has significant mixing of all 3 fluid flows, see fig. 35 a-k). The contour plots appear to indicate significant mixing of the 3 fluid flows with significant spread of flow towards the substrate surface. The velocity magnitude and kinetic turbulent kinetic energy plots of the AACVD inlet are significantly larger than the CVD inlets for the entire path length of the head design, see fig. 35 l-m). The probable synthesis outcome would be a uniform film with no or uniform inclusion of nanoparticles within the host metal oxide matrix thin film.

Figure 30: Head 4, fluid flow case 5: 3D view of the interior plane/plane of symmetry of the model, a and b) contours of velocity/ m/s, c and d) contours of turbulent kinetic energy/ m^2/s^2, e and f) contours of turbulent intensity/ %, g and h) contours of dissipation rate/ m^2/s^3, i) velocity vectors/ m/s, j and k) pathlines of velocity magnitude/ m/s, l) graph of velocity magnitude/ m/s, m) graph of turbulent kinetic energy/ m^2/s^2.

a) b)

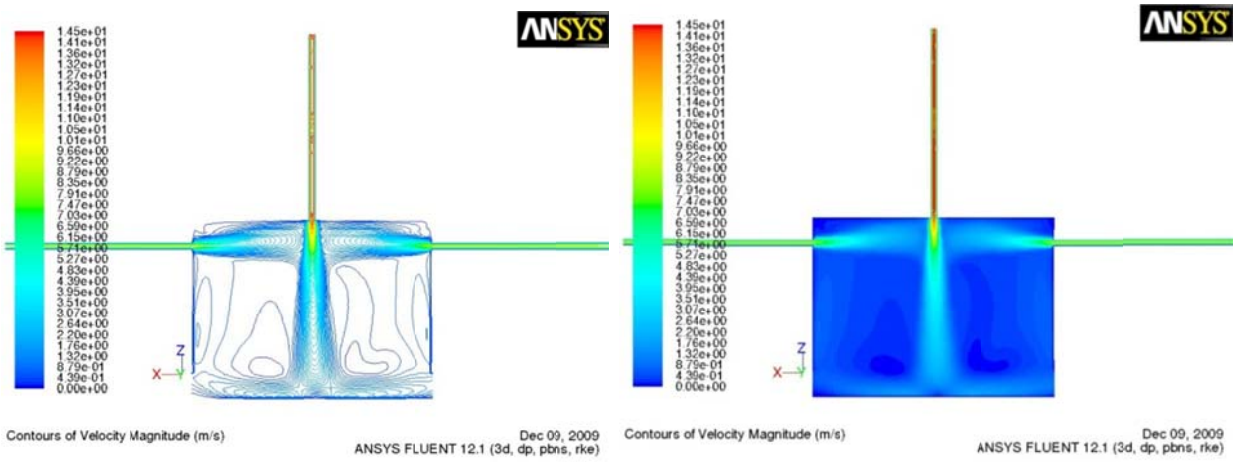

c)

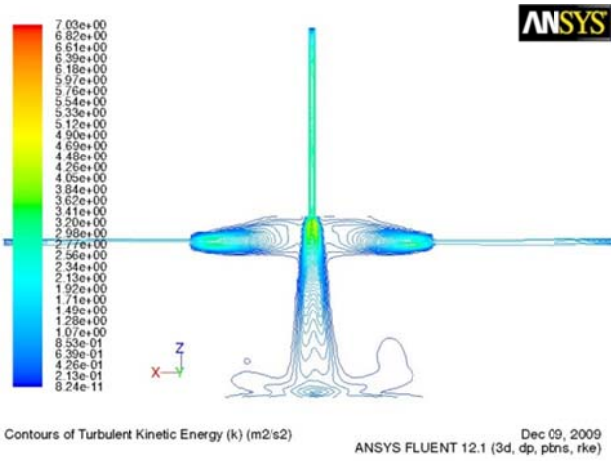

Contours of Turbulent Kinetic Energy (k) (m2/s2)

Dec 09, 2009
ANSYS FLUENT 12.1 (3d, dp, pbns, rke)

d)

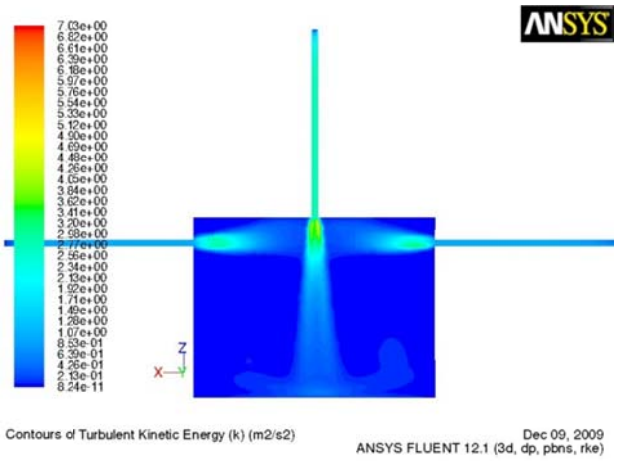

Contours of Turbulent Kinetic Energy (k) (m2/s2)

Dec 09, 2009
ANSYS FLUENT 12.1 (3d, dp, pbns, rke)

e)

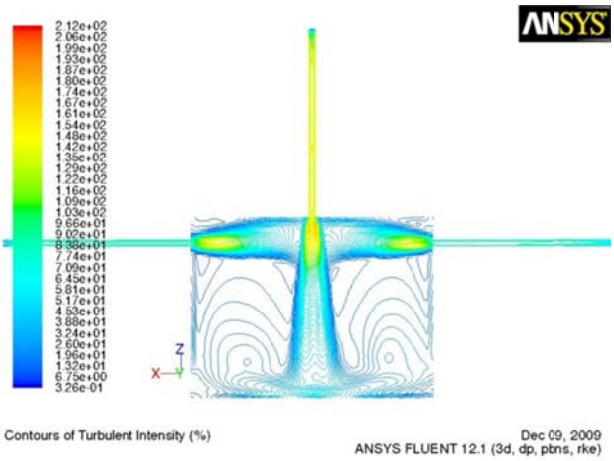

Contours of Turbulent Intensity (%)

Dec 09, 2009
ANSYS FLUENT 12.1 (3d, dp, pbns, rke)

f)

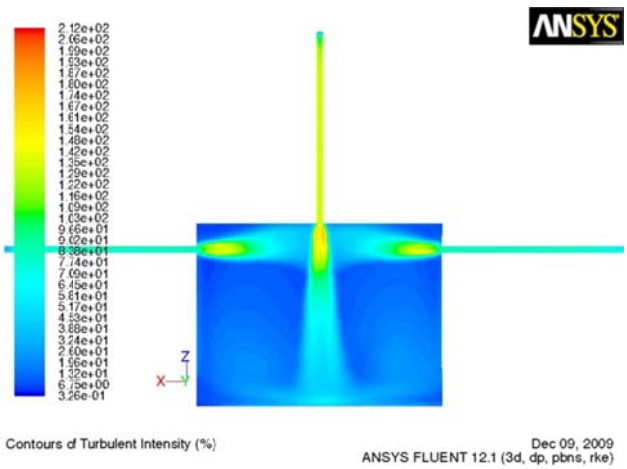

Contours of Turbulent Intensity (%)

Dec 09, 2009
ANSYS FLUENT 12.1 (3d, dp, pbns, rke)

g)

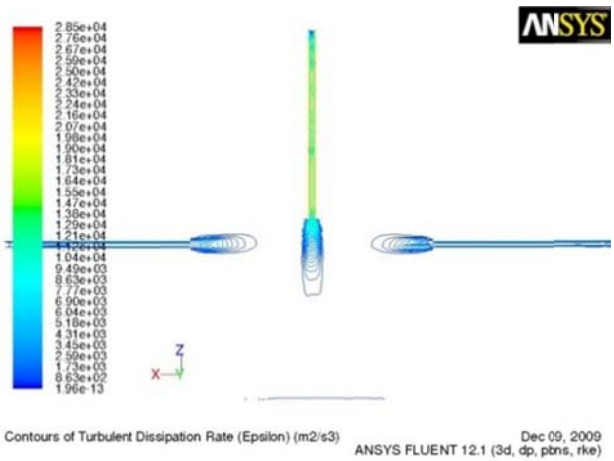

Contours of Turbulent Dissipation Rate (Epsilon) (m2/s3)

Dec 09, 2009
ANSYS FLUENT 12.1 (3d, dp, pbns, rke)

h)

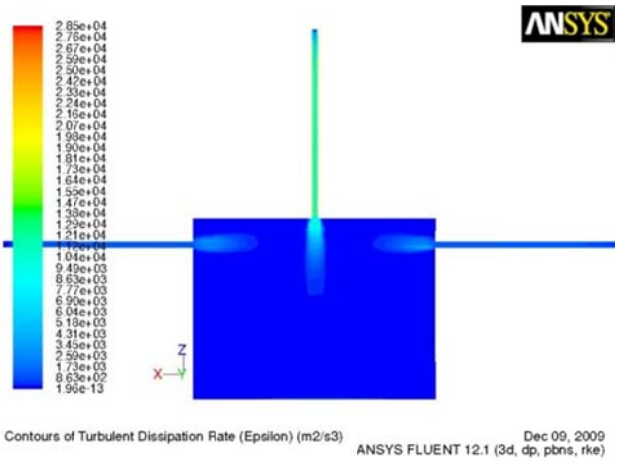

Contours of Turbulent Dissipation Rate (Epsilon) (m2/s3)

Dec 09, 2009
ANSYS FLUENT 12.1 (3d, dp, pbns, rke)

i)

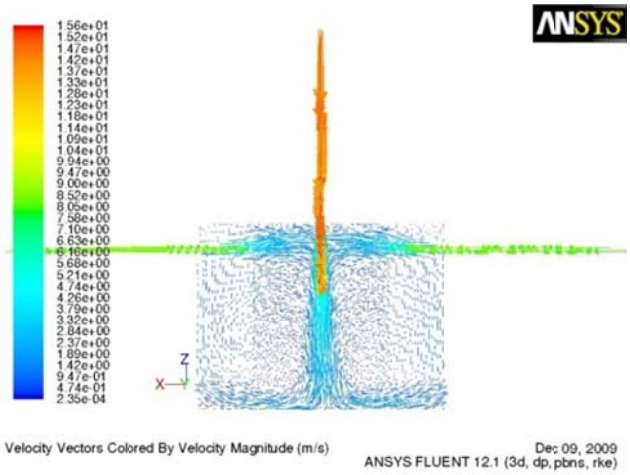
ANSYS
1.56e+01
1.52e+01
1.47e+01
1.42e+01
1.37e+01
1.33e+01
1.28e+01
1.23e+01
1.18e+01
1.14e+01
1.09e+01
1.04e+01
9.94e+00
9.47e+00
9.00e+00
8.52e+00
8.05e+00
7.58e+00
7.10e+00
6.63e+00
6.16e+00
5.68e+00
5.21e+00
4.74e+00
4.26e+00
3.79e+00
3.32e+00
2.84e+00
2.37e+00
1.89e+00
1.42e+00
9.47e-01
4.74e-01
2.35e-04
Z
X
Velocity Vectors Colored By Velocity Magnitude (m/s)
Dec 09, 2009
ANSYS FLUENT 12.1 (3d, dp, pbns, rke)

j)

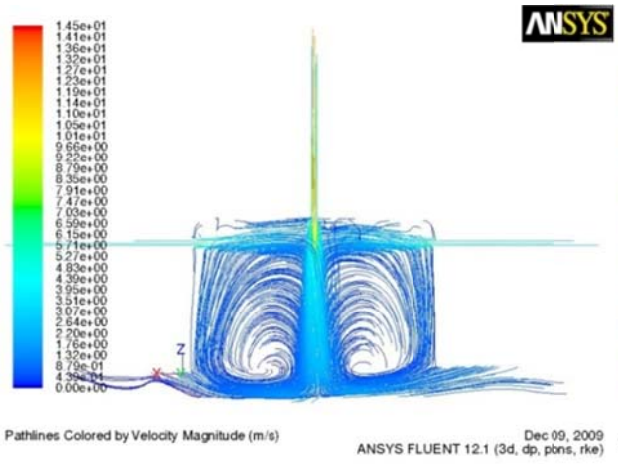
ANSYS
1.45e+01
1.41e+01
1.36e+01
1.32e+01
1.27e+01
1.23e+01
1.19e+01
1.14e+01
1.10e+01
1.05e+01
1.01e+01
9.66e+00
9.22e+00
8.79e+00
8.35e+00
7.91e+00
7.47e+00
7.03e+00
6.59e+00
6.15e+00
5.71e+00
5.27e+00
4.83e+00
4.39e+00
3.95e+00
3.51e+00
3.07e+00
2.64e+00
2.20e+00
1.76e+00
1.32e+00
8.79e-01
4.39e-01
0.00e+00
Z
X
Pathlines Colored by Velocity Magnitude (m/s)
Dec 09, 2009
ANSYS FLUENT 12.1 (3d, dp, pbns, rke)

k)

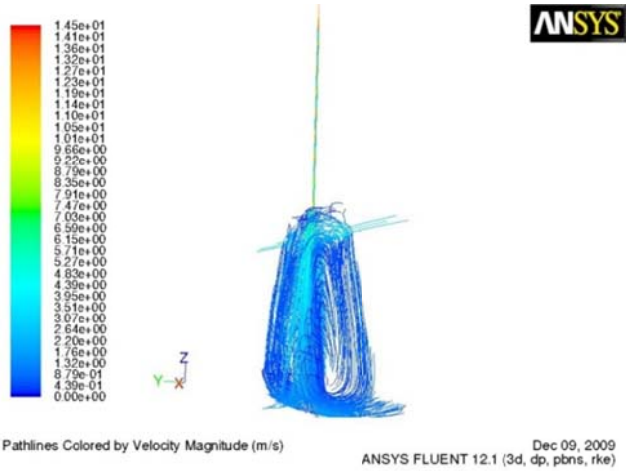
ANSYS
1.45e+01
1.41e+01
1.36e+01
1.32e+01
1.27e+01
1.23e+01
1.19e+01
1.14e+01
1.10e+01
1.05e+01
1.01e+01
9.66e+00
9.22e+00
8.79e+00
8.35e+00
7.91e+00
7.47e+00
7.03e+00
6.59e+00
6.15e+00
5.71e+00
5.27e+00
4.83e+00
4.39e+00
3.95e+00
3.51e+00
3.07e+00
2.64e+00
2.20e+00
1.76e+00
1.32e+00
8.79e-01
4.39e-01
0.00e+00
Z
Y
X
Pathlines Colored by Velocity Magnitude (m/s)
Dec 09, 2009
ANSYS FLUENT 12.1 (3d, dp, pbns, rke)

l)

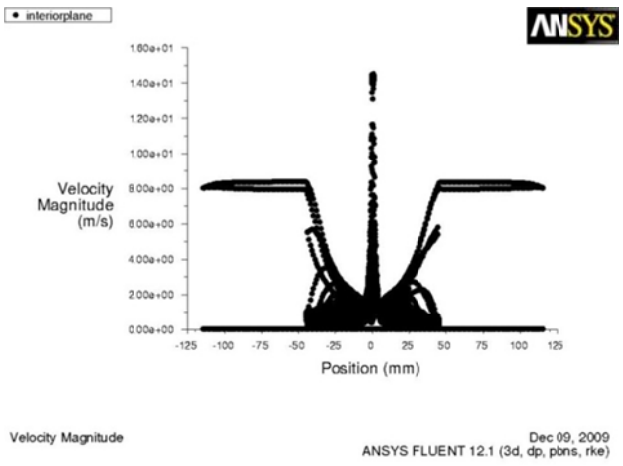
interiorplane
ANSYS
Velocity Magnitude (m/s)
1.60e+01
1.40e+01
1.20e+01
1.00e+01
8.00e+00
6.00e+00
4.00e+00
2.00e+00
0.00e+00
-125
-100
-75
-50
-25
0
25
50
75
100
125
Position (mm)
Velocity Magnitude
Dec 09, 2009
ANSYS FLUENT 12.1 (3d, dp, pbns, rke)

m)

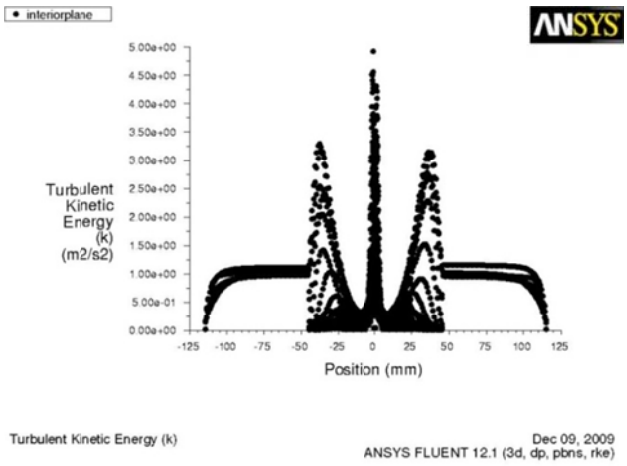
interiorplane
ANSYS
Turbulent Kinetic Energy (k) (m2/s2)
5.00e+00
4.50e+00
4.00e+00
3.50e+00
3.00e+00
2.50e+00
2.00e+00
1.50e+00
1.00e+00
5.00e-01
0.00e+00
-125
-100
-75
-50
-25
0
25
50
75
100
125
Position (mm)
Turbulent Kinetic Energy (k)
Dec 09, 2009
ANSYS FLUENT 12.1 (3d, dp, pbns, rke)

2.3.1.1.5 Reaction head design 5

The velocity, turbulent intensity, turbulent kinetic energy and dissipation rate results for fluid flow cases 1, 2, 3 and 4 for head design 5, see table 8, are displayed from the 3D view of the interior plane and indicate insufficient mixing of the central AACVD fluid flow with the two CVD fluid flows; the AACVD fluid flow appears to remain in the upper part of the reaction chamber head; indicating that the AACVD fluid flow would probably land on the upper surfaces of the reaction chamber, see fig. 31 a-e) and 151 a-d), 152 a-f), 153 a-e), appendix 3. The velocity magnitude and kinetic turbulent kinetic energy plots also indicate no significant mixing of the three fluid flows and a drop off in the velocity magnitude and turbulent kinetic energy for the central AACVD fluid flow, see fig. 31 f-g) and 151 e-f), 152 g-h), 153 f-g), appendix 3. The probable synthesis outcome would be either no inclusion or a non-uniform inclusion of nanoparticles within the host metal oxide matrix thin film.

Figure 31: Head 5, fluid flow case 1: 3D view of the interior plane/plane of symmetry of the model, a) contours of velocity/ m/s, b) velocity vectors/ m/s, c) contours of turbulent intensity/ %, d) contours of dissipation rate/ m^2/s^3, e) contours of turbulent kinetic energy/ m^2/s^2, f) graph of velocity magnitude/ m/s, g) graph of turbulent kinetic energy/ m^2/s^2.

a) b)

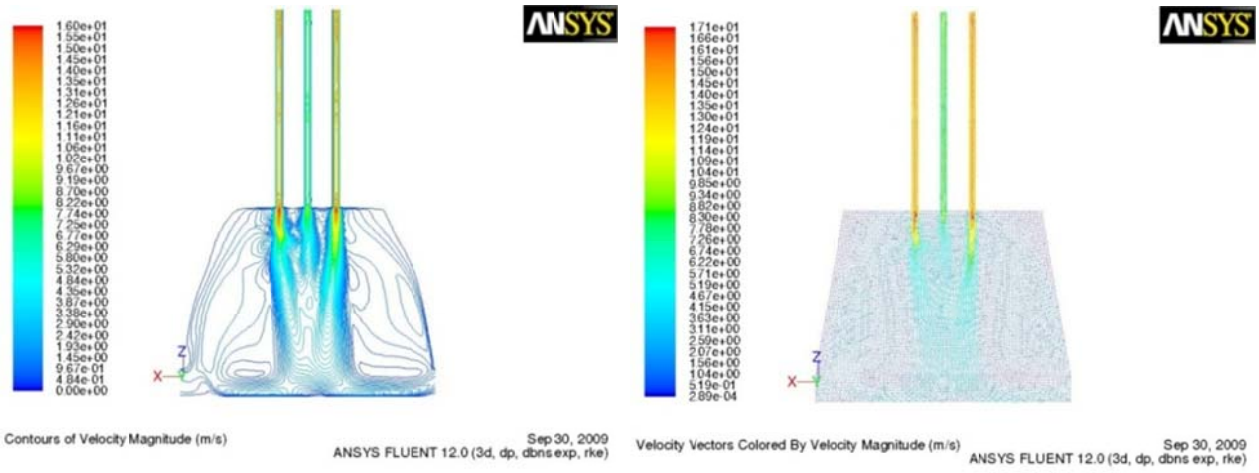

c)

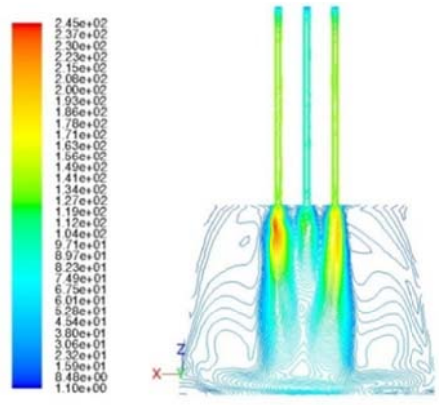

Contours of Turbulent Intensity (%)

Sep 30, 2009
ANSYS FLUENT 12.0 (3d, dp, dbns exp, rke)

d)

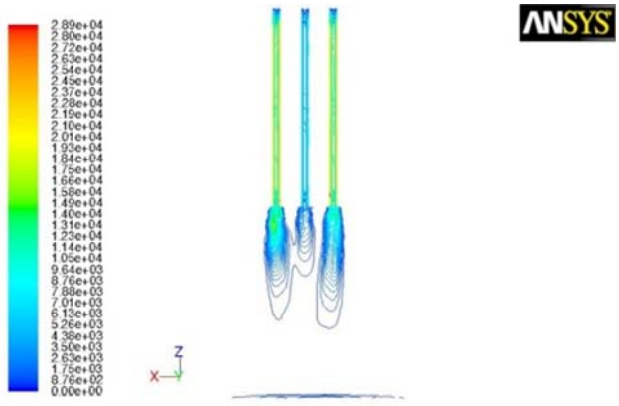

Contours of Turbulent Dissipation Rate (Epsilon) (m2/s3)

Sep 30, 2009
ANSYS FLUENT 12.0 (3d, dp, dbns exp, rke)

e)

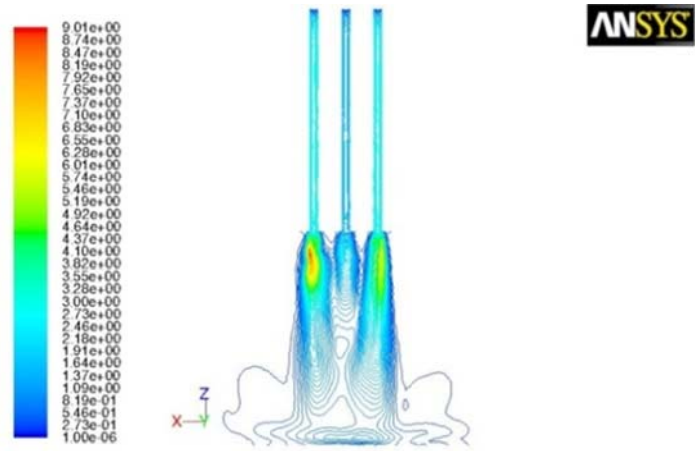

Contours of Turbulent Kinetic Energy (k) (m2/s2)

Sep 30, 2009
ANSYS FLUENT 12.0 (3d, dp, dbns exp, rke)

f)

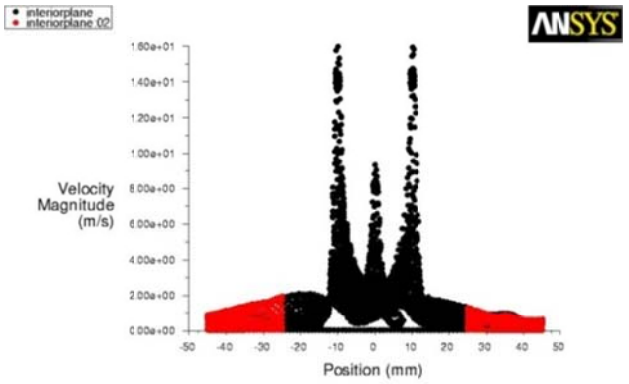

Velocity Magnitude

Sep 30, 2009
ANSYS FLUENT 12.0 (3d, dp, dbns exp, rke)

g)

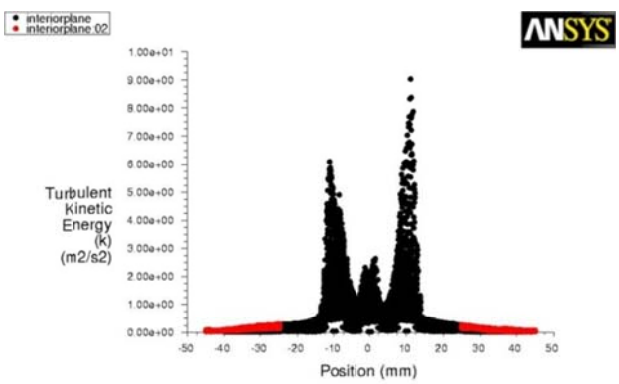

Turbulent Kinetic Energy (k)

Sep 30, 2009
ANSYS FLUENT 12.0 (3d, dp, dbns exp, rke)

2.3.1.2 Discussion on fluid flow (air model) results for the 5 AACVD/CVD head designs

Head designs 1, 2, 3, and 5 appear to have no significant mixing of the three fluid flows (air models), CVD and AACVD, and the most probable outcome of synthesis would be no inclusion or non-uniform inclusion of nanoparticles into the metal oxide host matrix thin film and formation of non-uniform thin film on the substrate surface. Head design 4 appears to indicate significant mixing of the three fluid flows and the most likely design to produce a uniform thin film with uniform inclusion of nanoparticles within the host metal oxide thin film on the substrate surface. According to the air modelling the inlet velocity rates most likely to produce even mixing of the AACVD fluid flow and the CVD fluid flows was case 5 which had a faster inlet velocity rate for the AACVD fluid flow (14.42 m/s) than the CVD fluid flow (8.00 m/s). Reaction head design 4 appeared to have the best fluid flow (air model) profile for producing a uniform film with the prospect of nanoparticle inclusion and was therefore used to in the calculate particle trajectory and evaporation modelling work below.

2.4.0 Particle trajectory and evaporation model results head 4, case 3

Head 4, Case 3: Heat model used: energy equations turned on, glass substrate set to 600 ºC, Discrete phase modelling turned on for particle trajectory modelling of solvent droplets (MeOH or water) and substrate surface boundary set to trap if hit by droplet (assumption that no droplet escapes once trapped).

Model parameters for discrete phase, particle AACVD inlet velocity (17.39 m/s), point properties include various droplet sizes (0.1-0.0001 mm), flow rate: 0.0001 kg/s (0.1 g/s), turbulent dispersion set at default, drag laws set to spherical, additional discrete model used was thermophoresis and the energy equation was used for the evaporation model with the glass substrate temperature set to 600 ºC. The surface injection of aerosol droplets at the top of the AACVD inlet gave 16 droplets per calculation, a statistical result, therefore each calculation with droplet sizes with variation in the numbers of trapped, escaped and/or evaporated droplets

were repeated 7 times to give 112 droplets and the results were averaged. Calculations of droplet sizes with no variation in the results such as 0.1/0.0001 mm *e.g.* where all droplets were either trapped, escaped or evaporated, were not necessarily repeated 7 times. The evaporation model was used with interaction with continuous phase turned on, the flow and turbulence models turned off (flow and turbulence model were previously solved in earlier calculations and did not require repeating for evaporation calculation), main assumption for turning off flow and turbulence, at this point, is that the droplet size will not affect the solved flow and turbulence model to any significant degree.

Table 10: Main droplet trajectory sizes/ mm and models, basic turbulence with/without thermophoresis and evaporation: chosen for evaluation for head design 4, case 3.

	κ-ε Realizable Model			
Droplet Size/ mm	**Without Thermophoretic**	**With Thermophoretic**	**Evaporation Model: Without Thermophoretic**	**Evaporation Model: With Thermophoretic**
0.0001	√	√	√	√
0.001	√	√	√	√
0.005*	√	√	√	√
0.01	√	√	√	√
0.02	√	√	√	√
0.03	√	√	√	√
0.031	√	-	-	-
0.032	√	-	-	-
0.033	√	-	-	-
0.034	√	-	-	-
0.035	√	-	-	-
0.036	√	-	-	-
0.037	√	-	-	-
0.038	√	-	-	-
0.039	√	-	-	-
0.04	√	√	√	√
0.1	√	√	√	√

Key: - No modelling performed at that droplet size, * average size of nebulised droplet

Combined graphs of droplet size versus percentage of droplets trapped, escaped and/or evaporated.

Figure 32: Head 4/Case 3: κ-ε realizable model of droplet size versus percentage of droplets (MeOH, 600 °C): trapped, escaped or evaporated: a) κ-ε realizable model with or without thermophoresis, b) κ-ε realizable model only, droplet size 0.03-0.04 mm) and c) κ-ε realizable model and evaporation model with/without thermophoresis.

a)

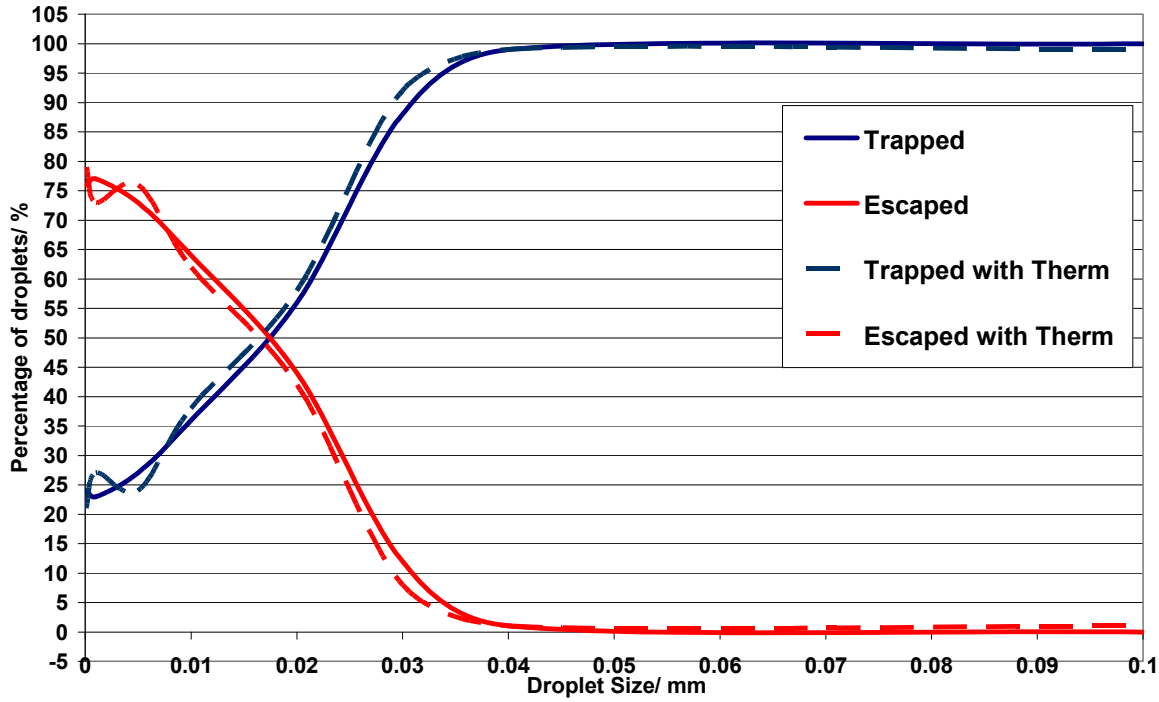

b)

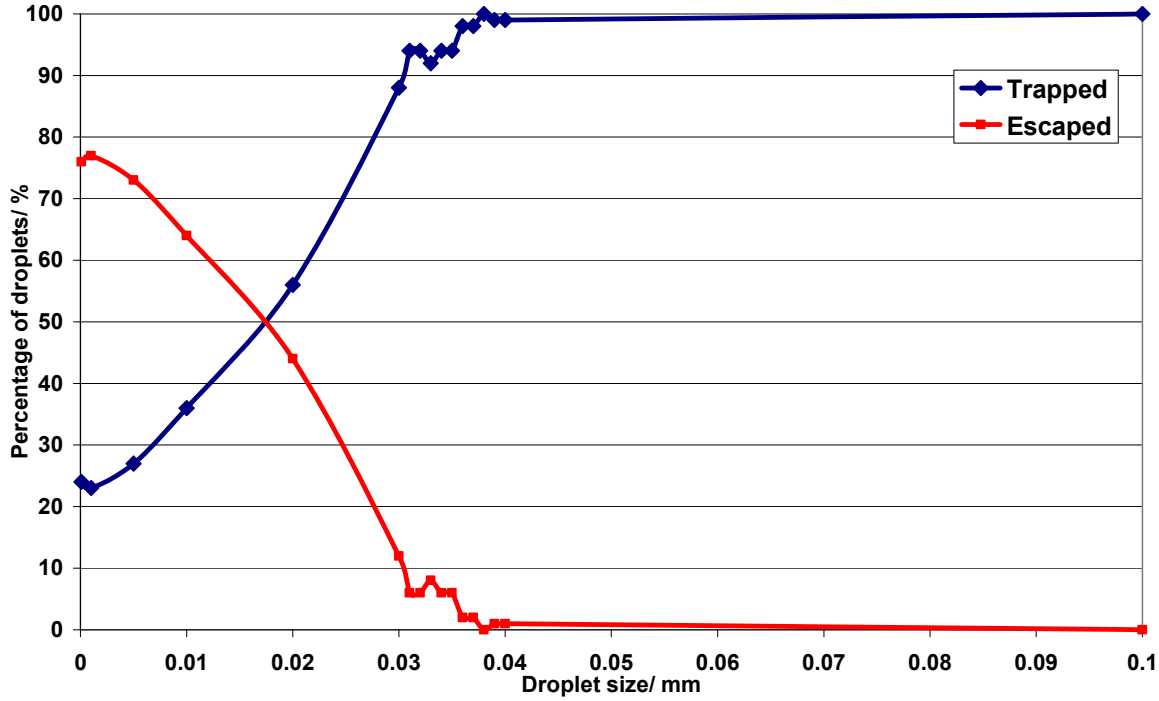
Trapped
Escaped
Percentage of droplets/ %
Droplet size/ mm
100
90
80
70
60
50
40
30
20
10
0
0
0.01
0.02
0.03
0.04
0.05
0.06
0.07
0.08
0.09
0.1

c)

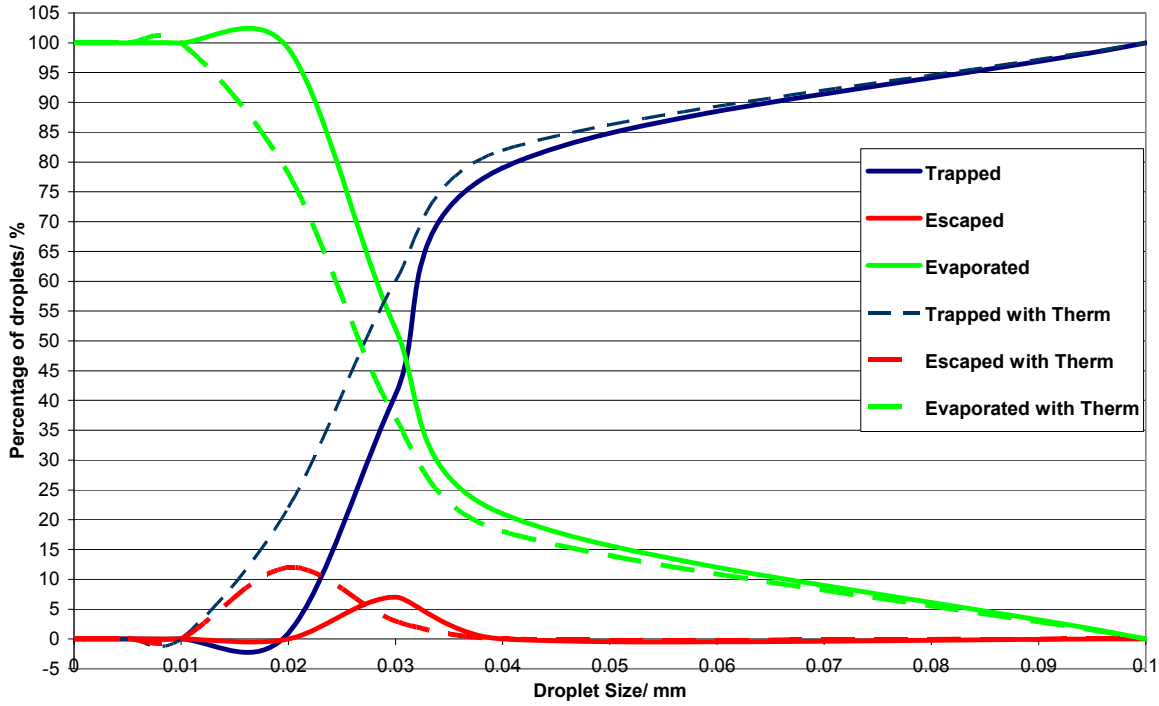
Trapped
Escaped
Evaporated
Trapped with Therm
Escaped with Therm
Evaporated with Therm
Percentage of droplets/ %
Droplet Size/ mm
105
100
95
90
85
80
75
70
65
60
55
50
45
40
35
30
25
20
15
10
5
0
-5
0
0.01
0.02
0.03
0.04
0.05
0.06
0.07
0.08
0.09
0.1

Figure 33: Head 4/Case 3: κ-ε realizable model of droplet size versus percentage of droplets (MeOH, 400 °C): trapped, escaped or evaporated: a) κ-ε realizable model with or without thermophoresis and b) κ-ε realizable model and evaporation model with/without thermophoresis.

a)

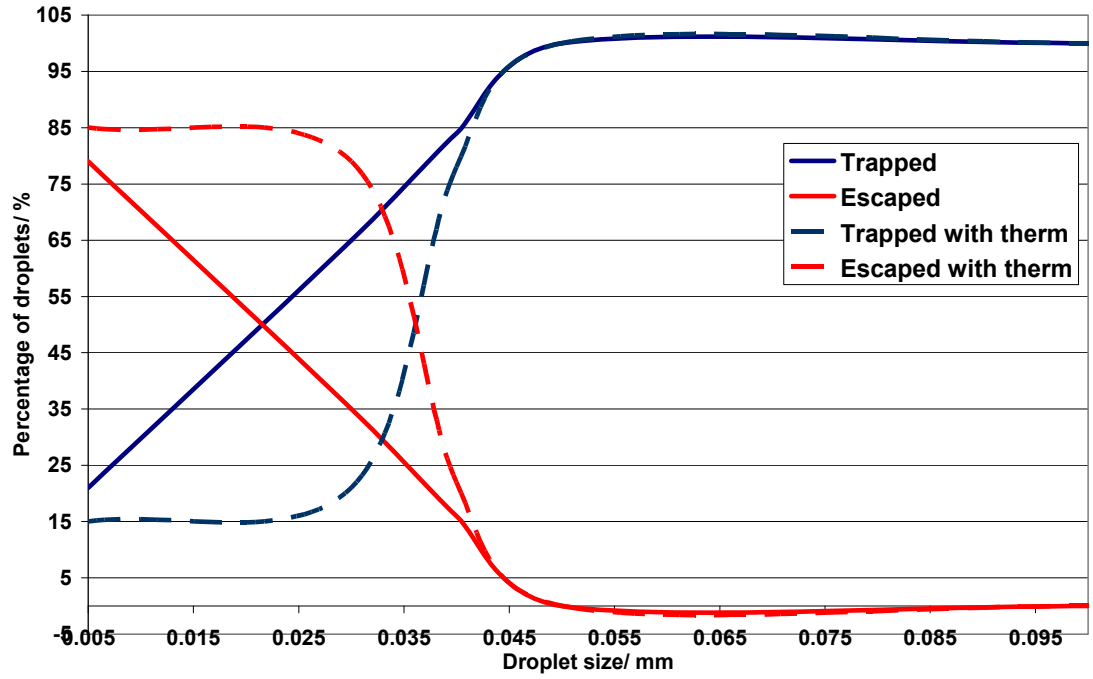

b)

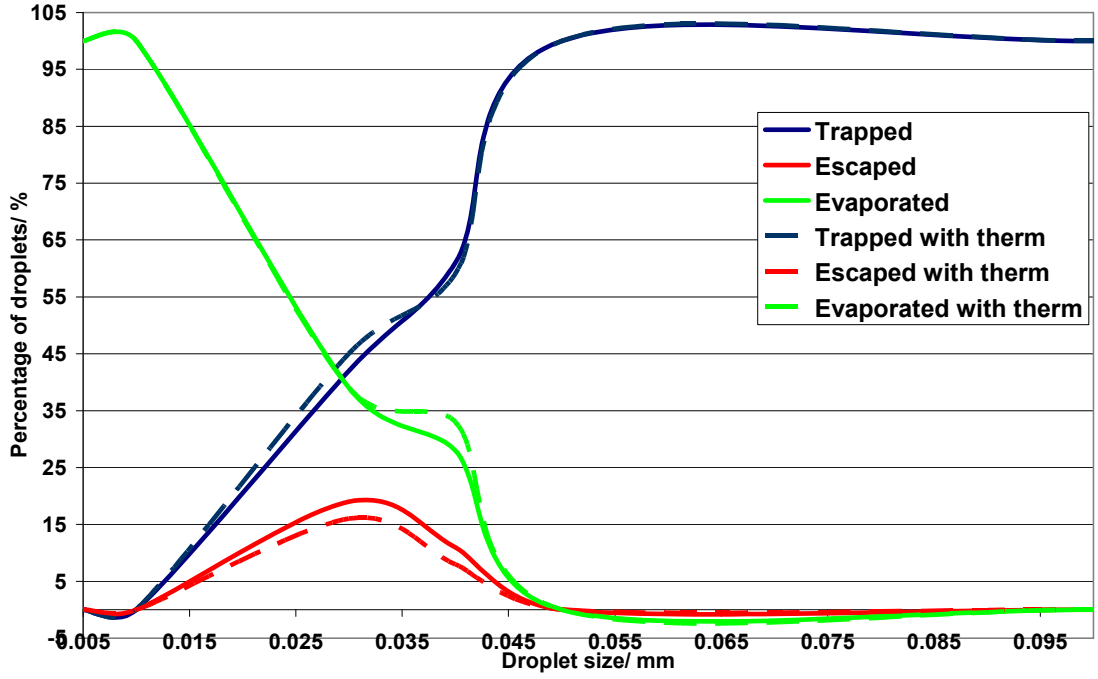

Figure 34: Head 4/Case 3: κ-ε realizable model of droplet size versus percentage of droplets (Water, 600 °C): trapped, escaped or evaporated: a) κ-ε realizable model with or without thermophoresis and b) κ-ε realizable model and evaporation model with/without thermophoresis.

a)

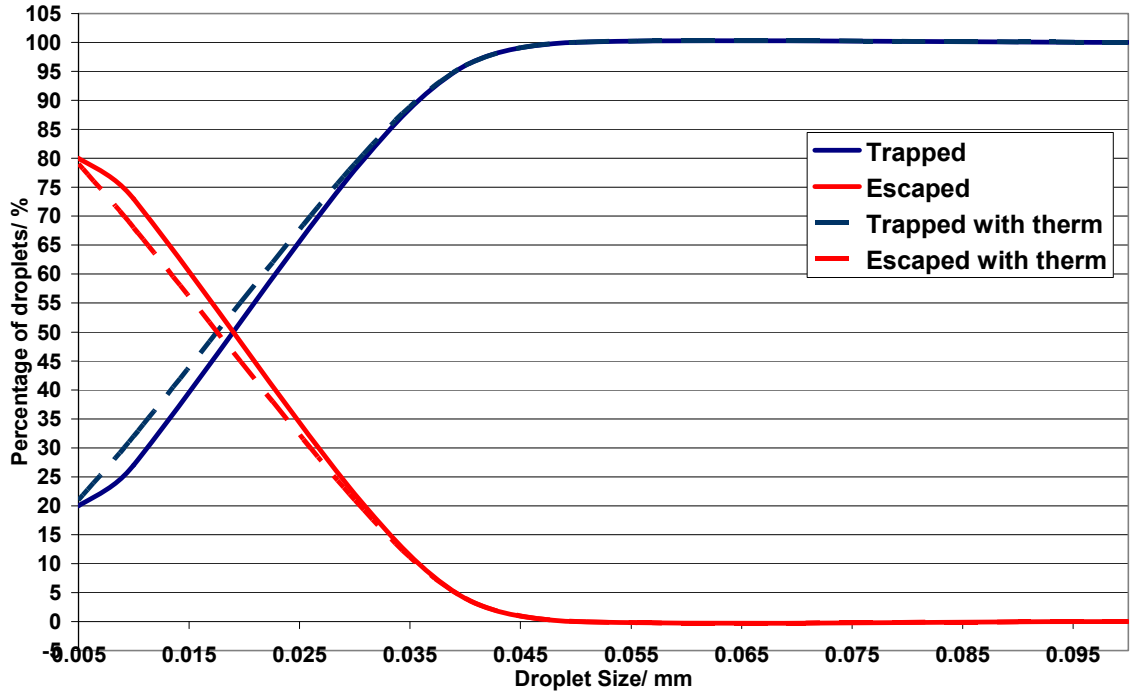

b)

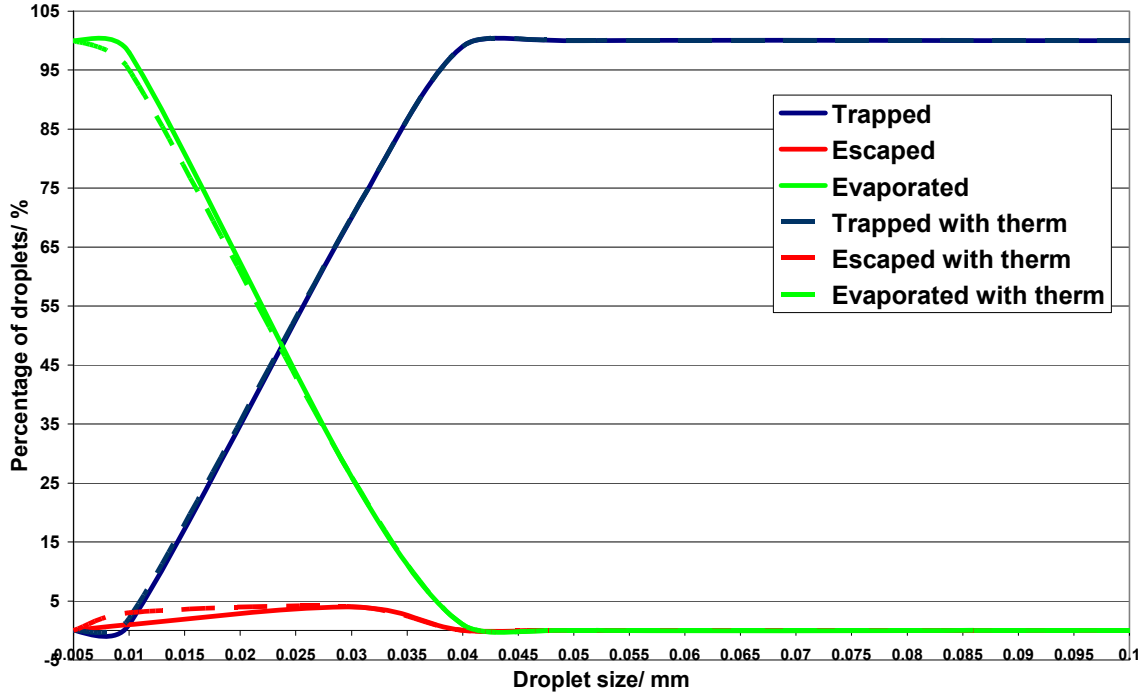

Figure 35: Head 4/Case 3: κ-ε realizable model of droplet size versus percentage of droplets (Water, 400 C): trapped, escaped or evaporated: a) κ-ε realizable model with or without thermophoresis and b) κ-ε realizable model and evaporation model with/without thermophoresis.

a)

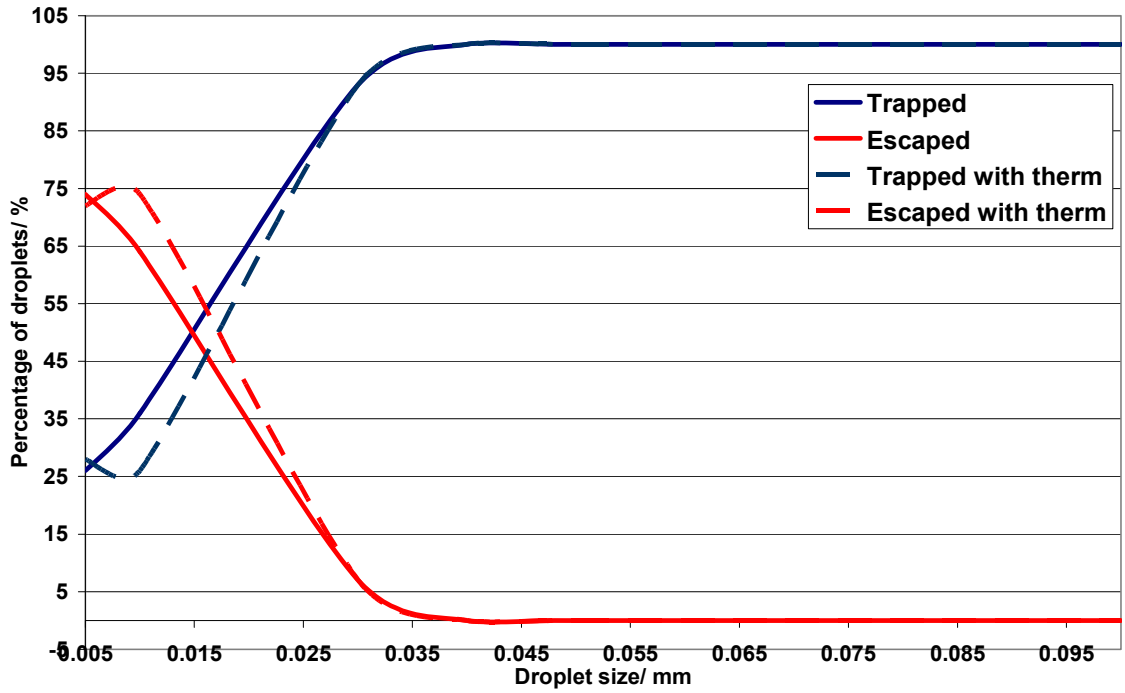

b)

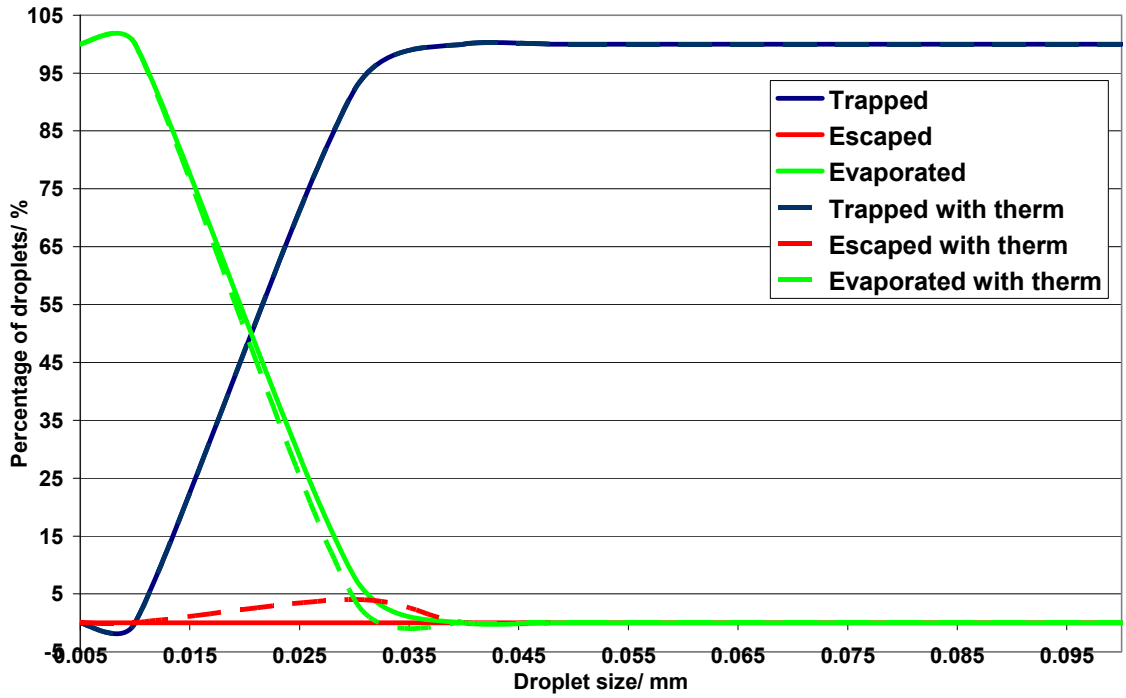

Figure 36: κ-ε realizable model comparison of MeOH and water droplets for the four simulation models, (600 °C).

a) κ-ε realizable model

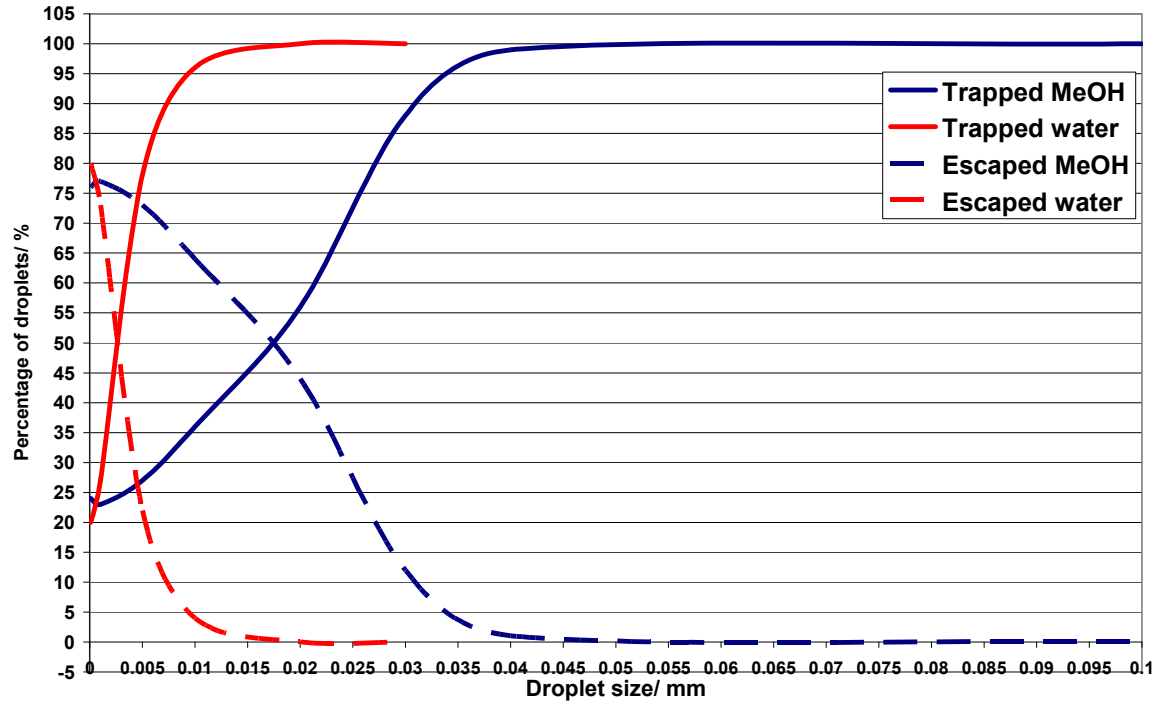

b) κ-ε realizable and thermophoretic models

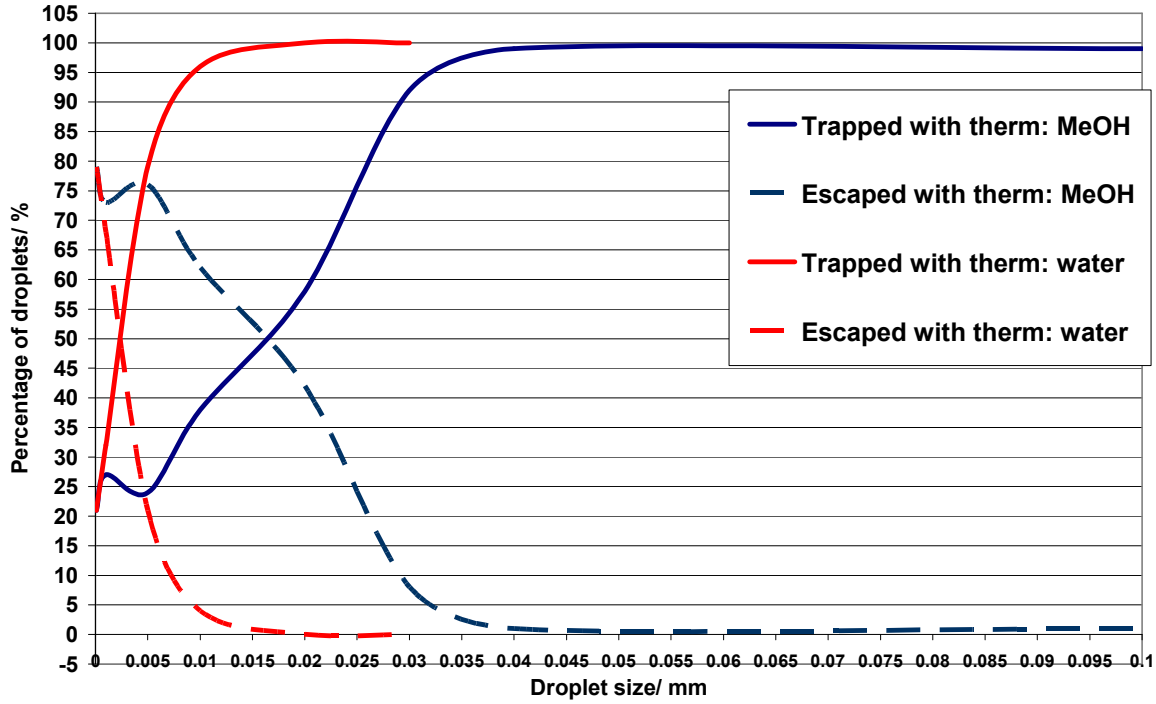

c) κ-ε realizable and evaporation models

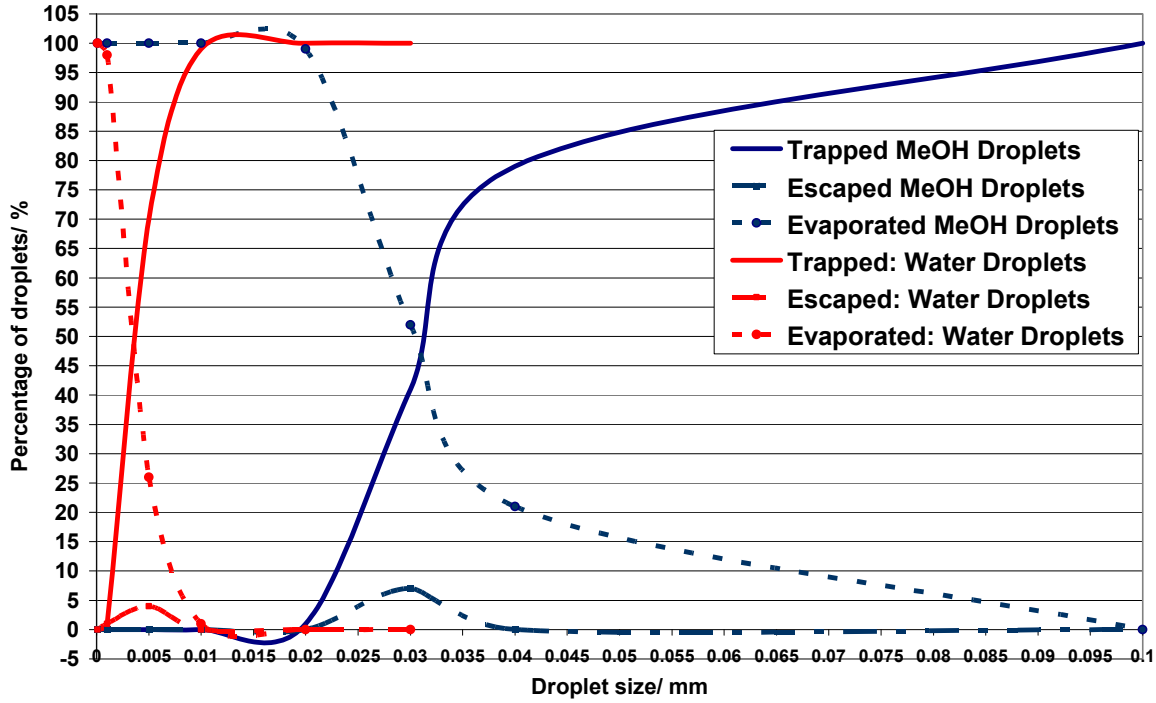

d) κ-ε realizable, evaporation and thermophoretic models

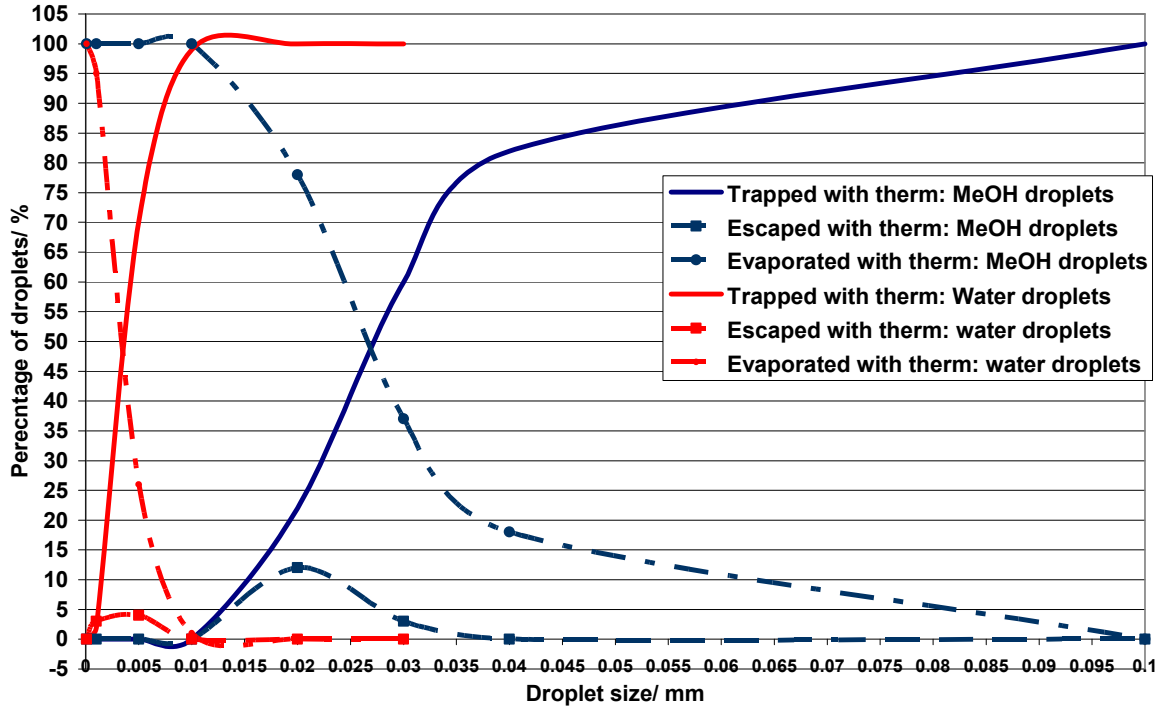

Figure 37: κ-ε realizable model comparison of MeOH and water droplets for the four simulation models used (400 °C).

a)* κ-ε realizable model: * straight lines on a) probably due to one missing data point

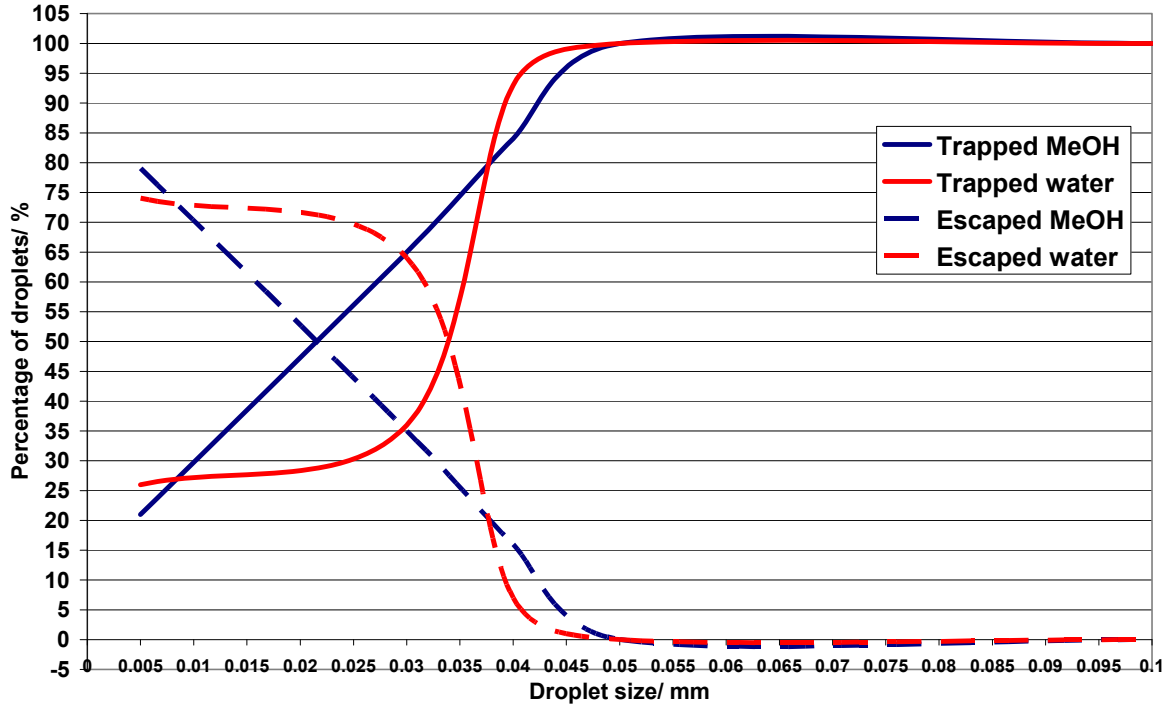

b) κ-ε realizable and thermophoretic models

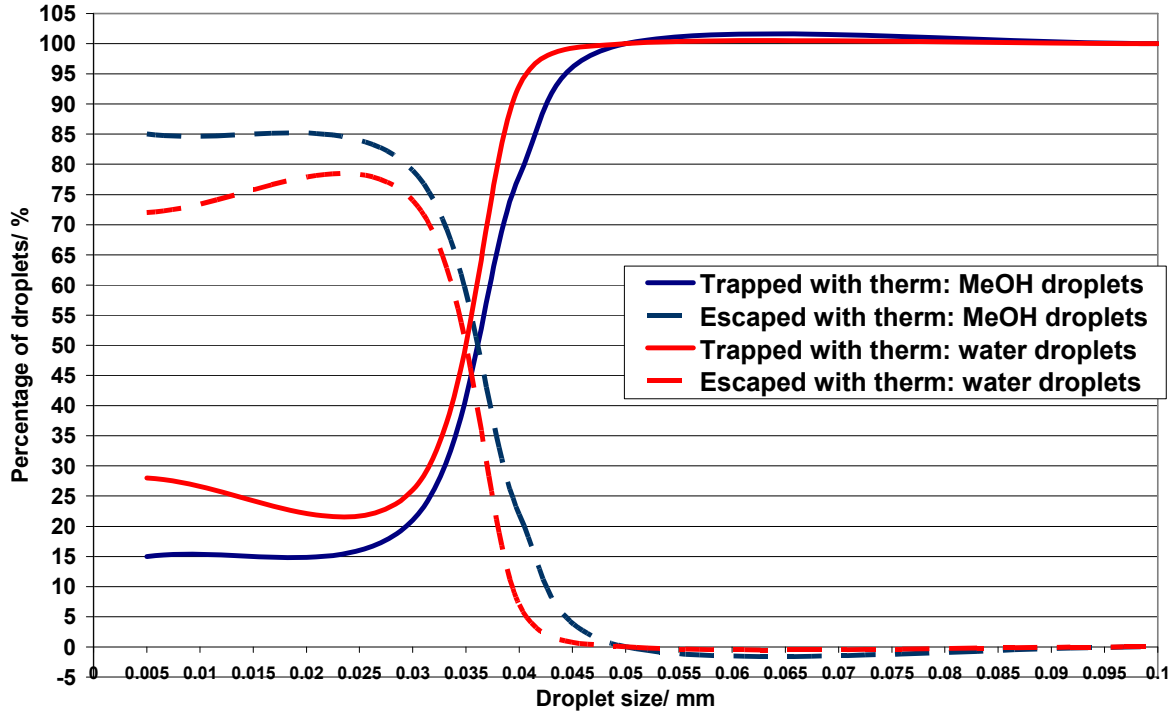

c) κ-ε realizable and evaporation models

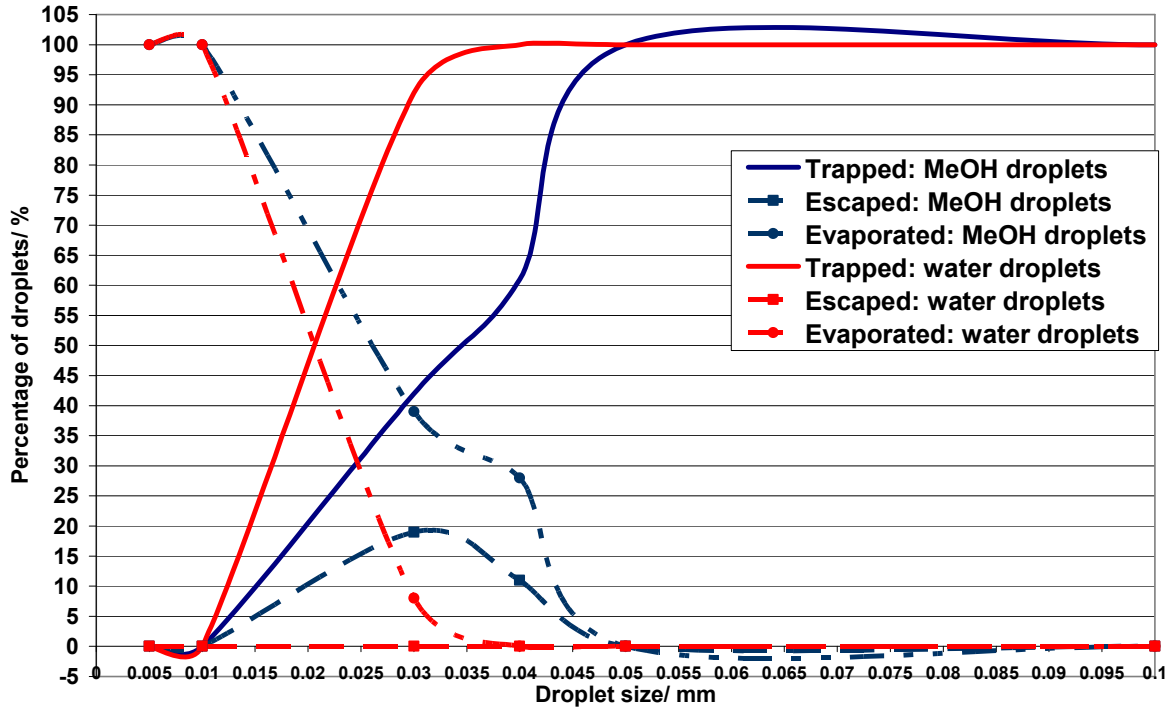

d) -ε realizable, evaporation and thermophoretic models.

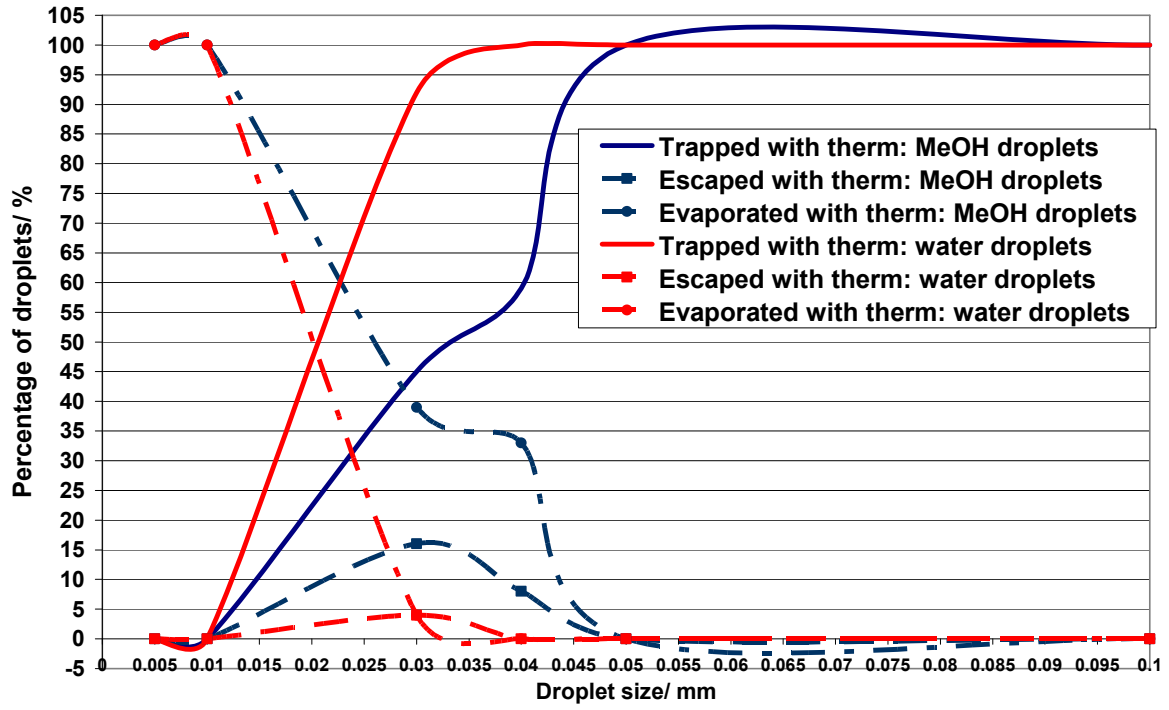

Figure 38: κ-ω SST model, head 4, case 3, (MeOH, 600 °C), turbulence model with/without thermophoretic effect.

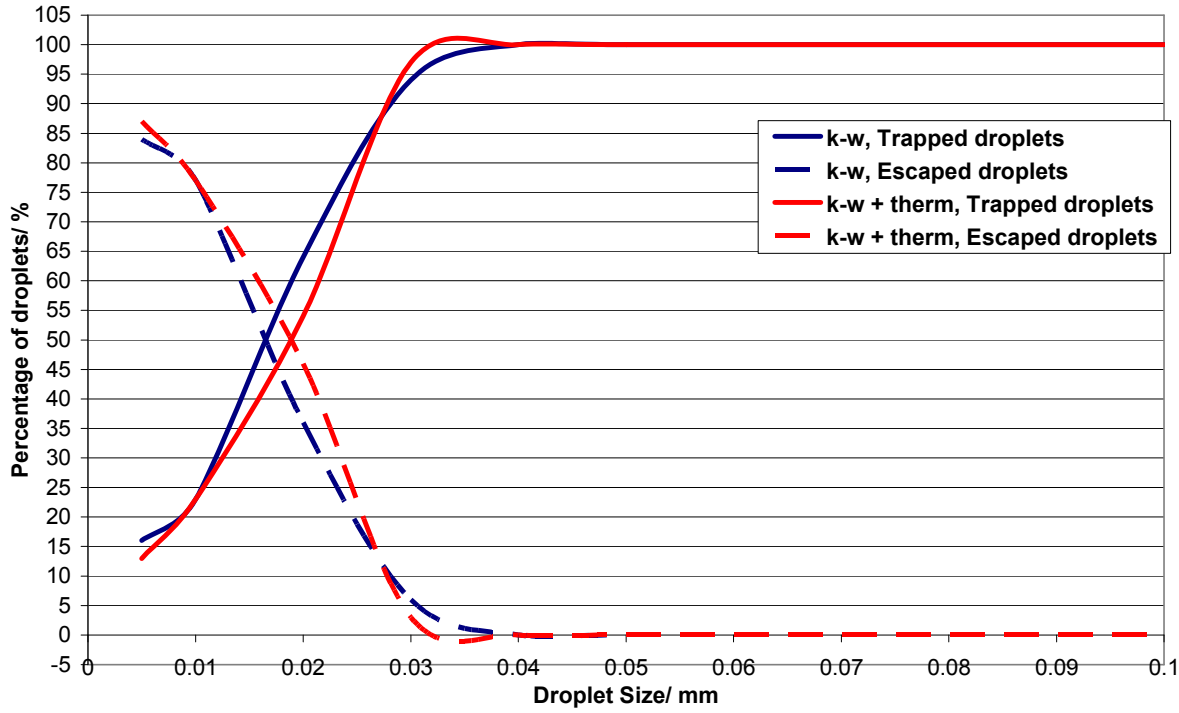

Figure 39: Comparison of κ-ε realizable and κ-ω SST model, (MeOH, 600 °C): a) basic turbulence model

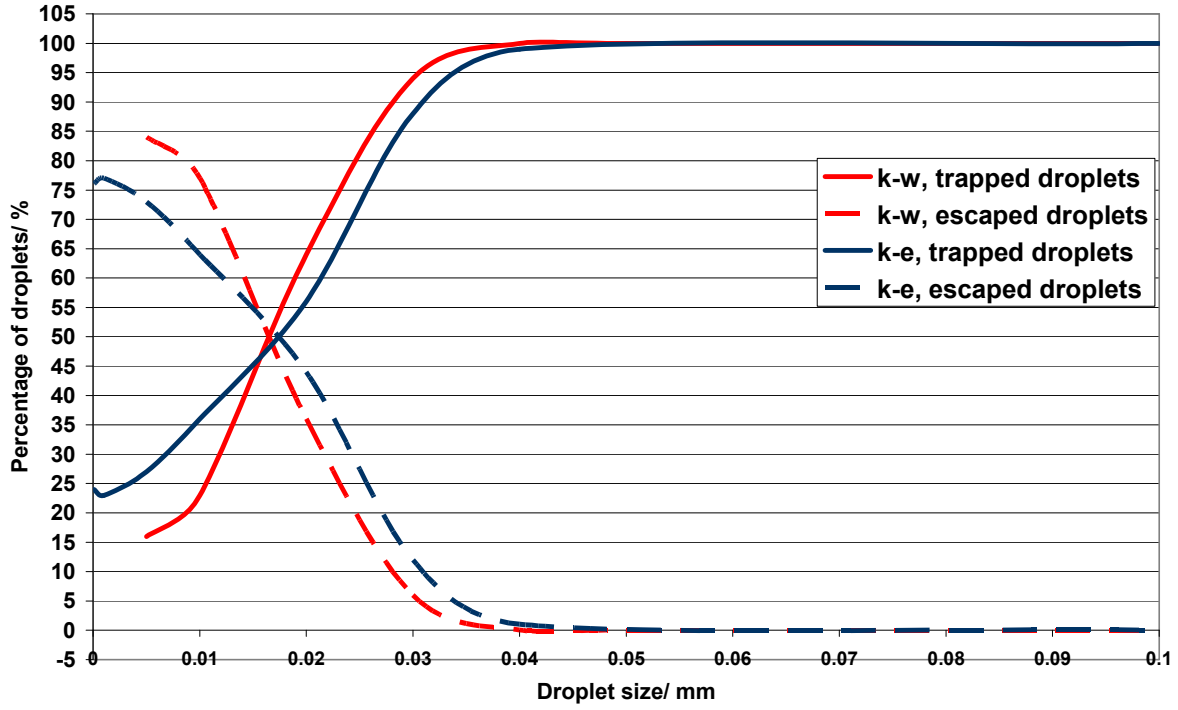

b) turbulence and thermophoretic simulations

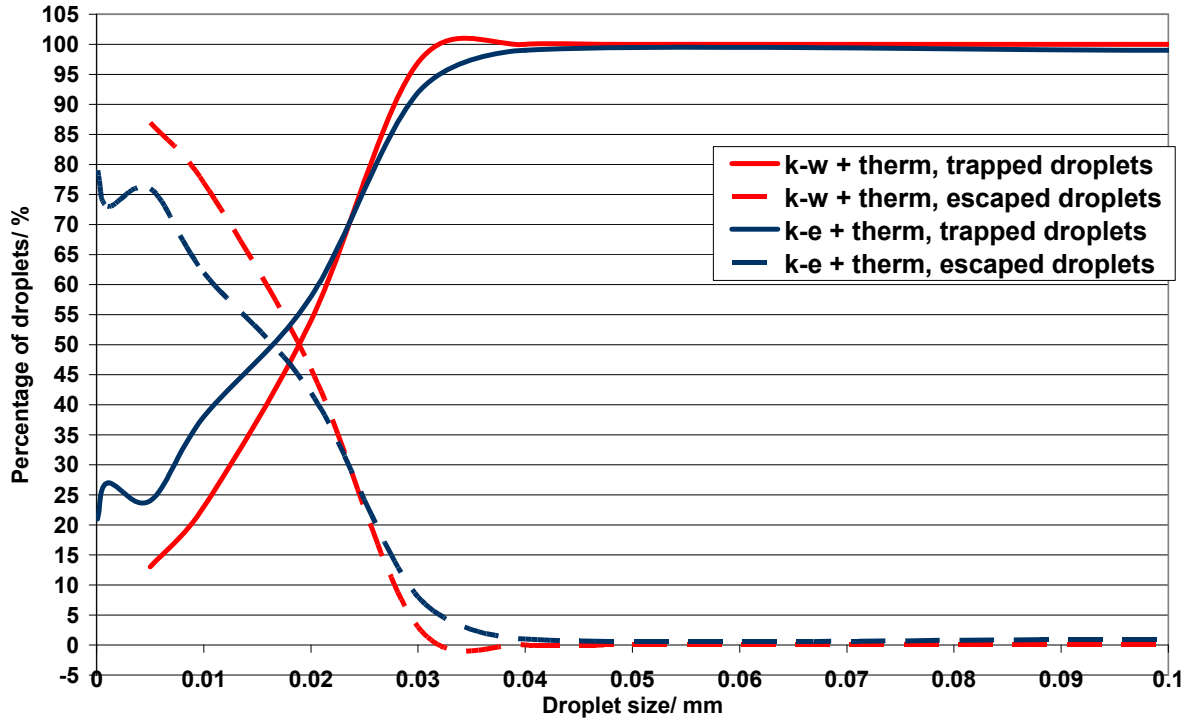

The agreement between the results for the κ-ε realizable and κ-ω SST turbulence modelling is remarkably close, droplet size required to reach substrate, 0.04 mm, this gives confidence that the results are repeatable and comparable across these two 2-equation models for basic turbulence and thermophoretic effects.

Figure 40: κ-ω SST model, head 4, case 3, MeOH, 600 °C, evaporation model with/without thermophoretic effect.

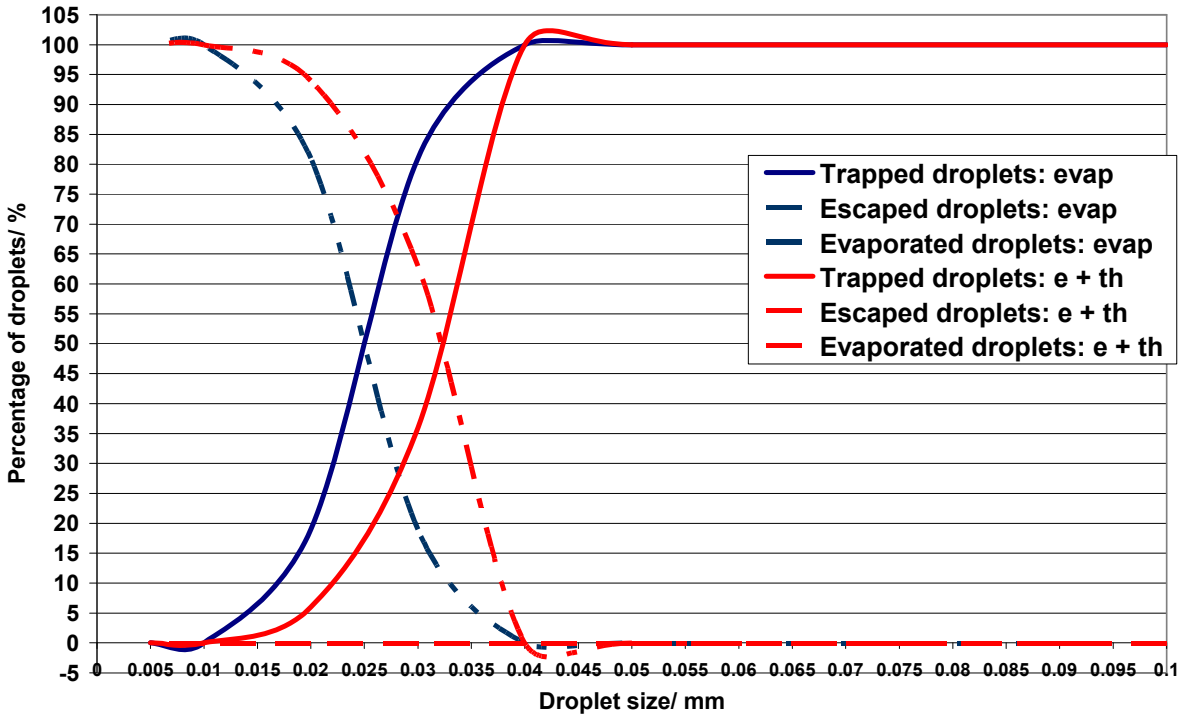

MeOH solvent droplet size required to reach the glass substrate surface 0.04 mm for evaporation with/without thermophoretic effects. Thermophoretic effects are more significant between 0.01 to 0.04 mm.

Figure 41: Comparison of κ-ε realizable and κ-ω SST model, (MeOH, 600 °C): a) evaporation and b) evaporation and thermophoretic simulations.

a)

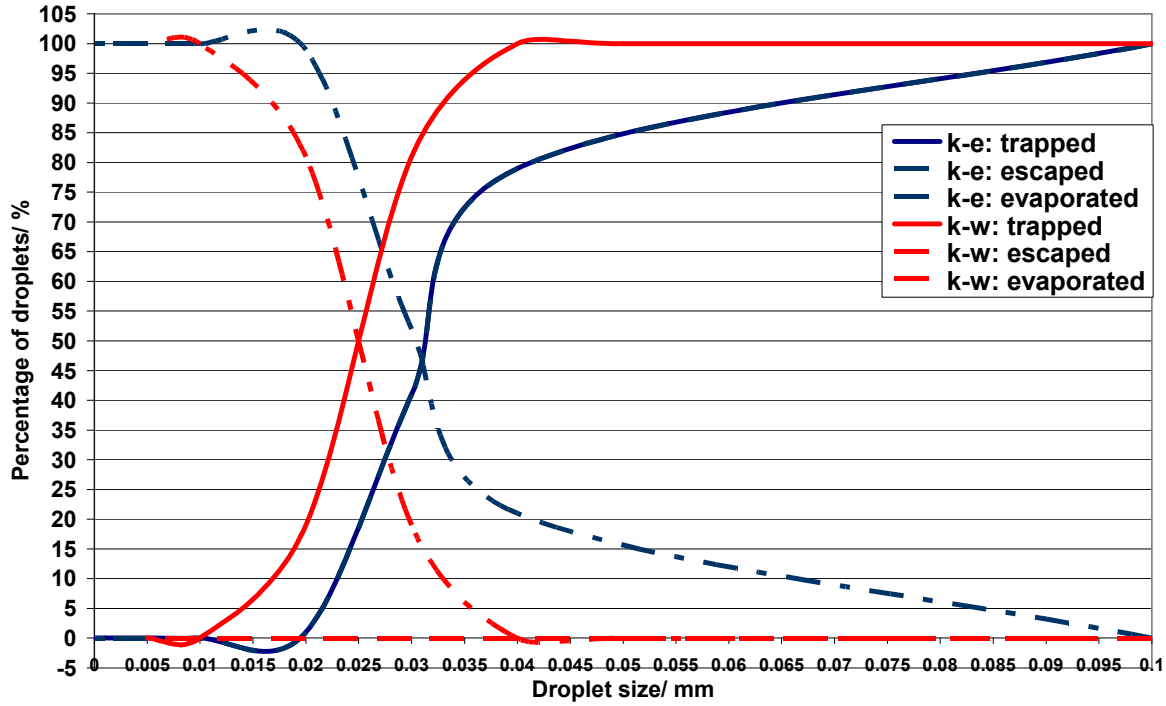

b)

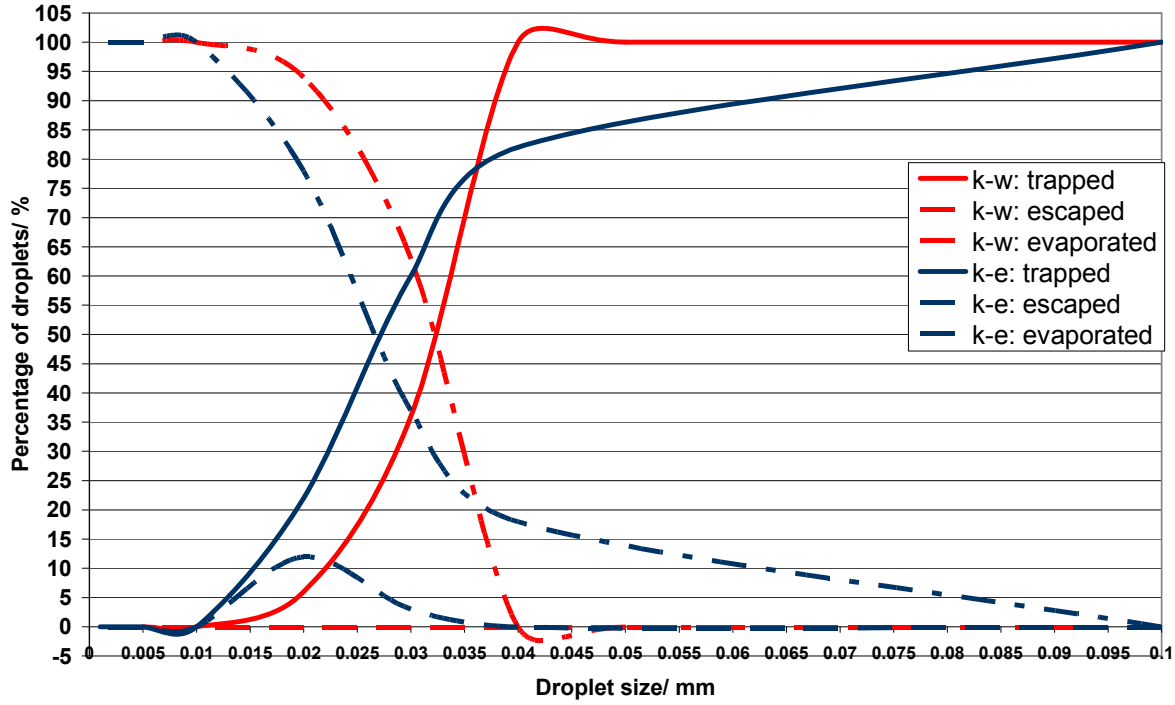

The lack of agreement between the two 2-equation models, κ-ε realizable and κ-ω SST for the evaporation effects with or without thermophoresis, may be due to the specialized nature of the κ-ω SST model near wall boundaries and the κ-ω SST may suit simulations with more complex flows near to the walls *e.g.* those with objects adjacent to the walls or complicated shaped sides than the simpler straight forward design simulated here. The κ-ε realizable evaporation results for this system appear to be more believable.

2.4.1 Discussion on particle trajectory results

2.4.1.1 Case 3, head 4, MeOH at 600 °C

The basic turbulence and evaporation simulation results, using the κ-ε realizable model for case 3 (all inlets: 17.39 m/s) have indicated a significant difference in the size of droplet required to reach the glass substrate surface (0.04 mm to 0.1 mm). The addition of the thermophoretic effects did not appear to affect the overall size of droplet required to reach the substrate surface but had more effect on droplets below the required size. According to the simulations the main effects on the droplets are aerodynamic drag and evaporation. The point, within the reactor head, where the solvent sheath is lost, through evaporation or swept away by aerodynamic drag, may well influence whether the nanoparticles reach the substrate surface for successful aerosol assisted CVD deposition within other host metal oxides being formed through conventional CVD methods.

2.4.1.2 Case 3, head 4, MeOH at 400 °C

The basic turbulence and evaporation simulation results, using the κ-ε realizable model for case 3 (all inlets: 17.39 m/s) have indicated a small difference in the size of solvent droplet required to reach the substrate surface (~0.05 mm for both simulations). Indicating that at lower temperatures evaporation is not as influential as aerodynamic drag. The addition of the thermophoretic effects did not appear to affect the overall size of droplet required to reach the substrate surface but had more effect on droplets below the required size. The main force of influence would therefore be aerodynamic drag for this simulation.

2.4.1.3 Case 3, head 4, water at 600 °C

The basic turbulence and evaporation simulation results, using the κ-ε realizable model for case 3 (all inlets: 17.39 m/s) have indicated a small difference in the size of solvent droplet required to reach the substrate surface (0.015 mm for basic turbulence and 0.01 mm with evaporation). The change in solvent, from MeOH to water at this temperature lowers the influence of evaporation and therefore aerodynamic drag was the main force of influence for this simulation. The addition of the thermophoretic effects did not appear to affect the overall size of droplet required to reach the substrate surface but had more effect on droplets below the required size.

2.4.1.4 Case 3, head 4, water at 400 °C

The basic turbulence and evaporation simulation results, using the κ-ε realizable model for case 3 (all inlets: 17.39 m/s) have indicated a small difference in the size of solvent droplet required to reach the substrate surface (0.036 mm for basic turbulence and 0.035 mm with evaporation). The change in solvent, from MeOH to water at this temperature lowers the influence of evaporation and therefore aerodynamic drag was the main force of influence for this simulation. The addition of the thermophoretic effects did not appear to affect the overall size of droplet required to reach the substrate surface but had more effect on droplets below the required size.

2.4.1.5 Comparison of water and methanol at 600 °C

The two equation κ-ε realizable turbulence model has shown that the solvent used has a significant effect on the size of droplet required to reach the substrate surface at 600 °C, see table 11.

Table 11: Comparison of κ-ε realizable model solvent (water, MeOH) droplet trajectory results:

For the four types of simulations, basic turbulence with/without thermophoresis and evaporation model with/without thermophoresis at 600 °C.

	MeOH	Water
Basic turbulence model	0.043 mm	0.015 mm
Basic and thermophoresis model	0.046 mm	0.016 mm
Basic turbulence and evaporation model	0.100 mm	0.010 mm
Basic turbulence, evaporation and thermophoresis model	0.100 mm	0.010 mm

The difference between water and MeOH for both the basic model with/without thermophoretic effects and the evaporation model with/without thermophoretic effects is an order of 10 magnitude greater.

2.4.1.6 Comparison of water and methanol at 400 °C

The two equation κ-ε realizable turbulence model has shown that the solvent used has a less significant effect on the size of droplet required to reach the substrate surface at 400 °C and the main force of influence at this temperature is aerodynamic drag, see table 12.

Table 12: Comparison of κ-ε realizable model water and MeOH droplet trajectory results:

For the four types of simulations, basic turbulence with/without thermophoresis and evaporation model with/without thermophoresis at 400 °C.

	MeOH	Water
Basic turbulence model	0.049 mm	0.046 mm
Basic and thermophoresis model	0.050 mm	0.050 mm
Basic turbulence and evaporation model	0.050 mm	0.040 mm
Basic turbulence, evaporation and thermophoresis model	0.050 mm	0.036 mm

2.4.1.7 κ-ω SST model, MeOH at 600 °C

The MeOH solvent droplet size required to reach the glass substrate surface for both the basic turbulence model and the evaporation model with or without thermophoretic effects is very similar (~0.032-0.04 mm), see figs. 42 and 43. The thermophoretic effect appears to be less significant for the required size to reach the substrate surface.

2.4.1.8 Comparison of κ-ε realizable and κ-ω SST, MeOH at 600 °C

Comparison of the basic κ-ε realizable and κ-ω SST turbulence models with or without thermophoretic effects gave remarkably similar results with droplet size required to hit the substrate for both models being ~0.035 to 0.04 mm. Comparison of the κ-ε realizable and κ-ω SST evaporation simulations with or without thermophoretic effects do share some similarities but the κ-ω SST model may not be suitable for evaporation modelling of this system due to change in the way boundary effects are modelled; the κ-ω SST predicts droplet size required to be about 0.04 mm compared to 0.1 mm of the κ-ε realizable model for MeOH at 600 °C, see figs. 44 and 45.

2.5.0 Individual results for head 4, case 3 simulations

The two equation κ-ε realizable model was used to produce the following individual results for head design 4, case 3 for both the basic turbulence model with/without thermophoresis and the evaporation model with/without thermophoresis for various droplet sizes (0.1, 0.04, 0.01 and 0.005 mm) at 600 °C, see figs. 46-49. Molar and mass fractions of MeOH and O_2 and XY plots of particle trajectories (0.1, 0.04, 0.01 and 0.005 mm) are also considered, see figs. 50 and 51.

Figure 42: Head 4/case 3, 3D view of individual droplet trajectory results (0.1 mm, κ-ε): From the AACVD inlet, droplet Size 0.1 mm: κ-ε realizable model.

a) Turbulence model

b) Turbulence & thermophoresis

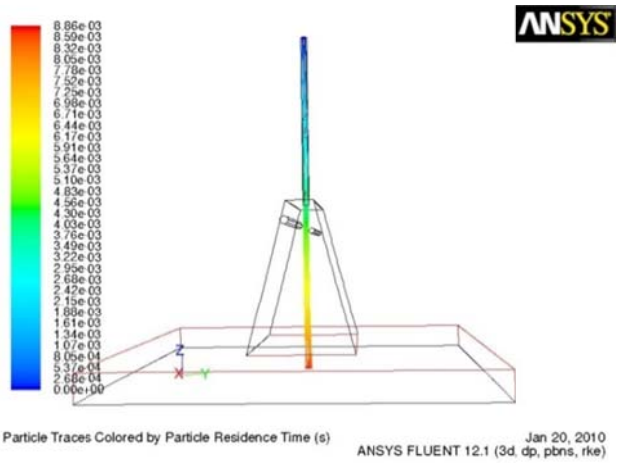

c) Turbulence & evaporation model

d) Turbulence, evaporation & thermophoresis

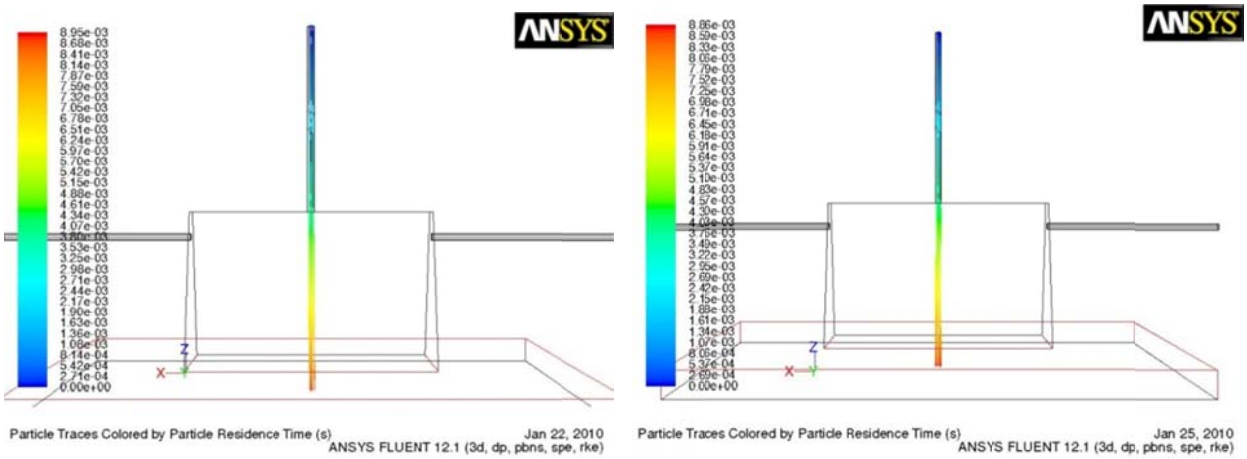

Figure 43: Head 4/case 3: 3D view of individual droplet trajectory results (0.04 mm, κ-ε): From the AACVD inlet: droplet Size 0.04 mm: κ-ε realizable model.

a) Turbulence model

b) Turbulence & thermophoresis

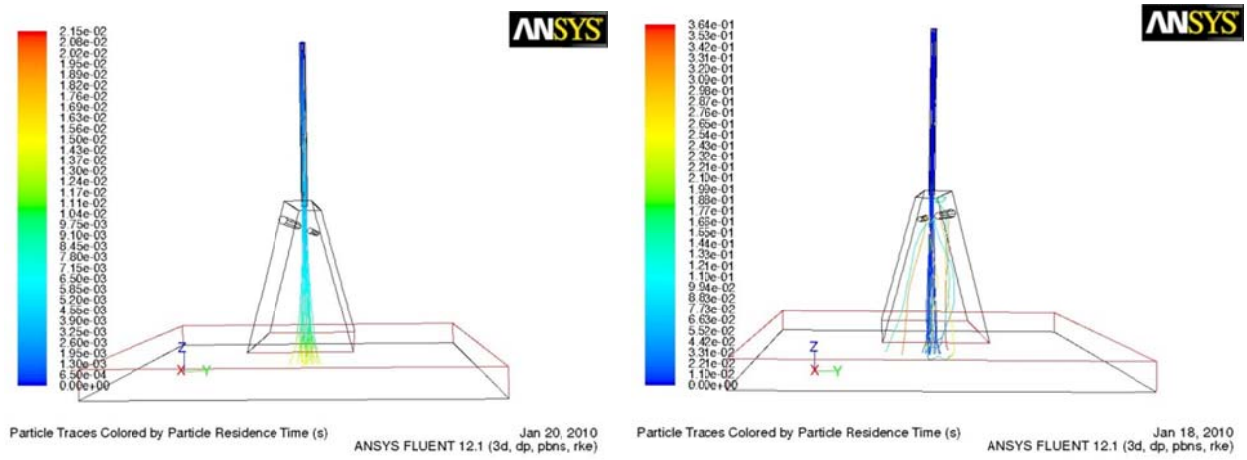

c) Turbulence & evaporation model

d) Turbulence, evaporation & thermophoresis

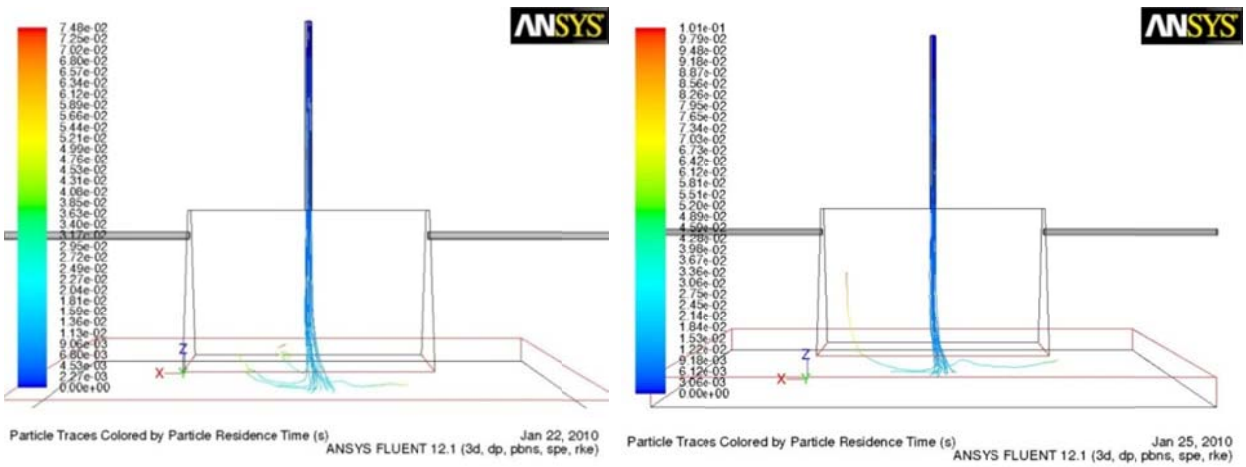

Figure 44: Head 4/case 3: 3D view of individual droplet trajectory results (0.01 mm, κ-ε): From the AACVD inlet: droplet Size 0.01 mm: κ-ε realizable model.

a) Turbulence model

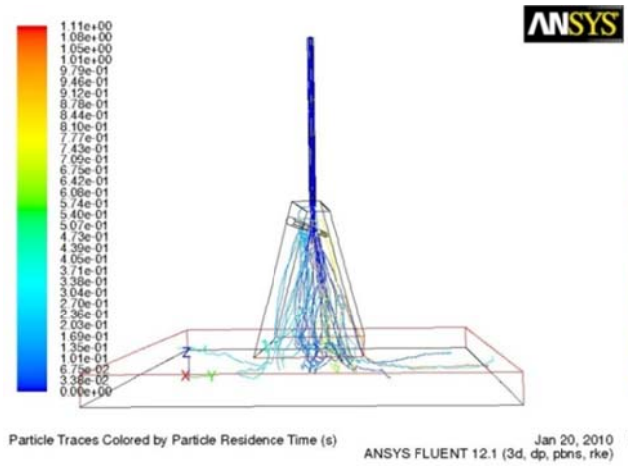

b) Turbulence & thermophoresis

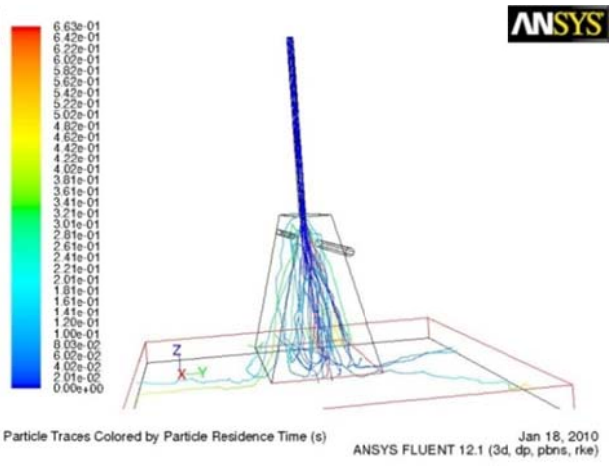

c) Turbulence & evaporation model

d) Turbulence, evaporation & thermophoresis

Figure 45: Head 4/case 3: 3D view of individual droplet trajectory results (0.005 mm, κ-ε): From the AACVD inlet: droplet Size 0.005 mm: κ-ε realizable model.

a) Turbulence model

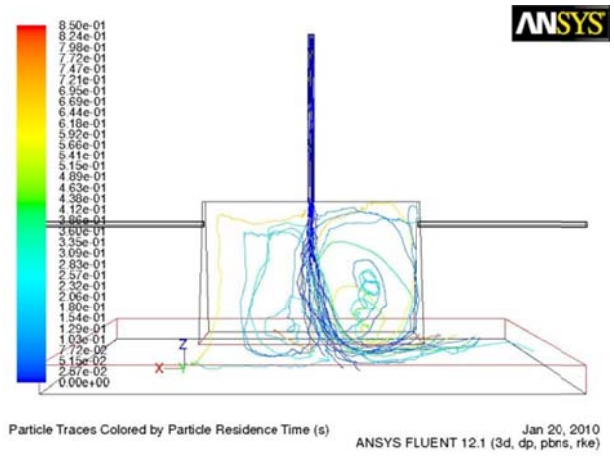

b) Turbulence & thermophoresis

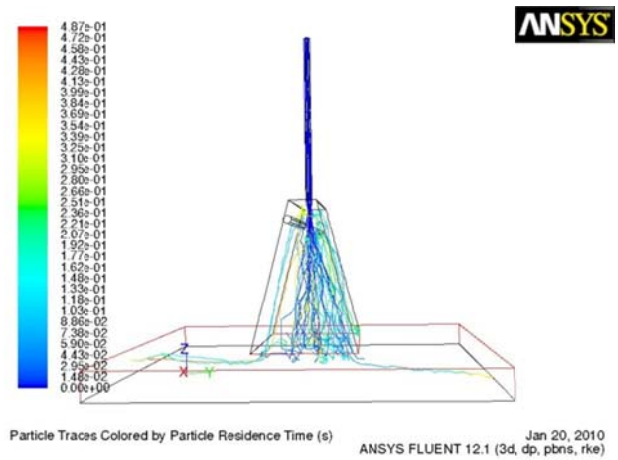

c) Turbulence & evaporation model

d) Turbulence, evaporation & thermophoresis

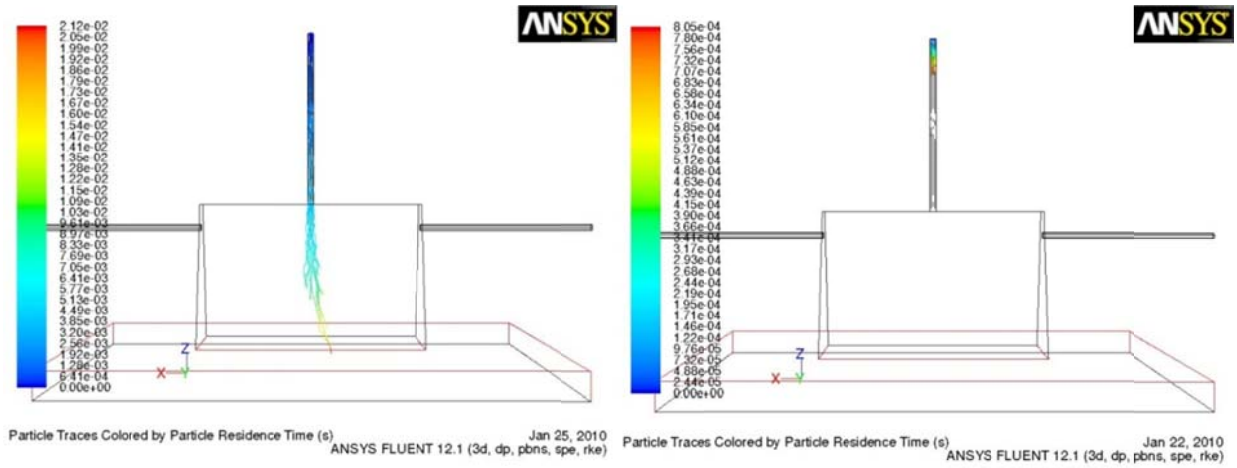

Figure 46: κ-ε realizable model, fluid flow case 3, head 4, (mass/mole fractions MeOH and O_2): a) mass of MeOH, b) mole fractions of MeOH, c) mass fractions of O_2, d) mole fractions of O_2.

a)

b)

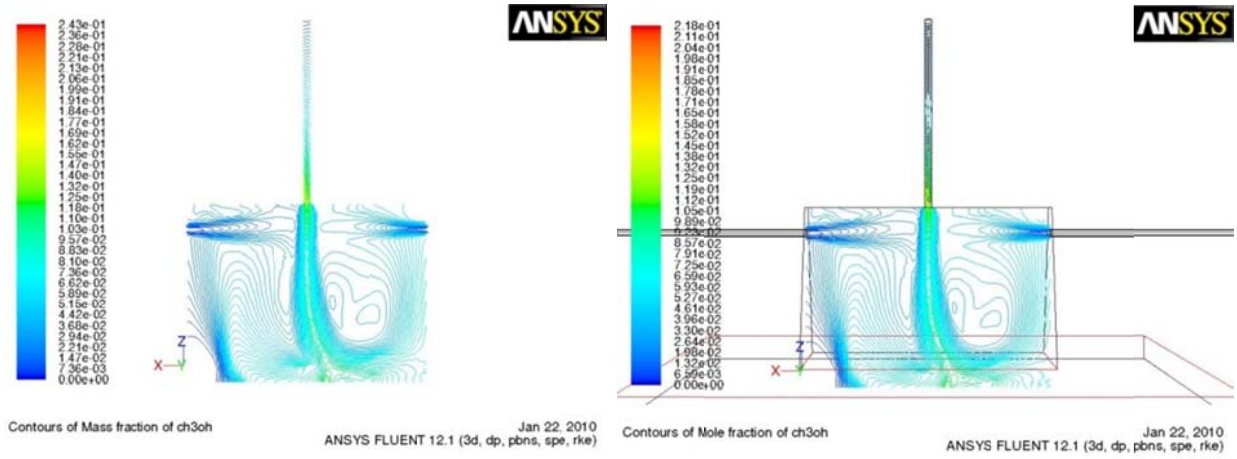

c)

d)

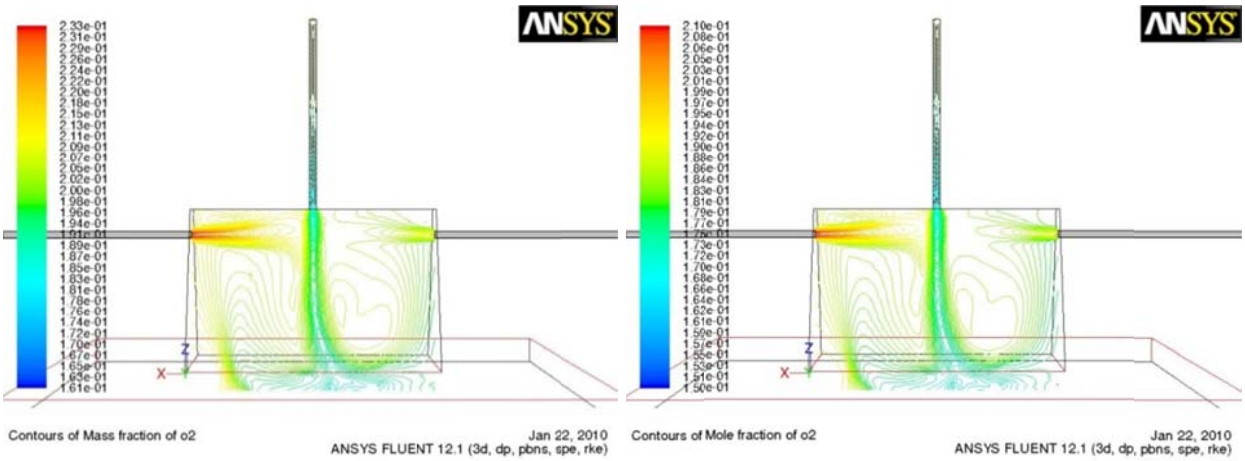

Figure 47: XY Plots: κ-ε model, evaporation with discrete thermophoretic model: a) droplet Size 0.1 mm, b) droplet Size 0.04 mm, c) droplet Size 0.005 mm.

a)

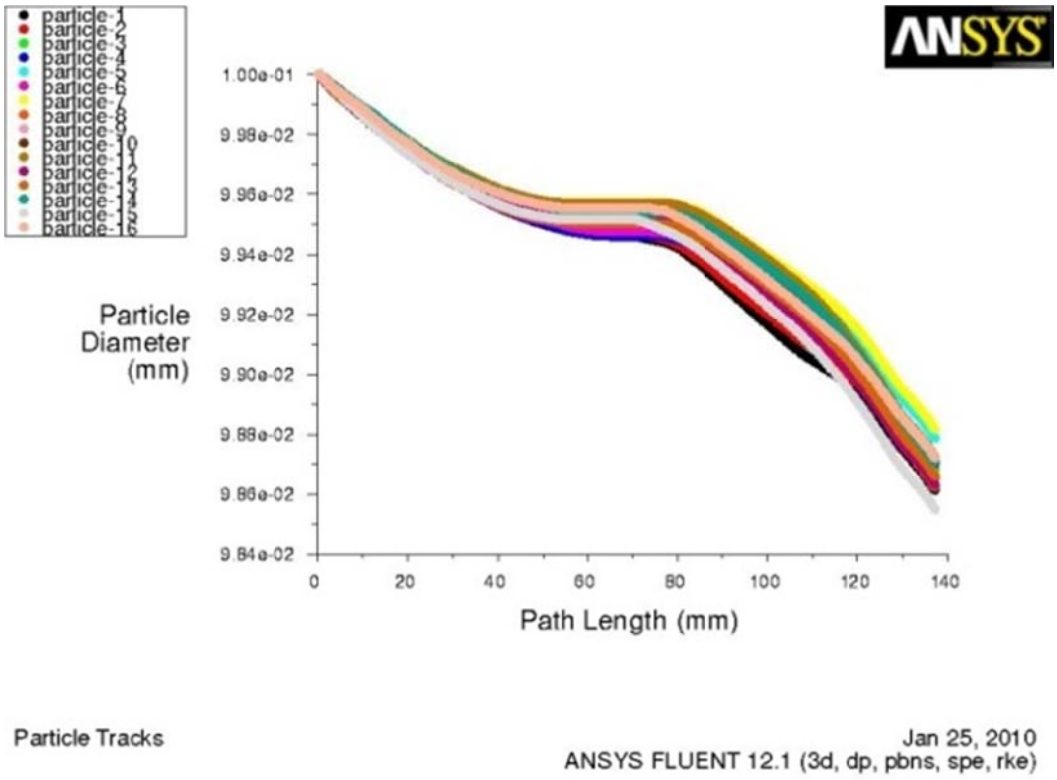

b)

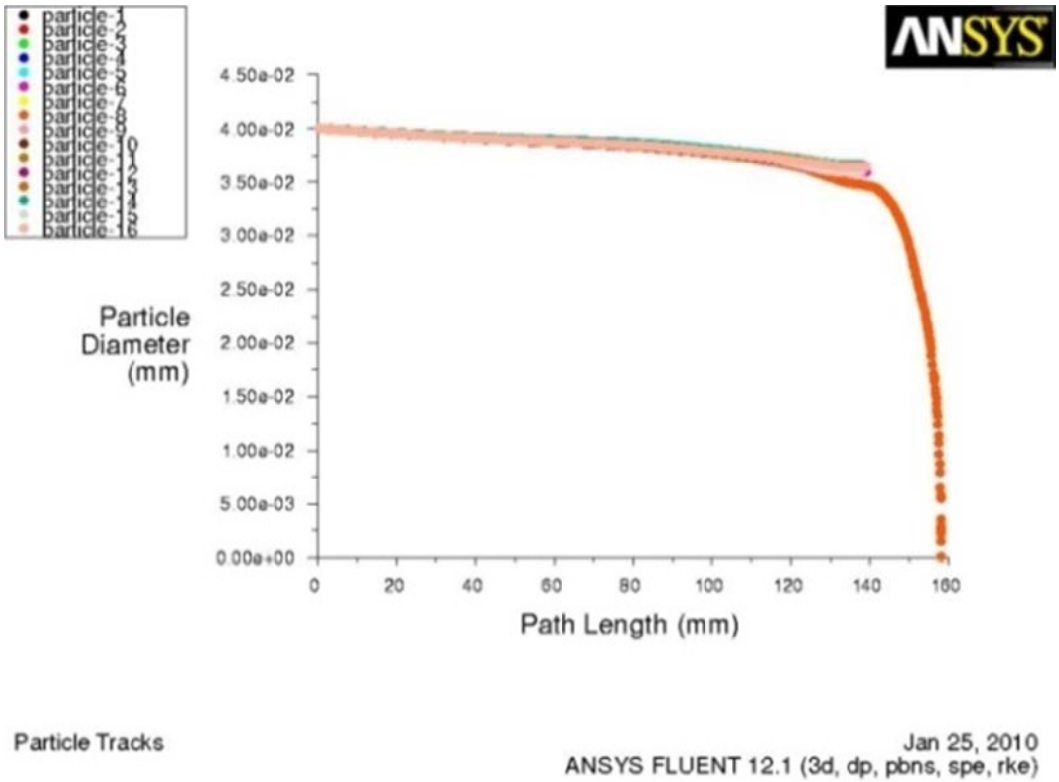

c)

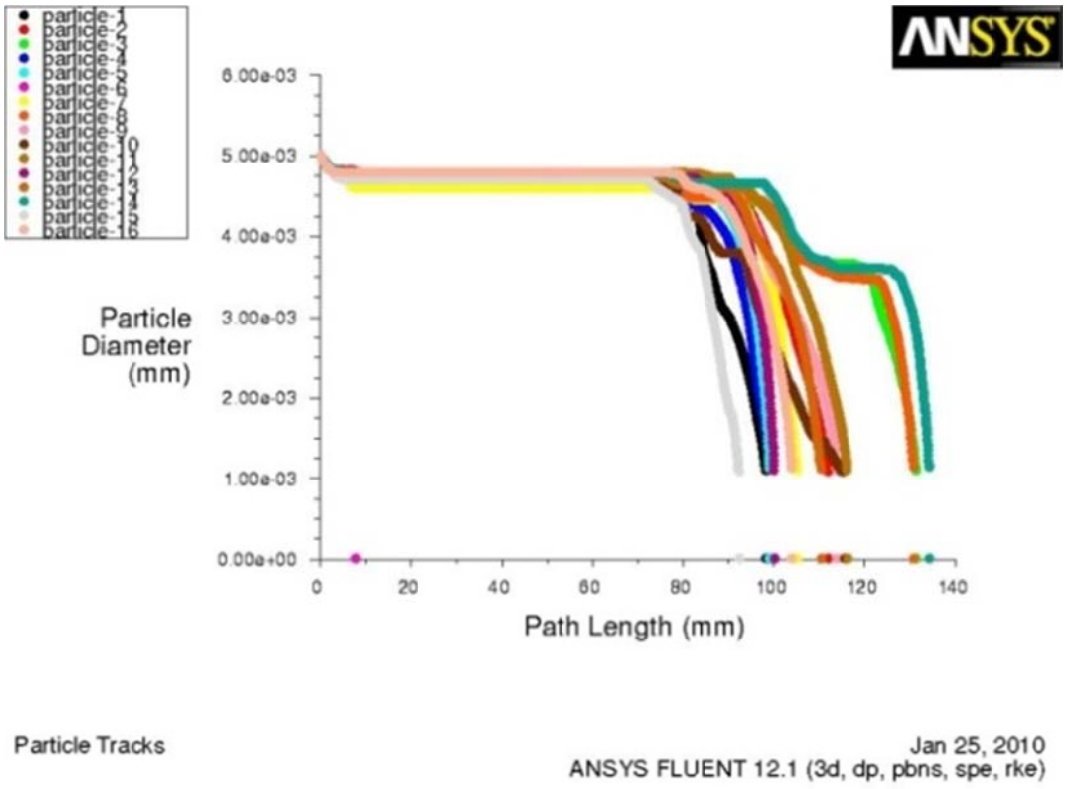

2.6.0 Discussion of the Five AACVD/CVD head designs

2.6.1 Fluid flow (air) model for the 5 designs

The numerical 2 equation 3ddp κ-ε realizable modelling for fluid flow (air) for head designs, 1, 3 and 5 with all three inlets (AACVD, CVD), running parallel to the head chamber did not produce streams of fluid flow that were particularly well mixed at any chosen sets of inlet velocities. Head 3 has the 3 inlets parallel to the head chamber at a 40º angle from the 'plumb line', results indicate that mixing of vapour streams was poor and no significant improvement on the results from heads 1 and 5. The two head designs that had the CVD inlets at 90 º (perpendicular) to the head chamber had far better mixing profiles which can be seen from the results of case 3 for head designs 2 and 4 both for velocity and turbulence contours and XY plots. Head design 4 appears to encourage the best mixing of all 3 inlets and has the necessary 15 º angle from the 'plumb line' for laminar flow towards the bottom of the head, so as to encourage uniform formation of a thin film on the glass substrate, head 2 on the other hand has a cubic shaped head chamber that does not encourage a good mix of vapours from all 3 inlets. The main effect of altering velocity of the fluid

flows between the AACVD and CVD confirmed that too little inlet velocity tended to leave the stream of fluid flow sat in the middle of the reactor head with a tendency to swirl into an upward direction; where in all probability the precursor materials would be deposited near the top, on the inside of the reactor walls. When the AACVD and CVD inlet flows are relatively fast and equal (17.39 m/s, 10 l/min) the fluid flow became unstable and there was a possibility of the fluid flow switching from side to side. The most favourable inlet velocities for the combined 90 ° vertical reactor head design was when the CVD inlet velocity (8.00 m/s) was lower than the AACVD inlet velocity (14.42 m/s).

2.6.2 Droplet trajectory and evaporation model for head design 4, case 3

The numerical 2-equation modelling with the κ-ε realizable model with or without the discrete thermophoretic model with both water and MeOH AACVD solvent droplets indicated that aerodynamic drag was the main force at 400 °C, the thermophoretic effect affects solvent droplet size below the required size to reach the heated substrate surface. At 600 °C the main forces of influence are aerodynamic drag and evaporation, the more volatile the solvent the more evaporation influences the size of droplet required to reach the heated substrate surface. The thermophoretic effect affects droplets that are smaller than the required size to hit the surface and is not the main force of influence. The droplet size/diameter is one of the most important factors for reaching the substrate surface and the main forces affecting droplet size are aerodynamic drag[122], turbulence[122] and at higher synthesis temperatures evaporation, hence the choice of AACVD solvent carrier is also critical. The work here for this system using all four evaporation model parameters, turbulence, aerodynamic drag, thermophoresis and evaporation, indicates that a droplet size of 0.1 mm is required for the AACVD solvent MeOH and 0.01 mm for water, at 600 °C; the difference between the solvents being one order of magnitude.

Comparison of the evaporation simulations using the κ-ε realizable model and the κ-ω SST model for MeOH at 600 °C does indicate similar trends but smaller droplet sizes reach the heated substrate using the κ-ω SST model, this may be due to the small sample size used or that the κ-ω SST model is a blended model that more accurately models nearer complicated boundary walls and

inlets than the chosen model of head 4[121]. Recent work by Aly *et al.* found that the κ-ε realizable model obtained the best agreement with experimental results for modelling droplet break up, aerodynamic drag forces on droplets, droplet size/diameter and fluid flow which was also found to be critical to droplet dispersion and angle[122]. According to recent droplet evaporation work by Katoshevski *et al.* a decrease in droplet size causes the phenomenon known as droplet grouping this could also be affecting the AACVD particle trajectory paths, as droplets of decreasing diameter group together and follow the inlet velocity path; the AACVD droplets may mix less well within the reactor head, although this effect may well be small when compared to the effect of evaporation at higher synthesis temperatures but droplet grouping is beyond the scope of the work presented here[123]. The mass and molar fractions of MeOH and O_2 demonstrate how the mass and concentration of these are more prevalent in the areas of fluid flow where mixing of the AACVD and two CVD flows has occurred in head design 4.

2.7.0 Conclusion for chapter 2

2.7.1 Combined AACVD/CVD head for experimental phase

Based on the modelling results above, head design 4 appeared to be the design that had a significant uniform mix of all three fluid flows and therefore had the most probable chance of forming a uniform CVD host metal oxide matrix thin film with uniform inclusion of AACVD nanoparticles. Although the average experimental AACVD nebulised droplet size is an order of ten below the required modelled droplet size (MeOH) to reach the heated substrate surface, useful experimental results have been obtained. There are a large number of CFD studies of atmospheric pressure CVD (APCVD) of various materials but there have been very few published studies that address how the fundamental flow structures, particle trajectory, evaporation and thermophoteric effects are observed in atmospheric pressure, APCVD reactors (mainly horizontal reactors) and there are no comparable literature results for the combined 90° vertical AACVD/APCVD reactor designs described here.

2.7.2 Experimental phase for AACVD and AACVD/CVD combined synthesis

The following chapters, 3, 4 and 5 detail the results of AACVD synthesis of host metal oxides with noble metal nanoparticles, see chapter 3, and the combined AACVD/CVD results obtained for prototype 1, see chapter 4 and prototype 2 (head design 4), see chapter 5.

Chapter 3

AACVD Synthesis of undoped and metal doped ZnO Thin Films

Chapter 3: AACVD Synthesis of undoped and metal doped ZnO Thin Films

3.0.0 Introduction

The host matrix and nanoparticle incorporation of dopants within a thin film gives coatings with specific physical and optical properties that are desired by the glass and semiconductor industries. There are a number of different types of intelligent coatings that are being investigated, these coatings can respond to external stimuli such as light intensity or temperature and include electrochromic, photochromic and thermochromic thin films[124-132]. Zinc oxide host matrix thin films on glass are one area of particular interest in thin film research, due to their transparent conductive oxide (TCO) properties. The films have exceptionally high transparency yet high electrical conductivity.

For photovoltaic technologies a transparent conducting oxide requires the bandgap > 3 eV for transmission in the short wavelength (UV, 400 nm) region *i.e.* to correspond to the fundamental bandgap of the material and for the free carrier plasma resonance absorption to lie in the near-infrared region *i.e.* the long wavelength (IR, 1500 nm) edge to correspond to the free carrier plasma resonance frequency[133, 134]. TCO's with a fundamental bandgap > 3 eV are insulators at 25 °C in the undoped state. Degenerately doped TCO's increase the free carrier density sufficiently enough to move the Fermi level into the conduction band giving a conducting TCO as the product. Native point defects *e.g.* oxygen vacancies, or impurities with an ionization energy close to the conduction band can provide the source of electrons required for degenerate doping. This requirement limits the number of suitable TCO materials. Native stoichiometric point defects *i.e.* oxygen vacancies readily exist in metal oxides with d^{10} cations *e.g.* Indium oxide, zinc oxide, tin oxide and cadmium oxide and are easily ionized to produce electrons for donation to the conduction band[132]. There are two main types of doping for TCO's cationic, on substitutional sites within the lattice or anionic *e.g.* replacing oxygen vacancies with fluorine. TCO's with the *n*-type host matrix and *p*-type dopants are the most common. The optimization of a doped TCO film is crucial and depends on a number of factors, increasing carrier density decreases resistivity but has the detrimental

effect of shifting the IR absorption edge towards the visible region, therefore narrowing the transmission window, too high a level of ionized impurities or impurity atoms can also lead to a decrease in the carrier mobility which can have a detrimental effect on the resistivity of the material[134]. Another key feature of TCO materials is the ability to control the growth orientation relative to a surface. This is particularly marked for materials such as F- doped SnO_2 which has three fold better solar control properties when grown with the preferred orientation.

ZnO is known to have a wurtzite structure (*a* = 3.25 Å, *c* = 5.206 Å) with a number of alternating planes composed of fourfold coordinated O^{2-} and Zn^{2+} ions stacked alternatively along the *c*-axis, thus it can be seen as two interpenetrating hexagonal closed-packed lattices of Zn and O. The vacancies in the oxygen sites and additional zinc atoms filling the interstitial sites in the wurtzite structure influence the electrical properties of ZnO. Common properties of TCO'S like ZnO are high optical transmittance over a wide spectrum including the visible region and low resistivity. Zinc oxide (ZnO) is a transparent *n*-type semiconductor with the necessary wide bandgap (3.3 eV) for transmission in the UV-Visible region, free carrier plasmon resonance absorption in the near-infrared, a large breakdown strength and a large saturation velocity. Undoped ZnO thin films are usually relatively conductive due to variations in composition and the resistivity values can have a large range (10^{-5} Ω cm to 10^{4} Ω cm)[135-137]. Doping of ZnO films with *n*-type dopants Al, Ga, In and Ge have been reported to improve the electrical properties[138]. Al doped ZnO films have been reported with low resistivity values which are comparable with indium tin oxide (ITO) films. Doping of ZnO films with noble metal nanoparticles, Au, Ag and metal dopant Cu and Al were investigated for possible surface plasmon resonance enhancement of non-linear optical properties.

This chapter describes an investigation into the use of the aerosol assisted chemical vapour deposition (AACVD) technique to synthesize new ZnO thin film coatings that exhibit high transparency in the visible region of the electromagnetic spectrum and high electrical conductivity. In particular to see how AACVD and dopants can affect preferred orientation. The synthesis and formation of ZnO, noble metal doped ZnO and aluminium oxide doped ZnO thin

films are reported. It will be shown that the dopant can direct the preferred orientation seen for ZnO films. The ability to be able control preferred growth is very important for functional applications. For example surface acoustic wave devices prefer c-axis orientated films and application of ZnO TCO materials within photovoltaic and LED devices are enhanced at specific orientation directions[138].

3.1.0 Experimental Methods

3.1 General experimental

3.1.1. Standard reagents and conditions

The host matrix precursor used for the investigation into the properties of ZnO thin films with and without the addition of the *p*-type dopant, Al and noble metal nanoparticles was [$Zn(acac)_2$] ~0.02 mol dm^{-3}. The most probable route for decomposition of the [$Zn(acac)_2$] precursor would be oxidative thermolysis within the reaction chamber. The metal precursors selected for incorporation into ZnO host matrix thin films included auric acid ($HAuCl_4$, 5.1 x 10^{-3} mol dm^{-3}) as a precursor to gold, silver nitrate ($AgNO_3$, 9.9 x 10^{-3} mol dm^{-3}) as a silver former and Copper (II) acetylacetonate, ($Cu(acac)_2$, $Cu(C_5H_7O_2)_2$, 7.6 x 10^{-3} mol dm^{-3}). The aluminium dopant precursor selected was $Al(NO_3)_3$, 2.14 x 10^{-3} mol dm^{-3}.

3.1.2. Analytical analysis

Scanning electron microscopy (SEM) analysis was carried out on a field emission JEOL 6301F instrument for both morphology and elemental analysis using the Energy Dispersive X-ray (EDX) analysis with uncoated and carbon/gold coated samples. SEM images used accelerating voltages from 5–20 kV. EDX analysis (typical voltage 20 kV with Cobalt as the standard element atomic ratio) was quantified using Oxford Link ISIS system. X-ray diffraction (XRD) analysis was carried out using a Bruker D8 discover reflection diffractometer with Cu Kα radiation (λ = 1.5406 Å) in reflection mode with glancing angle incidence beam of 1.5° or 5°. UV/Visible spectroscopy was carried out using a Helios Alpha Double Beam UV Spectrometer that allowed

direct comparison between the thin film and the glass substrate. Spectra were collected in the range between 300-1000 nm. Visible/IR transmittance and reflectance spectroscopy was carried out using A Zeiss miniature monolithic spectrometer (range 380–1150 nm) connected to a PC. Sheet resistivity/conductivity measurements were carried out using a 2-point-probe method for resistance (Ω).

3.1.3. Thin film growth

All synthesis was carried out using an aerosol assisted chemical vapour deposition technique with an ultrasonic nebuliser (Pifco xj 40 KHz). The general synthesis procedure involved dissolving precursors in methanol (50 ml) that were then nebulised to form an aerosol mist within either a glass or plastic bottle. The aerosol mist was transported by an inert gas (N_2) to a cold wall reaction chamber, where two clean parallel plates, 8 mm apart, of silica (50 nm) coated Float glass (dimensions 145 x 45 x 3 mm), previously cleaned with appropriate solvents (water, methanol or acetone) and dried in air, were heated (250-450 ºC), using a graphite block controlled by a thermostat (Tempatron TC4800), monitored by a Pt-Rh thermocouple. The aerosol droplets were then swept by a carrier gas into the reaction chamber where they were evaporated and a film deposited on the glass substrate. The reaction chamber was vented into the extraction system of a fume cupboard. The inert gas flow was allowed to continue for 10 min after either all the precursors had been used or 2 h had passed. The substrates and films were allowed to cool to room temperature *in-situ* and were stored in air.

3.2.0 Results

3.2.1 Synthesis and characterization

The ZnO films with and without additional phases were well adhered to the substrate, passed the Scotch tape test and could not be easily scratched with anything other than a hard surface (brass and steel).

3.2.2 Visible appearance and optical characterization

Zinc oxide *n*-type semiconducting films were synthesized as either undoped thin films at substrate temperatures of 400-600 °C or doped host matrix thin films with either Al_2O_3 or noble metal dopants Au, Ag, Cu at 400 °C from the AACVD of zinc acetylacetonate solutions. The macroscopic appearance by eye of all the films was transparent at thickness <1μm, with the films becoming white and opaque at a thickness above 4 μm; some of the films, especially the thinner ones displayed optical interference patterns that were indicative of areas of non-uniform thickness. The one exception was the ZnO thin film formed in the presence of copper, which was opaque and highly coloured (royal to navy blue). There appears to be a broad absorbance peak (600 nm) for Cu(CuO/Cu_2O) doped ZnO thin film sample deposited at 400 °C.

Transmittance results for undoped 400 nm thick ZnO thin films grown at 400 °C in the visible region were around 85%, scaled with thickness and were reproducible over sequential samples. The reflectance of these films rose to a maximum of ~20% in the infrared region (1500 nm) and similar results for transmittance were obtained for the ZnO film grown at 450 °C. Transmittance results for the visible region are >70% for the 500 nm thick ZnO-Al_2O_3 composite thin film grown at 400 °C. Transmittance for ZnO films incorporating Au and Ag doped ZnO thin films, even at very low incorporation levels, were lowered in the visible region compared to the undoped films. Reflectance results for both dopants lower reflectance in the IR region. The ZnO: Cu doped ZnO film at a thickness of 2 μm was very opaque (>85% film area) with visible transmission below 20%.

3.2.3 SEM and EDX analysis

3.2.3.1 Undoped films

The main purpose of the microscopy study was to see how temperature and addition of a secondary reagent to the AACVD precursor solution affected the morphology of the zinc oxide films deposited.

The shape, morphology and thickness of the doped and undoped ZnO thin films were determined on the majority of films synthesized at various magnifications (12,000–80,000x). Two samples of undoped ZnO films (400 °C) were assessed. The surface consisted mainly of spherical nanoparticles with a typical size of ~100 nm, see fig. 48 a). Thickness measurements showed mainly areas of consistent thickness (~395–450 nm) with occasional thicker areas (≥ 600 nm) from samples deposited in the middle of the substrate, see fig. 48 b). This thickness variation was a result of the reactor block on which the substrate sat; this block gave a *ca* 30 °C temperature difference from the centre to the edges at 400 °C. The thickest part of the film was formed at the centre of the block because this was the hottest part of the substrate. At higher magnification the ZnO particles were mainly rounded and spherical in shape with a tendency towards agglomeration, typical size ~100 nm, see fig. 48 c). This morphology is indicative of an aerosol assisted CVD process where extensive reaction has occurred in the gas phase, this tends to form spherical particles, the shape being influenced by the drop drying out process. EDX analysis for undoped ZnO films (400 °C), showed only Zn and O, see table 13.

Figure 48: Top-down and side-on SEM micrograph of ZnO film grown by AACVD (MeOH, 400 °C): a) Top-down SEM micrograph and b) Side-on SEM image of ZnO film grown by AACVD of $[Zn(acac)_2]$ in methanol at a substrate temperature of 400 °C . The scale bars represent the measured film thickness (380 nm).

a) b)

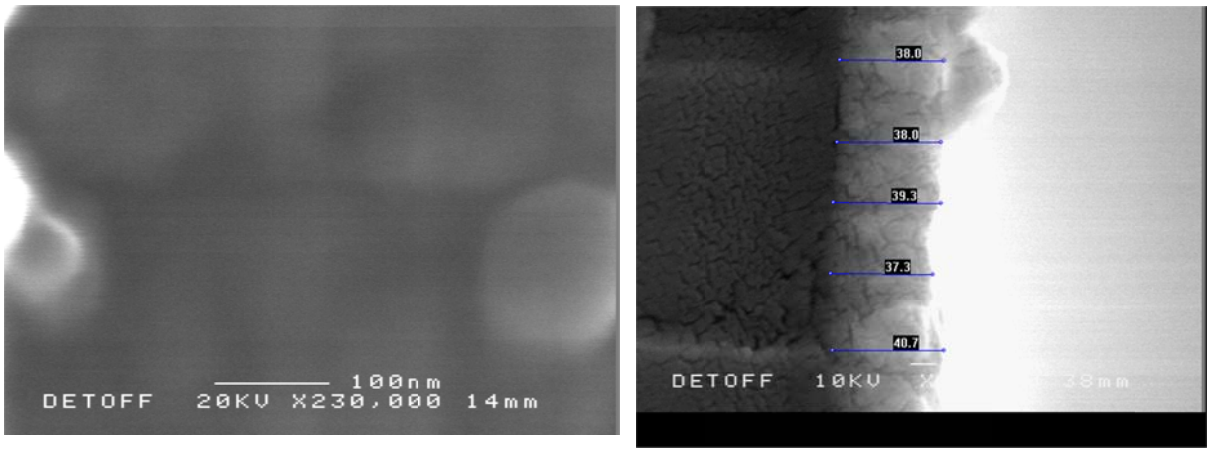

c) Top-down SEM micrograph of transparent undoped ZnO film formed from $[Zn(acac)_2]$ (MeOH, 400 °C).

i) Side closest to reactor inlet ii) furthest from the reactor inlet.

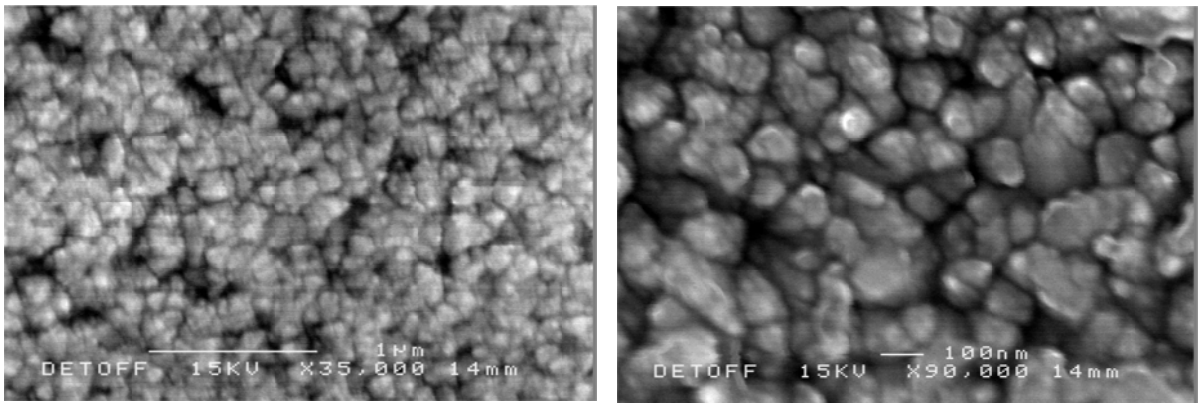

Table 13: Comparison of EDX analysis for ZnO thin films (400 °C) atomic % for Zn and O.

Sample No.	EDX Atomic %		Ratio	
	Zn	O	Calculation	Approximation
1, area 1	8.57	57.95	1 : 6.76	1 : 7
2, area 1	25.82	45.47	1 : 1.76	1 : 2
2, area 2	22.15	36.50	1 : 1.65	1 : 2
2, area 3	19.66	32.73	1 : 1.66	1 : 2

The surface morphology of the undoped ZnO thin films formed at 450 °C was again mainly spherical (300-400 nm) however occasional hexagonal nanoparticles 1-2 μm were seen, see fig. 49 a-c). The shaped particles are either the result of the growth of ZnO crystallites from the spherical particles although this seems unlikely as the films deposited at 400 °C maintained their rounded geometry or the result of surface growth. The film is more opaque towards the section of the glass substrate nearest to the exhaust vent and this corresponds to the agglomerated particles of dimension 100-200 nm, see fig. 49 d). The thickness differences of the transparent (~300-440 nm) and opaque (~800-1000 nm) areas of the film appear to be significant, see fig. 50 a-b).

Figure 49: Top-down SEM micrograph of ZnO film formed from [$Zn(acac)_2$] (MeOH, 450 °C): (a) transparent area of ZnO film nearest the reactor vent, (b) individual hexagonal nanoparticle, (c) transparent area of ZnO film, close up of a), (d) opaque area of ZnO film furthest from the reactor vent.

a)

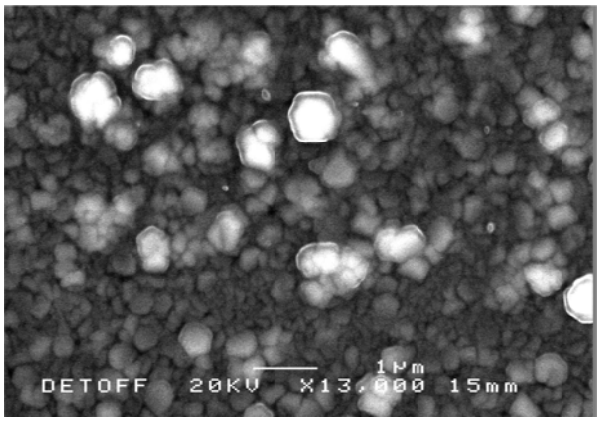

b)

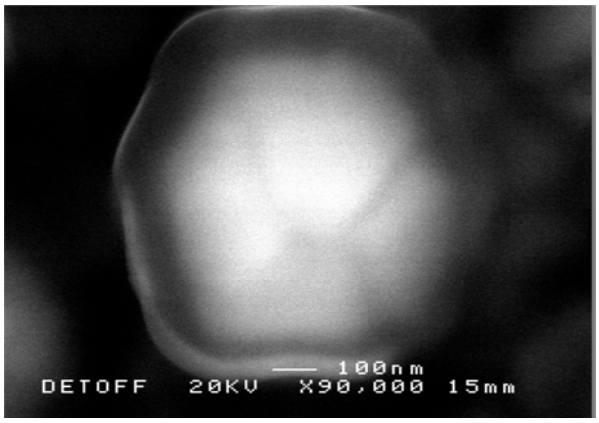

c)

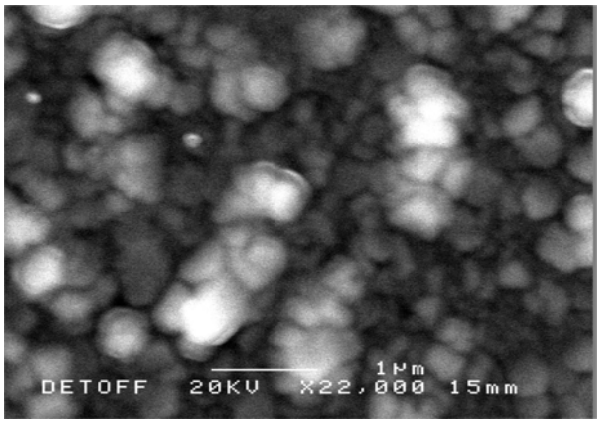

d)

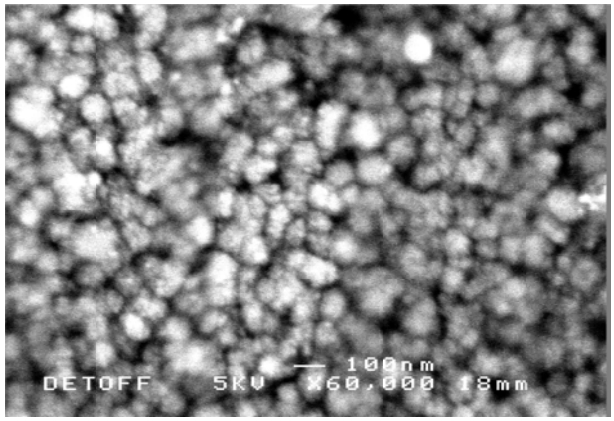

Table 14: EDX analysis for undoped ZnO thin film, 450 °C

Sample Type & Area	EDX Atomic %		Ratio	
	Zn	O	Calculation	Approximation
Bulk, area 1	24.55	50.62	1 : 2.06	1 : 2
Bulk, area 2	29.35	43.45	1 : 1.59	1 : 1.6
Hexagon, area 3	34.59	55.08	1 : 1.48	1 : 1.5

Figure 50: Side-on SEM image of ZnO film grown by AACVD of $[Zn(acac)_2]$ (MeOH, 450 °C): The scale bars represent the measured film thickness (380 nm). (a) transparent area of ZnO film, (b) opaque area of ZnO film.

a) b)

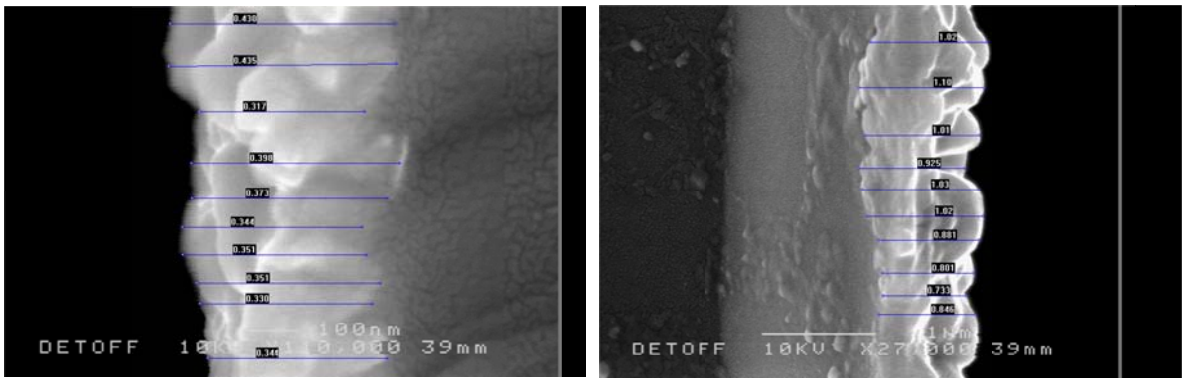

Table 15: EDX analysis: Comparison of undoped ZnO thin films, 400 °C, 500 °C

	Sample			
	Undoped ZnO (400 °C)		Undoped ZnO (500 °C)	
Element	Weight%	Atomic%	Weight%	Atomic%
O	37.60	57.95	30.19	50.31
Zn	22.72	8.57	26.60	10.85

The thinner regions were at the front of the substrate and the thicker regions at the back of the substrate; this variation has been seen before for AACVD processes[124-132]. EDX analysis of undoped ZnO thin film (450 °C) shows only Zn and O in the expected stoichiometric ratio, see table 14. The surface morphology and shape was clearer and easier to define in the film deposited at 500 °C than the ones made at 400- 450 °C, nearly all nanoparticles were spherical in shape (~200–400 nm) with some larger agglomerated particles (~500–1000 nm) again EDX confirmed only Zn and O in the films in the expected elemental ratio, see table 15.

3.2.3.2 Doped films

The addition of aluminium nitrate to the initial precursor solution produced a ZnO thin film with small amounts of readily identifiable Al_2O_3 from EDX analysis. The use of a an aluminium precursor in the initial AACVD mix induced significantly different ZnO morphology, mainly *ca* 100 nm spherical particles or oblong/rice shape particles with a long axis of 300 nm and with occasional cubic (~1 μm) particles, see fig. 51 a-d). Wide area EDX comparisons of the four different areas gave an Al content of 1.15 to 3.35 at. %, see table 16. The

aluminium was localized on the surface into readily identifiable regions consistent with formation of a composite of ZnO: Al_2O_3 rather than formation of a solid solution of Zn_xAl_yO.

Figure 51: SEM morphology of Al (Al_2O_3) doped ZnO film formed at 400 °C from the AACVD of [$Zn(acac)_2$] and $Al(NO_3)$ (MeOH): Micrographs were obtained from (a) to (d) moving lengthwise along the substrate from the reactor inlet (a) to outlet (d).

a) Spherical

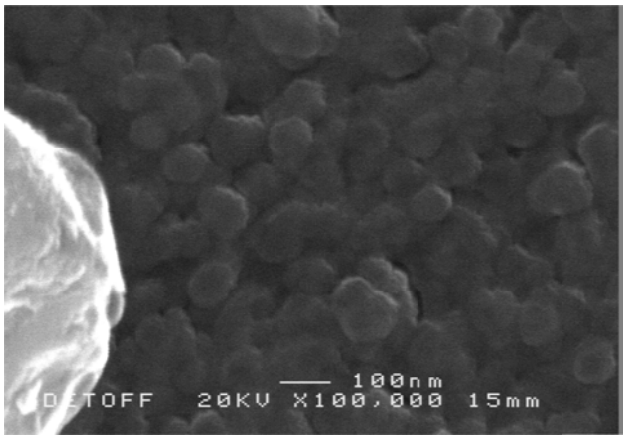

b) Oblong/rice shaped

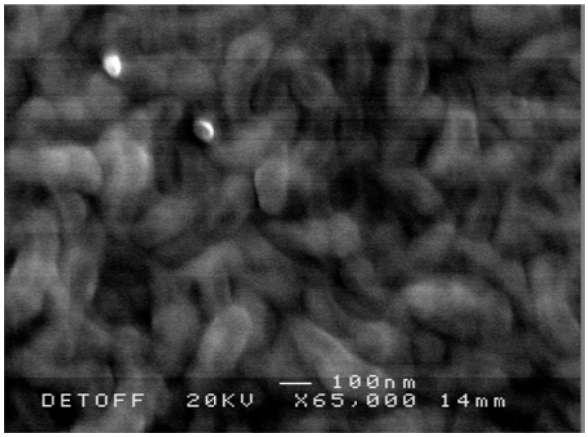

c) Spherical/Oblong

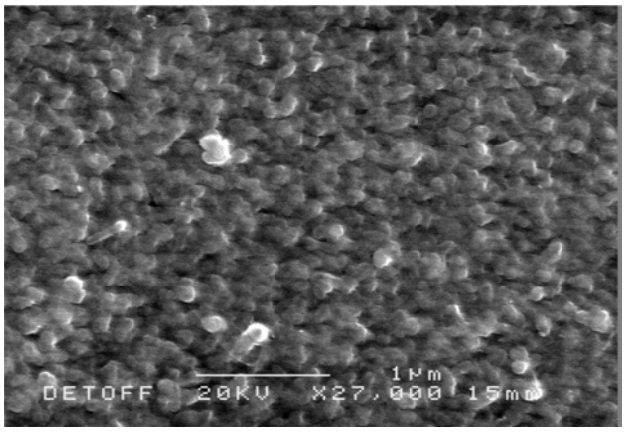

d) Cubic

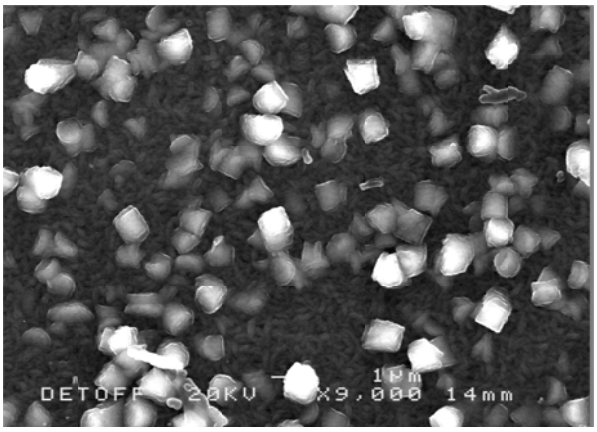

Table 16: EDX analysis for Al (Al_2O_3) doped ZnO thin films areas a), b), c) and d)

	Sample Area							
	a) spherical area		b) oblong/cigar shape		c) Spherical/oblong area		d) Cubic area	
Element	Weight%	Atomic%	Weight%	Atomic%	Weight%	Atomic%	Weight%	Atomic%
O	32.17	53.21	26.96	51.63	40.09	59.84	25.86	51.88
Al	2.41	2.36	2.99	3.39	1.30	1.15	2.31	2.75
Zn	28.79	11.66	48.63	22.79	19.63	7.17	54.51	26.77

The SEM surface morphology analysis for the ZnO thin films deposited in the presence of noble metal nanoparticles demonstrated quite different

morphologies dependent on the Au, Ag and Cu used. The ZnO thin film formed in the presence of auric acid gave rounded oblong nanoparticles ~100-1000 nm that were very agglomerated and intertwined on the substrate it was also noted that deposition in this case also occurred on the top guide plate analysis of these revealed nanoparticles that were more spherical in nature, fig. 52 a-b). The EDX analysis shows a gold atomic percentage of 0.15 atom% for the substrate and 0.31 atom% for the top plate, see table 17. The higher percentage gold doping is a probably a consequence of aerodynamic drag and/or the thermophoretic effect.

Figure 52: SEM morphology of Au doped ZnO thin films formed by the AACVD of $[Zn(acac)_2]$ (MeOH, 400 °C).

a) b) higher magnification of (a)

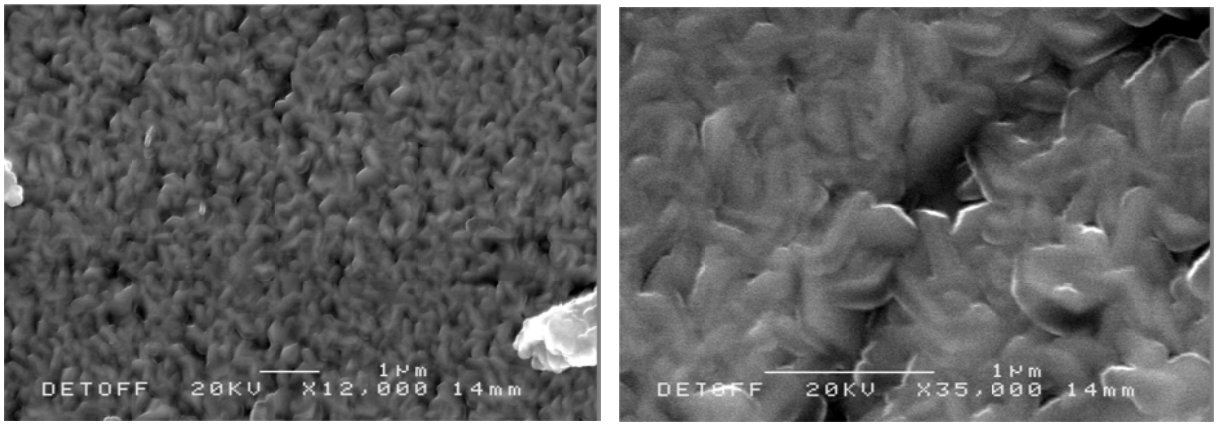

Table 17: EDX analysis: Au doped ZnO, 400 °C, bottom and top plate

	Sample			
	Bottom Plate		Top plate	
Element	Weight%	Atomic%	Weight%	Atomic%
O	22.37	45.18	38.93	57.48
Zn	48.52	23.99	11.37	4.11
Au	0.90	0.15	2.61	0.31

The ZnO thin films formed in the presence of silver nitrate mainly gave very well defined spherical nanoparticles, of ~ 200-500 nm, see fig. 53. EDX analysis shows 0.28 at. % Ag, on the substrate plate, again deposition was also noted on the top guide plate which showed a ZnO film by EDX with slightly more silver, 0.62% at.% Ag, see table 18. In both the Ag and Au cases, the predominant phase seen was ZnO and there was no direct evidence of silver or gold nanoparticle formation. SEM of ZnO thin films formed in the presence of

copper nanoparticles gave spherical nanoparticles (~200-1000 nm) with some agglomeration, see fig. 54. EDX analysis for ZnO: Cu thin film gave a significant amount of Cu (22.18 at. %), see table 19.

Figure 53: SEM morphology of Ag doped ZnO thin films formed by the AACVD of $[Zn(acac)_2]$ (MeOH, 400 °C).

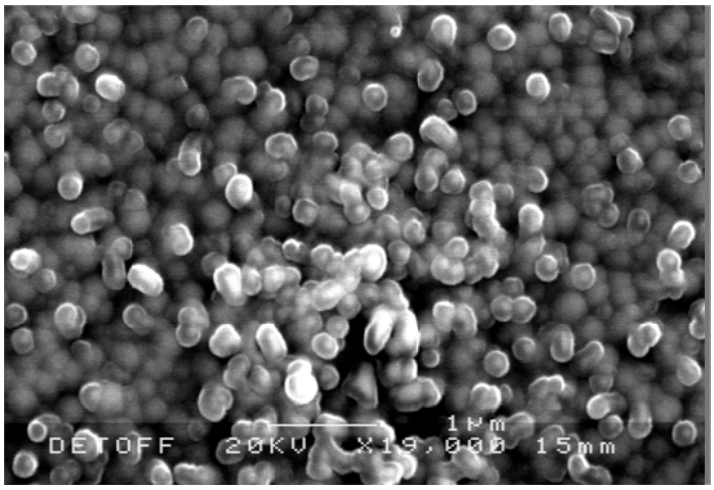

Table 18: Representative EDX analysis of bottom and top plates of Ag doped ZnO thin films

	Sample			
	Bottom Plate		Top plate	
Element	Weight%	Atomic%	Weight%	Atomic%
O	24.92	48.20	41.95	61.96
Zn	47.21	22.35	16.16	5.84
Ag	-0.40	-0.12	2.84	0.62

Figure 54: SEM morphology of Cu doped ZnO thin films formed by the AACVD of $[Zn(acac)_2]$ (MeOH, 400 °C).

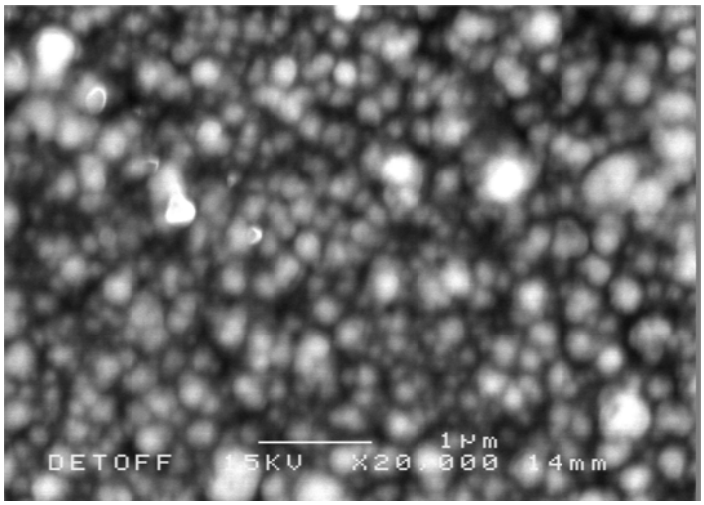

Table 19: EDX analysis for Cu doped ZnO thin film, 400 °C

Element	Weight%	Atomic%
O	20.64	45.83
Cu	39.67	22.18
Zn	24.13	13.11

The SEM surface analysis demonstrates the effect that synthesis temperature has on morphology, shape and thickness. Higher synthesis temperatures gave more defined nanoparticles. There is also an increase of white opaque areas of film with increasing synthesis temperature which correlates to an increase in film thickness. Film thickness also appears to increase towards the exhaust vent of the AACVD reaction chamber. EDX analysis confirmed the presence of Zn and O for the undoped ZnO thin films (400/450-500 °C). The attempted doped Al (Al_2O_3) ZnO thin film produced several different morphologies, spherical (~100 nm) or oblong/rice shaped (~300 nm) and a cubic (~1 μm) area. EDX comparisons of the four different areas give a range (1.15 to 3.35 at. %) of Al present. SEM morphology analysis of the noble metal into the ZnO host matrix film revealed interesting effects. Au was minimally incorporated into the substrate plate ZnO thin film, according to EDX, but still had a significant effect on morphology producing intertwined and agglomerated oblong ZnO nanoparticles, almost acting like a surfactant template. Ag was incorporated again at a low atomic % level, but definitely had an effect on the morphology of the ZnO nanoparticles which were spherical and well defined. Incorporation of Cu or copper oxide nanoparticles produced less well defined spherical nanoparticles with some agglomeration.

The variation in metal dopant incorporated in the films was somewhat surprising. Based on the molar ratios used in the reaction it was expected that between 5 and 10 at.% would be found in the films. The silver and gold were found to present at much lower levels. This can be explained by the fact that under similar conditions both precursors can generate nanoparticles that are difficult to incorporate into films due to aerodynamic drag and/or thermophoretic effects. The copper based precursor readily formed copper oxide in the process and this deposition seems to be kinetically faster than that of zinc oxide, whilst the corresponding aluminium oxide deposition is slightly slower than that for ZnO.

3.2.4 X-ray diffraction analysis

3.2.4.1. Affect of temperature

XRD analysis was carried out on the ZnO films formed at substrate temperatures of 400-600 °C. ZnO thin films deposited at temperatures 400-500 °C, showed a very distinct preferred crystal lattice orientation in the (002) direction. This orientation has been reported as the most electrically conductive orientation for ZnO. The preferred (002) crystal lattice orientation appears to be lost at films grown at above 500 °C and replaced with the expected random orientation pattern for hexagonal ZnO, see fig. 55 a). The ZnO thin film preferred crystal lattice orientation at lower temperatures could be expected due to the natural predilection of the interpenetrating hexagonal close packed lattice and the wurtzite structure. There are reports in the literature[125] theorizing that small amounts of ZnO have a catalytic effect, in this case a directional catalytic effect, almost like a *pro forma* laying down a template for the nanoparticles to line up with during AACVD synthesis.

3.2.4.2 Affect of dopant

Two XRD patterns were analysed from the ZnO: Al_2O_3 film grown at 400 °C. A comparison with the undoped ZnO XRD pattern grown at 400 °C with two XRD scans of an Al doped ZnO film grown at the same temperature clearly showed a marked change in preferred crystal lattice orientation, from the (002) direction in the ZnO film to the (101) direction in the composite, see fig. 55 b). The XRD pattern for the repeat film of the ZnO: Al_2O_3 composite clearly displays a shoulder on the (101) peak corresponding to the (002) direction whereas the first sample has no such shoulder, a probable explanation is that there is a difference in the thickness of the film between the two areas scanned. This has caused a slightly more complex crystal lattice orientation in the second film, although the (101) direction still predominates. In neither film was the pattern for Al_2O_3 clearly observed, probably because it is present in such low amounts (*ca* 2-3 mol%). Although the alumina was present in small amounts and from EDX was found to be inhomogeneously distributed, X-ray analysis did not pick up this variation because the spot size was too large; furthermore areas of

different alumina concentration could not be used to account for the variation of preferred orientation.

Metal, Au, Ag and Cu precursors were introduced in the same solution as [$Zn(acac)_2$] to attempt to produce noble metal doped ZnO films. The use of auric acid in the initial solution formed a ZnO film that had a complex preferred crystal orientation in the (002) and (101) direction, see fig. 55 c). The introduction of silver nitrate to the initial solution formed a ZnO film with a preferred crystal orientation in the (002) direction, see fig. 55 c). Cu, as copper oxide, nanoparticle incorporation into ZnO host matrix showed a preferred crystal orientation in the (002) direction for the top substrate plate and a random crystal orientation in the bottom substrate plate, see fig. 55 d). The copper phase was present in sufficient amounts to allow identification as cubic Cu_2O. This was surprising as the copper is formally reduced in the deposition, with no readily identifiable reducing agent.

Figure 55: XRD patterns: AACVD ZnO films of [$Zn(acac)_2$] (MeOH, 400 °C and 500 °C): (a) XRD: ZnO AACVD films, (MeOH, 400 °C and 500 °C). (b) XRD: Undoped and Ag doped AACVD films (MeOH, 400 °C (red and green lines)), (c) XRD: ZnO undoped and doped Au and Ag AACVD film (MeOH, 400 °C); (d) XRD: ZnO undoped and Cu doped AACVD film (MeOH), (BP = bottom substrate plate, TP = top substrate plate).

a)

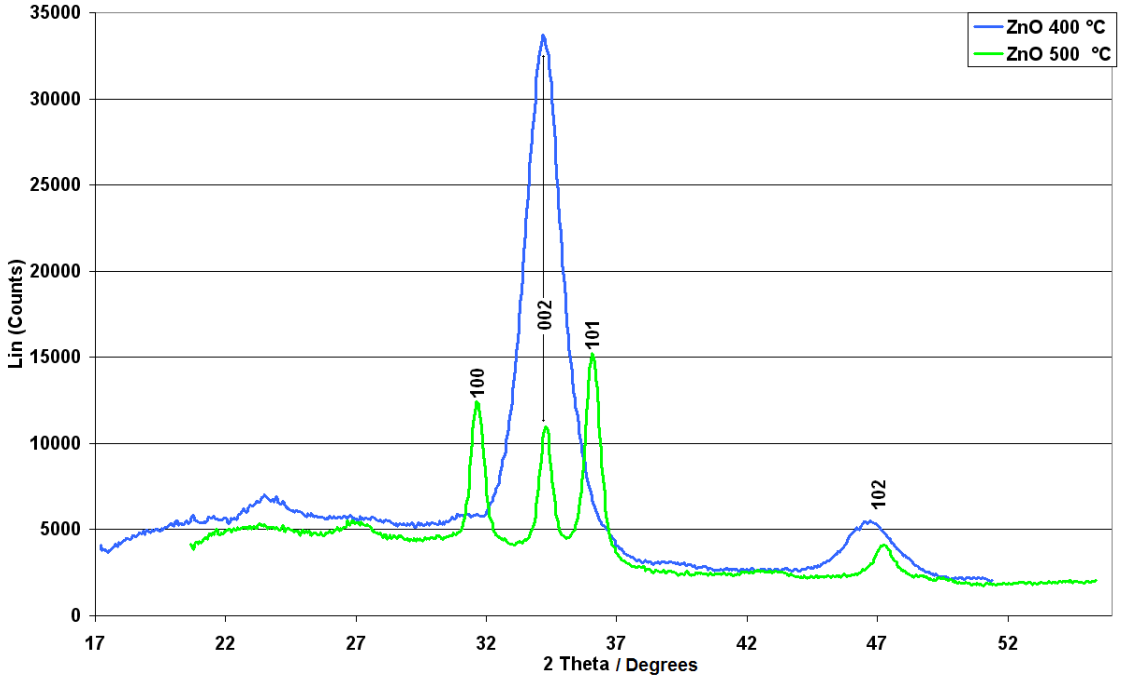

b)

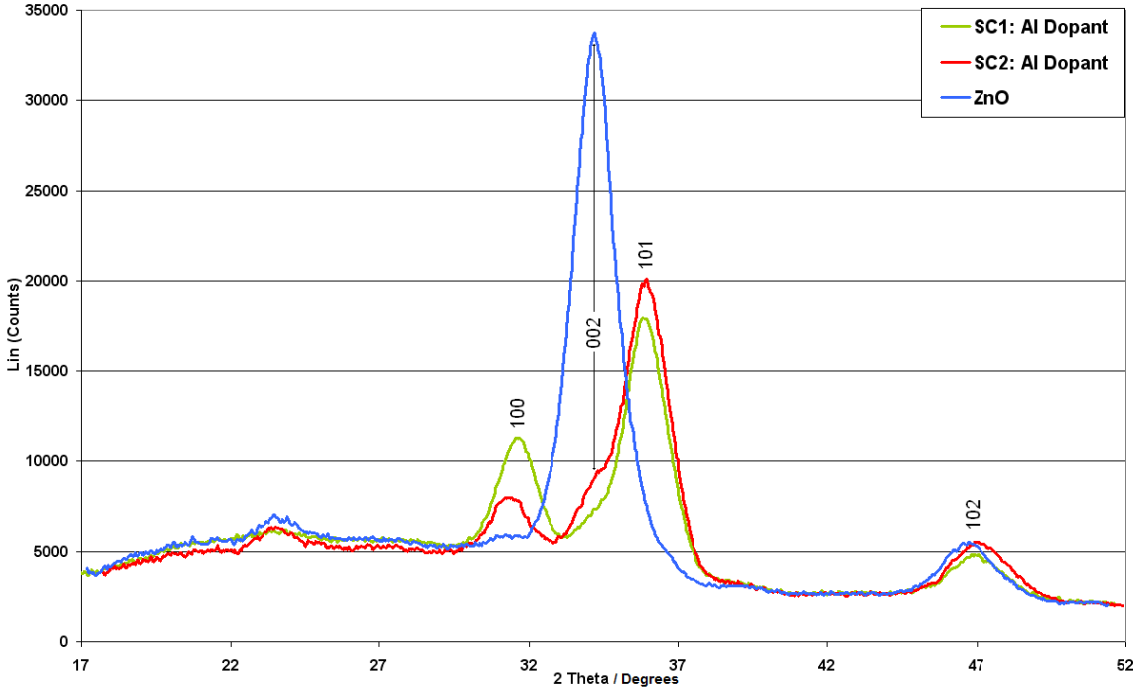
SC1: Al Dopant
SC2: Al Dopant
ZnO
Lin (Counts)
2 Theta / Degrees
100
002
101
102

c)

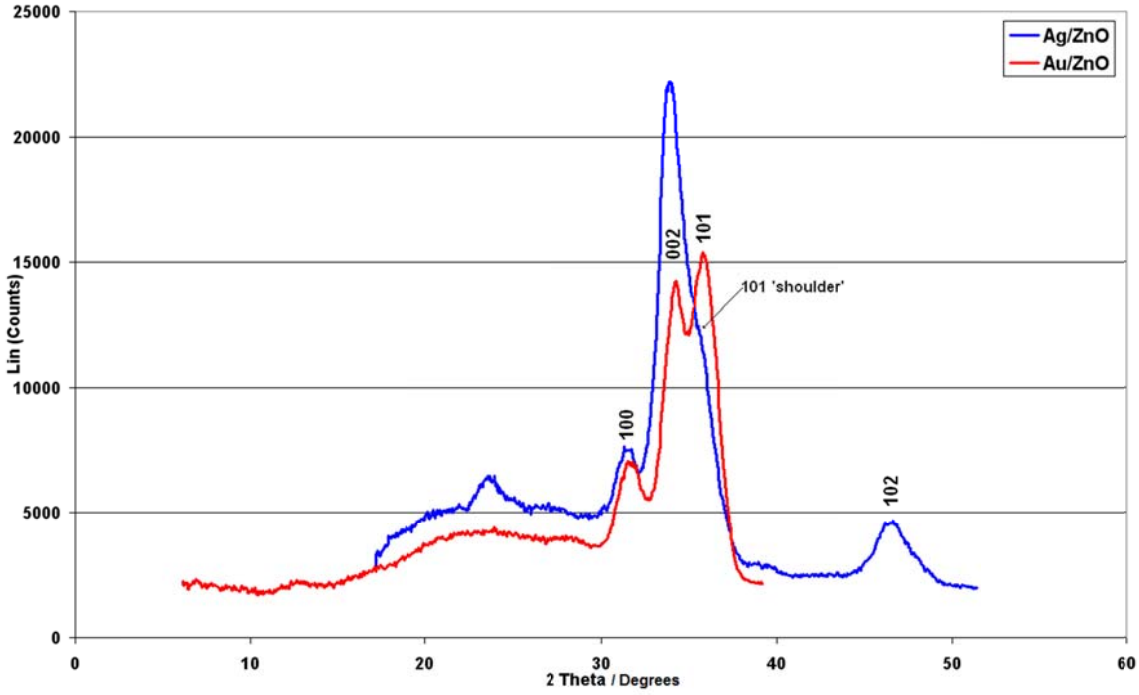
Ag/ZnO
Au/ZnO
Lin (Counts)
2 Theta / Degrees
100
002
101
101 'shoulder'
102

d)

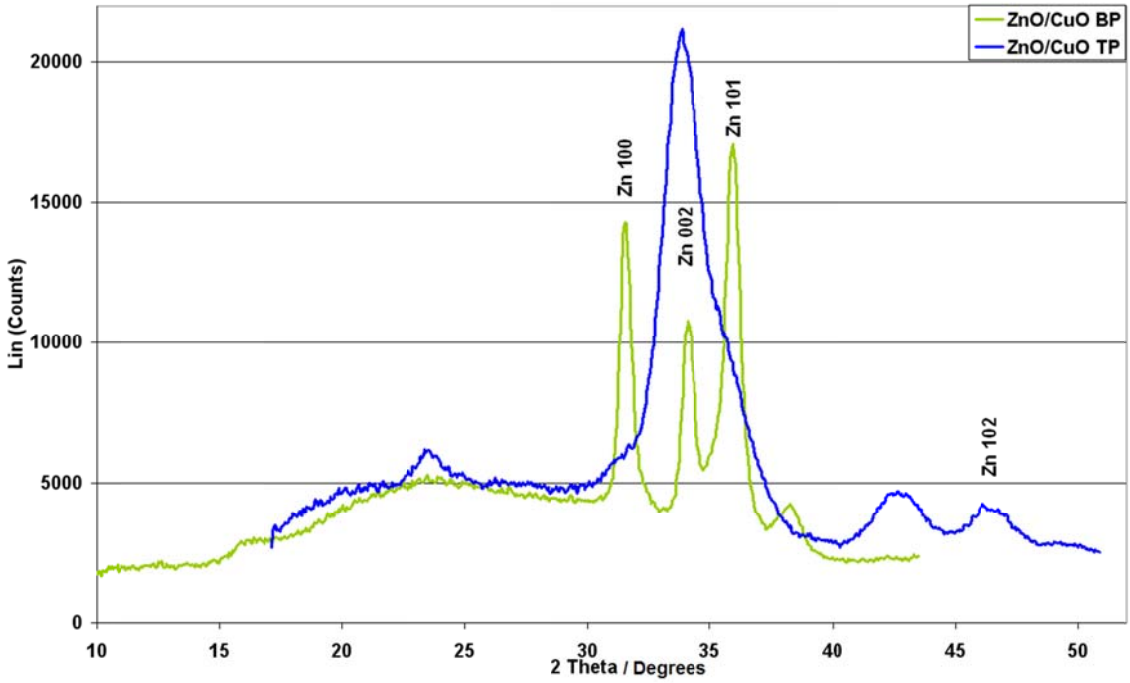

The undoped ZnO host matrix thin films (< 500 °C) display a preferred crystal lattice orientation in the (002) direction. The ZnO: Al_2O_3 composite film (400 °C) displayed a preferred crystal lattice orientation in the (101) direction. Noble metal dopants Ag and Cu as Cu_2O do not appear to effect the crystal lattice orientation to any great degree and follow the preferred (002) crystal lattice direction of undoped ZnO thin films (< 500 °C), although Au appears to produce a complex crystal lattice orientation in both the (002) and (101).

3.2.5. Resistance measurements

The lowest value obtained for sheet resistivity using the 2 point-probe method was 52.4 kΩ for a ZnO thin film where an attempt to incorporate Au nanoparticles into the host matrix was made. Although the EDX stoichiometric analysis shows that very little of Au nanoparticles were included in this film, the morphology had definitely been affected and maybe further indication of the effect shape and distance between ZnO nanoparticles have on conductance. Therefore no ZnO films with or without dopants grown by AACVD have low resistivity (20 kΩ, 2 point-probe).

3.3.0. Discussion of AACVD ZnO films

The ideal ZnO thin film, doped or undoped, should display a strong transmittance (≥ 70%) in the visible region and either a strong reflectance (≥ 70%) in the near IR region or high electrical conductivity. Undoped ZnO thin films (400-450 °C) and the Al (Al_2O_3) doped ZnO film achieved the transmittance criterion (>70%) but failed to achieve the reflectance criterion (>40%). Au and Ag doped ZnO thin films (nanoparticle <1% at. wt.%) appeared to have a slight detrimental effect on transmission in the visible region when compared to undoped ZnO films. Reflectance results for Au and Ag dopants indicate that incorporation into a ZnO host matrix thin film is detrimental to the percentage reflectance. ZnO thin films were deposited at a range of temperatures (400-500 °C), films grown below 500 °C showed a distinct preferred crystal lattice orientation in the (002) direction which has been reported as the most electrically conductive orientation for ZnO. At 500 °C XRD analysis showed the random orientation pattern for hexagonal ZnO and the preferred crystal lattice orientation of lower temperatures disappeared. Comparison of these results with the literature has shown the preferred (002) crystal lattice orientation to be at higher temperatures for undoped ZnO thin films using a sol-gel method where the ZnO film was annealed (~500) on quartz and sapphire substrates[139] and for flame CVD (>500 °C), on quartz substrates[136], and for the atmospheric pressure CVD (500-600 °C) technique on Pyrex glass substrates[140] which is the complete opposite of the results reported here for AACVD- where preferred orientation was only seen at lower substrate temperatures. Furthermore the use of aluminium nitrate in the initial precursor solution forms a composite film in which the predominant phase is ZnO, but that this ZnO shows strong (101) growth.

The lowest sheet resistivity value (52.4 kΩ) for a ZnO thin film was when Au nanoparticles had been attempted as inclusions to the host matrix. The EDX stoichiometric analysis shows that small amounts of Au nanoparticles were incorporated into the film, the morphology had changed, indicating the effect shape and distance between ZnO nanoparticles had on the mean free path for conductance. Therefore no ZnO films with or without dopants have the low resistivity required for good conductivity. There are four main technical difficulties with AACVD synthesis, effects of aerodynamic drag and

thermophoresis, low particle incorporation into the thin film and deposition time. One of the main issues includes thermophoresis effect[141, 142], drag, gravity and Brownian forces that occur in the reaction chamber due to the temperature gradient in both laminar and turbulent gaseous flow. The result is that deposition also occurs on the elevated surfaces above the actual surface that requires coating. There is also the technical difficulty of low particle incorporation due to the nebulized aerosol mist delivery system used for AACVD. The affinity of the raw material precursors for the solvent vapour state and the rate of evaporation of the solvent affects the amount of host matrix, transition metal dopants and noble metal nanoparticles deposited onto the desired surface. Precursors with a low affinity for the vapour state of the carrier solvent have difficulty forming the aerosol mist and tend to deposit precursor material on the inside of the nebuliser bottle and carrier tubes.

3.4.0 Summary of AACVD ZnO films

The majority of the undoped and doped ZnO host matrix thin films were highly transparent the transparency was lowered when higher temperatures (> 450 °C) were used or where film thickness increased (≥ 1 μm) with the exception of the Copper oxide doped ZnO film which was highly coloured and mainly opaque. Undoped and noble metal doped ZnO host matrix films had mainly spherical shaped morphology, which became more pronounced with dopants. Transmittance results for all undoped and doped ZnO thin films was sufficient to pass the criterion required for glass but inclusion of any dopants including Au, Ag and Al_2O_3 dopants appear to have a detrimental effect on the reflectance criterion. The attempted Al (Al_2O_3) doped ZnO film had varying morphology from spherical to cubic. The XRD pattern at lower temperatures (< 500 °C) showed a strong preferred (002) crystal lattice orientation for undoped and noble metal nanoparticle doped ZnO films not previously reported in the literature for these temperatures. The undoped ZnO film at 500 ºC exhibited a random crystal orientation pattern for hexagonal ZnO. The Al (Al_2O_3) doped ZnO thin film crystal lattice orientation had a (101) preferred direction in contrast to majority of the other ZnO films which displayed a strong preference for the (002) direction. The sheet resistivity values were high for nearly all the ZnO thin films and therefore these films were not conductive. Thermophoretic effects

have always been thought to be the main obstacle for incorporation of nanoparticles in high concentrations into the host matrices for ZnO thin films but aerodynamic drag, see chapter 2, is the more likely to be the main force responsible for the low particle incorporation into these host matrices.

Chapter 4

AACVD/APCVD Synthesis of TiO_2 Films: Prototype 1

Chapter 4: AACVD/APCVD Synthesis of TiO_2 Films: Prototype 1

4.0.0 Introduction

Titania films are of interest because of their potential and known uses as self-cleaning, photocatalytic, solar control and gas sensing coatings. There are two types of photocatalysis for titania films, involving photo-induced redox reactions (UV irradiation) and photo-induced hydrophilic inversion of TiO_2. The photocatalytic properties of titania are related to the crystal phase, grain size, morphology and band gap (3.1-3.3 eV), with smoother morphology possibly being the key to easier migration route for the photo electron hole pairs to reach the surface, for the $OH^{\cdot}$ radical cascade process to reduce/oxidise organic species[143]. Surface contact angle formed with water droplets also influences the self-cleaning property of titania films *e.g.* on archetypal glass with rougher surfaces being reported as more beneficial for superhydrophilic properties[144]. The most common phases of TiO_2 are rutile, which exhibits a slightly lower band gap (~3.0 eV) and can be irradiated by shorter wavelengths of light than the anatase phase with a slightly larger band gap of ~3.2 eV. The anatase phase has superior photocatalytic properties, due in part to the superior e^- h^+ mobility. Anatase-rutile mixtures appear to enhance electron pair separation, with the rutile phase trapping conduction electrons and improving photocatalytic activity[145].

Doping has been used to improve titania's properties in particular metal doping has been used to achieve a batho-chromic shift, a decrease in the band gap or introduction of intra-band gap states which result in more visible light absorption. Traditional doping with typical *n*-type dopants *e.g.* nitrogen have been one of the most common methods for titania film property enhancement with nitrogen interstitial doping favouring photocatalytic activity over substitutional[146, 147]. Typical *n*-type dopants have an excess of electrons *e.g.* Group 15 of the periodic table, P, N, and As that can be donated to the conduction band. Noble metal dopants Au, Ag and Cu are of great interest due to the surface plasmon resonance effect, the oscillation of conduction electrons in resonance with the electromagnetic field in thin films producing waves

travelling at the metal-surface interface and the donation of electrons into the conduction band which have been shown to enhance optical, physical and chemical properties of titania films such as photocatalytic activity.

The following chapter looks at the possible effects of the noble metal Au, Ag and Cu dopants on the physical and optical properties such as colour, morphology, transmittance/reflectance, surface contact angle and crystal lattice orientation on TiO_2 host matrix films. The titania films were synthesized using a combined AACVD/APCVD technique and analysed using a range of techniques such as UV-VIS spectroscopy, XRD, SEM, EDX, EDS, XPS and Raman to assess the possible influence "dopants" could have on physical, optical and chemical properties of these TiO_2 films. The titania films in chapter 4 are referred to as being doped even though the level of dopant, if present, may be below levels of detection for ease of understanding the thread of work and because the dopants were found to have such a profound effect on physical, optical and chemical properties such as morphology, water contact angle and colour.

4.1.0 Experimental Methods

4.1 General experiment

4.1.1 Standard reagents and conditions

The host matrix precursor used for the formation of the TiO_2 films with or without the addition of noble metal and/or *p*-type dopants were titanium tetraisopropoxide (TTIP, 10 l/min) for CVD synthesis. The noble metal precursors selected for incorporation into the AACVD/APCVD synthesis were $HAuCl_4$ (0.01 - 5.1 x 10^{-3} mol dm^{-3}), $AgNO_3$ (0.02-3.5 x 10^{-2} mol dm^{-3}), $Cu(acac)_2$ (7.6 x 10^{-3} mol dm^{-3}) and pre-formed Au nanoparticles [citrate method, citrate (0.4 mol dm^{-3}), $HAuCl_4$ (0.01 mol dm^{-3}), water 50 ml, see chapter 1].

4.1.2 Analytical Analysis

Scanning electron microscopy (SEM) analysis was carried out on a thermal field emission Philips XL30 instrument for both morphology and elemental analysis, using the Energy Dispersive Spectroscopy (EDS) analysis (EDAX Phoenix system), with uncoated/coated carbon/gold/platinum samples. SEM images used accelerating voltages from 10 to 30 kV and were captured at various magnifications (2-5 x 10^5 x). The voltage was reduced to 10kV (working distance: 10 mm) for surface sensitive work with the back scattered electron (BSE) detector. High resolution X-ray diffraction (HRXRD) analysis was carried out using a MRD diffractometer in reflection mode with Cu Kα radiation (λ =1.54 Å) with a glancing angle incidence beam of 1.5. Visible/IR transmittance and reflectance spectroscopy was carried out using a Hunterlab, Ultrascan XE, colour measurement spectrometer (range 360–750 nm) connected to a PC. Raman analysis was carried out using a Renishaw InVia Raman microscope System using a HeNe laser (excitation wavelength: 514.5 nm) calibrated against Neon emission lines, (x50 microscope objective, 10 s exposure). XPS analysis was carried with Kratos Axis 165 by using monochromated Al Kα X-ray source at 100 W (1486.6 eV). XPS surface analysis were carried out for undoped and doped TiO_2 films and analysed from 4-7 different points with analysis area < 1 mm^2. Low-resolution survey scans were used for elemental identification (10 mins). High-resolution scans of Ti $2p_{3/2}$, Cu 2p, O 1s and C 1s peaks were recorded at a pass energy of 20 eV (3.5 mins). All the binding energies were referenced to the C 1s peak at 283.0 Ev and the etching was performed using an argon ion beam.

Water surface contact angles were measured using an FTA-1000B-23A-141 Automated Drop Shape Analyser, 3 µL water droplets were used to minimise any gravitational effects. The water droplet images were analysed using a circular fitting method to obtain the contact angles on the surface. The surfaces were tested from a range of areas over the substrate plate. The water slip angle was measured by noting the angle to the horizontal at which a water droplet of known volume moved on the surface. Photographs were recorded using a video camera on the FTA-1000 instrument system to monitor the wetting process on the surface.

4.1.3 Thin film growth

All synthesis was carried out using an experimental rig consisting of a combination of CVD and AACVD synthesis technique; conventional thermal chemical vapour deposition and aerosol assisted chemical vapour deposition technique with bubbler, and nebuliser. The CVD synthesis procedure involved the evaporation of TTIP using a bubbler (160-170 °C) with a hotplate (~160 °C) and heated transport pipes (200 °C) to prevent condensation and the AACVD synthesis involved dissolving precursors in methanol (50 ml) that were then nebulised by an ultrasonic humidifier (Ultra-Neb 2000, DeVilbliss) with appropriate ultrasonic wave frequency (1.63 MHz) to form an aerosol mist within a plastic container. The CVD vapour was transported by inert gas, N_2, controlled by a gas flow meter (molar ratio rate: 10), the aerosol mist was transported by compressed air (0.3-0.6 l/min), to a 3 slot combined AACVD/CVD cold wall reaction chamber (synthesis head), see fig. 23, chapter 2.

One clean plate of silica (50 nm) coated glass (dimensions ~207 x 85 x 3 mm), previously cleaned with appropriate solvents (water, methanol or acetone) and dried in air, was heated (400-600 ºC), using a graphite block controlled by a thermostat, monitored by a Pt-Rh thermocouple attached to a conveyor belt for automated substrate movement. The substrate was either left stationary (1-3 mins) on the conveyor belt or passed forwards and backwards (8-20 passes) under the combination AACVD/CVD synthesis head. The vapour and aerosol droplets were then swept by a carrier gases into the reaction chamber where the vapour and aerosol droplets were evaporated and a film deposited on the Float glass substrate. The experimental rig chamber was vented into the inbuilt extraction system. The inert gas and compressed air flow was allowed to continue for 10 min after either timed stationary synthesis or a number of dynamic passes underneath the head had been counted. The substrates and films were allowed to cool to room temperature *in-situ* and were stored in air.

4.2.0 Results

4.2.1 Synthesis and characterization

The TiO_2 films with and without additional phases were well adhered to the substrate, passed the Scotch tape test and could not be easily scratched with anything other than a hard surface (brass and steel). The films were grown using a new combined AACVD/APCVD coater head that was designed and built on the basics of the standard numerical 2-equation CFD code (κ-ε Realizable and κ-ω SST models) study for a fluid flow that was reported in chapter 2.

4.2.2 Visible appearance and optical characterization

Titanium oxide films were synthesized as either undoped thin films at substrate temperatures of 400-600 °C from the CVD of titanium tetraisopropoxide (TTIP) or doped TiO_2 host matrix thin films with noble metal dopants Au, Ag, Cu at 400-600 °C from the AACVD of auric acid, silver nitrate and copper acetylacetonate solutions. The macroscopic appearance by eye of all the films was transparent at thickness < 1μm, with the films becoming white and opaque at a thickness above 4 μm. The static films exhibited optical interference patterns that were indicative of areas of non-uniform thickness whilst the dynamic films mainly displayed uniform surfaces at lower synthesis temperatures (400°C) and non-uniform surfaces for films synthesised at higher temperatures (500-600 °C); which tended to exhibit optical interference patterns that were indicative of areas of non-uniform thickness.

4.2.2.1 Transmittance and Reflectance analysis

The comparison of the films synthesised statically (1-3 mins) and dynamically (8-20 passes under the prototype head) at 400 °C and 600 °C with either 0.3 or 0.6 l/min AACVD flow rates are compared below. Transmittance and reflectance analysis was repeated to ensure conformity of the results.

4.2.2.1.1 Static film results

Cu and Au doped static films at 400 °C with a AACVD flow rate of 0.3 l/min showed an increase in transmittance (80-85%) when compared to the TiO_2 CVD control film (65%), Ag gave the same transmittance value (65%), see fig. 56 a). The reflectance values for Au, Ag and Cu doped TiO_2 films (20-30%) were above the TiO_2 control value (20%) but the reflectance value for the Au

doped film dropped towards the TiO_2 film control value (20%) in the near infrared region, see fig. 56 a). The transmittance values for all the doped TiO_2 films (60-80%) at 400 °C with an AACVD flow rate of 0.6 l/min were lower than the TiO_2 control film (80-85%), see fig. 56 b). The reflectance values for the doped TiO_2 rose or fell slightly (10-30%) when compared to the undoped TiO_2 films due to interference patterns but were not significant for reflectance properties in the infrared region, see fig. 56 b). The thickness of the static Au doped TiO_2 film (400 C, 0.6 l/min) using the Swanepoel method[148] was 138±9.6 nm.

Figure 56: Comparison of T/R %: static films with AACVD flow rates: 0.3 and 0.6 l/min, 400 °C: a) static film, 400 °C, AACVD flow rate: 0.3 l/min, b) static film, 400 °C, AACVD flow rate: 0.6 l/min.

a)

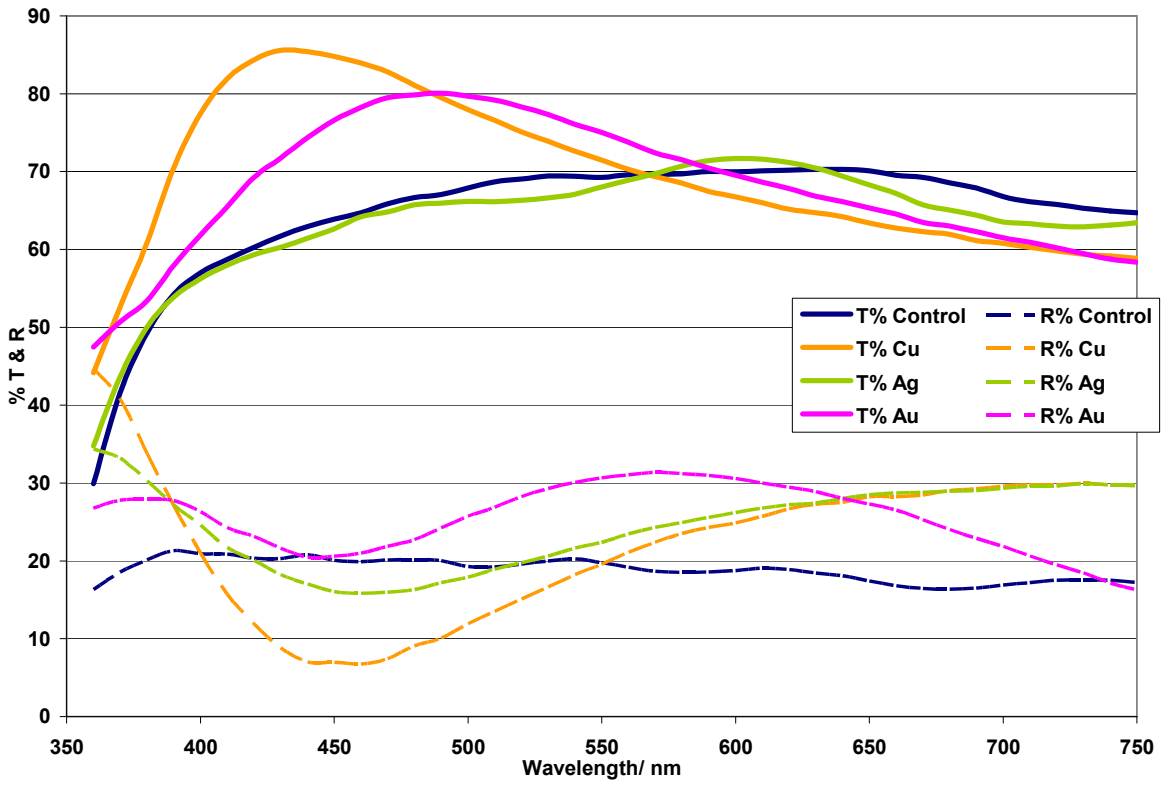

b)

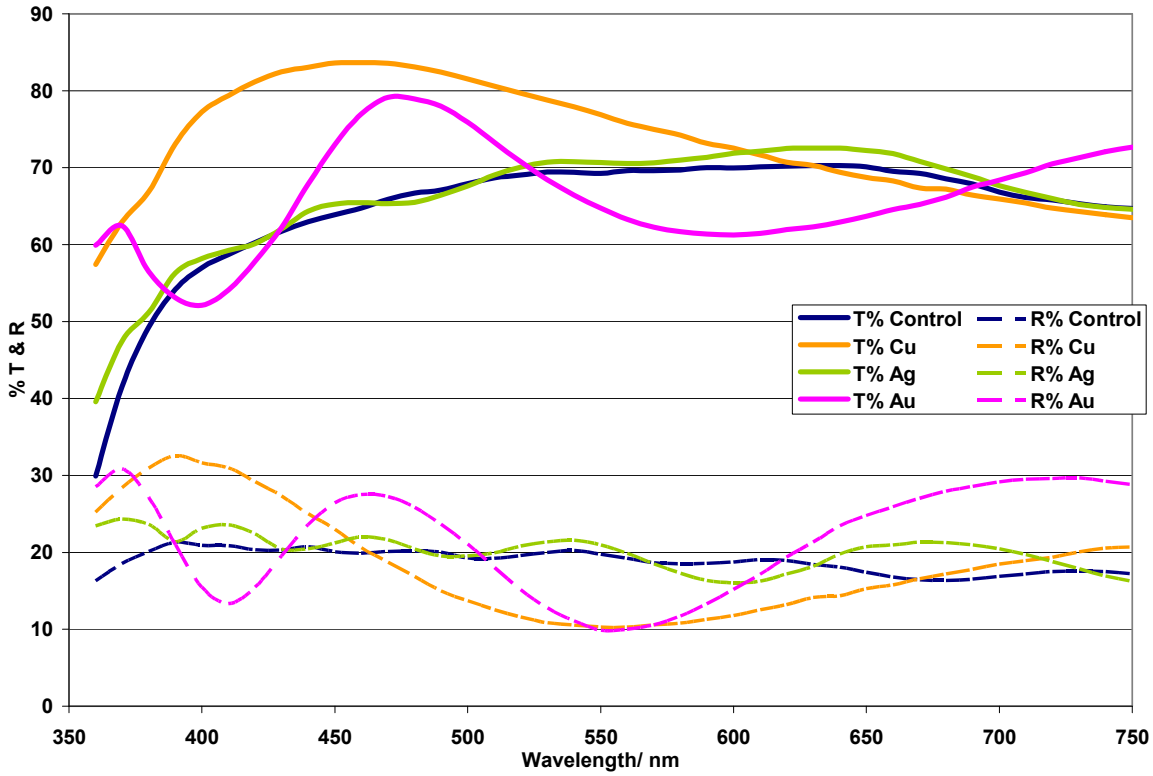

The transmittance values (400-500 nm) for doped TiO_2 films (60-70%) at 600 °C with an AACVD flow rate of 0.3 l/min showed a decrease when compared to the control TiO_2 film (75-80%). The films doped with pre-formed Au nanoparticles showed a significant increase in transmittance at wavelengths ≥ 480 nm, see fig. 57 a). The transmittance values (400-500 nm) for Au doped TiO_2 films (30-60%) with an AACVD flow rate of 0.6 l/min showed a drop that increased with increasing time underneath the prototype head due to the increasing thickness of the film; the Ag doped TiO_2 film had a similar transmittance value (400-500 nm) as the TiO_2 control film, see fig. 57 b).

Figure 57: Comparison of T/R %: static films with AACVD flow rates: 0.3 and 0.6 l/min, 600 °C: a) static film, 600 °C, AACVD flow rate: 0.3 l/min, b) static film, 600 °C, AACVD flow rate: 0.6 l/min.

a)

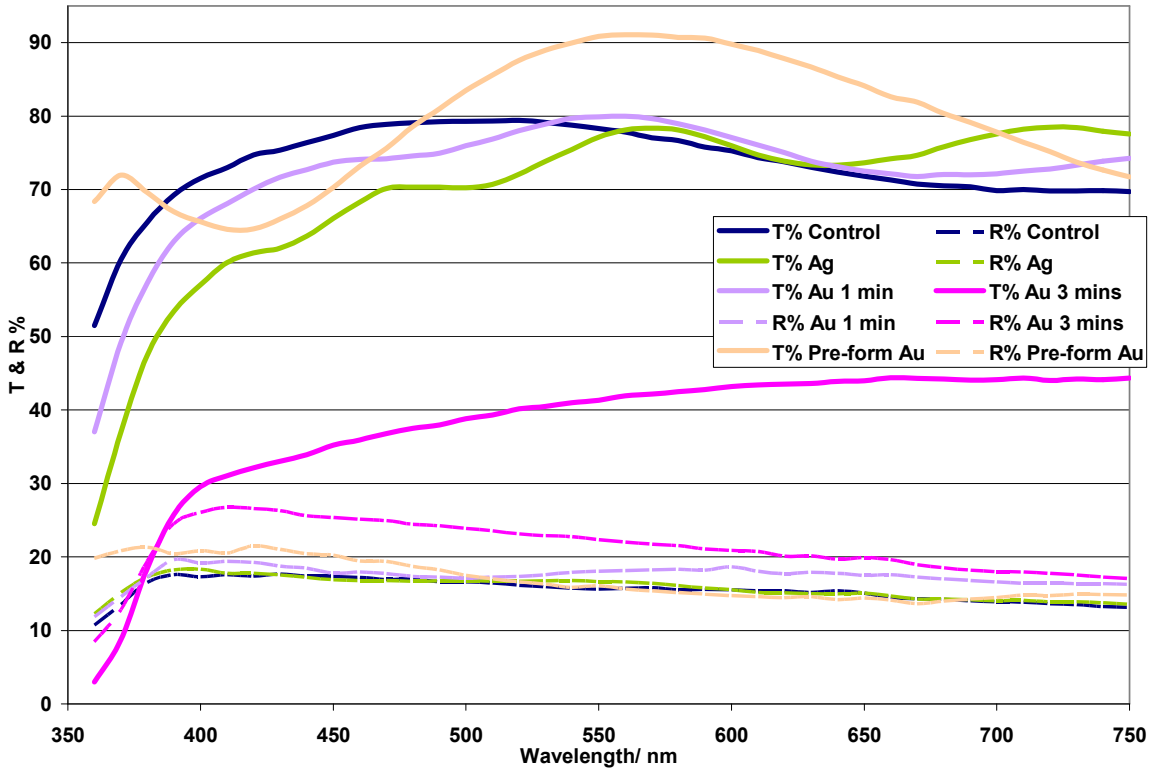

b)

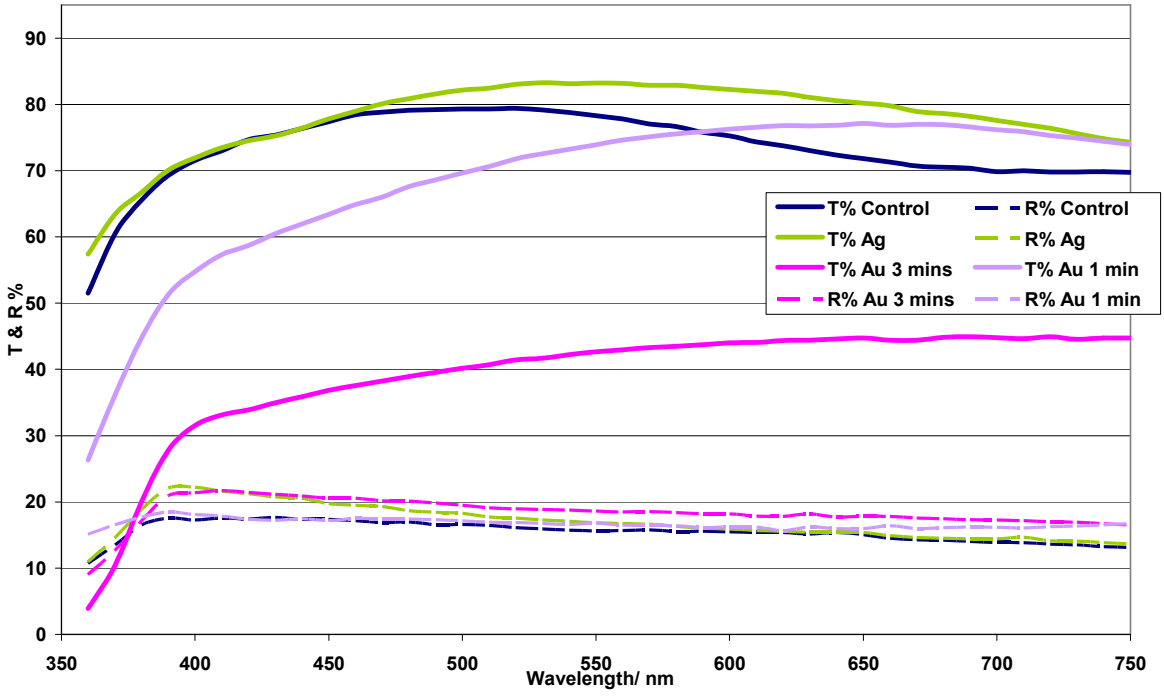

4.2.2.1.2 Dynamic Results

The transmittance value increases for Cu and Au doped films (70-85%) when compared to the TiO_2 control between 400–550 nm, whereas the Ag doped film has comparable transmittance values with the TiO_2 control (60-70%) with an AACVD flow rate of 0.3 l/min, order of increasing transmittance >Cu>Au>Ag, see fig. 58 a). Reflectance values for the Cu, Ag and Au doped films increase in the infrared (20–30%) when compared to the TiO_2 control (>20%) with an AACVD flow rate of 0.3 l/min, order of increasing reflectance Au>Ag>Cu, see fig. 58 a). The transmittance values of the Cu (60-75%), Ag (70-80) and Au (55-65%) doped TiO_2 films decrease when compared to the TiO_2 control (70-85%) between 450–550 nm when the AACVD flow rate is raised to 0.6 l/min, order of decreasing transmittance (Ag>Cu>Au), see fig. 58 b). The reflectance values appear to be better than the TiO_2 control although all three doped films reflectance values drop rapidly in the infra-red region in the order of decreasing reflectance Ag<Cu<Au, see fig. 58 b).

Figure 58: Comparison of T/R %: dynamic films (8-10 passes) with AACVD flow rates: 0.3 and 0.6 l/min, 400 °C: a) dynamic, 400 °C, 8 passes, 0.3 l/min, b) dynamic, 400 °C, 8 to 10 passes 0.6 l/min [Cu (8 passes), Ag (8 passes), Au (10 passes)].

a)

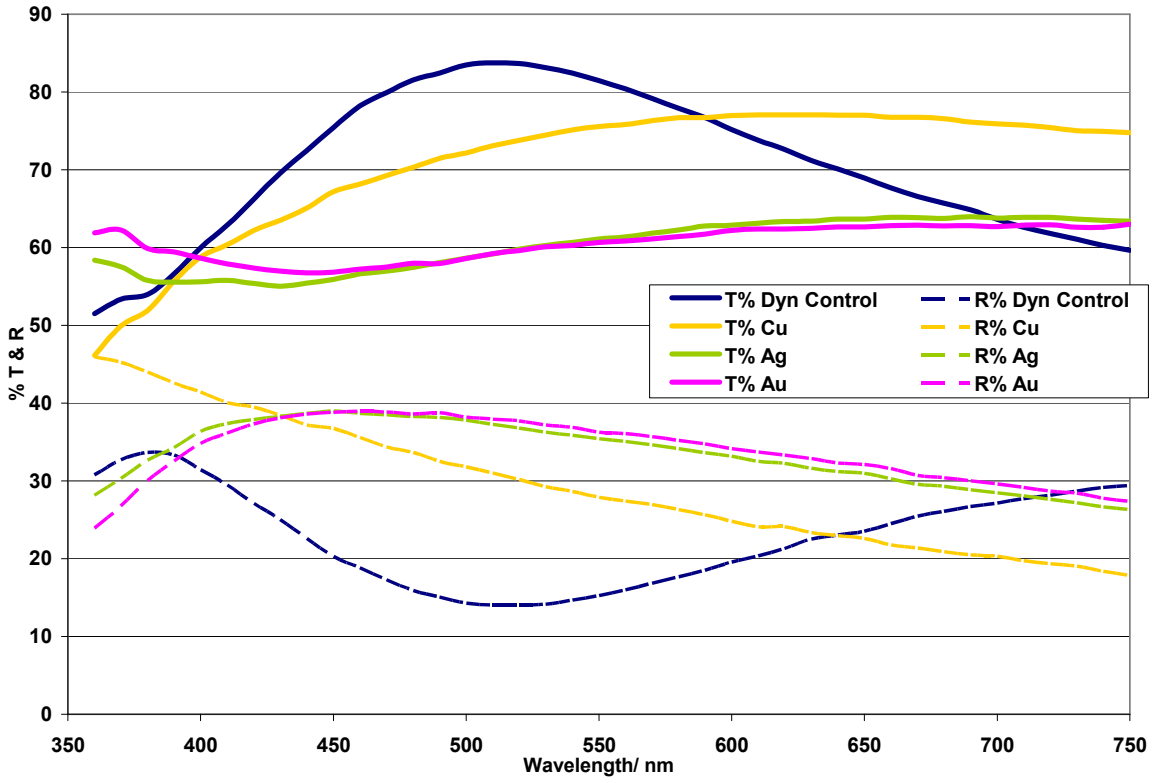

b)

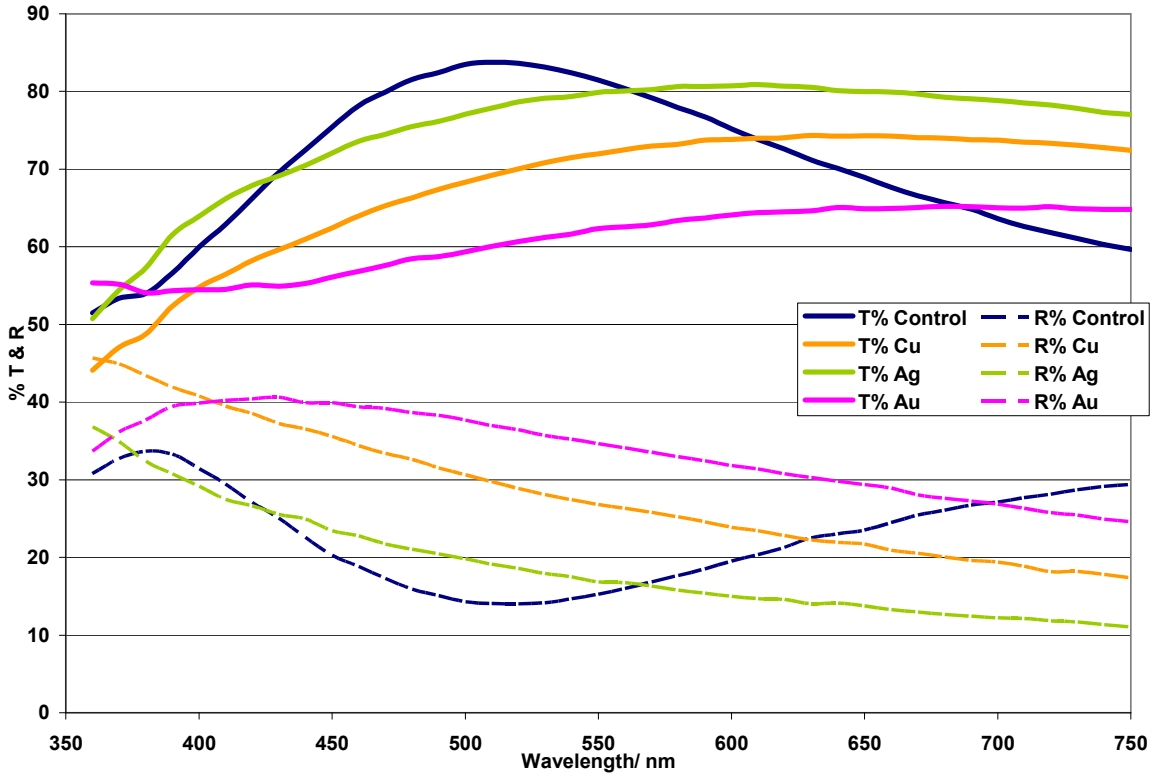

Transmittance values (400-500 nm) of the Ag, Au and Au pre-formed nanoparticle doped films (65-80%) have decreased when compared to the control TiO_2 film (70-90%) with the increase in temperature (600 °C) the dopants have had a negative effect on transmittance for an AACVD flow rate of 0.3 l/min, see fig. 59 a). The reflectance values for the Ag, Au and Au pre-formed nanoparticle doped TiO_2 films are above the TiO_2 control for a AACVD flow rate of 0.3 l/min but the improvement was not significant enough to be useful as a reflection coating, see fig. 59 a). Transmittance values (400-500 nm) for Au and Ag doped films worsen when a flow rate of 0.6 l/min is used when compared to the TiO_2 control, see fig. 59 b) and the reflectance values are better than the TiO_2 control but not significantly different when compared to the results from the 0.3 l/min AACVD flow rate, see fig. 59 a-b).

Figure 59: Comparison of T/R %: dynamic films (8 passes) with AACVD flow rates: 0.3 and 0.6 l/min, 600 °C: a) Dynamic, 600 °C, 8 passes, 0.3 l/min, b) Dynamic, 600 °C, 8 passes, 0.6 l/min.

a)

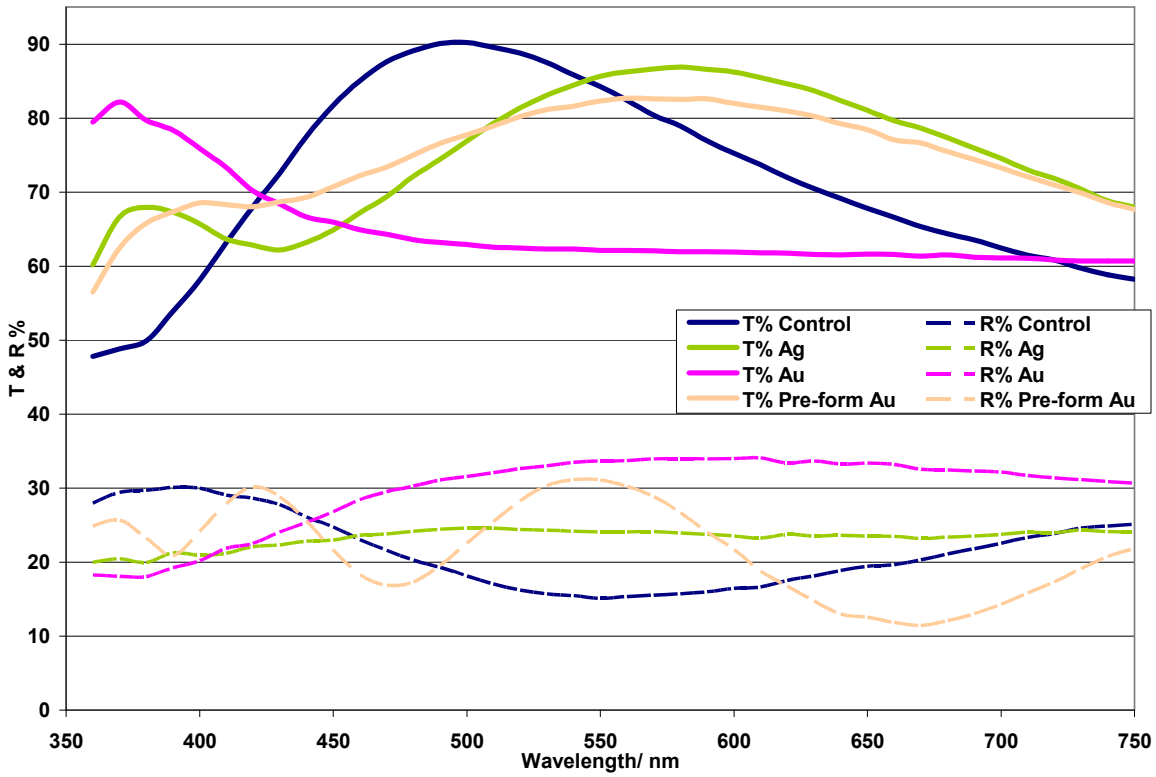

b)

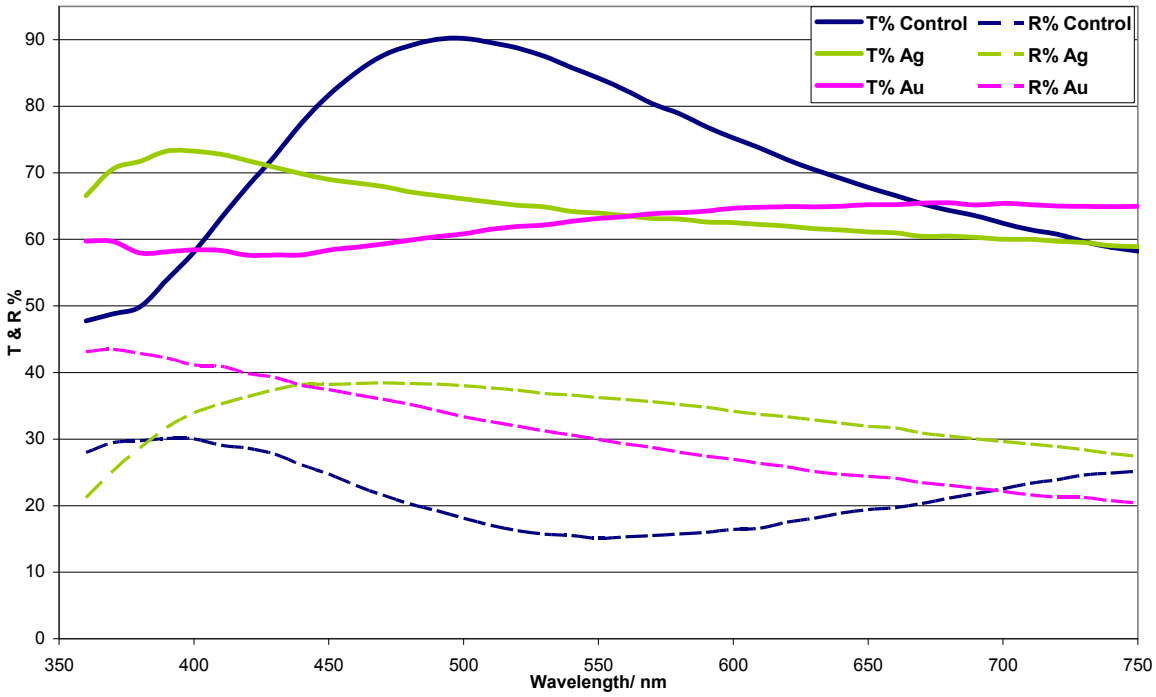

The transmittance values (400-500 nm) for the dynamic doped films at 600 °C with the increased number of passes (20) show some interference patterns for the Ag dopant and lower transmittance values for the Au and pre-formed Au nanoparticle dopants than the TiO_2 control with a 0.3 l/min AACVD flow rate, see fig. 60 a). The reflectance values for the pre-formed Au doped TiO_2 are higher than the TiO_2 control but the Au doped film values are lower than the TiO_2 control, see fig 60 a). Increasing the number of passes appears to detrimentally affect the transmittance and reflectance values for the doped TiO_2 films with a 0.3 l/min AACVD flow rate. Increasing the AACVD flow rate from 0.3 to 0.6 l/min reverses this trend making the Au and Ag doped TiO_2 films more comparable to the TiO_2 control film; there is a significant improvement and a shift in the transmittance value with the Au dopant (90% at about 440 nm) compared with the TiO_2 control (90% at 500 nm) and some improvement with the reflectance values when compared to the TiO_2 control, the Ag doped TiO_2 film shows a decrease in both transmittance and reflectance values when compared to the TiO_2 control, see fig. 60 b).

Figure 60: Comparison of T/R %: dynamic films (20 passes) with AACVD flow rates: 0.3 and 0.6 l/min, 600 °C: a) dynamic, 600 °C, 20 passes, 0.3 l/min, b) dynamic 600 °C, 20 passes 0.6 l/min

a)

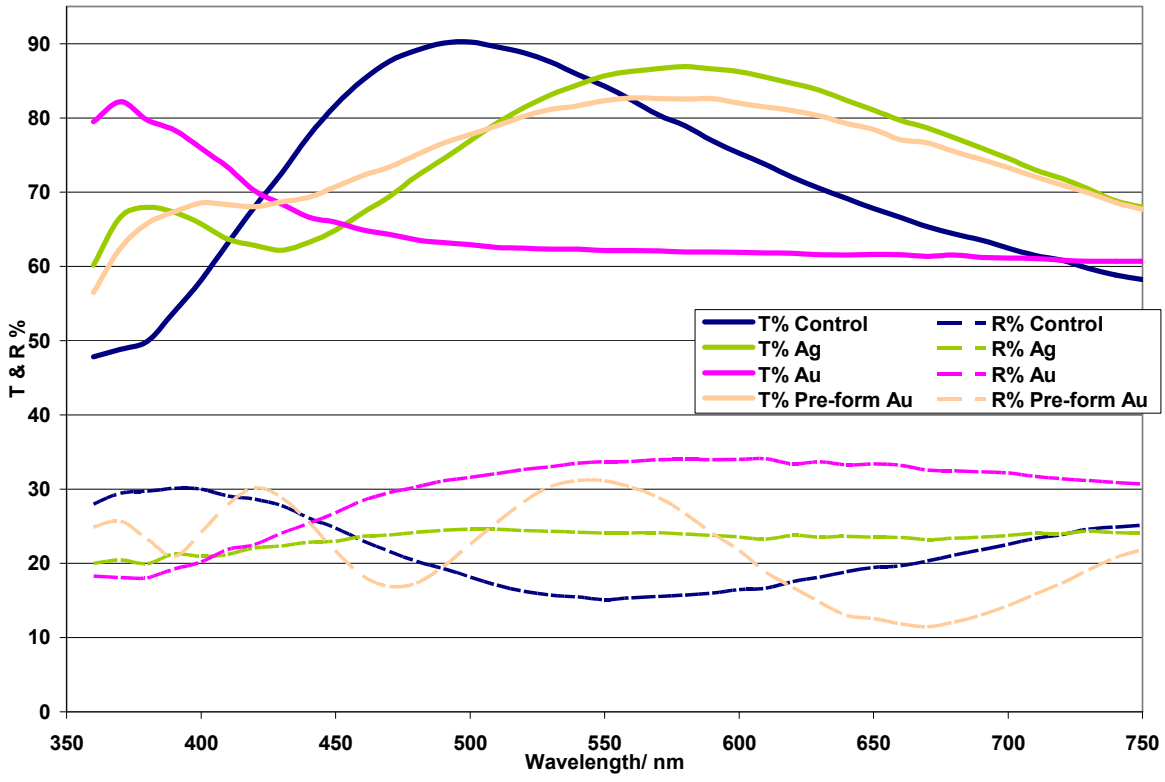

b)

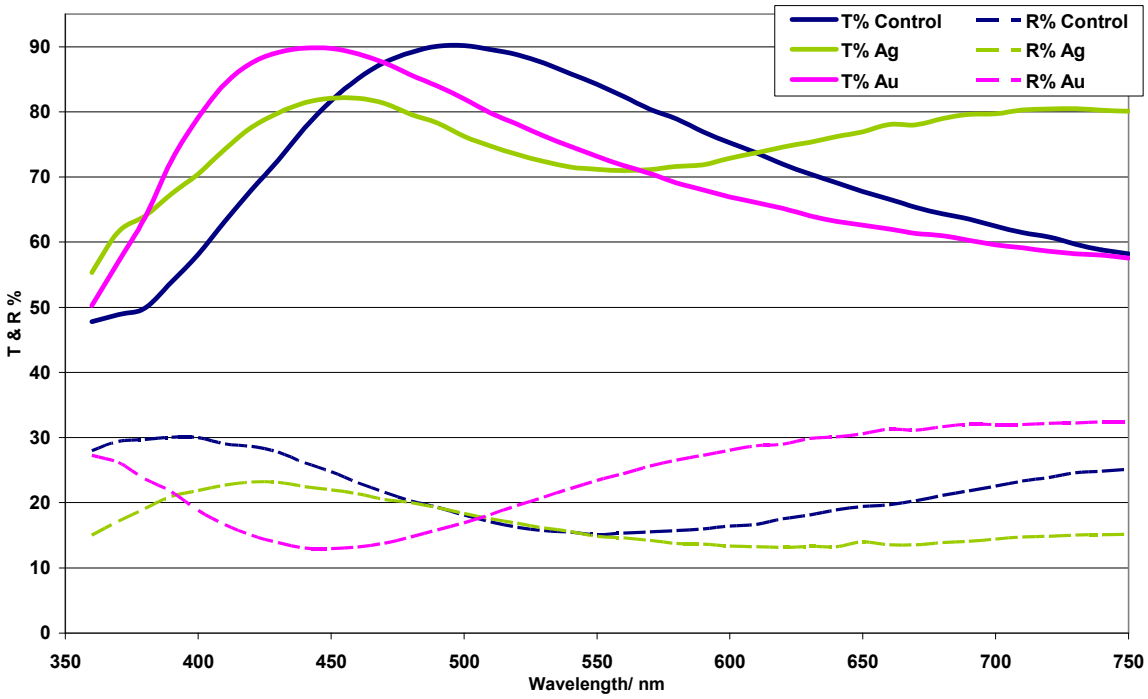

4.2.2.1.3 Comparison of Static and Dynamic Films

4.2.2.1.3.1 Comparison of AACVD flow rates

Comparison of the transmittance and reflectance analysis for thin films synthesised at different AACVD flow rates (0.3 and 0.6 l/min), see fig. 61 a-b) and 62 a-b).

The dynamic Au doped TiO_2 film at 400 °C gave a better reflectance value (30%) than the equivalent static film (18-30%) but a poor transmission value (55%) whereas the static film under these conditions has a much better transmission value (70-80%), see fig. 61 a). The Cu static and Ag dynamic doped TiO_2 films have higher transmission values (65-85%) than Au doped TiO_2 films (55 -80%) at 400 °C with 0.6 l/min AACVD flow rate, see fig. 61 b). For the Au doped TiO_2 films at 600 °C a higher AACVD flow rate, 0.6 l/min, appears to lower the transmission values and the Ag doped film appears to have a higher transmission value, see fig. 62 a-b).

Figure 61: Comparison of static and dynamic films at 400 °C, AACVD flow rates: 0.3 and 0.6 l/min:

a) films at 400 °C, AACVD: 0.3 l/min,

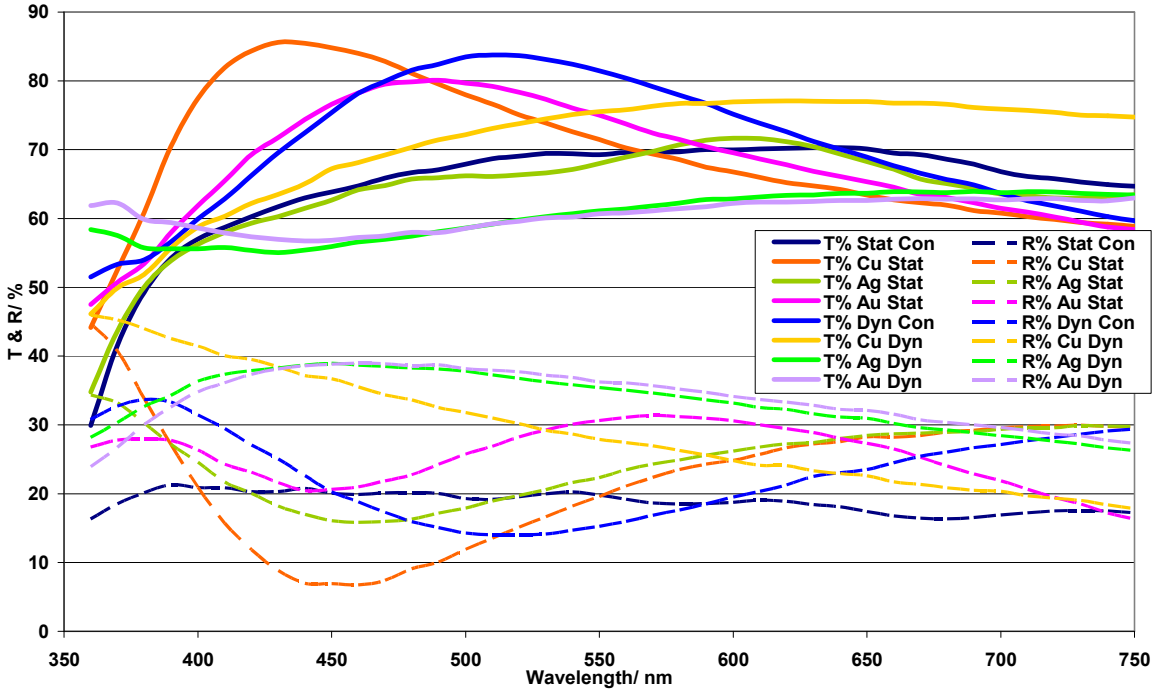

b) films at 400 °C, AACVD: 0.6 l/min

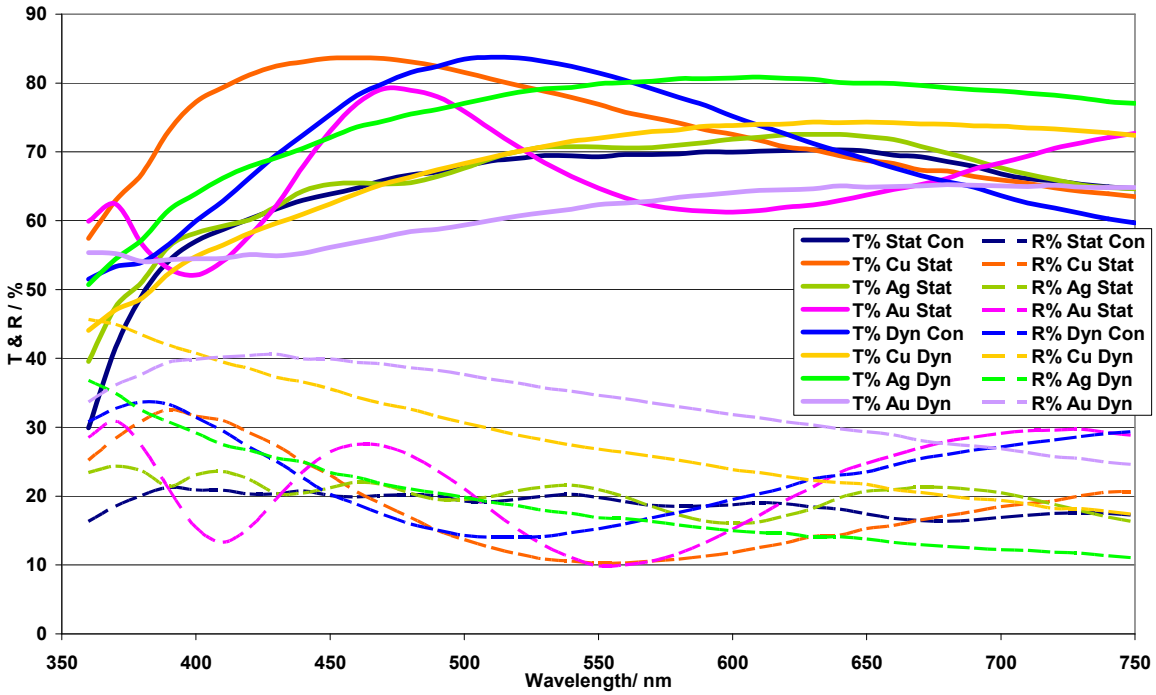

Figure 62: Comparison of static and dynamic films at 600 °C, AACVD flow rates: 0.3 and 0.6 l/min: a) films at 600 °C, AACVD: 0.3 l/min, b) films at 600 °C, AACVD: 0.6 l/min

a)

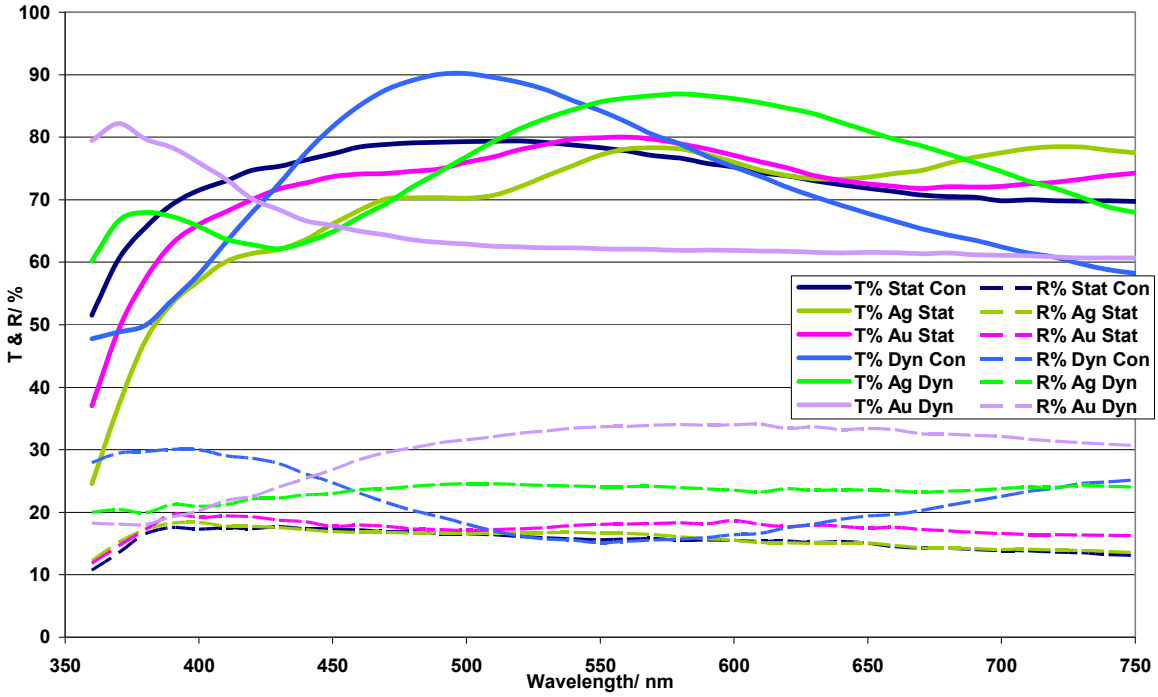

b)

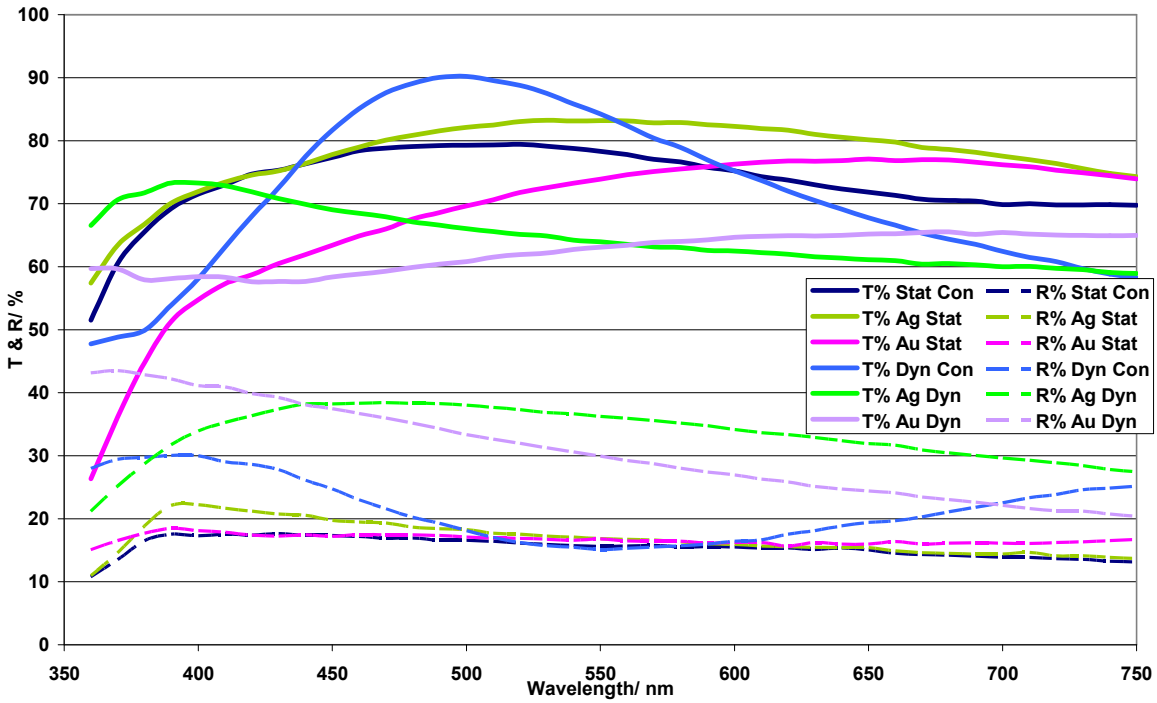

Individual comparison of the results of Au, Ag and Cu doped TiO_2 films at different AACVD flow rates confirm that static films have better transmission for Au doped films than dynamic but dynamic films produce slightly higher

reflectance values at 400 °C, see fig. 63 a). At 400 °C the faster AACVD flow rate, 0.6 l/min, does give better transmittance values for the Ag doped TiO_2 films but reflectance values drop, see fig. 63 b). The static Cu doped TiO_2 films at 400 °C gave better transmission values than the dynamic films but the reflectance values were <30% for all films and an increased AACVD flow rate, 0.6 l/min, also lowered the transmittance values, see fig. 63 c). At 600 °C the slower AACVD flow rate gave better transmittance values for the Au doped TiO_2 films but the higher AACVD flow the rate gave better transmission values for the Ag doped TiO_2 films, reflectance values were low for both Au and Ag doped TiO_2 films, see fig. 63 d) and e).

Figure 63: Comparison of Au and Ag doped static and dynamic films, AACVD flow rates: 0.3 and 0.6 l/min, 400 and 600 °C: a) Au doped films at 400 °C and 0.3, 0.6 l/min, b) Ag doped static and dynamic films at 400 °C and 0.3, 0.6 l/min, c) Cu doped static and dynamic films at 400 °C and 0.3, 0.6 l/min, d) Au doped static and dynamic films at 600 °C and 0.3, 0.6 l/min, e) Ag doped static and dynamic films at 600 °C and 0.3, 0.6 l/min.

a) Au, static/dynamic, 400 °C

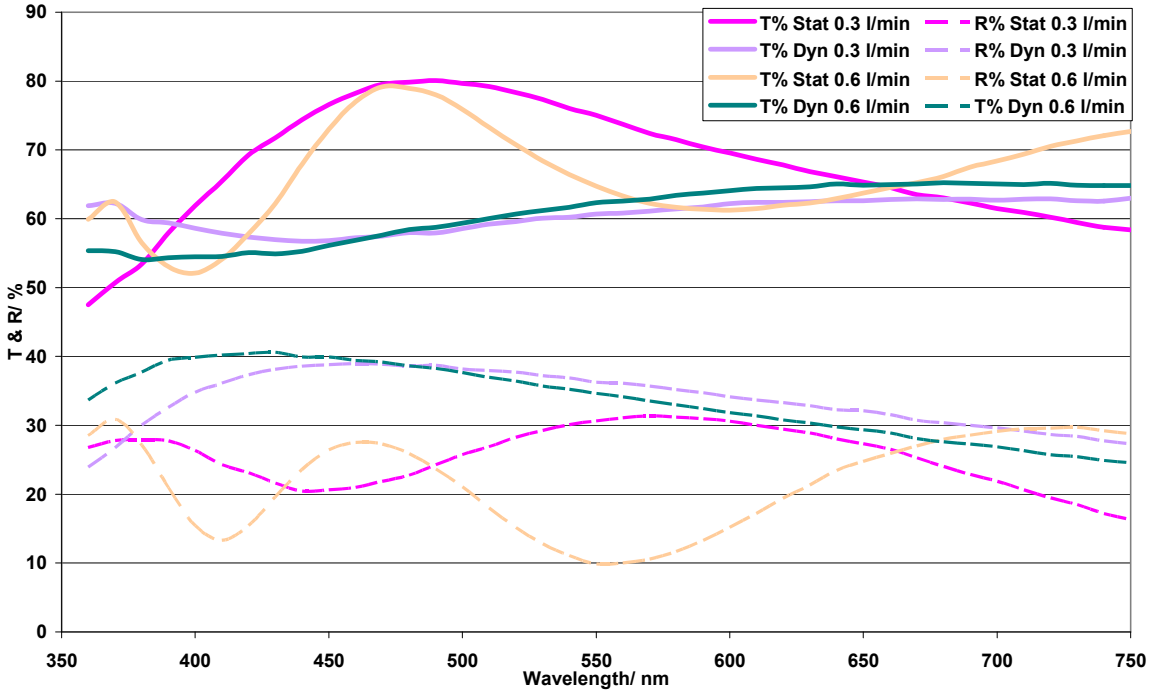

b) Ag, static/dynamic, 400 °C

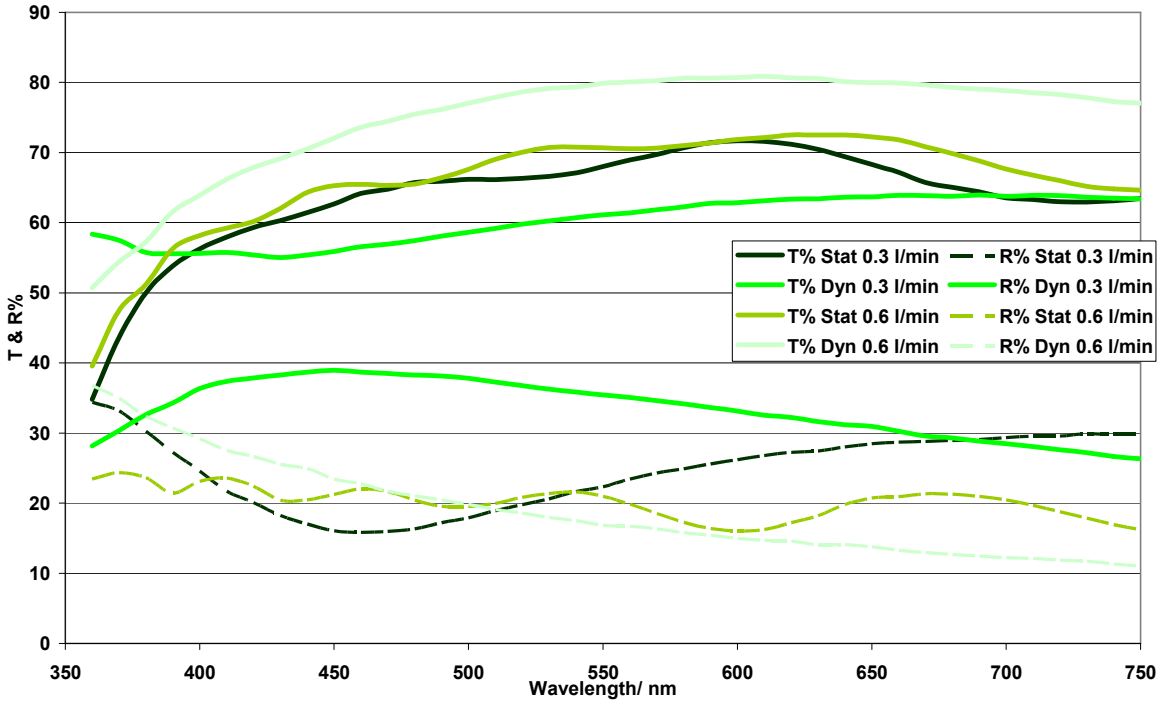

c) Cu, static/dynamic, 400 °C

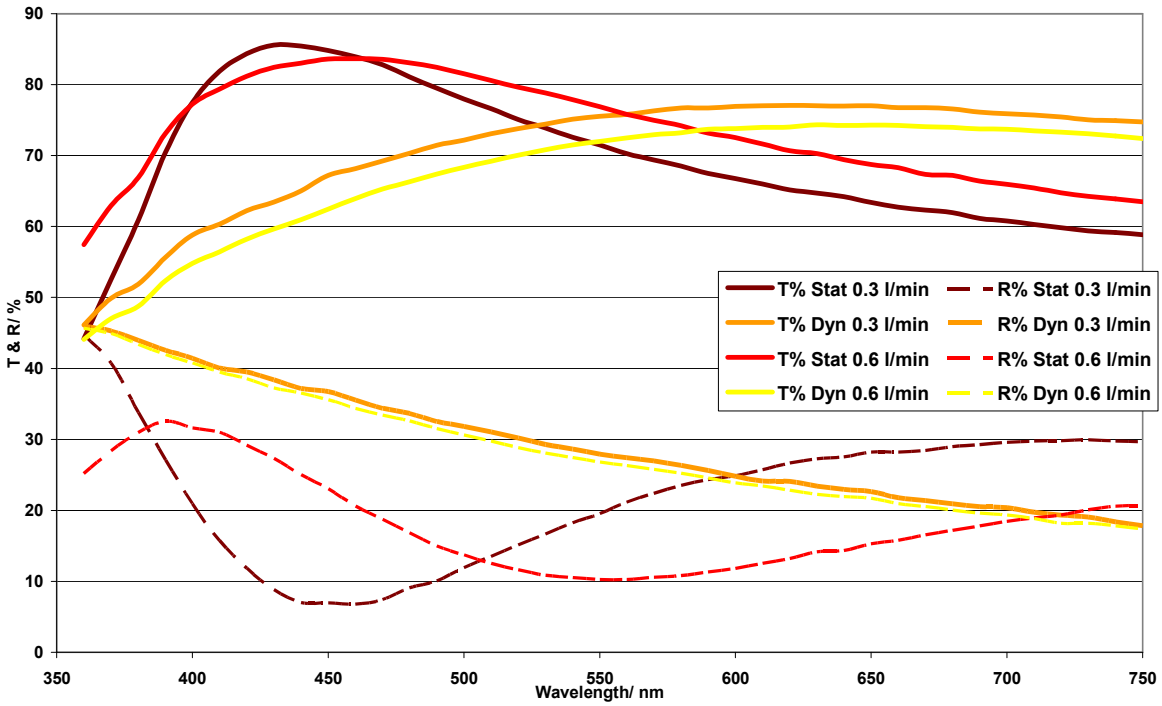

d) Au, static/dynamic, 600 °C

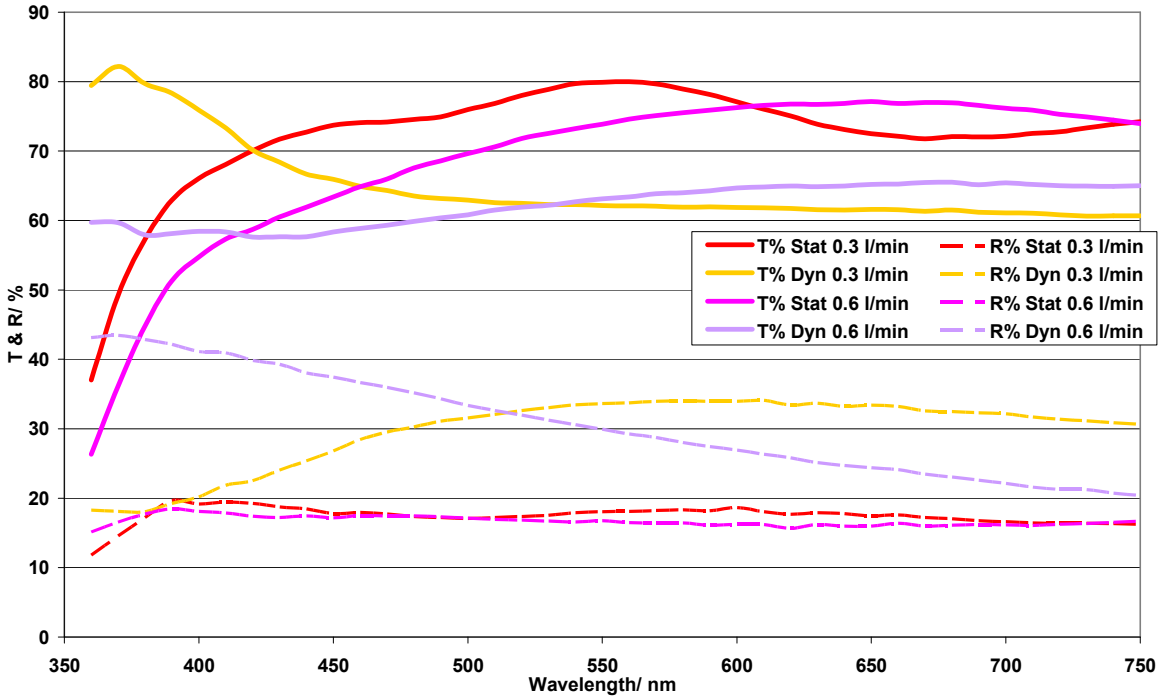

e) Ag, static/dynamic, 600 °C

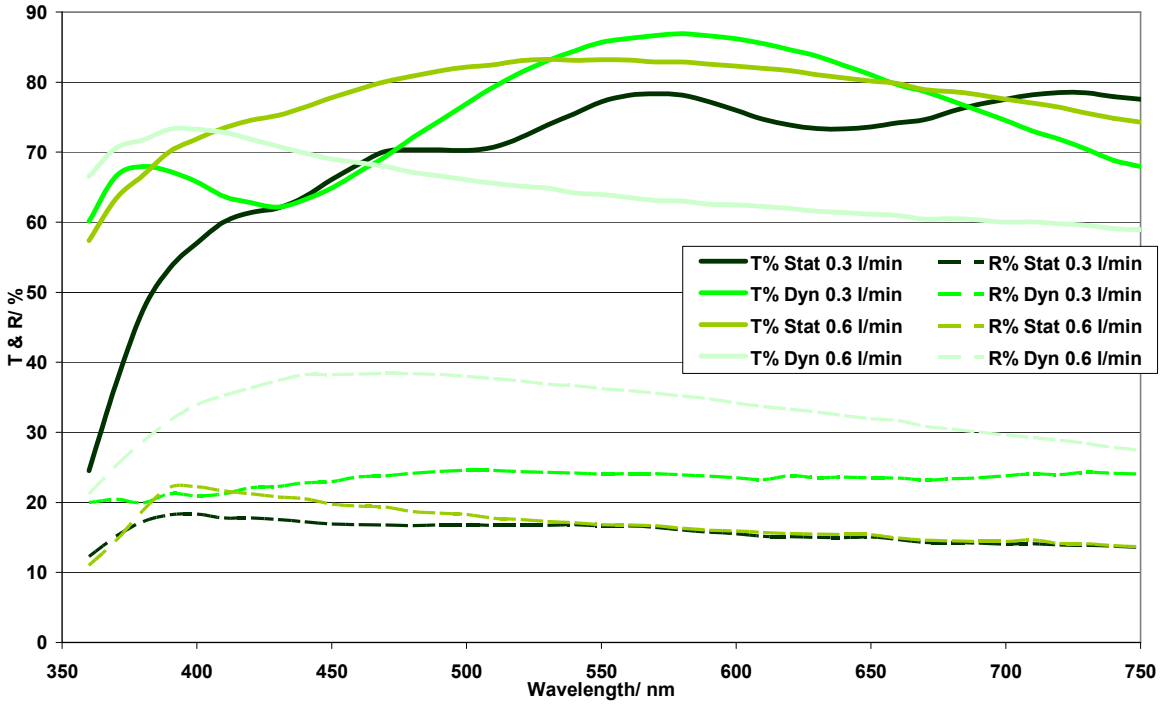

4.2.2.1.3.1 Comparison of the temperature, AACVD flow rate and dopant effect

Comparison of the temperature effect (400 and 600 °C) on the transmittance and reflection values of Au and Ag doped TiO_2 films synthesised with the

combined AACVD/CVD technique. The overall effect of an elevated temperature (600 °C) appeared to give higher transmittance values but a detrimental effect on the reflectance values in the infra-red, see fig. 64 a-c) and d). Static films at an elevated temperature for both Ag and Au doped films tended to give the best transmittance values, the dynamic films at elevated temperature produced worse transmittance results but improved reflectance values. The Au doped TiO_2 films at 400 °C appear to be have interference waves which are indicative of a thick uneven area of film as well as high transmission values in the visible region, see fig. 64 a-c). Lower temperatures (400 °C) for both Au and Ag dynamic results in 3 out of the four results displayed a higher reflectance value, see fig. 64 a-c), than the equivalent dynamic result and the dynamic at higher temperatures, see fig. 64 a-b) and d), (3 out of 4 results) displayed higher reflectance but not quite as good as the static films at lower temperatures.

Figure 64: Comparison of Au and Ag doped TiO_2 films AACVD flow rates and temperature: a) Au doped TiO_2 film with AACVD flow rate of 0.3 l/min, b) Ag doped TiO_2 film with AACVD flow rate of 0.3 l/min, c) Au doped TiO_2 film with AACVD flow rate of 0.6 l/min, d) Ag doped TiO_2 film with AACVD flow rate of 0.6 l/min.

a) Au, 0.3 l/min (400-600 °C)

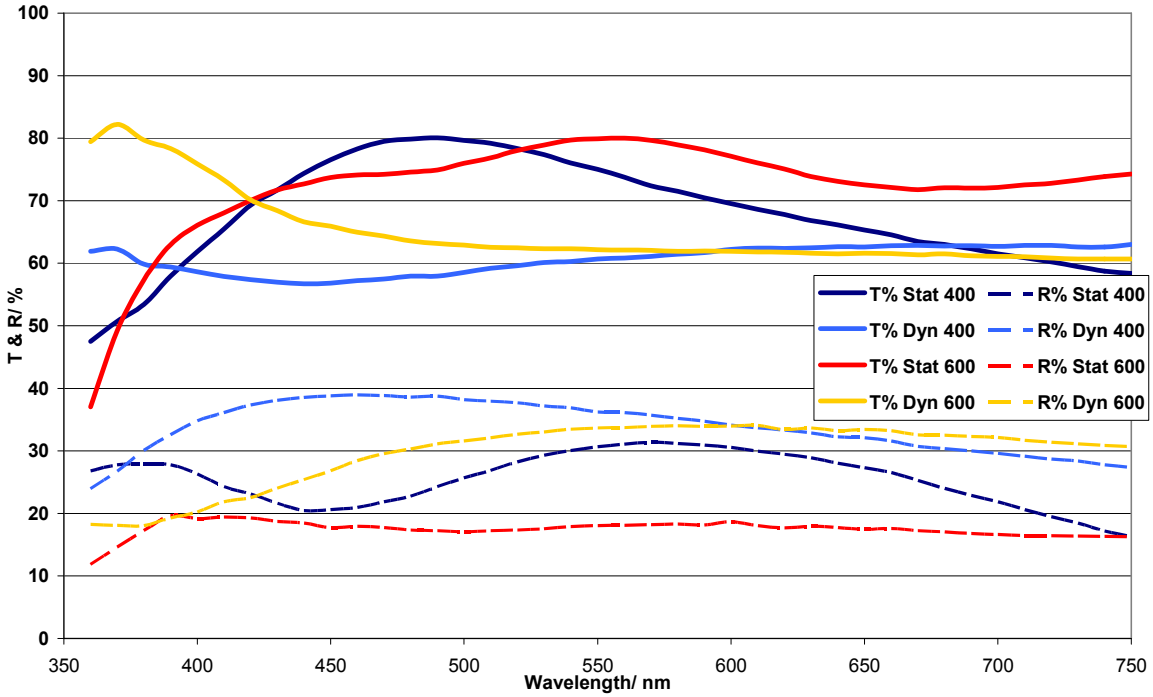

b) Ag, 0.3 l/min (400-600 °C)

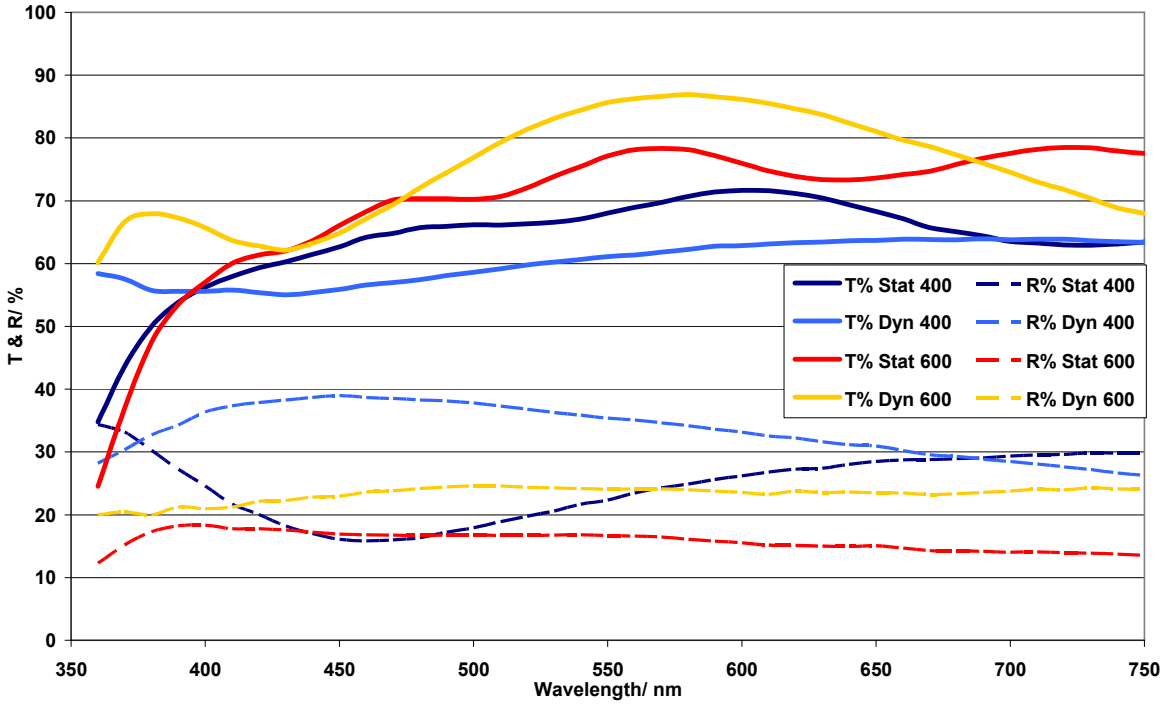

c) Au, 0.6 l/min (400-600 °C)

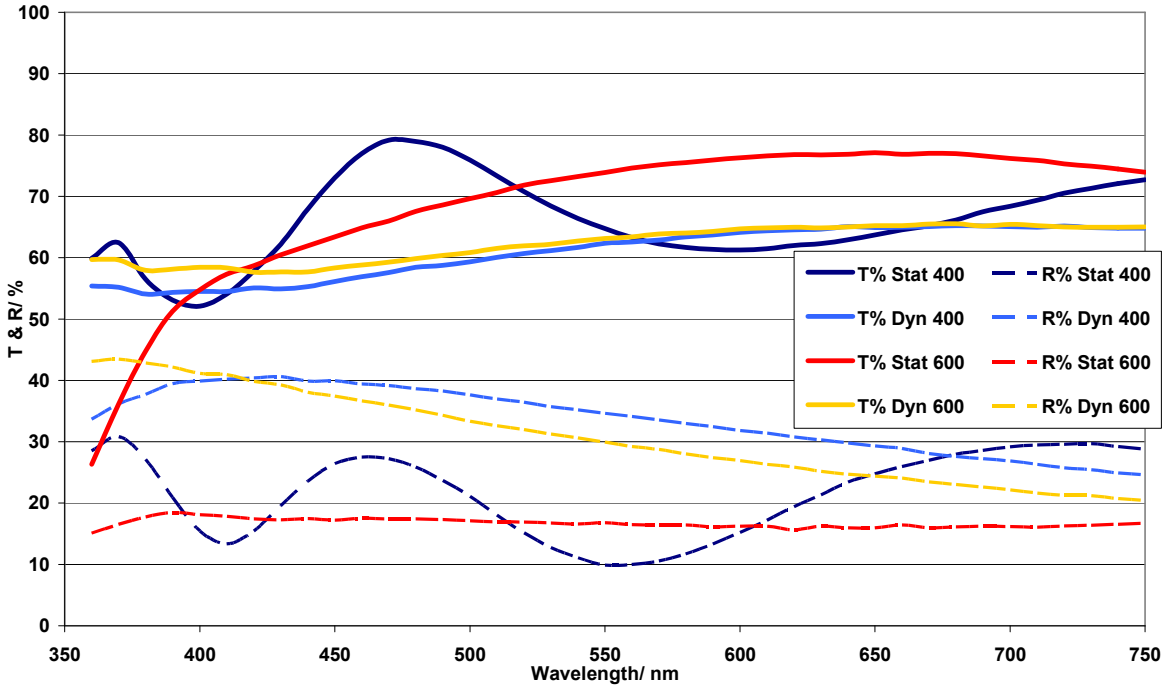

d) Ag, 0.6 l/min (400-600 °C)

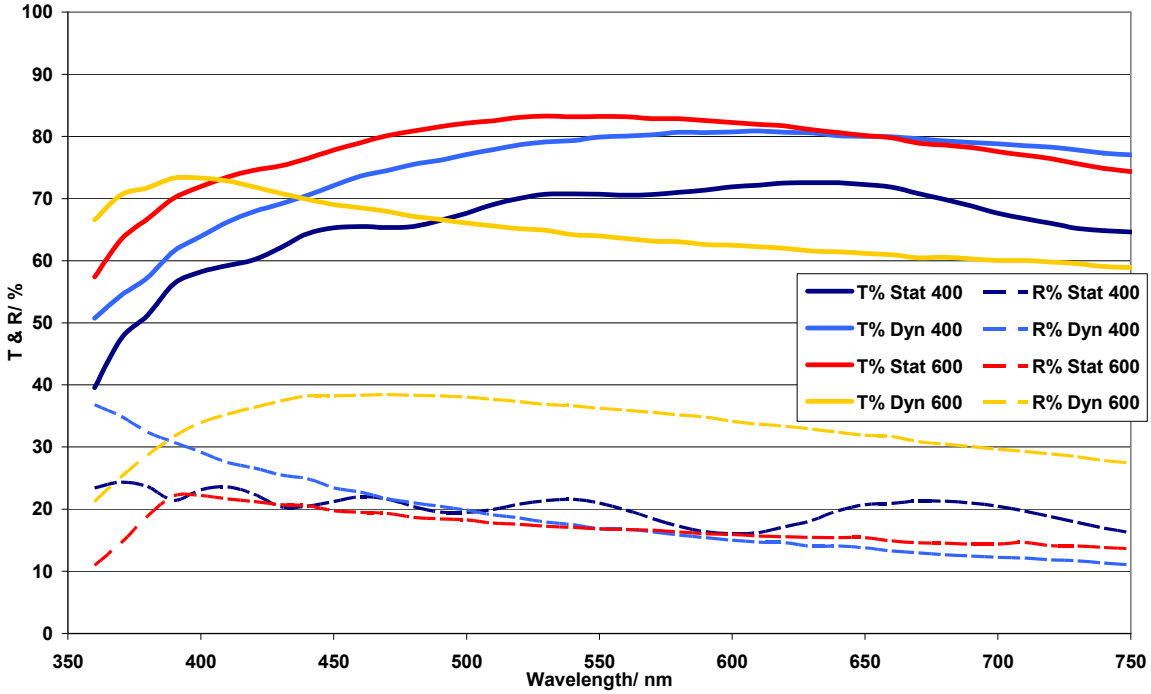

Comparison of the film thicknesses, using the Swanepoel method[148], reveals that static films synthesised at a higher temperature are thicker, (≈35-90 nm) reflecting the increased crystallinity of the films. The Ag dynamic films at 600 °C appear to have less variation in thickness with the film increasing by approximately 25 nm from 8 to 20 passes under the reaction chamber head, see table 20.

Table 20: Comparison of TiO_2 film thickness, calculated with the Swanepoel method: The reagents used for the synthesis of the TiO_2 films were TTIP, HAuCl and $AgNO_3$, static film deposition times were 1 min at 400 °C and 600 °C and dynamic films were deposited with 8 or 20 substrate passes under the reaction head at 600 °C.

TiO_2 Film Conditions				Maximum		Film Thickness*/ nm
Dopant	Temperature / °C	Static or Dynamic	AACVD Flow Rate/ l/min	T%	R%	
Au	400	Static	0.3	80	31	163.3 ± 6.7
Au	400	Static	0.6	80	30	138.0 ± 9.6
Ag	400	Static	0.3	72	29	190.4 ± 42.6
Ag	400	Static	0.6	70	21	226.6 ± 55.8
Au	600	Static	0.3	80	29	174.4 ± 31.2
Ag	600	Static	0.3	72	29	200.5 ± 46.8
Pre-formed Au	600	Dynamic: 8 passes	0.3	83	31	181.9 ± 29.5
Ag	600	Dynamic: 8 passes	0.3	87	25	161.6 ± 8.2
Ag	600	Dynamic: 20 passes	0.3	85	26	184.8 ± 30.8

* errors calculated from the Swanepoel method

4.2.2.1.4 Summary of transmittance and reflectance results

A higher synthesis temperature can improve transmission but lower reflectance values; a higher AACVD flow rate can improve transmission but detrimentally effect reflectance. Static films can give better transmission and in some cases better reflectance values but the film is thick and uneven. Au appears to be a better dopant at a lower AACVD flow rate for transmission values whereas Ag doped TiO_2 film appears to be better at a faster AACVD flow rate for transmission values. A number of static films displayed interference fringes, sinusoidal wave forms due to the thickness of the film and therefore film thickness was calculated, using the Swanepoel method[148]. For the static films the increase in temperature and crystallinity appears to be linked to an increase in film thickness and for the one comparable set of dynamic results (Ag, 600 °C, 0.3 l/min) displayed approximately a 20 nm (±6.7-55.8 nm)[148] increase in film thickness and crystallinity has been calculated when the number of passes under the reaction head was increased from 8 to 20. Comparison of the film thicknesses reveals that static films synthesised at a higher temperature are thicker, (≈35-90 nm) reflecting the increased crystallinity of the films. To a lesser extent the dynamic film thickness also appears to increase with increasing crystallinity. All film synthesis was repeated and re-tested for transmittance and reflectance analysis and the results were found to be repeatable.

4.2.3 SEM and EDX analysis

The results from the dynamic and static substrate samples of the AACVD/CVD synthesis technique doped and undoped titania thin films produced highly transparent clear films with visible transmission >85% at various temperatures (400 - 600 ºC). Undoped titania films were synthesized at 400 °C and 600 °C as static films (1 or 3 min) and then the glass substrate was passed under the reaction chamber head (8 dynamic passes) at 400 °C and 600 °C to act as controls for doped titania films. The morphology of titania thin films were found to be influenced by the attempted addition of Au, Ag and Cu dopants.

4.2.3.1 Undoped and doped static TiO_2 films at 400 °C

The static films at 400 °C displayed larger aligned elongated nanoparticles in a basket type weave pattern morphology with typical TiO_2 composition, see fig. 65 a-b).

Figure 65: Morphology and composition of static control at 400 °C

a) Morphology (scale: 500 nm)

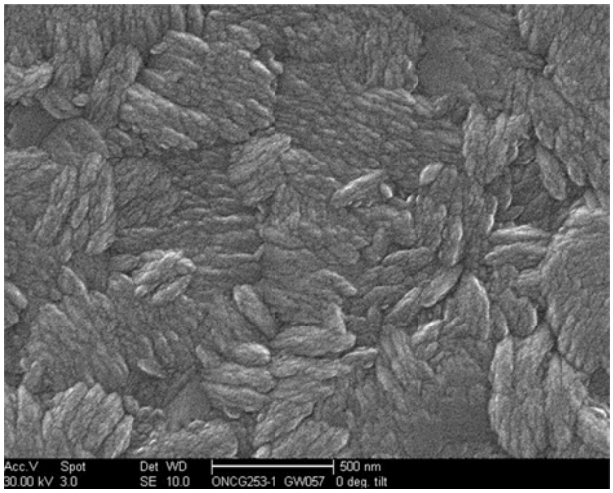

b) Composition: *Pt coating used

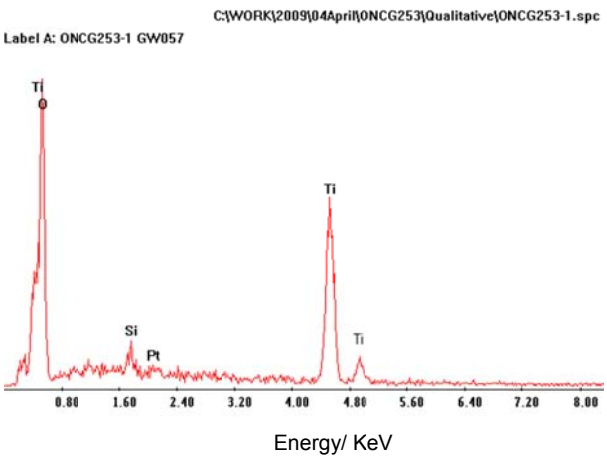

One Au doped static TiO_2 film, (static, 400 C, AACVD flow rate: 0.3 l/min) was found to include Au at a detectable level, the Au dopant changes the morphology to a much more uniform rounded granular microstructure with bright spots (nanoparticle size 10-20 nm): see fig. 66, a-d).

Figure 66: Morphology and composition of the static Au doped TiO_2 film at 400 °C, AACVD flow rate: 0.3 l/min.

a) morphology (scale: 1 µm)

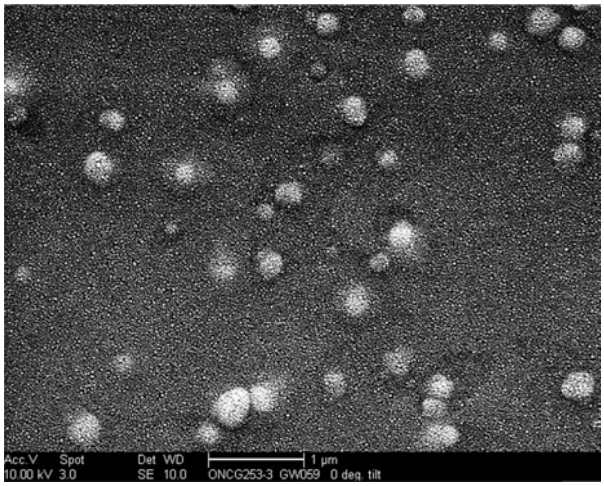

b) morphology (scale: 500 nm)

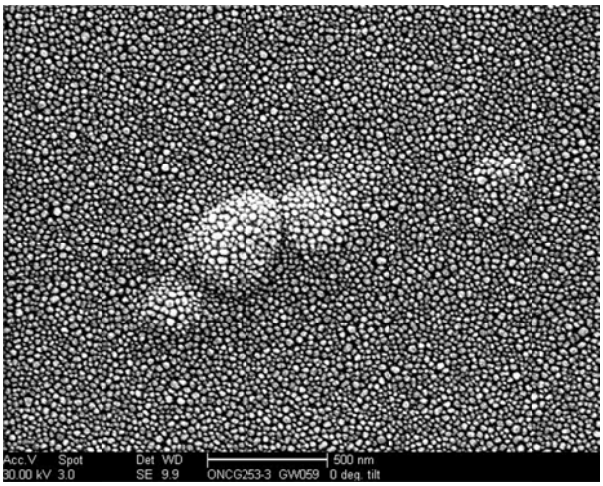

c) composition (bright areas)

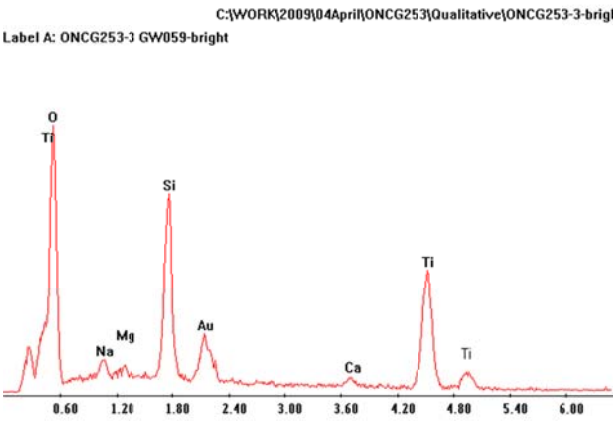

Energy/ KeV

d) composition (grey areas)

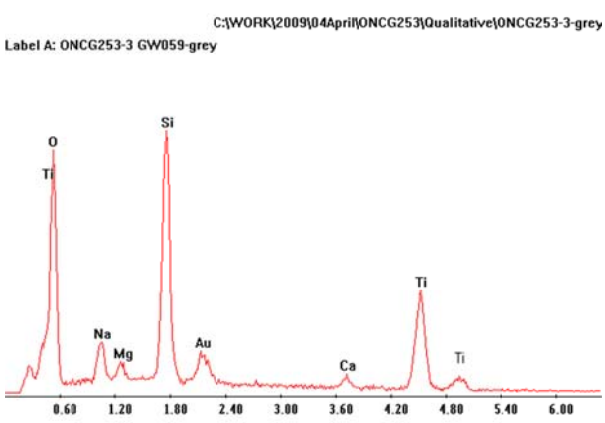

Energy/ KeV

The inclusion of Au nanoparticles within the host titania matrix were confirmed, the brighter areas contained a higher rate of Au than the greyer areas, see fig. 66 c-d).

The increased AACVD flow rate (0.6 l/min) affects the morphology of the titania film with a significant decrease in nanoparticle size when compared to both the CVD control and the Au doped titania film (0.3 l/min) and the lack of inclusion of the Au dopant, see fig. 67.

Figure 67: Morphology static Au doped TiO_2 films at 400 °C, AACVD flow rate: 0.6 l/min

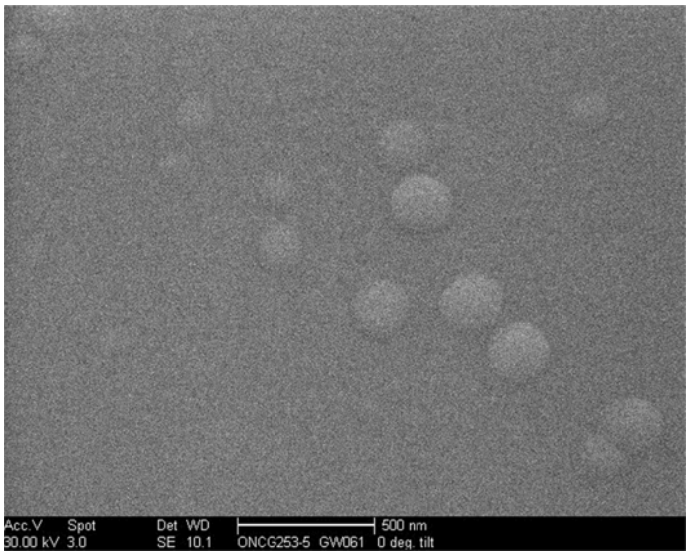

Increasing the AACVD flow rate of the titania films formed in the presence of Ag appears to increase agglomeration of the nanoparticles (size: 500 nm–1 μm), see figs. 68 a-b).

Figure 68: Morphology static TiO_2 film formed in the presence of Ag at 400 °C: a) AACVD flow rate: 0.3 l/min, b) AACVD flow rate: 0.6 l/min.

a) morphology: AACVD: 0.3 l/min (500 nm) b) morphology: AACVD: 0.6 l/min (1 µm)

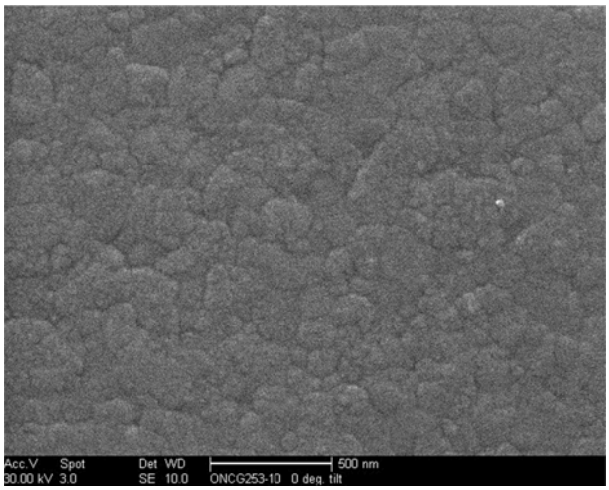

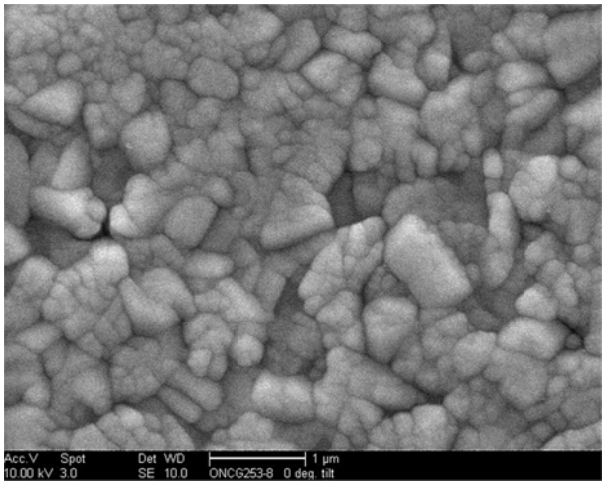

Increasing the AACVD flow rate of the titania films formed in the presence of Cu appeared to have little effect on the morphology of small nanoparticles making up large platelet type areas, see fig. 69 a-b).

Figure 69: Comparison of the morphology of static TiO_2 films, formed in the presence of Cu, 400 °C, with AACVD flow rates of 0.3 and 0.6 l/min: a) morphology static TiO_2 film formed in the presence of Cu at 400 °C, AACVD flow rate: 0.3 l/min, b) morphology static TiO_2 film formed in the presence of Cu at 400 °C, AACVD flow rate: 0.6 l/min.

a) morphology (scale: 500 nm) b) morphology (scale: 500 nm)

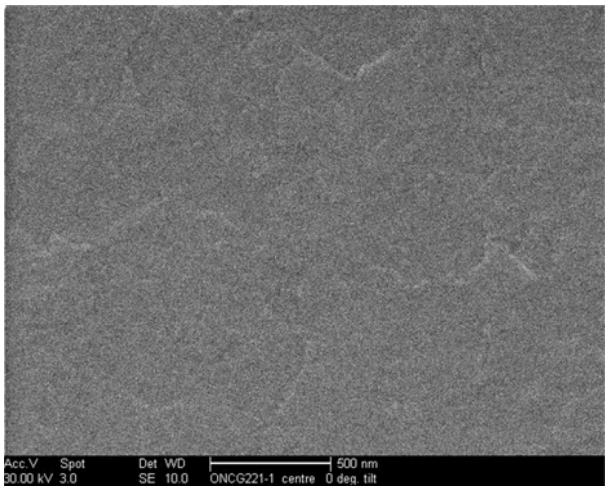

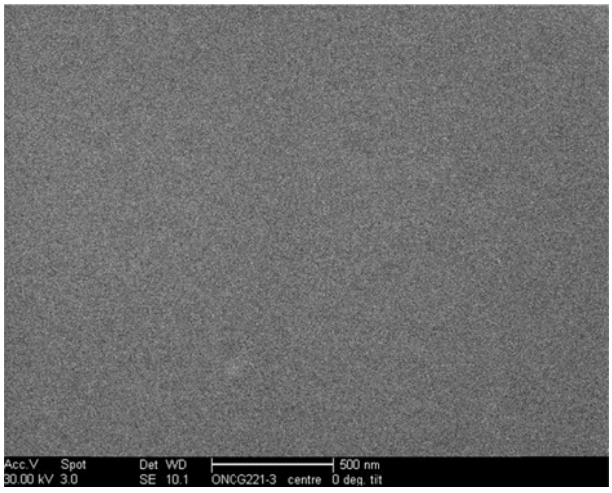

4.2.3.1.1 Summary of static TiO_2 films at 400 °C

Dopants do affect the overall morphology of the titania host matrix film even when the dopant is not actually included at detection level within the titania host matrix and the AACVD flow rate has a significant effect on morphology with the attempted Au and Ag doped titania films, less so with attempted Cu doped films. Increasing AACVD flow rate with the Au dopant appears to decrease nanoparticle size whereas the size of nanoparticle with Ag dopant increases nanoparticle size. Since Cu, under these conditions would be oxidised in the gas phase (CuO/Cu_2O) it could be said that the size of the dopant (Au: atomic radius 146 pm, Ag: atomic radius 160 pm) in the gas phase could be used to determine some aspects of expected film morphology until a critical size is reached and no further significant effect can be seen. The same solvent (MeOH) is used throughout the synthesis of all the TiO_2 films whether a dopant is present or not and therefore an assumption is made that the changes observed in morphology are an effect of flow rate, temperature and any dopants present.

4.2.3.2 Undoped and doped dynamic TiO_2 films, at 400 °C

The dynamic CVD titania control has some interesting morphology of both spherical nanoparticles and large platelet type structures, see fig. 70. The thickness of the titania film varies from about 96-127 nm, see fig. 70 c), with typical titania film composition, see fig. 70 d).

Figure 70: Morphology, thickness and composition of dynamic TiO_2 control film, substrate passes: 8, 400 °C.

a) morphology (scale: 500 nm)

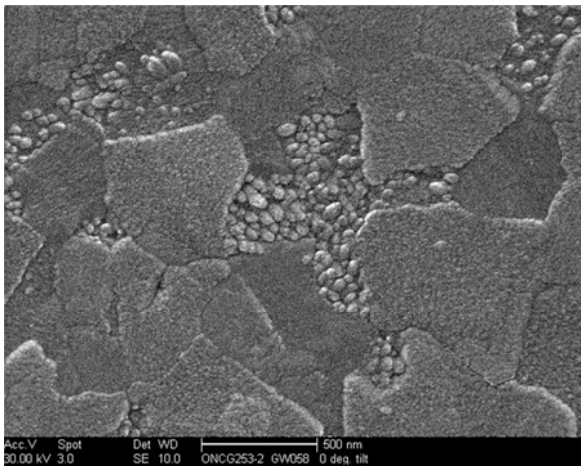

b) Thickness (scale: 1 µm)

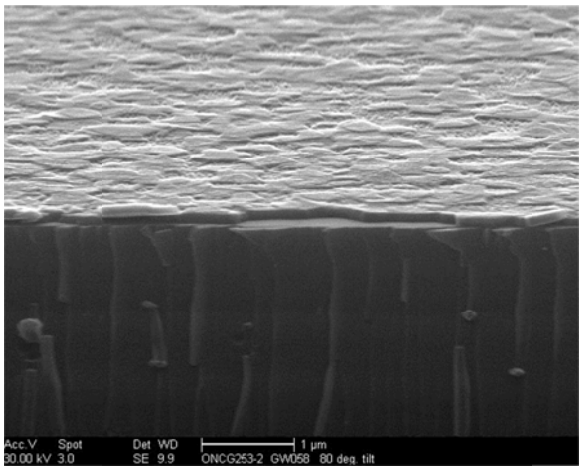

c) Thickness (96-127 nm)

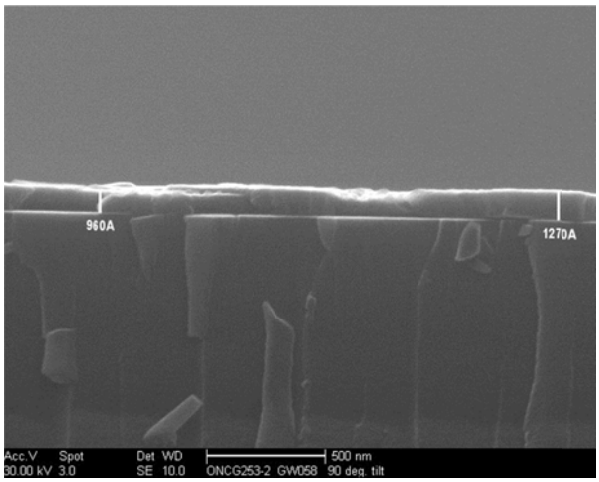

d) composition: *Pt coating used

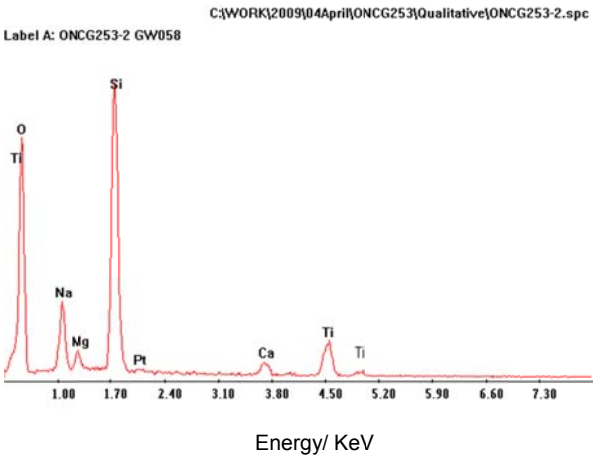

The titania host matrix films formed in the presence of Au have significantly decreased numbers of individually visible spherical nanoparticles with increased platelet structures appearing, increasing the AACVD flow rate appears to diminish the size of any spherical nanoparticles and smoothes the edges of the large platelet structures, see fig. 71 a-b).

Figure 71: Comparison of the morphology of dynamic (8-10 substrate passes) TiO_2 film formed in the presence of Au (400 °C) with different AACVD flow rates: 0.3 and 0.6 l/min: a) no. of passes: 8, AACVD flow rate: 0.3 l/min, b) no. of passes: 10, AACVD flow rate: 0.6 l/min.

a) morphology (scale: 500 nm)

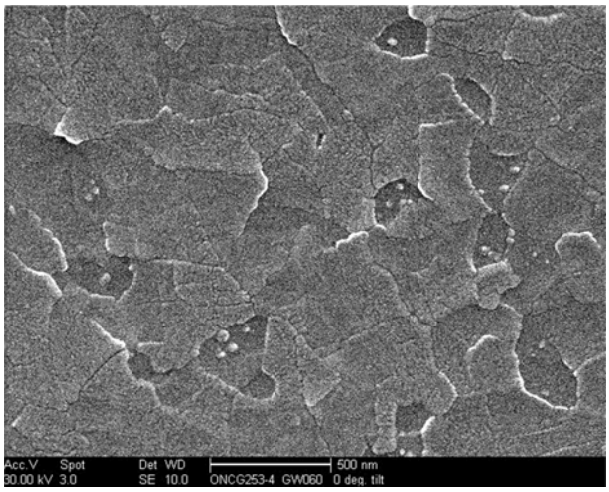

b) morphology (scale: 500 nm)

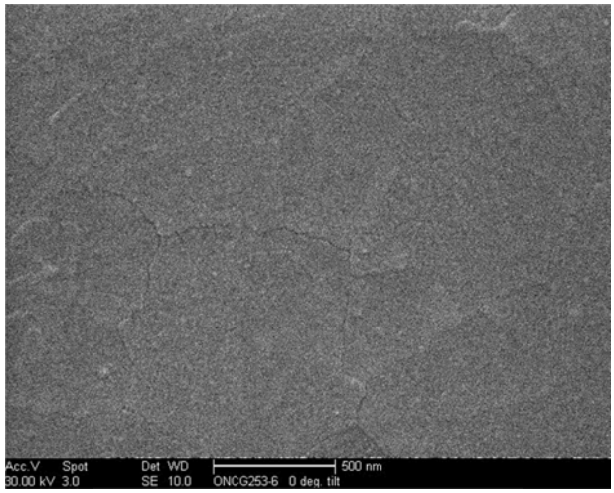

Increasing the number of passes (20) of the substrate under the synthesis head, thickens the titania film and makes the platelet boundary areas more prominent, see fig. 72.

Figure 72: Morphology of dynamic TiO_2 film formed in the presence of Au at 400 °C, substrate passes: 20, AACVD flow rate: 0.6 l/min.

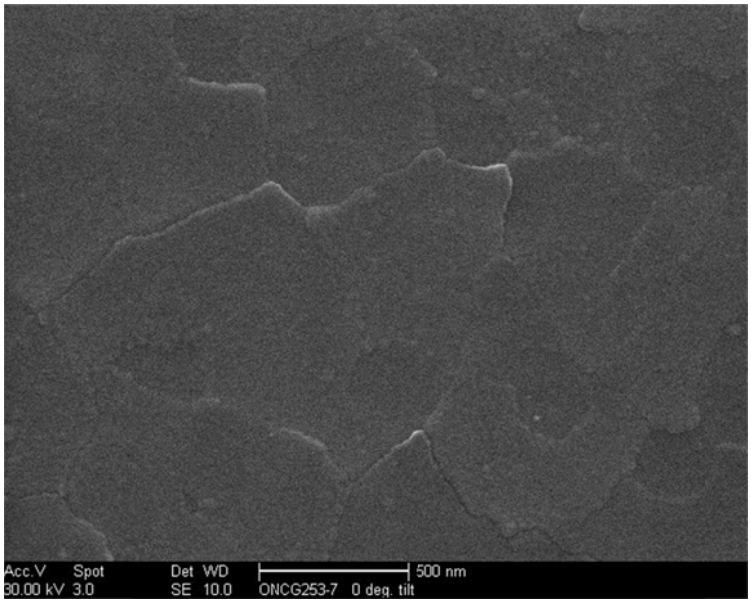

The film formed in the presence of Ag precursors had a very similar morphology to the Au doped film, less spherical nanoparticles and larger platelet structures, see fig. 73 a). An increase of the AACVD flow rate (0.6 l/min) led to individual spherical nanoparticles which are very much smaller (5-10 nm) and harder to discern as are the platelet type boundary structures, see fig. 73 b).

Figure 73: Comparison of the morphology of dynamic (8 substrate passes) TiO_2 film formed in the presence of Ag at 400 °C with different AACVD flow rates 0.3 and 0.6 l/min: a) AACVD flow rate: 0.3 l/min, b) AACVD flow rate: 0.6 l/min.

a) morphology (scale: 500 nm)

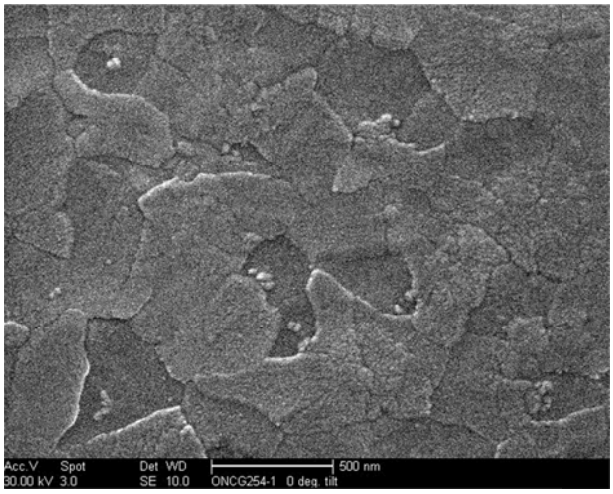

b) morphology (scale: 500 nm)

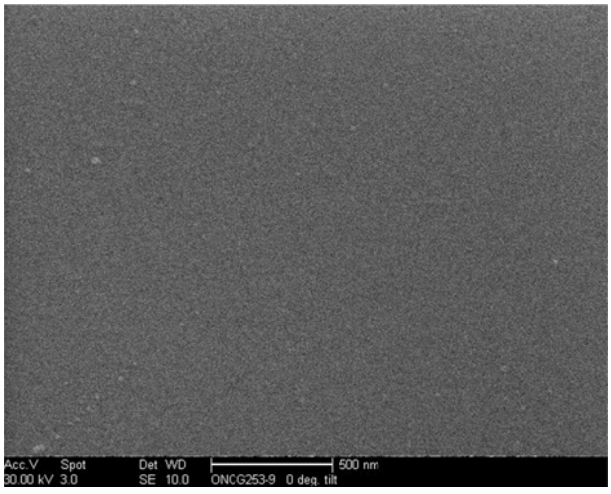

Increasing the number of passes (20) of the substrate under the reaction chamber head only increase thickness of the film and makes the platelet structures more prominent, see fig. 74.

Figure 74: Morphology of dynamic (substrate passes: 20) TiO_2 film formed in the presence of Ag at 400 °C, AACVD flow rate: 0.6 l/min: scale: 500 nm.

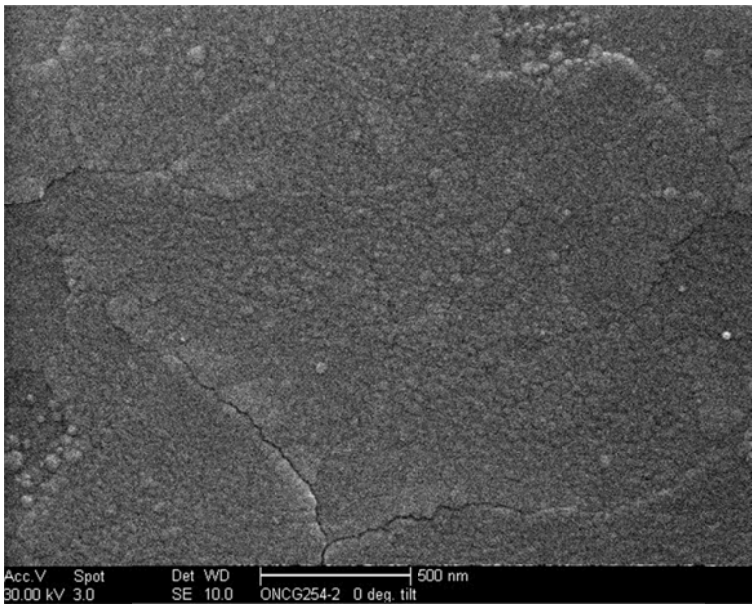

The titania films formed in the presence of Cu have the large platelet type structures with smaller agglomerated spherical nanoparticles, increased AACVD flow rate appears to have no significant effect on morphology, see fig. 75 a-b).

Figure 75: Comparison of the morphology of dynamic (substrate passes: 8) TiO_2 films formed in the presence of Cu at 400 °C with different AACVD flow rates 0.3 and 0.6 l/min: a) AACVD flow rate: 0.3 l/min, b) AACVD flow rate: 0.6 l/min.

a) morphology (scale: 500 nm)

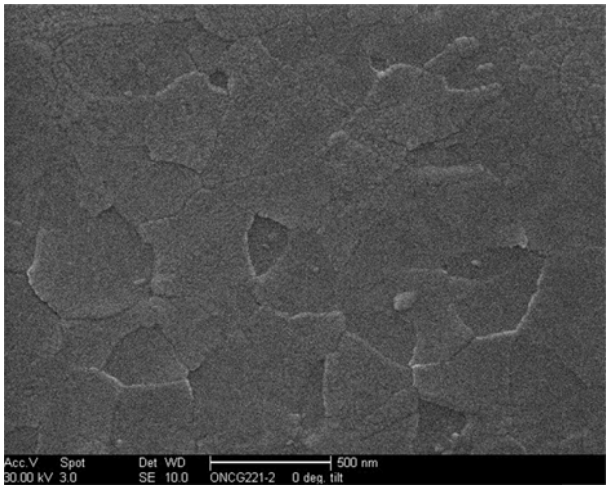

b) morphology (scale: 500 nm)

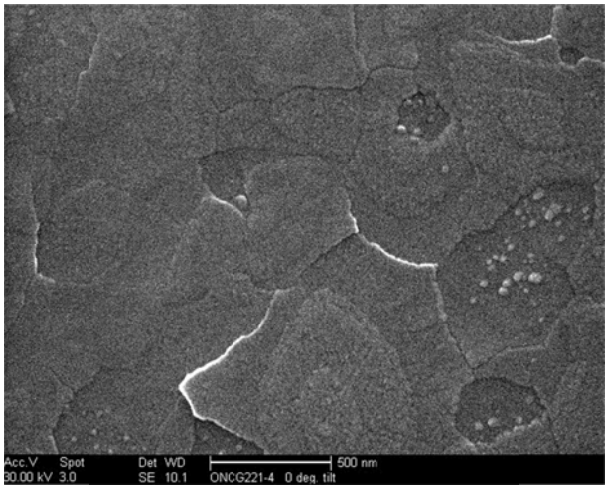

4.2.3.2.1 Summary of undoped and doped dynamic TiO_2 films at 400 °C

Control samples for dynamic films (400 ºC) showed plate structures with smaller granular/spherical areas and the static samples were granular/spherical and agglomerated in shape. Plate structures were seen for dynamic thin film samples formed in the presence of Au, Ag and Cu, dopants at 400, all dopants were below detection level within the film, whereas spherical nanoparticle structures (100-800 nm) were observed for static substrate samples at 400 ºC and one sample that contained Au nanoparticles had uniform spherical structures (50–100 nm) with bright spots.

4.2.3.3 Undoped and doped static TiO_2 films at 600 °C

The static CVD titania control at 600 °C, formed from TTIP, had elongated nanoparticles (50-100 nm) with a typical thickness of 402 nm for transparent areas of film, see fig. 76 a-d). Opaque areas of the titania control displayed agglomerated columns of angular fractal floret type structures, fractals with typical thickness of 1857 nm, see fig. 76 e-h). Transparent and opaque areas of the TiO_2 films correlate to the optical interference patterns and the non-uniform surface due to change in thickness of the films *i.e.* opaque areas are thicker than transparent areas of the films.

Figure 76: SEM static TiO_2 control film at 600 °C: a) and e) Morphology; b), c), f) and g) thickness; d) and h) composition.

a) Morphology (scale: 500 nm)

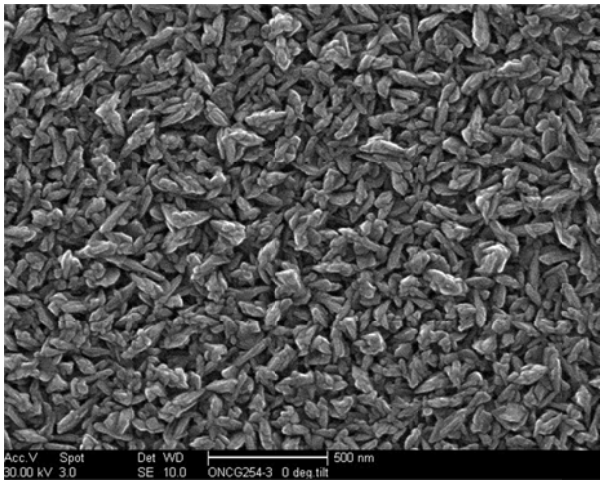

b) Thickness (scale: 500 nm)

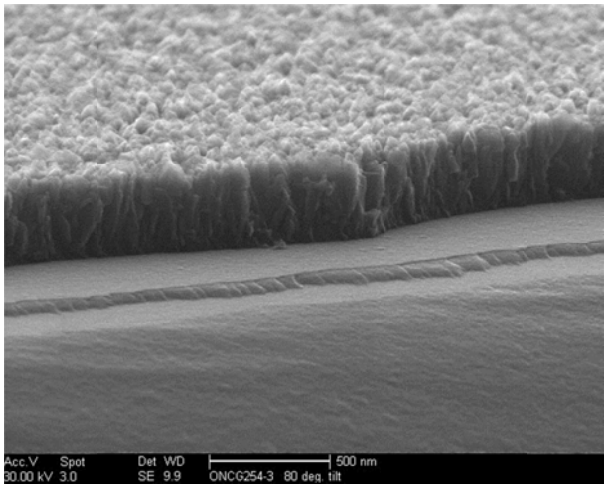

c) Thickness: 402 nm

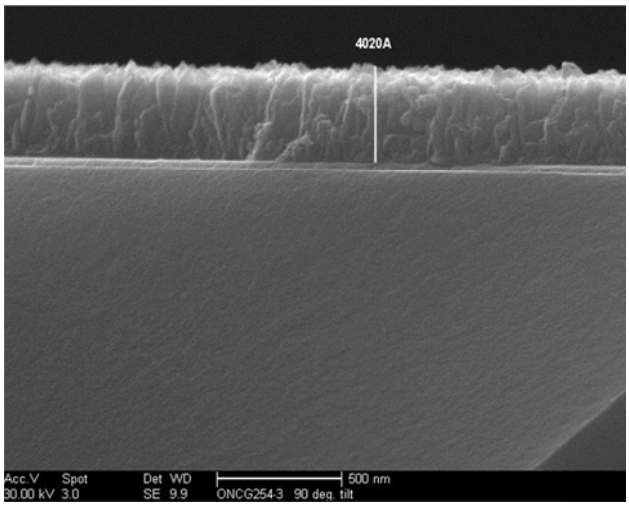

d) Composition (* Pt coating used)

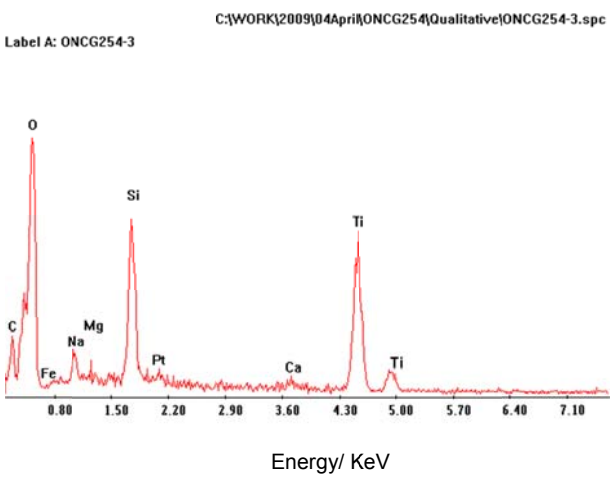

e) Morphology: opaque area (scale: 500nm)

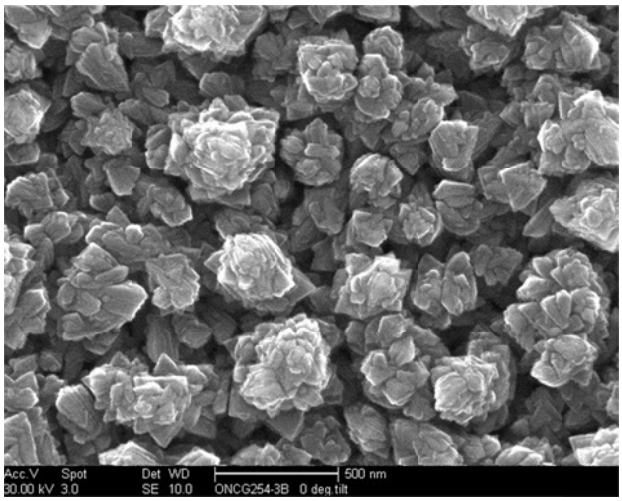

f) Thickness: opaque area

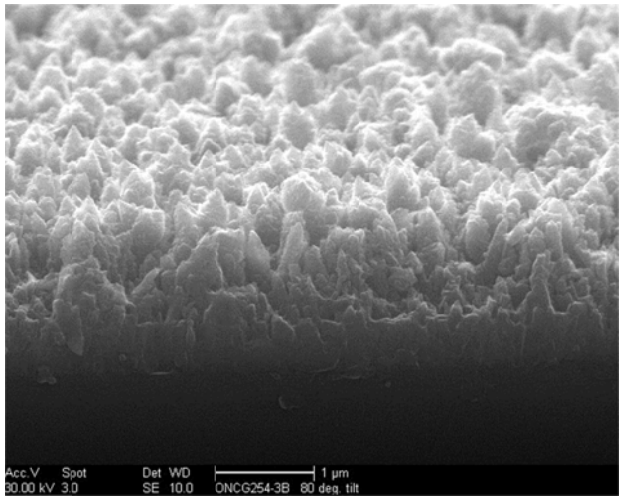

g) Thickness: opaque area: 1875 nm

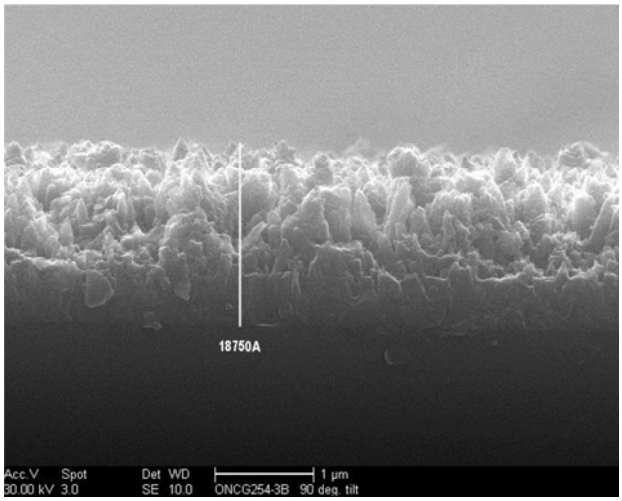

h) Composition: opaque area

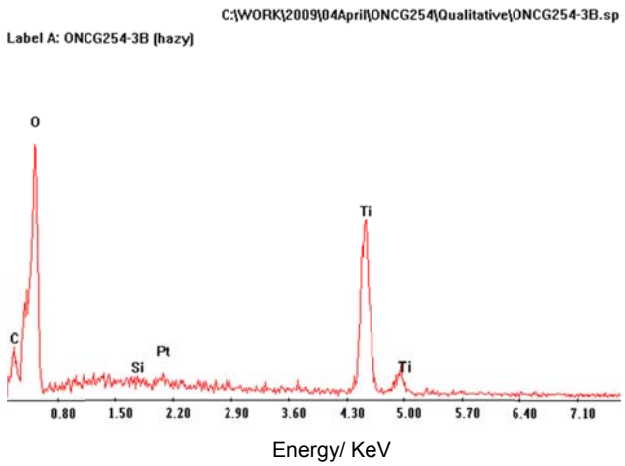

The static titania film formed in the presence of Au has very similar morphology to the APCVD titania control for both transparent and opaque areas of film, see

fig. 77 a-b). The amount of Ti increased slightly for the opaque areas of the film.

Figure 77: Comparison of the transparent and opaque morphology of static (1 min) TiO_2 filmed formed in the presence of Au (600 °C, AACVD: 0.3 l/min).

a) morphology (middle: transparent) b) morphology (edge: opaque film)

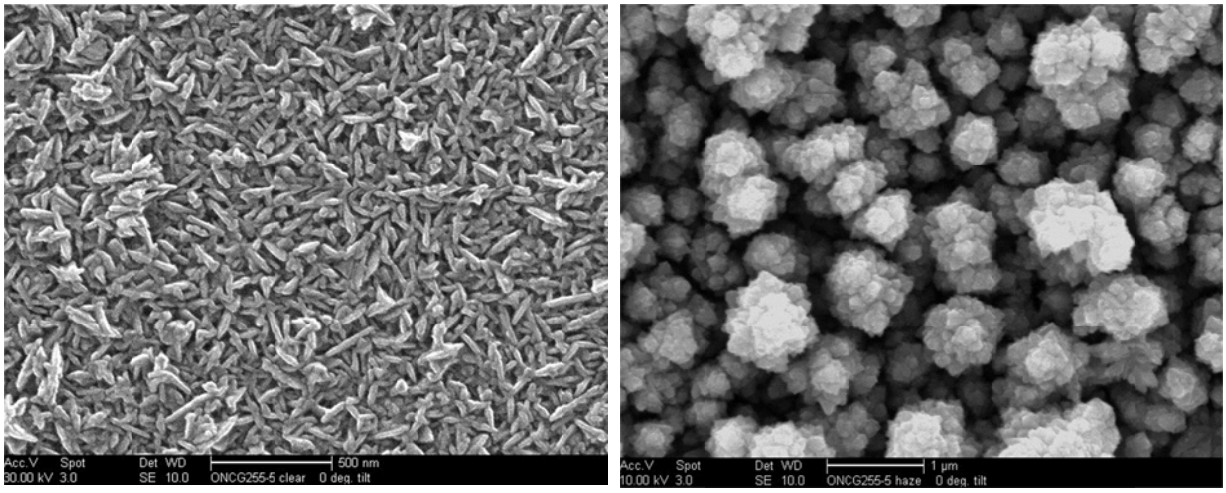

No Au nanoparticles were detected. An increase in the amount of time the substrate is exposed under the reaction chamber appears to only increase the agglomeration and size of the nanoparticle structures indication of the increase of thickness of the film, see fig. 78 a-b).

Figure 78: Comparison of the transparent and opaque morphology and composition of static (3 min) TiO_2 film formed in the presence of Au (600 °C, AACVD: 0.3 l/min). The amount of Ti increases slightly in the opaque area of the film, see fig. 113 c) and d).

a) morphology (middle: transparent) b) morphology (edge: opaque)

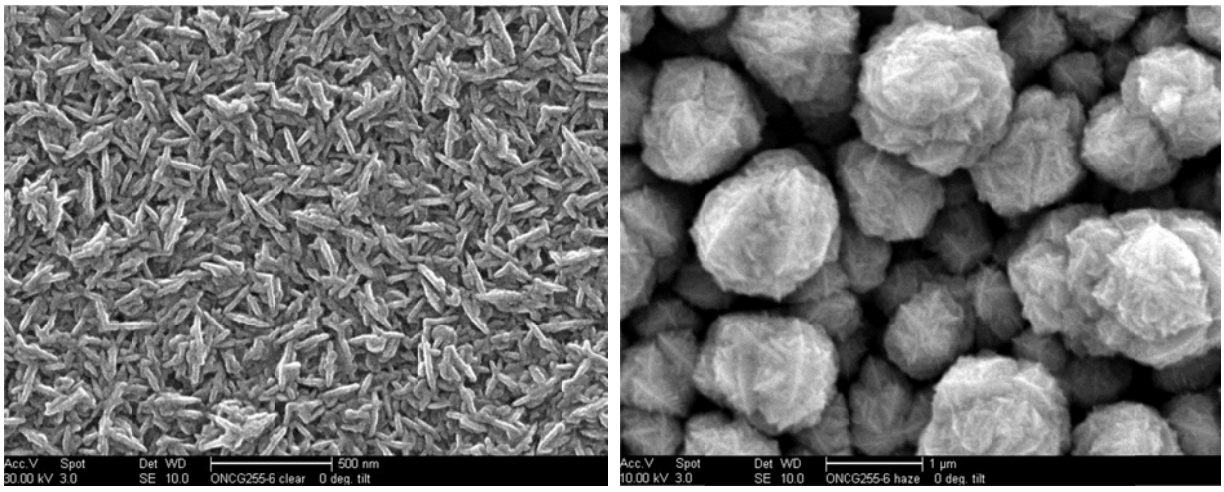

c) composition (transparent area): (* Pt coating used)

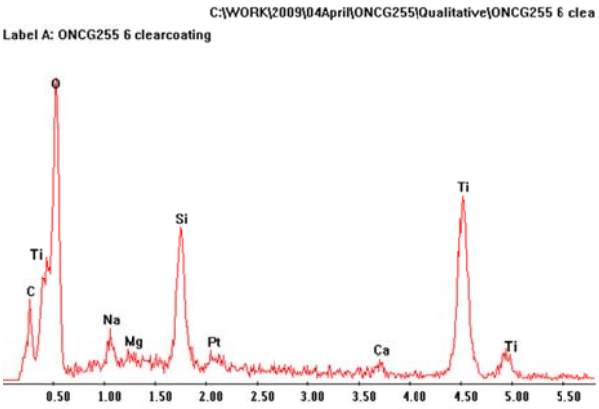

d) composition (opaque area)

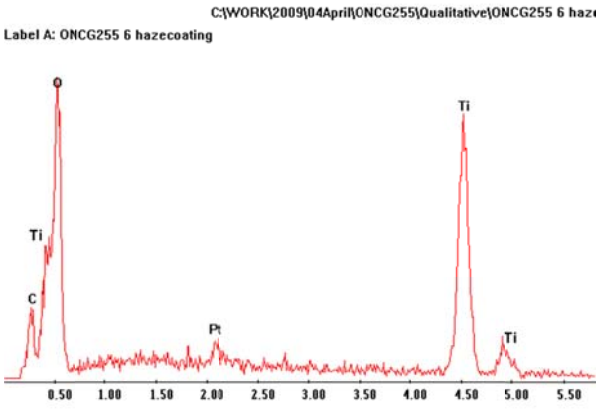

No Au nanoparticles were detected the titania films formed in the presence of Au had agglomerated spherical nanoparticles in the transparent area of the film and columns of rounded fractal floret type structures in the opaque areas of the film, the amount of Ti increases slightly in the opaque areas of the film see fig. 79 a-d).

Figure 79: Comparison of the transparent and opaque morphology and composition of static (1 min) TiO_2 film formed in the presence of pre-formed Au (AACVD flow rate: 0.3 l/min, 600 °C).

a) morphology (middle: transparent)

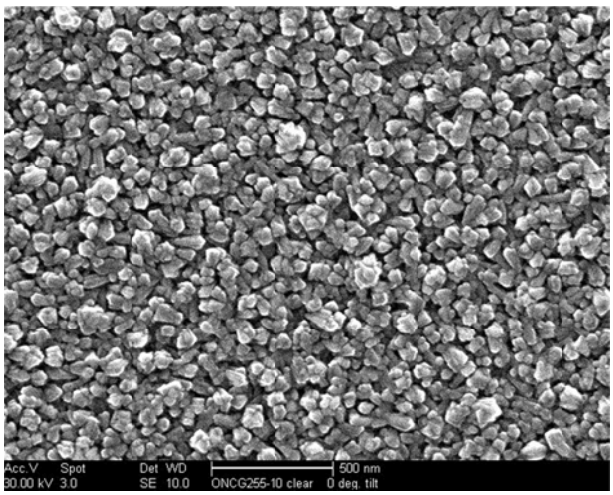

b) morphology (edge: opaque)

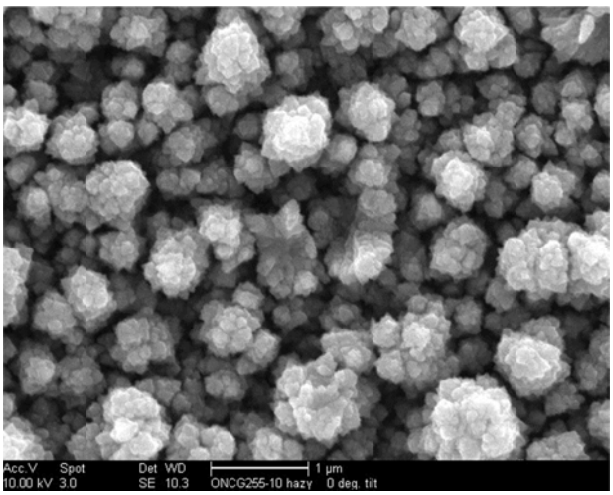

c) composition transparent film area: (* Pt coating used)

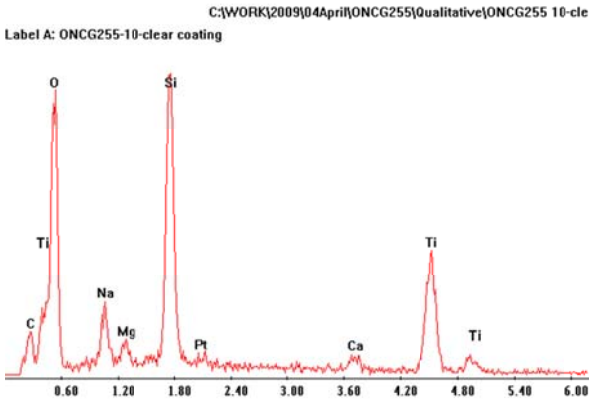

Energy/ KeV

d) composition opaque film area

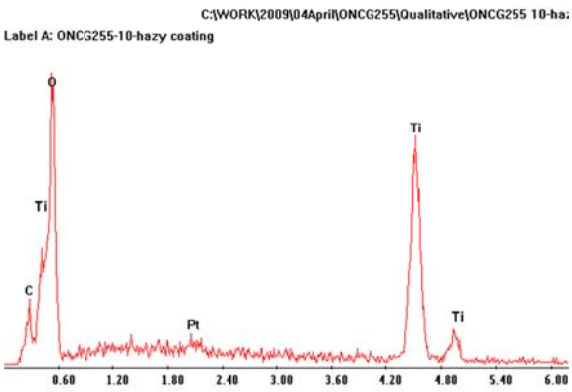

Energy/ KeV

No Au nanoparticles were detected. An increase in the AACVD flow rate (0.6 l/min) of the Au dopant appears to alter the morphology of the titania film to more angular nanoparticles, see fig. 80.

Figure 80: Morphology of TiO_2 film formed in the presence of Au at 600 °C, static (1 min), AACVD flow rate: 0.6 l/min, 600 °C.

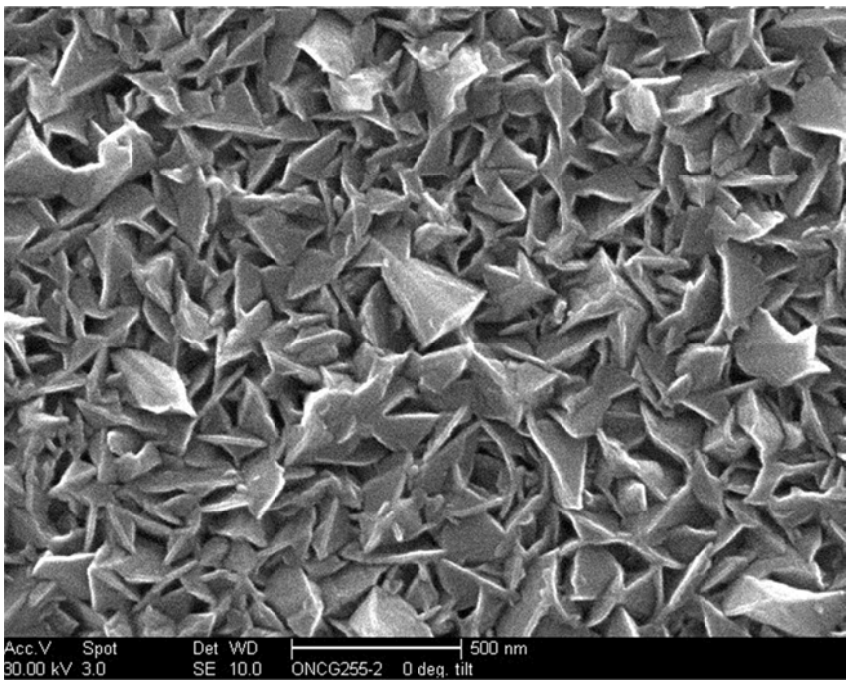

No Ag nanoparticles were detected, the titania film formed in the presence of Ag had nanoparticles (size: 50–100 nm) in the transparent area whereas the opaque areas have agglomerated column type structures (size: 500 nm–1 µm), the Ti content increases in the opaque area of the film, see fig. 81 a-b).

Figure 81: Comparison of the transparent and opaque morphology of static (1 min) TiO_2 film formed in the presence of Ag (AACVD flow rate: 0.3 l/min, 600 °C).

a) morphology (middle: transparent) b) morphology (edge: opaque)

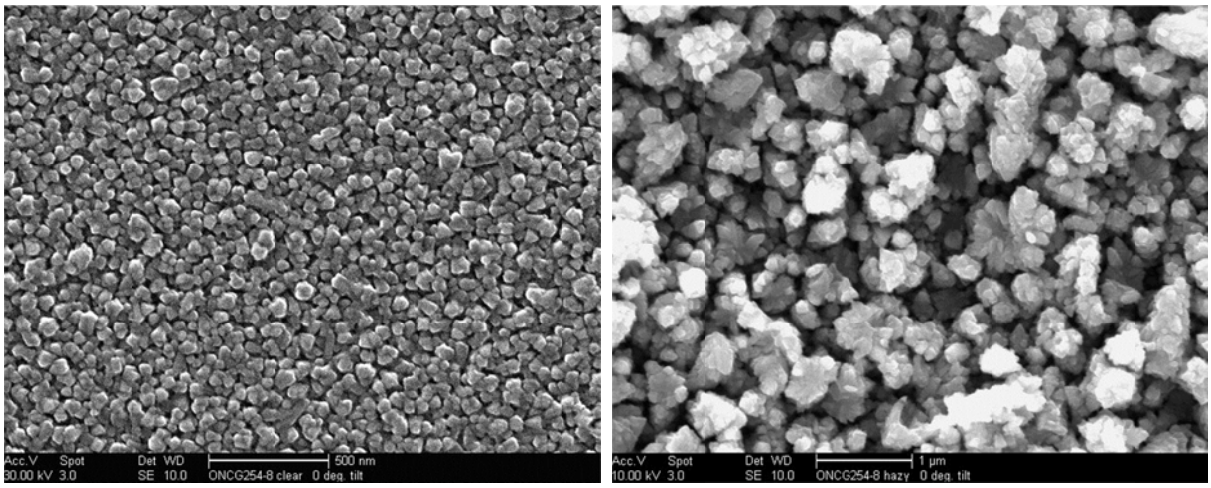

No Ag nanoparticles were detected. An increased AACVD flow rate (0.6 l/min) changes the morphology to more angular nanoparticle structures (50–500 nm) with groups of large crystals (size: ~1 µm) with no significant difference in composition between the overall morphology and large crystal groups, see fig. 82 a-b).

Figure 82: Morphology of TiO_2 film formed in the presence of Ag, static (1 min), AACVD flow rate: 0.6 l/min, 600 °C.

a) morphology (scale: 500 nm) b) morphology (scale: 1 µm)

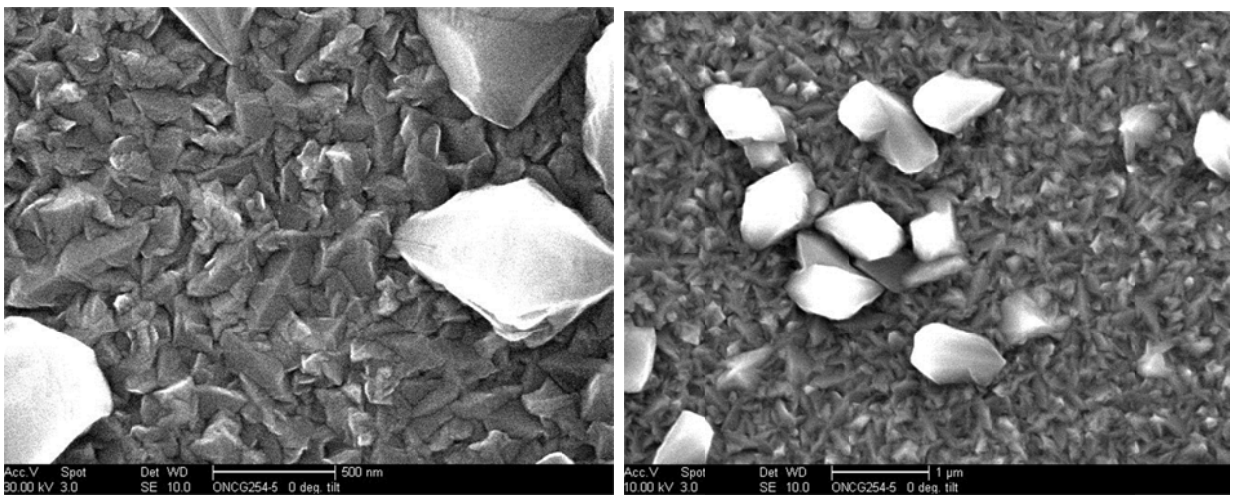

4.2.3.4 Undoped and doped dynamic TiO_2 films at 600 °C

The titania CVD control film has an angular nanoparticle structure (size: 100–250 nm) with a typical thickness (219 nm) and composition, see fig 83 a-d).

Figure 83: Morphology, thickness and composition of the TiO_2 dynamic (8 substrate passes) control film, 600 °C.

a) morphology (scale: 500 nm)

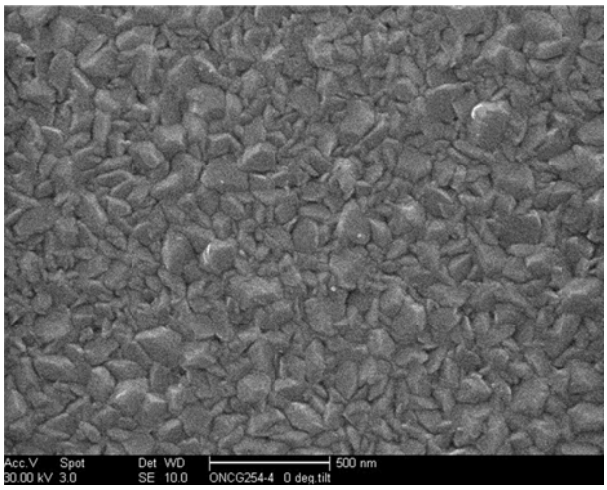

b) Thickness

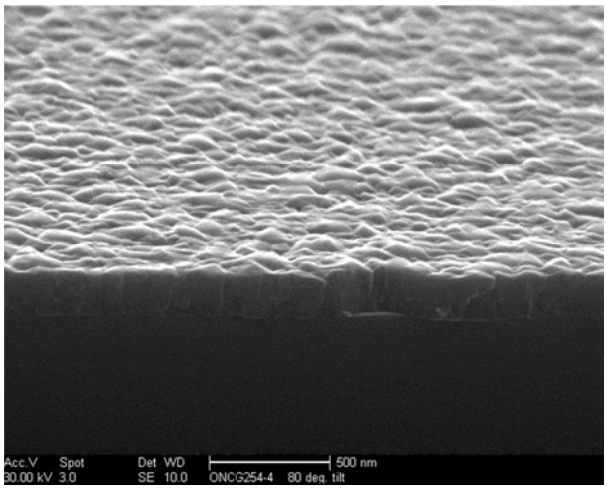

c) Thickness: 219 nm (scale: 500 nm)

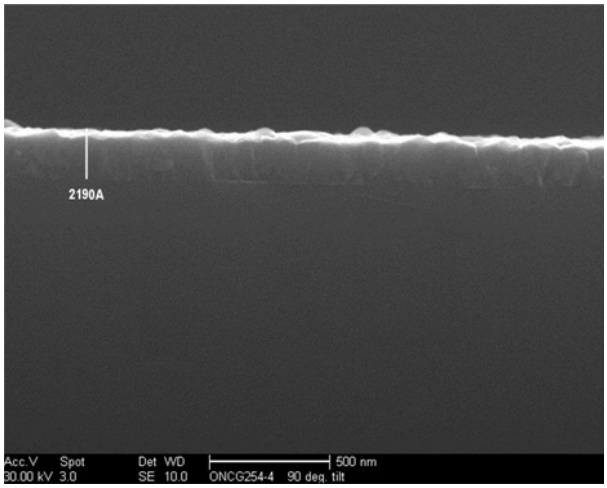

d) Composition

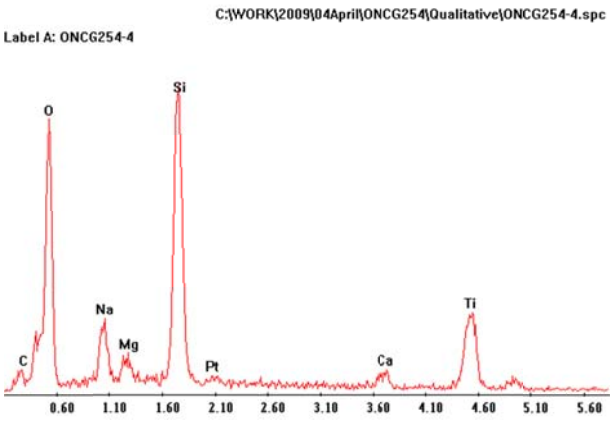

The titania film with lower AACVD flow rate (0.3 l/min) formed in the presence of Au has elongated nanoparticle structure with decreased size (50–100 nm) and lower levels of Ti in the composition when compared with the APCVD titania control film, see fig. 84. No Au nanoparticles were detected. An increased number of passes under the reaction chamber head only enlarged the nanoparticle size (100–150 nm) when compared to the Au doped film with 8 substrate passes under the reaction chamber head, see fig. 84 a-b).

Figure 84: Comparison of the morphology of dynamic TiO_2 films formed in the presence of Au, AACVD flow rate: 0.3 l/min with either 8 or 20 substrate passes under the reaction head:

a) 8 substrate passes (scale: 500 nm) b) 20 substrate passes (scale: 500 nm)

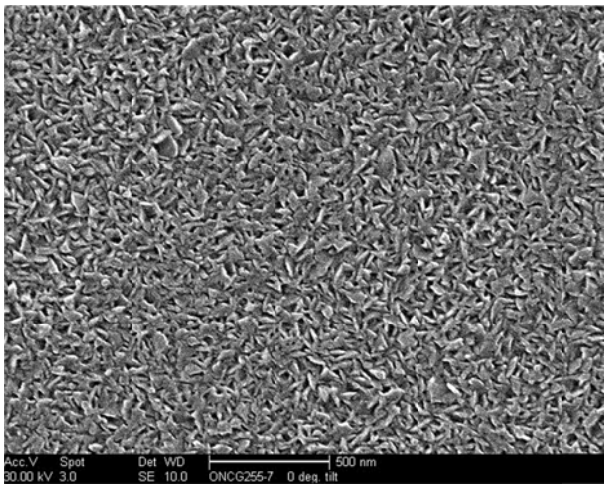

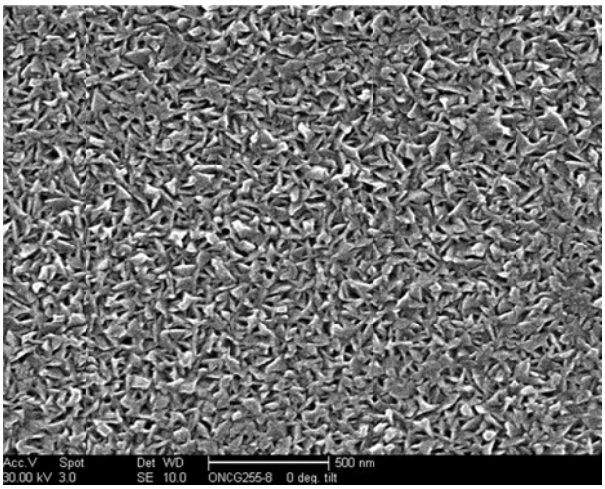

The titania film formed in the presence of pre-formed Au nanoparticle dopant gave a more interlocked angular nanoparticle (size 100-300 nm) morphology than the *in-situ* Au dopant with additional interspersed large lumps of rounded off angular agglomerated nanoparticles (size: 500 nm-1µm) lying on the surface, see fig. 85 a-b).

Figure 85: Morphology and composition of TiO_2 doped film, formed in the presence of pre-formed Au; number of passes under reaction chamber head: 8 passes, AACVD flow rate: 0.3 l/min.

a) morphology (scale: 500 nm) b) morphology (scale:1µm)

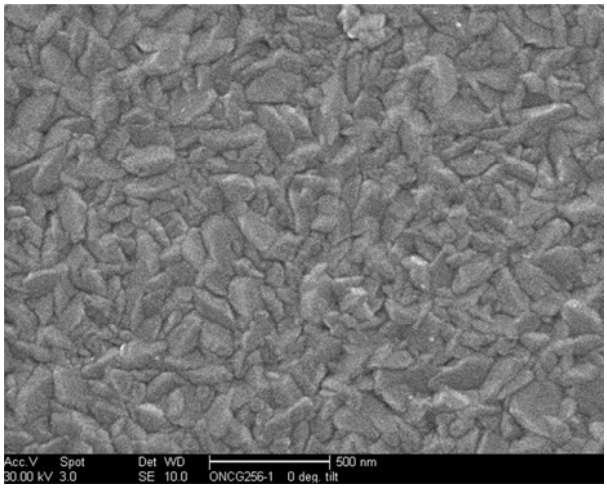

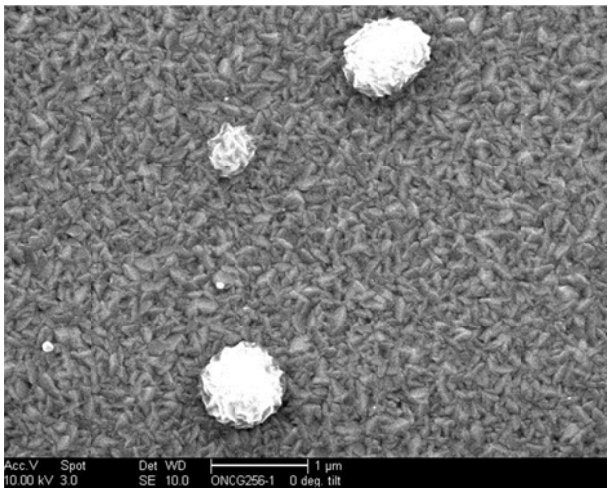

No Au nanoparticles were detected. An increase in the number of substrate passes under the reaction chamber head with the pre-formed Au dopant increases the thickness of the film and increases the size of the morphology

seen when compared to the *in-situ* Au doped film with 8 passes under the reaction chamber head, see fig. 86 a-b).

Figure 86: Morphology of TiO_2 film formed in the presence of pre-formed Au, number of passes under reaction chamber head: 20 passes, AACVD flow rate: 0.3 l/min.

a) morphology (scale: 500 nm) b) morphology (scale: 1 µm)

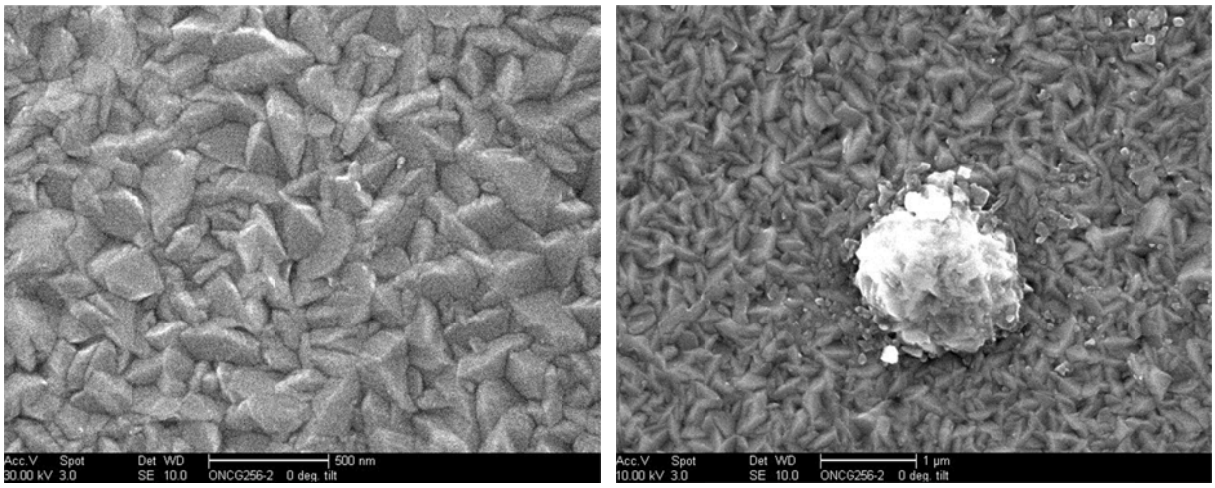

For the dynamic (8 passes) TiO_2 film formed in the presence of Au, no Au nanoparticles were detected, increasing the AACVD flow rate (0.6 l/min) for the *in-situ* Au dopant had the effect of increasing film thickness and the size of the nanoparticle morphology (size: 100–400 nm), see fig. 87.

Figure 87: Morphology of TiO_2 film formed in the presence of Au, substrate passes 8, AACVD flow rate: 0.6 l/min.

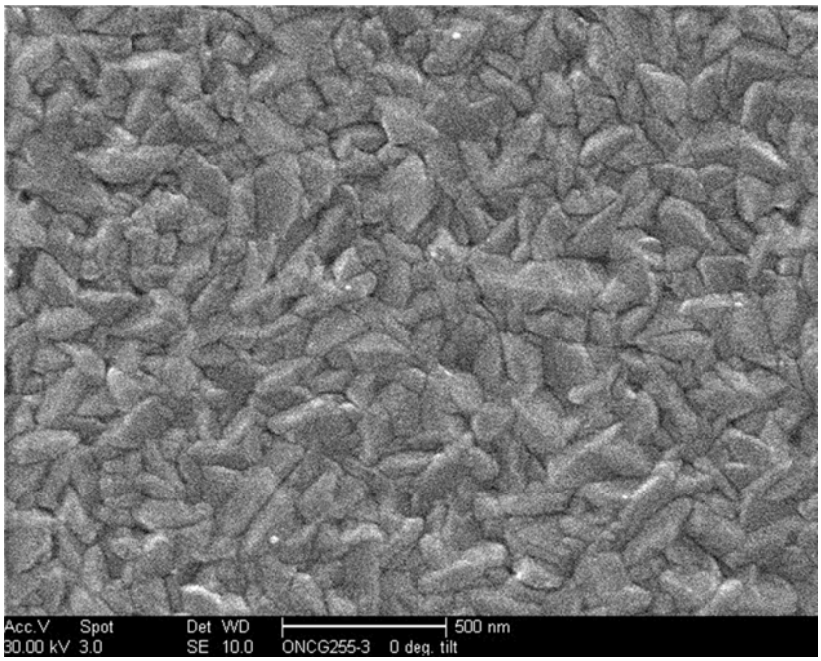

No Au nanoparticles were detected. An increase in the number of substrate passes increases the nanoparticle size when compared to Au doped films with less number of substrate passes, see fig. 88.

Figure 88: Morphology and composition of TiO_2 film formed in the presence of Au, substrate passes: 20 passes, AACVD flow rate: 0.6 l/min.

a) morphology (scale: 500 nm)

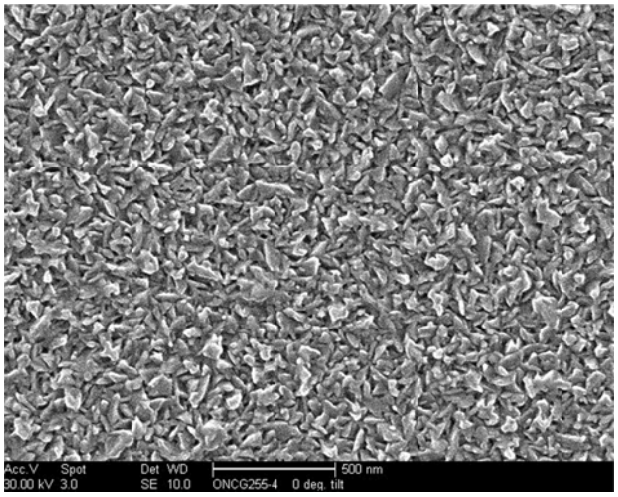

b) composition

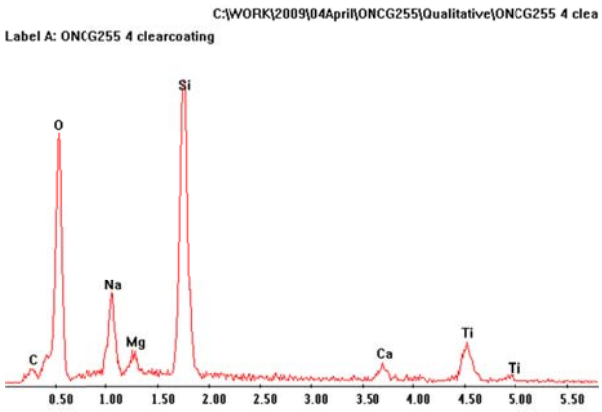

No Ag nanoparticles were detected. Ag doped titania film has elongated nanoparticles (size: 50–100 nm) with lower Ti content than the CVD titania control film, see fig. 89.

Figure 89: Morphology of TiO_2 film formed in the presence of Ag, substrate passes: 8, AACVD flow rate: 0.3 l/min.

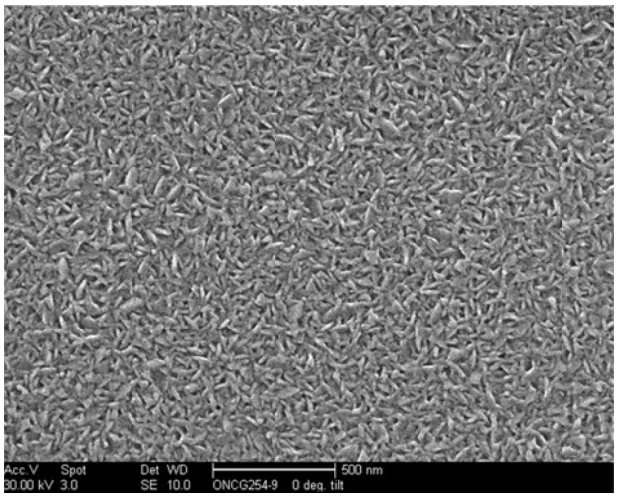

No Ag nanoparticles were detected. An increase in the number of substrate passes (20) under the reaction chamber head for the Ag doped titania film enlarges the size of the angular shaped nanoparticles in the transparent area of

the film and forms columns of agglomerated fractal floret type structures in the opaque areas of the film, an indication in the increase of thickness, there are no significant differences in composition between transparent and opaque areas of the film, see fig. 90 a-b).

Figure 90: Morphology of TiO_2 film, formed in the middle and at the edge of the glass substrate, in the presence of Ag, number of passes under reaction chamber head: 20 passes, AACVD flow rate: 0.3 l/min

a) morphology, (middle: transparent)

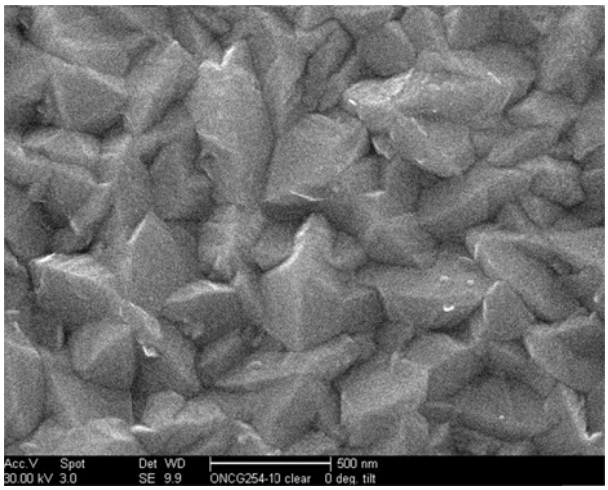

b) morphology, (edge: opaque)

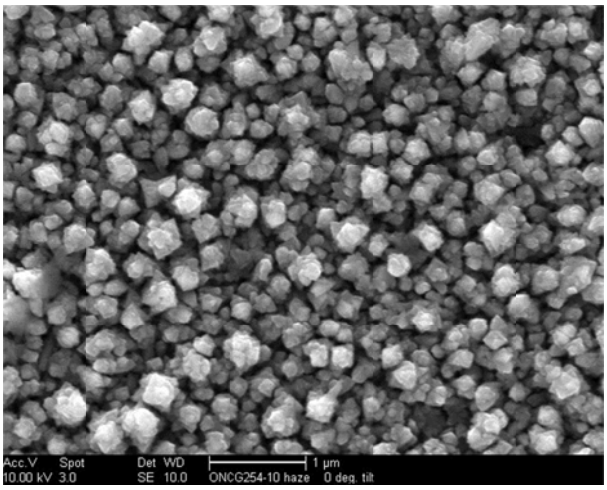

No Ag nanoparticles were detected. An increase in the AACVD flow rate (0.6 l/min) of the Ag doped film decreases the size of the angular nanoparticle morphology (50 nm) from the lower flow rate of 0.3 l/min, see fig. 91.

Figure 91: Morphology of TiO_2 film formed in the presence of Ag, substrate passes: 8, AACVD flow rate: 0.6 l/min.

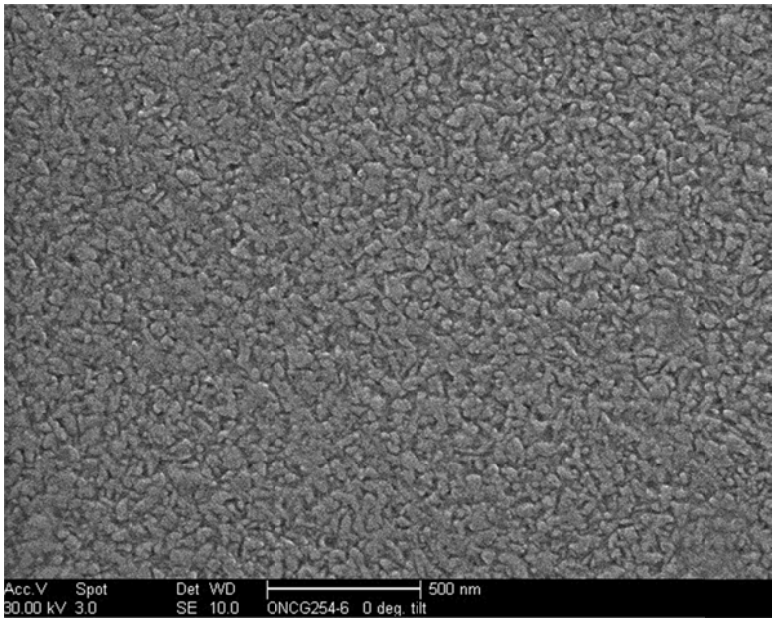

No Ag nanoparticles were detected. An increased AACVD flow rate (0.6 l/min) and an increased number of substrate passes (20) under the reaction chamber head increase the overall size of the angular nanoparticle morphology (200-300 nm) and Ti content, see fig. 92 a-b).

Figure 92: Morphology and composition of a TiO_2 film formed in the presence of Ag, substrate passes: 20, AACVD flow rate: 0.6 l/min.

a) morphology (scale: 500 nm) b) composition

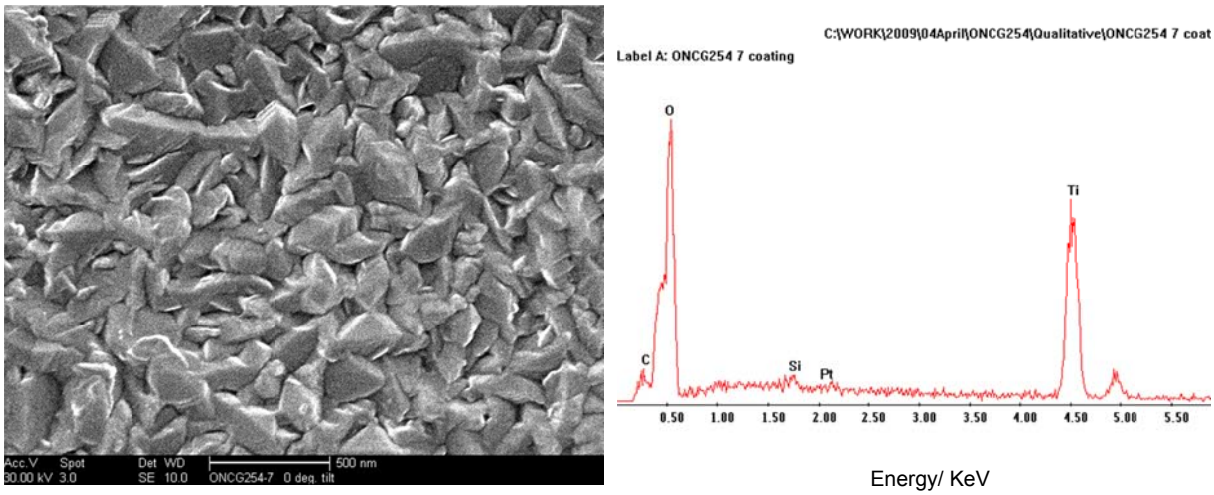

4.2.3.5 Summary of undoped and doped TiO_2 films at 600 °C

The static APCVD control film at 600 °C consisted of angular nanoparticle morphology; the films formed in the presence of Au and Ag nanoparticles also displayed this morphology differing in size in transparent areas of the films and forming large columns of angular floret fractal nanoparticles in opaque areas of the films. An increase in the time duration under the reaction chamber head correlated to an increase in nanoparticle size. The dynamic APCVD control TiO_2 film, at 600 °C, consisted of elongated angular nanoparticle morphology. The doped dynamic films at 600 °C formed elongated nanoparticles between larger interlocking platelet type morphology. An increase in the number of passes under the reaction chamber head increased the nanoparticle size, due to increasing thickness of film and an increase in the AACVD flow rate decreased the size of the nanoparticle size. Control samples for dynamic films (600 ºC) showed angular grain structures (100–150 nm) and static films were agglomerated angular in shape with larger embedded Neolithic spear structures (400 nm). Au and Ag dopants for both dynamic and static films had angular structures (50-500 nm) with agglomeration and angular floret fractal structures

forming in the static samples with increasing film thickness (402–1875 nm). Au dopants tended to decrease nanoparticle size and Ag dopants tended to increase nanoparticle size. The film produced at 600 °C much larger crystalline structures than those at 400 °C.

The morphologies observed for static and dynamic TiO_2 films formed at 600 °C are affected by the fluid flow, see chapter 2, time duration (1-3 mins) for static films and/or number of passes (8-20) for dynamic films under the reaction chamber head. The differences and effect on the morphology that could be expected to be observed by using different solvent systems was negated by using the same solvent MeOH throughout the synthesis of these films.

4.2.3.5 Overall summary for undoped and doped TiO_2 films

Direct comparison of TiO_2 films formed in the presence of the noble metal dopants Au, Ag and Cu are discussed below. The titania films formed at 400 ºC under static conditions show a stark contrast of morphologies when compared to the CVD control film and each other, see fig. 93 a-e).

Figure 93: Comparison of Static TiO_2 film morphology at 400 °C, 1 min.

a) control

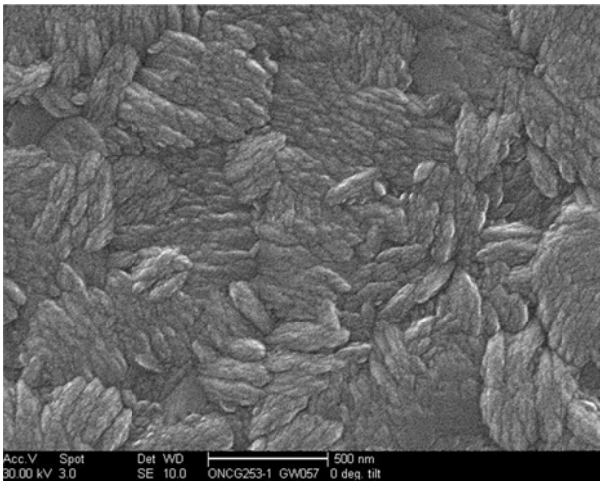

b) Au

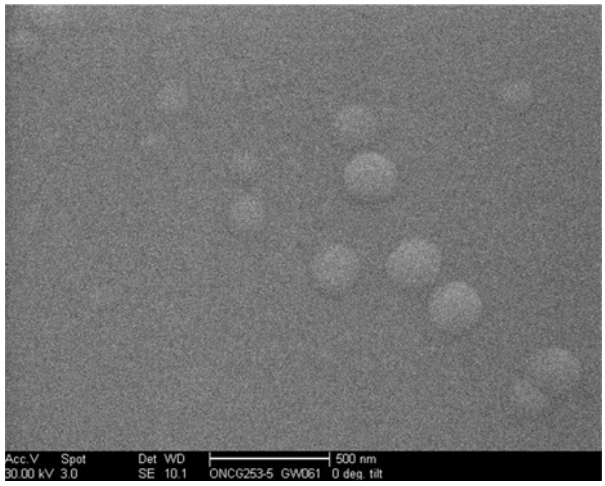

c) Au (present)

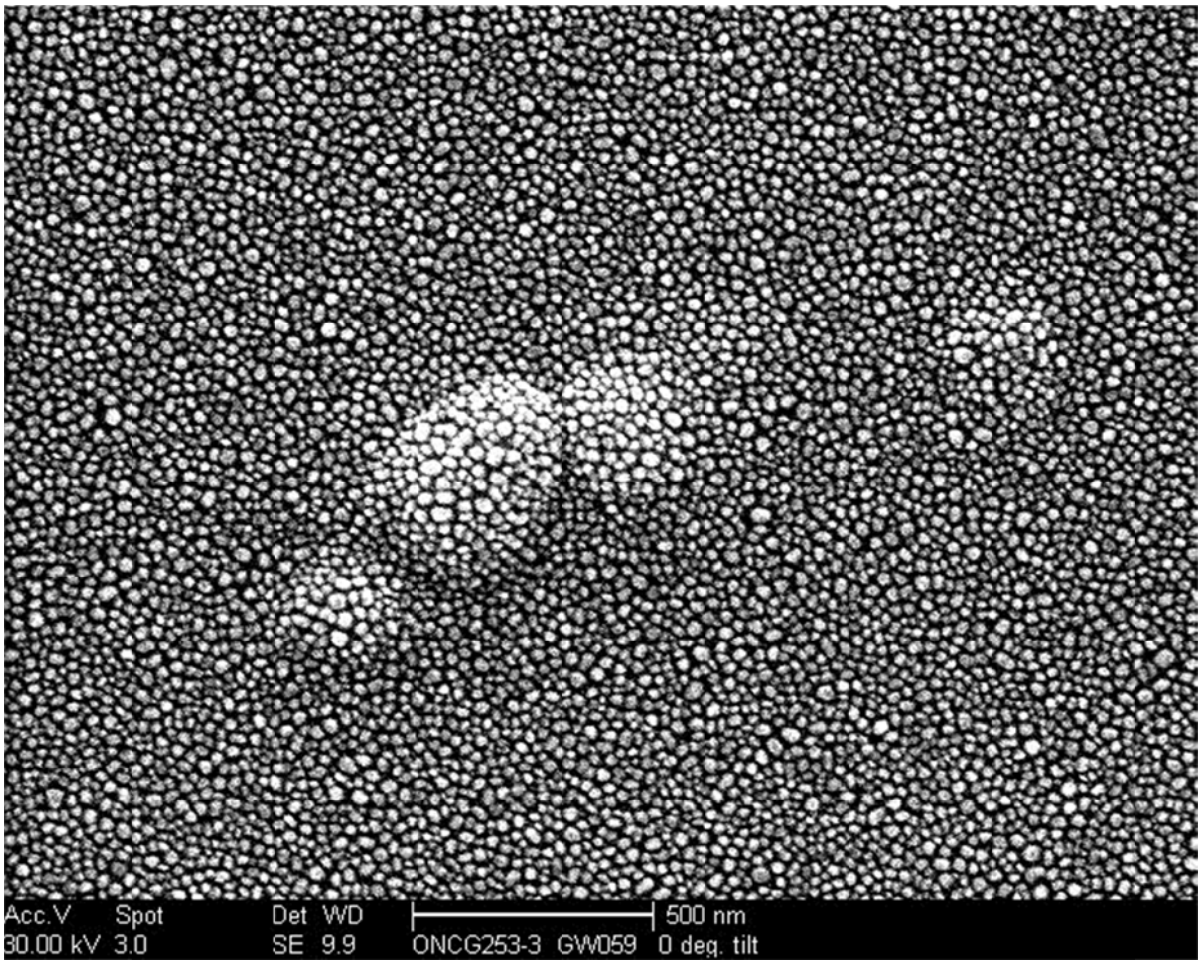

d) Ag

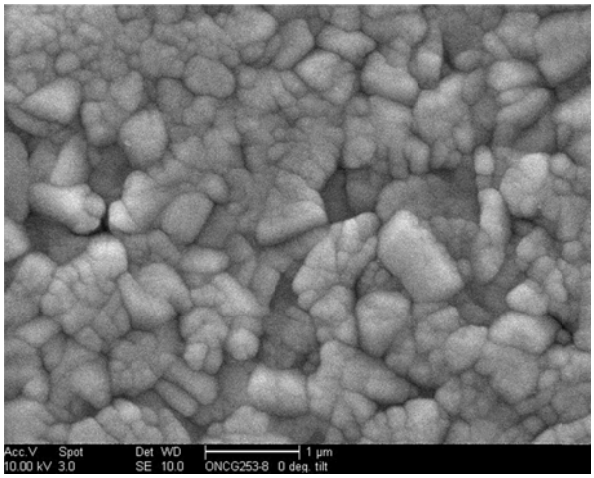

e) Cu

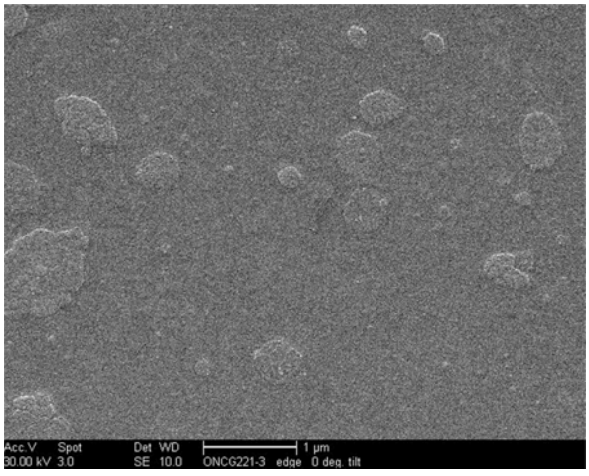

Ag appears to produce larger structures than Au, whereas Au's influence appears to smooth the morphological structures. These apparent differences are not so apparent once the substrate moves under the reaction chamber head and all morphologies appear to be very similar flat platelet type microstructures, see fig. ii, 94 a)-d).

Figure 94: Comparison of dynamic TiO_2 film morphology at 400 °C, 8 substrate passes.

a) control

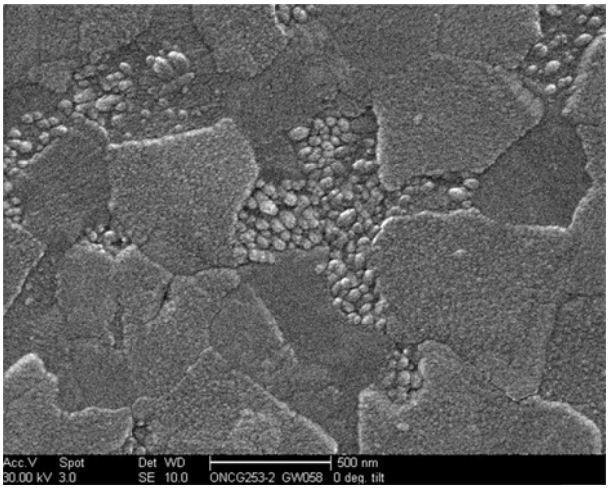

b) Au

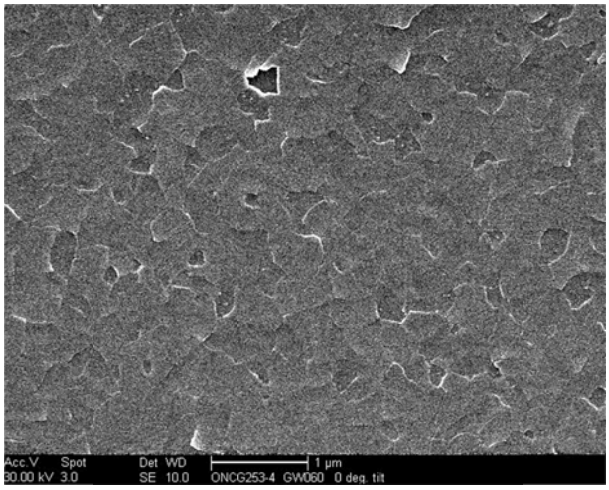

c) Ag

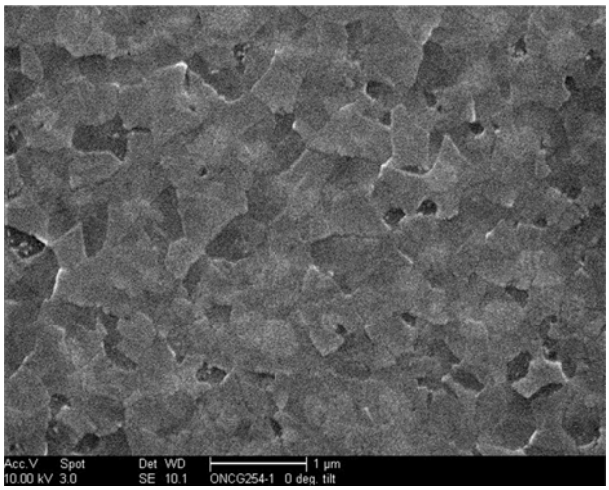

d) Cu

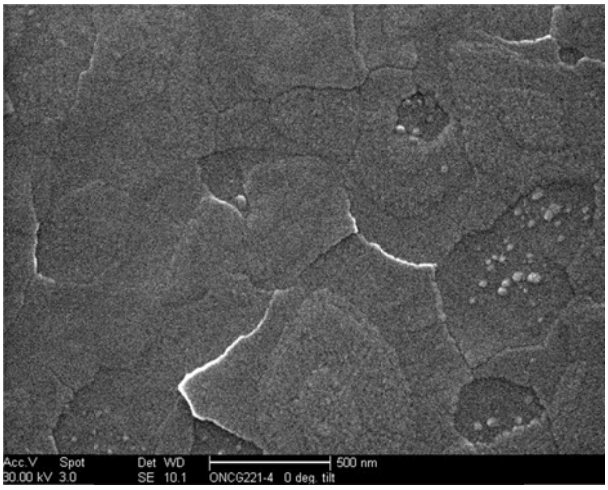

The titania films formed at 600 ºC under static conditions show a stark contrast of morphologies when compared to the APCVD control film and each other, see fig. 95 a-d).

Figure 95: Comparison of static TiO_2 film morphology at 600 °C, 1 min.

a) control

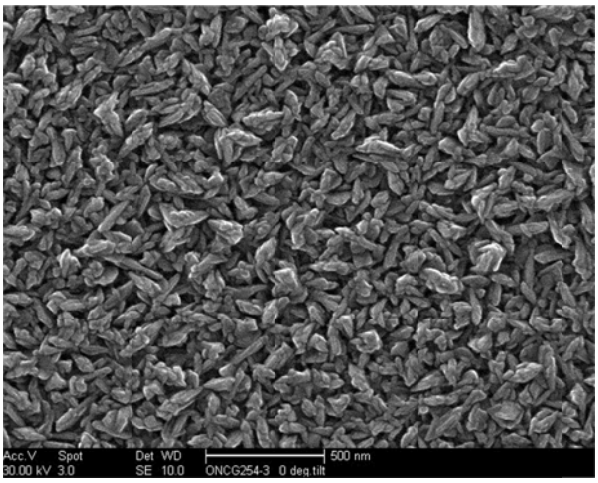

b) Au

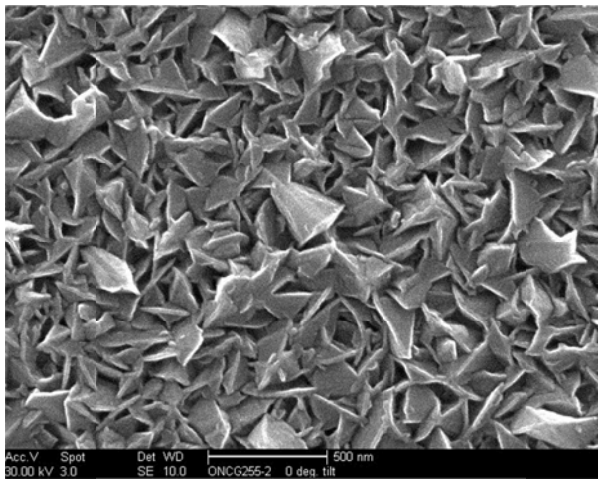

c) Ag

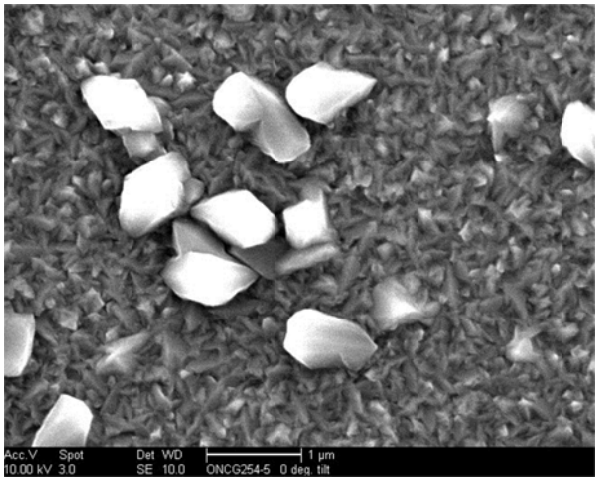

d) pre-formed Au

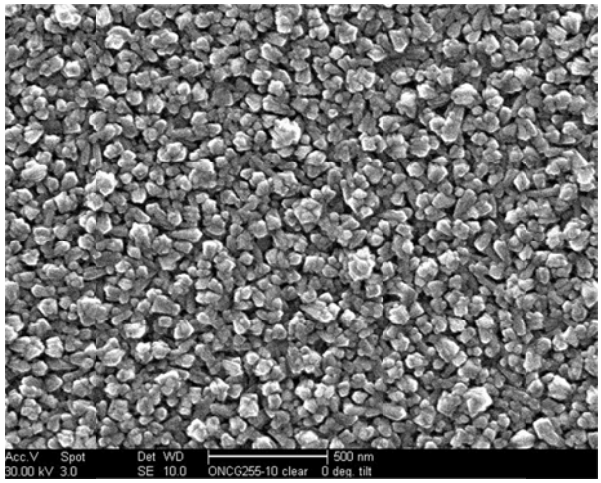

Opaque areas of the films for all static's formed at 600 °C form exhibit typical columnar fractal type patterns in common with work using various CVD techniques including Goossens *et al.*1998[149], Jung *et. al*, 2005[150] using low-pressure MOCVD, Kim *et al.*, 2009[151], Mathur *et.al*, 2006[152] using plasma CVD (PACVD), Seifried *et.al*., 2000[153]. Yung's work also illustrates that increasing the amount of synthesis time increases the size and structure of the columnar type microstructure growth seen in titania films[150]. The titania films formed under dynamic conditions at 600 °C had remarkably similar crystalline morphologies, see fig. 96 a-d).

Figure 96: Comparison of dynamic TiO_2 film morphology at 600 ºC, 8 substrate passes

a) control

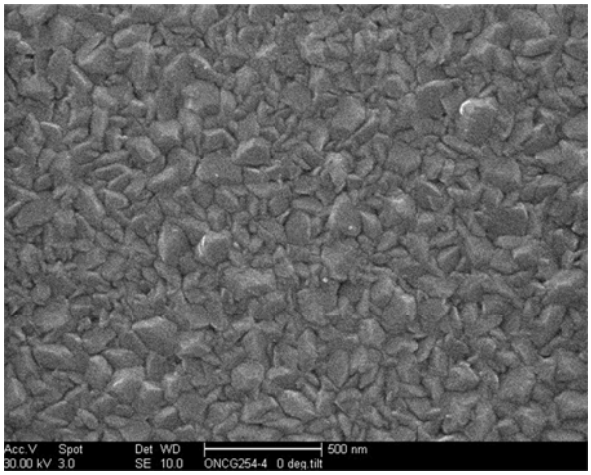

b) Au

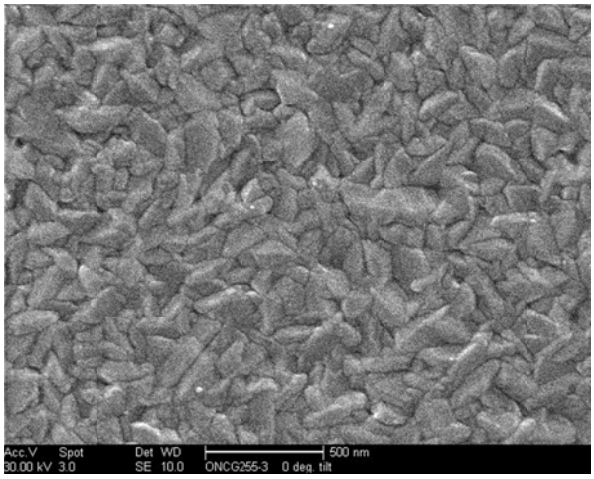

c) Ag

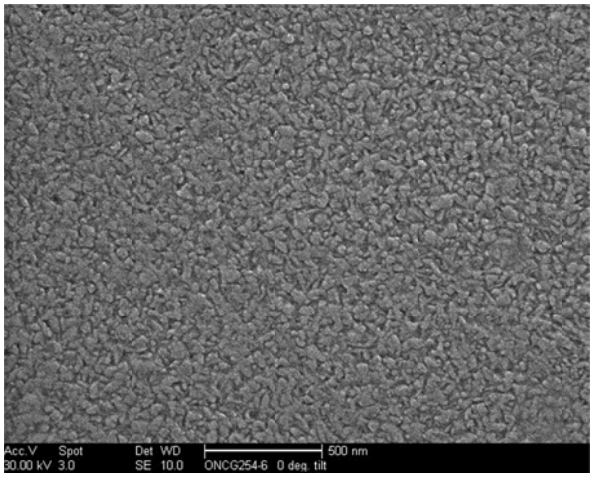

d) pre-formed Au

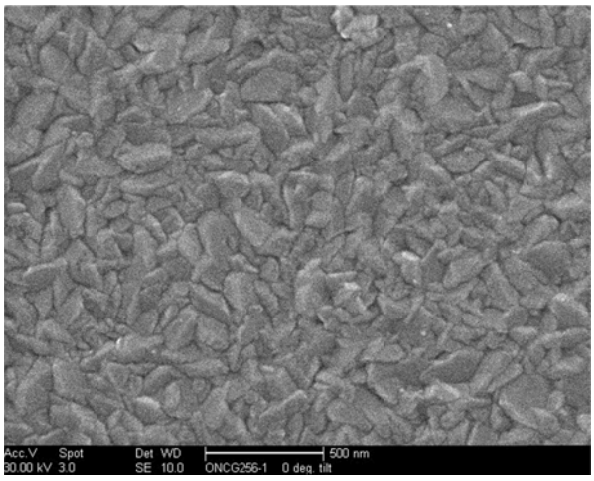

The large angular and agglomerated microstructures seen for the dynamic titania films at 600 °C bore some similarities with those seen in work done by Rosas *et. al*, 2010, on steel using MOCVD[154].

The titania films synthesized at higher temperatures (600 ºC) whether undoped or formed in the presence of a dopant were more crystalline than the titania films at lower temperatures (400 ºC). A moving substrate somewhat negates the effect of the dopant on morphology particularly at higher temperatures. Only one film sample was found to contain Au nanoparticles suggesting that a lower temperature (400 ºC), slower AACVD velocity (0.3 l/min) and static conditions are better for noble metal nanoparticle inclusion into the host matrix than higher temperatures (600 ºC), faster AACVD velocities (0.6 l/min) and a moving substrate. Thickness of the TiO_2 films also affects the microstructure; for static films the longer time periods (3 mins) create more agglomerated

massive structures, particularly on the columnar structures seen at 1 minute intervals and for dynamic films increasing the number of substrate passes (20 passes) under the reaction chamber head has a similar effect of creating more agglomerated massive structures already seen at a lower number of passes (8-10 passes). The morphologies observed for static and dynamic TiO_2 films formed at 400-600 °C are affected by the fluid flow, see chapter 2, time duration (1-3 mins) for static films and/or number of passes (8-20) for dynamic films under the reaction chamber head, the dopant and synthesis temperature. The fluid flow for prototype head 1 was demonstrated to be ineffective at mixing the AACVD fluid flow with the two APCVD fluid flows, in part due to the inner separating walls between these three flows, the consequence of the ineffective mixing of prototype head 1 can be seen in the TiO_2 films synthesised above and the differences in non-uniform surfaces are particularly apparent in the static film morphology, see chapter 2. For static films an increment in the duration of time (1-3 mins) and for dynamic films an increment in the number of passes (8-20) correlates to an increase in the thickness of the film. The Ag doped films appear to cause particularly thick films on the static samples (>200 nm) according to the Swanepoel calculations and lower the maximum transmittance seen (~70%) at both 400 °C and 600 °C. The effect of any dopant can be more clearly seen at higher temperatures (600 °C) and particularly with static films; a moving substrate lessens the overall effect on the microstructure. An increase in synthesis temperature correlates to an increase in the crystallinity of the film. The differences and effect on the morphology that could be expected to be observed by using different solvent systems was negated by using the same solvent, methanol, throughout the synthesis of these films.

4.2.4 XPS analysis

XPS analysis was carried out on TiO_2 films formed in the presence of Cu, Ag and Au dopants (400-450 °). All dopants were below detectable limits except for one Cu doped film at 400 °C were a small amount was detected.

4.2.4.1 XPS analysis of doped TiO_2 film, 450 °C

The XPS spectra of a TiO_2 film formed in the presence of Au dopant exhibited no Au, the composition after etching (3.5 mins) was titania, (Ti: 38 at.%, O: 59 at.%) with carbon contamination present (C: 2.8 at.%) at the surface. No Au was seen on the spectra, even with slow acquisition of the gold 3d peak region, see fig. 97.

Figure 97: XPS depth profile of titania film with Au dopant, 450 °C.

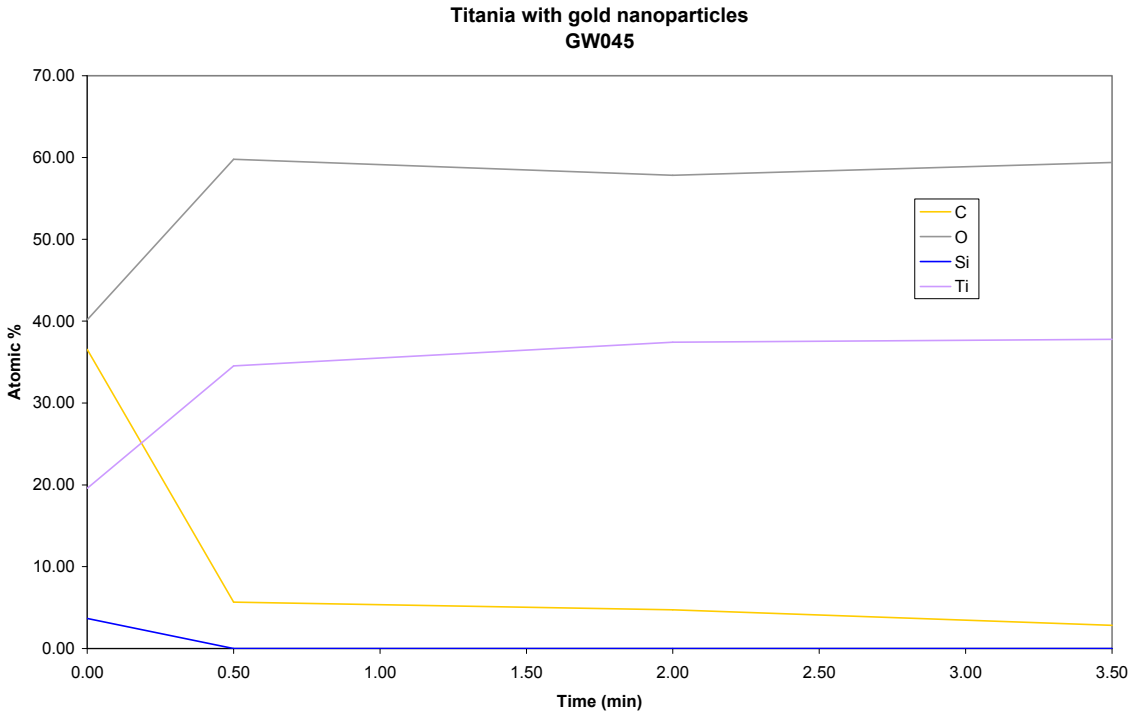

The XPS spectra of other TiO_2 thin films formed in the presence of Ag and Cu at 450 °C exhibited no detectable dopants, after etching (30 s), the composition of two titania films with Ag dopants was titania (Ti ~33 at.%, O ~59 at.%) and the composition of the remaining Cu doped TiO_2 was also titania (Ti: 32 at.%, O: 58 at.%). The binding energies determined from the high-resolution XPS measurements (peak positions: 456.0 eV for Ti $2p_{3/2}$ and 528.0 eV for O 1s) were in fair agreement with published values for TiO_2[152, 155].

4.2.4.2 XPS analysis of Cu doped titania films, 400 °C

The XPS spectra of TiO_2 thin films formed in the presence of Cu, at 400 °C exhibited typical titania and only one sample contained Cu dopant but at too low a level to ascertain the oxidation state, see tables 21, 22, 23.

Table 21: Type of Cu doped titania samples at 400 °C.

Sample Number	Static/ 1 min or Dynamic/ 8 substrate passes	AACVD Flow Rate/ l/min
1	Static	0.3
2	Dynamic	0.3
3	Static	0.6
4	Dynamic	0.6

Table 22: XPS analysis of the composition of Cu doped titania films, 400 °C. Before etching

Sample	C	Cu	O	Ti	[O] / [Ti]
1 centre	42	0.55	41	17	2.5
1 side	35	--	46	20	2.3
2	37	--	42	21	1.9
3 centre	39	--	42	19	2.2
3 side	40	--	40	20	2.1
4	44	--	37	19	2.0

Table 23: XPS analysis of the composition of Cu doped titania films, 400 °C. After etching (~2 mins)

Sample	C	Cu	O	Ti	[O] / [Ti]
1 centre	15	--	56	30	1.9
1 side	14	--	57	29	1.9
2	7	--	58	36	1.6
3 centre	13	--	55	32	1.7
3 side	14	--	53	33	1.6
4	3.3	--	59	38	1.5

*Carbon contamination probably originated from the coating or handling.

The binding energies determined from the high-resolution XPS measurements for the peak position of Cu 2p was 933.0 eV.

4.2.4.3 Summary of XPS Analysis

Nearly all TiO_2 films formed in the presence of Au, Ag and Cu (400-450 °) only exhibited TiO_2, only one Cu doped TiO_2 (400 °C) exhibited Cu but at too low a level to ascertain the oxidation state.

4.2.5 X-ray diffraction analysis

X-ray diffraction analysis was carried out on both undoped and attempted doped samples (400-600 °C). The tetragonal form of anatase titania was exhibited on every film, one or two films produced a small number of reflections corresponding to the tetragonal form of rutile titania and no other reflections were observed. All crystallite orientations have an opportunity to produce diffraction intensity and it is only those crystallographic planes that are parallel to the surface that produce diffraction intensity at the detector (according to Bragg's Law). The diffractograms were obtained by scanning each sample for 30 minutes from 5 to 75 degrees 2-theta using the X'Celerator detector, see figs. 98-107.

4.2.5.1 TiO_2 films (400 °C)

X-ray diffraction analysis for undoped and doped Au, Ag and Cu TiO_2 films at 400 ºC are below, see figs. 98-100.

Figure 98: XRD diffractograms for static and dynamic TiO_2 film controls at 400 ºC

Legend line colours: red (XT12775): static CVD control; blue (XT12776): dynamic CVD control.

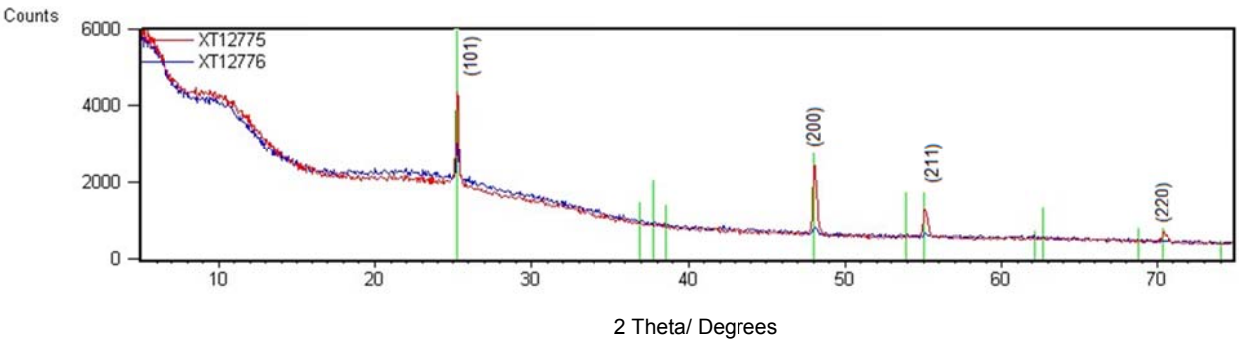

No.	Ref. Code	Compound Name	Chemical Formula
1	00-021-1272	Anatase, syn	Ti O2

Anatase form of titania for both dynamic and static APCVD TiO_2 film controls.

Figure 99: XRD diffractograms for static and dynamic TiO_2 films in the presence of Au and Ag at 400 ºC.*

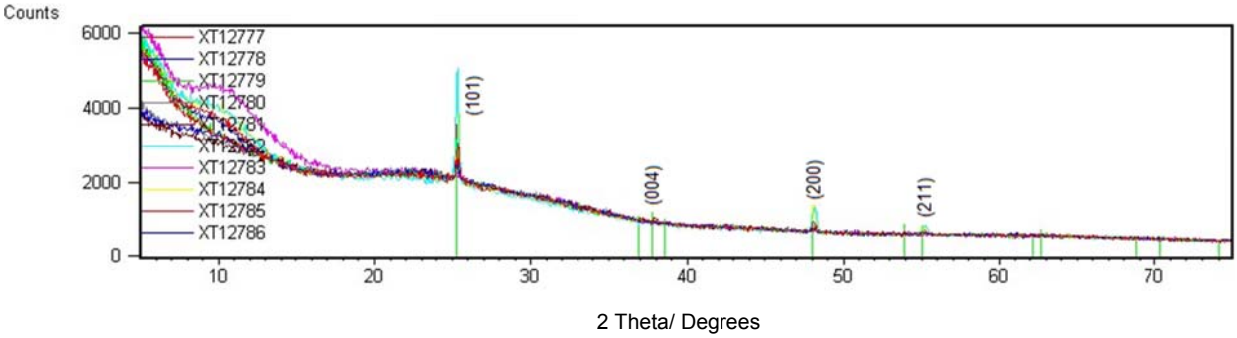

No.	Ref. Code	Compound Name	Chemical Formula
1	00-021-1272	Anatase, syn	Ti O2

*Legend line colours: red [(XT12777), (static: 1 min)], blue [(XT12778), (dynamic: 8 passes)], green [(XT12779), (static: 1 min)] and grey [(XT12780), (dynamic: 10 passes)]: formed in the presence of Au. Brown [(XT12781), (dynamic: 20 passes)], turquoise [(XT12782), (static: 1 min)] pink [(XT12783), (dynamic: 8 passes)], yellow [(XT12784), (static: 1 min)], purple [(XT12786), (dynamic: 8 passes)] and red [(XT12785), (dynamic: 20 passes)]: formed in the presence of Ag.

All TiO_2 films formed in the presence of Au and Ag (400 ºC) had the tetragonal form of anatase.

Figure 100: XRD diffractograms for static and dynamic TiO_2 films formed in the presence of Cu at 400 ºC.*

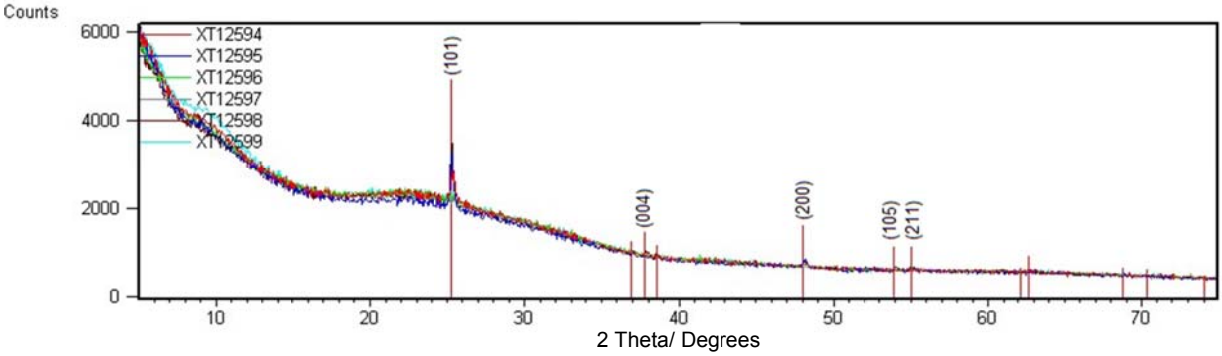

No.	Ref. Code	Compound Name	Chemical Formula
1	00-021-1272	Anatase, syn	Ti O2

*Legend line colours: red (XT12594, centre) and blue (XT12595, edge) static film (1 min), green (XT12596), (dynamic film: 8 passes)], grey (XT12597, centre) and brown [(XT12598, edge), (static film: 1 min)], turquoise (XT12599), (dynamic: 8 passes)].

All TiO_2 films formed in the presence of Cu (400 ºC) had the tetragonal form of anatase.

4.2.5.2 TiO_2 films (600 °C)

X-ray diffraction analysis for undoped and doped Au, Ag and preformed Au TiO_2 films at 600 ºC are below, see figs. 101-103.

Figure 101: XRD diffractograms for static and dynamic control TiO_2 film controls at 600 ºC.*

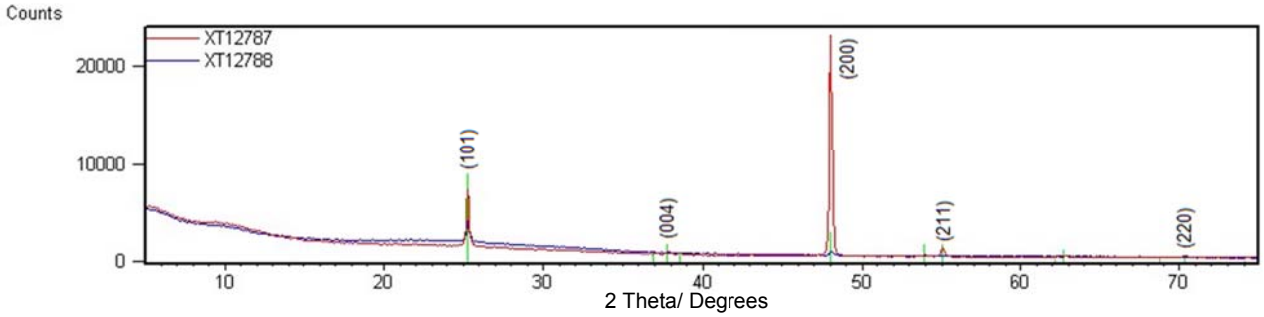

No.	Ref. Code	Compound Name	Chemical Formula
1	00-021-1272	Anatase, syn	Ti O2

* Legend line colours: red: static, blue: dynamic

Figure 102: XRD diffractograms for static and dynamic TiO_2 films in the presence of Au and Ag at 600 ºC.*

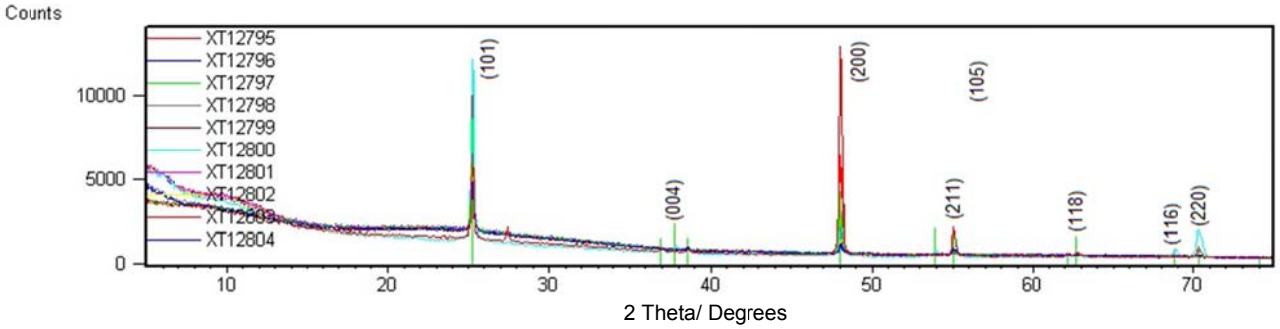

No.	Ref. Code	Compound Name	Chemical Formula
1	00-021-1272	Anatase, syn	Ti O2

* Legend line colours: red [(XT12795) (static: 3 min)]; blue [(XT12796), (static: 1 min)]; green [(XT12797), (dynamic: 8 passes]; grey [(XT12798), (dynamic: 20 passes)]; brown [(XT12799) (static: 1 min)]; turquoise [(XT12800), (static; 3 min)]; pink [(XT12801) (dynamic: 8 passes)]; yellow [(XT12802), (dynamic: 20 passes)]; red [(XT12803), (dynamic 16 passes)]; formed in the presence of Au and purple [(XT12804), (static 1 min)] formed in the presence of pre-formed Au.

b) Static (3 mins) TiO2 film formed in the presence of Au at 600 ºC.

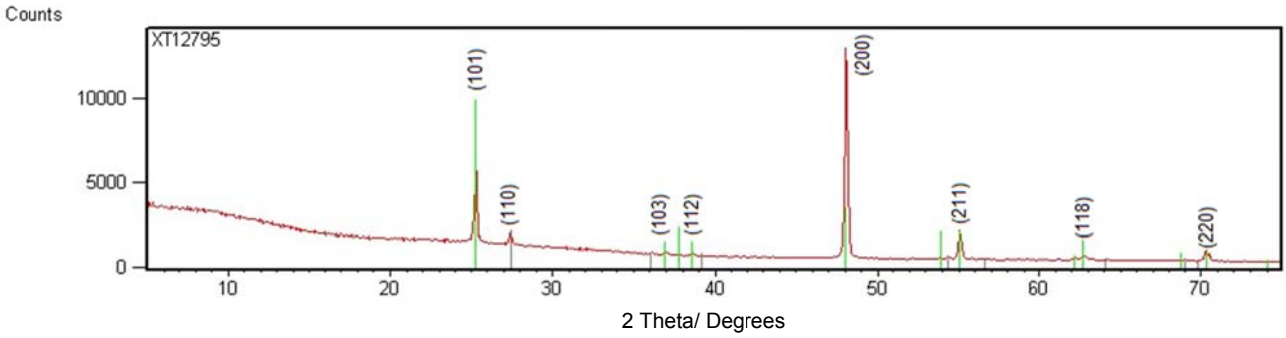

No.	Ref. Code	Compound Name	Chemical Formula
1	00-021-1272	Anatase, syn	Ti O2
2	00-034-0180	Rutile, syn	Ti O2

All TiO_2 films formed in the presence of Au and Ag (600 ºC) exhibited the tetragonal form of anatase and one static (3 mins) TiO_2 film formed in the presence of Au (600 ºC) exhibited both the rutile and anatase form of titania.

Figure 103: XRD diffractograms for dynamic TiO_2 films (8-20 passes underneath the reaction head) formed in the presence of pre-formed Au, 600 ºC.*

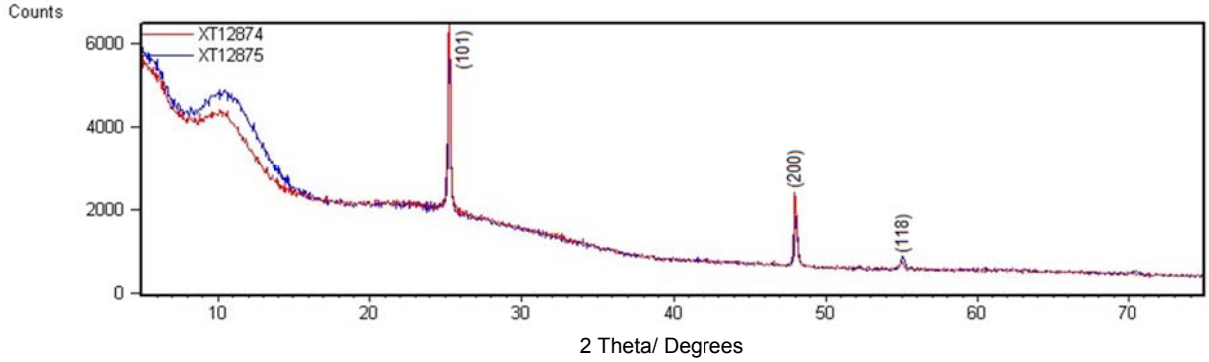

* Legend line colours: red [(XT12874), (dynamic, 8 passes)], blue [(XT12875), (dynamic, 20 passes)]

All dynamic TiO_2 films formed in the presence of pre-formed Au (600 ºC) had the tetragonal form of anatase.

4.2.5.3 Summary of XRD analysis

The dominant anatase form of titania was exhibited on every diffractogram apart from one static TiO_2 film formed in the presence of Au at 600 ºC. According to the XRD diffractograms; the dopants Au, Ag and Cu appeared to have little effect on the form of titania observed. This is in direct contrast to the work of many people were mixtures of anatase/rutile and brookite were seen particularly at lower synthesis temperatures (<600 °C)[155-161]; this includes work by Hyett and Edusi where anatase/rutile mixtures were seen from a similar precursor set[157]. However the work of Siefried *et al*., 2000, found that at about 400 °C, anatase was dominant, at 700 °C anatase with some rutile phase was found and ≥1000 °C only the rutile phase was observed[153] this is due to the rutile phase being thermodynamically stable; the anatase phase is metastable and usually observed for thin films with thicknesses below 10 μm[162], or particles >30 nm[163].

4.2.6 Raman analysis

Raman spectra analysis was carried out for TiO_2 films formed in the presence of Cu, Ag and Au at 400 °C and TiO_2 films formed in the presence of Ag, Au and pre-formed Au at 600 °C. Typical peaks for the anatase phase were observed for all samples, except for the Cu film, 400 °C, were no peaks were observed.

4.2.6.1 Comparison of Raman spectra for TiO_2 films, 400 °C

Raman spectra for both static and dynamic TiO_2 films, formed in the presence of Cu, Ag and Au, at 400 °C, display typical wavelengths for the anatase phase of titania, peaks (144, 197, 394, 512, 635 cm^{-1}), see fig 104 a-b) and table 24. Dynamic TiO_2 film formed in the presence of Cu dopant displayed no spectra attributable to titania, see fig. 104 b).

Figure 104: Comparison of Raman spectra of static and dynamic TiO_2 films formed in the presence of Au, Ag and Cu at 400 °C: a) static (1 min) and b) dynamic (8 passes) titania films in the presence of Au, Ag and Cu at 400 °C.

a) Static (1 min)

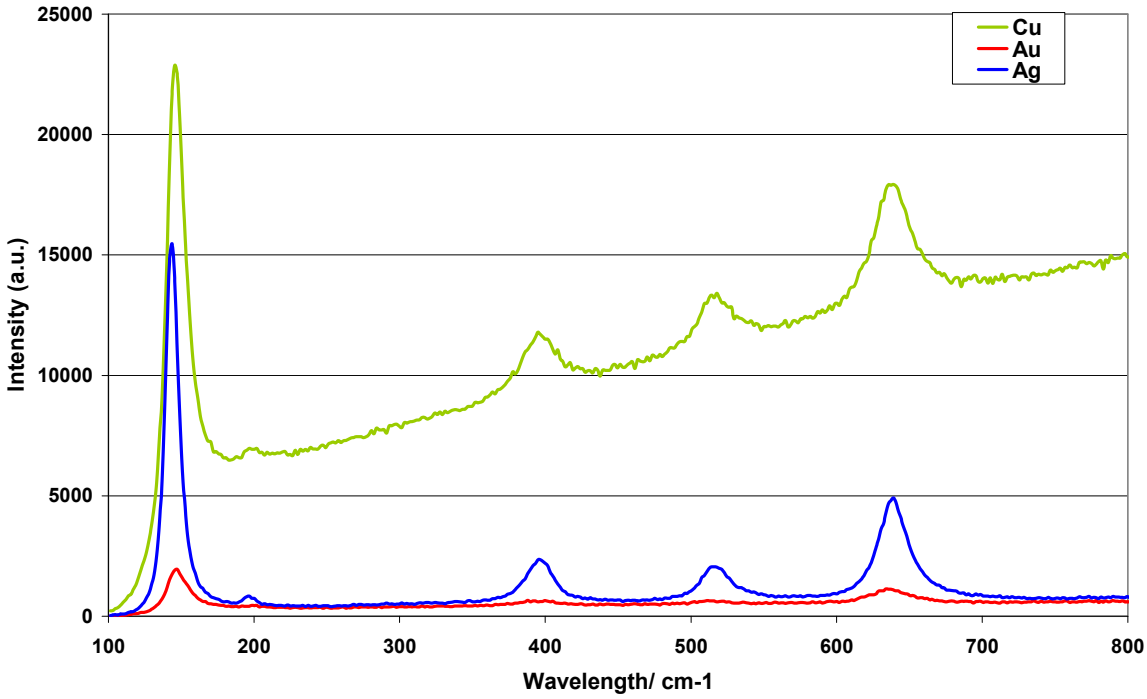

b) Dynamic (8 passes)

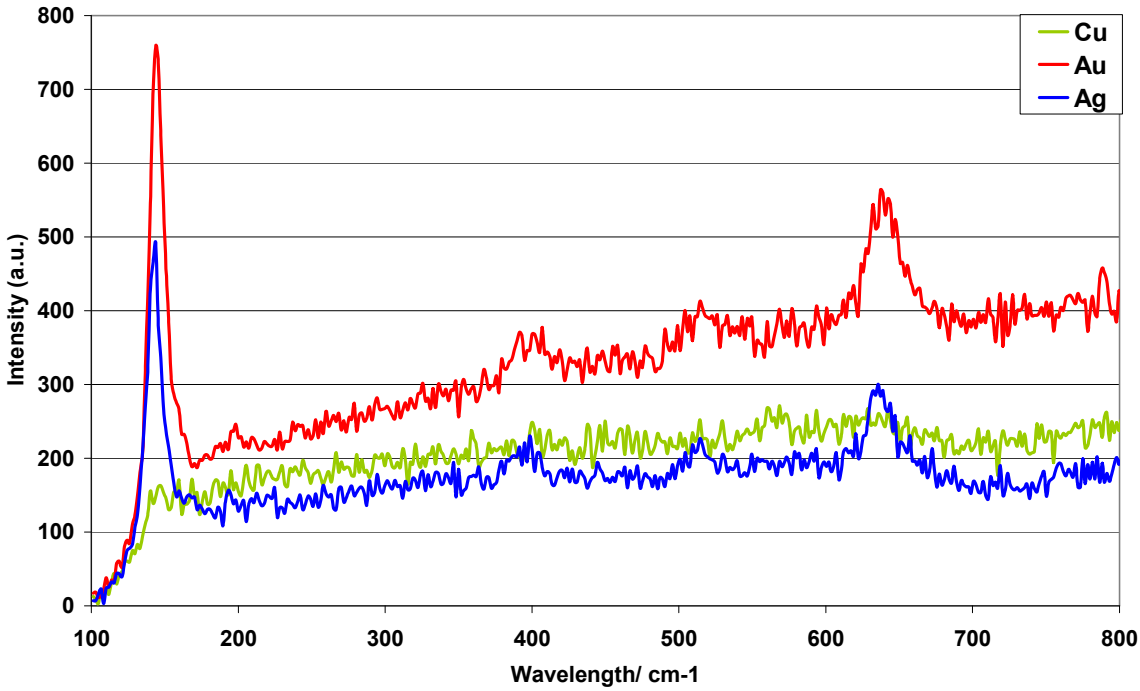

Table 24: Raman peak phase values for dynamic TiO_2 films formed in the presence of Au, Ag and Cu at 400 °C:

Static Dopant	Peak 1 /cm^{-1}	Phase A/R	Peak 2 /cm^{-1}	Phase A/R	Peak 3 /cm^{-1}	Phase A/R	Peak 4 /cm^{-1}	Phase A/R	Peak 5 /cm^{-1}	Phase A/R
Cu	145	A	196	A	394	A	514	A	635	A
Ag	143	A	193	A	394	A	512	A	635	A
Au	143	A	-	-	-	-	-	-	633	A
Dynamic Dopant	Peak 1/cm^{-1}	Phase A/R	Peak 2/cm^{-1}	Phase A/R	Peak 3/cm^{-1}	Phase A/R	Peak 4/cm^{-1}	Phase A/R	Peak 5/cm^{-1}	Phase A/R
Cu	-	-	-	-	-	-	-	-	-	-
Ag	143	A	193	A	394	A	514	A	635	A
Au	143	A	198	A	391	A	514	A	637	A

A = anatase, R = Rutile, - no TiO_2 film or peak detected

4.2.6.2 Comparison of Raman spectra for TiO_2 films, 600 °C

Raman spectra for both static and dynamic TiO_2 films formed in the presence of Ag, Au and pre-formed Au, at 600 °C display typical wavelengths for the anatase phase of titania, peaks (144, 197, 394, 512, 635 cm^{-1}), see fig. 105 a-b) and table 25.

Figure 105: Comparison of Raman spectra of static and dynamic TiO_2 films formed in the presence of Au, Ag and Cu at 600 °C: a) static (1 min) and b) dynamic (8 passes) titania films formed in the presence of Ag, Au and pre-formed Au at 600 °C.

a) Static (1 min)

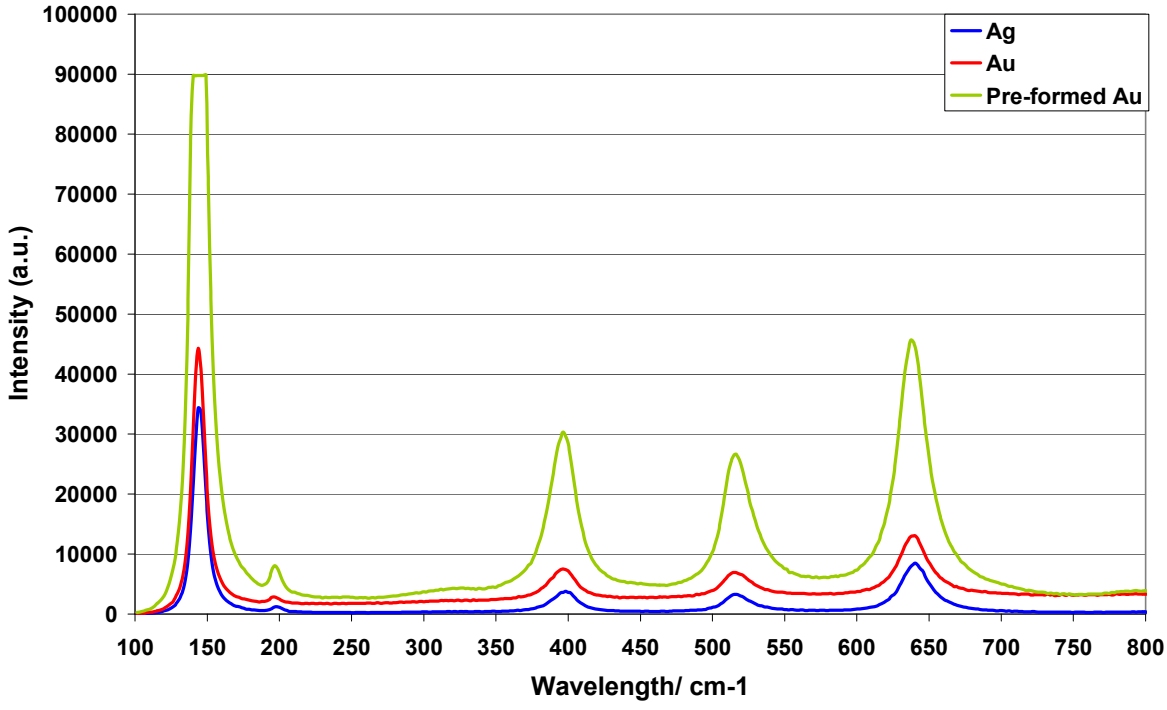

b) Dynamic (8 passes)

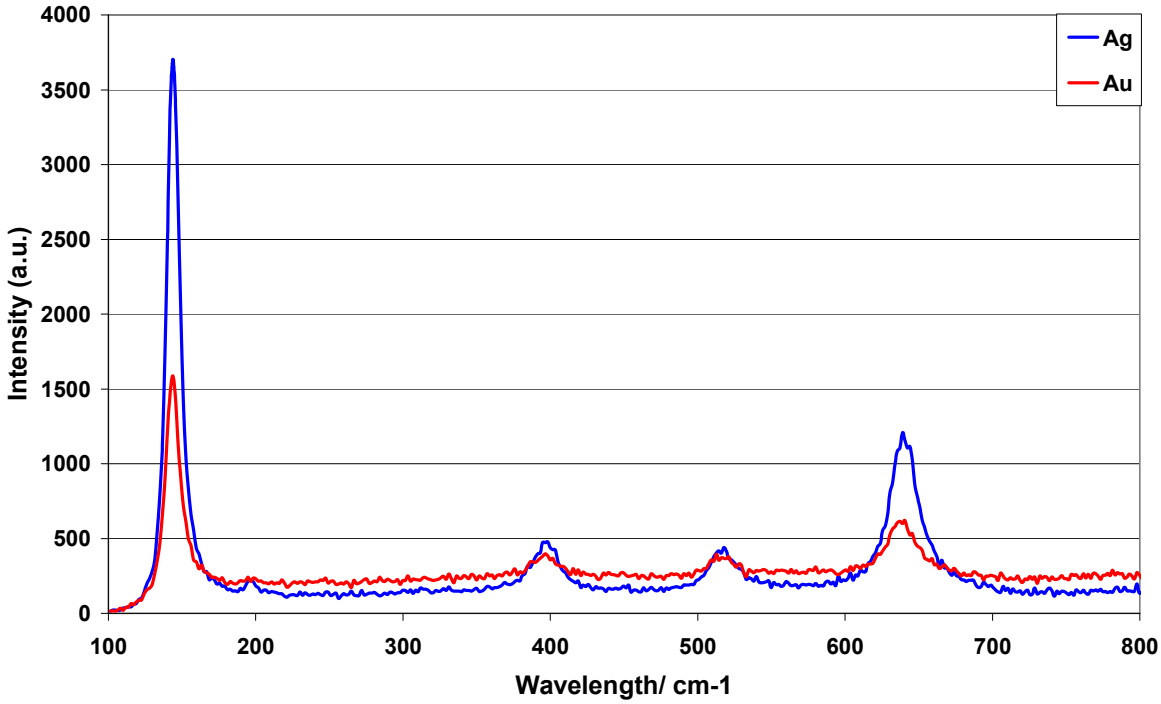

Table 25: Raman peak phase values for the titania films formed in the presence of Ag and Au at 600 °C.

Dynamic Static	Peak 1/cm^{-1}	Phase A/R	Peak 2/cm^{-1}	Phase A/R	Peak 3/cm^{-1}	Phase A/R	Peak 4/cm^{-1}	Phase A/R	Peak 5/cm^{-1}	Phase A/R
Ag	143	A	194	A	394	A	512	A	637	A
Au	143	A	193	A	394	A	512	A	637	A
P-Au	142	A	196	A	396	A	514	A	637	A
Dynamic Dopant	Peak 1/cm^{-1}	Phase A/R	Peak 2/cm^{-1}	Phase A/R	Peak 3/cm^{-1}	Phase A/R	Peak 4/cm^{-1}	Phase A/R	Peak 5/cm^{-1}	Phase A/R
Ag	143	A	193	A	394	A	514	A	638	A
Au	143	A	193	A	394	A	514	A	635	A

A = anatase, R = Rutile

The Raman band frequencies for these titania films (400-600 °C) are assigned the following vibration modes:

- 143 ±2 cm^{-1} E_g phononic mode (*v6*)
- 195 ±3 cm^{-1} E_g phononic mode (*v5*)
- 393 ±3 cm^{-1} B_{1g} phononic mode (*v4*)
- 513 ±2 cm^{-1} $A_{1g} + B_{1g}$ phononic mode (*v2* + *v3*)
- 635 ±4 cm^{-1} E_g phononic mode (*v1*)

The change in intensity of the Raman bands could be related to the thickness of the film or the crystallinity of the film but these dynamic films appear to be more uniform than static films and therefore the dopant used may have affected the intensity of the bands.

4.2.6.3 Summary of Raman analysis

Raman spectra for TiO_2 films formed in the presence of Cu, Ag, Au, (400 °C) and Ag, Au and pre-formed Au, (600 °C) exhibit typical anatase phase peaks[21, 146-147, 156-161]. According to the work by Yee Hong Chee, *et.al.* the anatase phase should be dominant up to a synthesis temperature of about 700 °C but the rutile phase should still be formed between the temperature range of 420-700 °C; there is no apparent evidence of the rutile phase being formed at the higher temperatures here[156]. The AACVD/CVD prototype reaction chamber head used does not confine the substrate within a confined or enclosed space, all gaseous vapours, at standard atmospheric pressure, are allowed to vent to a much larger area; the duration of the substrate under the reaction chamber is also short; resembling the production process more accurately and therefore the conditions required for the formation of the rutile phase, even at higher temperatures, may not be supported. The presence of Au or Ag metallic/oxide phase was not expected as they are poor Raman scatterers. The presence of Cu oxide either as CuO[164-170], Cu_2O[166-174] or Cu_3O_2[169, 170] was also not detected[165-174].

4.2.7 Contact Angle Analysis

A surface water contact angles > 90° are classed as hydrophobic and surface contact angles < 90° are classed as hydrophilic[175-178]. Thin film coatings with either a superhydrophilic (θ: <10°) or superhydrophobic (θ~≥ 150°) surface contact angle are of interest as self-cleaning surfaces. There are two main models used to describe the wetting behaviour of hydrophobic surfaces, the Wenzel[175] and Cassie–Baxter models[144, 176, 177]. Titania films often become superhydrophilic, (θ < 10°), when exposed to ultraviolet (UV) light, a phenomenon termed photoinduced superhydrophilicity (PSH)[1775-185] and the morphology of the film may also influence superhydrophilicity, particularly if it has rough surfaces[144].

The change in contact angle when exposed to 254 nm UVA irradiation was measured on undoped and Au, Ag and Cu doped titania films at 400 °C and on undoped and Au, pre-formed Au and Ag doped films at 600 °C.

4.2.7.1 Contact angles of TiO_2 films at 400 °C

The TiO_2 control and TiO_2 films formed in the presence of Au and Ag at 400 °C did not have contact angles (< 15 °) that dropped sufficiently after irradiation (254 nm) for superhydrophilicity to be exhibited, see fig. 106. The titania films formed in the presence of Au and Ag at 400 °C appear to have a detrimental effect on the contact angle observed for titania. Water surface contact angles were measured 3 to 5 times to achieve an average with standard deviation (Stdv), the largest variations of Stdv were exhibited by static films, see table 26.

Figure 106: Comparison of doped and undoped titania thin films average contact angles (400 °C) before and after irradiation at 254 nm.

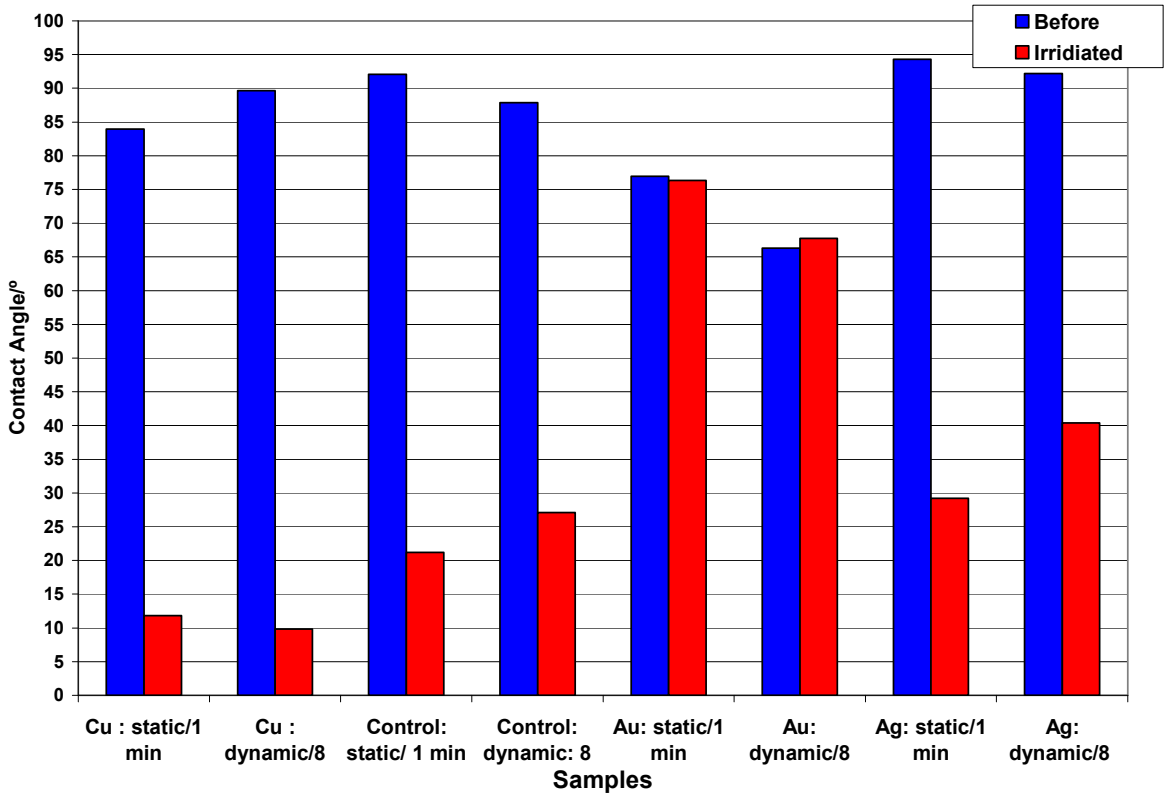

Table 26: Average water surface contact angles (θ) for TiO_2 films grown at 400 °C.

Conditions and Dopants	Contact Angle before irradiation/º		Contact Angle after irradiation/º, 254 nm	
	Average	Stdv	Average	Stdv
Cu: static/1 min	84	11	12	6
Cu: dynamic/8 passes	90	2	10	0
Control: static/ 1 min	92	9	21	4
Control: dynamic: 8 passes	88	4	27	7
Au: static/1 min	77	3	76	11
Au: dynamic/8 passes	66	1	68	5
Ag: static/1 min	94	9	29	4
Ag: dynamic/8 passes	92	5	40	2

The TiO_2 films formed at 400 °C in the presence of Cu exhibited surface water contact angles before irradiation of ~84° ±10.75 for static film and ~90° ±2.06 for dynamic film; therefore the contact angles for the Cu doped films were >80 ° before irradiation and ~10° after irradiation (254 nm) and formed a superhydrophilic film coating, see fig.s 107 a-d).

Figure 107: Comparison of TiO_2 dynamic control and dynamic Cu doped TiO_2 contact angles (400 °C): a) TiO_2 control, (θ >85°), b) TiO_2 control, (θ <30°), after irradiation (254 nm), c) TiO_2 film in the presence of Cu, (θ >85°), d) TiO_2 film in the presence of Cu, (θ <10°), after irradiation (254 nm).

a) TiO_2 control

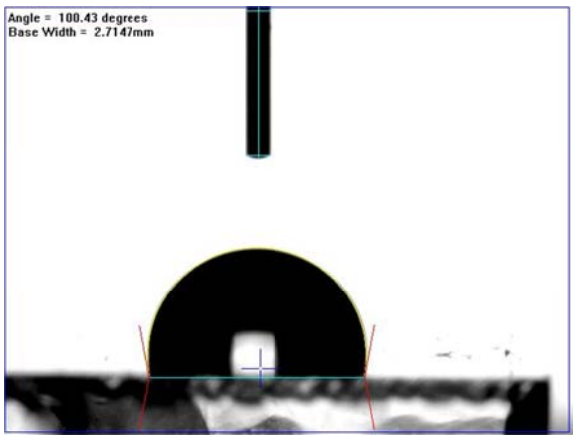

b) TiO_2 control irradiated (254 nm)

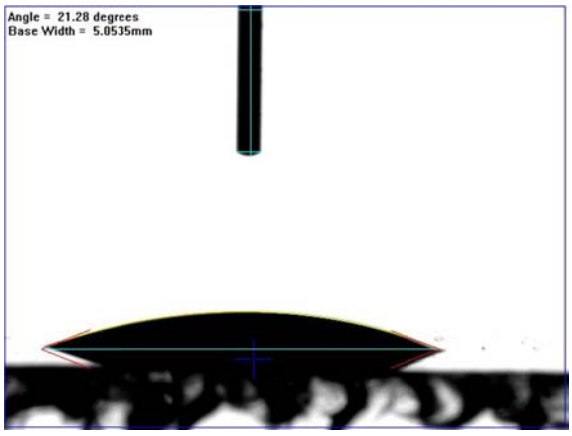

c) Cu TiO_2

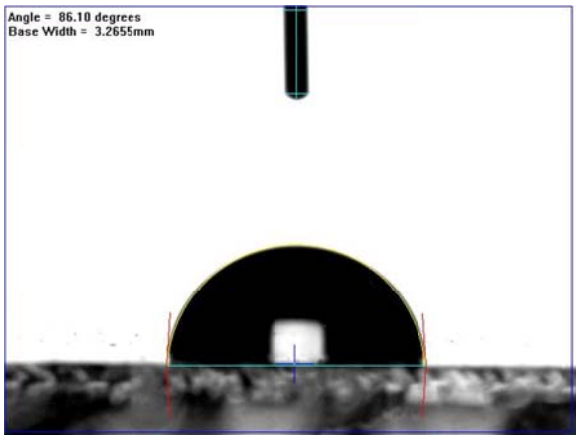

d) Cu TiO_2 irradiated (254 nm)

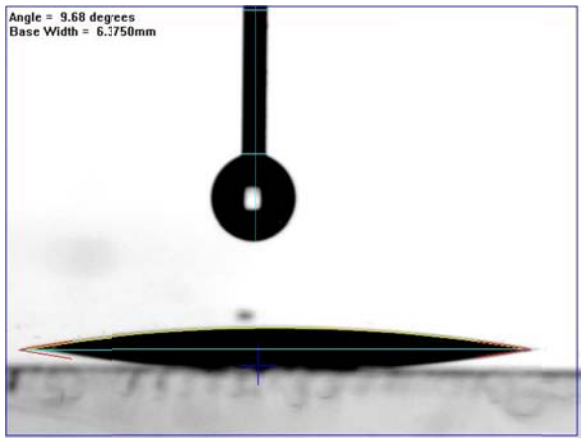

4.2.7.2 Contact angles of TiO_2 films at 600 °C

The comparison of contact angles for titania films either formed in the presence of Au, pre-formed Au and Ag at 600 °C. The control, Ag and Au titania films all exhibited hydrophilic surface contact angles >15 ° after irradiation. The TiO_2 control exhibited the largest before and after irradiation difference in contact angle and therefore addition of Au and Ag nanoparticles or films formed in the presence of Au and Ag do not enhance the TiO_2 film superhydrophilic properties, see fig. 108 and table 27. Water surface contact angles were measured 3 to 5 times to achieve an average with standard deviation (Stdv), the largest variations of Stdv were exhibited by static films, see table 27.

Figure 108: Comparison of doped and undoped titania thin films surface contact angles (600 °C) before and after irradiation at 254 nm.

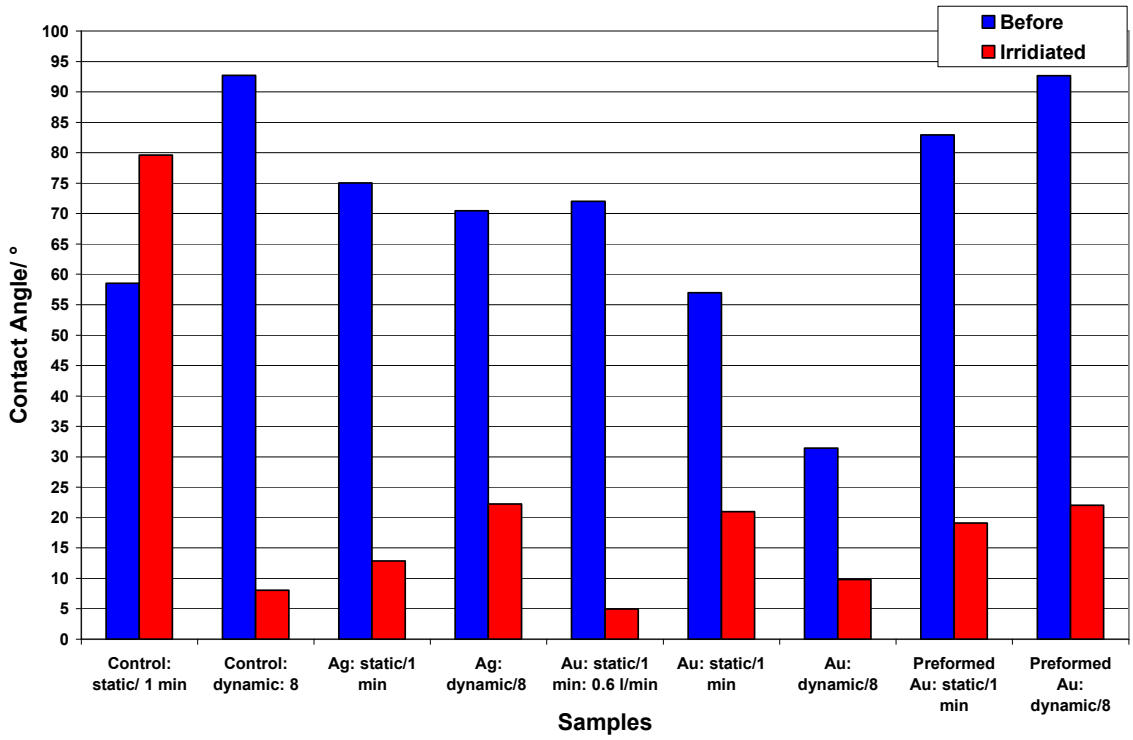

Table 27: Average water surface contact angles (θ) for TiO_2 films grown at 600 °C.

Conditions and Dopants	Contact Angle before irradiation/°		Contact Angle after irradiation/°, 254 nm	
	Average	Stdv	Average	Stdv
Control: static: 1 min	59	1	80	11
Control: dynamic: 8 passes	93	4	8	1.0
Ag: static: 1 min	75	18	13	2
Ag: dynamic: 8 passes	70	3	22	6
Au: static: 1 min: 0.6 l/min	72	6	5	1
Au: static: 1 min	57	11	21	3
Au: dynamic: 8 passes	31	5	10	1
Preformed Au: static/1 min	83	17	19	1
Preformed Au: dynamic: 8 passes	93	7	22	3

The water surface contact angle for the static TiO_2 film control increased from about 59° before irradiation to 80° after irradiation (254 nm), all other TiO_2 films contact angles reduced after irradiation, see table 27. A possible explanation could include that the area of film analysed was particularly thick with floret fractal type morphology, typically seen on opaque areas of the static films where the thickness ~≥ 1 μm. After irradiation (254 nm) the dynamic control, Au doped static (1 min, 0.6 l/min) and Au doped dynamic TiO_2 films exhibited

superhydrophilic properties (contact angle ≤10°), see table 27. Therefore the presence of the Au precursor, HAuCl4, did not adversely affect the contact angle normally exhibited by undoped TiO_2 films.

4.2.7.3 Summary of contact angle results

The titania thin film coatings change from being hydrophobic to hydrophilic after irradiation, apart from one static control film at 600 °C and have the superhydrophilic property necessary for self-cleaning glass, addition of Au and Ag (400 °C) and Au, preformed Au and Ag (600 °C) did not exhibit any significant enhancement of this property, however addition of Cu or titania films formed in the presence of Cu, at 400 °C, did show a possible slight enhancement.

4.3.0 Discussion of prototype 1 AACVD/CVD results

The results from the dynamic and static substrate samples of the AACVD/CVD synthesis technique doped/undoped titania thin films produced highly transparent clear films with visible transmission (>85%) at various temperatures (400 - 600 ºC). The morphology of titania thin films were found to be influenced by the attempted addition of dopants but had no apparent influence over the preferred anatase form of titania except for one Au titania film synthesized at a lower temperature (400 ºC). Control samples for dynamic films (400 ºC) showed plate structures with smaller granular/spherical areas and the static samples were granular/spherical and agglomerated in shape.

Plate structures were seen for dynamic thin film samples with Au, Ag, Cu and Al, dopants at 400, 450 ºC, all dopants were below detection level, whereas spherical structures (100-800 nm) where observed for static substrate samples at 400 ºC and one sample that contained Au nanoparticles had uniform spherical structures (50–100 nm) with bright spots. Control samples for dynamic films (600 ºC) showed angular grain structures (100–150 nm) and static films were agglomerated angular in shape with larger embedded Neolithic spear structures (400 nm). Au and Ag dopants for both dynamic and static films had angular structures (50-500 nm) with agglomeration and angular fractal floret structures forming in the static samples with increasing film thickness (402–1875 nm). The titania thin film coatings formed in the presence of Au,

preformed Au and Ag at 600 °C did not exhibit any significant enhancement of superhydrophilicity, however titania films formed in the presence Cu, at 400 °C, did show a possible slight enhancement. XRD and Raman spectra for TiO_2 films formed in the presence of Cu, Ag, Au, (400 °C) and Ag, Au and pre-formed Au, (600 °C) mainly exhibit typical anatase phase peaks. The anatase phase is often seen as the majority phase for TiO_2 ≤ at 500 ◦C for short sinter periods; the rutile phase becomes dominant at higher temperatures or when TiO_2 is sintered for longer and at higher temperatures[153, 156]. However this is in contrast to all the TiO_2 thin films synthesised here at 600 °C; all of which exhibited the anatase phase as the dominant phase whether they were synthesised under a static reaction chamber head or as a moving substrate. No dopant, Au, Ag or Cu metallic/oxides were detected with Raman. XPS spectra for nearly all TiO_2 films formed in the presence of Au, Ag and Cu (400-450 °C) only exhibited TiO_2, only one Cu doped TiO_2 (400 °C) exhibited Cu but at too low a level to ascertain the oxidation state.

4.4.0 Conclusion of Chapter 4

No TiO_2 film synthesised had significant amounts of any dopants present apart from one static Au doped titania film (400 ºC, 3 mins) and nearly all dopants were below the analytical detection level but the morphology was affected by dopants and film thickness, even when the dopant was not detected in the film although the influence of the dopant lessened with a moving substrate. Increasing either substrate time (3 mins) for static films under the reaction chamber head or increasing the number of passes for dynamic films under the reaction chamber head exaggerated the agglomeration and size of the microstructure seen at lower time intervals (1 min) or at a lower number of passes (8-10 passes). A slight enhancement of superhydrophilicity was seen for one TiO_2 film formed in the presence of Cu, at 400 °C, all other films formed in the presence of dopants showed no enhancement of this property. XRD and Raman spectra exhibited typical peaks for the anatase phase of titania. XPS spectra exhibited typical titania composition and only detected one very low level Cu dopant (400 °C). Dopants of Au and Cu were only detected in static films at 400 °C, higher temperatures and moving substrate appear to negate any success of inclusion of these noble metal nanoparticles using this particular

design of AACVD/APCVD combined synthesis technique. The following physical and chemical parameters fluid flow, moving substrate, synthesis temperature and the presence of dopants during the reaction all affect the morphology observed in the TiO_2 films synthesised with prototype reaction head 1. Fluid flow due to the negligible mixing of the AACVD and two APCVD fluid flows and the dopants, Au, Ag appear to have the greatest effect on the microstructure. The effect of the solvent on the microstructure has been negated by using methanol throughout the synthesis of the TiO_2 films. Low or negligible incorporation of the dopants were the probable consequence of the size of the droplets formed by the nebuliser; the droplets were of an order of 1 magnitude too small to overcome the main forces and effects of aerodynamic drag and at higher synthesis temperatures evaporation, see chapter 2.

The following chapter, 5, investigates a new model of the AACVD/APCVD technique designed using computational fluid software for a more successful result of including noble metal dopants within the TiO_2 host matrix film.

Chapter 5

Combined AACVD/APCVD Synthesis of TiO_2 Films: Prototype 2

Chapter 5: AACVD/APCVD Synthesis of TiO_2 Films: Prototype 2

5.0.0 Introduction

This chapter looks at the second prototype for synthesizing metal oxide thin films on glass designed using computational fluid dynamic (CFD) software, see chapter 2. Titania is used again as the host metal oxide matrix and the films synthesised are investigated for their physical, optical and chemical properties, particularly the effect of dopants, metal Au, Ag, Cu and Al dopants on the properties such as colour, morphology, transmittance/reflectance, surface contact angle, crystal lattice orientation and photocatalytic activity on TiO_2 host matrix films. Al was included as a dopant to see if inclusion was possible within the host matrix film using this combined reaction head for possible future work with ZnO. The titania films were synthesized using a combined AACVD/APCVD technique and analysed using a range of techniques such as UV-VIS spectroscopy, XRD, SEM, EDX, FTIR and Raman to assess the possible influence dopants could have on physical, optical and chemical properties of these TiO_2 films. The results were then compared to literature for many of the well known metal oxide host matrix film synthesis techniques including APCVD, FACVD, Sol-gel (sintering/annealing), LPCVD, PECVD, MOCVD and CVD.

The titania films in chapter 5 are referred to as being doped even though the level of dopant, if present, may well be below levels of detection for ease of understanding the thread of work and because the dopants were found to have such a profound effect on physical, optical and chemical properties such as morphology, photocatalysis and colour.

Chapter 5

5.1.0 Experimental Methods

5.1 General Experiment

5.1.1 Standard reagents and conditions

The host matrix precursor used for the formation of the TiO_2 films with or without the addition of metal dopants were titanium tetraisopropoxide (TTIP, 10 l/min) for CVD synthesis. The metal precursors selected for incorporation into the AACVD/CVD synthesis were $HAuCl_4$ (0.01 mol dm^{-3}), $AgNO_3$ (0.12–3.5 x 10^{-2} mol dm^{-3}), $Cu(acac)_2$ (1.6 x 10^{-2} mol dm^{-3}) and $Al(acac)_3$ (1.6 x 10^{-2} mol dm^{-3}).

5.1.2 Analytical analysis

Scanning electron microscopy (SEM) analysis was carried out on a thermal field emission Philips XL30 instrument for both morphology and elemental analysis, using the Energy Dispersive Spectroscopy (EDS) analysis (EDAX Phoenix system), with uncoated/coated carbon/gold/platinum samples. SEM images used accelerating voltages from 10 to 30 kV and were captured at various magnifications (2-5 x 10^5 x), samples were coated with thin layer of Pt. The voltage was reduced to 10 kV (working distance: 10 mm) for surface sensitive work with the back scattered electron (BSE) detector.

High resolution X-ray diffraction (HRXRD) analysis was carried out using a MRD diffractometer in reflection mode with Cu Kα radiation (λ =1.540 Å) with a glancing angle incidence beam of 5 or 1.5°. Visible/IR transmittance and reflectance spectroscopy was carried out using a Hunterlab, Ultrascan XE, colour measurement spectrometer (range 360–750 nm) connected to a PC. Raman analysis was carried out using a Renishaw InVia Raman microscope System using a HeNe laser (excitation wavelength: 514.5 nm) calibrated against Neon emission lines, (x50 microscope objective, 10 s exposure).

Water surface contact angles were measured using an FTA-1000B-23A-141 Automated Drop Shape Analyser, 3 µL water droplets were used to minimise any

gravitational effects. The water droplet images were analysed using a circular fitting method to obtain the contact angles on the surface. The surfaces were tested from a range of areas over the substrate plate. The water slip angle was measured by noting the angle to the horizontal at which a water droplet of known volume moved on the surface. Photographs were recorded using a video camera on the FTA-1000 instrument system to monitor the wetting process on the surface. Resazurin (Rz) and dichloroindophenol (DCIP) indicator inks were used to assess Photocatalytic activity and prepared in the same way as formulated by Mills and McGrady[187]. The ink consisted of 3 g of a 1.5 wt.% aqueous solution of HEC polymer, 0.3 g of glycerol and 4 mg of Rz redox dye. Test films were washed in distilled water, subsequently rinsed with isopropanol and photocatalytically cleaned after 1 h of 254nm irradiation. The photocatalytic reductions were monitored via UV–visible absorption spectroscopy. Measurement of the photo-oxidation of an applied saturated solution of stearic acid (methanol) to film samples was analysed using a Perkin Elmer Spectrum RX1 FTIR spectrometer (2800-3000cm^{-1}). Photocatalytic activity was also assessed using the more conventional stearic acid test, a saturated solution (methanol) applied to the film surface and was then allowed to evaporate, the film surface was irradiated (254 nm) and analysed using FTIR (1 hr, at 15 min intervals).

5.1.3 Thin film growth

All synthesis was carried out using an experimental rig consisting of a combination of APCVD and AACVD synthesis techniques; conventional atmospheric chemical vapour deposition and aerosol assisted chemical vapour deposition technique with bubbler, and nebuliser. The CVD synthesis procedure involved the evaporation of TTIP using a bubbler (160-170 °C) with a hotplate (~160 °C) and heated transport pipes (200 °C) to prevent condensation and the AACVD synthesis involved dissolving precursors in methanol (50 ml) that were then nebulised by an ultrasonic humidifier (Ultra-Neb 2000, DeVilbliss) with appropriate ultrasonic wave frequency (1.63 MHz) to form an aerosol mist within a plastic container. The APCVD vapour was transported by inert gas, N_2, controlled by a gas flow meter (molar ratio rate: 10, derived from the Antoine equation), the aerosol mist was transported by

compressed air (1.2 l/min), to a combined AACVD/CVD cold wall reaction chamber (synthesis head), see fig. 109 a) and b).

Figure 109: Diagram and photograph of prototype 2.

a) Diagram

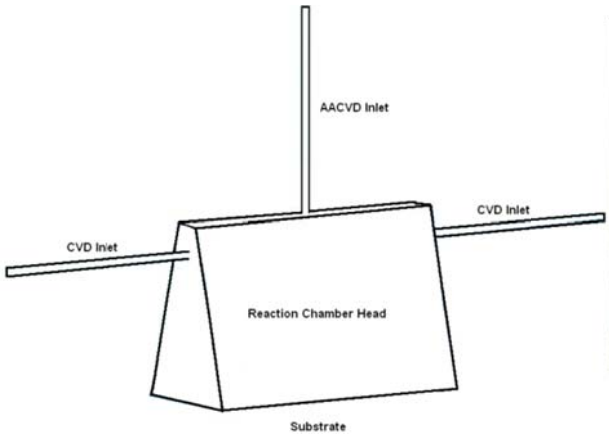

b) Photograph

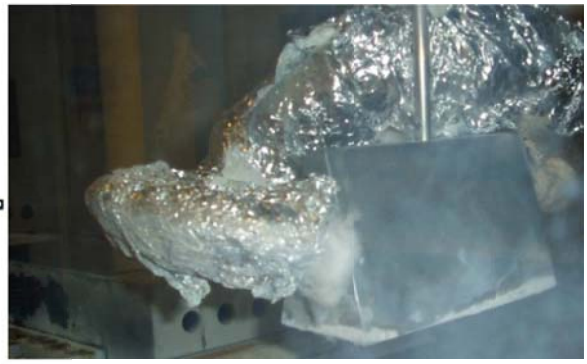

One clean plate of silica (50 nm) coated glass (dimensions ~207 x 85 x 3 mm), previously cleaned with appropriate solvents (water, methanol or acetone) and dried in air, was heated (300-600 ºC), using a graphite block controlled by a thermostat, monitored by a Pt-Rh thermocouple attached to a conveyor belt for automated substrate movement. The substrate was either left stationary (1-3 mins) on the conveyor belt or passed forwards and backwards (4-10 passes) under the combination AACVD/APCVD synthesis head. The vapour and aerosol droplets were then swept by carrier gases into the reaction chamber where the vapour and aerosol droplets were evaporated and a film deposited on the Float glass substrate. The experimental rig chamber was vented into the inbuilt extraction system. The inert gas and compressed air flow was allowed to continue for 10 min after a number of dynamic passes underneath the head had been counted. The substrates and films were allowed to cool to room temperature *in-situ* and were stored in air.

5.2.0 Results

5.2.1 Synthesis and characterisation

The TiO_2 films formed by AACVD/CVD prototype 2 reaction head with and without additional phases were well adhered to the substrate, passed the Scotch tape test and could not be easily scratched with anything other than a hard surface (brass and steel).

5.2.2 Visible appearance and optical characterisation

Titanium oxide films were synthesized as either undoped thin films at substrate temperatures of 400-600 °C from the APCVD of titanium tetraisopropoxide (TTIP) or doped TiO_2 host matrix thin films with noble metal nanoparticle dopants Au, Ag, Cu at 400-600 °C from the AACVD of auric acid, silver nitrate, copper acetylacetonate and aluminium acetylacetonate solutions. The macroscopic appearance by eye of all the films was transparent at thickness < 1 μm, many of the films synthesised below 500 °C were coloured, eventually turning opaque in areas where the film thickness (>4 μm) increased with the number of passes underneath the reaction chamber head. The films synthesised at lower substrate temperatures (<500 °C) displayed a very uniform surface with little or no optical interference patterns that were indicative of areas of non-uniform thickness.

5.2.2.1 Transmittance and reflectance analysis

The transmittance and reflectance analysis of the undoped and Au, Ag, Cu and Al doped TiO_2 films synthesised dynamically (10 passes) under the prototype head (300-600 °C) with 1.2 l/min AACVD flow rates are compared below.

5.2.2.1.1 Comparison of undoped and doped TiO_2 films at 300 °C

Transmittance values for the Ag and Cu doped TiO_2 films (60-70 %) were considerably less than the undoped TiO_2 film (90%). The transmittance values of one Au doped TiO_2 film was comparable to the TiO_2 control but the second Au doped TiO_2 film sample transmittance value dropped <70 % (350-425 nm) and

then rose at 500 nm (90%), see fig. 110. Reflectance values did not show a particularly strong IR reflectance for any TiO_2 film (~30%), see fig. 110.

Figure 110: Comparison of transmittance/reflectance analysis of undoped and Au, Ag and Cu doped TiO_2 films, 300 °C.

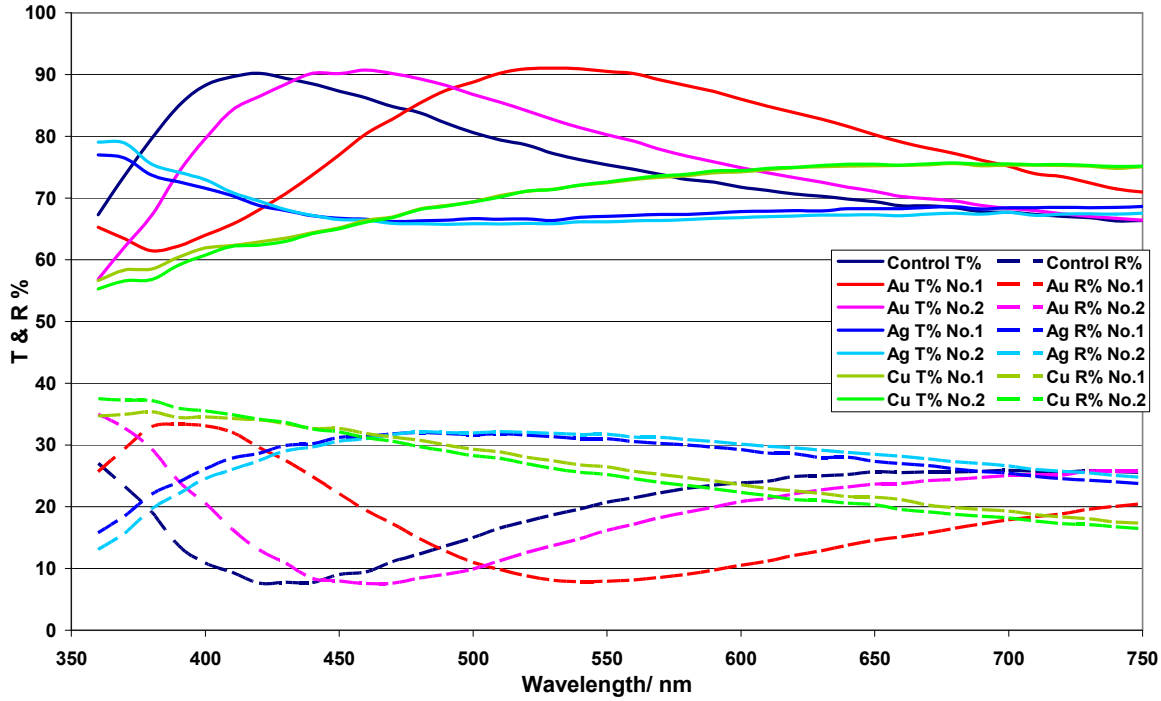

5.2.2.1.2 Comparison of undoped and doped TiO_2 films at 400 °C

The maximum transmittance value for the Cu doped TiO_2 film (90%) sample was slightly higher than the undoped TiO_2 film (85%) with Au and Ag transmittance values are comparable to the undoped TiO_2 film control, see fig. 111. Reflectance values did not show a particularly strong IR reflectance for any TiO_2 film (~30%), see fig. 111. The shape of the spectra is due to interference patterns indicating different areas of film thickness.

Figure 111: Comparison of transmittance/reflectance analysis of undoped and Au, Ag and Cu doped TiO_2 films, 400 °C.

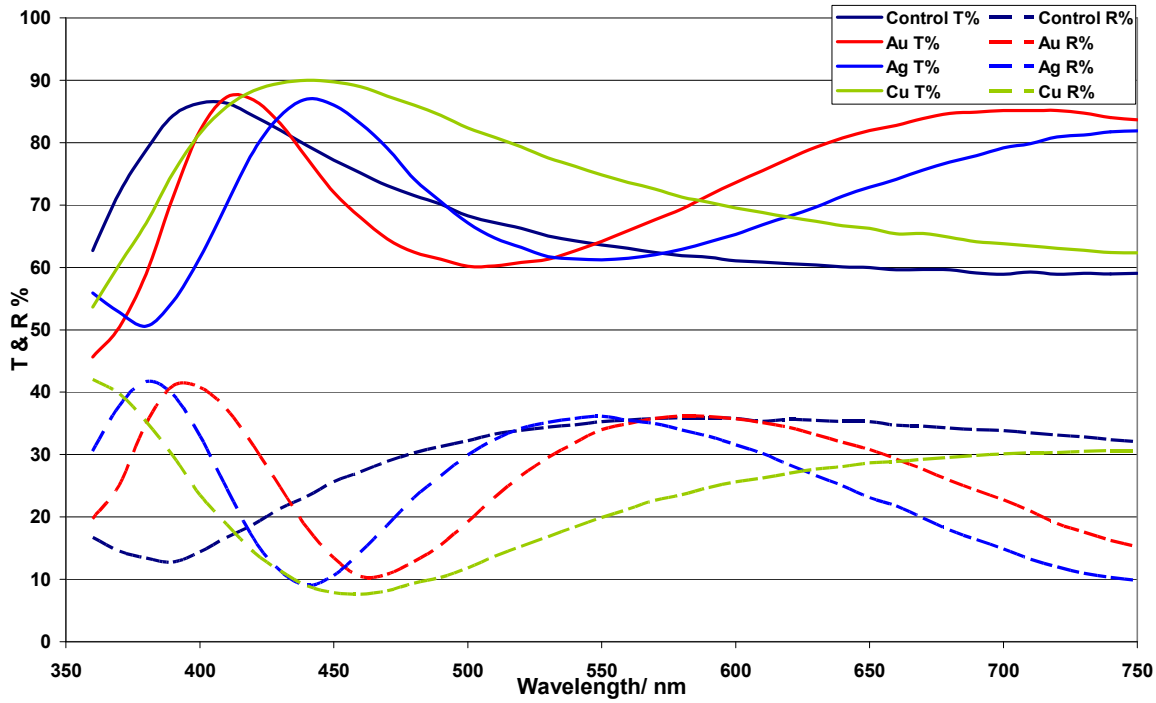

5.2.2.1.3 Comparison of undoped and doped TiO_2 films at 500 °C

Interference patterns are displayed on all transmittance and reflectance values for undoped and Au, Ag and Cu doped TiO_2 films formed at 500 °C, the shape of the spectra could be due to reflection of very uniform films, see fig. 112. Transmittance values for the Ag and Cu TiO_2 films (70 and 65 % respectively) were higher than the undoped and Au doped TiO_2 films (55 %) in the 350-450 nm range, see fig. 112. Reflectance values did not show a particularly strong IR reflectance for any TiO_2 film (~30%), see fig. 112.

Figure 112: Comparison of transmittance/reflectance analysis of undoped and Au, Ag and Cu doped TiO_2 films, 500 °C.

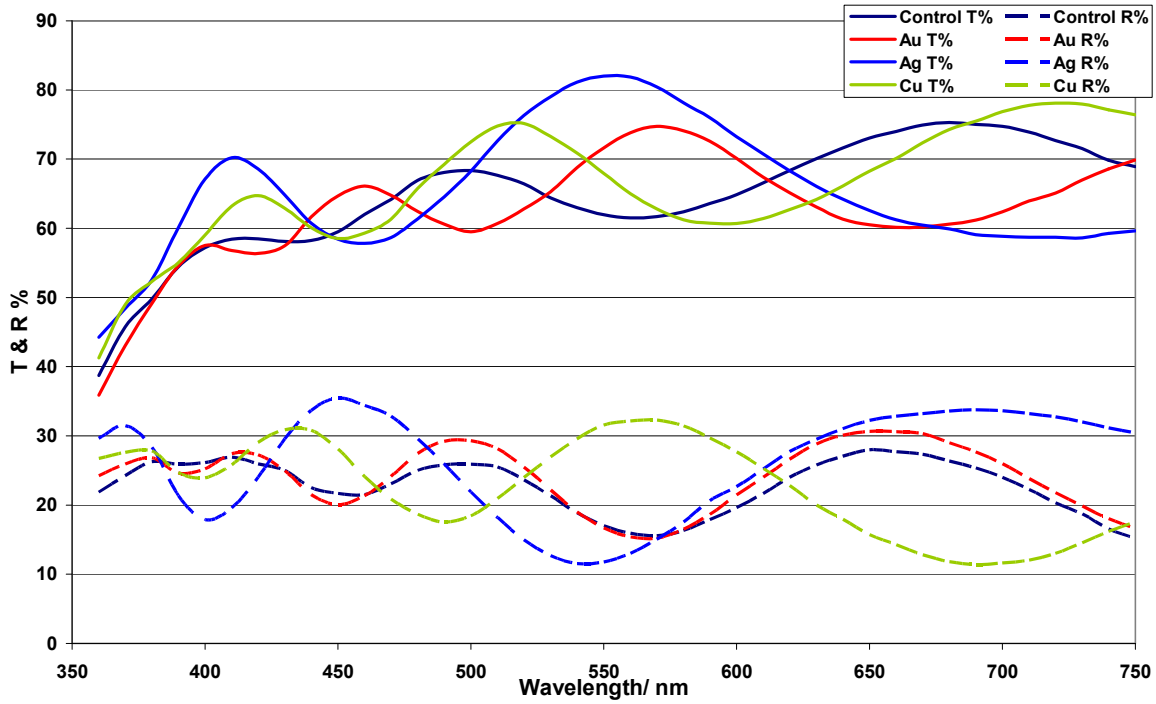

The average film thickness's were calculated for the undoped (184.3 nm) and doped Au (224.5 nm), Ag (167.6 nm) and Cu (193.0 nm) TiO_2 films (500 °C) using the Swanepoel method[148].

5.2.2.1.4 Comparison of undoped and doped TiO_2 films at 600 °C

Interference patterns are displayed on all transmittance and reflectance values for undoped and Au, Ag, Cu and Al doped TiO_2 films, 600 °C, indicating a change in thickness of the film across the substrate, see fig. 113 a-b). The Ag doped TiO_2 maximum transmittance value (~90%) appears slightly higher than the undoped TiO_2 film (~85%), all other dopants had slightly lower transmittance values, Au (~80-90%), Cu and Al (~75-85%), see fig. 113 a-b). Reflectance values did not show a particularly strong IR reflectance for any TiO_2 film (~30%), see fig. 113 a-b).

Figure 113: Comparison of transmittance/reflectance analysis of undoped and doped Au, Ag, Cu and Al doped TiO_2 films, 600 °C.

a) TiO_2 control and Au, Ag, Cu doped TiO_2 films

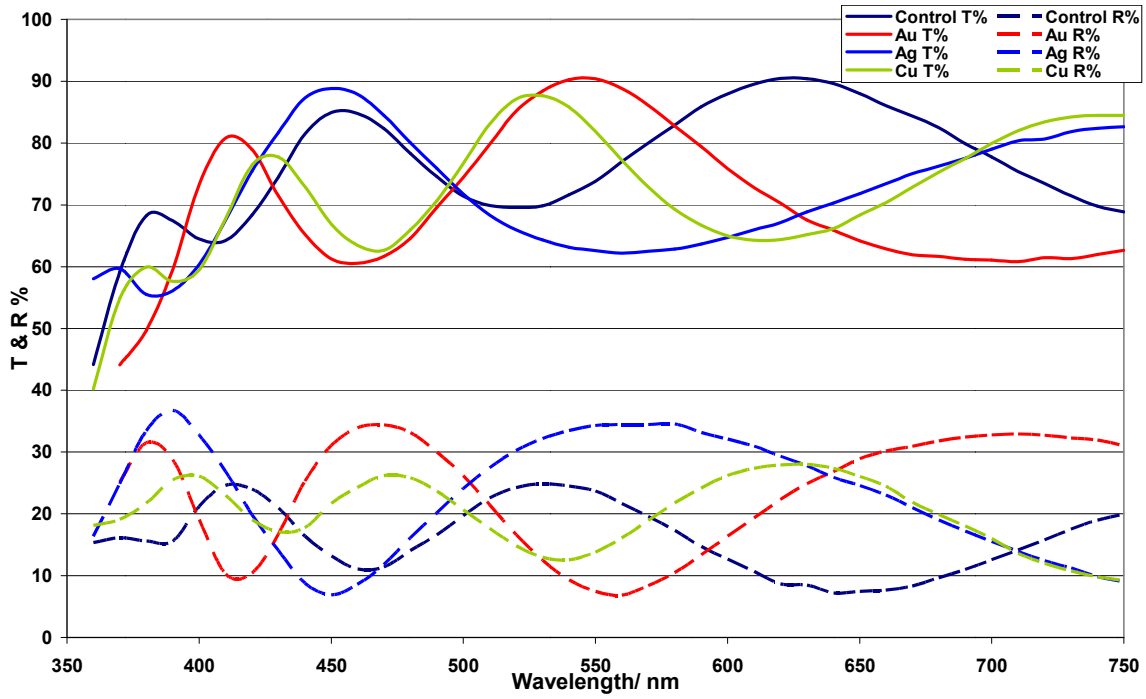

b) TiO_2 control and Al doped TiO_2 films

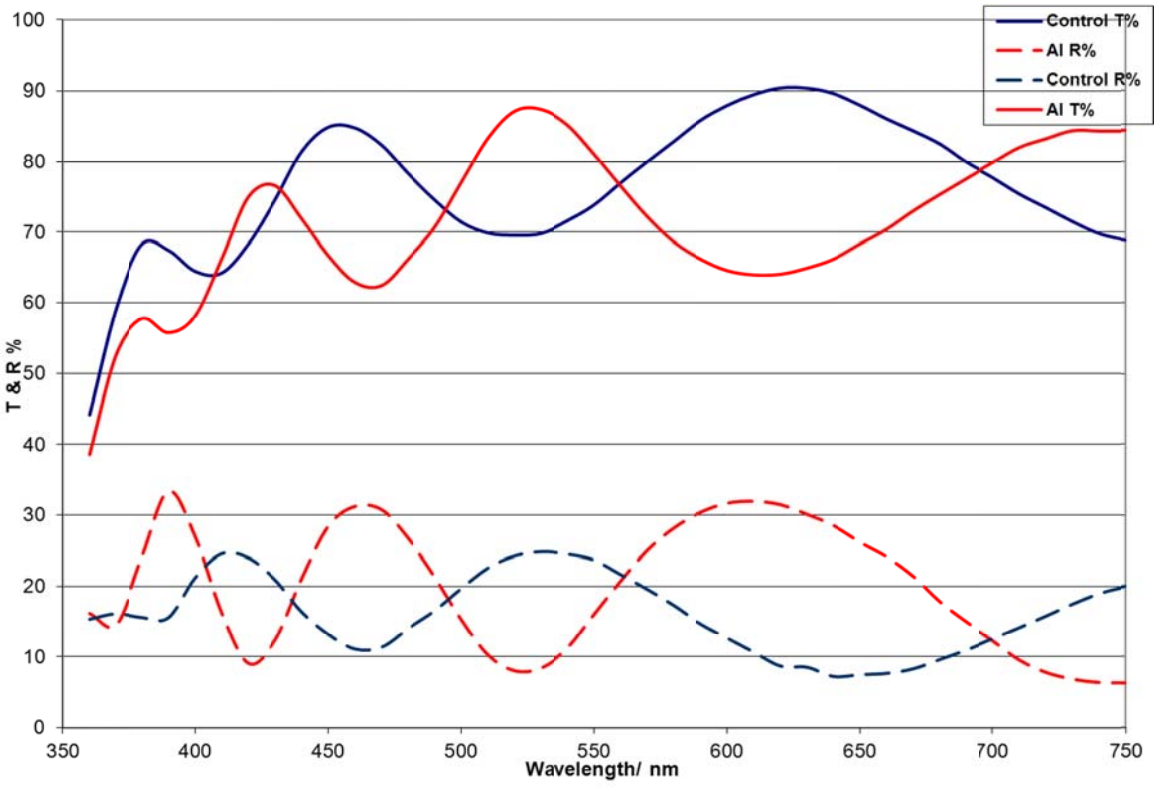

The average film thickness's were calculated for the undoped (165.7 nm) and doped Au (165.6 nm), Ag (168.7 nm), Cu (215.4 nm) and Al (214.6 nm) TiO_2 films (600 °C) using the Swanepoel method[148].

5.2.2.1.5 Summary of transmittance and reflectance results

The Au doped TiO_2 film, at 300 °C, had the only comparable T% value to the TiO_2 control. The transmittance value for the Cu doped TiO_2 film (90%) sample was slightly higher than the undoped TiO_2 film (85%) with Au and Ag transmittance values are comparable to the undoped TiO_2 film control. The Ag and Cu doped TiO_2 films at 500 °C appear to have higher transmission values than the control, whereas only the Ag doped TiO_2 film has a higher transmission at 600 °C, see table 28.

Table 28: Comparison of Transmittance values (300-600 °C).

	Maximum T% Values			
Film sample	300 °C	400 °C	500 °C	600 °C
Control	90	85	55	85
Au	90	85	55	80-90
Ag	65	85	70	90
Cu	70	90	65	75-80
Al	-	-	-	75-85

- Al films not synthesised at these temperatures

The results for transmittance values appears to display that not only does the presence of a dopant effect the T% value but synthesis temperature, with films synthesised at 500 °C having the most detrimental effect. Interference patterns are displayed on all transmittance and reflectance values for undoped and doped Au, Ag, Cu and Al doped TiO_2 films across separate portions of the substrate, 500-600 °C, indicating a relatively non-uniform film across the substrate. Reflectance values did not show a particularly strong IR reflectance for any TiO_2 film (~30%) for the whole temperature range studied (300-600 °C). A range of film thickness calculations (165.7-224.5 nm) were calculated from the interference patterns for the TiO_2 films synthesised at 500 °C and 600 °C.

5.2.3 SEM and EDX analysis

The SEM and EDX analysis from the dynamic undoped and doped TiO_2 film samples from the AACVD/CVD synthesis technique, prototype 2, produced highly transparent clear films with visible transmission from 60-90% at various temperatures (300-600 ºC). Undoped titania films were synthesized between 300 °C and 600 °C; the glass substrate was passed under the reaction chamber head (normally 10 passes) to act as controls/comparison for doped titania films. The morphology of titania thin films were found to be influenced by the attempted addition of Au, Ag, Cu and Al dopants (≥400 °C). Pt or Au coatings were used. The TiO_2 films synthesised at lower temperatures (≤500 °C) displayed a uniform transparent pale blue colour; films synthesised at higher temperatures (≥500 °C) displayed typical optical interference patterns indicative of a non-uniform surface of varying thickness.

5.2.3.1 Comparison of undoped and doped TiO_2 films, 300 °C

Undoped and Au, Ag and Cu doped TiO_2 doped films were analysed at 300 °C, the morphology is very uniform and shallow with no discernible nanoparticle structure (500 nm), see figs. 114 a), 115 a-c). EDX analysis showed no incorporation of any dopants, see fig. 114 b).

Figure 114: SEM analysis of undoped TiO_2 film (300 °C)

a) Morphology undoped (500 nm)

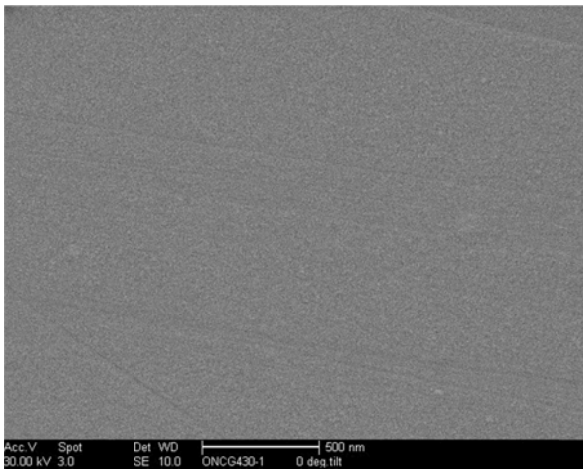

b) EDX analysis undoped: *Pt coating used

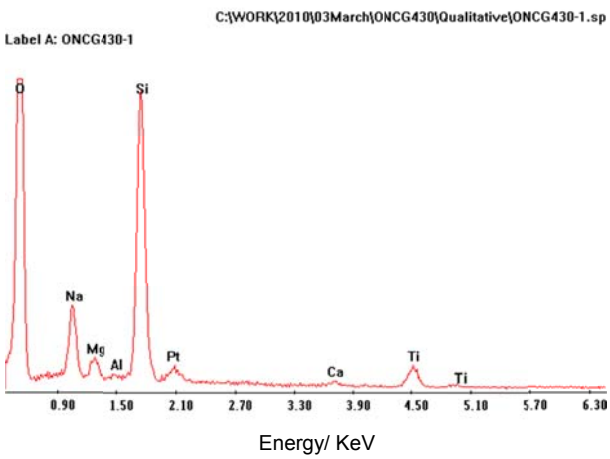

Figure 115: SEM analysis of Au, Ag and Cu TiO_2 doped films at 300 °C.

a) Morphology Au doped (500 nm)

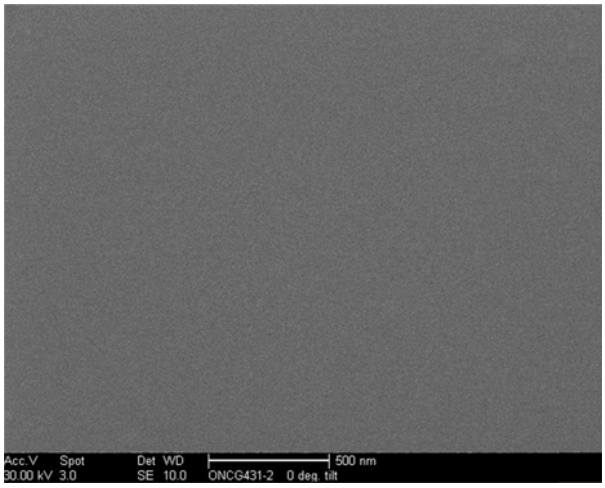

b) Morphology Ag doped (500 nm)

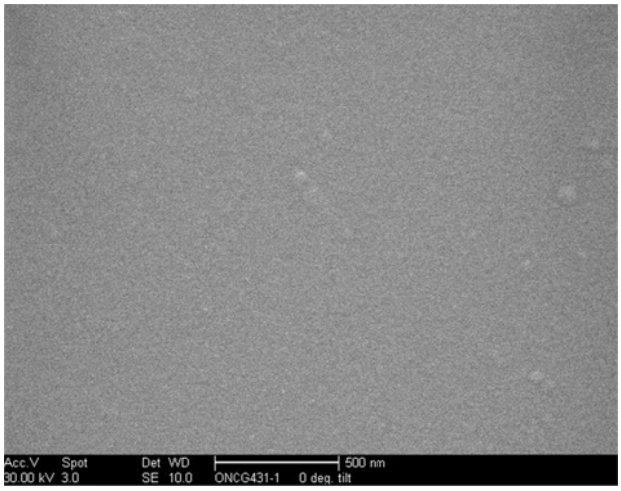

c) Morphology Cu doped (500 nm)

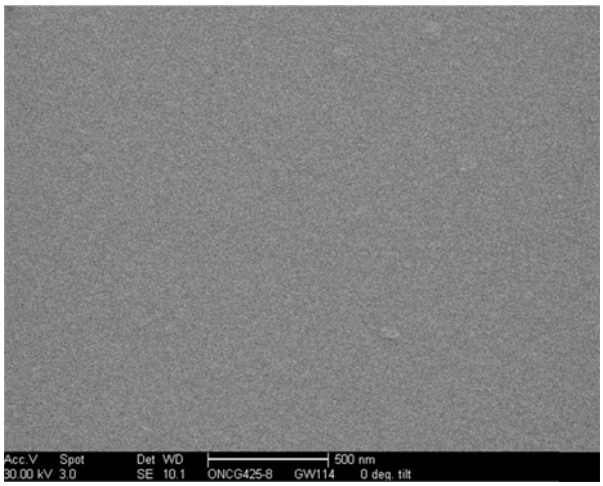

5.2.3.1.1 Summary of 300 °C results

Morphology and analysis very similar, the coatings had very, very fine shallow structures, not discernible at the magnification used (500 nm), apart from the odd bump shape seen on the Ag and Cu doped films, no dopants detected. The lack of visible morphology for all the titania films synthesised at 300 °C could be due to the very uniform and amorphous nature of the films, since all these films were highly coloured, transparent pale blue and TiO_2 was detected using EDX.

5.2.3.2 Comparison of undoped and doped TiO_2 films, 400 °C

Undoped and Au, Ag and Cu TiO_2 doped films were analysed at 400 °C, the morphology is very uniform with no discernible nanoparticle structure (500 nm), see figs. 116 a), 117 a-c), 118 a-b). EDX analysis showed incorporation of Au dopant on one film, see fig. 117 b) and all other EDX analysis showed no incorporation of dopants, see fig. 117 d). There are NaCl crystals present with an organic phase on the Au doped TiO_2 film formed through contamination, see fig. 117 c). Pt coatings were used on the samples.

Figure 116: SEM analysis of undoped TiO_2 film, 400 °C

a) Morphology undoped (500 nm) b) EDX analysis undoped

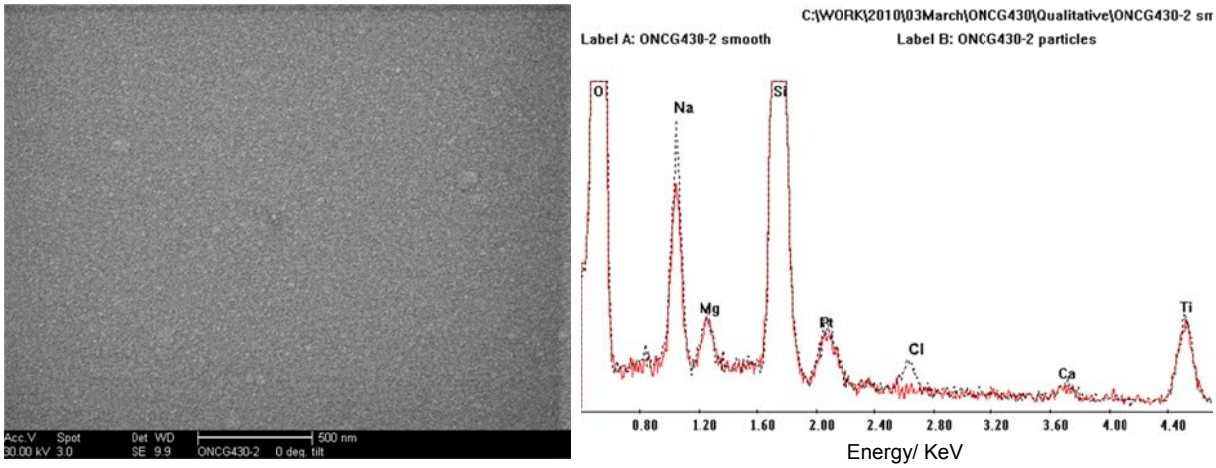

Figure 117: SEM analysis of Au doped TiO_2 film, 400 °C

a) Morphology Au doped (500 nm) b) Au doped EDX analysis

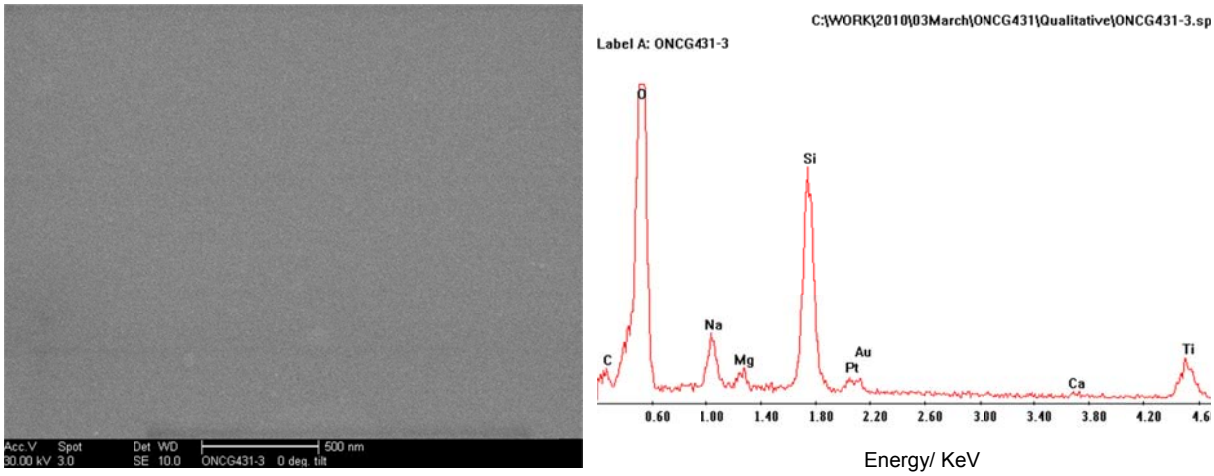

c) Morphology Au doped (500 nm)

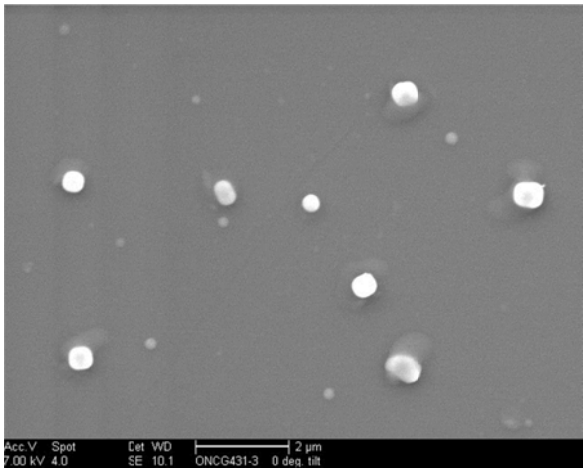

d) Au doped EDX analysis: * Pt coating used

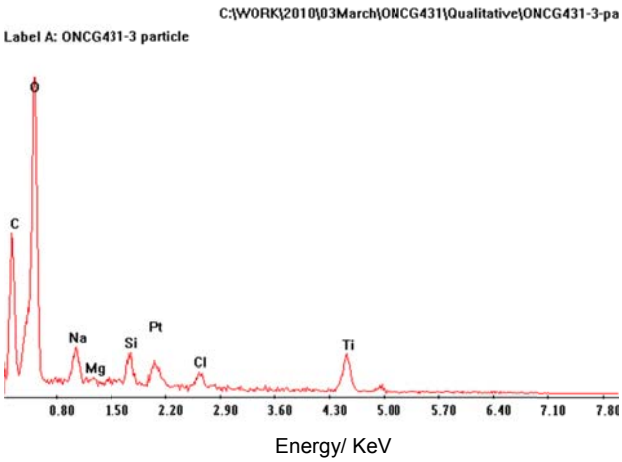

* NaCl contaminant crystals present on the surface

Figure 118: SEM analysis of Ag and Cu TiO_2 doped films, 400 °C.

a) Morphology Ag doped (500 nm)

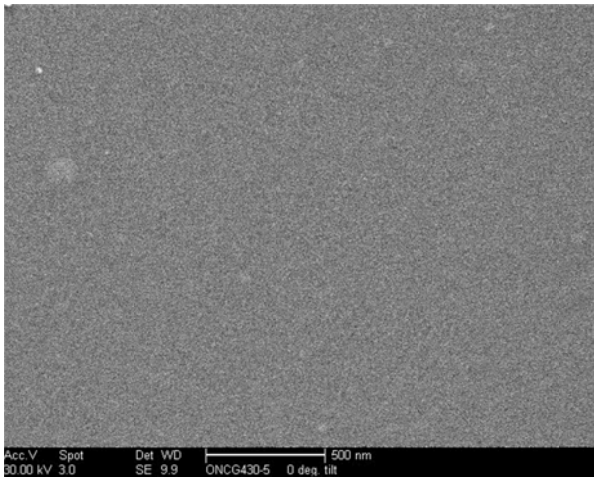

b) Morphology Cu doped (500 nm)

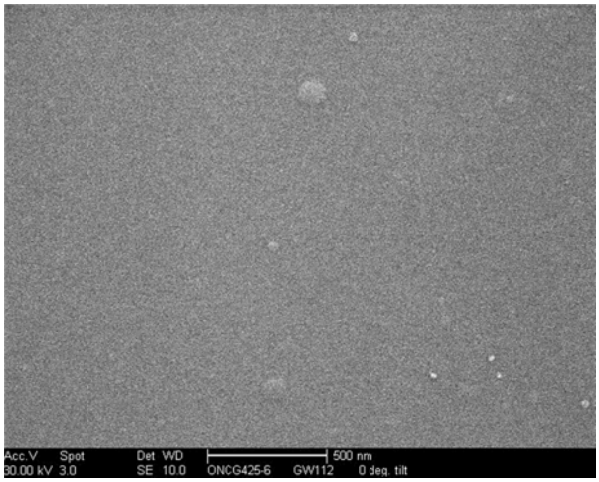

5.2.3.2.1 Summary of TiO_2 films at 400 °C

Very fine morphology for the bulk areas of the coatings, similar composition, NaCl crystals found on the surface of several films and the Au dopant was detected on one TiO_2 film sample. One Au doped film was contaminated with NaCl crystals and associated with an organic phase due to the diffusion of Na ions to the surface of the glass reacting with Cl ions from the gaseous phase. The morphology of recent undoped titania film AACVD work (400 °C) by Edusi *et al*. gave a very different result from the undoped TiO_2 film above, Edusi's morphology had large angular structures embedded within a granular matrix[157]. Recent LPCVD work on

Ag doped TiO_2 films by Munkalasiri *et al.* also gave very different morphology with large agglomerated structures seen compared with the smooth morphology seen here[188].

5.2.3.3 Comparison of undoped and doped TiO_2 films, 500 °C

Comparison of the undoped and doped Au, Ag and Cu TiO_2 films, 500 °C, appear to display a distinct change in morphology, the undoped TiO_2 film had very angular, aggregated nanoparticle structure, see fig. 119 a), whilst the TiO_2 films formed in the presence of Au, Ag and Cu appear to have large platelet conglomerates with smaller nanoparticles formed between them see fig. 119 c-d), g-i) and j), suggesting a change in height, see fig. 119 e-f).

Figure 119: SEM analysis of undoped TiO_2 film, 500 °C.

a) Morphology Undoped TiO_2 (500 nm)

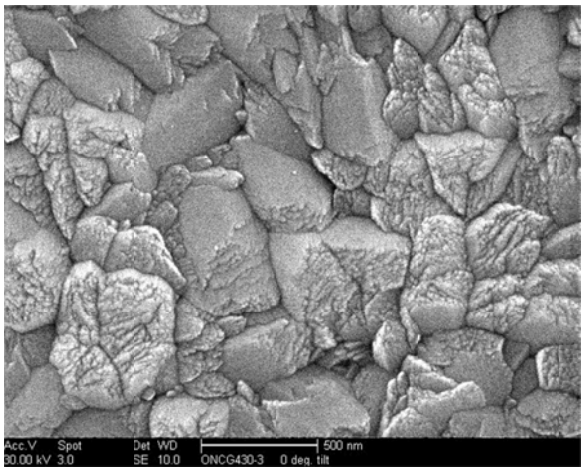

b) Undoped TiO_2 EDX analysis

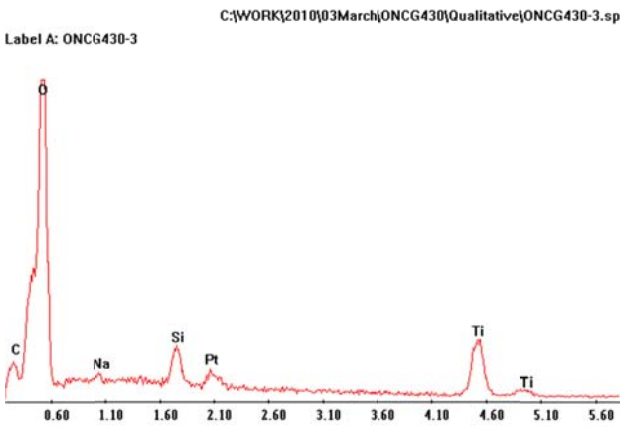

c) Morphology Au doped (1 µm)

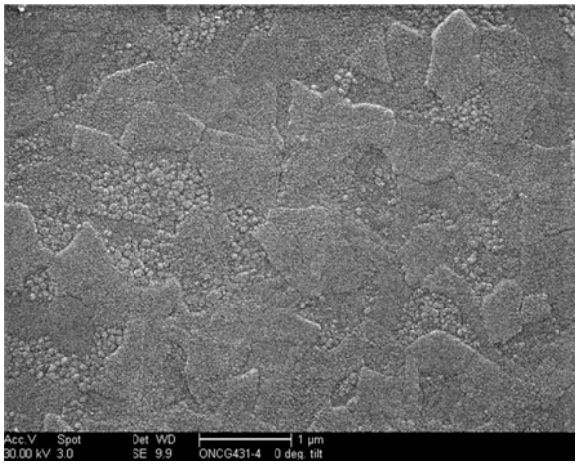

d) Morphology Au (500 nm)

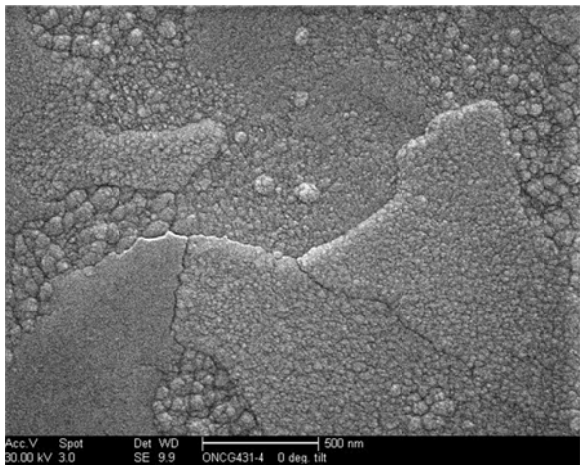

e) Thickness Au doped

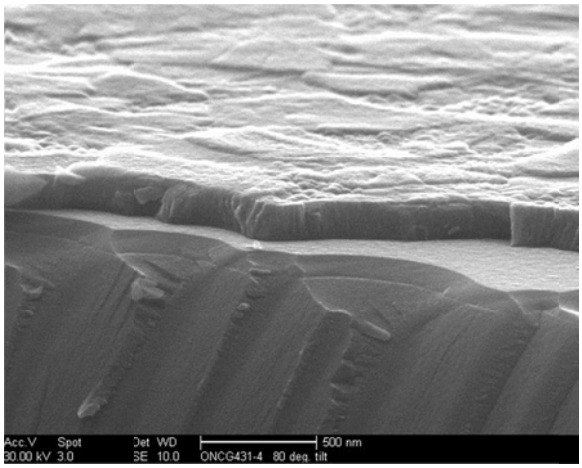

f) Thickness Au (185-197 nm)

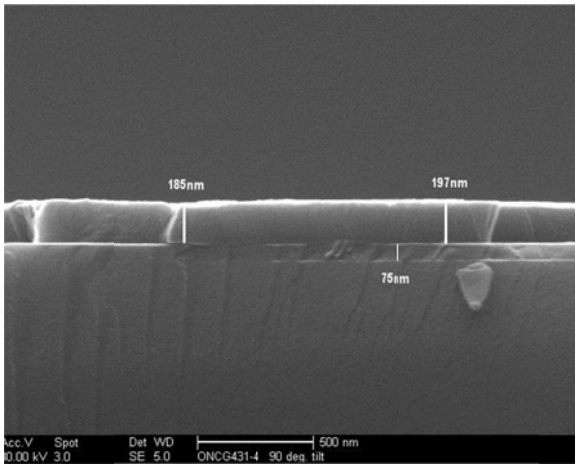

g) Morphology Ag doped (1 µm)

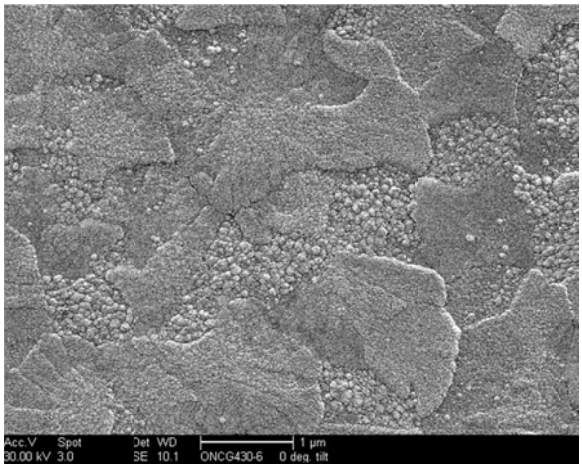

h) Morphology Ag doped (500 nm)

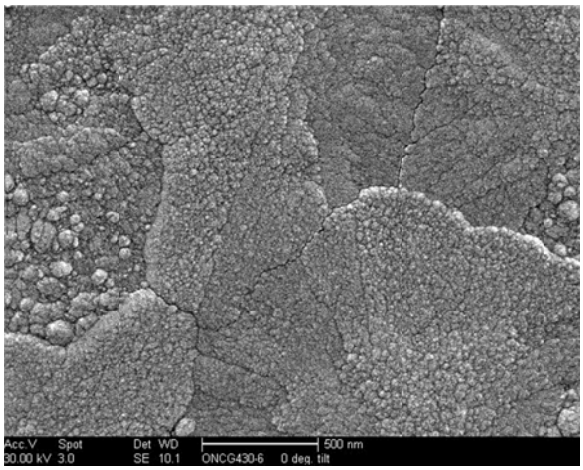

i) Morphology Cu doped (1 µm)

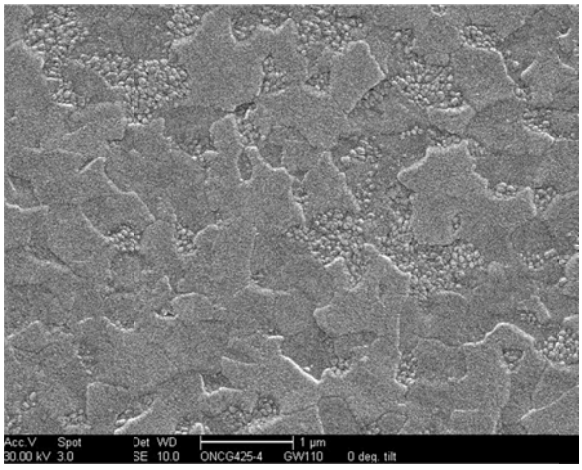

j) Morphology Cu doped (500 nm)

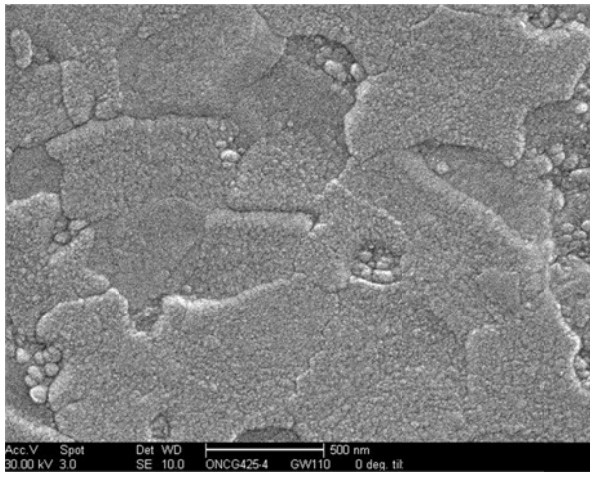

5.2.3.3.1 Summary of doped TiO_2 films. 500 °C

Morphology of the coatings were much more defined with the undoped TiO_2 film, 500 °C, having very a very rough angular, aggregated nanoparticle structure (100-500 nm) and appears to be faceted in one direction, similar to recent work by Rosas *et al.* on a steel substrate (600 °C) forming a highly orientated crack-free film[154]. The doped Au, Au, and Cu TiO_2 films displayed large platelet areas (> 500nm) with smaller finer crystal structures (50-100 nm) found in-between, suggesting a change in height (~185-200 nm). The characteristic one direction faceting seen in the undoped TiO_2 film appears to be lost in the TiO_2 films formed in the presence of dopants. The experimental thickness (185-197 nm) of the Au doped film does not appear to agree with the calculated Swanepoel value (224.5 nm), this could be due to different areas of the film being used to produce the transmittance/reflectance values to the area used for SEM analysis. All EDX analysis proved to be very similar with only TiO_2 detected, no dopants were detected. The morphology of recent titania film AACVD work (500 °C) by Edusi *et al*. gave a very different result from the undoped TiO_2 film, Edusi's morphology had smaller angular type nanoparticle structures and was not as compacted and agglomerated as the undoped TiO_2 film shown here[157]. Comparison to other recent literature using various CVD techniques also showed very different morphological structures[189] to the films shown here including recent work by Sheel *et. al*, where the Ag doped TiO_2 film (500 °C) structures were either smaller and

elongated or had more angular nanoparticles[190], similar to the static films in chapter 4.

5.2.3.4 Comparison of undoped and doped Au, Ag, Cu and Al TiO_2 films, 600 °C

Comparison of the undoped and doped Au, Ag and Cu TiO_2 films, 600 °C, appear to display a distinct change in morphology, the undoped TiO_2 film had very angular, aggregated nanoparticle structure, see fig. 120 a), whilst the TiO_2 films formed in the presence of Au are much smaller angular and resemble neolithic spear heads, see fig. 120 c). The Ag TiO_2 film displays aggregated angular structures and plate nanoparticles which are slightly larger than the Au TiO_2 film, see fig. 120 d). The Cu and Al TiO_2 films display large platelet conglomerates with smaller nanoparticles formed between them, similar to the morphology seen at 500 °C also suggesting a change in height between the plates and smaller nanoparticles, see fig. 120 e-f). No dopants were detected using EDX analysis.

Figure 120: SEM analysis of undoped TiO_2 film, 600 °C.

a) Morphology undoped (500 nm)

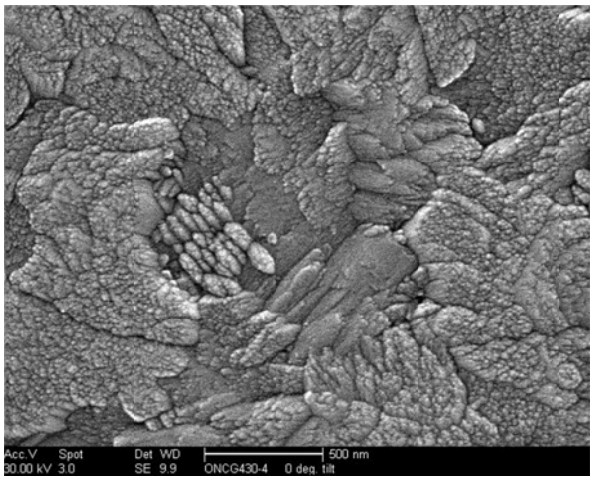

b) Undoped EDX analysis: * Pt coating used

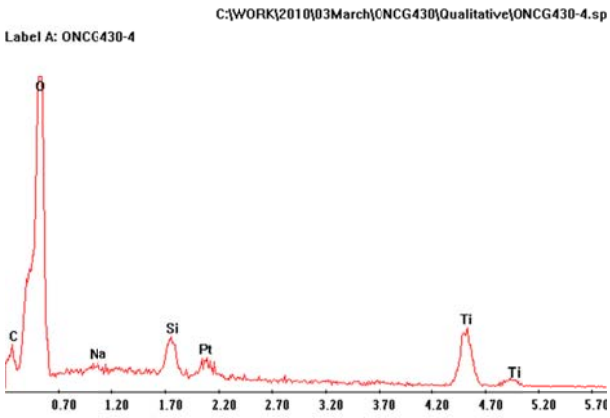

c) Morphology Au doped (500 nm)

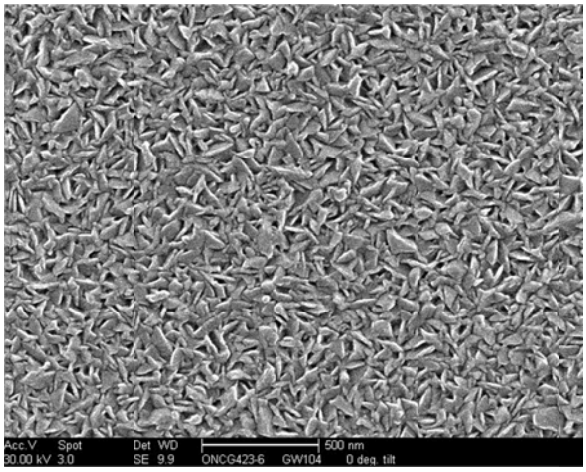

d) Morphology Ag doped (500 nm)

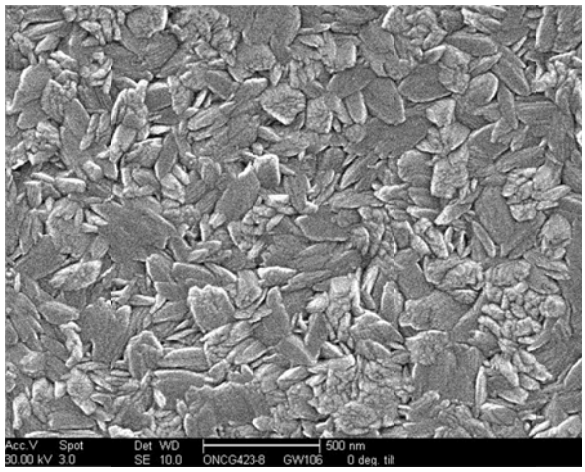

e) Morphology Cu (500 nm)

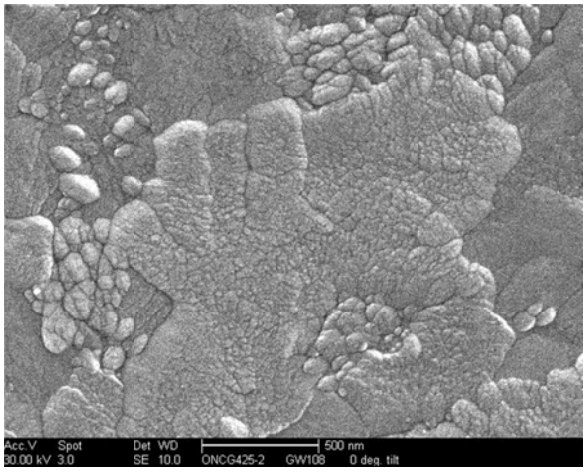

f) Morphology Al (500 nm)

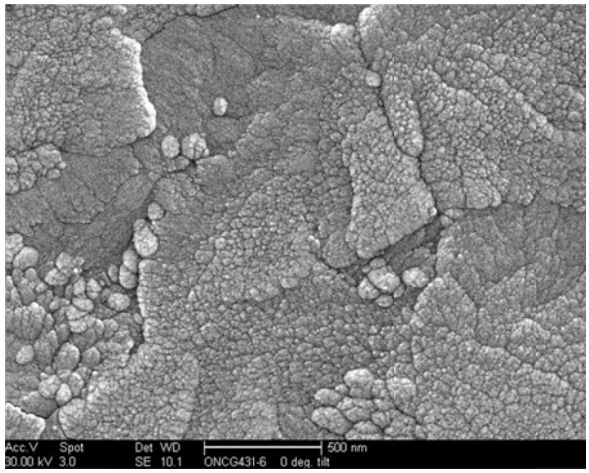

5.2.3.4.1 Summary of the TiO_2 doped films, 600 °C

The morphology of the films was crystalline, the control and TiO_2 film formed in the presence of Cu and Al have very similar massive platelet structures with areas of smaller crystal structures between. These morphologies are representative of the whole film area examined. The Au and Ag dopants have affected the morphology with far more angular, smaller structures visible the larger platelet crystal structures seen to dominate in the undoped TiO_2 film and Cu, Al doped TiO_2 films are not present; smaller angular crystal structures dominate the Au and Ag doped TiO_2 film morphology, this effect is slightly less angular with Ag. All EDX analysis proved to be very similar with only TiO_2 detected, no dopants were detected (EDX detection level *ca* 0.5 atom%). The morphology of the undoped TiO_2 film appears to be very

different to results reported in literature with large agglomerated platelets dominating the surface[159, 189]; for *e.g.* the morphology found in Hyett *et al.* CVD work on mixed anatase/rutile phase titania films showed much less agglomeration with smaller angular structures[159]. Comparison of similar Al doped TiO_2 films by Kuo *et al.* (350-500 °C) displayed very different morphologies, *e.g.* agglomerated granular structures which are very unlike the large plate structure morphology displayed in this work[191]. Recent work by Kim *et al*. with TiO_2 films, on an alumina substrate, at higher synthesis temperatures (500 °C, deposition time: 10 mins) have columnar prismatic facets that are much in tune with what is observed with static films in chapter 4, see chapter 4[151]. Other recent work by Kuo *et al.* using Al as the dopant (350-500 °C) had agglomerated granular structures unlike the large plate structure morphology displayed in this work[191].

5.2.3.5 Summary of the SEM and EDX analysis

TiO_2 films undoped and formed in the presence of dopants at lower temperatures (<500 °C) appear to have very uniform fine structures with very similar morphology. TiO_2 films formed in the presence of Au, Ag, Cu and Al dopants at 500 °C had very similar large platelet, conglomerated type structures that differed from the smaller more angular, aggregated structures seen in the undoped TiO_2 film; all dopants had a very similar effect on the morphology. At 600 °C the dopants used had a profound effect on the morphology with Au and Ag producing very different morphologies from the undoped TiO_2 film and the TiO_2 films formed in the presence of Cu and Al displayed very similar large platelet conglomerated structures also seen at 500 °C and for dynamic films in chapter 4, see chapter 4. The Au dopant was detected by EDX, at 400 °C, but no other dopants were detected using EDX analysis for the rest of the temperature range (300-600 °C).

5.2.4 X-ray diffraction analysis

X-ray diffraction analysis was carried out on both undoped and doped Au, Ag, Cu and Al TiO_2 films (300-600 °C). The tetragonal form of anatase titania was exhibited on every film (400-600 °C), all other films below 400 °C exhibited no crystallinity. All crystallite orientations have an opportunity to produce diffraction

intensity and it is only those crystallographic planes that are parallel to the surface that produce diffraction intensity at the detector (according to Bragg's Law). The diffractograms were obtained by scanning each sample for 30 minutes from 5 to 75 degrees 2-theta using the X'Celerator detector, see fig's 121 a-b), 122 a-b), 123 a-b), 124 a-b). All X-ray diffraction patterns were matched to the anatase phase of TiO_2.

5.2.4.1 Undoped (300-600 °C) and Ag doped TiO_2 films (400-500 °C)

Figure 121: X-ray diffraction spectra for undoped TiO_2 control films, 300-600 °C and Ag, 400-500 °C

a)

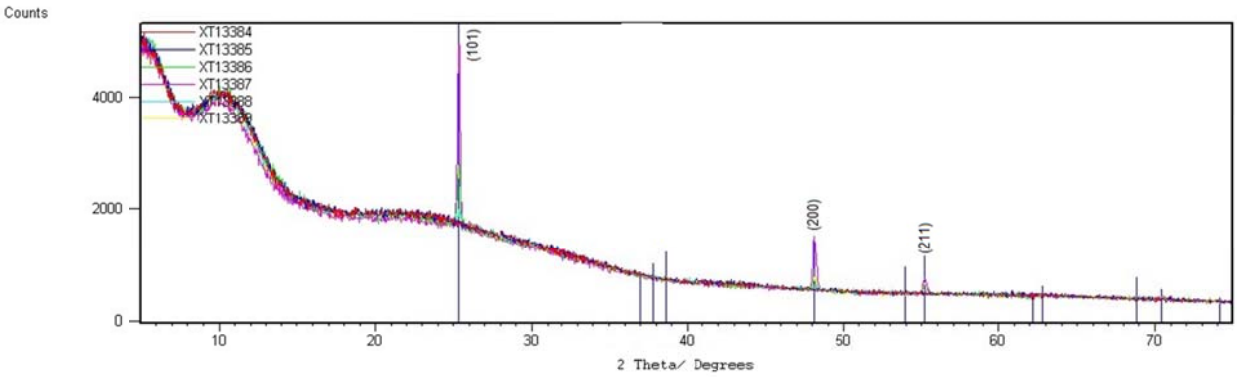

No.	Ref. Code	Compound Name	Chemical Formula
1	01-083-2243	Anatase, syn	Ti O2

b)

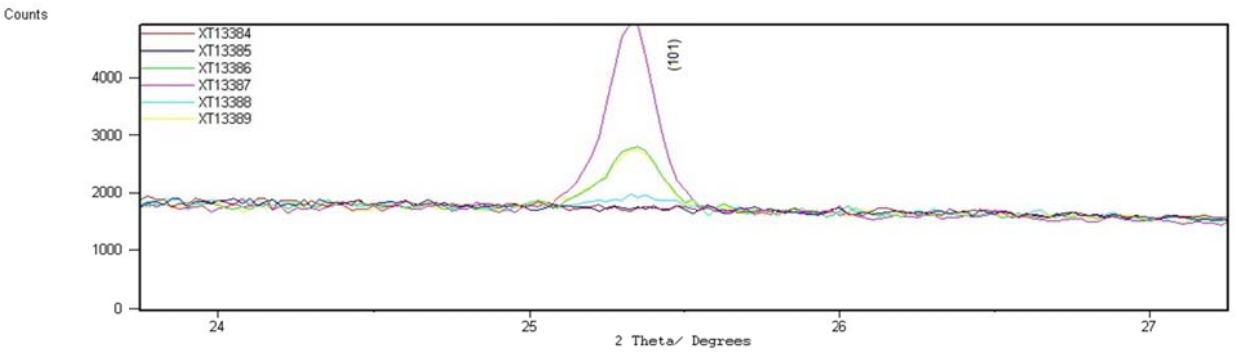

Sample: Control 300 °C: XT13384 (red), Control 400 °C: XT13385 (blue), Control 500 °C: XT13386 (green), Control 600 °C: XT13387 (pink), Ag 400 °C: XT13388 (light blue), Ag 500 °C (yellow).

All the undoped (400-600°C) and doped Ag TiO_2 films (400-500 ºC) had the tetragonal anatase phase form. The undoped TiO_2 films (300-400 °C) were not crystalline. The reflection observed for Ag doped TiO_2 film (400 °C) appeared to correspond with TiO_2 (101). The reflections observed for undoped TiO_2 (500 °C) and doped Ag TiO_2 film (500 °C) appeared to correspond with TiO_2 (101), (200) and (211). The reflections observed for undoped TiO_2 (600 °C) appeared to correspond with TiO_2 (101), (112), (200), (211) and (220).

5.2.4.2 Au, Ag and Al TiO_2 doped films (300-600 °C)

Figure 122: X-ray diffraction spectra for Au, Ag and Al, TiO_2 doped films, 300-600 °C

a)

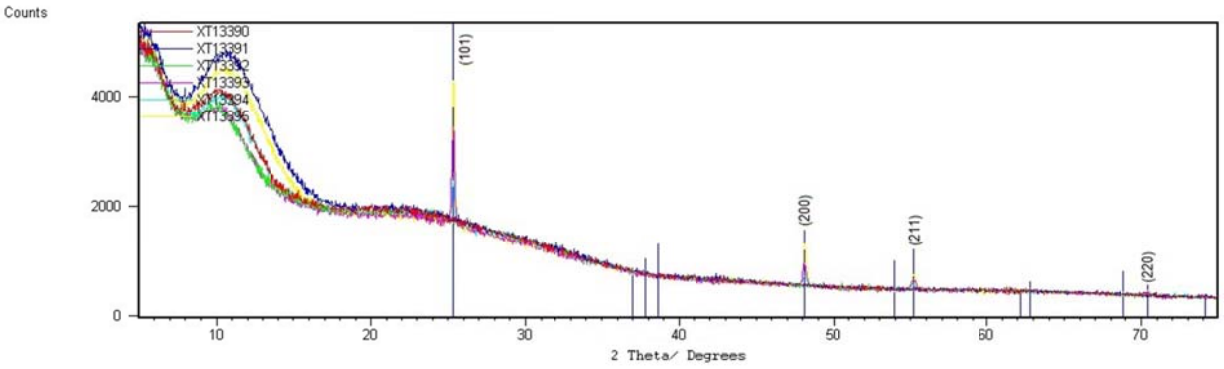

No.	Ref. Code	Compound Name	Chemical Formula
1	01-083-2243	Anatase, syn	Ti O2

b)

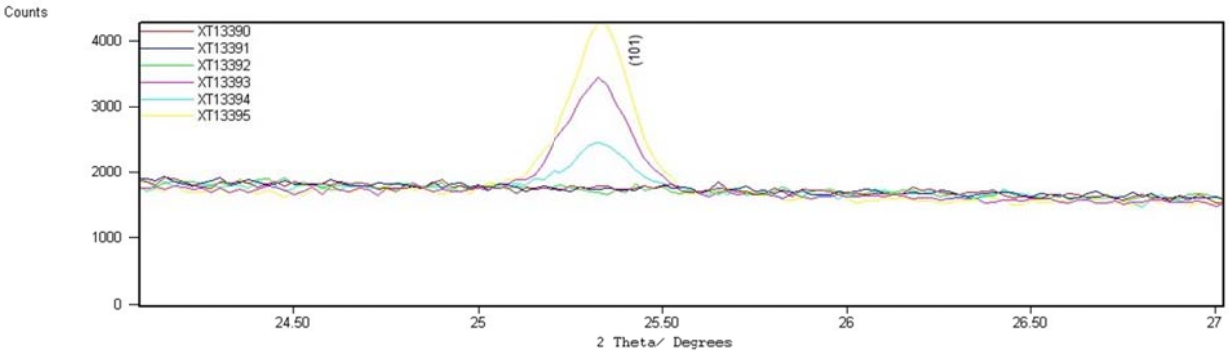

Sample: Ag 300 °C: XT13390 (red), Au 300 °C: XT13391 (blue), Au 400 °C: XT13392 (green), Au 500 °C: XT13393 (pink), Au 500 °C (4 passes): XT13394 (light blue), Al 600 °C: XT13395 (yellow).

All Au, Ag and Al doped TiO_2 films (500-600 ºC) had the tetragonal anatase phase form. No crystalline reflections were observed for Au, Ag doped TiO_2 film (300 °C) and Au doped TiO_2 film (400 °C). The reflections observed for Au doped TiO_2 (500 °C, 10 and 4 passes) and Al doped TiO_2 appeared to correspond with TiO_2 (101), (200) and (211) with an extra reflection observed for the Al doped TiO_2 film that appeared to correspond with TiO_2 (220).

5.2.4.3 Doped Au and Ag TiO_2 films (600 °C)

Figure 123: X-ray diffraction spectra for Au and Ag doped TiO_2 films, 600 °C

a)

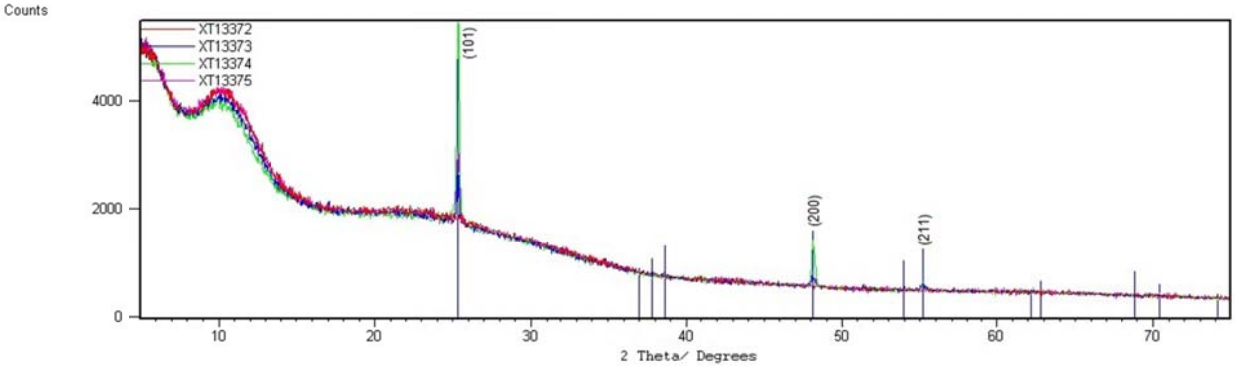

No.	Ref. Code	Compound Name	Chemical Formula
1	01-083-2243	Anatase, syn	Ti O2

b)

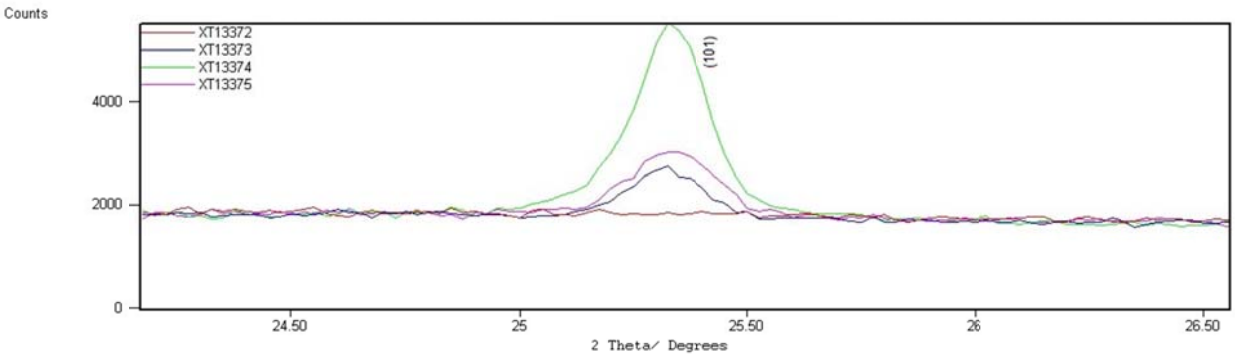

Sample: Au 600 °C (20 passes) : XT13372 (red), Au 600 °C: XT13373 (blue), Au 600 °C: XT13374 (green), Ag 600 °C: XT13375 (pink).

All Au and Ag doped TiO_2 films (600 ºC) had the tetragonal anatase phase form corresponding to TiO_2 (101), (200) and (211) and the intensity of the reflections increased in the order >Ag >Au.

5.2.4.4 Doped Cu TiO_2 films (300-600 °C)

Figure 124: X-ray diffraction spectra for Cu doped TiO_2 films, 300-600 °C

a)

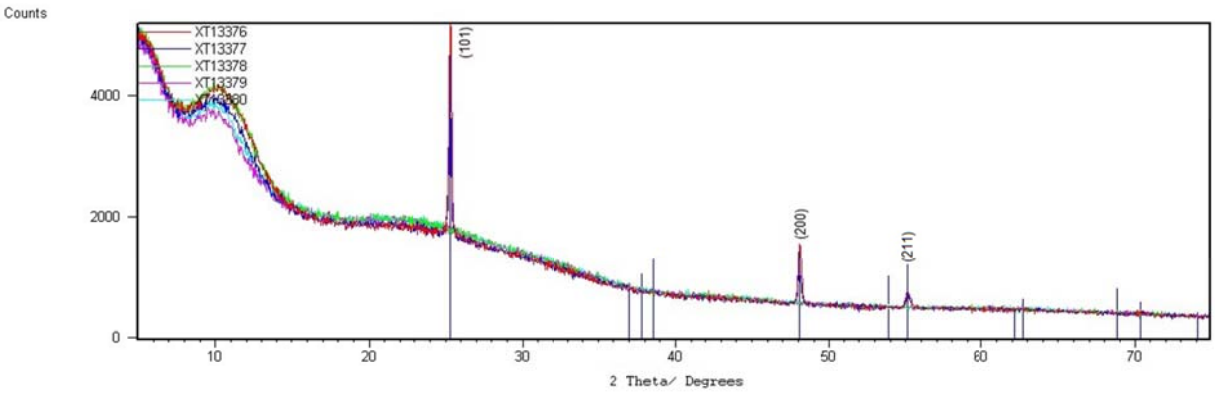

No.	Ref. Code	Compound Name	Chemical Formula
1	01-083-2243	Anatase, syn	Ti O2

b)

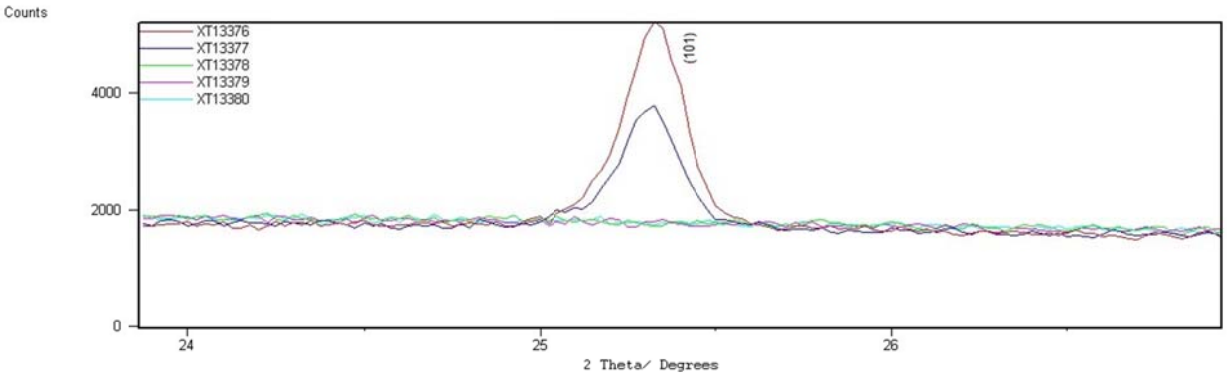

Sample: Cu, 600 °C: XT13376 (red), Cu, 500 °C: XT13377 (blue), Cu, 400 °C: XT13378 (green), Cu, 300 °C: XT13379 (pink), Cu, 375 °C: XT13380 (light blue).

All Cu doped TiO_2 films (300-600 ºC) had the tetragonal anatase phase form. The reflections observed for Cu, (500-600 °C) appeared to correspond with TiO_2 (101),

(200) and (211) with a high angle low intensity peak at 500 °C corresponding to (220), Cu (300-400 °C) films were not crystalline and the greatest intensity occurred with Cu at 600 °C.

5.2.4.5 Summary of XRD analysis

The dominant tetragonal anatase form of titania was exhibited on all diffractograms for undoped and doped Au, Ag, Cu and Al TiO_2 films (400- 600 ºC). TiO_2 films formed below 400 °C were not crystalline. According to the XRD diffractograms; the dopants Au, Ag, Cu and Al appeared to have little effect on the form of titania observed. Notably no Rutile was formed even at 600 °C. This is in direct contrast to the work of Hyett and Edusi where anatase/rutile mixtures were seen from a similar precursor set[157-160].

5.2.5 Raman Analysis

Raman spectra analysis was carried out for TiO_2 films formed in the presence of Au, Ag and Cu (400 °C, 600 °C). Typical peaks for the tetragonal anatase phase were observed for all samples, see figs. 125, 126, tables 29 and 30.

5.2.5.1 Au, Ag and Cu doped TiO_2 films, 400 °C

Raman spectra for dynamic TiO_2 films (10 passes), formed in the presence of Au, Ag and Cu, at 400 °C, display typical wavelengths for the tetragonal anatase phase of titania, peaks (144, 197, 394, 512, 635 cm^{-1}), see fig. 125 and table 29.

Table 29: Raman band frequencies for dynamic (10 passes) undoped and Au, Ag and Cu doped TiO_2 films, (400 °C)

Dopant	Band 1/cm^{-1}	Phase A/R	Band 2/cm^{-1}	Phase A/R	Band 3/cm^{-1}	Phase A/R	Band 4/cm^{-1}	Phase A/R	Band 5/cm^{-1}	Phase A/R
Au	147	A	-	-	-	-	-	-	639	A
Ag	147	A	203	A	396	A	519	A	640	A
Cu	145	A	-	-	400	A	517	A	640	A

Key: A = anatase, R = Rutile, - spectrum weak due to thin film

Figure 125: Comparison of Raman spectra for Au, Ag and Cu doped dynamic TiO_2 films (10 passes), 400 °C

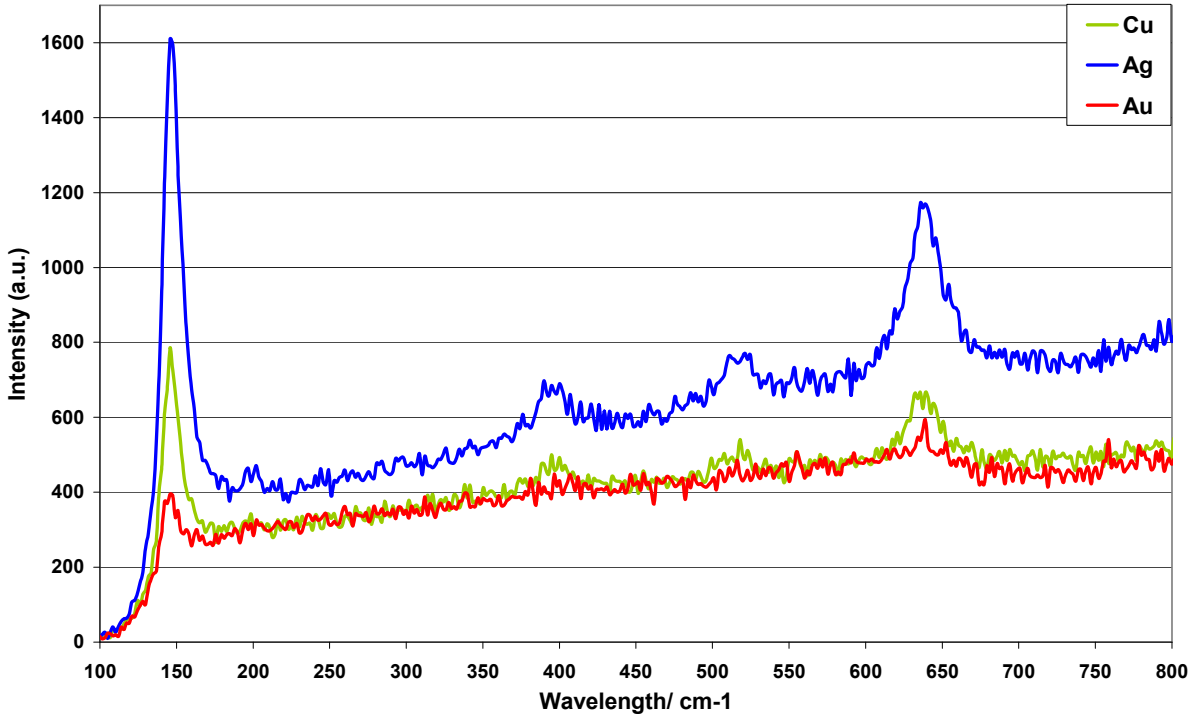

5.2.5.2 Au, Ag and Cu doped TiO_2 films, 600 °C

Raman spectra for dynamic TiO_2 films formed in the presence of Ag, Au and Cu at 600 °C display typical wavelengths for the tetragonal anatase phase of titania, peaks (144, 197, 394, 512, 635 cm^{-1}), see fig. 126 and table 30.

Table 30: Raman band frequencies for dynamic (10 passes) undoped and Au, Ag and Cu doped TiO_2 films, (600 °C)

Dopant	Band 1/cm^{-1}	Phase A/R	Band 2/cm^{-1}	Phase A/R	Band 3/cm^{-1}	Phase A/R	Band 4/cm^{-1}	Phase A/R	Band 5/cm^{-1}	Phase A/R
Au	144	A	200	A	400	A	519	A	644	A
Ag	-	-	-	-	-	-	-	-	-	-
Cu	144	A	200	A	398	A	519	A	639	A

Key: A = anatase, R = Rutile, - No spectrum/peak found

Figure 126: Comparison of Raman spectra for Au, Ag and Cu doped dynamic (10 passes) TiO_2 films (600 °C).

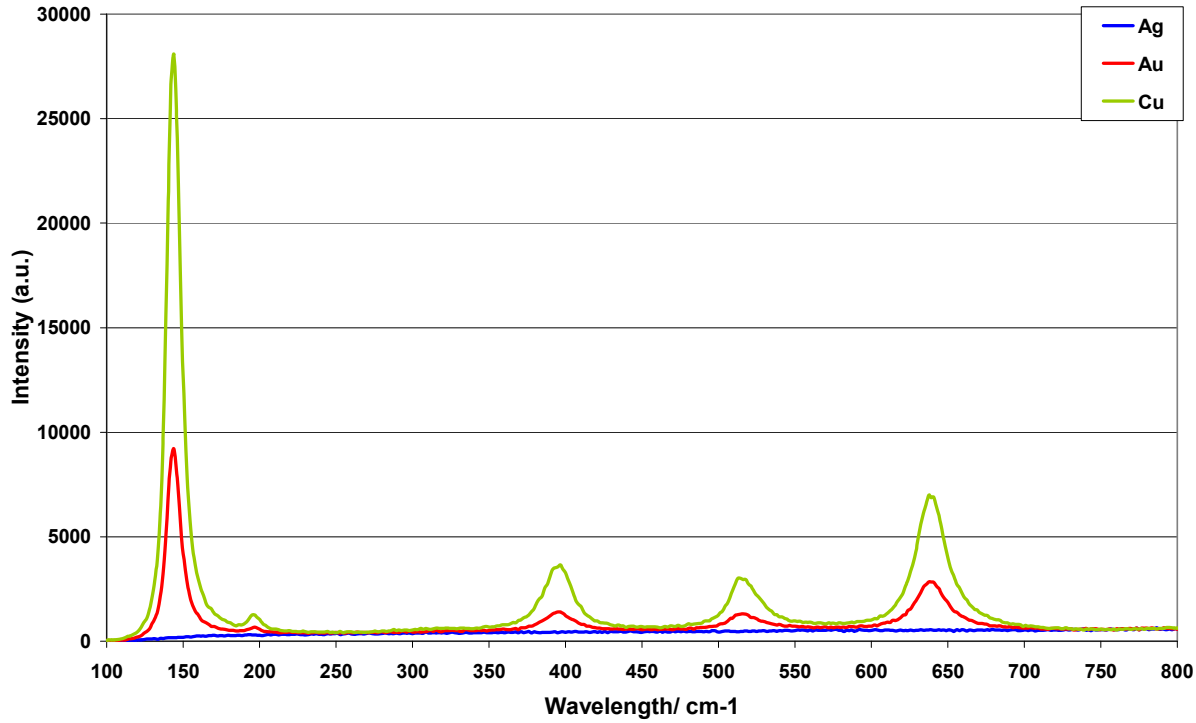

The Raman band frequencies for these titania films (400-600 °C) are assigned the following vibration modes:

147 ±2 cm^{-1}	E_g	phononic mode (*v6*)
200 ±3 cm^{-1}	E_g	phononic mode (*v5*)
396 ±4 cm^{-1}	B_{1g}	phononic mode (*v4*)
517 ±2 cm^{-1}	$A_{1g} + B_{1g}$	phononic mode (*v2* + *v3*)
640 ±4 cm^{-1}	E_g	phononic mode (*v1*)

The change in intensity of the Raman bands could be related to the thickness of the film or the crystallinity of the film but these dynamic films appear to be more uniform than static films and therefore the dopant used may have affected the intensity of the bands. The intensity trend with dopant Ag >Cu >Au, at 400 °C, the

intensity trend at 600 °C is probably the same but unfortunately no Ag spectra could be ascertained on the sample.

5.2.5.3 Summary of Raman analysis

Raman spectra for TiO_2 films formed in the presence of Cu, Ag, Au, (400 °C) and Ag, Au and Cu, (600 °C) exhibit typical anatase phase peaks[146, 147, 161]. According to the work by Yee Hong Chee, *et al.* the anatase phase should be dominant up to a synthesis temperature of about 700 °C but the rutile phase should still be formed between the temperature range of 420-700 °C; there is no apparent evidence of the rutile phase being formed at the higher temperatures here[156]. The AACVD/CVD prototype reaction chamber head used does not confine the substrate within a confined or enclosed space, all gaseous vapours, at standard atmospheric pressure, are allowed to vent to a much larger area; the duration of the substrate under the reaction chamber is also short; resembling the commercial production process more accurately and therefore the conditions required for the formation of the rutile phase, even at higher temperatures, may not be supported. The XRD spectra were much more amorphous in nature whereas the Raman spectra are easier to identify with the anatase phase. The presence of Au or Ag metallic/oxide phase was not expected as they are poor Raman scatterers. The presence of Cu metallic/oxide either as Cu, CuO[164-170], Cu_2O[166-174] or Cu_3O_2[169, 170] was also not detected[165-190].

5.2.6 Contact angle analysis

5.2.6.1 Undoped and doped Au, Ag and Cu TiO_2 films, 400-600 °C

Both the undoped and Au, Ag and Cu doped TiO_2 films at 400 °C had very similar contact angles (θ~80°) before irradiation, after irradiation the Au and Ag doped TiO_2 films contact angles (θ~37°) were slightly less than the undoped TiO_2 control (θ~40°) and the Cu doped TiO_2 film contact angle (θ~55 °) was significantly larger than the control, see fig. 127 a). Similar trends were observed for the contact angles (θ>80°) before irradiation for the undoped and Au, Ag and Cu doped TiO_2

films at 500 °C, see fig. 127 b). When compared to the results at 400 °C there was a significant drop in contact angle after irradiation for both the undoped TiO_2 film (θ~30°) and Au, Ag and Cu doped TiO_2 films (θ = 24°, 26° and 30°, respectively) at 500 °C, see fig. 127 b). At 600 °C the contact angles for the undoped and Ag, Cu doped TiO_2 films before irradiation were >105°; the contact angles for the Au and Al doped TiO_2 films before irradiation were ~85-90°. After irradiation there was a much more significant drop in contact angle compared to the initial non-irradiated results for all TiO_2 films formed at 600 °C, with the Al doped TiO_2 film contact angle of ~14° the lowest angle and in line with the undoped control (θ = 15°). The Au and Ag doped TiO_2 film contact angles after irradiation were about 20° and the Cu doped TiO_2 film was 30°, see fig. 127 c). The most obvious trend was the decrease in irradiated contact angle with increasing temperature, see table 31.

The titania films either undoped or doped exhibit hydrophilic behaviour when irradiated but do not exhibit the expected superhydrophilicity often seen for many irradiated titania films (≤10°). Increasing crystallinity of the microstructure corresponds to a decrease in the irradiated hydrophilic contact angle and an increase in the non-irradiated hydrophobic contact angles. Water surface contact angles were measured 3 to 5 times to achieve an average with standard deviation (Stdv), the largest variations of Stdv were exhibited by static films, see table 32.

Table 31: Comparison of irradiated θ

	Irradiated Contact Angle, θ/°				
Temperature/ °C	Control	Au	Ag	Cu	Al
400	40	37	37	55	-
500	30	24	26	30	-
600	15	20	20	30	14

- no film made with this dopant at this temperature

Figure 127: Comparison of contact angles, θ, for undoped TiO_2 and TiO_2 films formed in the presence of Au, Ag and Cu (400-600 °C).

a) 400 °C

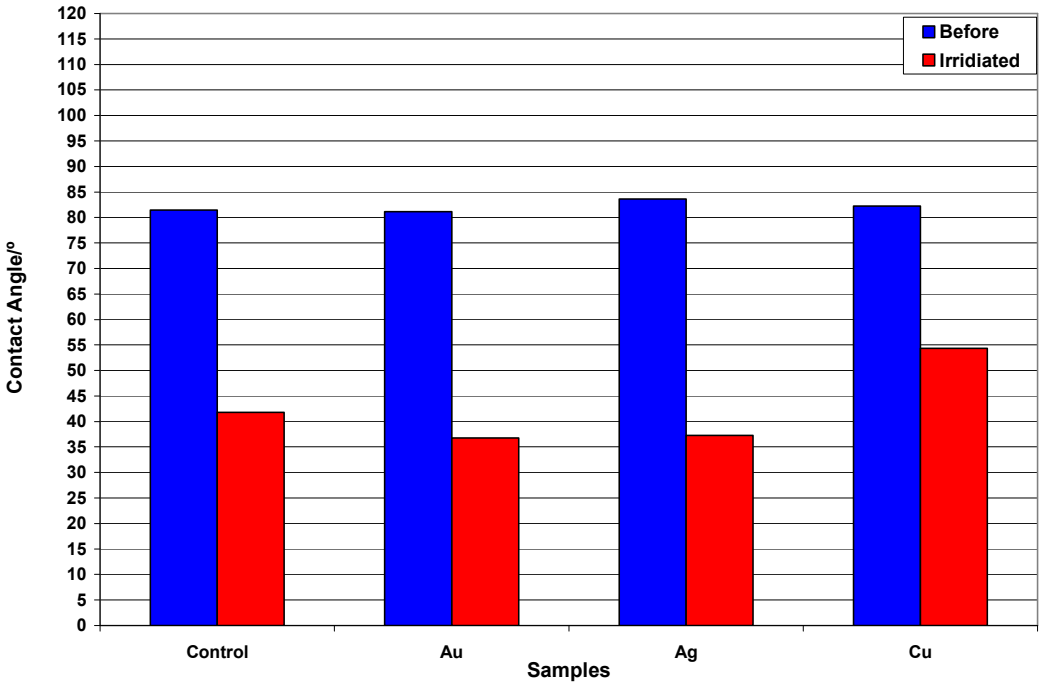

b) 500 °C

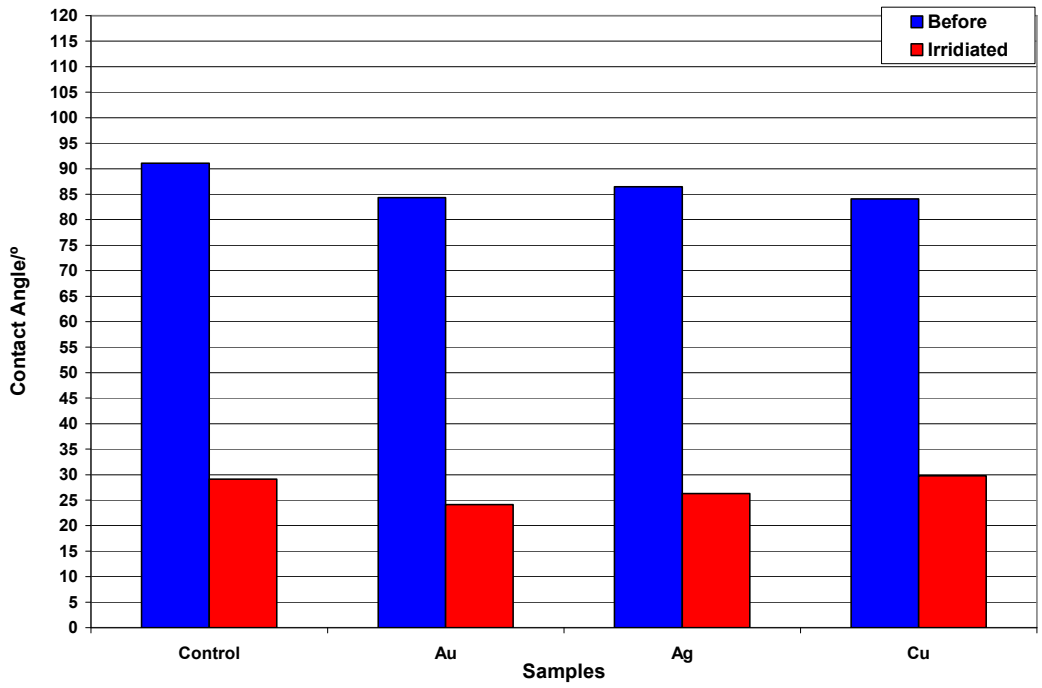

c) 600 °C

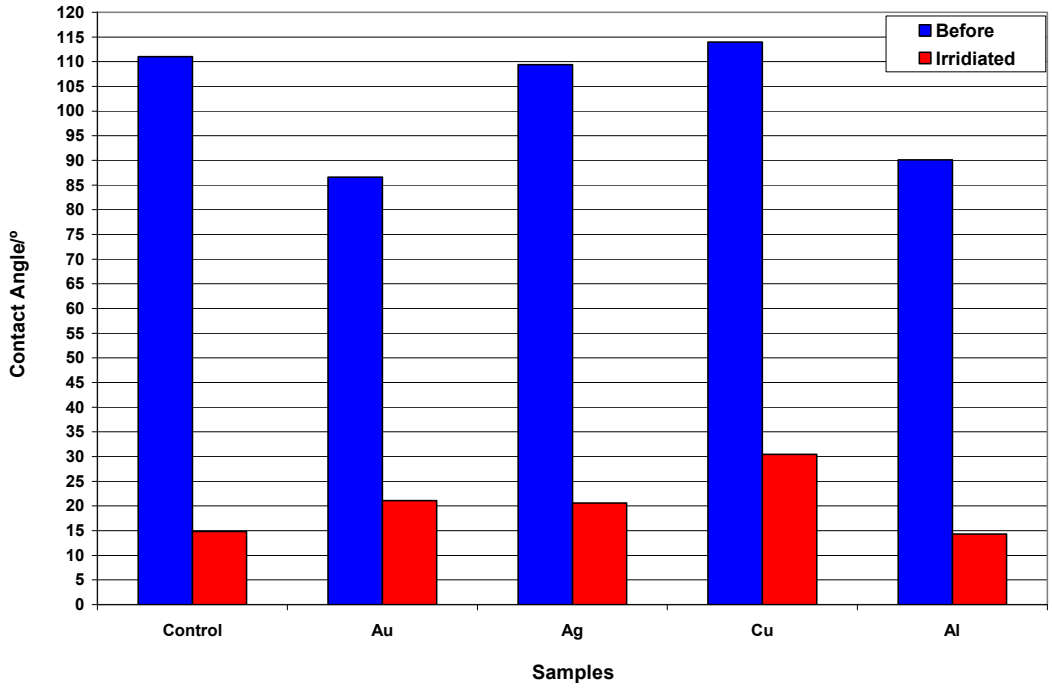

Table 32: Average water surface contact angles (θ) for TiO_2 films grown at 400 °C, 500 °C, 600 °C.

Conditions and Dopants		Contact Angle before irradiation/º		Contact Angle after irradiation/º, 254 nm	
		Average	Stdv	Average	Stdv
600 ºC	Control	111	17	15	6
	Au	87	5	21	2
	Ag	109	5	21	0
	Cu	114	1	31	2
	Al	90	12	14	2
500 °C	Control	91	3	29	12
	Au	84	1	24	1
	Ag	86	1	26	1
	Cu	84	2	30	3
400 °C	Control	81	1	42	7
	Au	81	6	37	9
	Ag	84	2	37	7
	Cu	82	2	54	11

Figure 128: Photographic comparison of the contact angles of undoped and Cu doped TiO_2 films after irradiation (254 nm) at 600 °C: a) TiO_2 control, (θ >90°), b) TiO_2 control, (θ ≤15°), after irradiation (254 nm), c) TiO_2 film in the presence of Cu, (θ >110°), and d) TiO_2 film in the presence of Cu, (θ ≤30°), after irradiation (254 nm) at 600 °C.

a) TiO_2 control

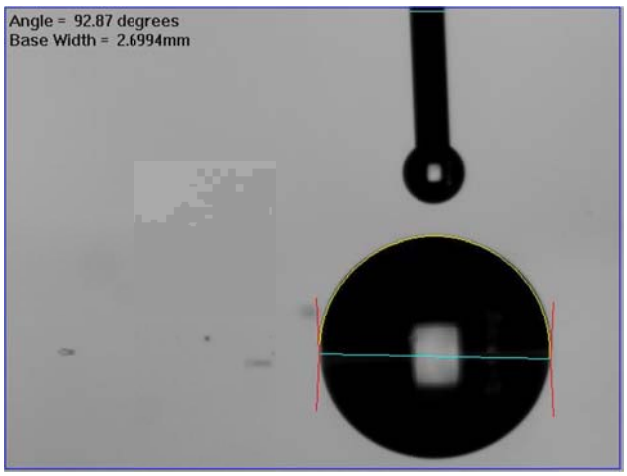

b) TiO_2 control irradiated (254 nm)

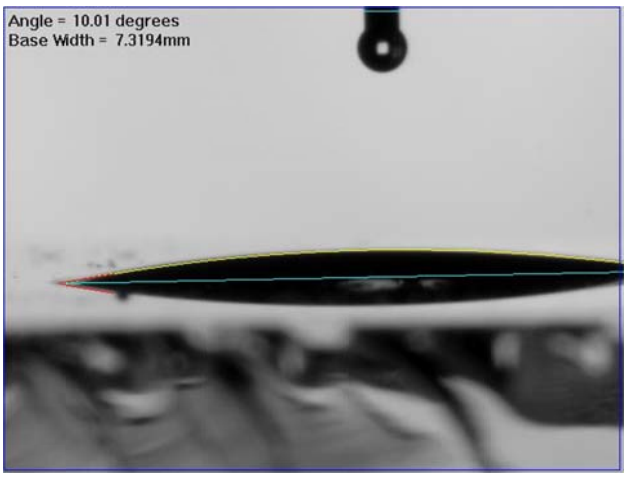

c) Cu TiO_2

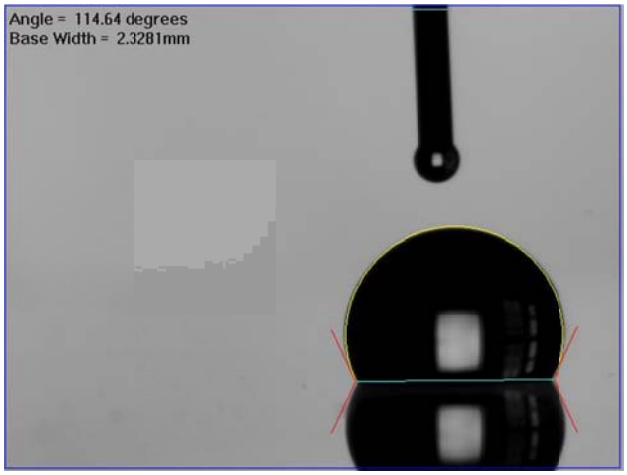

d) Cu TiO_2 irradiated (254 nm)

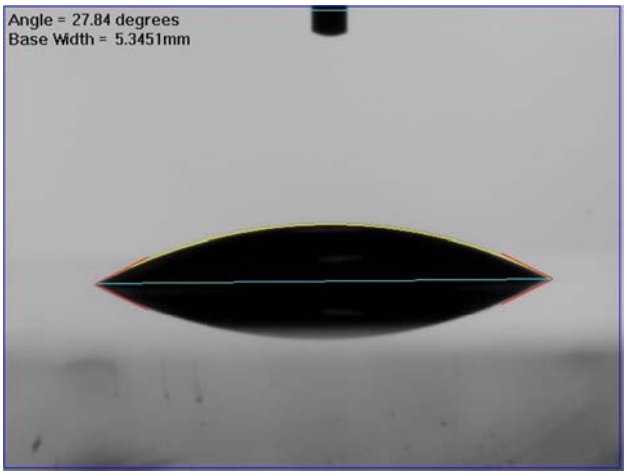

The before and after irradiated contact angles for the TiO_2 and the Cu doped TiO_2 films, at 600 °C, can be seen above, demonstrating the two extremes of values seen, see fig. 128 a-d).

5.2.6.2 Summary of contact angle analysis

The undoped and doped TiO_2 films non-irradiated contact angles at lower synthesis temperatures (400-500 °C) gave very similar hydrophobic results (θ~80°)[157, 192], however an increase in synthesis temperature (600 °C) increased the observed contact angle (θ>105°) becoming superhydrophobic, a result also seen in the recent work by Edusi (Edusi, *et al.*, 2011)[157]. Typical Float glass *e.g.* Pilkington Activ™, would be expected to have a water contact angle of about 70°[178, 193, 194]. The synthesis temperature and the dopant both have an effect on the irradiated value for the contact angle; increasing temperature reflects a decrease in the TiO_2 irradiated contact angle (θ≤15°) as seen in many other examples of TiO_2 thin film synthesis[178, 180, 182, 183, 185, 193-203].

The irradiated contact angle for the Cu doped TiO_2 films appear to not go below 30°, even when synthesis temperature is increased (600 °C), therefore this dopant appears to be detrimental for the superhydrophilic properties of TiO_2 films. At lower synthesis temperatures (400-500 °C) Au and Ag dopants either appear to enhance or at least have no significant negative effect on the superhydrophilicity of TiO_2 films, at higher temperatures (600 °C) the irradiated contact angles rose slightly for Au and Ag doped TiO_2 films (θ~20°), this is in contrast to other TiO_2 synthesis results in the literature where the irradiated contact angles for Ag and Au doped TiO_2 drops ≤ 15°[192, 193]. The Al dopant, if present, also appeared to have no detrimental effect on the irradiated contact angle of TiO_2 film. When compared to other literature results the type of dopant used on a dynamic moving substrate appears to have a more significant effect on the non-irradiated and irradiated contact angle than seen in other TiO_2 low concentration doped films synthesised by either static substrate CVD methods[157, 178, 182, 194-199, 201], Sol-Gel (Dip-Coating or Spray Pyrolysis via annealing/calcining)[179, 185, 192, 193, 202, 203], radical-enhanced atomic layer deposition (RE-ALD)[200] or Magnetron Sputtering[199]. The increase in synthesis temperature correlates to an increase in the crystallinity of the film and the lower, more hydrophilic, surface water contact angles observed upon irradiation (254 nm).

5.2.7 Photocatalytic analysis

5.2.7.1 Resazurin intelligent ink analysis

The Photocatalytic activity of the films was also qualitatively measured using a resazurin-based (Rz) intelligent ink[204, 205]. The intelligent ink was then spray-coated evenly over the surface of the thin-films. The arrays were subsequently irradiated under 365 nm UVA light in-between regular intervals of flat-bed digital scanning. The redox dye in the intelligent ink is photo-reduced in a two-step mechanism from resazurin (Rz), royal blue, to resorufin (Rf), pink, to bleached intermediates, colourless; these reductions were monitored via UV-visible absorption spectroscopy. If a film rapidly turned the ink pink and then colourless, it was highly photoactive, and if it took longer, it was less photoactive. A comparison between reaction rates of undoped and doped Au, Ag, Cu and Al TiO_2 films were made for the synthesis temperature range (400-600 °C). Changes at λ ~630 nm are indicative of complete Rz conversion to Rf and changes at λ ~510 nm are indicative of a maximum formation of the Rf intermediate[204, 205].

5.2.7.1.1 Comparison of the change of absorbance at 600 nm, Abs_{600}

The comparison of the change of absorbance at 600 nm (Abs_{600}), at lower synthesis temperatures (400, 500 °C), follow an almost expected set of results, see figs. 129 a-a) i, ii b-b) i, ii where the Ag doped TiO_2 films have the fastest observed absorbance changes but the results at a higher synthesis temperature (600 °C) appear to have very different absorbance trends, see fig. 129 c-c) i, ii:

Abs_{600} trends:

- 400 °C Ag >Cu >Au >control
- 500 °C Ag >Au >Cu >control
- 600 °C Cu >Al >Ag >control >Au

Figure 129: Comparison of Rz indicator ink change in Absorbance at 600 nm, Abs_{600}, and First-order rate plots (s^{-1}) a) 400 °C, b) 500 °C, c) 600 °C.

a) i) 400 °C

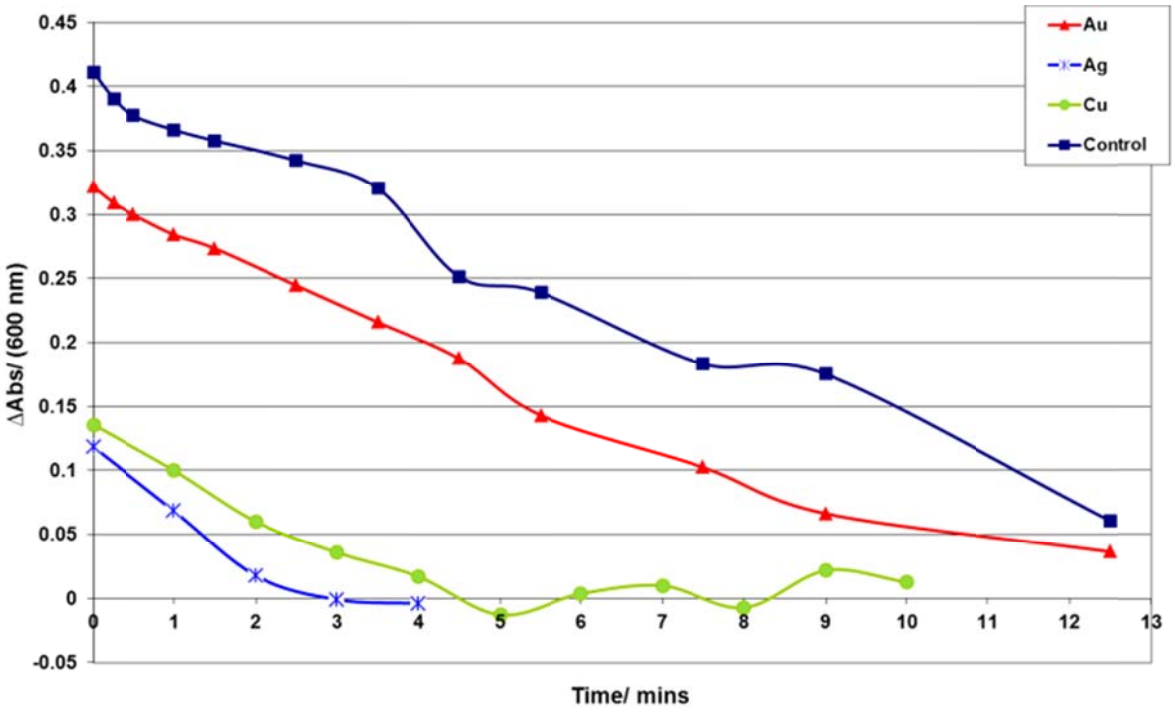

ii) First-order plot

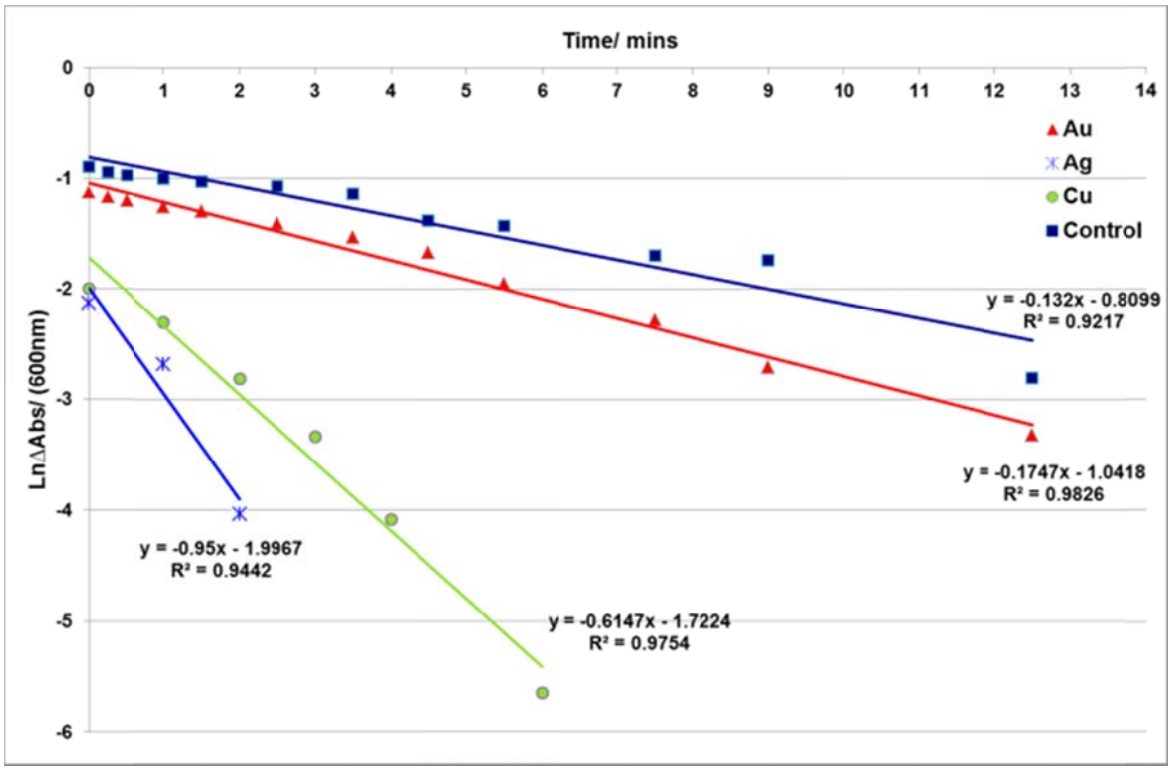

b) i) 500 °C

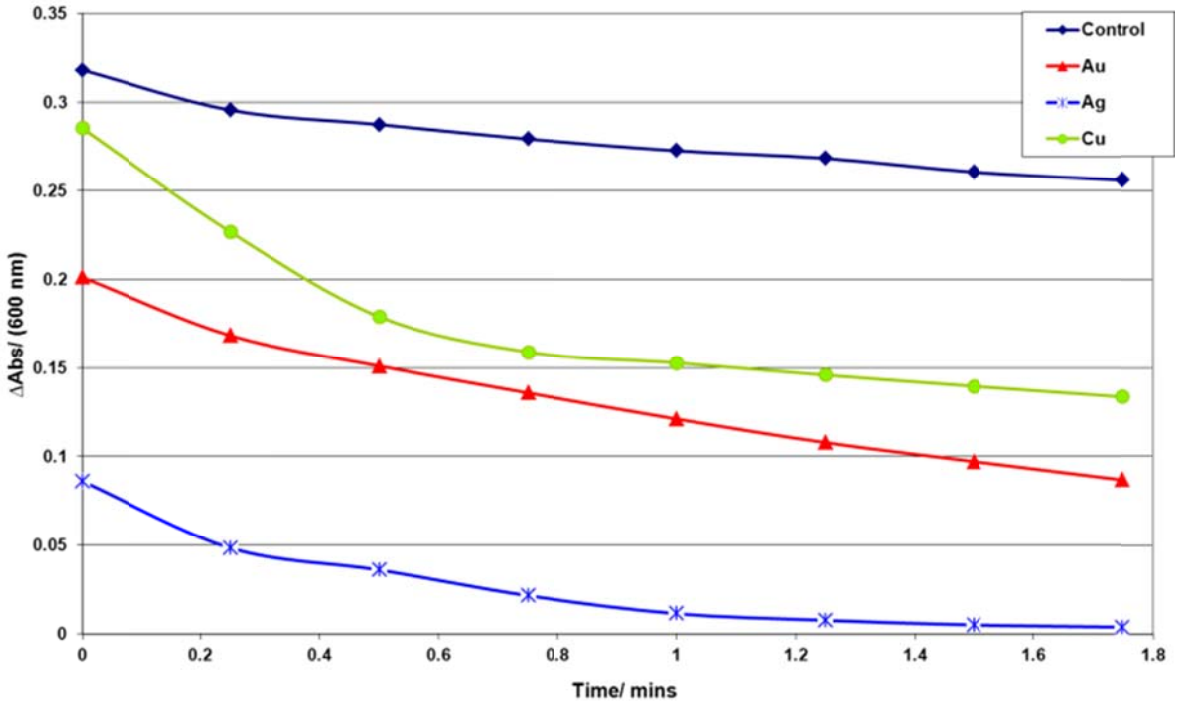

ii) First-order plot

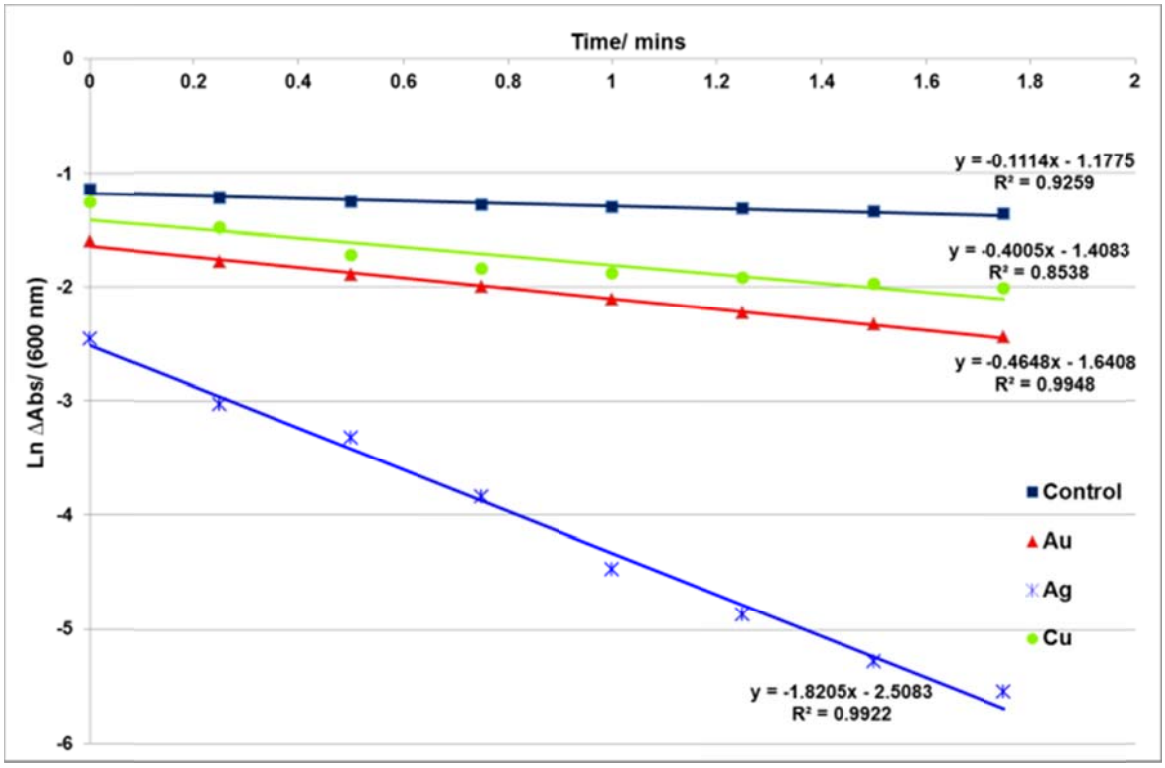

c) i) 600 °C

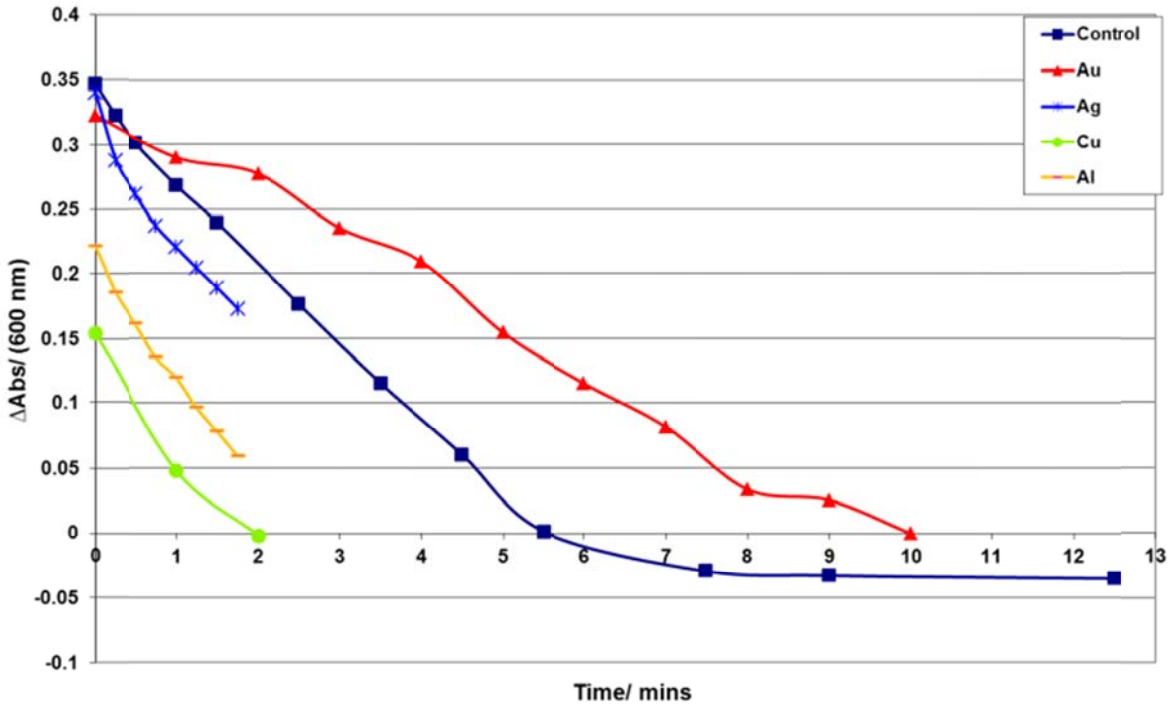

ii) First-order plot

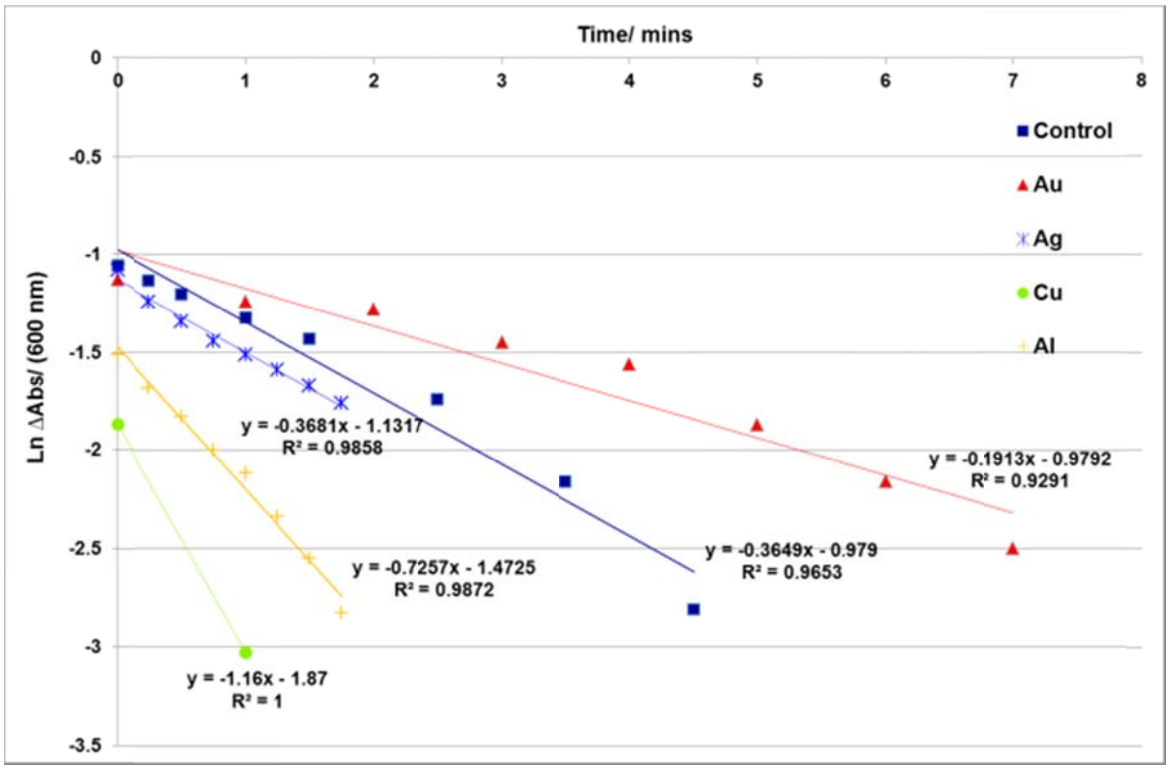

The first-order plots give the following rate constants, k_1, (s^{-1}), see table 33.

Table 33: Table of rate constants, k_1, (s^{-1}) for undoped and Au, Ag, Cu and Al doped TiO_2 films, 400-600 °C first-order rate plots.

TiO_2 Film	Rate constant (s^{-1}) at 400 °C	Rate constant (s^{-1}) at 500 °C	Rate constant (s^{-1}) at 600 °C
Control	1.46×10^{-2}	1.50×10^{-2}	1.16×10^{-2}
Au	1.40×10^{-2}	1.05×10^{-2}	1.38×10^{-2}
Ag	6.45×10^{-3}	2.68×10^{-3}	1.15×10^{-2}
Cu	9.04×10^{-3}	1.12×10^{-2}	5.19×10^{-3}
Al	-	-	8.05×10^{-3}

– no Al doped TiO_2 films made at this temperature

The rate constants, k_1, (s^{-1}) reported here are a relative measure they are not fundamental constants and will vary with light intensity and sample orientation. The results for the change in absorbance at 600 nm shows that both temperature and dopant have an effect on the order of fastest observed decrease.

5.2.7.1.2 Comparison of UV-Vis absorbance, 400-600 °C

A comparison of UV-Vis absorption spectra for undoped and doped Au, Ag, Cu and Al TiO_2 films are described below for the synthesis temperature range 400-600 °C. The Rz indicator reaction has a characteristic decreased absorbance transition from Rz (royal blue; λ_{max} ≈608 nm) to Rf (pink; λ_{max} ≈584 nm) for photomineralisation of the Rf intermediate; therefore a peak shoulder shift within the red part of the spectrum to lower wavelengths signifies the transition from Rz to Rf [204, 205].

5.2.7.1.2.1 UV-Vis absorbance, 400 °C

Comparison of UV-Vis absorption spectra for undoped and Au, Ag and Cu doped TiO_2 films (400 °C) are described below, see fig. 130 a-d). The undoped TiO_2 film has a substantial decrease in absorption in the red part of the spectrum within 1.75 mins, the only doped film to come close to this result is the Ag doped film, at 4 mins, films formed in the presence of Au (12.5 mins) and Cu (10 mins) appear to increase the time required for photomineralisation.

Figure 130: Comparison of the UV-Vis absorption spectra (400-800 nm) of the reduction of the Rz indicator ink for undoped and doped Au, Ag and Cu TiO_2 films, (400 °C).

a) Control

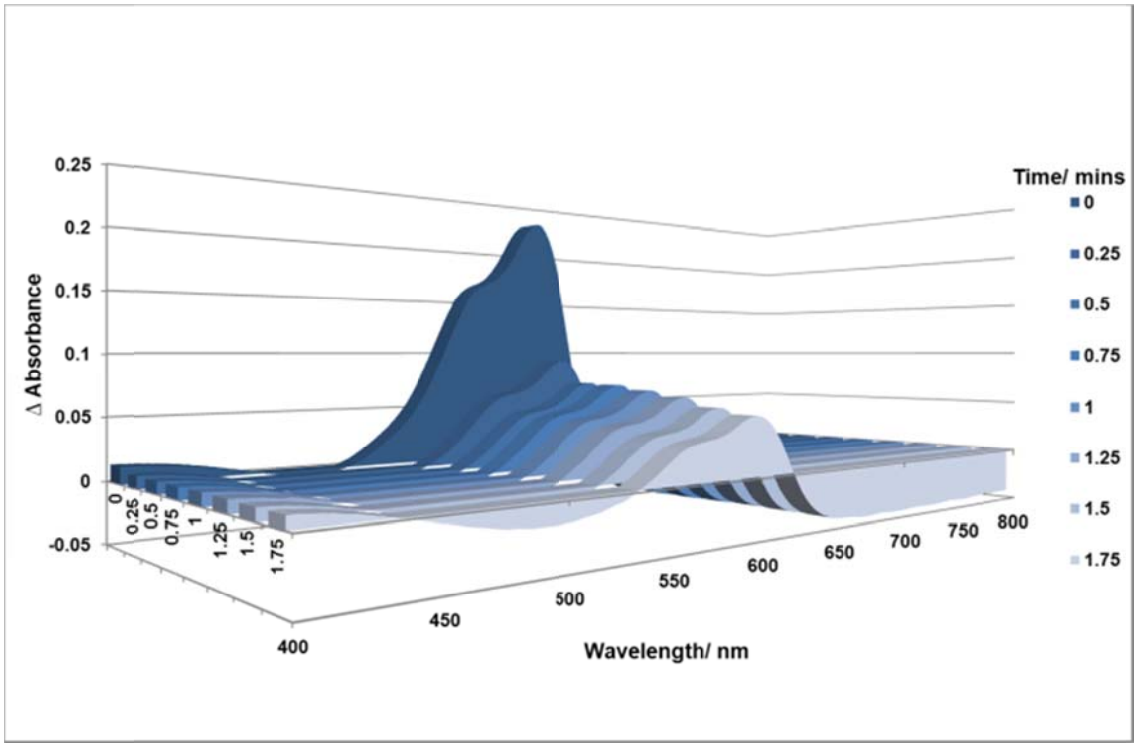

b) Au

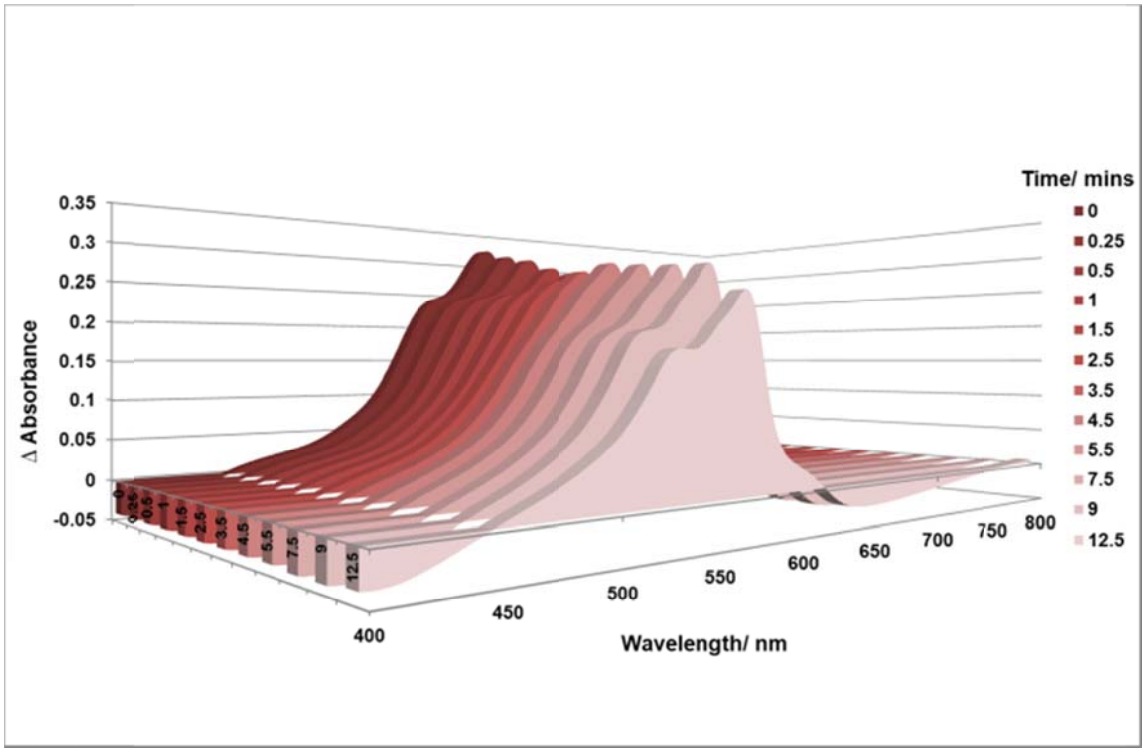

c) Ag

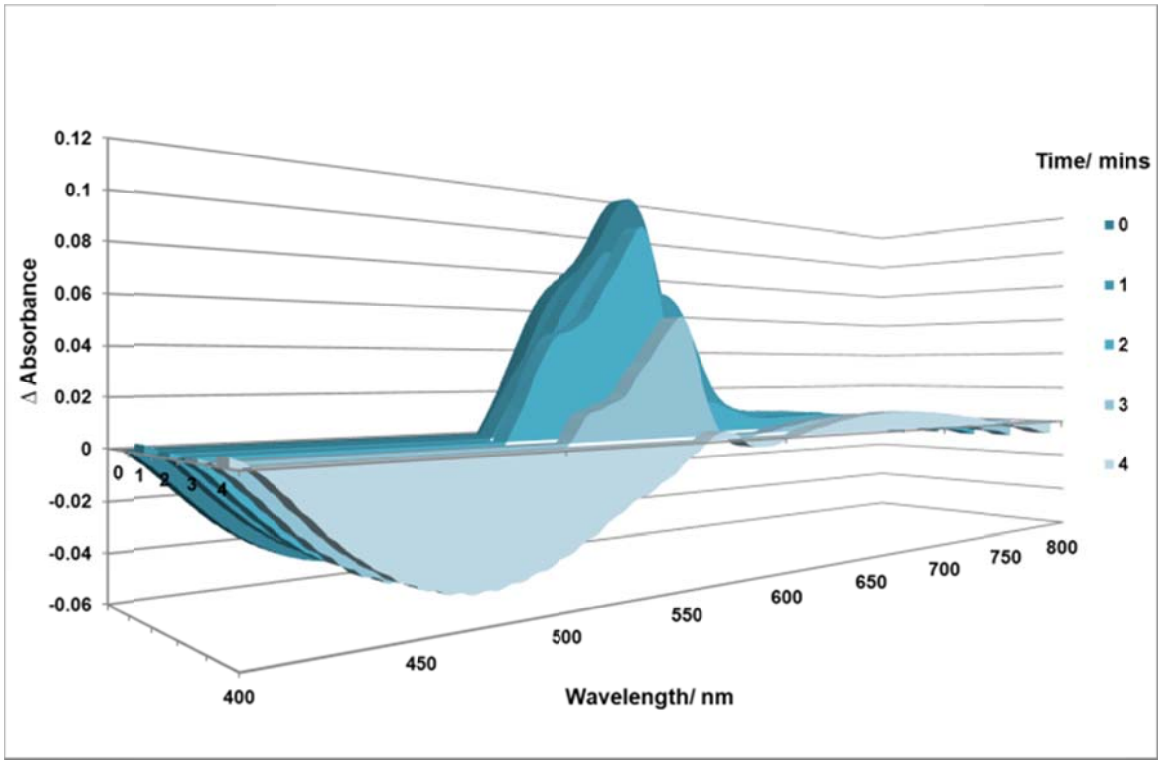
Time/ mins
0
1
2
3
4
Δ Absorbance
0.12
0.1
0.08
0.06
0.04
0.02
0
-0.02
-0.04
-0.06
400
450
500
550
600
650
700
750
800
Wavelength/ nm

d) Cu

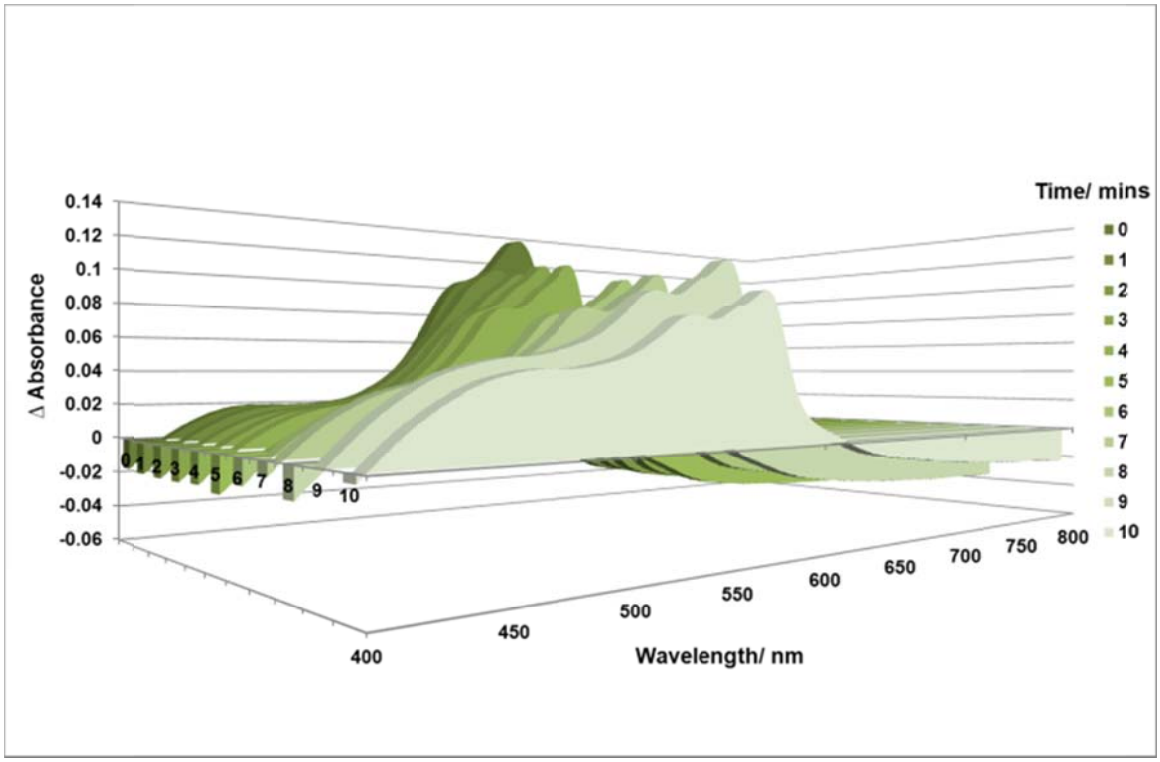
Time/ mins
0
1
2
3
4
5
6
7
8
9
10
Δ Absorbance
0.14
0.12
0.1
0.08
0.06
0.04
0.02
0
-0.02
-0.04
-0.06
400
450
500
550
600
650
700
750
800
Wavelength/ nm

5.2.7.1.2.2 UV-Vis absorbance, 500 °C

Comparison of UV-Vis absorption spectra for undoped and Au, Ag and Cu doped TiO_2 films (500 °C) are described below, see fig. 131 a-d). The TiO_2 films formed at higher temperatures (500 °C) in the presence of dopants (Au, Ag, Cu) appear to enhance the photomineralisation with the TiO_2 film formed in the presence of Ag displaying a significant decrease in absorption for the red part of the spectrum.

Figure 131: Comparison of dye absorbance over time for undoped and doped Au, Ag and Cu TiO_2 film at 500 °C.

a) Control

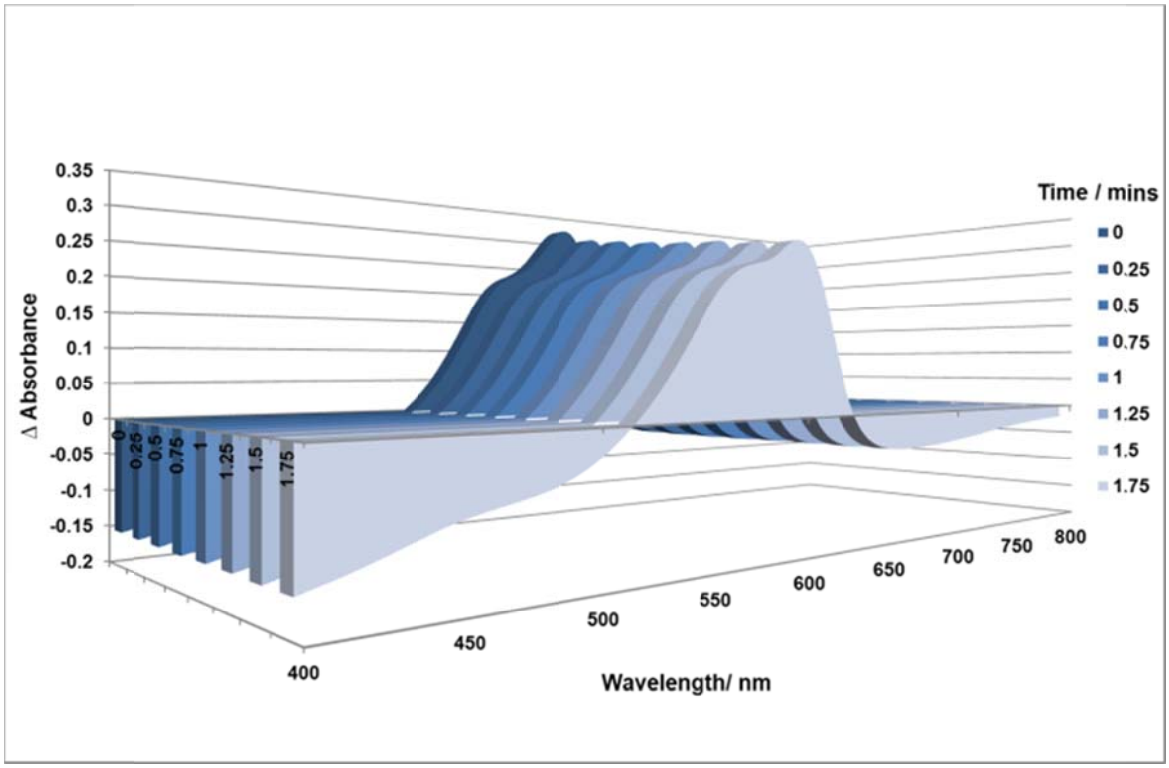

b) Au

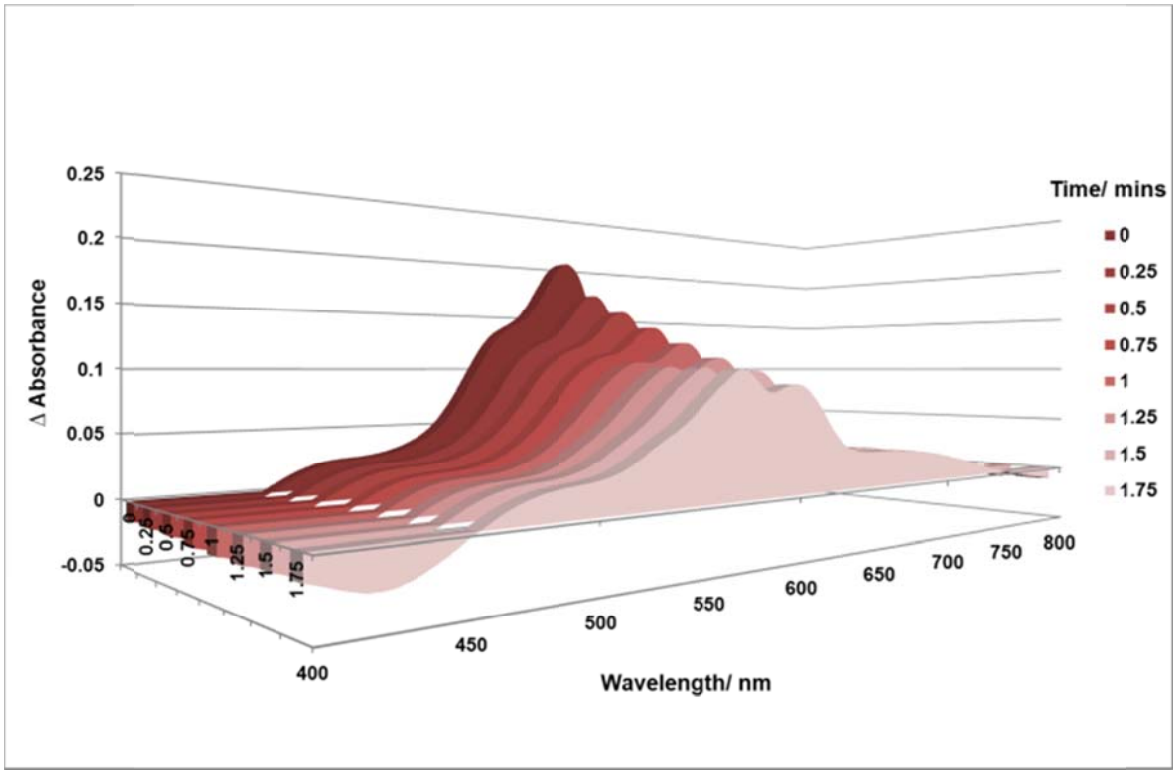
Time/ mins
0
0.25
0.5
0.75
1
1.25
1.5
1.75
Δ Absorbance
0.25
0.2
0.15
0.1
0.05
0
-0.05
400
450
500
550
600
650
700
750
800
Wavelength/ nm

c) Ag

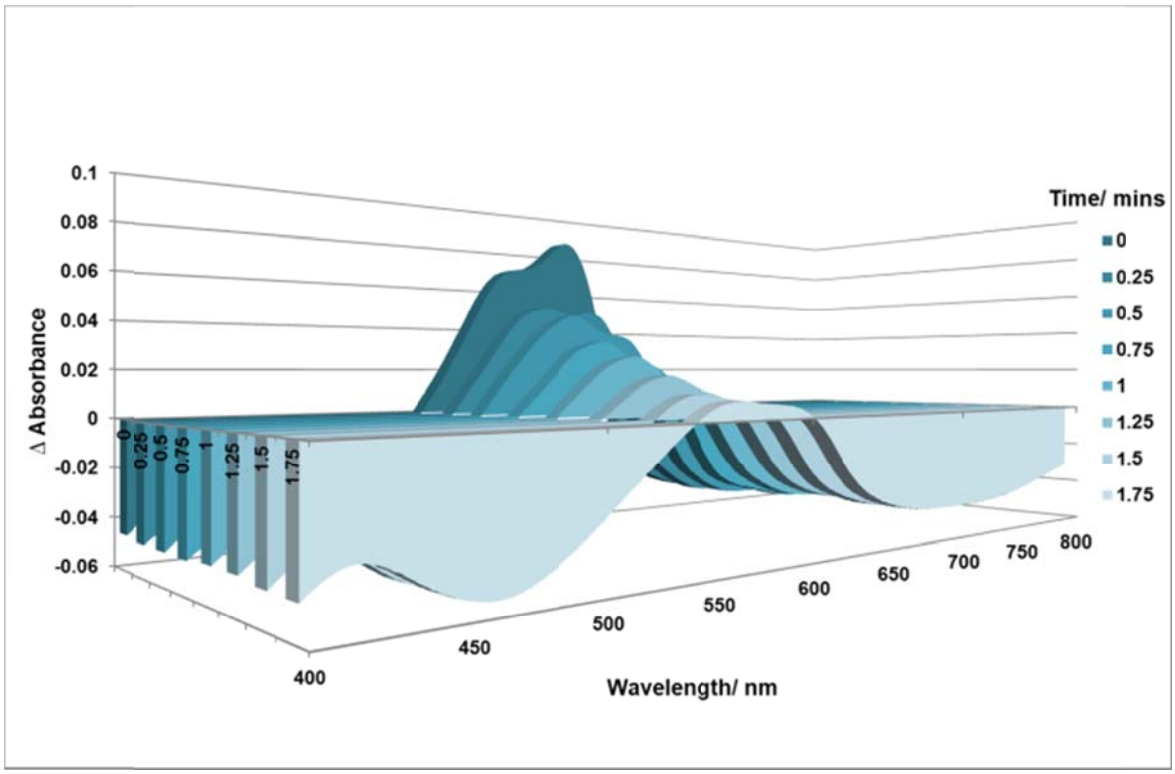
Time/ mins
0
0.25
0.5
0.75
1
1.25
1.5
1.75
Δ Absorbance
0.1
0.08
0.06
0.04
0.02
0
-0.02
-0.04
-0.06
400
450
500
550
600
650
700
750
800
Wavelength/ nm

d) Cu

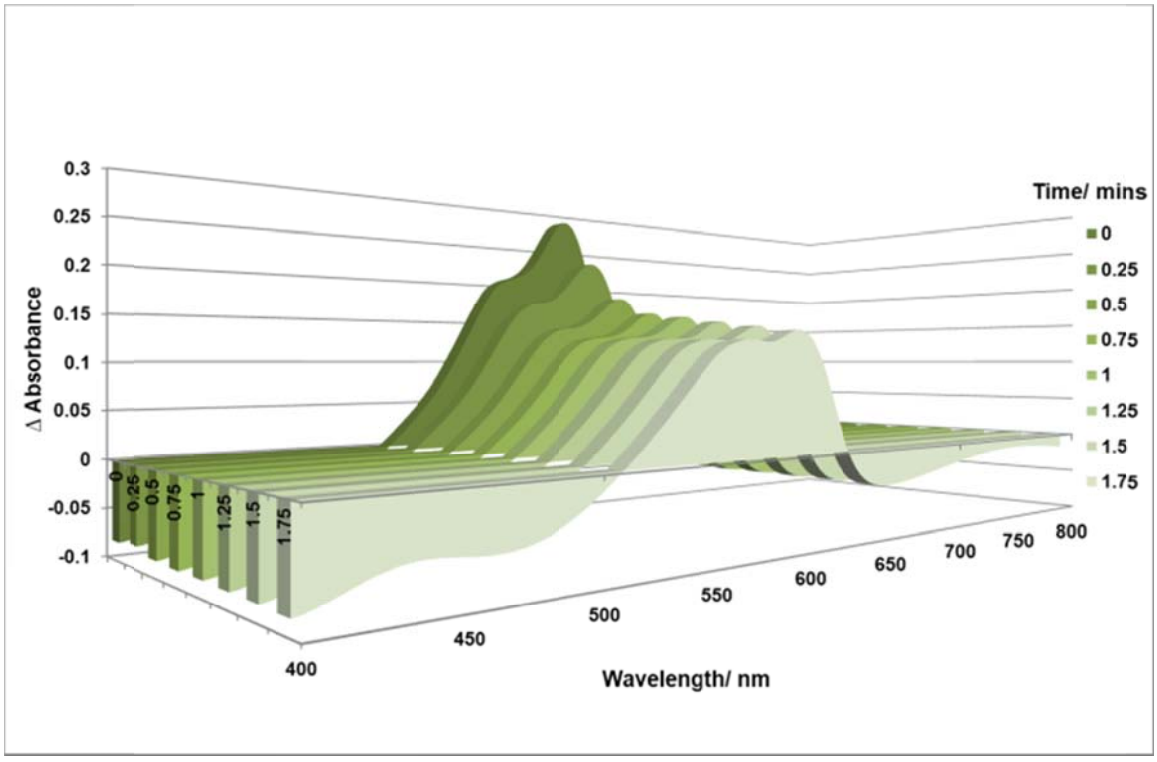

5.2.7.1.2.3 UV-Vis absorbance, 600 °C

Comparison of UV-Vis absorption spectra for undoped and Au, Ag, Cu and Al doped TiO_2 films (600 °C) are described below, see fig. 132 a-e). At this temperature (600 °C) the largest and most rapid decrease in absorption of the red spectrum appears to occur with TiO_2 film formed in the presence of Cu. The Ag doped film has a steady decline in absorption over 1.75 mins but not as significant as the undoped TiO_2 film over a longer time period (12.5 mins); the Au (10 mins) and Al (1.75 mins) doped films appear not to decrease in red absorbance to any significant degree.

Figure 132: Comparison of dye absorbance over time for undoped and doped Au, Ag, Cu and Al TiO_2 film at 600 °C

a) Control

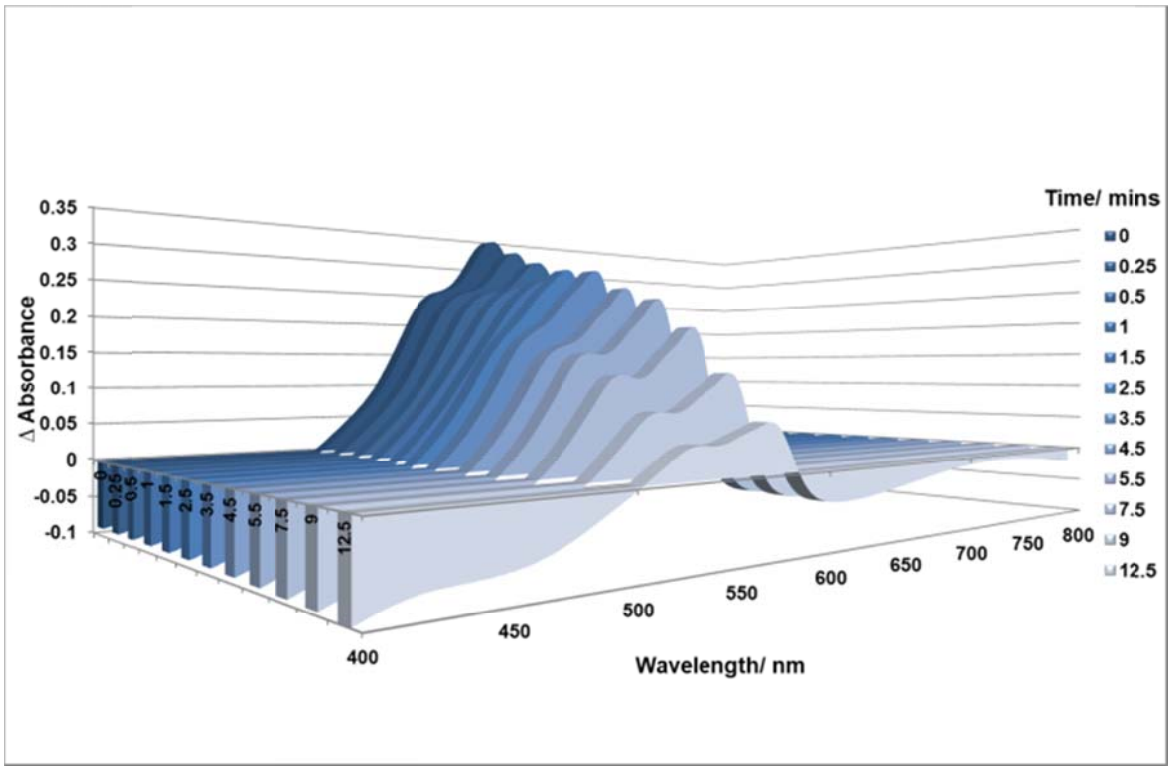

b) Au

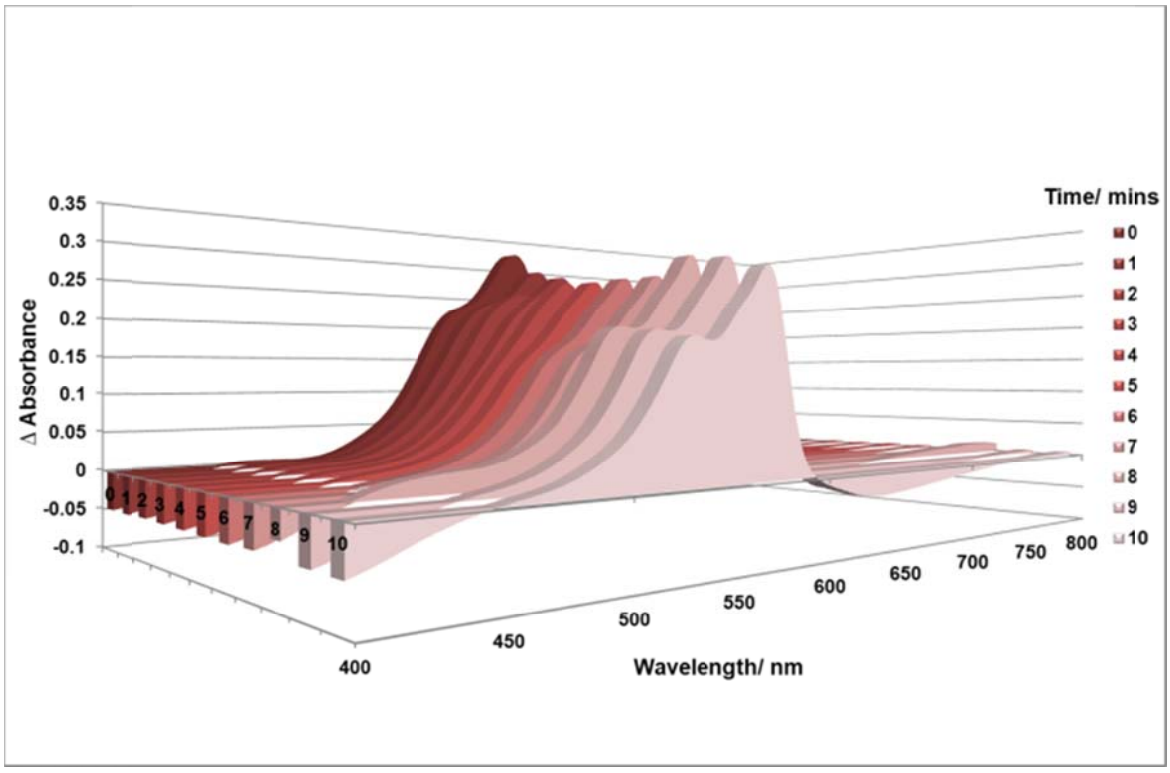

c) Ag

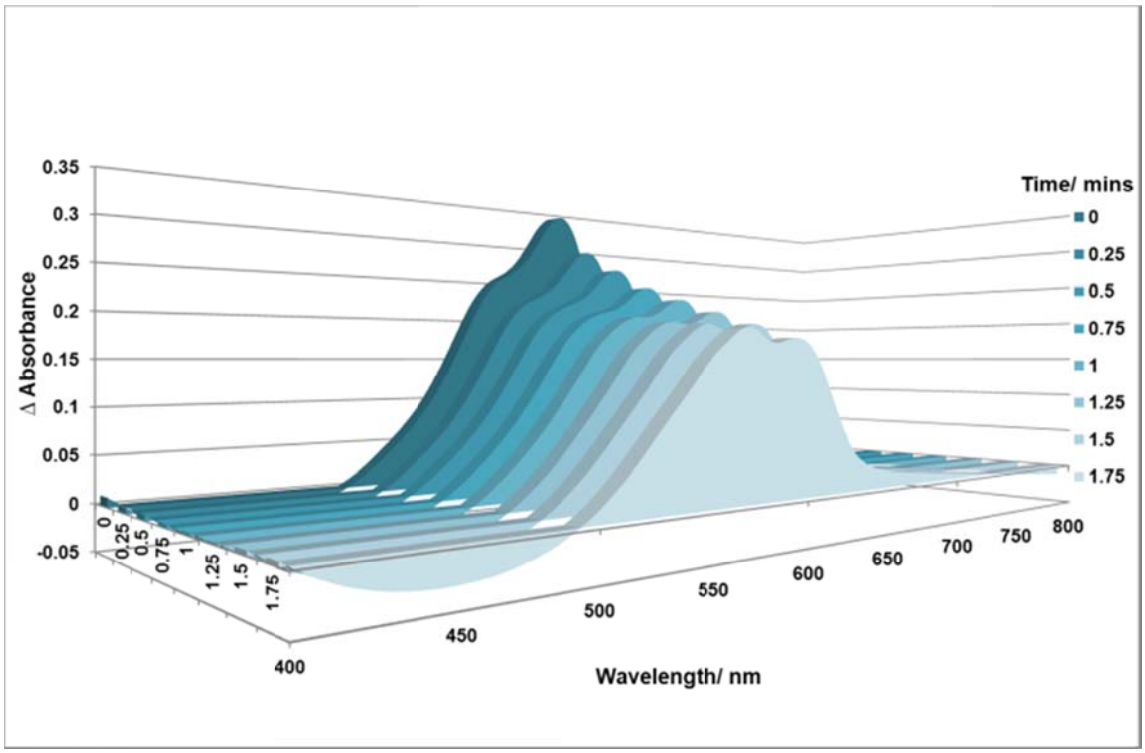
Time/ mins
0
0.25
0.5
0.75
1
1.25
1.5
1.75
Δ Absorbance
0.35
0.3
0.25
0.2
0.15
0.1
0.05
0
-0.05
Wavelength/ nm
400
450
500
550
600
650
700
750
800

d) Cu

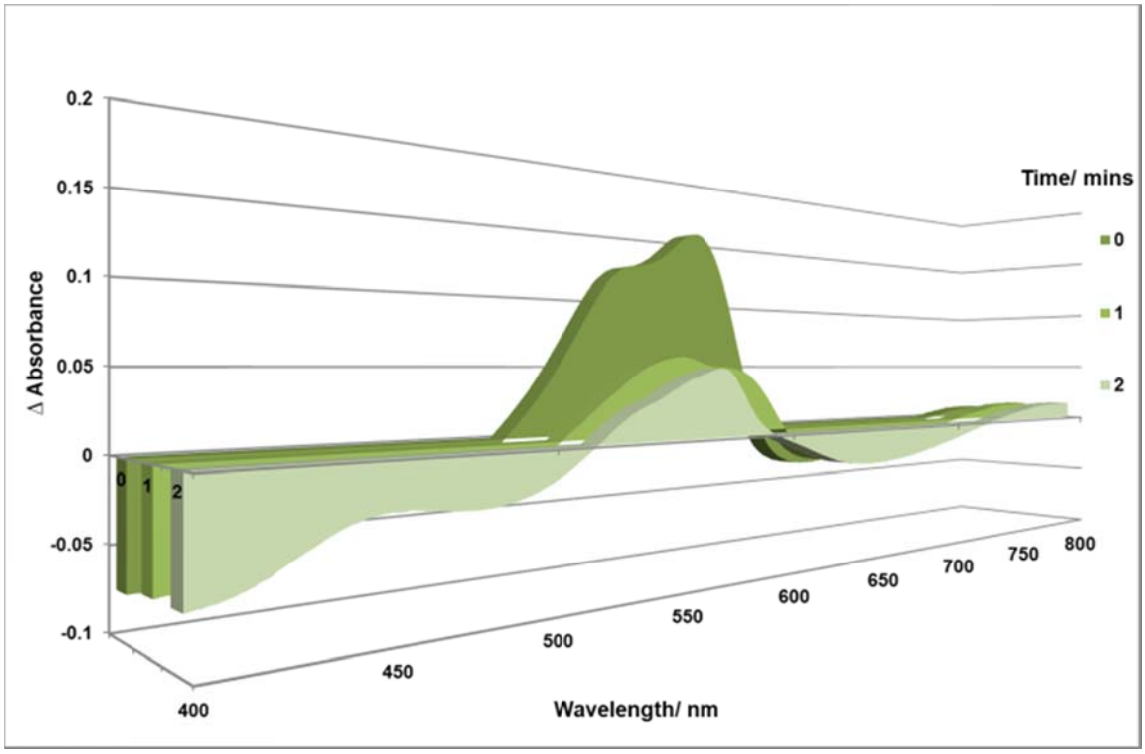
Time/ mins
0
1
2
Δ Absorbance
0.2
0.15
0.1
0.05
0
-0.05
-0.1
Wavelength/ nm
400
450
500
550
600
650
700
750
800

e) Al

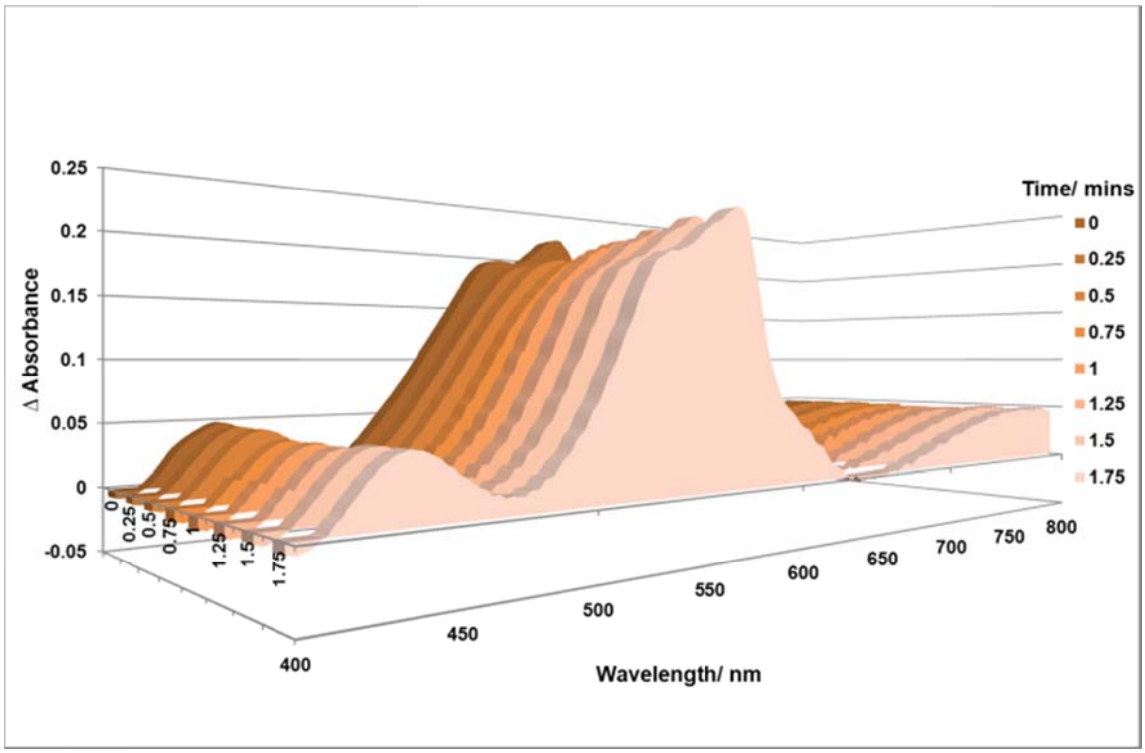

There may be some evidence of Au, Ag and Cu SPR peaks for TiO_2 films synthesised at 400 °C; there are only two main peaks seen in the TiO_2 control film whereas there are several absorbance's seen for TiO_2 films formed in the presence of Au, Ag and Cu (~530, 555 and 570 nm), see table 24. An extra peak absorbance is also observed for Au doped TiO_2 film (~478 nm) at 500 °C. For TiO_2 films synthesised at 600 °C extra absorbance peaks (~435, 770 nm) are only observed with the Al dopant.

5.2.7.2.3 Comparison of photocatalytic activity, Rz test, (400-600 °C, 365 nm)

Comparison of photocatalytic activity of undoped and doped Au, Ag, Cu and Al TiO_2 films (400-600 °C) using the Rz test (UVC 365 nm), see fig. 133. Synthesis temperature affects photocatalytic rate; the general trend indicates that higher synthesis temperatures corresponds to an increase in photocatalytic activity, dopants do have an effect with the Ag doped TiO_2 (600 °C) appearing to have the greatest molecule destruction rate (4.08×10^{12}) above that of the undoped TiO_2 at 600 °C, (2.90×10^{12}).

Figure 133: Comparison: number of molecules destroyed (UVC 365 nm) of undoped and doped Au, Ag, Cu and Al TiO_2 films (400-600 °C).

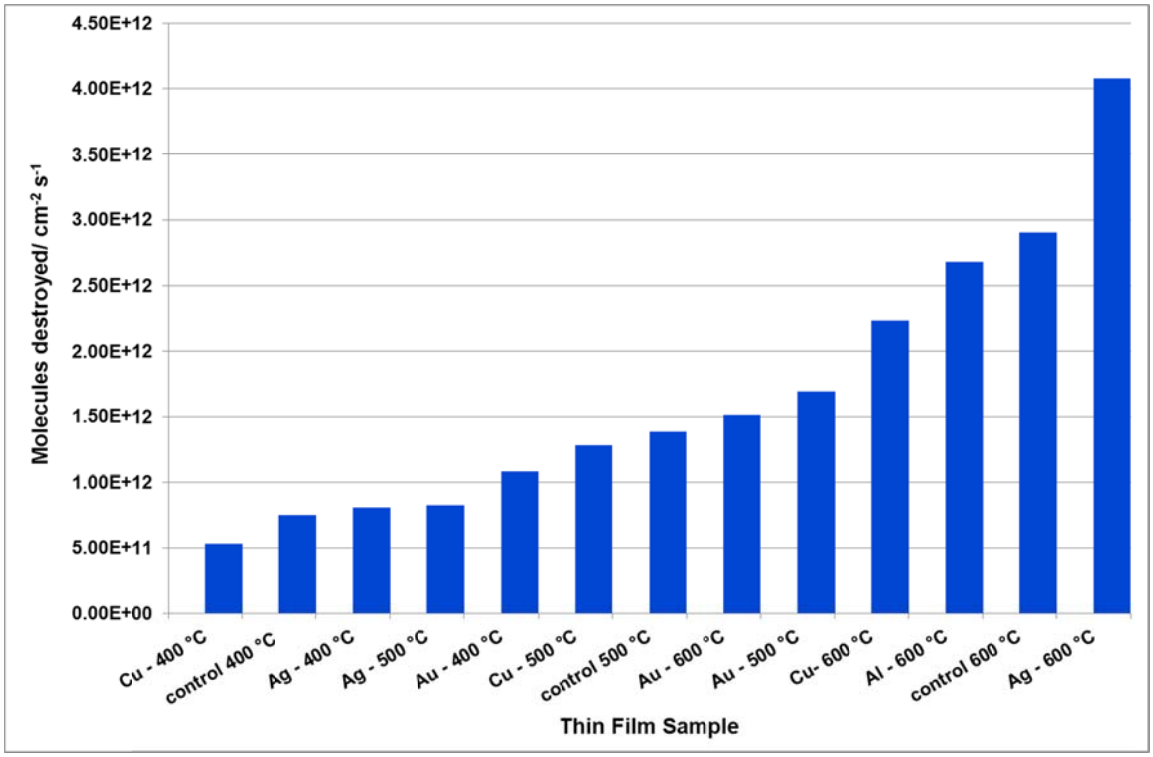

5.2.7.1.3.1 Summary of photocatalytic activity, RZ test, (400-600 °C, 365 nm)

These results appear to show that synthesis temperature, (higher crystallinity), film thickness and dopants all have an effect on the molecule destruction rate, photocatalytic rate.

General Photocatalytic Dopant Trends

- 600 °C Ag >control >Al >Cu >Au
- 500 °C Au >control >Cu >Ag
- 400 °C Au >Ag >control >Cu

General Thickness Trends (Swanepoel calculations)

- 600 °C Cu >Al >Ag >control >Au
- 500 °C Au >Cu >control >Ag

Films prepared at higher synthesis temperatures (600 °C) appear to increase the molecule destruction rate. At 600 °C Ag is the only dopant to really increase

activity above the control all other dopants appear to have a detrimental effect on activity when compared to the undoped TiO_2. Interestingly once the synthesis temperature drops to 500 °C the dopant used appears to have a greater effect with the Au dopant appearing to enhance the molecule destruction rate more than Ag, a result also seen in the 400 °C films. Extra absorbance peaks are observed with doped TiO_2 films mainly synthesised at 400 °C, these do not occur to the same degree with TiO_2 films synthesised at higher temperatures. This could be evidence of SPR peaks but the absorbance of the host matrix and/or the absorbance shift seen for the Rz to Rf conversion could well be masking this effect at higher temperatures or a reflection of the fact no dopants were included into the TiO_2 host matrix in any significant quantity at higher temperatures (≥ 500 °C).

Recent work by Kundu *et. al*, 2011, confirmed that the rate of photocatalysis is dependent upon film thickness and the addition of noble metal dopants Au/Ag did not give conclusive evidence of an enhancement of photocatalytic activity when compared to plain anatase glass[161]. At higher synthesis temperatures (≥600 °C) the work here appears less dependent on film thickness whereas the thickness of the film at lower temperatures does appear to have a greater effect on photocatalytic behaviour. The effect of the addition of dopants is more discernible at higher synthesis temperatures. Ag, Au do appear to have an enhancement effect upon the photocatalytic rate[161].

Therefore generally photocatalysis of TiO_2 films at:

- Higher synthesis temperatures is dopant dependent
- Lower synthesis temperatures is film thickness dependent

However these are very generalised statements for this specific set of results.

5.2.7.2 Stearic acid test

The analysis of the photodegradation of stearic acid is a convenient method for determining a relative rate of photocatalytic activity of a film[206-210].

Equation 6

The overall reaction corresponds to:

$$C_{17}H_{35}COOH + 26O_2 \xrightarrow{TiO_2/hv} 18CO_2 + 18H_2O$$

A solution of stearic acid ($C_{17}H_{35}COOH$, 0.1M) in methanol was used to deposit a coating of stearic acid by evaporation onto the titania films. The titania films were irradiated with a UV lamp (254 nm, BDH, 2x8 germicidal lamp) at 15 min intervals for 1 hr and IR absorption spectroscopy was used to assess the concentration of stearic acid on the surface of the undoped and doped Au, Ag, Cu and Al TiO_2 films (400-600 °C). The lamp wavelength of 254 nm (4.88 eV) ensures that the radiation exceeds TiO_2 band gap (3.2 eV). Rates of catalysis (molecules cm^{-2} s^{-1}) were calculated when the stearic acid decay profile fitted an appropriate rate law[187, 194, 211, 212]. Typical stearic acid absorptions are given below, see table 34.

Table 34: Stearic acid IR absorptions.

Type of vibration	**Absorption/ cm^{-1}**
C–H Stretch CH_3	2958
symmetric C–H stretch CH_2	2923
asymmetric C–H stretch CH_2	2853

Integration of the peaks gives an approximate concentration of stearic acid on the surface. An integrated area of 1 cm^{-1} between 2800 and 3000 cm^{-1} corresponds to approximately 9.7×10^{15} molecules cm^{-2}[211]. The stearic acid zero-order rate of decay can then be measured by the decrease in concentration over time. The data is given in terms of the raw IR data plotted to show the decrease in integrated area over 1 hr.

5.2.7.2.1 Comparison of photocatalytic absorbance, 400 °C

The absorbance of undoped and doped Au, Ag and Cu TiO_2 (400 °C) films were compared. The area under the curve corresponds to the amount of stearic acid

on the surface and the heights of the lines represent time (0, 15, 30, 45 and 60 mins), see fig.134 a-d).

Figure 134: Comparison of the change in integrated intensity of the C-H stretching region of stearic acid (2800-2960 cm^{-1}) against irradiation time (hrs, 254 nm) for undoped and doped Au, Ag and Cu TiO_2 films, 400 °C.

a) Control

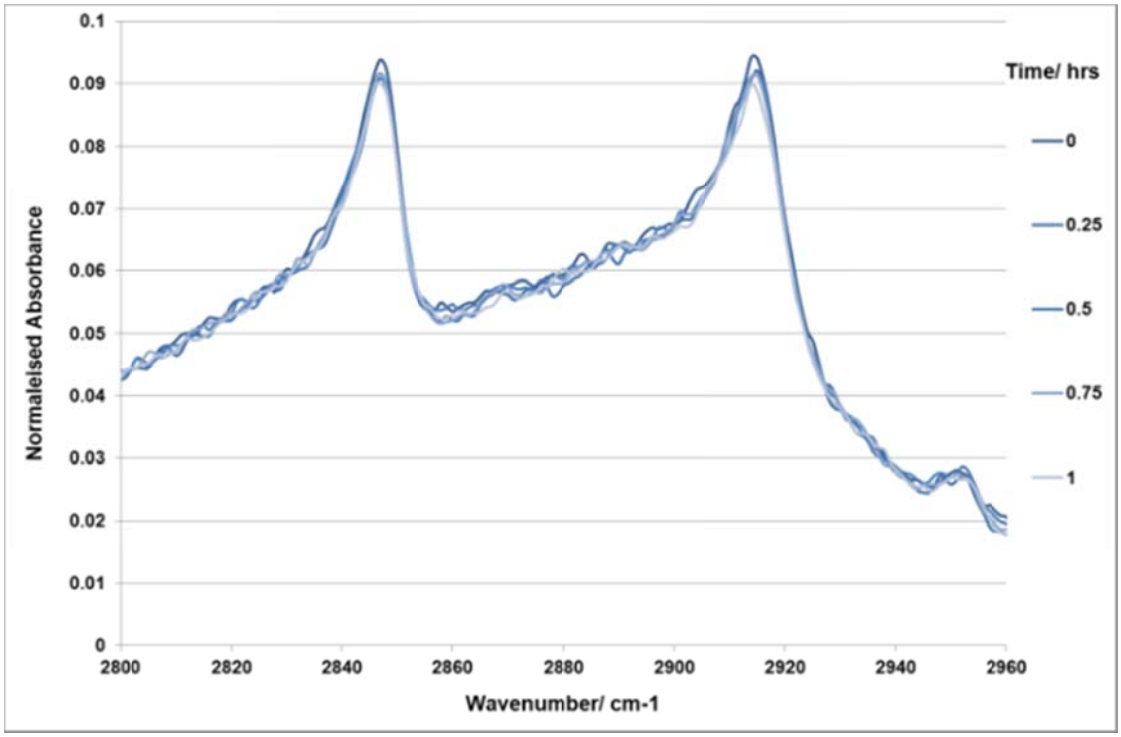

b) Au

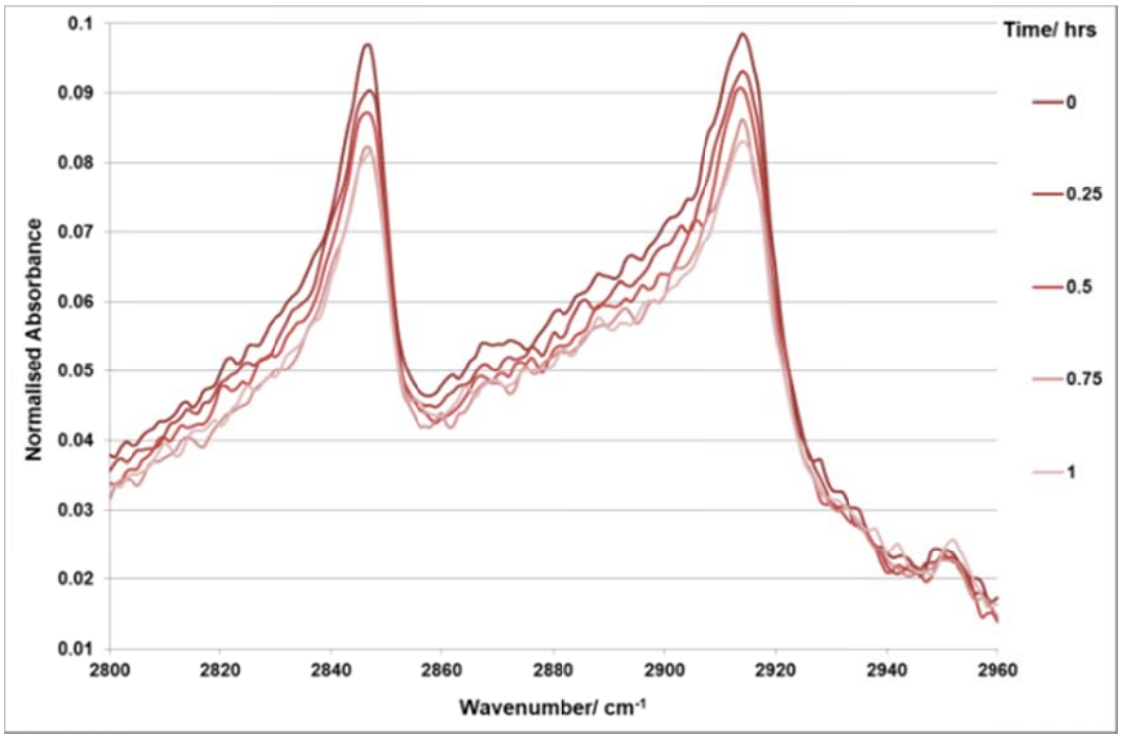

c) Ag

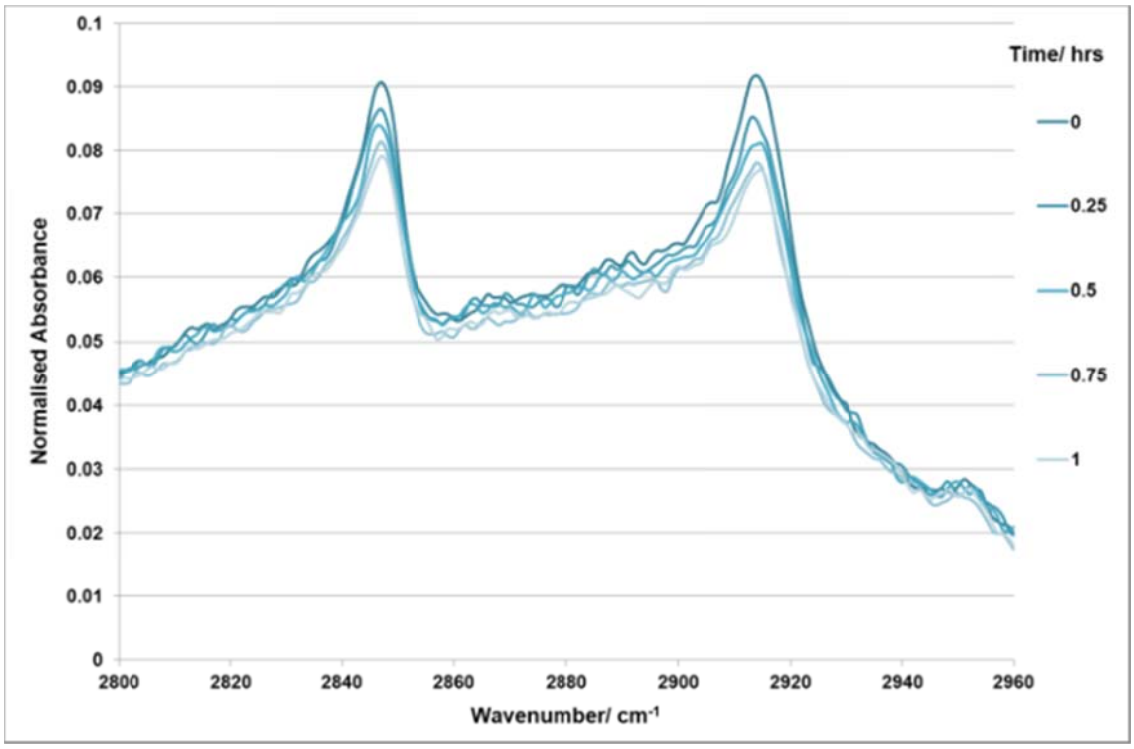

d) Cu

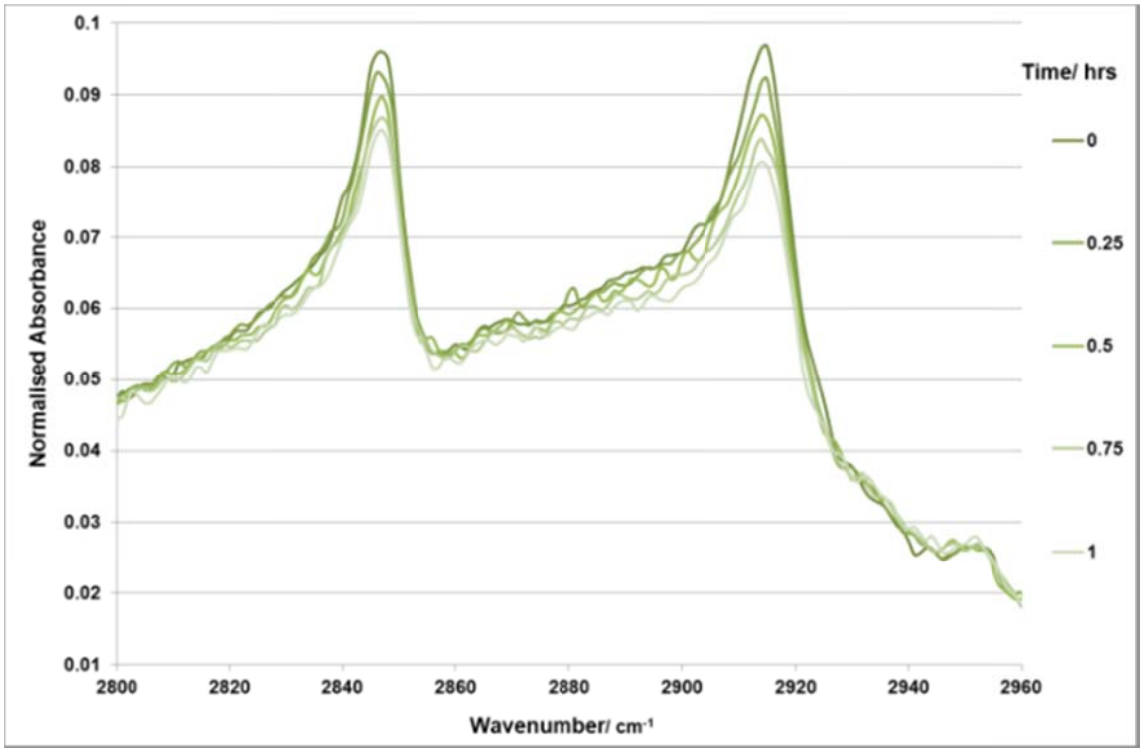

There appears to be little change in the absorbance values for the control, this may be due to the stearic acid layer being too thick *i.e.* no oxygen reaching the surface.

5.2.7.2.2 Comparison of photocatalytic absorbance, 500 °C

The absorbance of undoped and doped Au, Ag and Cu TiO_2 (500 °C) films were compared. The area under the curve corresponds to the amount of stearic acid on the surface and the heights of the lines represent time (0, 15, 30, 45 and 60 mins), see fig.135 a-d).

Figure 135: Comparison of the stearic acid C-H region for irradiated undoped and Au, Ag and Cu doped TiO_2 films, 500 °C. Integrated intensity C-H stretching region: 2800-2960 cm^{-1} and irradiation time/hrs: 254 nm.

a) Control

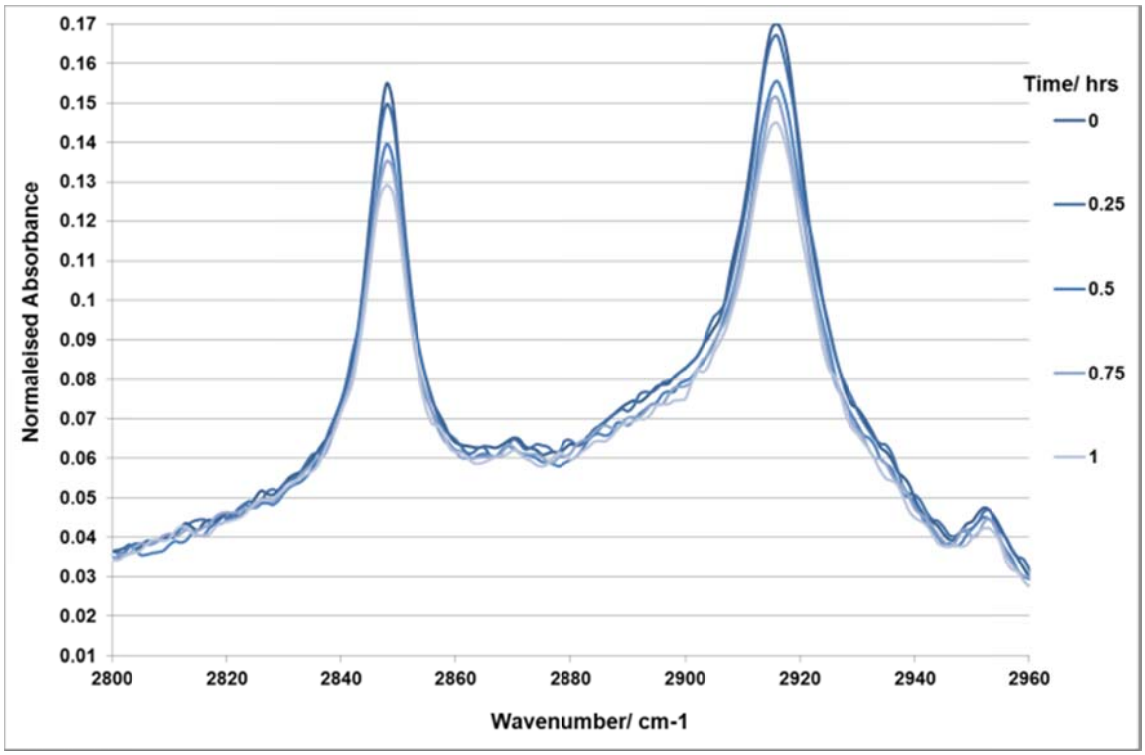

b) Au

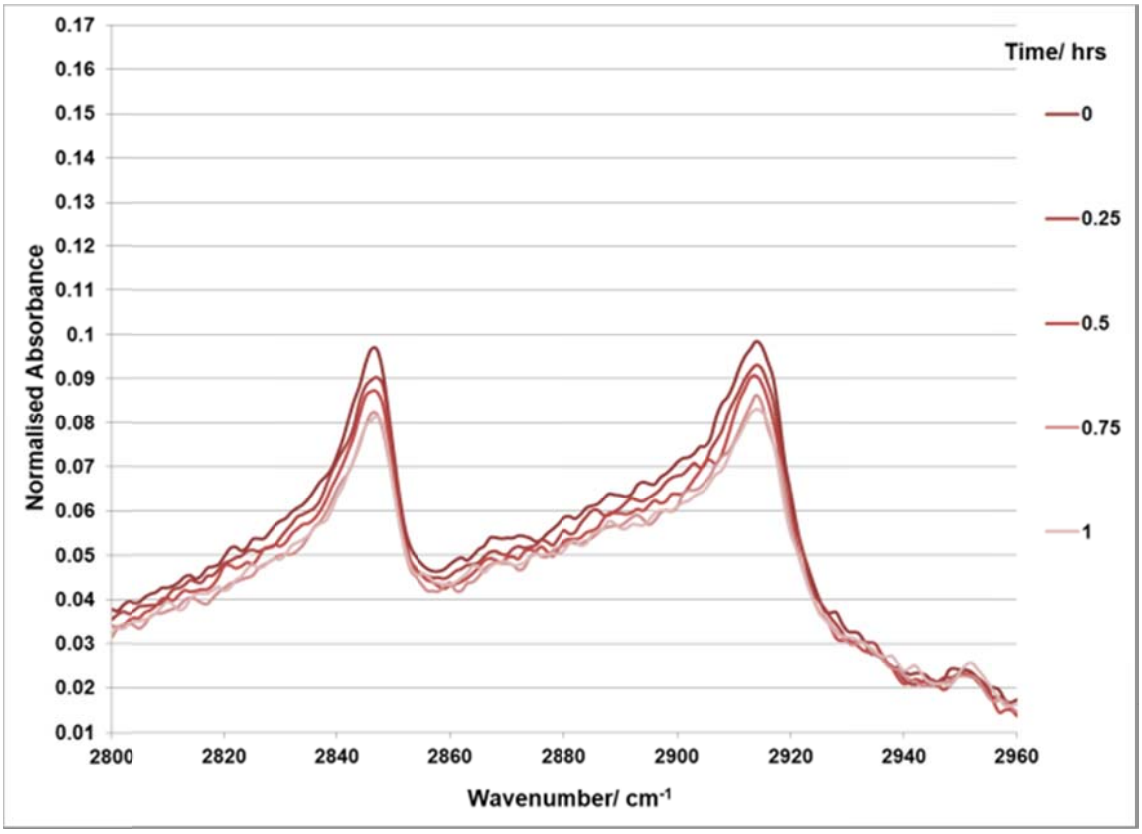
Time/ hrs
0
0.25
0.5
0.75
1
Normalised Absorbance
0.17
0.16
0.15
0.14
0.13
0.12
0.11
0.1
0.09
0.08
0.07
0.06
0.05
0.04
0.03
0.02
0.01
2800
2820
2840
2860
2880
2900
2920
2940
2960
Wavenumber/ cm-1

c) Ag

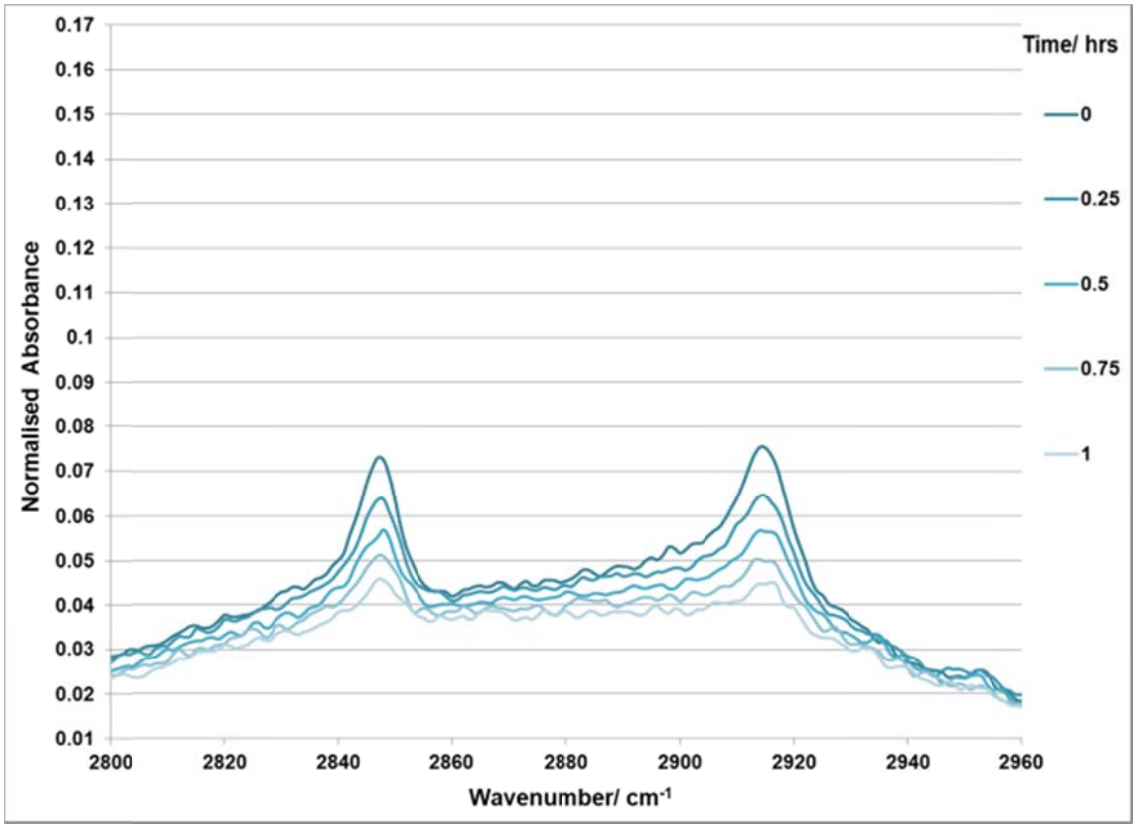
Time/ hrs
0
0.25
0.5
0.75
1
Normalised Absorbance
0.17
0.16
0.15
0.14
0.13
0.12
0.11
0.1
0.09
0.08
0.07
0.06
0.05
0.04
0.03
0.02
0.01
2800
2820
2840
2860
2880
2900
2920
2940
2960
Wavenumber/ cm-1

d) Cu

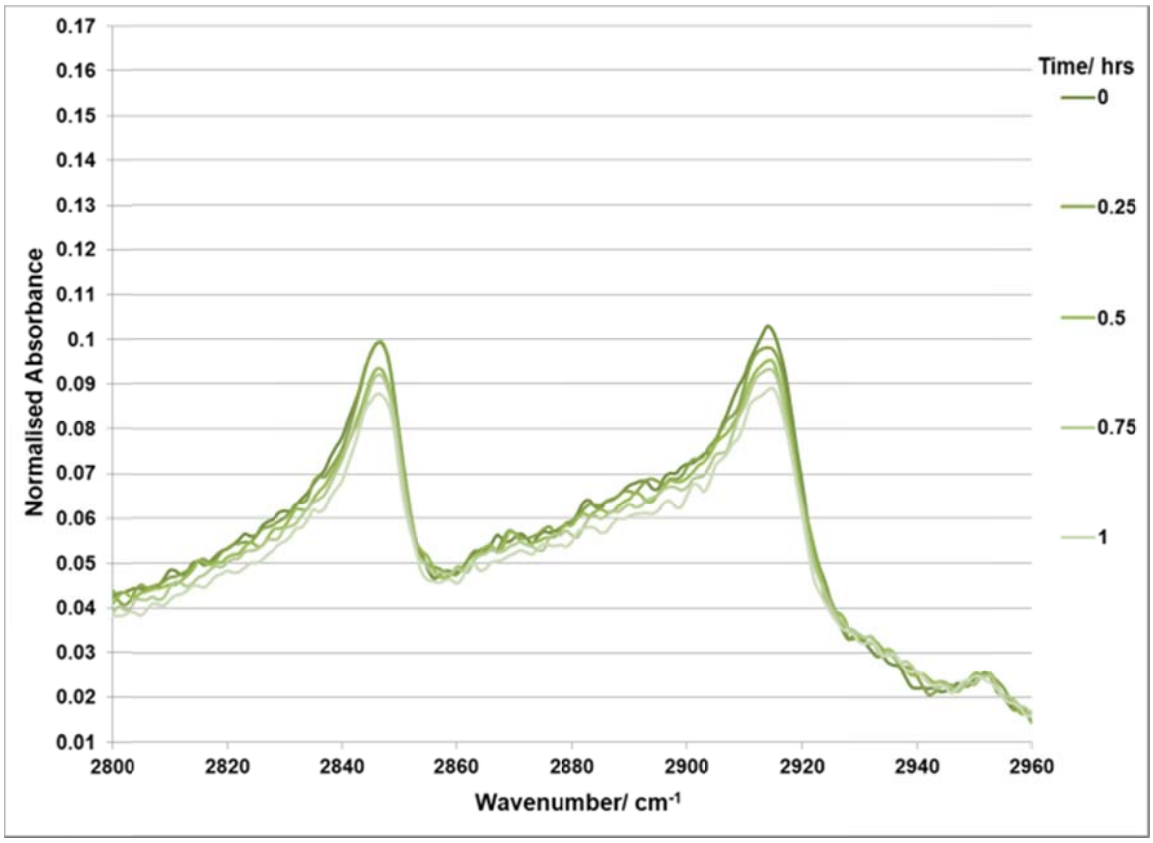

5.2.7.2.3 Comparison of photocatalytic absorbance, 600 °C

The absorbance of undoped and doped Au, Ag, Cu and Al TiO_2 (600 °C) films were compared. The area under the curve corresponds to the amount of stearic acid on the surface and the heights of the lines represent time (0, 15, 30, 45 and 60 mins), see fig.136 a-e).

Figure 136: Comparison of the stearic acid C-H region for irradiated undoped and Au, Ag and Cu doped TiO_2 films, 600 °C: Integrated intensity C-H stretching: 2800-2960 cm^{-1} and irradiation time/hrs: 254 nm.

a) Control

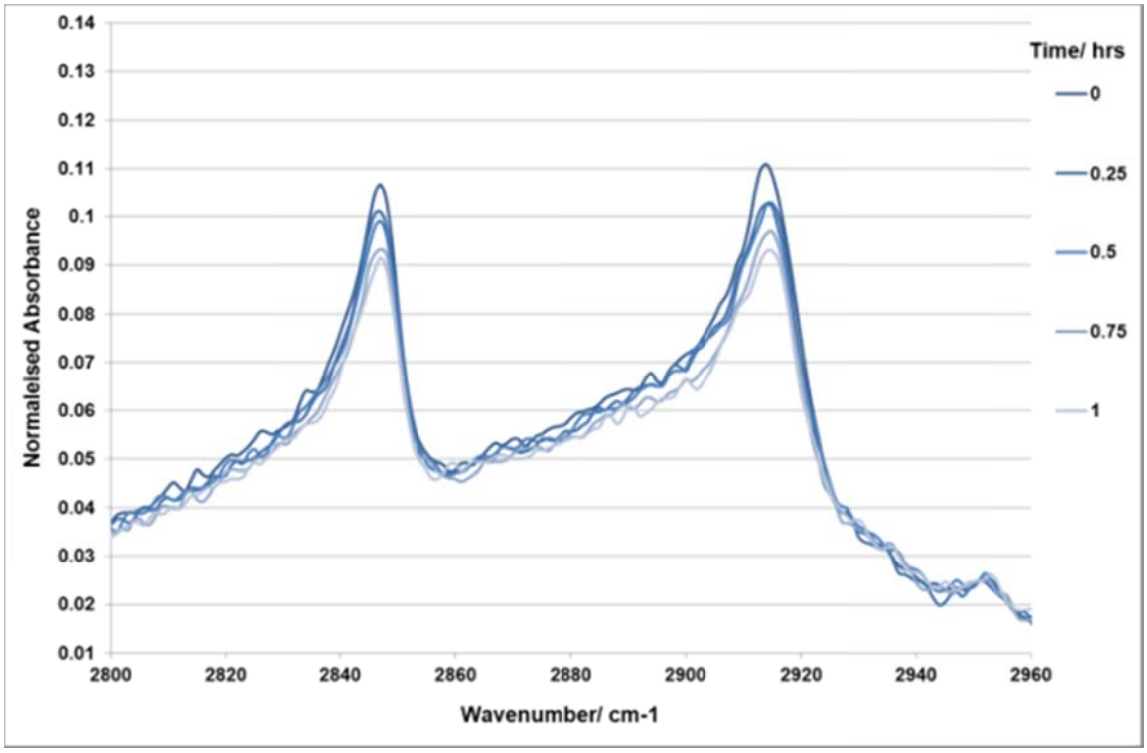

b) Au

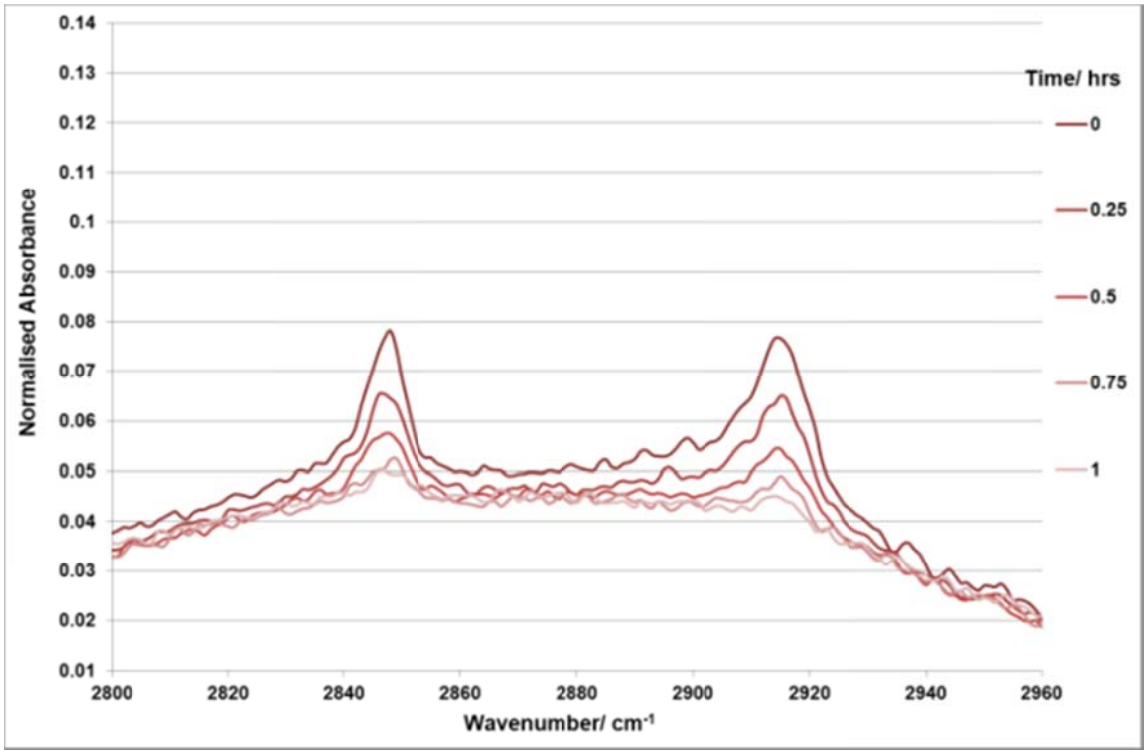

c) Ag

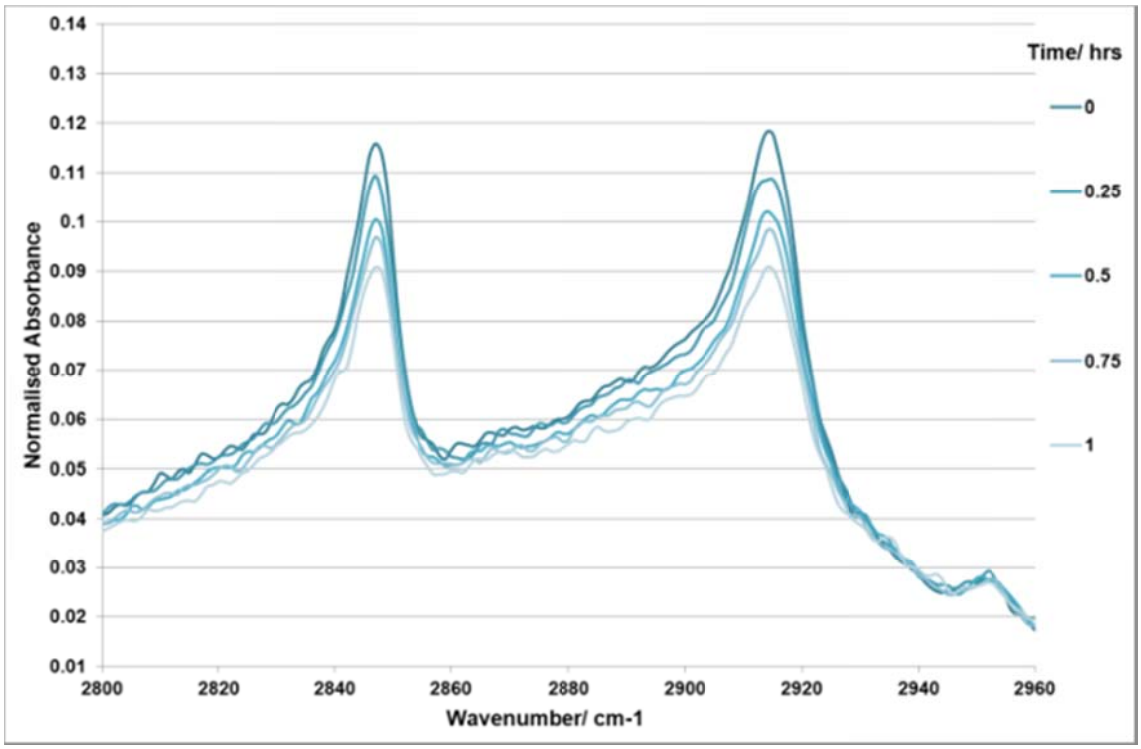
Normalised Absorbance
0.14
0.13
0.12
0.11
0.1
0.09
0.08
0.07
0.06
0.05
0.04
0.03
0.02
0.01
2800
2820
2840
2860
2880
2900
2920
2940
2960
Wavenumber/ cm-1
Time/ hrs
0
0.25
0.5
0.75
1

d) Cu

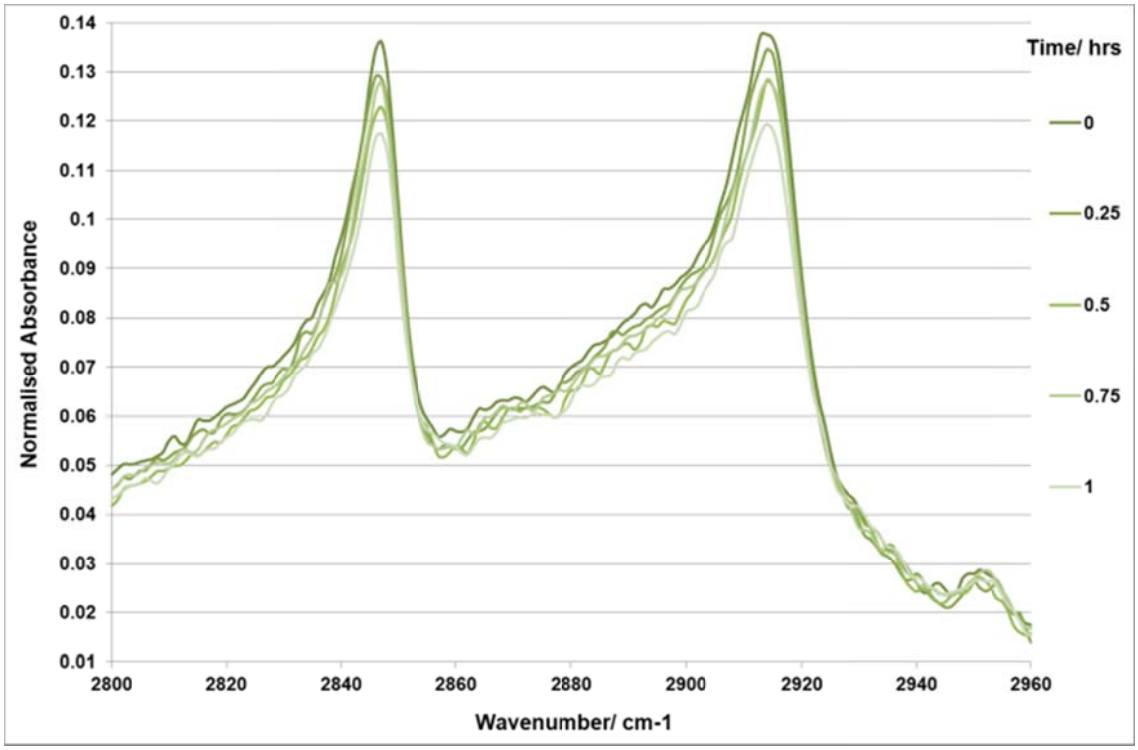
Normalised Absorbance
0.14
0.13
0.12
0.11
0.1
0.09
0.08
0.07
0.06
0.05
0.04
0.03
0.02
0.01
2800
2820
2840
2860
2880
2900
2920
2940
2960
Wavenumber/ cm-1
Time/ hrs
0
0.25
0.5
0.75
1

e) Al

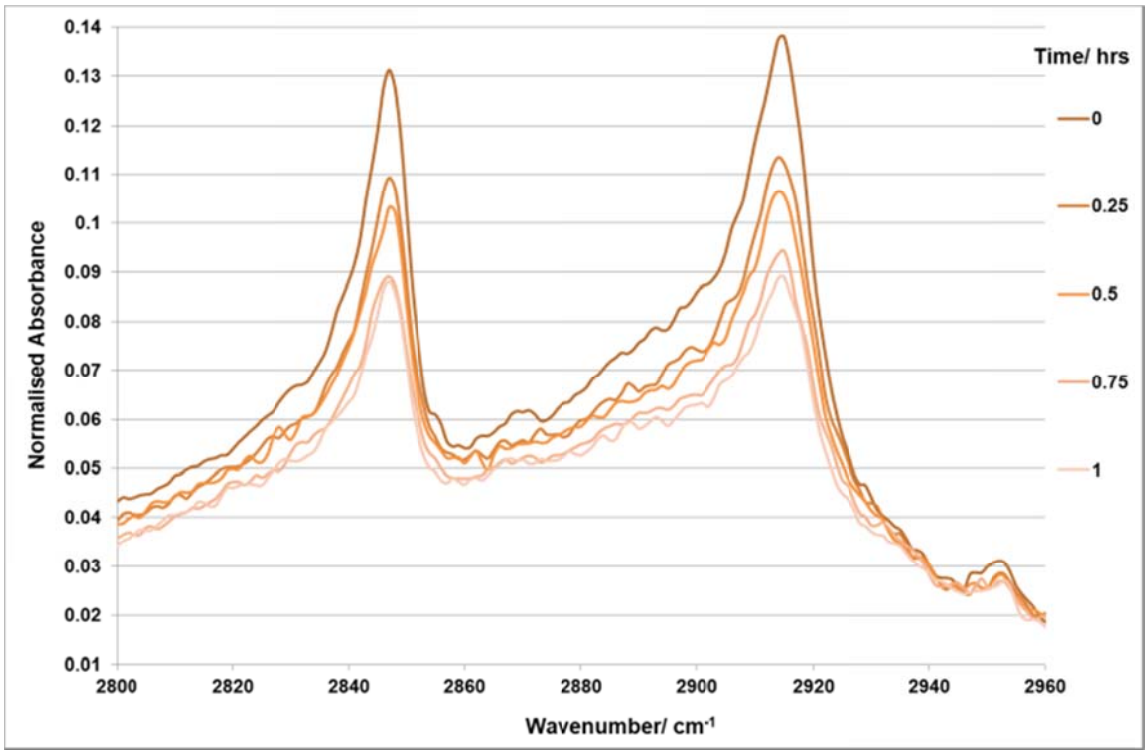

5.2.7.2.4 Comparison of Photocatalytic activity, Stearic Acid test, (400-600 °C, 254 nm)

Comparison of photocatalytic activity of undoped and doped Au, Ag, Cu and Al TiO_2 films (400-600 °C) using the stearic acid test (UVC 254 nm), number of stearic acid molecules destroyed, cm^{-2} s^{-1}, see fig. 137.

Figure 137: A comparison of the rate of stearic acid molecules destroyed (UVC 254 nm), on undoped and doped Au, Ag, Cu and Al TiO_2 films, (400-600 °C).

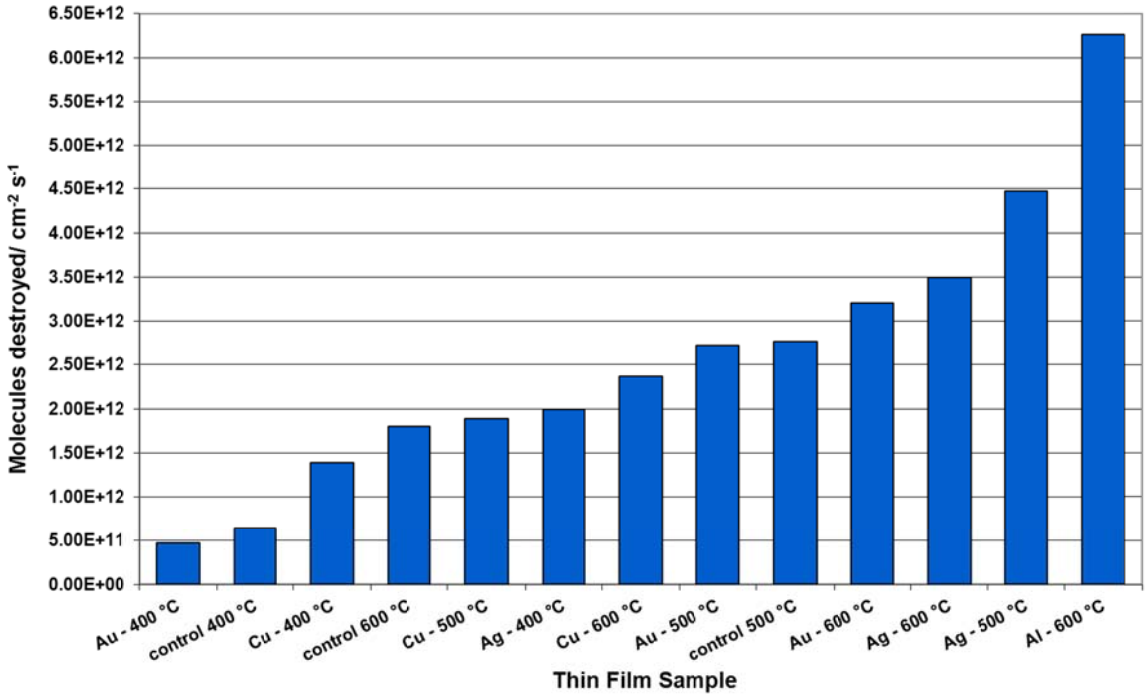

The comparison of the stearic acid molecule destruction rates for both undoped and doped TiO_2 films (400-600 °C) in general appear to support the RZ indicator results, with both temperature and dopant having an effect on the rate. In general the higher the synthesis temperature the better the photocatalytic activity with the Al (6.27×10^{12} molecules cm^{-2} s^{-1}) and Ag (4.48×10^{12} molecules cm^{-2} s^{-1}) dopants having the greatest effect at 600 and 500 °C respectively. Although the effect of the dopant appears to be more significant than with the undoped TiO_2 films which do not appear to perform well against those with dopants present.

Comparison of the molecule destruction rate with recent work by Dunnill *et al.*, 2011, (TiO_2 and Ag doped TiO_2: ~3.05×10^{10} molecules cm^{-2} s^{-1}), shows a distinct increase with the AACVD/APCVD synthesis technique used in this thesis compared to the Sol-gel sintered method[193]. Other work by Foster *et al.*, 2010, with Ag and Cu doped TiO_2 films (FACVD-APCVD, 300-500 °C) showed some agreement with these results that the Cu dopant is detrimental to the photocatalytic activity of TiO_2 films[213]. Recent work by Kafizas *et al.*, 2009, using the same light source and intensity also showed some agreement with the results reported here, Ag doped TiO_2 film (Sol-gel, annealed: 500 °C) exhibited the greatest rate of stearic acid destruction rate and the introduction of the Au

dopant to the Ag doped film decreased the destruction rate[192]. Other work by Page *et al*., 2007, also demonstrated that Ag doped TiO_2 films (Sol-gel, annealed 500 °C) are more photocatalytically active than undoped TiO_2 films [zero-order rate: 5.85 x 10^{12} molecules cm^{-2} min^{-1}, (9.75 x 10^{10} molecules cm^{-2} s^{-1})][211]. There are many examples of photocatalytically enhanced TiO_2 films by the use of Ag as a dopant and the work here confirms that in general Ag does enhance this physical property[190, 192, 193, 213- 215]. Hence the CVD films here have amongst the fastest rate of photodegradation of RZ and stearic acid reported in the literature.

5.2.7.2.5 Summary of photocatalysis analysis

The photoreduction of the Rz indicator ink is reduced irreversibly and should be less likely to be affected by the presence of oxygen. The Rz indicator ink kinetic results in the form of the relative change in absorbance (λ = 600 nm) as a function of irradiation time, see figs. 133, a), b) and c), appear to be first order (rate constant = k) but this is subject to light intensity, sample orientation and possibly the direct reaction of O_2 with photogenerated e^- therefore the results should be treated as a measure of relative efficiency. The first order kinetics appear to support the results found by Mills (Mills *et al*., 2008) that the rate-determining step is the diffusion of oxidised Rz dye to the titania surface[187]. For the Rz ink indicator results synthesis temperature affects photocatalytic rate; the general trend indicates that higher synthesis temperatures corresponds to an increase in photocatalytic activity, dopants do have an effect with the Ag doped TiO_2 (600 °C) appearing to have the greatest effect on molecule destruction rate (4.08 x 10^{12} cm^{-2} s^{-1}). The RZ results also indicate that the rate of photocatalysis at higher synthesis temperatures is dopant dependent and the lower synthesis temperatures is film thickness dependent. There may also be some evidence for the presence of SPR at the lower synthesis temperatures (400-500 °C).

For the stearic acid destruction results higher synthesis temperatures (500-600 °C) increased the photocatalytic activity and dopants appeared to have a more significant effect particularly the Ag and Al dopants which displayed the fastest zero-order destruction rates (4.48 x 10^{12} cm^{-2} s^{-1}, 6.27 x 10^{12} cm^{-2} s^{-1}, respectively). The choice of 254 nm lamp (4.88 eV) ensured that the energy

exceeded the TiO_2 band gap (3.2 eV), a 365 nm lamp (340 eV) supplies energy that falls on the O^2-Ti^{4+} boundary which is not as effective at electronic excitation as energy supplied above the boundary[192]. Direct comparison with literature results for photocatalytic indicator ink tests are not always useful as these indicators are known to be sensitive to the amount of oxygen presence *e.g.* stearic acid and the amount of humidity present *e.g.* Rz ink, therefore the quantitative results stated here are valid for this set of experimental parameters but some caution is needed in comparison against other literature[187].

5.3.0 Discussion of prototype 2 AACV/CVD results

The results from the dynamic substrate samples of the AACVD/CVD synthesis technique (300-400°C) undoped/doped Au, Au and Cu titania thin films produced highly transparent clear film with a blue hint with visible transmission (65-90%). The transmittance values at 500 °C lost some transmittance (55-70%) which was regained at the higher synthesis temperature of 600 °C (75-90%). Therefore the results for transmittance values appears to display that both the presence of a dopant and synthesis temperature have an effect, with films synthesised at 500 °C having the most detrimental effect. Interference patterns are displayed on all transmittance and reflectance values for undoped and doped Au, Ag, Cu and Al doped TiO_2 films, 500-600 °C, indicating a change in thickness of the film across the substrate and film thickness calculations (165.7-224.5 nm) were calculated (500-600 °C). Reflectance values did not show a particularly strong IR absorbance for any TiO_2 film (~30%) for the whole temperature (300-600 °C).

Very fine uniform morphology was observed for TiO_2 films undoped and formed in the presence of dopants at lower temperatures (<500 °C). At 500 °C large platelet conglomerated morphology was observed for TiO_2 films formed in the presence of Au, Ag, Cu and Al dopants that differed from the smaller angular, aggregated structures seen in the undoped TiO_2 film. At 600 °C the morphology was significantly different with dopants having a profound effect on the morphology with Au and Ag producing very different morphologies from the undoped TiO_2 film and the TiO_2 films formed in the presence of Cu and Al displayed very similar large platelet conglomerated structures also seen at 500

°C and for dynamic films in chapter 4. Only one Au dopant was detected by EDX, at 400 °C, no other dopants were detected using EDX analysis.

XRD analysis on all diffractograms exhibited the tetragonal anatase form of titania for undoped and doped Au, Ag, Cu and Al TiO_2 films (400-600 ºC). TiO_2 films formed below 400 °C were not crystalline. According to the XRD diffractograms; the dopants Au, Ag, Cu and Al appeared to have little effect on the form of titania observed. Raman spectra for TiO_2 films formed in the presence of Cu, Ag, Au, (400 °C) and Ag, Au and Cu, (600 °C) exhibit typical anatase phase peaks. As expected the presence of Au or Ag metallic/oxide phase was not detected they are poor Raman scatterers and the presence of Cu metallic/oxides was also not detected.

The contact angles at lower synthesis temperatures (400-500 °C) gave very similar hydrophobic results (θ~80°), an increase in synthesis temperature (600 °C) increased the observed contact angle (θ>105°) becoming superhydrophobic. The synthesis temperature and the dopant both have an effect on the irradiated value for the contact angle; increasing temperature reflects a decrease in the TiO_2 irradiated contact angle ($\theta \leq 15°$). Cu appears to be a detrimental dopant for the superhydrophilic properties of TiO_2, as contact angles of <30°, were not achievable across the whole synthesis temperature range (400-600 °C). Au and Ag dopants either appear to enhance or at least have no significant negative effect on the superhydrophilicity of TiO_2 films (400-500 C) with only a slight detrimental effect seen at higher temperatures (600 °C) The Al dopant appeared to have no detrimental effect on the irradiated contact angle of TiO_2 film.

The Rz indicator ink photocatalytic results appear to support first-order kinetics with mainly Ag doped films appearing to give the greatest enhancement to photocatalytic activity. Both Rz and stearic acid indicator results indicate that higher synthesis temperatures corresponds to an increase in photocatalytic activity, dopants do have an effect with the Ag doped TiO_2 (600 °C) appearing to have the greatest effect. The rate of photocatalysis for doped films at higher synthesis temperatures appears to be dependent on the dopant used and the lower synthesis temperatures appears to be dependent on film thickness. There may also be some evidence for the presence of SPR at the lower

synthesis temperatures (400-500 °C). For the stearic acid destruction results higher synthesis temperatures (500-600 °C) increased the photocatalytic activity and dopants appeared to have a more significant effect particularly the Ag and Al dopants which displayed the fastest zero-order destruction rates

5.4.0 Conclusion for chapter 5

All films synthesized <500 °C were highly transparent, highly uniform with no obvious interference patterns and pale blue in colour. Very fine morphology was observed for films synthesised <500 °C. The effect of both dopants and temperature on morphology at higher synthesis temperatures (>500 °C) is profound with dopants like Cu and Al reflecting the TiO_2 controls with large agglomerated plate structures and Au and Ag creating much smaller angular nanoparticles. Only one dopant, Au, in a TiO_2 film synthesised at a lower temperature (400 °C) was detected by EDX analysis but the effect of the dopants on structure was obvious and may well indicate their presence at a level not detectable by the analytical methods used here. XRD and Raman analysis confirmed that the presence of dopants or change in synthesis temperature did not affect the anatase crystal structure of the TiO_2 host matrix.

At lower synthesis temperatures (400-500 °C) the Au and Ag dopant appear to enhance the TiO_2 films contact angle properties whereas the Cu dopant appeared to have a detrimental effect at all synthesis temperatures, the Al dopant appeared to have no significant effect. The photocatalytic results appear to support first-order kinetics with mainly Ag doped films appearing to give the greatest enhancement to photocatalytic activity. Higher synthesis temperatures corresponds to an increase in photocatalytic activity, dopants do have an effect with Ag dopant (600 °C) appearing to have the greatest effect. The rate of photocatalysis for doped films at higher temperatures appears to be dependent on the dopant used and the lower synthesis temperatures appears to be dependent on film thickness. There may also be some evidence for the presence of SPR at the lower synthesis temperatures (400-500 °C).

Chapter 6

Conclusion

Chapter 6

Conclusion

An investigation was carried out using both computational fluid dynamics modelling technique (κ-ε realizable, κ-ω SST, discrete thermophoresis) and AACVD, AACVD/CVD experimental results into the inclusion of noble metal and or *n*-type nanoparticles in metal oxides such as ZnO. This was to generate thin metal oxide films with new or enhanced physical and chemical properties such as photocatalysis, resistivity and colour. The CFD investigation reveals that the main force acting on the formation of such thin films was aerodynamic drag, at lower temperatures and aerodynamic drag with evaporation, at higher temperatures (600 °C), the more volatile the solvent the more evaporation influences the size of droplet required to reach the heated substrate surface and not thermophoresis, as previously assumed in some literature. The thermophoretic effect affects droplets that are smaller than the required size to hit the surface and is not the main force of influence. Therefore AACVD droplet size in the reaction chamber is crucial in whether or not a dopant reaches the surface of the substrate. The separation of the CVD flow from the AACVD flow in the combined synthesis technique caused non-uniformity and complete lack of detectable noble metal or metal nanoparticles in the host matrix film. The idea of increasing/decreasing flow rate to increase/decrease the rate of inclusion of nanoparticles was dismissed, this simply makes the nanoparticle material either leave the reaction chamber at an increased or decreased rate, it has no effect on the amount actually hitting the substrate surface and being included within the host metal oxide film. Although the average experimental AACVD nebulised droplet size is an order of ten below (0.005 mm) the required modelled droplet size (0.04 mm) to reach the heated substrate surface at lower synthesis temperatures (400 °C) and two orders of ten below the required droplet size (0.1 mm) for higher synthesis temperatures (600 °C), useful experimental results have been obtained.

The experimental work for ZnO thin films was carried out using AACVD (due to health & safety concerns of using the AACVD/CVD pilot plant rig, which is far more open to the ‘atmosphere’ than a single cold-wall quartz tube reactor within

a fume cupboard. The results for these two metal oxide host matrices inferred that temperature was the main factor for inclusion of noble metal or metal nanoparticles but even low reaction temperatures did not produce much higher inclusion rates, somewhat confirming the results of the CFD investigation that the main force is still aerodynamic drag and aerodynamic drag with evaporation at higher temperatures. The work carried out using the AACVD/CVD pilot plant rig using titania as the host metal matrix produced interesting results, confirming the CFD findings that separated AACVD/CVD flows in the reaction chamber produce non-uniform films with little or no detectable inclusion of noble metal or *p*-type dopants. The faster two different synthesis raw material flows can be mixed the better the result, especially for dynamically moving substrates, this leads to uniform, reproducible results at set substrate synthesis temperatures (300-600 °C). The second AACVD/CVD prototype tested, designed via CFD, produced highly, uniform, blue transparent titania host films with or without doping. There was also some very small detectable dopant inclusion, Au, at 400 °C, in one film, also indicating the small influence substrate reaction temperature has over the likelihood of nanoparticle dopant inclusion within this system.

The AACVD films were mainly non-uniform indicating the difficulty of relying on any of the results being reproducible at a pilot plant or production type level for Float glass. The ZnO host matrices had no inclusion of dopants or very low level of included dopants; the only films to really buck the trend were the mainly opaque ZnO host matrix films with Cu as the dopant, present as copper oxide (Cu_2O). Undoped and noble metal doped ZnO produced thin films with a strong preferred (002) crystal lattice orientation, this orientation is known to enhance conductivity, the addition of Al, as Al_2O_3, produced a preferred crystal lattice growth along the (101). In the main ZnO undoped or noble metal doped produced spherical morphology; the Al dopant produced a range of morphologies.

TiO_2 was used as a test model for inclusion of noble metal and/or *p*-type dopants for the development of AACVD/CVD reaction head chambers primarily for a moving substrate, the first prototype had separate chambers for both the AACVD and CVD gas flows, the second prototype, based on CFD design allowed these gas flows to mix as soon as practicable. Neither prototype

proved particularly successful at including any nanoparticles introduced through the AACVD system on a regular or uniform basis. This was an expected result after the CFD results indicated that the droplet size required to reach the substrate surface was in the order of 10 magnitude too small, aerosol drag at lower temperatures and aerosol drag plus evaporation were the over-riding forces that any AACVD reaction head, open to the atmosphere, as these prototypes would be on a Float glass line. Simply put AACVD, with methanol as the solvent, produces droplet sizes that are too small to overcome aerosol drag and evaporation using the nebuliser system available for this work.

For prototype 1, no TiO_2 film synthesised had significant amounts of any dopants present apart from one static Au doped titania film (400 ºC, 3 mins) and nearly all dopants were below the analytical detection level but the morphology and film thickness appeared to be affected by dopants. Increasing either substrate time for static films or increasing the number of passes for dynamic films under the reaction chamber head exaggerated the agglomeration and size of the microstructure seen. Columnar fractal microstructures were seen for static films. A slight enhancement of superhydrophilicity was seen for one TiO_2 film formed in the presence of Cu, at 400 °C, all other films formed in the presence of dopants showed no enhancement of this property. XRD and Raman spectra exhibited typical peaks for the anatase phase of titania. XPS spectra exhibited typical titania composition and only detected very low level of Cu dopant (400 °C). For prototype 2 all films synthesized <500 °C were highly transparent, highly uniform with no obvious interference patterns and pale blue in colour. Very fine morphology was observed for films synthesised <500 °C. Morphology at higher synthesis temperatures (>500 °C) was affected by dopants, Cu and Al exhibiting similar platelet morphology to the TiO_2 controls; Au and Ag creating much smaller angular nanoparticle microstructure. One dopant, Au, in a TiO_2 film synthesised (400 °C) was detected by EDX analysis but the effect of the dopants on structure was obvious and may well indicate their presence at a level not detectable by the analytical methods used here. XRD and Raman analysis confirmed that the presence of dopants or change in synthesis temperature did not affect the anatase crystal structure of the TiO_2 host matrix. Both the RZ and stearic acid photocatalyst test results indicate that

photocatalysis appears to be enhanced by Ag in the precursor stream whether the element was detectable or not.

Further Work

Further work would include the computational fluid modelling of cold-wall static reaction chambers for the influence of aerosol drag versus the influence of thermophoresis. Design a complete new AACVD/CVD reaction chamber with aerosol drag in mind, probably place the reaction head at different angles to the substrate surface and place the AACVD inlets close to substrate surface with an enclosing 'curtain' type system to encourage the possibility of some inclusion of nanoparticles into the main metal oxide host matrix. Develop the knowledge on solvent drop size necessary to reach the substrate surface for different solvents. Design a Spray pyrolysis/CVD combination head with CFD. Experimental work would include further AACVD/CVD combined synthesis experiments with SnO_2 and ZnO for the effects of noble metal nanoparticles and/or *p*-type dopants on those metal oxide host matrices morphology and crystal orientation. Development and testing of new combination reaction AACVD/CVD and a spray pyrolysis/CVD prototypes based on CFD results. Further experimentation with different aerosol nebulizers to produce larger droplet sizes would also be advantageous; one of the main obstacles for the AACVD precursors physical deposition onto the substrate surface is the critical droplet size, dependent upon the solvent system, required.

References

References

1. M.C. Daniel and D. Astruc, *Chem. Rev*. 2004, **104**, 293.

2. G. Walters, I. P. Parkin, *J. Mater. Chem*., 2009, **19**, 574–590.

3. J. Zhao, S. Wu, J. Liu, H. Liu, S. Gong, D. Zhou, *Sensors and Actuators B: Chemical*, 2010, **145,** 2, 788-793.

4. G. Korotcenkov, V. Tolstoy, J. Schwank, *Meas. Sci. Technol*., 2006**, 17**, 1861 – 1869.

5. M. Green, *Chem. Commun*., 2005, 3002-3011.

6. P. K. Jain, C. P. Huang, M. A. El Sayed and Y. Y. Zhu, *Plasmonics*, 2007, **2**, 107-118.

7. G. Hyett, M. A. Green and I. P. Parkin, *J. Am. Chem. Soc*., 2007, **129**, 15541-15548.

8. G. Hyett, C. Blackman and I. P. Parkin, *Faraday Trans*., 2007, **136**, 329-343.

9. S. Ashraff, C. Blackman, S. C. Naisbitt, I. P. Parkin, *Meas. Sci. Technol.,* 2008, **19**, 205-211.

10. B. Houng, *App. Phys. Lett,* 2005, **87**, 251922.

11. K. Mallik, M. J. Witcomb, M.S. Scurrel, *Mat. Sci. and Eng., C,* 2005, **26**, 87 – 91.

12. C.-S. Hong, H.-H. Park, S.-J. Wang, H.-H. Park, R. H. Hill, *App. Surface Sci.,* 2006, **252**, 7739 – 7742.

13. C.-S. Hong, H.-H. Park, J. Moon and H.-. Park, *Thin Solid Films,* 2006, **515**, 957–960.

14. R. Ravindran, K. Gangopadhyay, S. Gangopadhyay, *App. Phys. Lett.,* 2006, **89**, 263511.

15. R. E. Dávila-Martínez, L. F. Cueto, E. M. Sánchez, *Surface Science,* 2006, **600**, 17, 3427–3435.

16. S.-W. Kim and S. Fujita, *Appl. Phys. Lett*., 2005, **86**, 153119.

17. S. S. Yi, G. Girolami, J. Amano, M. Saif Islam, S. Sharma, T. I. Kamins, I. Kimukin, *App. Phys. Lett.,* 2006, **89**, 133121.

18. X. Feng, J. Kang, W. Inami, X. Yuan, M. Terauchi, T. Sekiguchi, S. Tsunekawa, S. Ito and T. Sakurai, *Crystal Growth & Design,* 2006, **7**, 3, 564–568.

19. A. K. Sharma, B. D. Gupta, *J. Opt. A: Pure Appl*. Opt., 2007, **9**, 180–185.

20. A. Panacek, L. Kvitek, R. Prucek, M. Kolar M, R. Vecerova, N. Pizurova, V. K. Sharma, T. Nevecna, R. Zboril, *J. Phys. Chem. B,* 2006*,* **110,** 33, 16248–16253.

21. K. Page, R. G. Palgrave, M. Wilson, I. P. Parkin, *J. Mater. Chem*., 2007, **17**, 95-104.

22. J. Chen, J. Tang, F. Yan, H. Ju, *Biomaterials,* 2006, **27,** 10, 2313–21.

23. J. Zheng, C. Zhang, R. M. Dickson, *Phys. Rev. Lett.,* 2004, 13, **93**, 7, :077402

24. A.-Q. Wang, C.-M.Chang, C.-Y. Mou, *J. Phys. Chem. B,* 2005, **109**, 18860-18867.

25. D. T. Thompson, *Nanotoday,* 2007, **2,** 4, 40–43.

26. W. B. Kim, G. J. Rodriquez-Rivera, T. Voitl, S. T. Evans, J. J. Einspahr, P. M. Voyles, J. A. Dumesic, *J. Catal*., 2005, **235**, 327–332.

27. M. D. Hughes, Xu Yi-Jun., P. Jenkins, P. McMorn, P. Landon, D. I. Enache, A. F. Carley, G. A.. Attard, G. J. Hutchings, F. King, E. H. Stitt, P. Johnston, K. Griffin, C. J. Kiely, *Nature,* 2005, **437**, 1132–1135.

28. C.-C. Huang, Z. Yang, K.-H. Lee and H.-T. Chang, *Angew. Chem. Int. Ed.,* 2007, **46**, 6824–6828.

29. R. Narayannan, M. A. El-Sayed, *J. Phys. Chem. B,* 2005, **109**, 12663-12672.

30. M. Shahid, M. Mazhar, M. Hamid, P. O'Brien, M. A. Malik, M. Helliwell, J. Raftery, *Dalton Trans*., 2009, **28,** 5487-94

31. A. Tao, F. Kim F, C. Hess, J. Goldberger, R. He, Y. Sun, Y. Xia, P. Yang, *Nano Letters,* 2003, **3,** 9, 1229–1233.

32. Y. Xia, P. Yang, Y. Sun, Y. Wu, B. Mayers, B. Gates, Y. Yin, F. Kim, H. Yan, *Adv. Mater.*, 2003, **15**, 353-389.

33. K. Graf and H. Riegler, *Colloids and surfaces A: Physicochemical and Engineering Aspects*, 1998, **131**, 215–224.

34. F. Kim, S. Kwan, J. Akana, P. *Yang, J. Am. Chem. Soc.,* 2001, **123**, 4360-4361.

35. K. Graf, H. Riegler, *Langmuir*, 2000, **16,** 11, 5187-5191.

36. A. Wijaya, K. A. Brown, J. D. Alper and K. Hamid-Schifferli, *J. Magn. Magn. Mater.,* 2007, **309**, 15-19.

37. J. Turkevitch, P. C. Stevenson, J. Hillier, *Discuss Faraday Soc*. 1951, **11**, 55–75.

38. G. Frens, *Nature: Phys. Sci.,* 1973, **241**, 20–22.

39. J. Kimling, M. Maier, B. Okenve, V. Kotaidis, Ballot, A. Plech, A. *J. Phys. Chem. B*., 2006, **110**, 15700–15707.

40. M. Brust, M. Walker M, D. Bethell, D. J. Schiffrin, R. J. Whyman, *Chem. Soc. Chem. Comm*., 1994, 801–802.

41. J. E. Park, M. Atobe, T. Fuchigami, *Ultrason. Sonochem.,* 2006, **13,** 3, 237–241.

42. V. Amendola, S. Polizzi, M. Meneghetti, *J. Phys. Chem. B.,* 2006, **110**, 7232–7237.

43. M. Tsuji, M. Hashimoto, Y. Nishizawa, M. Kubokawa and T. Tsuji, *Chem. Eur. J*., 2005, **11**, 440 – 452.

44. P. Raveendran, J. Fu, S. C. Wallen, *Green Chem*., 2006, **8**, 34–38.

45. N. N. Mallikarjuna, R. S. Varma, *Crystal Growth & Des.,* 2007*,* **7**, 686-690.

46. T. Nakamura, Y. Tsukahara, T. Sakata, H. Mori, Y. Kanbe, H. Bessho, Y. Wada, *Bull. Chem. Soc. Jpn*., 2007, **80,** 1, 224–232.

47. H. Jiang, K. Moon, Z. Zhang, S. Pothukuchi, C. P. Wong, *J. Nanoparticle Res*., 2006, **8,** 1, 117–124.

48. T. Yamamoto, Y. Wada, T. Sakata, H. Mori, M. Goto, S. Hibino, S.Yanagida, *Chem. Lett*., 2004, **33,** 2, 158-159.

49. N. R. Jana, *Small*., 2005, **1,** 8-9, 875–882.

50. N. Arimitsu, A. Nakajima, Y. Kameshima, Y. Shibayama, H. Ohsaki, K. Okada, *Mat. Letts*., 2007, **61**, 2173–2177.

51. C.-H. Dai, Y.-L. Wu, Y.-H. Lee, C.-J. Chang and W.-F. Su, *J. Crsty. Growth,* 2006, **288**, 128–136.

52. Z. Y. Li, J. Yuan, Y. Chen, R. E. Palmer, J. P. Wilcoxon, *Appl. Phys. Lett*., 2005, **87**, 243103.

53. A. P. Herrera, O. Resto, J. G. Briano, C. Rinaldi, *Nanotechnology, 20*05, **16**, S618-S625.

54. M. F. Lengke, G. Southam, *Geochim. Cosmochin. Acta.,* 2005, **69**, 3759.

55. M. F. Lengke, M. E. Fleet, G. Southam, *Langmuir,* 2006, **22**, 2780.

56. Y. Konishi, T. Tsukigamo, K. Ohno, T. Saitoh, Normura, S. Nagamine, *Hydrometallurgy,* 2006, **81**, 24.

57. Y. Konishi, K. Ohno, N. Saitoh, T. Nomurar, S. Nagamine, *Mater. Res. Soc. Symp. Proc.,* 2006, 942, 0942-W13-01 (5 pages).

58. K. Yang, H. Fan, K. J. Malloy, C. J. Brinker, T. W. Sigmon, *Thin Solid Films,* 2005, **491**, 38–42.

59. D.-Y. Wang, H.-C. Lin, C.-C. Yen, *Thin Solid Films,* 2006, **515**, 1047–1052.

60. T.-H. Kao, J.-M. Song, I.-G. Chen, H.-H. Wu, T.-Y Dong, *Nanotechnology,* 2006, **17** 1416–1420.

61. V. V. Gurin, A. A. Alexeenko, V. B. Prakapenka, D. L. Kovalenko, K. V. Yumashev, P. V. Prokoshin, *Mat. Sci.,* 2002, **20**, 2.

62. B. Houng and C.-H. Huang, *Surface & Coatings Technology,* 2006, **201**, 3188–3192.

63. W. Huang, J. Shi, *Superficies y Vacio,* 2004, **17,** 1, 13–16.

64. H. Y. Y. Ko, M. Mizuhata, A. Kajinami, S. Deki, *Thin Solids Films,* 2005, **491**, 86-90.

65. M. F. V. Silva, J. R. Nicholls, *Surface and Coatings Technology,* 2001, **142-144**, 934-938.

66. H. Liao, W. Wen, G. K. L. Wong, *Opt. Soc. Am. B,* 2006, **23,** 12, 2518-2521.

67. E. György, G. Sauthier, A. Figureras, A. Giannoudakos, M. Kompitsas, I. N. Mihailescu, *J. Appl Phys*., 2006, **100**, 114302.

68. K. Frey, A. Beck, G. Pëto, G. Molná, O. Gestzi, L. Guczi, *Catalysis Communications,* 2006, **7**, 64–67.

69. Z. Konstantinovic, M. G. Muro del, M. Varela, X. Batlle, A. Labarta, *Nanotechnology,* 2006, **17**, 4106-4111.

70. R. Serna, A. Suarez-Garcia, C. N. Afonso, D. Babonneau, *Nanotechnology,* 2006, **17**, 4588-4593.

71. R. Chein, W. Liao, *Heat Mass Transfer,* 2005, **47**, 71-79.

72. I. P. Parkin, G. R. Palgrave, *J. Am. Chem. Soc*., 2006, **128**, 1587-1597; R. Palgrave, I. P. Parkin, *Gold Bull*., 2008, **41**, 66-69.

73. I. Matsui and H. Fujimori, *Chem. Lett*., 2007, **36,** 1, 80.

74. C. Hong, D. S. Kim, M. Choi, *Chem. Vap. Deposition,* 2006, **12**, 627-630.

75. S. Bet, A. Kar, *Mat. Sci. Eng., B,* 2006, **130**, 228-236.

76. A. Moores, F. Goettmann, *New J. Chem.,* 2006, **30**, 1121-1132.

77. R. H. Doremus, *Langmuir*, 2002, **18,** 6, 2436-2437.

78. M. Otter, *Physik*, 1961, **161**, 163-178.

79. L. K. Kelly, A. A. Lazarides, G. C. Schatz, *Nanotechnology*, 2001, **3,** 4, 67-73.

80. Z.-Y. Zang, Y.-P. Zao, *Appl. Phys Lett.,* 2006, **89,** 2, 023110.

81. K. L. Shuford, M. A. Ratner, G. C. Schatz, *J. Chem. Phys.,* 2005, **123,** 11, 114713.

82. B. O. Dabbousi, J. Rodriguez-Viegjo, F. V. Mikulec, J. R. Heine, H. Mattoussi, R. Ober, K. F. Jensen, M. G. Bawendi, *J. Phys. Chem. B*, 1977, **101**, 9463-9475.

83. S. K. Medda, S. De, G. De, *J. Mater. Chem*., 2005, **15**, 3278-3284.

84. S. Eustis, M. A. El-Sayed, *Chem. Soc. Rev*., 2006, **35**, 209-217.

85. J. L. Elichiguerra, J. Reyes-Gasga, M. J. Yacaman, *J. Mater. Chem*. 2006, **16**, 3906-3919.

86. A. Singh, M. Chaudhari, M. Sastry, *Nanotechnology*, 2006, **17**, 2399-2405.

87. K-C. Lee, S-J. Lin, C-H. Lin, C-S. Tsai, Y-J. Lu, *Surface & Coatings Technology*, 2008, **202,** 5339–5342.

88. T. A. El-Brolossy, T. Abdallah, M. B. Mohamed, S. Abdallah, K. Easawi, S. Negm, H. Talaat, *Eur. Phys. J. Special Topics*, 2008, **153**, 361–364.

89. F-K. Liu, P-W. Huang, Y-C. Chang, C-J. Ko, F-H. Ko and T-C. Cho, *J. Cryst. Growth,* 2005, **273**, 439-445.

90. Y. Yang, L. Xiong, J. Shi, M. Nogami, *Nanotechnology,* 2006, **17**, 2670-2674.

91. X. Yang, S. Chen, S. Zhao, D. Li, H. Ma, *J. Serb. Chem. Soc*., 2003, **68,** 11, 843-847.

92. R -L. Zong, J. Zhou, B. Li., M. Fu, S-K. Shi, L-T. Li, *J. Chem. Phys*., 2005, **123,** 9, 094710.

93. C. Noguez, *J. Phys. Chem. C,* 2007, **111***,* 3806-3819.

94. C. Burda C, X. Chen, R. Narayanam, M. A. El-Sayed, *Chem. Rev*., 2005, **105**, 1025-1102.

95. C. L. Nehl, H. Liao, J. H. Hafner, *Nano. Lett*., 2006, **6**, 4, 683-687.

96. A. Mooradian, *Phys. Rev. Lett*., 1969, **22**, 185.

97. I. Sakaguchi, H. Ryoken, T. Nakagawa, Y. Sato, H. Haneda, *Surf. Interface Anal.,* 2005, **38**, 1-5.

98. D. Basak, S. Karan, B. Mallick, *Chem. Phys. Lett*., 2006, **420**, 115-119.

99. S. Zhao, Y. Zhou, K. Zhao, Z. Liu, P. Han, S. Wang, W. Xiang, Z. Chen, H. Lu, B. Cheng, G. Yang, 2006, *Physica B*, **373**, 154–156.

100. H. Liao, W. Wen, G. K. Wong, 2006, *JOSA B*, **23**, 12, 2518-2521.

101. C. Damen, A. N. Sprafke, H. Dieker, M. Wuttig, G. von Plesson, *App. Phys. Lett.,* 2006, **88**, 011923.

102. G. Speranza, S. N. B. Bhaktha, A. Chiappini, A. Chiasera, M. Ferrari, C. Goyes, Y. Jestin, Minata L. Mattarelli, M. Montagna, G. N. Conti, S. Pelli, G. C. Righini, C. Tosello, K. C. Vishunubhatla, *J. Opt A: Pure Appl. Opt*., 2006, **8**, S450-S454.

103. T. He, Y. Ma, Y. Cao, P. Jiang, X. Zhang, W. Yang, J. Yao, *Langmuir***,** 2001, ***17,*** 8024-8027.

104. Y-C. Nah, S-S. Kim, J-H. Park and D-Y. Kim, *Electrochem. Solid State Lett.,* 2007, **10**, 1, J12-J14.

105. L. Eurenius, C. Haggland, E. Olsson, B. Kaesmo, D. Chakarov, *Nat. Photon*., 2008, **2**, 360-364.

106. M. Kim, G. H. Jeong, K. Y. Lee, K. Kwon, S. W. Han, *J. Mater. Chem*., 2008, **18**, 2208-2212.

107. S. Kodaira, S. W. Lee, T. Kunitake, *Chem. Lett*., 2008, **37**, 168-190.

108. R. Binions, C. Piccirllo, R. Palgrove, I. P. Parkin, *Chem. Vap. Deposition*, 2008, **14**, 33-39.

109. R. Gentle, P. Edwards, W. Bolton, *Mechanical Engineering Systems*, 1st edn, Oxford, UK: Butterworth-Heineman, 2001, 136-145.

110. R. L. Daugherty, J. B. Franzini, E. J. Finnemore, *Fluid Mechanics with Engineering Applications*, 8th edn., Singapore: McGraw-Hill, 1989, 188-189

111. Ansys Inc, *Fluent™ 6.3 User's Guide*, 6.3 edn., USA: PA, Canonsburg: Ansys Inc, 2010.

112. T.-H. Shih, w. w. Liou, A. Shabbir, Z. Yang, J. Zhu, *Comput. Fluids*, 1995, **24**(3), 227-238.

113. S. E. Kim, D. Choudhury, B. Patel, 'Computations of complex turbulent flows using the commercial code FLUENT'. In Proceedings of the ICASE/LARC/AFOSR Symposium on Modelling Complex Turbulent Flows, Hampton, Virginia, 1997.

114. J. O. Hinze, Turbulence, McGraw-Hill Publishing Co., New York, 1975.

115. L. Talbot *et al*., Thermophoresis of Particles in a Heated Boundary Layer. *J. Fluid Mech.*, 1980, **101**, 4, 737-758.

116. Ansys Inc, *Gambit™ 2.3 User's Guide*, 2.3 edn., USA: PA, Canonsburg, Ansys Inc., 2006.

117. Ansys Inc, *Gambit™ 2.3 Modeling Guide*, 2.3 edn., USA: PA, Canonsburg: Ansys Inc., 2006

118. W. M. Kays, *J. Heat Transfer*, 1994, **116**, 284-295.

119. D. C. Wilcox, Turbulence Modelling for CFD, DCW Industries, Inc., La Canada, California, 1998.

120. F. R. Menter, *AIAA Journal*, 1994, **32**, 8, 1598-1605

121. F. R. Menter, M. Kuntz, R. Langtry, Ten Years of Experience with the SST Turbulence Model. In K. Hanjalsc, Y. Nagano, M. Tummers, editors, *Turbulence, Heat and Mass Transfer*, 2003, 625-632, Begell House Inc.

122. H. S. Aly, Y. A. Eldrainy, T. M. Lazim, M. N. M. Jaafar, *CFD Letters*, 2010, 2, **2**, 97-105.

123. D. Katoshevski, T. Shakked, S. S. Sazhin, C. Crua, M. R. Heikal, *International Journal of Heat and Fluid Flow*, 2008, 29, 415–426

124. C. G. Granqvist, *Sol. Energy Mater. Sol. Cells,* 2007, **91**, 1529

125. T. D. Manning, I. P. Parkin, R. J. H. Clark, *J. Mater. Chem.,* 2002, **12**, 2936.

126. T. D. Manning, I. P. Parkin, M. E. Pemble, D. Sheel, D. Vernadou, *Chem. Mater.*, 2004, **16**, 744.

127. C. J. Carmalt, A. Newport, I. P. Parkin, *J. Mater. Chem.*, 2003, **13**, 84.

128. C. S. Blackman, I. P. Parkin, *Chem. Mater.,* 2005, **17**, 1583.

129. W. B. Cross, I. P. Parkin, *Chem. Commun.*, 2003, **14**, 1696.

130. T. D. Manning, I. P. Parkin, *J. Mater. Chem.*, 2004, **14**, 2554.

131. R. G. Palgrave, I. P. Parkin, *J. Am. Chem. Soc.*, 2006, **128**, 1587.

132. R. G. Palgrave, I. P. Parkin, *J. Mater. Chem*., 2004, **14**, 2864.

133. A. Moores, F. Goettmann, *New J. Chem*., 2006, **30**, 1121.

134. H. Kostlin, R. Jost, W. Lems, *Phys. Status Solidi* A., 1975, **29**, 87.

135. E. Fortunato, D. Ginley, H. Hosono, D. C. Paine, *MRS Bull*., 2007, **32**, 242-247.

136. T. A. Polley, W. B. Carter, D. B. Poker, *Thin Solid Films***,** 1999, **357**, 132-136.

137. B. Ataev, A. M. Bagamadova, A. M. Djabrailov, V. V. Mamedov, R. A. Rabadanov, *Thin Solid Films,*1995, **260**, 19-20.

138. L. C. Olsen, H. Aguilar, F. W. Addis, W. Lei, J. Li, *PVSCC***,** 1996, **25**, 997-1000.

139. G. Srinvasan, J. Kumar, *Cryst. Res. Technol*., 2006, **9**, 893-896.

140. M. F. Ogawa, Y. Natsume, T .J. Hirayama, *J. Mater. Sci. Lett*., 1990, **9**, 1351-1353.

141. R. Chein, W. Liao, *Heat Mass Transfer,* 2005*,* **47**, 71-79.

142. F. J. Jenson, E. O. Einset, D. I. Fotiadis, *Ann. Rev. Fluid Mech*., 1991, **23**, 197-232.

143. F. Meng, F. Lu, *Vacuum*, 2010, **85**, 84-88.

144. W. Huang, W. Deng, M. Lei, H. Huang, *Applied Surface Science*, 2011, **257**, 4774–4780

145. D. Hanaor, C. Sorrell, *J. Mat. Sci*, 2011, **46**, 4, 1-20.

146. C. W. Dunnill, I. P. Parkin, *Dalton Trans,.* 2011, **40**, 1635-1640.

147. C. W. Dunnill, Z. A. Aiken, J. Pratten, M. Wilson, D. J. Morgan, I. P. Parkin, *J. Photochemistry and Photobiology A: Chemistry*, 2009, **207**, 2-3, 244-253.

148. R. Swanepoel, *J. Phys. E: Sci. Instrum*., 1983, 16, 1214.

149. A. Goossens, E-L. Maloney, J. Schoonman, *Chem. Vap. Dep*, 1998, **4**, 3, 109-114.

150. S-C. Jung, B-H. Kim, S-J. Kim, N. Imaishi, Y-I.Chu, *Chem. Vap. Dep*., 2005, **3**, 11, 137-141.

151. J-S. Kim, C-W. Ham, *J. Ceramic Society of Japan*, 2009, **117**, 5, 570-573.

152. S. Mathur, P. Kuhn, *Surface & Coatings Technology*, 2006, **201**, 807-814.

153. Seifred, M. Winterer, H. Hahn, *Chem. Vap. Dep*., 2000, **6**, 5, 239-244.

154. E. R. Rosas, L. M. Apátiga, V. Rodríguez-Lugo, *Acta Microscopica*, 2010, **19**, 1, 89-93.

155. V. G. Bessergenev, R. J. F. Pereira, M. C. Mateus, I. V. Khmelinskii, D. A. Vasconcelos, R. Nicula, E. Burkel, A. M. Botelho do Rego, A. I. Saprykin, *Thin Solid Films*, 2006, 503, 29-39.

156. Y. H. Chee, R. P. Cooney, R. F Howe, P. A. W. van der Heide, *Journal of Raman Spectroscopy*, 1992, 23, 161-166.

157.. C. Edusi, G. Hyett, G. Sankar, I. P. Parkin, *Chem. Vap. Deposition*, 2011, **17**, 30–36.

158. G. Hyett, M. Green, I. P. Parkin, *J. Am. Chem. Soc*., 2006, **128,** 12147- 12155.

159. G. Hyett, M. A. Green, I. P. Parkin, *J. Photochem. Photobiol. A*, 2009, **203**, 199-203.99.

160. G. Hyett, J. A. Darr, A. Mills, I. P. Parkin, *Chem. Vap. Dep*., 2010, 16, 301-304.

161. S. Kundu, A. Kafizas, G. Hyett, A. Mills, J. A. Darra, I. P. Parkin, *J. Mater. Chem*, 2011, **21**, 6854-6863

162. Y. Takahashi, H. Suzuki, M. Nasu, *J. Chem. Soc., Faraday Trans*., 1985, **1**, 81, 3117.

163. K-N. P. Kumar, *Scr. Metall. Mater*., 1995, 32, 873.

164. L. Burgio, R. H. J. Clark, *Spectrochim. Acta. Part A*, 2001, ***57***, 1491-1521.

165. T. Wei, "*Raman Scattering of Cupric Oxide (CuO)"*, MSc Thesis, Peking University, China, 1990.

166. Z. H. Gan, G. Q. Yu, B. K. Tay, C. M. Tan, Z. W. Zhao, Y. Q. Fu, *J. Phys. D: Appl. Phys*., 2004, **37**

167. Y. S. Gong, C.Lee, C. K. Yang, *J. Appl. Phys.* 1995, **77**, 5422.

168. B. Balamurugan, B. R. Mehta, D. K. Avasthi, F. Singh, A. K. Arora, M. Rajalakshmi, G. Raghavan, A. K. Tyagi, S. M. Shivaprasad, *J. Appl. Phys.,* 2002, **92**, 3304.

169. C. R. Lordanescu, D. Tenciu, I. D. Feraru, A. Kiss, M. Bercu, D. Savastru, R. Notonier, C. E. A. Grigoreescu, *Digest J. Nanomaterials and Biostructures*, 2011, **6**, 2, 863–868.

170. R. Schennach, A. Gupper, *Mat. Res. Soc. Symp. Proc*. Vol. 766, Materials Research Society, 2003.

171. G. Niaura, *Electrochimica Acta 45,* 2000, 3507.

172. J. F. Xu, W. Ji, Z. X. Shen, S. H. Tang, X. R. Ye, D. Z. Jia, X. Q. Xin, *J. Solid State Chem*., 1999, **147**, 516.

173. F. Texier, L. Servant, J. L. Bruneel, F. Argoul, *J. Electroanal. Chem*., 1998, **446**, 189.

174. Y. S. Gong, Chiapyng Lee, C. K. Yang, *J. Appl. Phys*., 1995, **77**, 5422

175. R. N. Wenzel, *Ind. Eng. Chem.,* 1936, **28**, 988.

176. A. B. D. Cassie, S. Baxter, *Trans. Faraday Soc*., 1944, **40**, 546.

177. C. R. Crick, I. P. Parkin, *Thin Solid Films*, 2011, **519**, 2181–2186.

178. A. Mills, M. Crow, *International Journal of Photoenergy*, Hindawi Publishing Corporation, 2008, Article ID 470670, 6 pages.

179. M. Langlet, S. Permpoon, D. Riassetto, G. Berthom´e, E. Pernot, J. C. Joud, *J. Photochem.Photobiol.A*, 2006, **181**, 2-3, 203–214.

180. A. Mills, G. Hill, S. Bhopal, I. P. Parkin, S. A. O'Neill, *J. Photochem. Photobiol. A*, 2003, **160**, 3, 185–194.

181. M. Miyauchi, A. Nakajima, T. Watanabe, K. Hashimoto, *Chem. Maters.*, 2002, **14**, 6, 2812–2816.

182. I. P. Parkin, R. G. Palgrave, *J. Mater. Chem.*, 2005, **15**, 17, 1689–1695.

183. R-D. Sun, A. Nakajima, A. Fujishima, T. Watanabe, K.Hashimoto, *J. Phys. Chem. B*, 2001, **105**, 10, 1984–1990.

184. R. Wang, K. Hashimoto, A. Fujishima, et al., *Nature*, 1997, **388**, 6641, 431–432.

185. N. Stevens, C. I. Priest,R. Sedev, J. Ralston, *Langmuir*, 2003, **19**, 8, 3272–3275.

186. A. Rampaul, I. P. Parkin, S. A. O Neill, J. Desouza, A. Mills, N. Elliott, *Polyhedron*, 2003, **22** , 1, 35-44.

187. A. Mills, M. McGrady, *J. Photochem. Photobiol*. *A*, 2008, 193, 228.

188. J. Mungkalasiri, L. Bedel, F. Emieux, J. Dore´, F. N. R. Renaud, C. Sarantopoulos, F. Maury, *Chem. Vap. Deposition*, 2010, 16, 35-41.

189. P. Babelona, A.S. Dequiedt, H. Moste´fa-Sba, S. Bourgeois, P. Sibillot, M. Sacilotti, *Thin Solid Films*, 1998, 322, 63–67.

190. D. W. Sheel, L. A. Brook, I. B. Ditta, P. Evans, H. A. Foster, A. Steele, H. M. Yates, *International Journal of Photoenergy*, 2008, Article ID 168185, 11 pages.

191. D-H. Kuo, C-N. Shueh, *Journal of Non-Crystalline Solids*, 2004, 336, 120–127

192. A. Kafizas, S. Kellici, J. A. Darr, I. P. Parkin, *Photochem. Photobiol. A,* 2009, 204, 183-190.

193. C. W. Dunnill, K. Page, Z. A. Aiken, S. Noimark, G. Hyett, A. Kafizas, J. Pratten, M. Wilson, I. P. Parkin, *J. Photochem. Photobiol. A,* 2011, 220, 113-123.

194. A. Mills, A. Lepre, N. Elliott, S. Bhopal, I. P. Parkin, S. A. O'Neill, *J. Photochem. Photobiol*., 2003, 160, 213-224.

195. D. L. Cho, H. Min, J-H. Kim, G-S. Cha, G-S. Kim, B. H. Kim, S-H Ohk, *J. Ind. Eng. Chem*., 2007, 13, **3**, 434-437

196. M. Horáková, A. Kolouch, P. Špatenka, *Czechoslovak Journal of Physics*, 56, Suppl. B, 2006, 1185-1191.

197. G. Hyett, M. A. Green, I. P. Parkin, *J. Photochem. Photobiol. A,* 2009, 203, 199-203.

198. A. Mills, N. Elliott, I. P. Parkin, S. A. O'Neill, R.J. Clark, *J. Photochem. Photobiol. A,* 2002, 151, 171-179.

199. B. A. Nejand, S. Sanjabi, V. Ahmadi, *Transaction F: Nanotechnology*, 2010, 17, **2**, 102-107

200. A. Niskanen, K. Arstila, M. Leskelä, M. Ritala, *Chem. Vap. Deposition,* 2007, 13, 152–157

201. S. A. O'Neill, I. P. Parkin, R. J. H. Clark, Andrew Mills, N. Elliott, *J. Mater. Chem.*, 2003, 13, 56–60

202. J-K. Park, H-K. Kim, *Bull. Korean Chem. Soc.,* 2002, 23, **5**, 745-748.

203. A. Rampaul, I. P. Parkin, S. A. O'Neill, J. DeSouza, A. Mills, N. Elliott, *Polyhedron*, 2003, 22, 35-44.

204. A. Mills, J. Wang, S-K Lee, M. Simonsen, *Chem. Commun*., 2005, 2721-2723

205. A. Kafizas, A. Mills and I. P. Parkin, *Anal. Chim. Acta*., 2010, 663, 69– 76.

206. A. Kafizas, D. Adriaens, A. Mills, I. P. Parkin, *Phys. Chem. Phys. Chem.*, 2009, 11, **37**, 8367-8375.

207. Y. Paz, Z. Luo, L. Rabenberg, A. Heller, *J. Mater. Res*., 1995, 10, 2842.

208. P. Sawunyama, L. Jiang, A. Fujishima, K. Hashimoto, *J. Phys. Chem. B,* 1997, 101, 11000.

209. A. Mills, S. K. Lee, A. Lepre, I. P. Parkin, S. A. O'Neill, *Photochem. Photobiol. Sci.* 2002, 1, 865.

210. A. Mills, J. Wang, M. McGrady., *J. Phys. Chem. B*, 2006, 110, 18324-18331.

211. A. Mills, M. McFarlane, *Catalysis Today,* 2007, 129, 22–28.

212. A. Mills, J. Wang, *J. Photochem. Photobiol. A: Chem*., 2006, **182**, 181–186.

213. H.A. Foster, D.W. Sheel, P. Sheel, P. Evans, S. Varghesea, N. Rutschkea, H.M. Yates, *J. Photochem. Photobiol. A: Chem*., 2010, **216**, 283-289.

214. K. Page, R. G. Palgrave, I. P. Parkin, M. Wilson, S. L. P. Savin, A. V. Chadwick, *J. Mater. Chem.*, 2007, **17**, 95-104.

215. H. M. Yates, L. A. Brook, D. W. Sheel, *International Journal of Photoenergy*, 2008, 1-8.

Acknowledgements

My partner, Mr. Mark Mullins and my mother, Mrs. Jean Walters are thanked for their unrelenting support and encouragement. My friends Mr. Jon Cook, Mrs. Sheila Biederman and Ms. Alex Saran are thanked for their support and provision of accommodation when required and Mr. Geoff Beech is thanked for his support and role of chauffeur when I was in dire need.

Both EPSRC are thanked for an Eng. D. award to G.W. and I.P.P. Mr. Kevin Reeves for the help with Scanning Electron Microscopy. The Royal Society/Wolfson Trust is thanked for a merit award to IPP. Dr. Geoffrey Hyett is thanked for his help with the XRD, Mr. Andreas Kafizas is thanked for his help on photocatalysis and Raman. Pilkington Ltd are also thanked for the use of their laboratories and analytical department, particular thanks to Mr. Simon Hurst (ONC Group), Mr. Michael Baines for his help with Scanning Electron Microscopy and all of the Computational Fluids Group.

Appendices

Appendices

Appendix 1

The following mathematical explanations are provided as background information and a guide from the Ansys Fluent™ Technical Manual[102]. For a complete mathematical explanation of all expressions and terms refer to the Ansys Fluent™ Technical Manual[102].

Equation 7: The Mass Conservation Equation

$$\frac{\partial \rho}{\partial t} + \nabla . (\rho \vec{v}) = S_m \tag{7}$$

Where S_m = additional mass *e.g.* due to vaporization of liquid droplets added to the continuous phase from the dispersed second phase, ρ = density, t = time, v = velocity[102].

Equation 8: The Momentum Conservation Equation

Conservation of momentum in an inertial (non-accelerating) is given by:

$$\frac{\partial}{\partial t}(\rho \vec{v}) + \quad . (\rho \vec{v} \vec{v}) = - \; p + \quad . (\bar{\bar{\tau}}) + \rho \vec{g} + \vec{F} \tag{8}$$

where p is the static pressure, $\bar{\bar{\tau}}$ is the stress tensor (described below), and $\rho \vec{g}$ and $\vec{F}$ are the gravitational body force and external body forces (*e.g.*, that arise from interaction with the dispersed phase)[102].

Equation 9

$$\bar{\bar{\tau}} = \mu \left[(\quad \vec{v} + \quad \vec{v}^{T}) - \frac{2}{3} \quad . \vec{v} I \right] \tag{9}$$

where μ is the molecular viscosity, I is the unit tensor, and the second term on the right hand side is the effect of volume dilation[102].

- Heat Transfer Theory

The heat transfer theory is used in the following form to solve for energy when required in CFD simulations in Fluent™ software.

Equation 10: The Energy Equation is given by:

$$\frac{\partial}{\partial t}(\rho E) + \nabla \cdot \left(k_{eff} \nabla T - \sum_j h_j \vec{J}_j + \left(\bar{\bar{\tau}}_{eff} \cdot \vec{v} \right) \right) + S_h \qquad (10)$$

Where k_{eff} = effective conductivity, $(k + k_t)$, k_t = turbulent thermal conductivity, $\vec{J}_j$ = diffusion flux of species j, S_h = heat of chemical reaction. The first three terms on the right-hand side of equation represent energy transfer due to conduction, species diffusion, and viscous dissipation, respectively[102].

- Inclusion of the Species Diffusion Term

The effect of enthalpy transport due to species diffusion includes the following term when the pressure-based solver is used:

Equation 11

$$\nabla \cdot \left(\sum_j h_j \vec{J}_j \right) \qquad (11)$$

- Diffusion at inlets

The net transport of energy at inlets consists of both the convection and diffusion components[102]. The convection component is fixed by the inlet temperature by the user. The diffusion component depends on the gradient of the computed temperature field therefore the diffusion component and therefore the net inlet transport is not specified a priori[102].

- Turbulent Models

    - κ-ε Realizable model

Transport equations

Turbulent kinetic energy, κ is given by:

Equation 12: Turbulent kinetic energy, κ

$$\frac{\partial}{\partial t}(\rho k) + \frac{\partial}{\partial x_i}(\rho k u_j) = \frac{\partial}{\partial x_i}\left[\left(\mu + \frac{\mu t}{\sigma k}\right)\frac{\partial k}{\partial x_j}\right] + G_k + G_b - \rho\epsilon - Y_m + S_k \quad (12)$$

And

Dissipation rate, ε is given by:

Equation 13: Dissipation rate, ε

$$\frac{\partial}{\partial t}(\rho\epsilon) + \frac{\partial}{\partial x_j}(\rho\epsilon u_j) = \frac{\partial}{\partial x_j}\left[\left(\mu + \frac{\mu t}{\sigma\epsilon}\right)\frac{\partial \epsilon}{\partial x_j}\right] + \rho C_1 S_\epsilon - \rho C_2 \frac{\epsilon^2}{k + \sqrt{v\epsilon}} + C_{1\epsilon}\frac{\epsilon}{k} C_{3\epsilon} G_b + S_\epsilon \quad (13)$$

where:

Equation 14

$$C_1 = \max\left[0.43, \frac{\eta}{\eta + 5}\right], \quad \eta = S = \frac{k}{\epsilon}, \quad S = \sqrt{2 S_{ij} S_{ij}} \quad (14)$$

where G_κ = the generation of turbulence kinetic energy due to the mean velocity gradients, G_b = the generation of turbulence kinetic energy due to buoyancy, Y_m = the contribution of the fluctuating dilation in compressible turbulence to the overall dissipation rate, $C_{1\varepsilon}$, $C_{2\varepsilon}$ and $C_{3\varepsilon}$ are constants, σ_κ and σ_ε are the turbulent Prandtl numbers for κ and ε respectively and S_κ and S_ε are user-defined source terms[102].

The model Constants are given by $C_{1\varepsilon} = 1.44$, $C_2 = 1.9$, $\varepsilon_k = 1.0$, $\sigma_\varepsilon = 1.2$

- κ-ε Realizable model

Transport equations

Turbulent kinetic energy, κ is given by:

Equation 15

$$\frac{\partial}{\partial t}(\rho k) + \frac{\partial}{\partial x_i}(\rho k u_j) = \frac{\partial}{\partial x_i}\left[\left(\mu + \frac{\mu t}{\sigma k}\right)\frac{\partial k}{\partial x_j}\right] + G_k + G_b - \rho\epsilon - Y_m + S_k \quad (15)$$

and

Dissipation rate, ε is given by:

Equation 16

$$\frac{\partial}{\partial t}(\rho\epsilon) + \frac{\partial}{\partial x_j}(\rho\epsilon u_j) = \frac{\partial}{\partial x_j}\left[\left(\mu + \frac{\mu t}{\sigma\epsilon}\right)\frac{\partial \epsilon}{\partial x_j}\right] + \rho C_1 S_\epsilon - \rho C_2 \frac{\epsilon^2}{k + \sqrt{v\epsilon}} + C_{1\epsilon}\frac{\epsilon}{k} C_{3\epsilon} G_b + S_\epsilon \quad (16)$$

where:

Equation 17

$$C_1 = \max\left[0.43, \frac{\eta}{\eta + 5}\right], \quad \eta = S = \frac{k}{\epsilon}, \quad S = \sqrt{2 S_{ij} S_{ij}} \quad (17)$$

where G_κ = the generation of turbulence kinetic energy due to the mean velocity gradients, G_b = the generation of turbulence kinetic energy due to buoyancy, Y_m = the contribution of the fluctuating dilation in compressible turbulence to the overall dissipation rate, $C_{1\varepsilon}$, $C_{2\varepsilon}$ and $C_{3\varepsilon}$ are constants, σ_κ and σ_ε are the turbulent Prandtl numbers for κ and ε respectively and S_κ and S_ε are user-defined source terms[102]. The model Constants are given by $C_{1\varepsilon}$ = 1.44, C_2 = 1.9, ε_k = 1.0, σ_ε = 1.2

- κ-ω SST model

The κ-ω SST model effectively blends the standard κ-ω model with the κ-ε model via a conversion of the κ-ε model into a κ-ω formulation making the κ-ω SST model more accurate and reliable for a wider class of flows than the standard κ-ω model[109]. There is also an additional cross-diffusion term in the ω equation and a blending function for both near wall and far-field zones[102].

Transport equations

The turbulent kinetic energy, κ, is given by:

Equation 18

$$\frac{\partial}{\partial t}(\rho\kappa) + \frac{\partial}{\partial x_i}(\rho\kappa u_i) = \frac{\partial}{\partial x_j}\left(\Gamma_\kappa \frac{\partial \kappa}{\partial x_j}\right) + \tilde{G}_\kappa - Y_\kappa + S_\kappa \quad (18)$$

and

The specific dissipation rate, ω, is given by:

Equation 19

$$\frac{\partial}{\partial t}(\rho\omega) + \frac{\partial}{\partial x_i}(\rho\omega u_i) = \frac{\partial}{\partial x_j}\left(\Gamma_\omega \frac{\partial \omega}{\partial x_j}\right) + G_\omega - Y_\omega + D_\omega + S_\omega \quad (19)$$

Where $\bar{G}_\kappa$ = generation of turbulence kinetic energy due to the mean velocity gradient, G_ω = generation of ω, Γ_κ and Γ_ω = effective diffusivity of κ and ω, respectively, Y_κ and Y_ω = dissipation of κ and ω due to turbulence, respectively, D_ω = cross-diffusion term and the S_κ and S_ω = user-defined source terms[102].

The model Constants are defined as:

$\sigma_{\kappa,1}$ = 1.176, $\sigma_{\omega,1}$ = 2.0, $\sigma_{\kappa,2}$ = 1.0, $\sigma_{\omega,2}$ = 1.168, a_1 = 0.31, $\beta_{i,2}$ = 0.075, $\beta_{i,2}$ = 0.0826,
α^*_∞ = 1, α_∞ = 0.52, α_0 = 1/9, β^*_∞ = 0.09, β_i 0.072, R_β = 8, R_κ = 6, R_ω = 2.95, ζ* = 1.5, Mt_0 = 0.25, σ_κ = 2.0 and σ_ω = 2.0[102].

For wall boundary equations refer to Fluent™ Technical Manual[102].

- Thermophoretic modelling

The thermophoretic effect on particles in the additional acceleration (force/unit mass) term F_x is defined by:

Equation 20

$$F_x = -D_{T,p}\frac{1}{M_p T}\frac{\partial T}{\partial x} \quad (20)$$

Where using the form from Talbot *et al*. gives[110]:

Equation 21

$$F_x = -\frac{6\pi d_p \mu^2 C_S (K + C_t Kn)}{\rho (1 + 3C_m Kn)(1 + 2K + 2C_t Kn)}\frac{1}{m_p T}\frac{\partial T}{\partial x} \quad (21)$$

Where Kn = Knudsen number = 2 λ/d_p, λ = mean free path of the fluid, K = k/kp, k = fluid thermal conductivity based on based on translational energy only =

(15/4)μR, k_p = particle thermal conductivity, C_S = 1.17, C_t = 1.14, m_p = particle mass, T = local fluid temperature and μ = fluid viscosity[102].

- κ-ω SST model

The κ-ω SST model effectively blends the standard κ-ω model with the κ-ε model via a conversion of the κ-ε model into a κ-ω formulation making the κ-ω SST model more accurate and reliable for a wider class of flows than the standard κ-ω model[109]. There is also an additional cross-diffusion term in the ω equation and a blending function for both near wall and far-field zones[102].

Transport equations

The turbulent kinetic energy, κ, is given by:

Equation 22

$$\frac{\partial}{\partial t}(\rho\kappa) + \frac{\partial}{\partial x_i}(\rho\kappa u_i) = \frac{\partial}{\partial x_j}\left(\Gamma_\kappa \frac{\partial \kappa}{\partial x_j}\right) + \tilde{G}_\kappa - Y_\kappa + S_\kappa \quad (22)$$

and

The specific dissipation rate, ω, is given by:

Equation 23

$$\frac{\partial}{\partial t}(\rho\omega) + \frac{\partial}{\partial x_i}(\rho\omega u_i) = \frac{\partial}{\partial x_j}\left(\Gamma_\omega \frac{\partial \omega}{\partial x_j}\right) + G_\omega - Y_\omega + D_\omega + S_\omega \quad (23)$$

Where $\tilde{G}_\kappa$ = generation of turbulence kinetic energy due to the mean velocity gradient, G_ω = generation of ω, Γ_κ and Γ_ω = effective diffusivity of κ and ω, respectively, Y_κ and Y_ω = dissipation of κ and ω due to turbulence, respectively, D_ω = cross-diffusion term and the S_κ and S_ω = user-defined source terms[102].

The model Constants are defined as:

$\sigma_{\kappa,1}$ = 1.176, $\sigma_{\omega,1}$ = 2.0, $\sigma_{\kappa,2}$ = 1.0, $\sigma_{\omega,2}$ = 1.168, a_1 = 0.31, $\beta_{i,2}$ = 0.075, $\beta_{i,2}$ = 0.0826,
α^*_∞ = 1, α_∞ = 0.52, α_0 = 1/9, β^*_∞ = 0.09, β_i 0.072, R_β = 8, R_κ = 6, R_ω = 2.95, ζ* = 1.5, Mt_0 = 0.25, σ_κ = 2.0 and σ_ω = 2.0.[102]

For wall boundary equations refer to Fluent™ Technical Manual[102].

- Discrete Models

The thermophoretic model

The thermophoretic effect on particles in the additional acceleration (force/unit mass) term F_x is defined by:

Equation 24

$$F_x = -D_{T,p} \frac{1}{M_p T} \frac{\partial T}{\partial x} \tag{24}$$

Where using the form from Talbot *et al*. gives[110]:

Equation 25

$$F_x = -\frac{6\pi d_p \mu^2 C_S (K + C_t Kn)}{\rho (1 + 3 C_m Kn)(1 + 2K + 2 C_t Kn)} \frac{1}{m_p T} \frac{\partial T}{\partial x} \tag{25}$$

Where Kn = Knudsen number = 2 λ/d_p, λ = mean free path of the fluid, K = k/kp, k = fluid thermal conductivity based on based on translational energy only = (15/4)μR, k_p = particle thermal conductivity, C_S = 1.17, C_t = 1.14, m_p = particle mass, T = local fluid temperature and μ = fluid viscosity[102]. The assumption is that the particle is a sphere and the fluid behaves like an ideal gas.

Appendix 2

The Reynolds Number

The Reynolds number is dimensionless that can give an indication of the transition point between laminar and turbulent flow for a particular system. Laminar flows have a low velocity with a low Re number, turbulent flows have low viscosity and high velocity with a high Re number.

Reynold's Number

Equation 26

$$\mathbf{Re} = \mathbf{\rho v D/\mu} \quad (26)$$

Where: ρ = fluid density, v = fluid velocity, D = tube diameter, μ = fluid viscosity

Turbulent flow requires large applied pressures and that can lead to high energy losses. Find area of the burred inlet pipe where $A = \pi r^2$, diameter 4.5 mm unburred, burred 3.5 mm, used burred pipe diameter for calculations

Burred: Area = $\pi.0.00175^2$, A = 9.62×10^{-6} m^2

Conversion of flow rate l/min into m^3/s

1.0 l/min = 1.66×10^{-5} m^3/s

Conversion of flow rate, l/min, into velocity, m/s use the following

Equation 27

$$\text{Velocity, v, m/s} = \frac{\text{Flow Rate of pipe } m^3/s}{\text{Area of pipe } m^2} \quad (27)$$

Convert actual flow rates used from l/min to m^3/s:

0.3 l/min = 5×10^{-6} m^3/s, 0.6 l/min = 1.0×10^{-5} m^3/s, 1.2 l/min = 2.0×10^{-5} m^3/s, 10.0 l/min = 1.6×10^{-4} m^3/s

For 0.3 l/min flow rate with a burred pipe:

$$v = \frac{5 \times 10^{-6}\ m^3/s}{9.62 \times 10^{-6}\ m^2} = 0.5197 \text{ m/s}$$

v = 0.52 m/s

For 0.6 l/min flow rate with a burred pipe:

$$v = \frac{1 \times 10^{-5}\ m^3/s}{9.62 \times 10^{-6}\ m^2} = 1.039\ m/s$$

$$v = 1.04\ m/s$$

For 1.2 l/min flow rate with a burred pipe:

$$v = \frac{2.0 \times 10^{-5}\ m^3/s}{9.62 \times 10^{-6}\ m^2} = 2.079\ m/s$$

$$v = 2.0\ 8\ m/s$$

For 10.0 l/min flow rate with a burred pipe:

$$v = \frac{1.6 \times 10^{-4}\ m^3/s}{9.62 \times 10^{-6}\ m^2} = 17.324\ m/s$$

$$v = 17.\ 32\ m/s$$

Calculate Reynold's number for actual flow rates used 0.6 l/min, density of air (1.1 kg/m^3) with a burred pipe diameter 3.5 mm, a velocity of 1.04 m/s and the viscosity, 1.85 x 10^{-5} Pa s of air at 25 ºC:

$$Re = \frac{1.1\ kg/m^3 \times 1.04\ m/s \times 3.5 \times 10^{-3}\ m}{1.85 \times 10^{-5}\ Pa\ s}$$

$$Re = 216.43$$

Calculate Reynold's number for actual flow rates used 0.3 l/min, density of methanol, 791.4 kg/m^3 with a burred pipe, diameter 3.5 mm, a velocity of 0.52 m/s and the viscosity, 1.85 x 10^{-5} Pa s of air at 25 ºC:

$$Re = \frac{1.1\ kg/m^3 \times 0.52\ m/s \times 3.5 \times 10^{-3}\ m}{1.85 \times 10^{-5}\ Pa\ s}$$

$$Re = 108.22$$

Theoretical flow rate from Re number 3000 gives a theoretical velocity for a burred diameter of:

$$\rho vD/\mu = \frac{791.4\ kg/m^3 \times v \times 3.5 \times 10^{-3}\ m}{1.85 \times 10^{-5}\ Pa\ s} = 3000$$

$$v = 3000 \times \frac{1.85 \times 10^{-5}\ Pa\ s}{1.1\ kg/m^3 \times 3.5 \times 10^{-3}\ m}$$

$$v = 14.42\ m/s$$

Convert 14.42 m/s into a flow rate l/min:

Flow rate of pipe m^3/s = Velocity m/s x Area of pipe m^2

Flow rate = 14.42 m/s x 9.62×10^{-6} m^2

Flow Rate = 1.39×10^{-4} m^3/s

Convert m^3/s into l/s

$1.39 \times 10^{-4} \times 1000 = 0.139$ l/s

Convert l/s into l/min

0.139 l/s x 60 = 8.342 l/min

Therefore from calculation a flow of approximately 8.32 l/min should give turbulent flow.

Table 35: Flow rates used for turbulence modelling.

Theoretical flow rate for modelling/ m/s	Experimental flow rate/ l/min	Significance
17.39	10.0	Flow rate of CVD inlets with equipment
14.42	8.34	Re = 3000
0.52	0.3	Flow rate of AACVD inlet achieved with equipment
1.04	0.6	Flow rate of AACVD inlet achieved with equipment
2.08	1.2	Flow rate of AACVD inlet achieved with equipment

Appendix 3

Figure 138: Head 1, fluid flow case 2: 3D view of the interior plane/plane of symmetry of the model, a) Contours of velocity/ m/s, b) velocity vectors/ m/s, c) pathlines of velocity/ m/s, d) contours of turbulent intensity/ %, e) graph of velocity magnitude/ m/s, f) graph of turbulent kinetic energy/ m^2/s^2.

a)

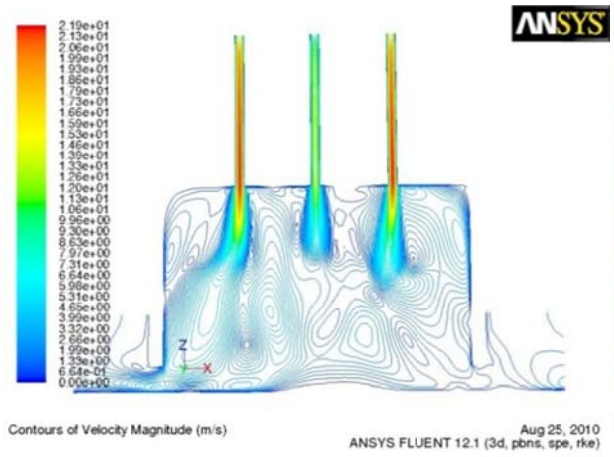

b)

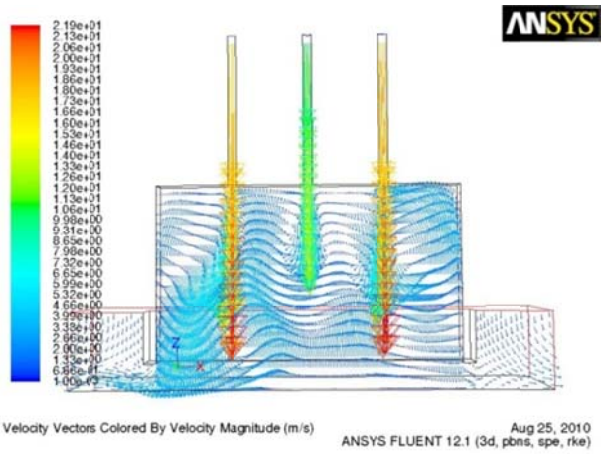

c)

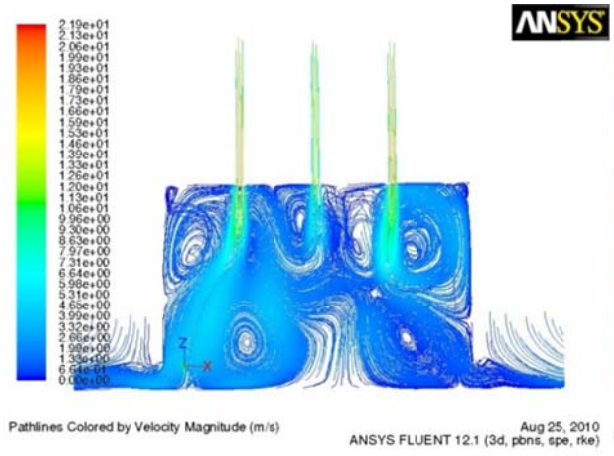

d)

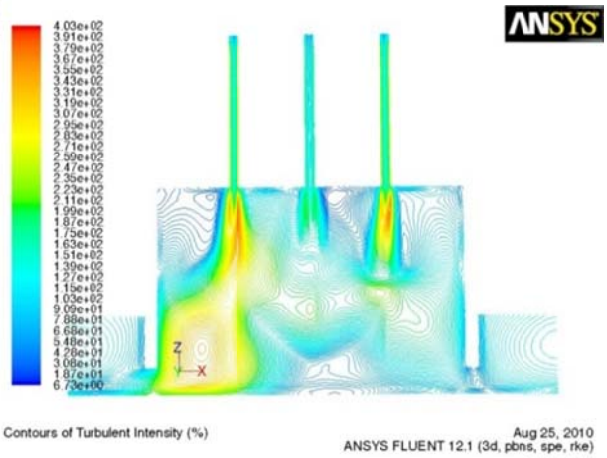

e) f)

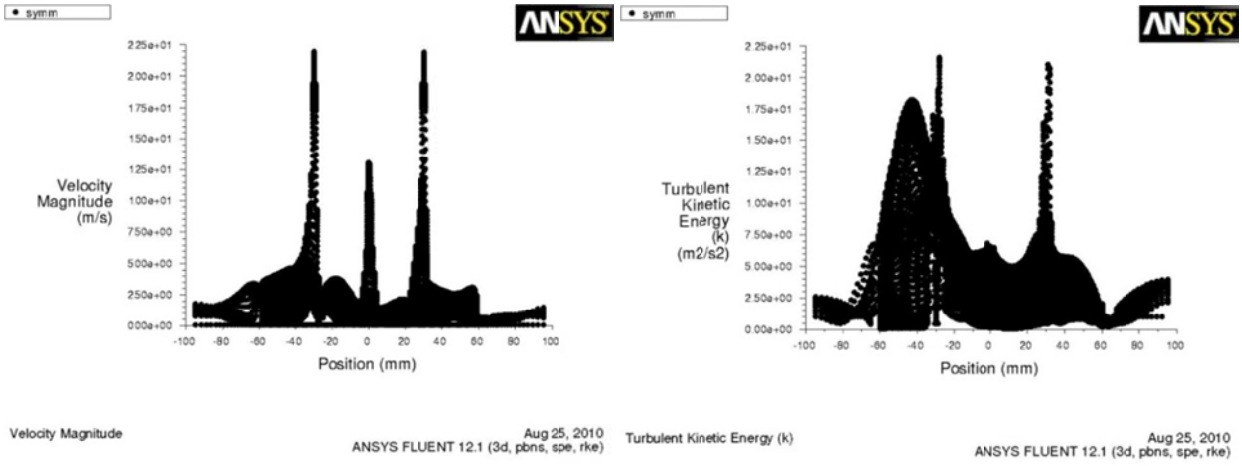

Figure 139: Head 1, fluid flow case 3: 3D view of the interior plane/plane of symmetry of the model, a) contours of velocity/ m/s, b) velocity vectors/ m/s, c) pathlines of velocity/ m/s, d) contours of turbulent intensity/ %, e) contours of dissipation rate/ m^2/s^3, f) contours of turbulent kinetic energy/ m^2/s^2, g) graph of velocity magnitude/ m/s, h) graph of turbulent kinetic energy/ m^2/s^2.

a) b)

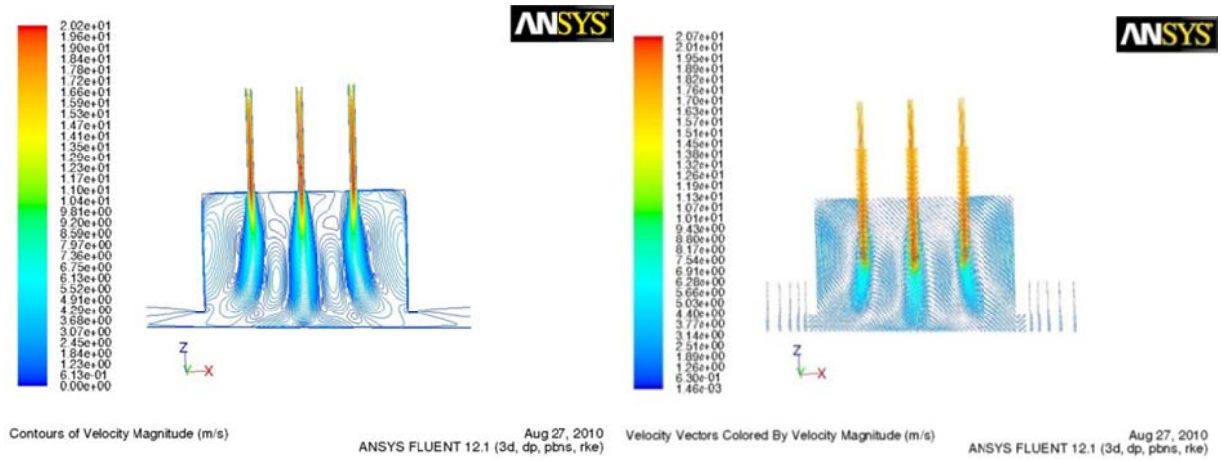

c)

Pathlines Colored by Velocity Magnitude (m/s)

Aug 27, 2010
ANSYS FLUENT 12.1 (3d, dp, pbns, rke)

d)

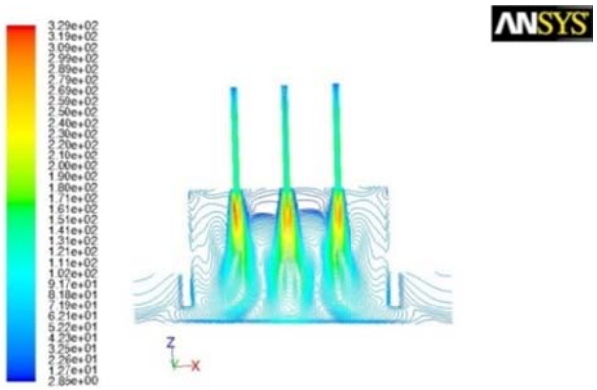

Contours of Turbulent Intensity (%)

Aug 27, 2010
ANSYS FLUENT 12.1 (3d, dp, pbns, rke)

e)

Contours of Turbulent Dissipation Rate (Epsilon) (m2/s3)

Aug 27, 2010
ANSYS FLUENT 12.1 (3d, dp, pbns, rke)

f)

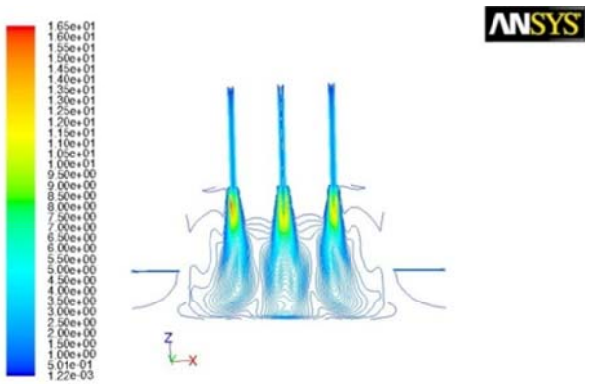

Contours of Turbulent Kinetic Energy (k) (m2/s2)

Aug 27, 2010
ANSYS FLUENT 12.1 (3d, dp, pbns, rke)

g)

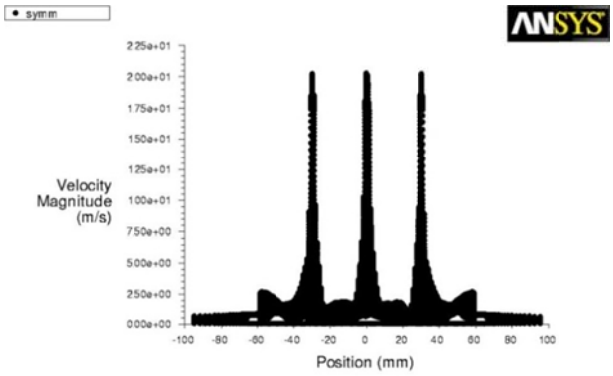

Velocity Magnitude

Aug 27, 2010
ANSYS FLUENT 12.1 (3d, dp, pbns, rke)

h)

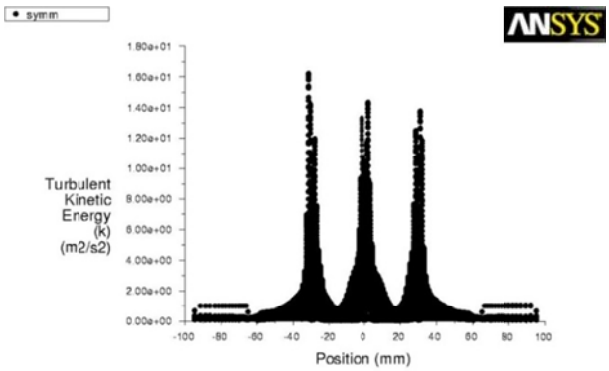

Turbulent Kinetic Energy (k)

Aug 27, 2010
ANSYS FLUENT 12.1 (3d, dp, pbns, rke)

Figure 140: Head 1, fluid flow case 4: 3D view of the interior plane/plane of symmetry of the model, a) contours of velocity/ m/s, a) contours of velocity/ m/s, b) velocity vectors/ m/s, c) pathlines of velocity/ m/s, d) contours of turbulent intensity/ %, e) contours of dissipation rate/ m^2/s^3, f) contours of turbulent kinetic energy/ m^2/s^2, g) contours of turbulent viscosity kg/ms^{-1}, h) graph of velocity magnitude/ m/s, i) graph of turbulent kinetic energy/ m^2/s^2.

a)

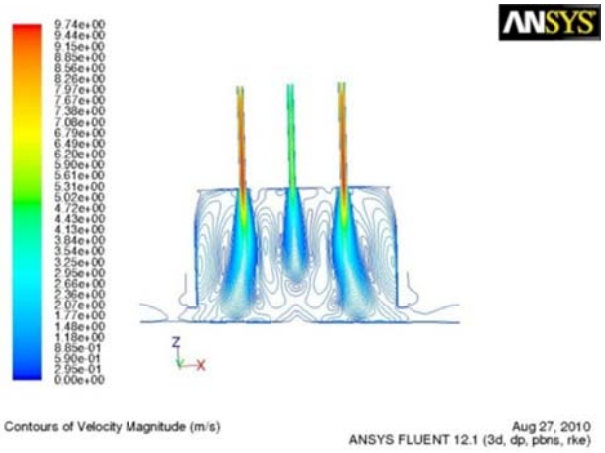

b)

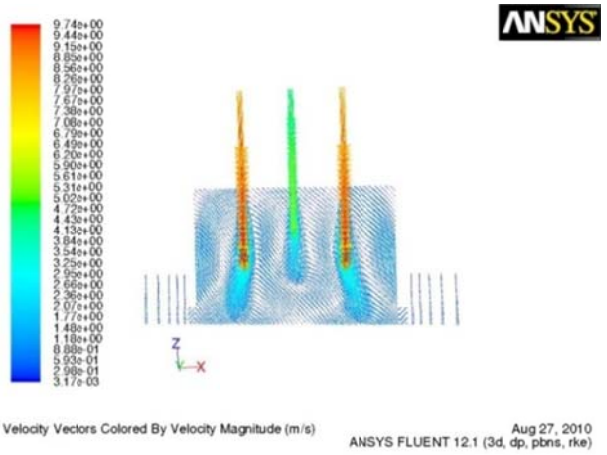

c)

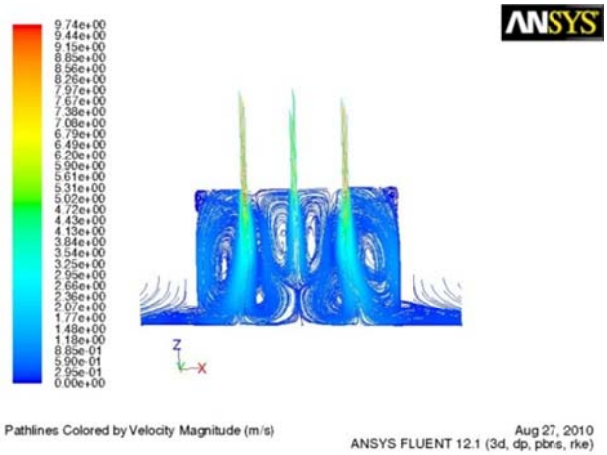

d)

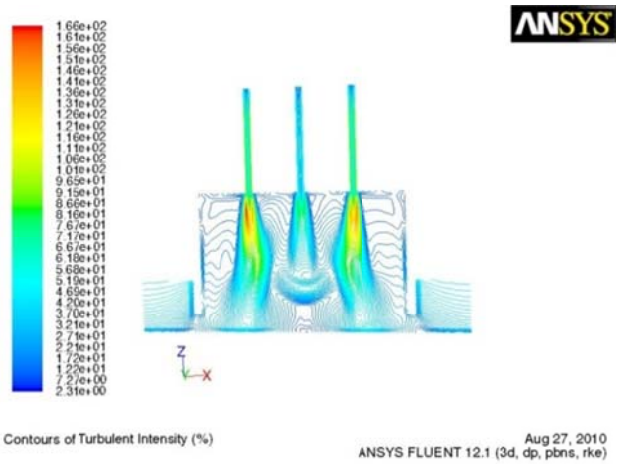

e)

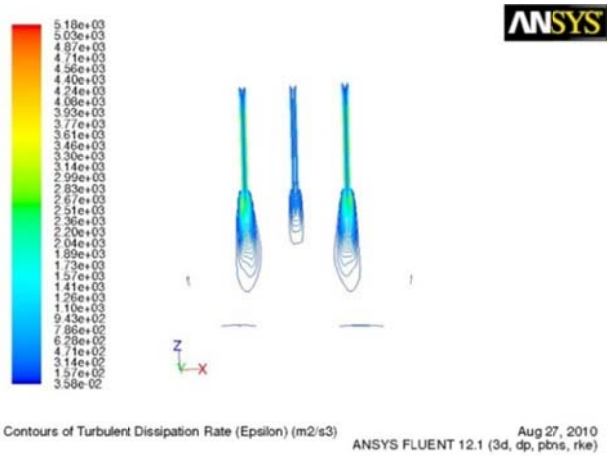

Contours of Turbulent Dissipation Rate (Epsilon) (m2/s3)

Aug 27, 2010
ANSYS FLUENT 12.1 (3d, dp, pbns, rke)

f)

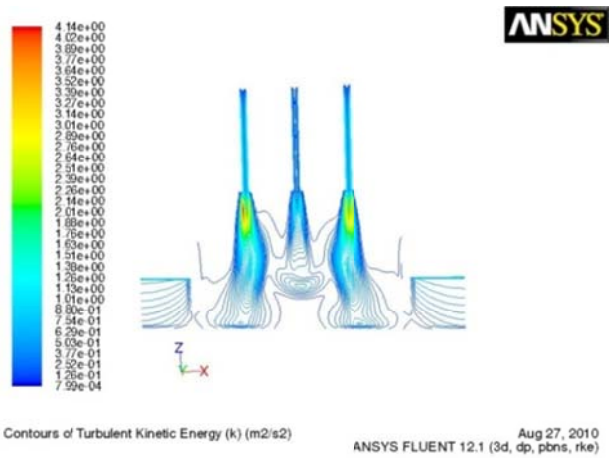

Contours of Turbulent Kinetic Energy (k) (m2/s2)

Aug 27, 2010
ANSYS FLUENT 12.1 (3d, dp, pbns, rke)

g)

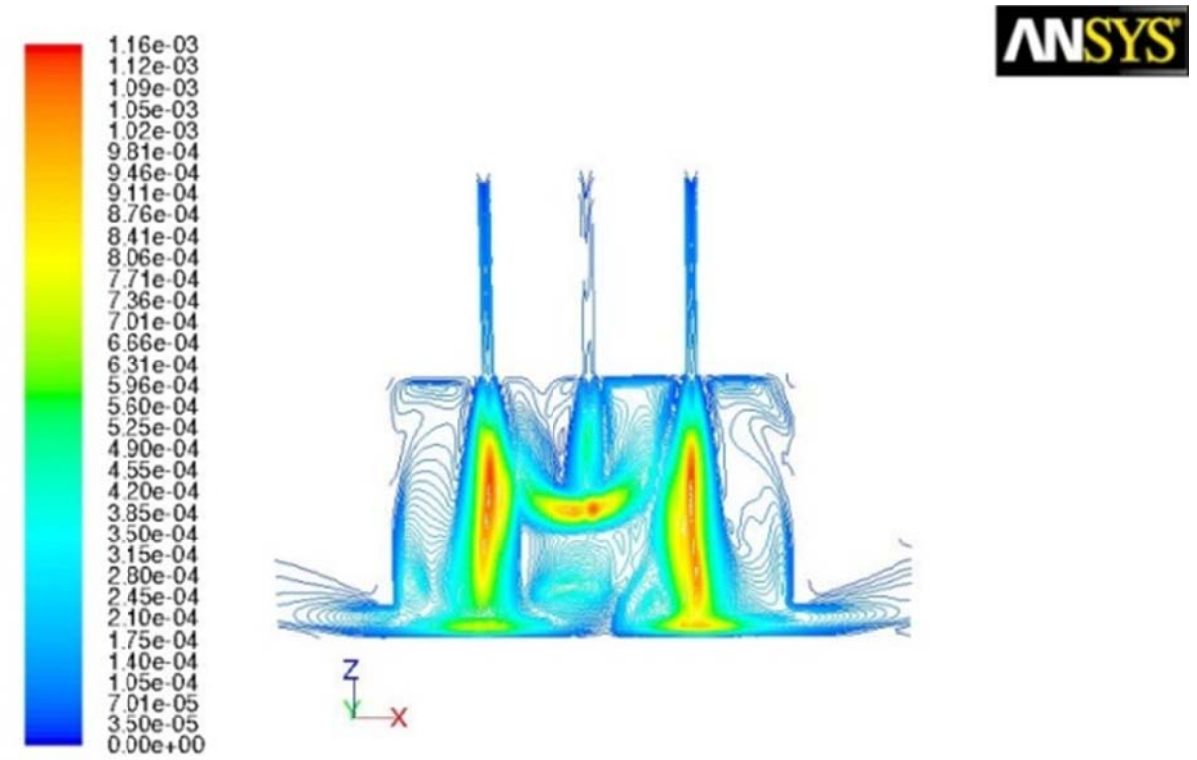

Contours of Turbulent Viscosity (kg/m-s)

Jul 29, 2009
ANSYS FLUENT 12.0 (3d, dp, pbns, rke)

h) i)

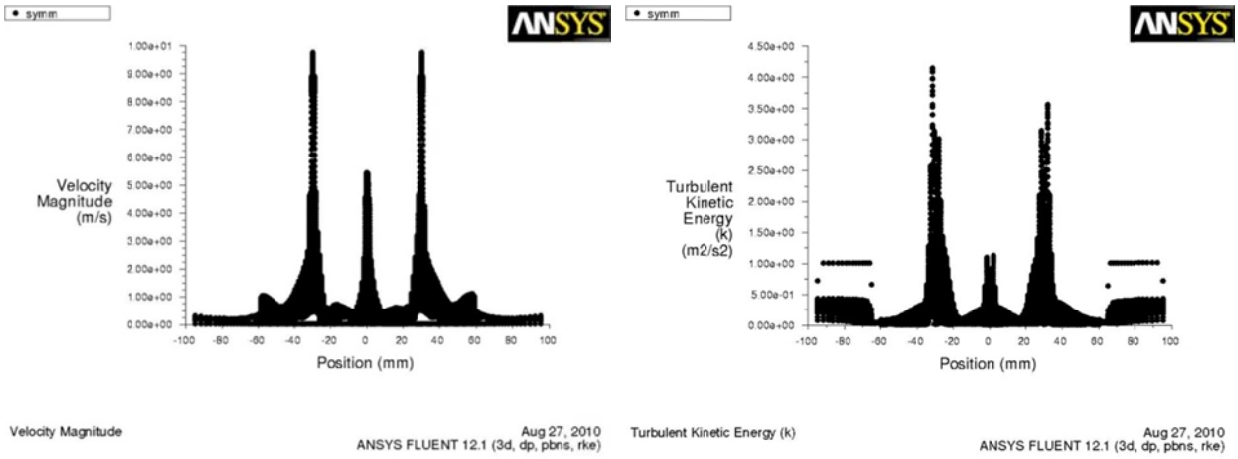

Figure 141: Head 2, fluid flow case 2: 3D view of the interior plane/plane of symmetry of the model, a) contours of velocity/ m/s, b) velocity vectors/ m/s, c) pathlines of velocity/ m/s, d) contours of turbulent intensity/ %, e) contours of dissipation rate/ m^2/s^3, f) contours of turbulent kinetic energy/ m^2/s^2, g) graph of velocity magnitude/ m/s, h) graph of turbulent kinetic energy/ m^2/s^2.

a) b)

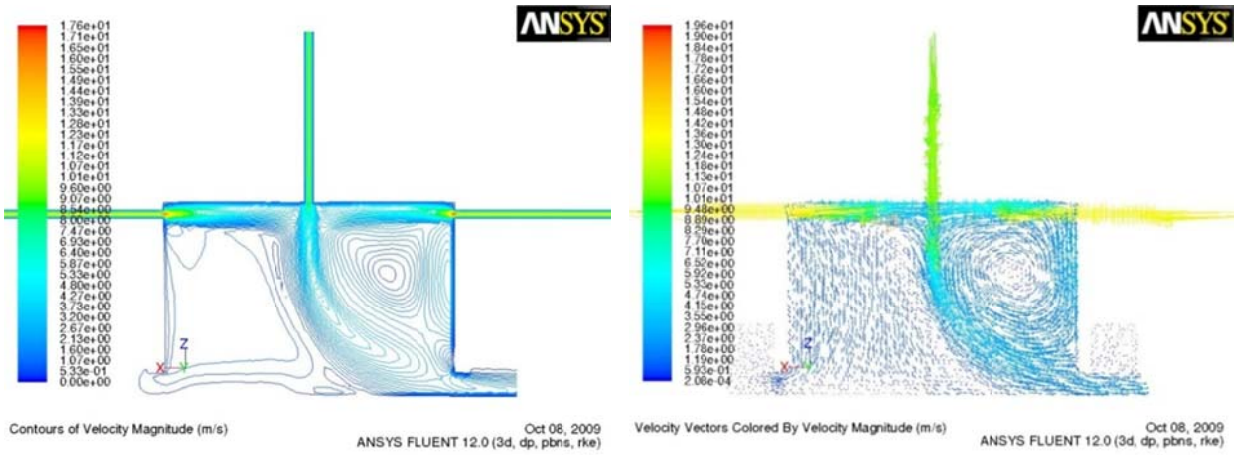

c) d)

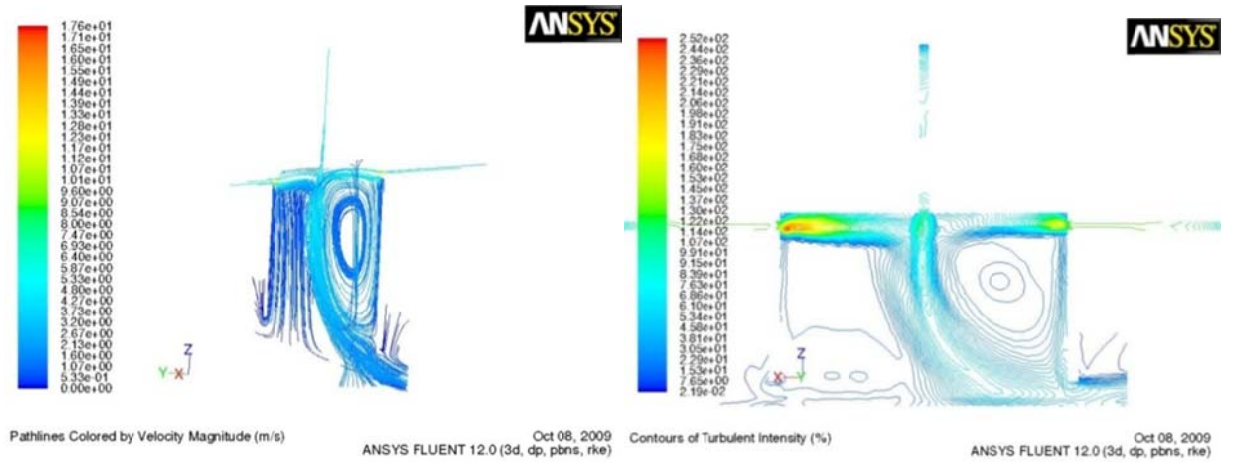

e)

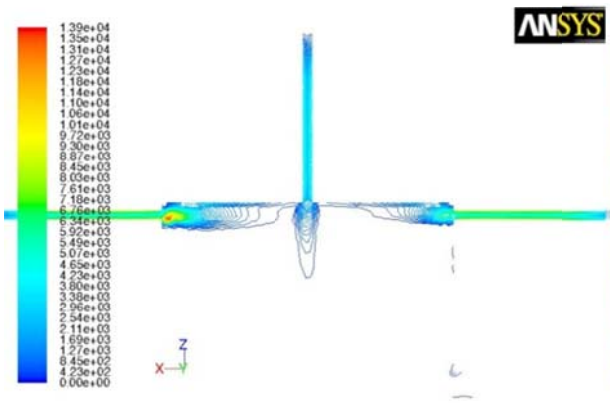

Contours of Turbulent Dissipation Rate (Epsilon) (m2/s3)

Oct 08, 2009
ANSYS FLUENT 12.0 (3d, dp, pbns, rke)

f)

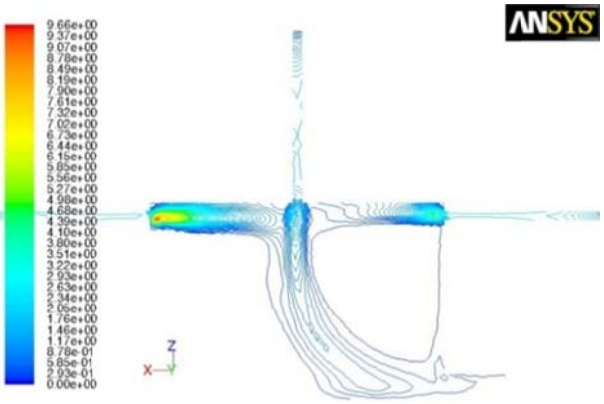

Contours of Turbulent Kinetic Energy (k) (m2/s2)

Oct 08, 2009
ANSYS FLUENT 12.0 (3d, dp, pbns, rke)

g)

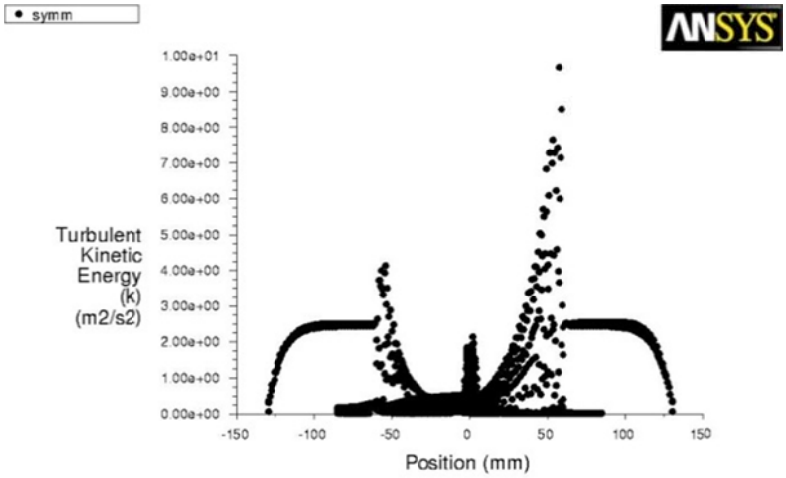

Turbulent Kinetic Energy (k)

Oct 08, 2009
ANSYS FLUENT 12.0 (3d, dp, pbns, rke)

h)

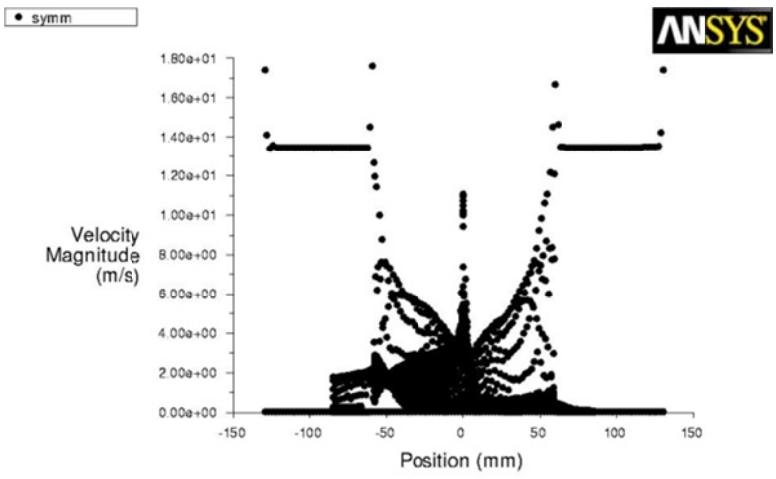

Velocity Magnitude

Oct 08, 2009
ANSYS FLUENT 12.0 (3d, dp, pbns, rke)

Figure 142: Head 2, fluid flow case 3: 3D view of the interior plane/plane of symmetry of the model, a) contours of velocity/ m/s, b) velocity vectors/ m/s, c) pathlines of velocity/ m/s, d) contours of turbulent intensity/ %, e) contours of dissipation rate/ m^2/s^3, f) contours of turbulent kinetic energy/ m^2/s^2, g) graph of velocity magnitude/ m/s, h) graph of turbulent kinetic energy/ m^2/s^2.

a)

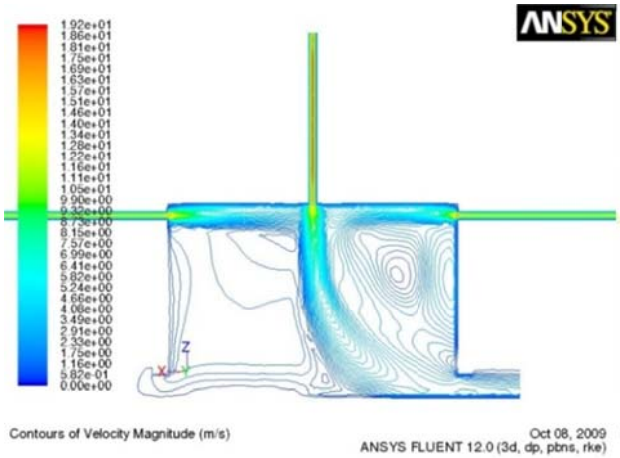

b)

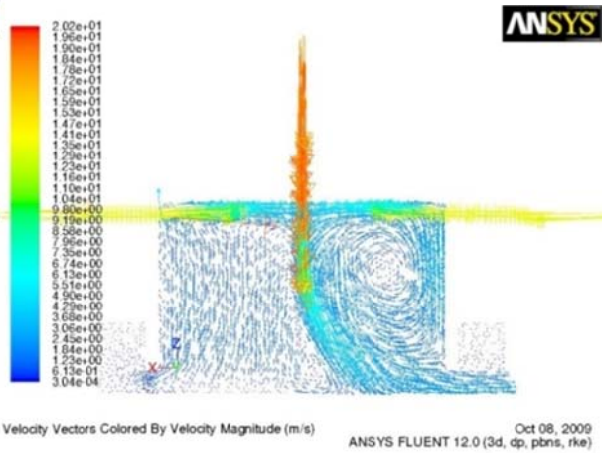

c)

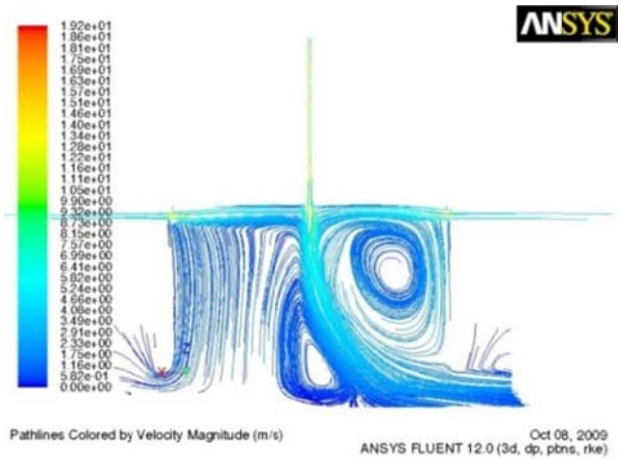

d)

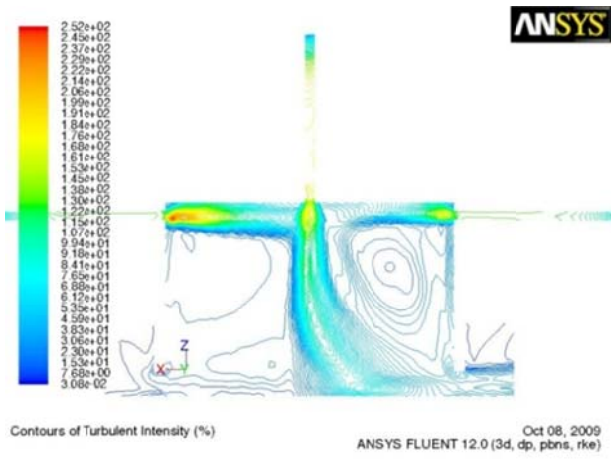

e)

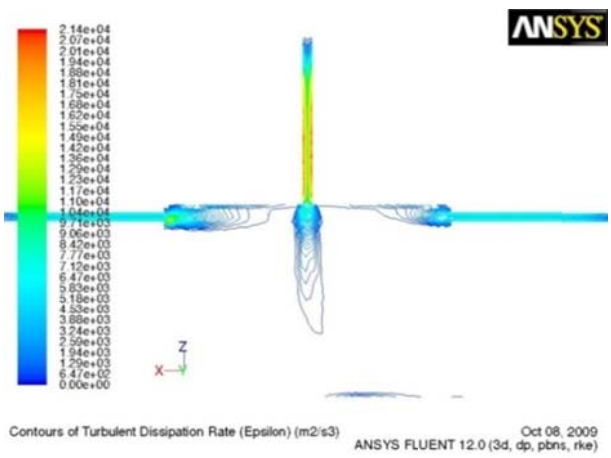

f)

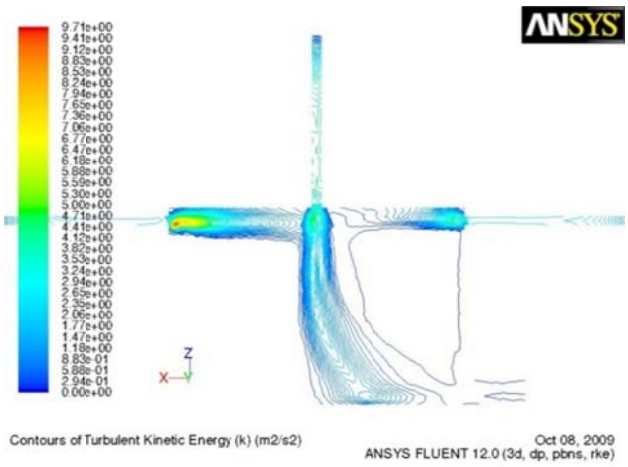

g)

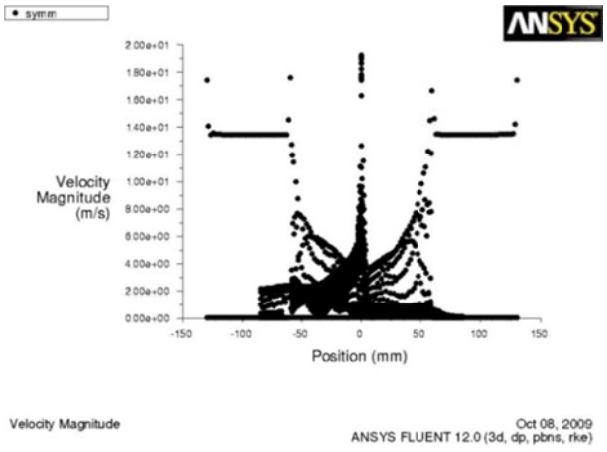

h)

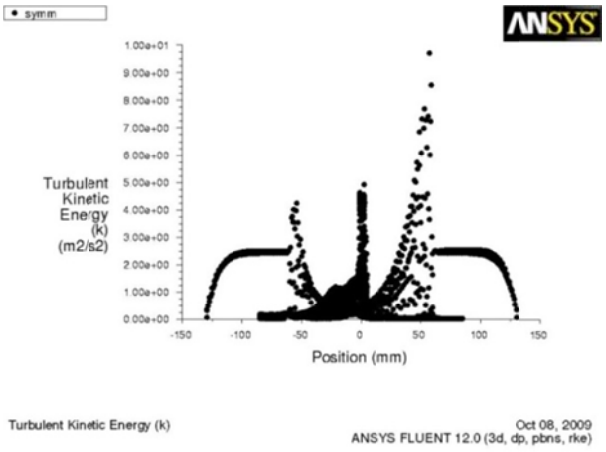

Figure 143: Head 2, fluid flow case 4: 3D view of the interior plane/plane of symmetry of the model, a) contours of velocity/ m/s, b) velocity vectors/ m/s, c) pathlines of velocity/ m/s, d) contours of turbulent intensity/ %, e) contours of dissipation rate/ m^2/s^3, f) contours of turbulent kinetic energy/ m^2/s^2, g) graph of velocity magnitude/ m/s, h) graph of turbulent kinetic energy/ m^2/s^2.

a)

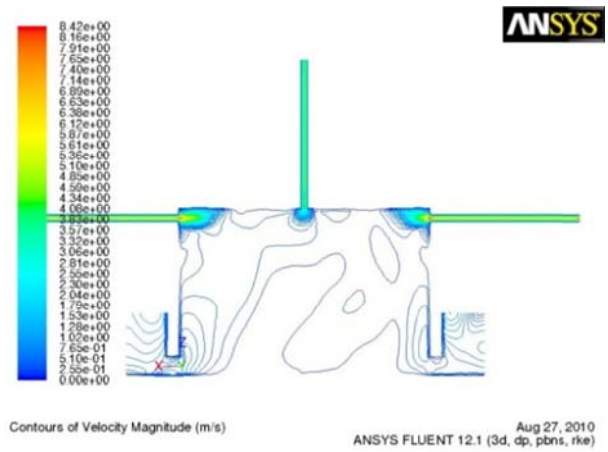

b)

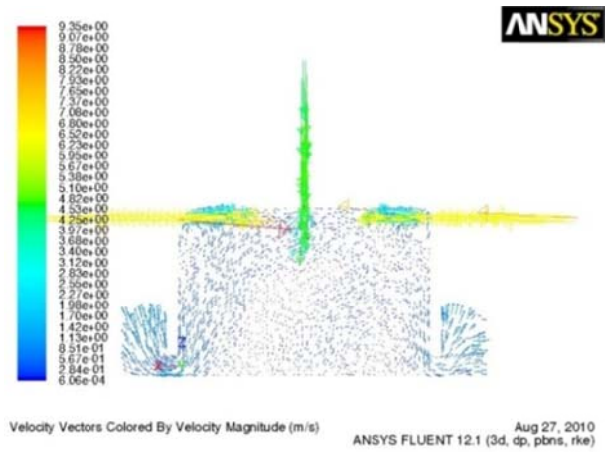

c)

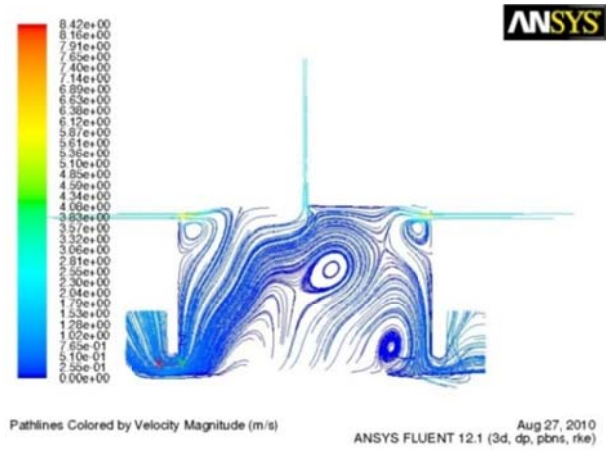

d)

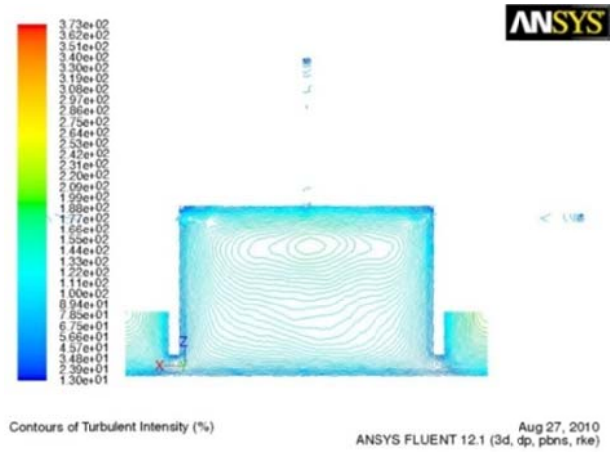

e)

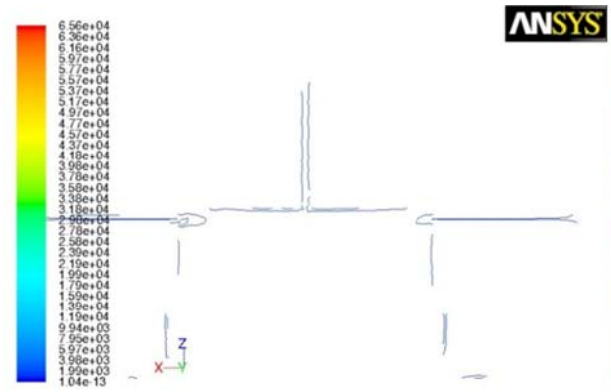

Contours of Turbulent Dissipation Rate (Epsilon) (m2/s3)

Aug 27, 2010
ANSYS FLUENT 12.1 (3d, dp, pbns, rke)

f)

Contours of Turbulent Kinetic Energy (k) (m2/s2)

Aug 27, 2010
ANSYS FLUENT 12.1 (3d, dp, pbns, rke)

g)

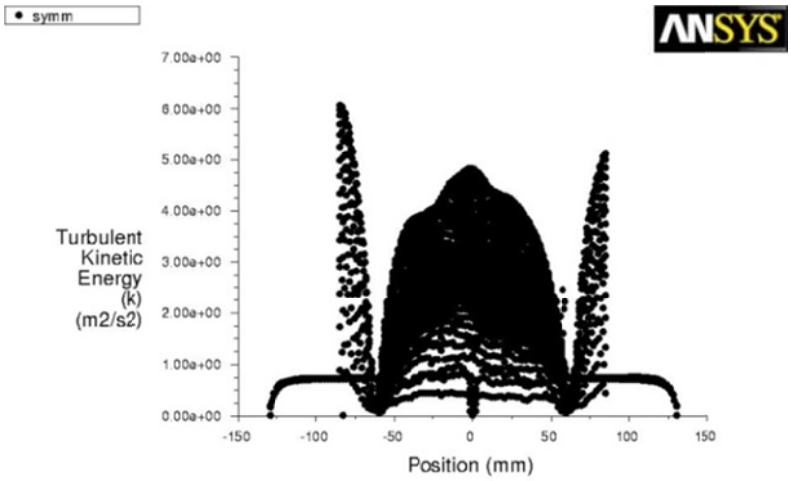

Turbulent Kinetic Energy (k)

Aug 27, 2010
ANSYS FLUENT 12.1 (3d, dp, pbns, rke)

h)

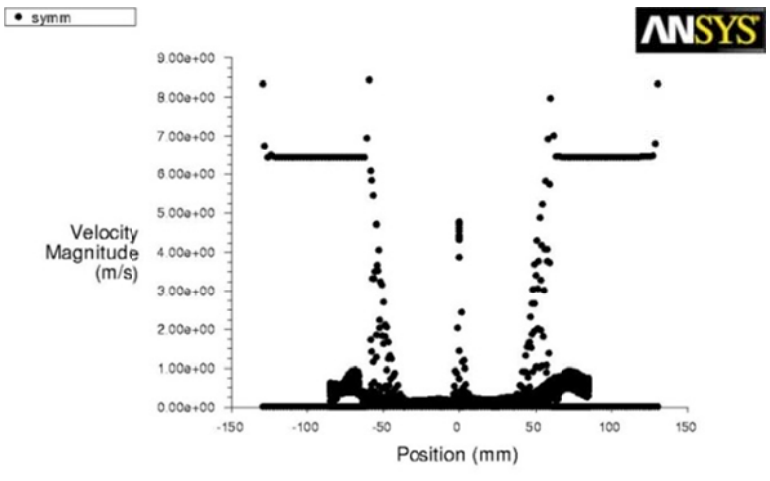

Velocity Magnitude

Aug 27, 2010
ANSYS FLUENT 12.1 (3d, dp, pbns, rke)

Figure 144: Head 3, fluid flow case 2: 3D view of the interior plane/plane of symmetry of the model, a) contours of velocity/ m/s, b) velocity vectors/ m/s, c) pathlines of velocity/ m/s, d) contours of turbulent intensity/ %, e) contours of dissipation rate/ m^2/s^3, f) contours of turbulent kinetic energy/ m^2/s^2, g) graph of velocity magnitude/ m/s, h) graph of turbulent kinetic energy/ m^2s^2.

a)

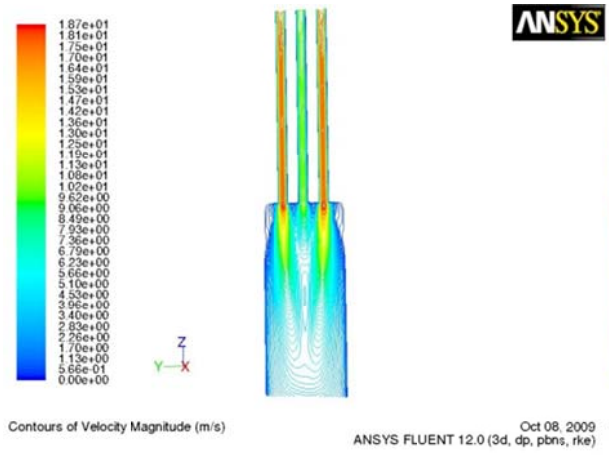

b)

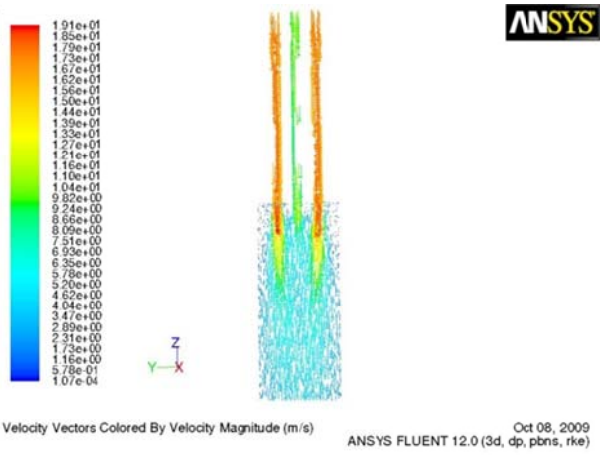

c)

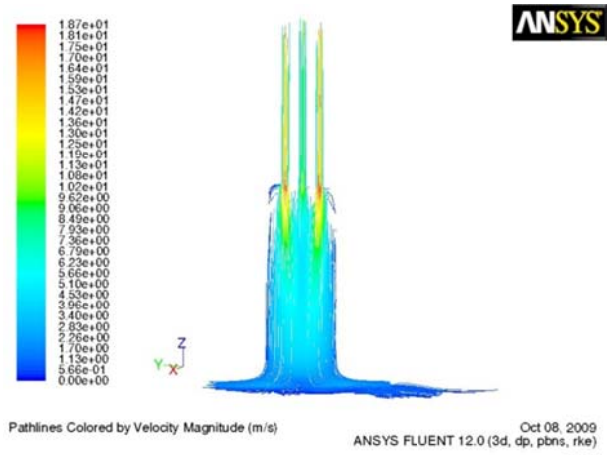

d)

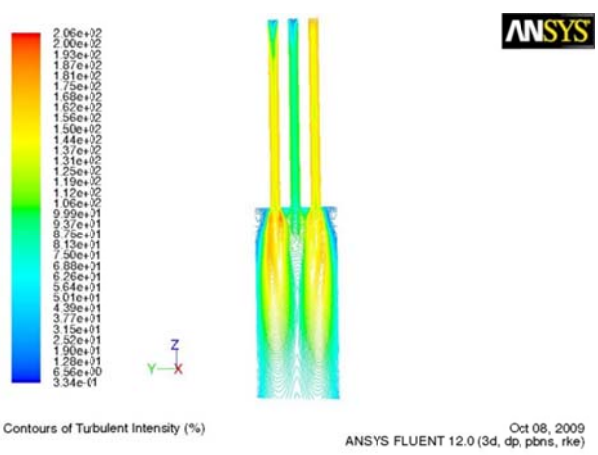

e)

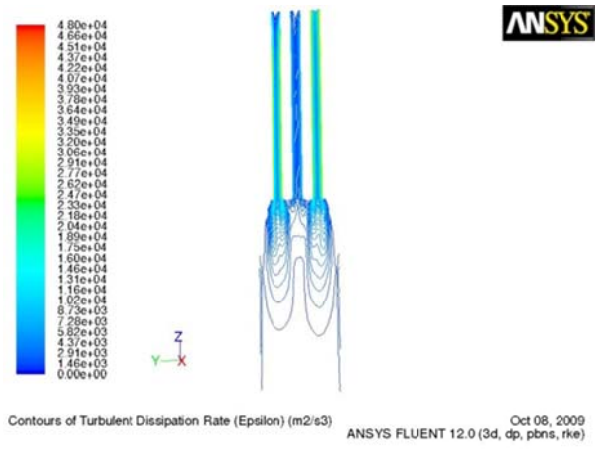

f)

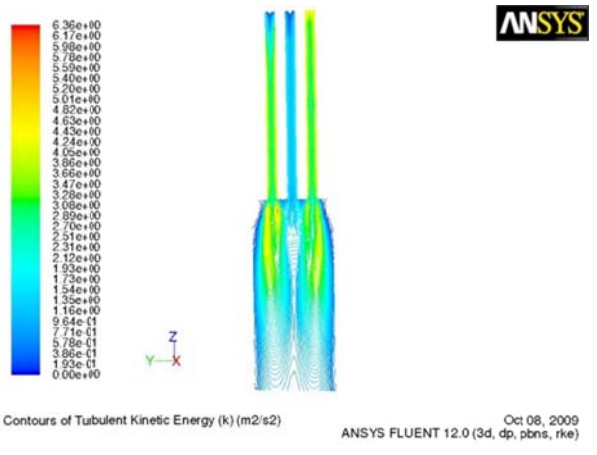

g)

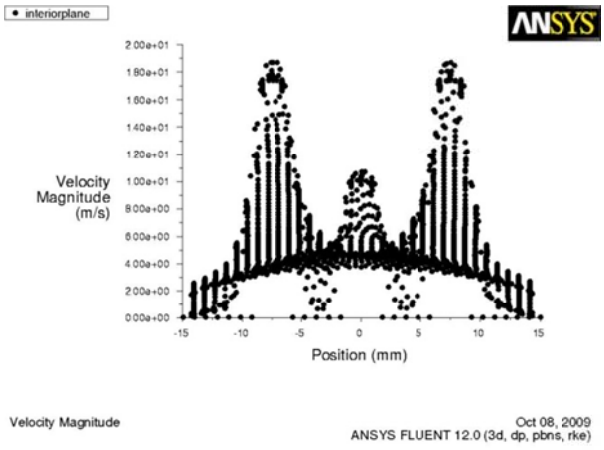

h)

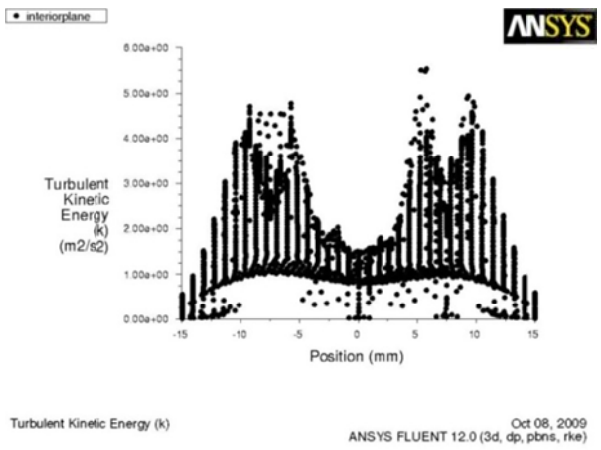

Figure 145: Head 3, fluid flow case 3: 3D view of the interior plane/plane of symmetry of the model, a) contours of velocity/ m/s, b) velocity vectors/ m/s, c) pathlines of velocity/ m/s, d) contours of turbulent intensity/ %, e) contours of dissipation rate/ m^2/s^3, f) contours of turbulent kinetic energy/ m^2/s^2, g) graph of velocity magnitude/ m/s, h) graph of turbulent kinetic energy/ m^2/s^2.

a)

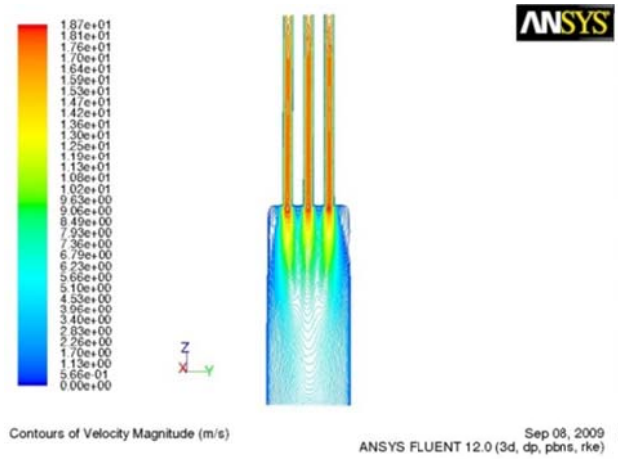

b)

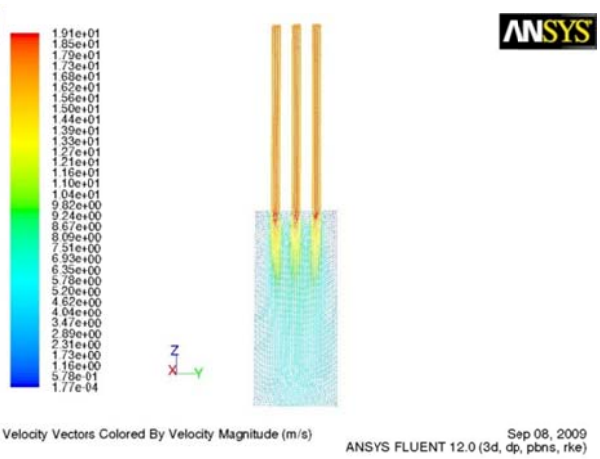

c)

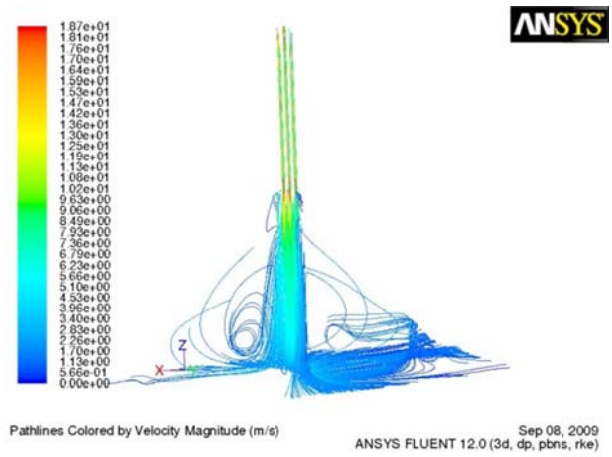

d)

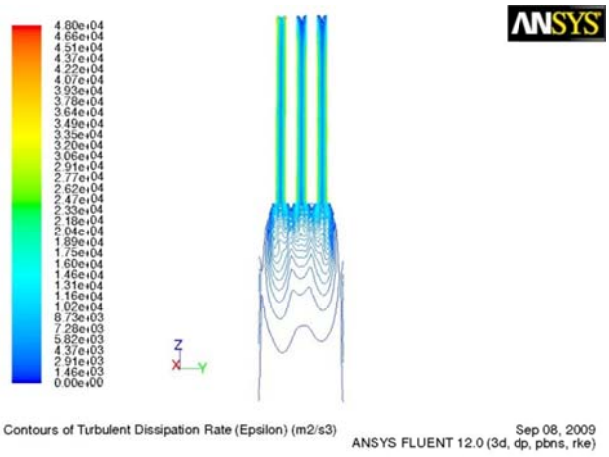

e)

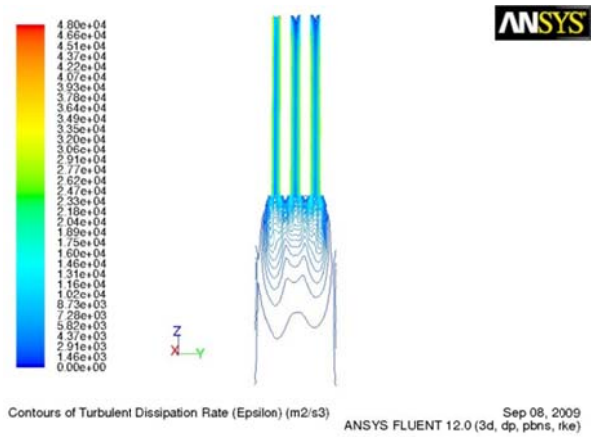

f)

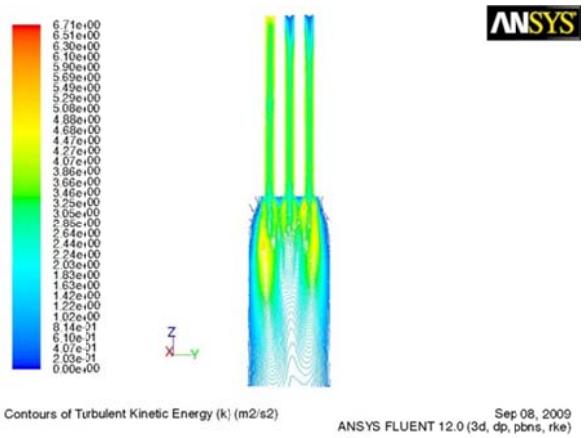

g)

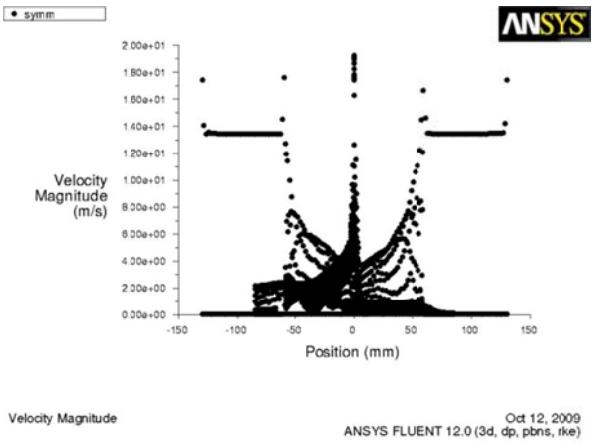

h)

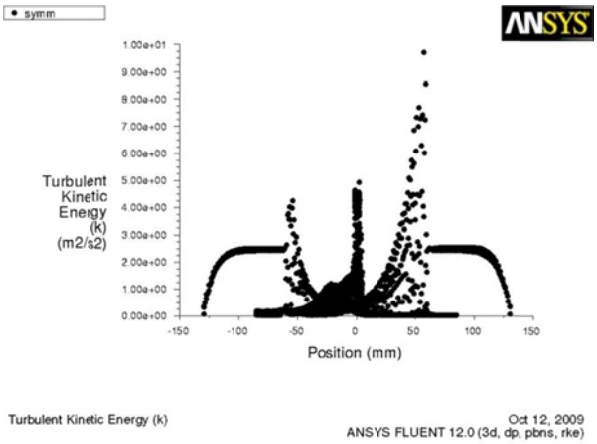

Figure 146: Head 3, fluid flow case 4: 3D view of the interior plane/plane of symmetry of the model, a) contours of velocity/ m/s, b) velocity vectors/ m/s, c) pathlines of velocity/ m/s, d) contours of turbulent intensity/ %, e) contours of dissipation rate/ m^2/s^3, f) contours of turbulent kinetic energy/ m^2/s^2, g) graph of velocity magnitude/ m/s, h) graph of turbulent kinetic energy/ m^2/s^2.

a)

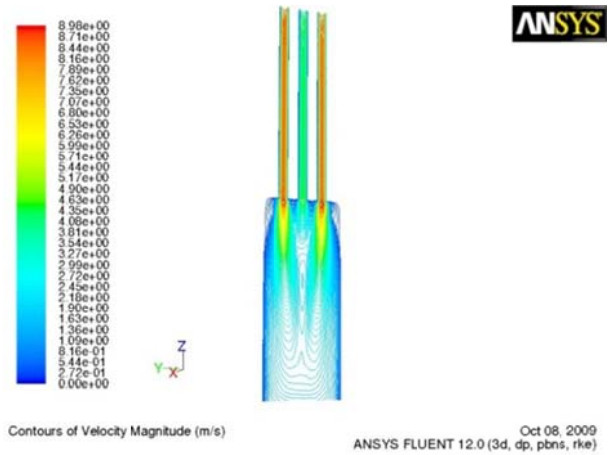

b)

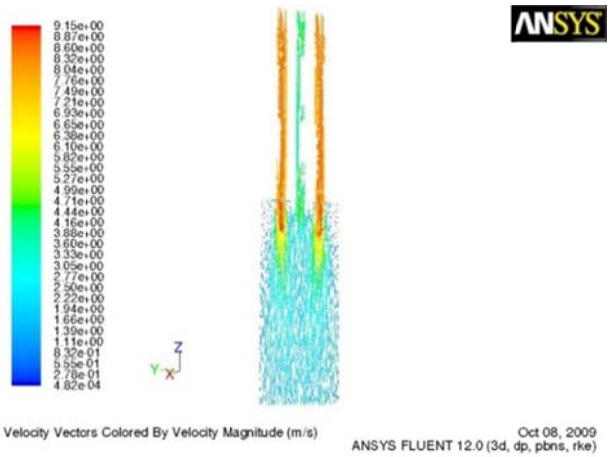

c)

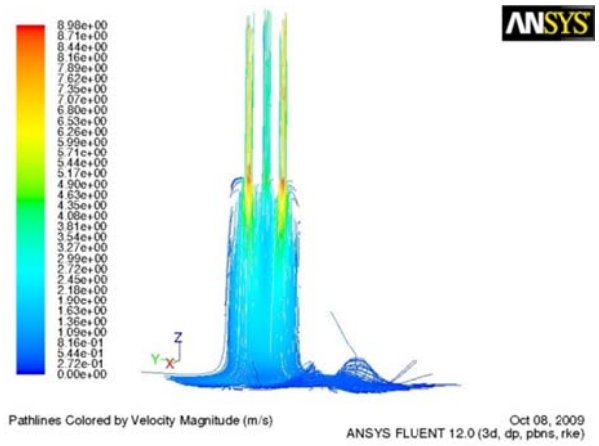

Pathlines Colored by Velocity Magnitude (m/s)

Oct 08, 2009
ANSYS FLUENT 12.0 (3d, dp, pbns, rke)

d)

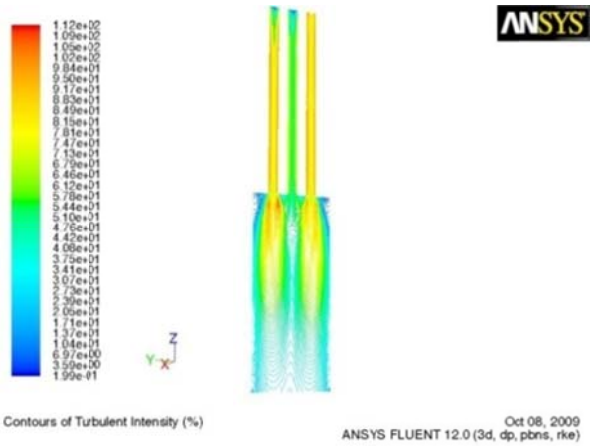

Contours of Turbulent Intensity (%)

Oct 08, 2009
ANSYS FLUENT 12.0 (3d, dp, pbns, rke)

e)

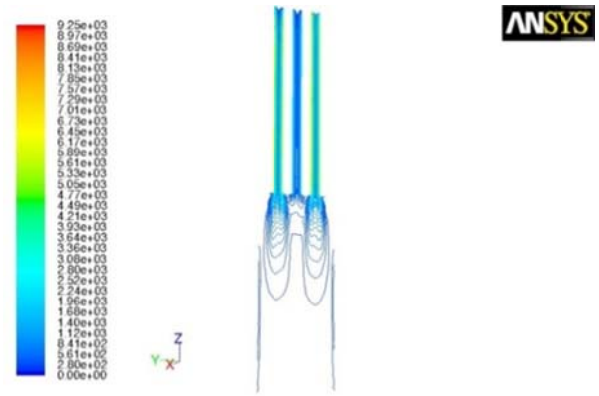

Contours of Turbulent Dissipation Rate (Epsilon) (m2/s3)

Oct 08, 2009
ANSYS FLUENT 12.0 (3d, dp, pbns, rke)

f)

Contours of Turbulent Kinetic Energy (k) (m2/s2)

Oct 08, 2009
ANSYS FLUENT 12.0 (3d, dp, pbns, rke)

g)

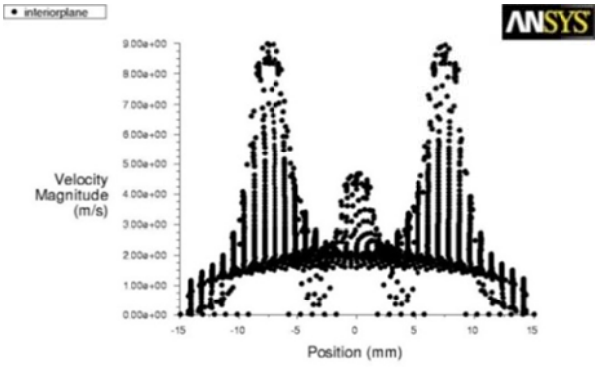

Velocity Magnitude

Oct 08, 2009
ANSYS FLUENT 12.0 (3d, dp, pbns, rke)

h)

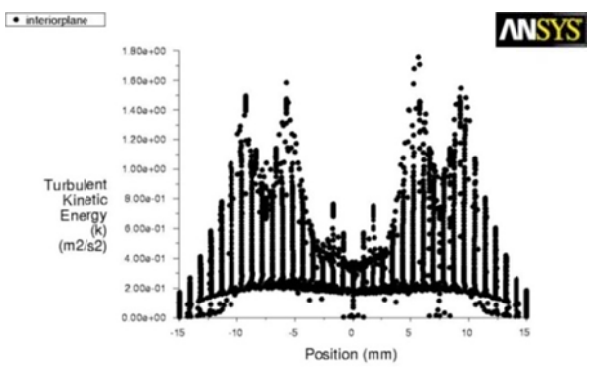

Turbulent Kinetic Energy (k)

Oct 08, 2009
ANSYS FLUENT 12.0 (3d, dp, pbns, rke)

Figure 147: Head 4, fluid flow case 1: 3D view of the interior plane/plane of symmetry of the model, a) contours of velocity/ m/s, b) velocity vectors/ m/s, c) pathlines of velocity/ m/s, d) contours of turbulent intensity/ %, e) contours of dissipation rate/ m^2s^3, f) contours of turbulent kinetic energy/ m^2/s^2 g) graph of velocity magnitude/ m/s, h) graph of turbulent kinetic energy/ m^2/s^2.

a)

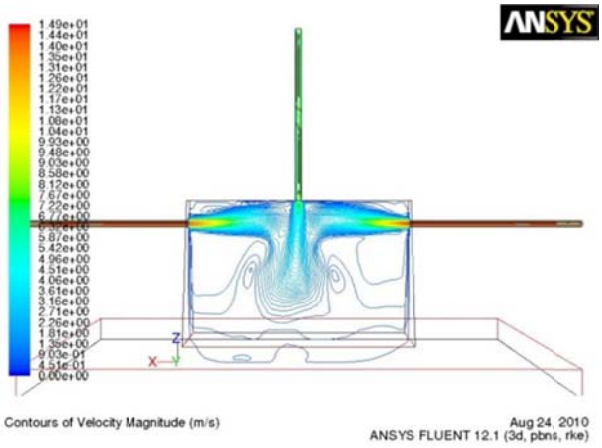

b)

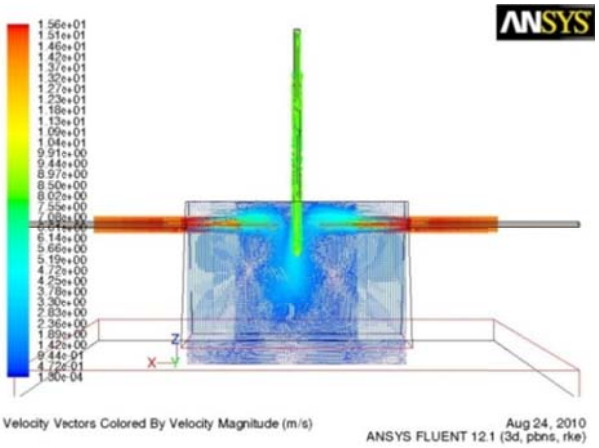

c)

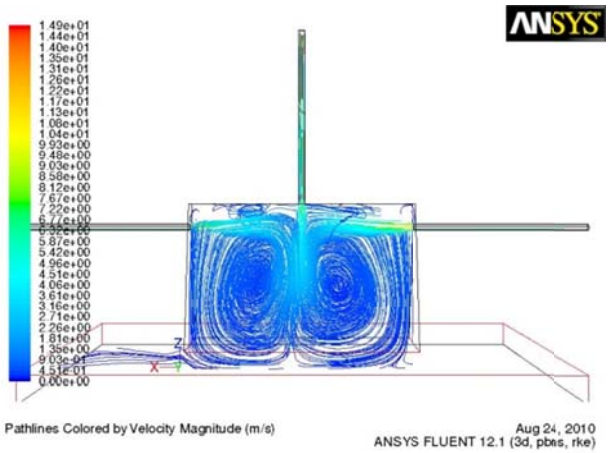

d)

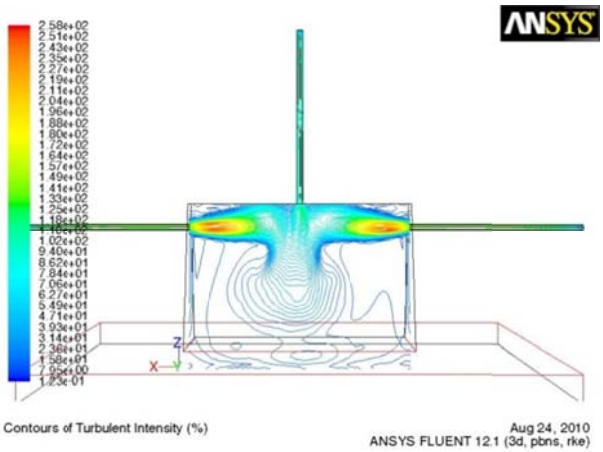

e)

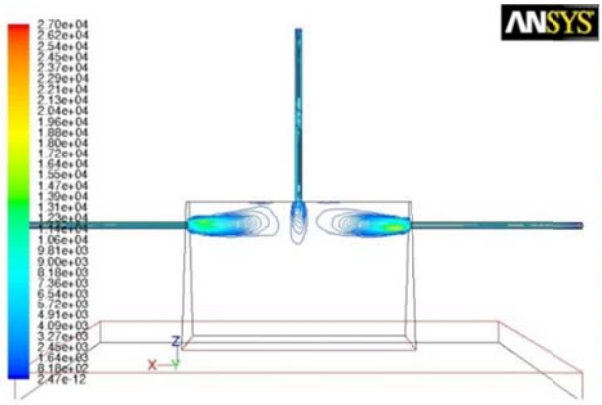
ANSYS
2.70e+04
2.62e+04
2.54e+04
2.45e+04
2.37e+04
2.29e+04
2.21e+04
2.13e+04
2.04e+04
1.96e+04
1.88e+04
1.80e+04
1.72e+04
1.64e+04
1.55e+04
1.47e+04
1.39e+04
1.31e+04
1.23e+04
1.06e+04
9.81e+03
9.00e+03
8.18e+03
7.36e+03
6.54e+03
5.72e+03
4.91e+03
4.09e+03
3.27e+03
2.45e+03
1.64e+03
8.18e+02
2.47e-12
Z
X
Contours of Turbulent Dissipation Rate (Epsilon) (m2/s3)
Aug 24, 2010
ANSYS FLUENT 12.1 (3d, pbns, rke)

f)

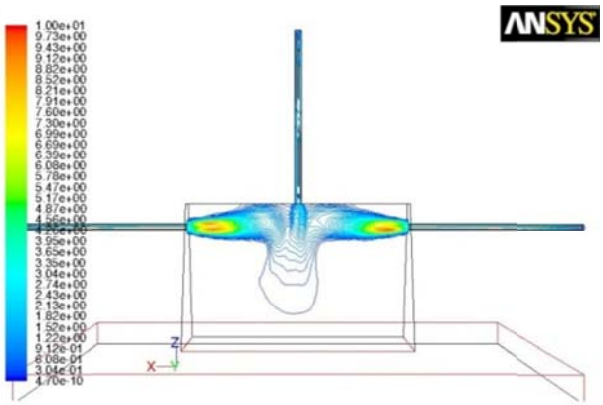
ANSYS
1.00e+01
9.73e+00
9.43e+00
9.12e+00
8.82e+00
8.52e+00
8.21e+00
7.91e+00
7.60e+00
7.30e+00
6.99e+00
6.69e+00
6.39e+00
6.08e+00
5.78e+00
5.47e+00
5.17e+00
4.87e+00
4.56e+00
3.95e+00
3.65e+00
3.35e+00
3.04e+00
2.74e+00
2.43e+00
2.13e+00
1.82e+00
1.52e+00
1.22e+00
9.12e-01
6.08e-01
3.04e-01
4.70e-10
Z
X
Contours of Turbulent Kinetic Energy (k) (m2/s2)
Aug 24, 2010
ANSYS FLUENT 12.1 (3d, pbns, rke)

g)

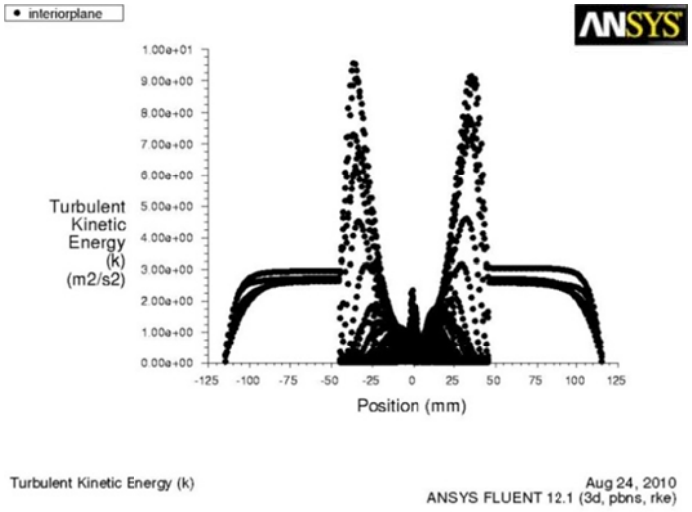
interiorplane
ANSYS
1.00e+01
9.00e+00
8.00e+00
7.00e+00
6.00e+00
5.00e+00
4.00e+00
3.00e+00
2.00e+00
1.00e+00
0.00e+00
Turbulent Kinetic Energy (k) (m2/s2)
-125
-100
-75
-50
-25
0
25
50
75
100
125
Position (mm)
Turbulent Kinetic Energy (k)
Aug 24, 2010
ANSYS FLUENT 12.1 (3d, pbns, rke)

h)

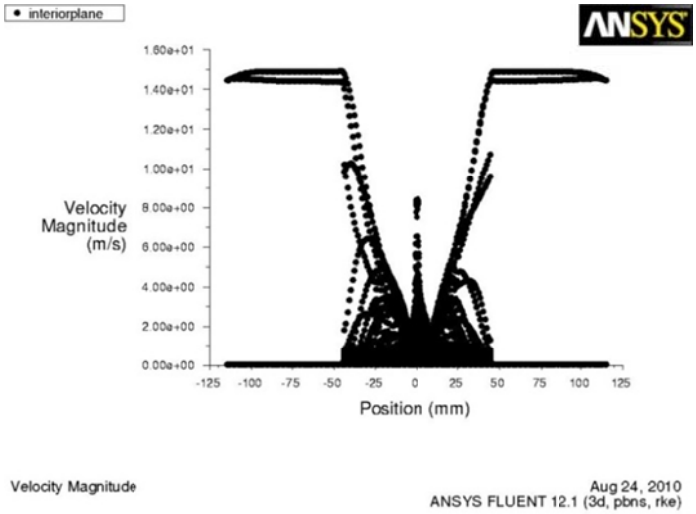
interiorplane
ANSYS
1.60e+01
1.40e+01
1.20e+01
1.00e+01
8.00e+00
6.00e+00
4.00e+00
2.00e+00
0.00e+00
Velocity Magnitude (m/s)
-125
-100
-75
-50
-25
0
25
50
75
100
125
Position (mm)
Velocity Magnitude
Aug 24, 2010
ANSYS FLUENT 12.1 (3d, pbns, rke)

Figure 148: Head 4, fluid flow case 2: 3D view of the interior plane/plane of symmetry of the model, a) contours of velocity/ m/s, b) velocity vectors/ m/s, c) pathlines of velocity/ m/s, d) contours of turbulent intensity/ %, e) contours of dissipation rate/ m^2/s^3, f) contours of turbulent kinetic energy/ m^2/s^2, g) graph of velocity magnitude/ m/s, h) graph of turbulent kinetic energy/ m^2s^2.

a)

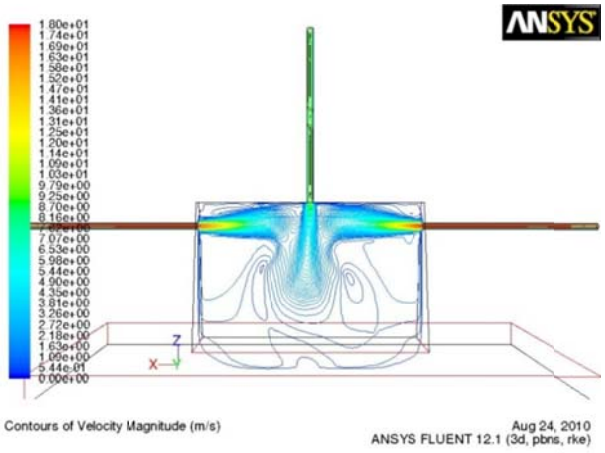

b)

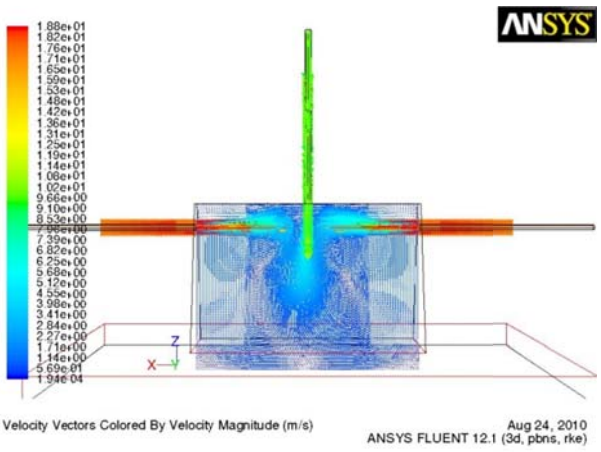

c)

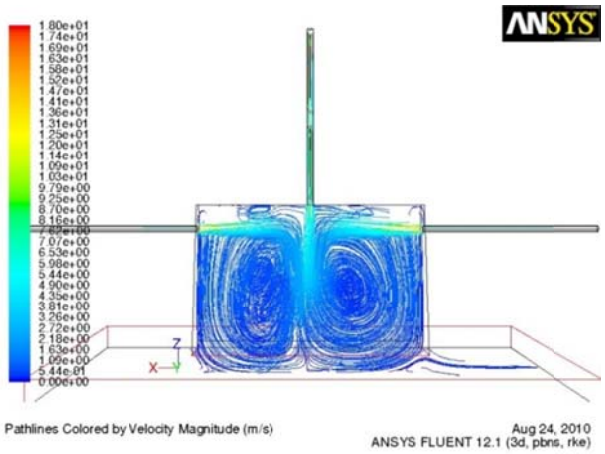

d)

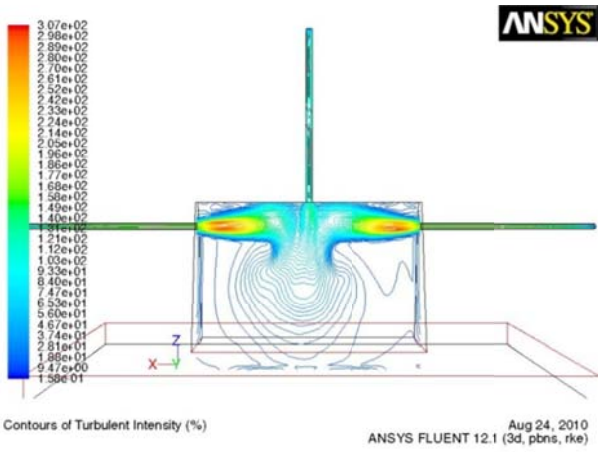

e)

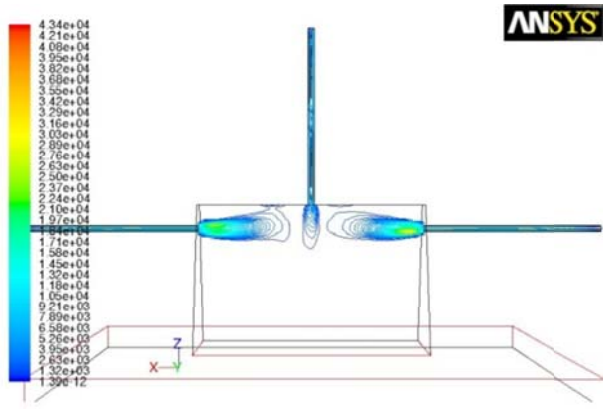

Contours of Turbulent Dissipation Rate (Epsilon) (m2/s3)

Aug 24, 2010
ANSYS FLUENT 12.1 (3d, pbns, rke)

f)

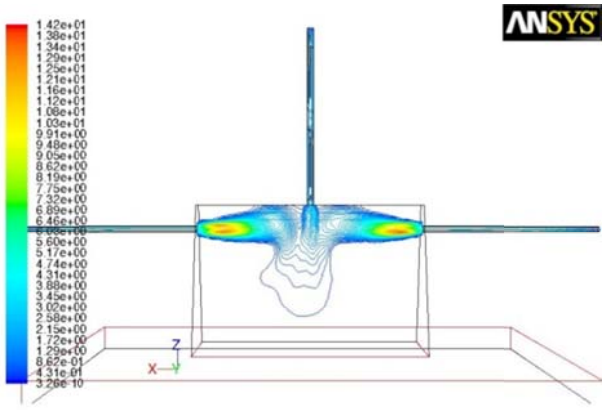

Contours of Turbulent Kinetic Energy (k) (m2/s2)

Aug 24, 2010
ANSYS FLUENT 12.1 (3d, pbns, rke)

g)

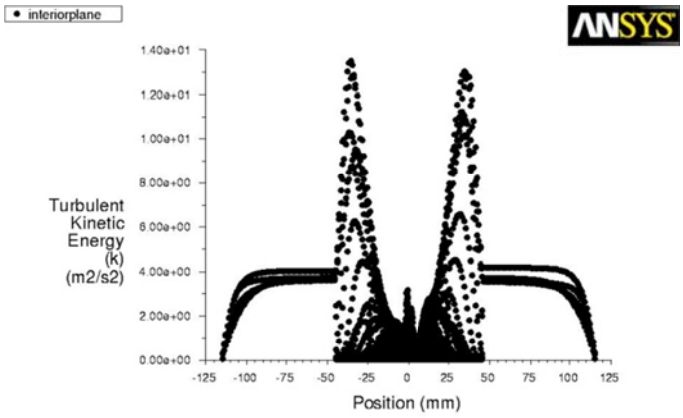

Turbulent Kinetic Energy (k)

Aug 24, 2010
ANSYS FLUENT 12.1 (3d, pbns, rke)

h)

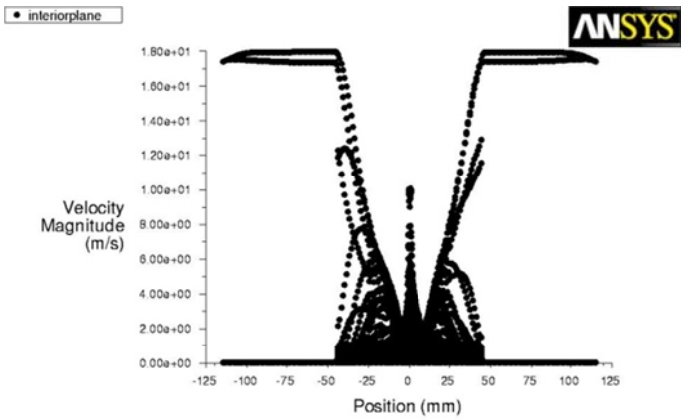

Velocity Magnitude

Aug 24, 2010
ANSYS FLUENT 12.1 (3d, pbns, rke)

Figure 149: Head 4, fluid flow case 3: 3D view of the interior plane/plane of symmetry of the model, a) contours of velocity/ m/s, b) velocity vectors/ m/s, c) pathlines of velocity/ m/s, d) contours of turbulent intensity/ %, e) contours of dissipation rate/ m^2/s^3, f) contours of turbulent kinetic energy/ m^2/s^2, g) graph of velocity magnitude/ m/s, h) graph of turbulent kinetic energy/ m^2/s^2.

a)

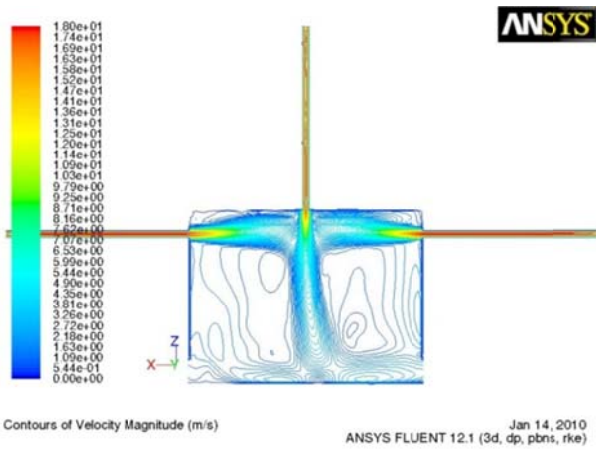

b)

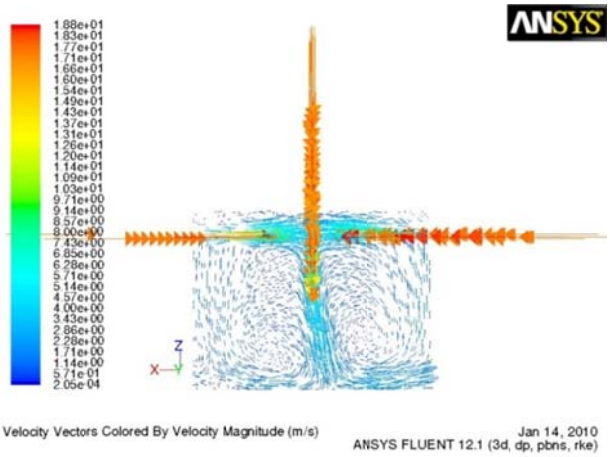

c)

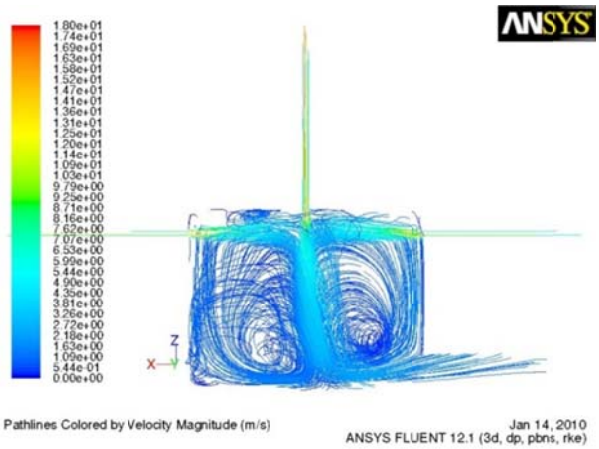

d)

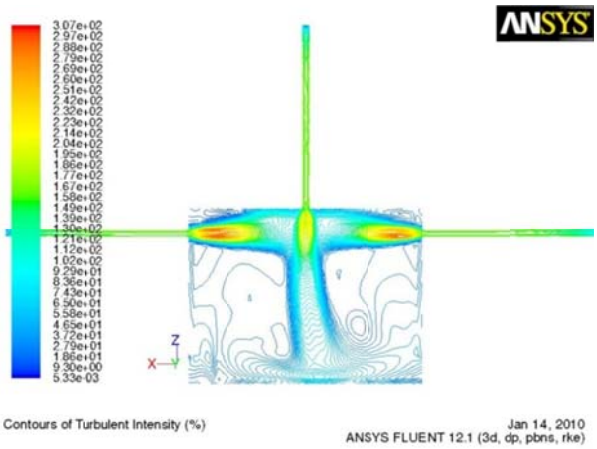

e)

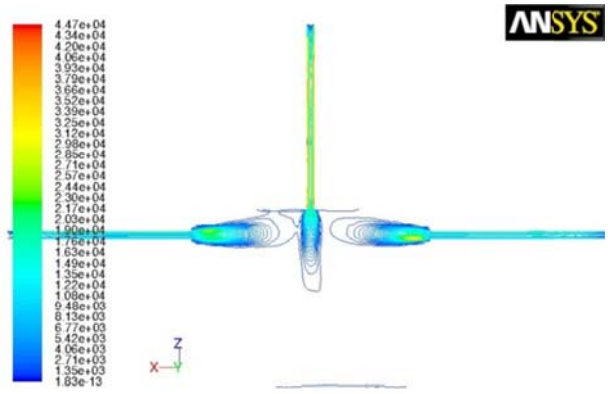

Contours of Turbulent Dissipation Rate (Epsilon) (m2/s3)

Jan 14, 2010
ANSYS FLUENT 12.1 (3d, dp, pbns, rke)

f)

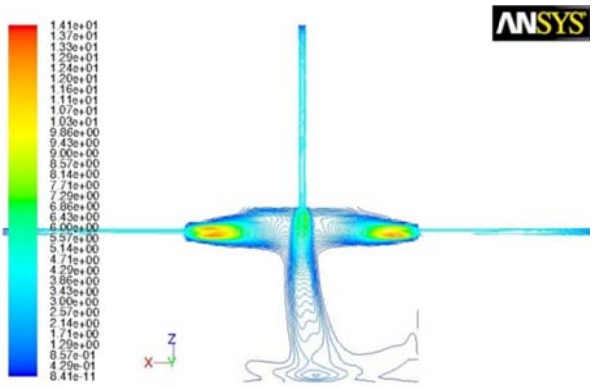

Contours of Turbulent Kinetic Energy (k) (m2/s2)

Jan 14, 2010
ANSYS FLUENT 12.1 (3d, dp, pbns, rke)

g)

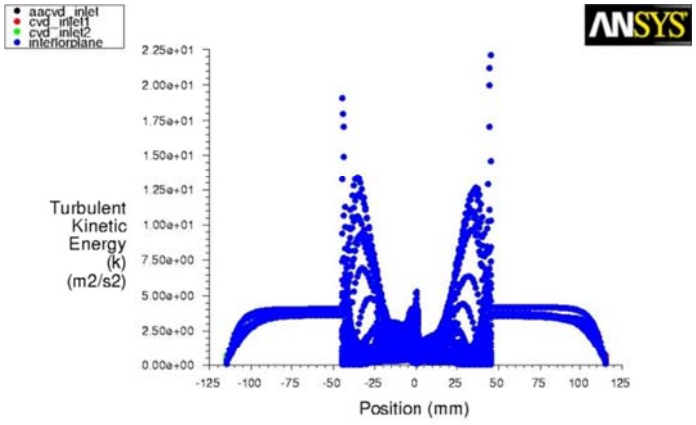

Turbulent Kinetic Energy (k)

Sep 21, 2009
ANSYS FLUENT 12.0 (3d, dp, pbns, rke)

h)

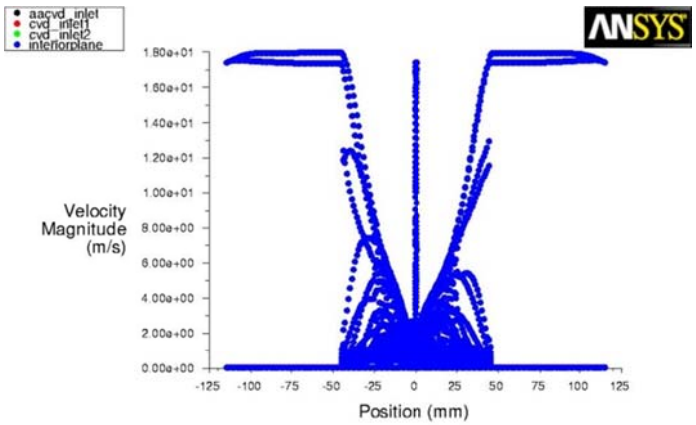

Velocity Magnitude

Sep 21, 2009
ANSYS FLUENT 12.0 (3d, dp, pbns, rke)

Figure 150: Head 4, fluid flow case 4: 3D view of the interior plane/plane of symmetry of the model, a) contours of velocity magnitude/ m/s, b) vectors of velocity/ m/s, c) pathlines of velocity/ m/s, d) contours of turbulent intensity/ %, e) contours of dissipation rate/ m^2/s^3, f) contours of turbulent kinetic energy/ m^2/s^2, g) graph of velocity magnitude/ m/s, h) graph of turbulent kinetic energy/ m^2/s^2.

a)

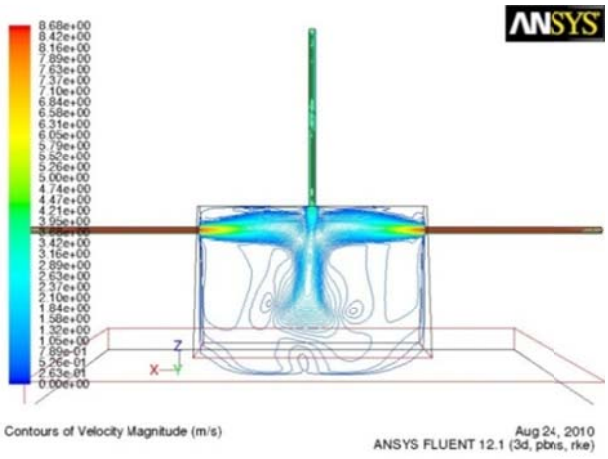

b)

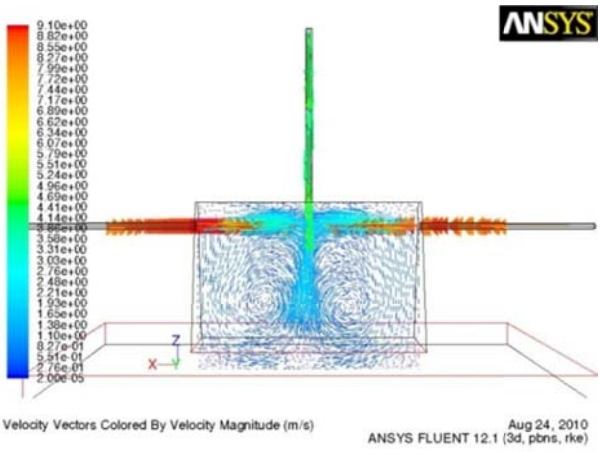

c)

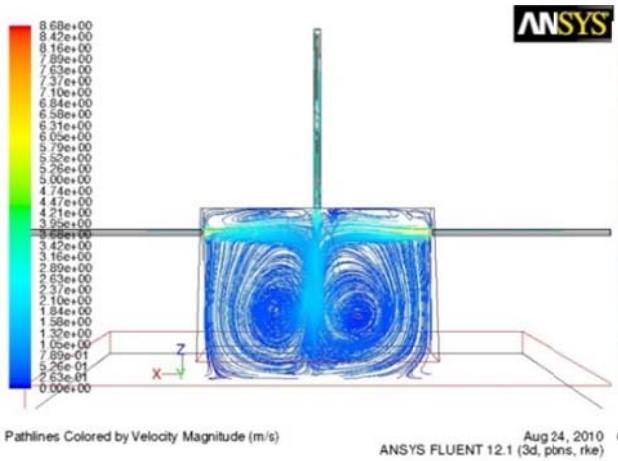

d)

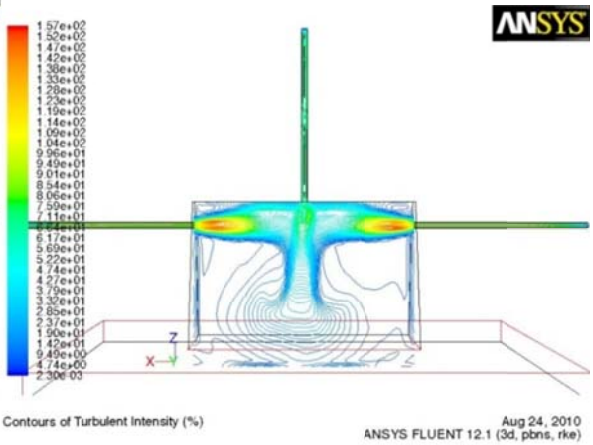

e)

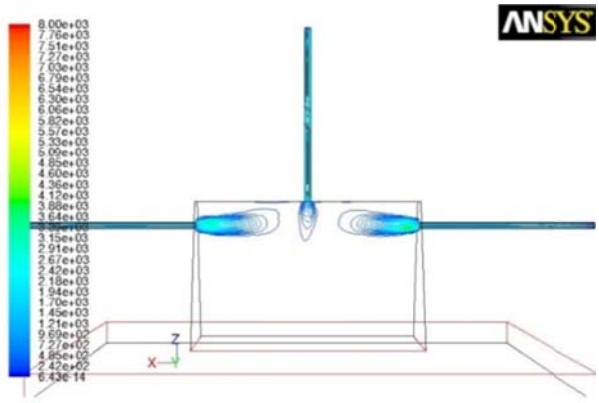
ANSYS
Contours of Turbulent Dissipation Rate (Epsilon) (m2/s3)
Aug 24, 2010
ANSYS FLUENT 12.1 (3d, pbns, rke)

f)

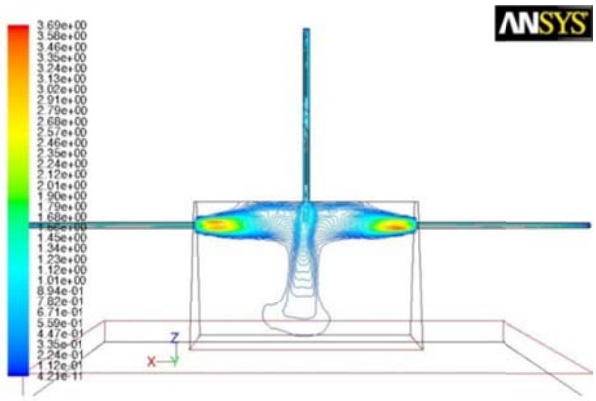
ANSYS
Contours of Turbulent Kinetic Energy (k) (m2/s2)
Aug 24, 2010
ANSYS FLUENT 12.1 (3d, pbns, rke)

g)

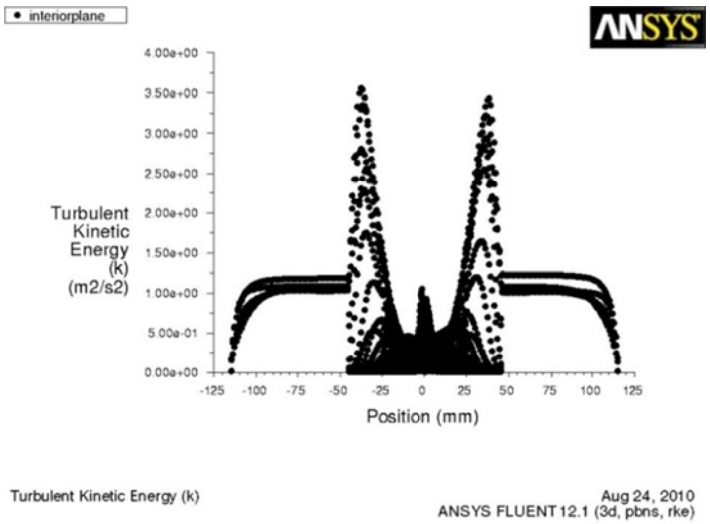
interiorplane
ANSYS
Turbulent Kinetic Energy (k) (m2/s2)
Position (mm)
Turbulent Kinetic Energy (k)
Aug 24, 2010
ANSYS FLUENT 12.1 (3d, pbns, rke)

h)

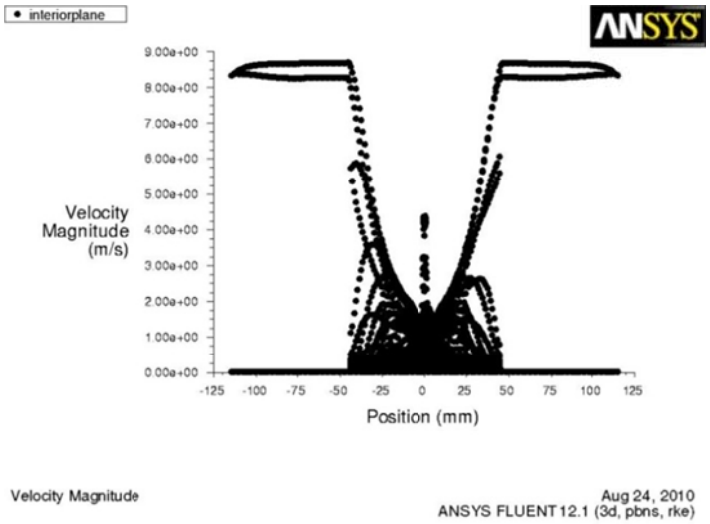
interiorplane
ANSYS
Velocity Magnitude (m/s)
Position (mm)
Velocity Magnitude
Aug 24, 2010
ANSYS FLUENT 12.1 (3d, pbns, rke)

Figure 151: Head 5, fluid flow case 2: 3D view of the interior plane/plane of symmetry of the model, a) contours of velocity/ m/s, b) velocity vectors/ m/s, c) contours of turbulent intensity/ %, d) contours of dissipation rate/ m^2/s^3, e) graph of velocity magnitude/ m/s, f) graph of turbulent kinetic energy/ m^2/s^2.

a)

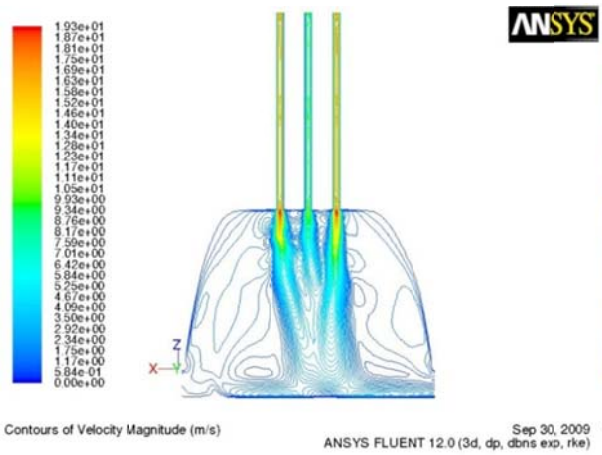

b)

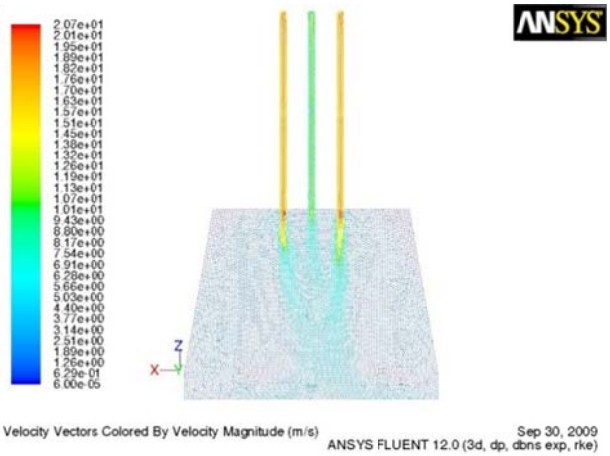

c)

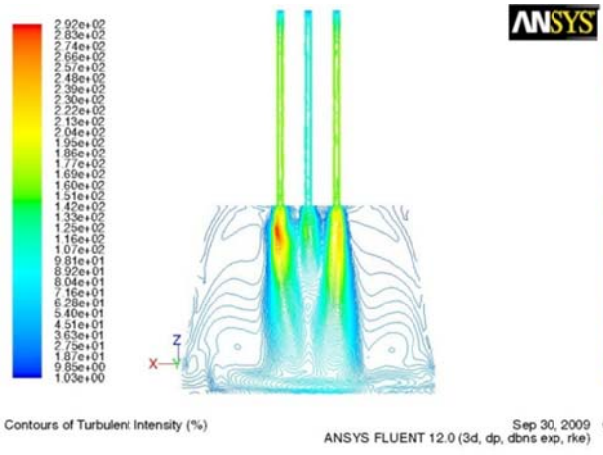

d)

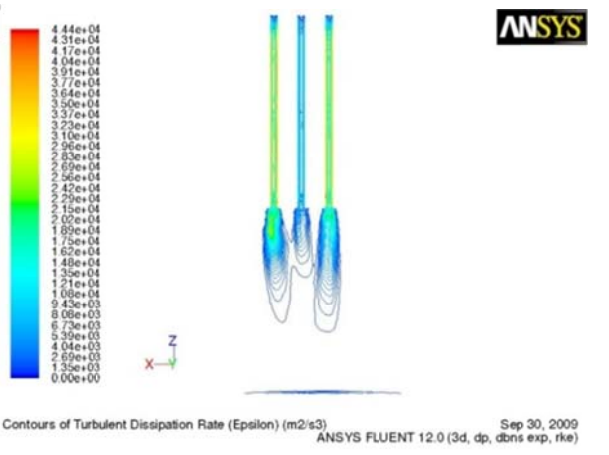

e) f)

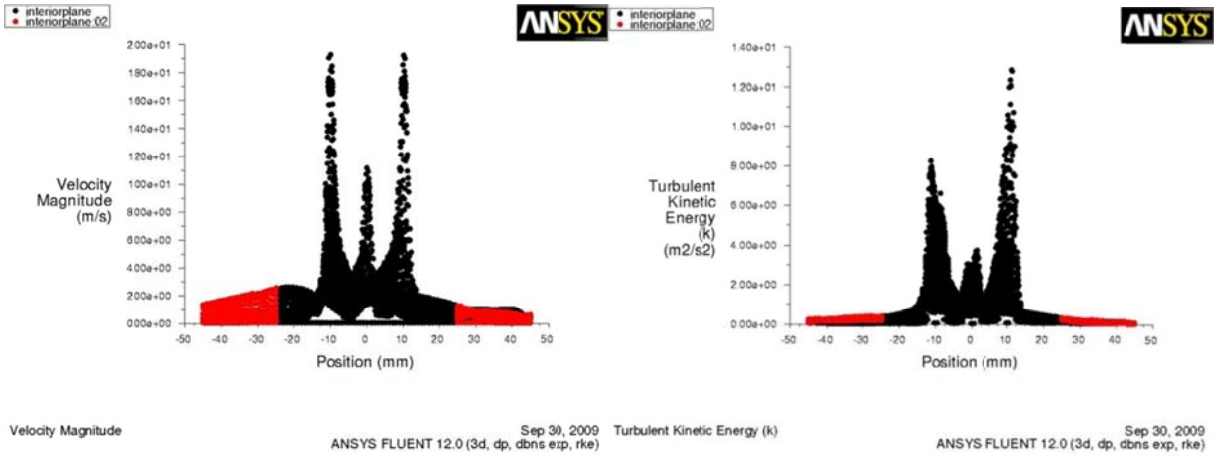

Figure 152: Head 5, fluid flow case 3: 3D view of the interior plane/plane of symmetry of the model, a) contours of velocity/ m/s, b) velocity vectors/ m/s, c) contours of turbulent intensity/ %, d) contours of dissipation rate/ m^2/s^3, e) pathlines of velocity/ m/s, f) pathlines of velocity/ m/s, g) graph of velocity magnitude/ m/s, h) graph of turbulent kinetic energy/ m^2s^2.

a) b)

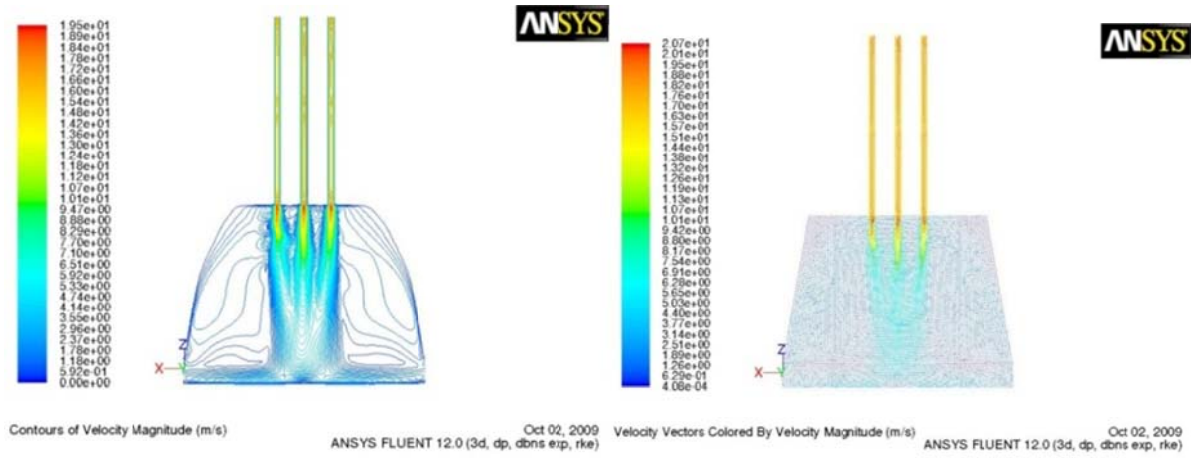

c)

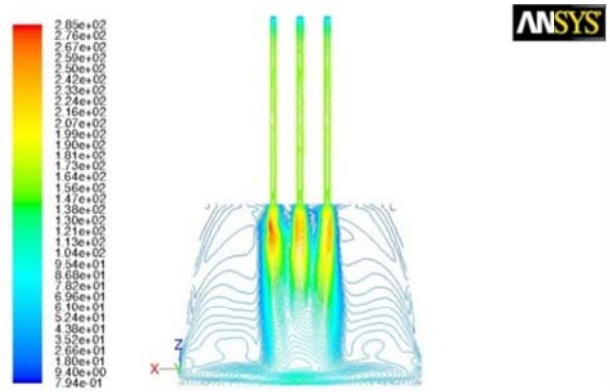

Contours of Turbulent Intensity (%)

Oct 02, 2009
ANSYS FLUENT 12.0 (3d, dp, dbns exp, rke)

d)

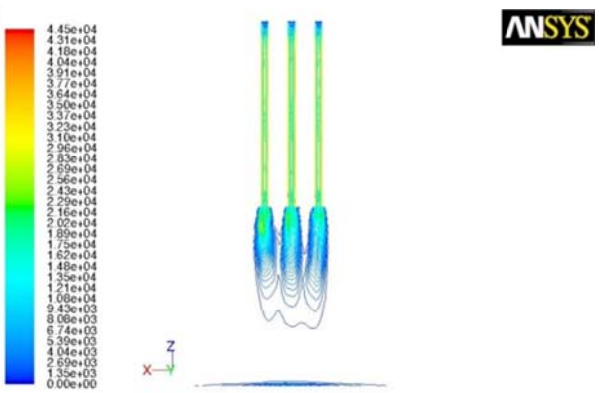

Contours of Turbulent Dissipation Rate (Epsilon) (m2/s3)

Oct 02, 2009
ANSYS FLUENT 12.0 (3d, dp, dbns exp, rke)

f)

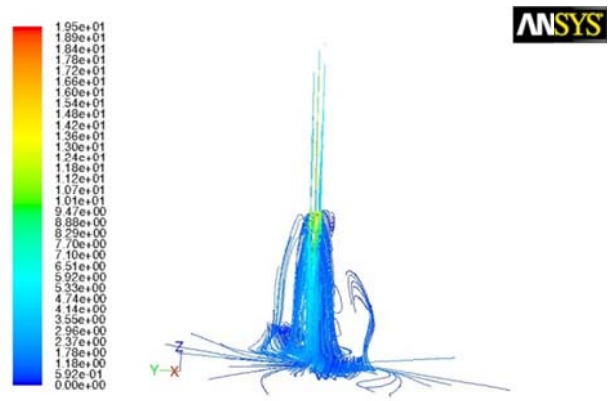

Pathlines Colored by Velocity Magnitude (m/s)

Oct 12, 2009
ANSYS FLUENT 12.0 (3d, dp, dbns exp, rke)

g)

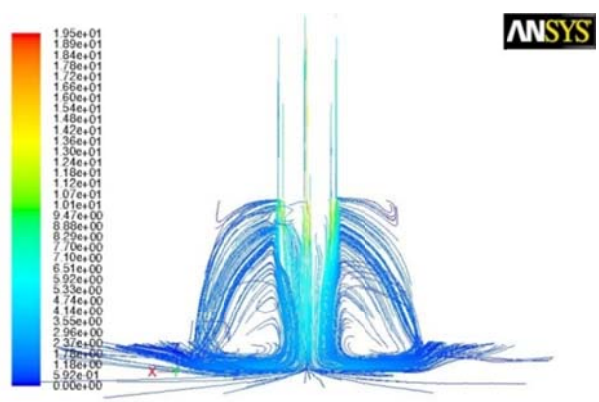

Pathlines Colored by Velocity Magnitude (m/s)

Oct 12, 2009
ANSYS FLUENT 12.0 (3d, dp, dbns exp, rke)

h)

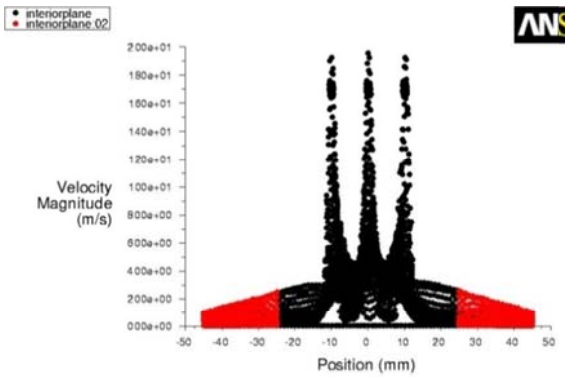

Velocity Magnitude

Oct 06, 2009
ANSYS FLUENT 12.0 (3d, dp, dbns exp, rke)

i)

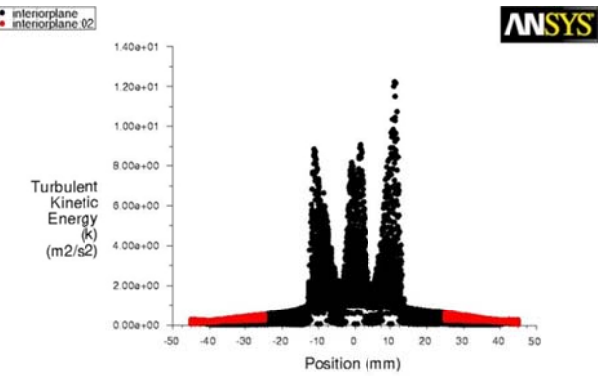

Turbulent Kinetic Energy (k)

Oct 06, 2009
ANSYS FLUENT 12.0 (3d, dp, dbns exp, rke)

Figure 153: Head 5, fluid flow case 4: 3D view of the interior plane/plane of symmetry of the model, a) contours of velocity/ m/s, b) velocity vectors/ m/s, c) contours of turbulent intensity/ %, d) contours of dissipation rate/ m^2/s^3, e) contours of turbulent kinetic energy/ m^2/s^2, f) graph of velocity magnitude/ m/s, g) graph of turbulent kinetic energy/ m^2/s^2.

a)

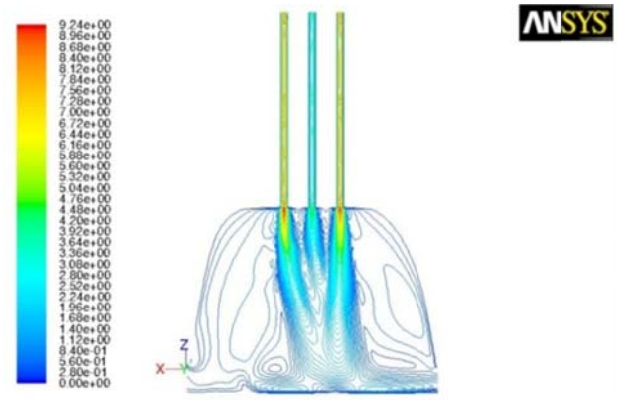

Contours of Velocity Magnitude (m/s)

Oct 02, 2009
ANSYS FLUENT 12.0 (3d, dp, dbns exp, rke)

b)

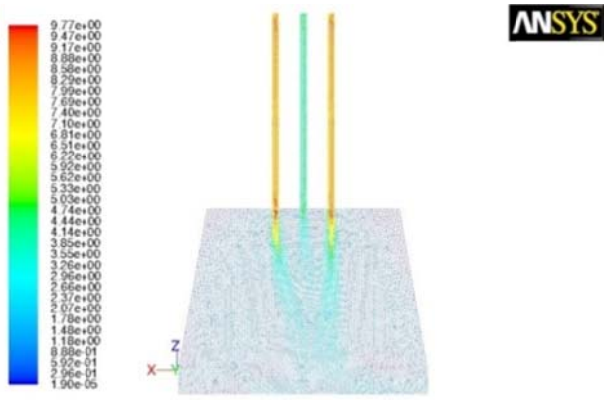

Velocity Vectors Colored By Velocity Magnitude (m/s)

Oct 02, 2009
ANSYS FLUENT 12.0 (3d, dp, dbns exp, rke)

c)

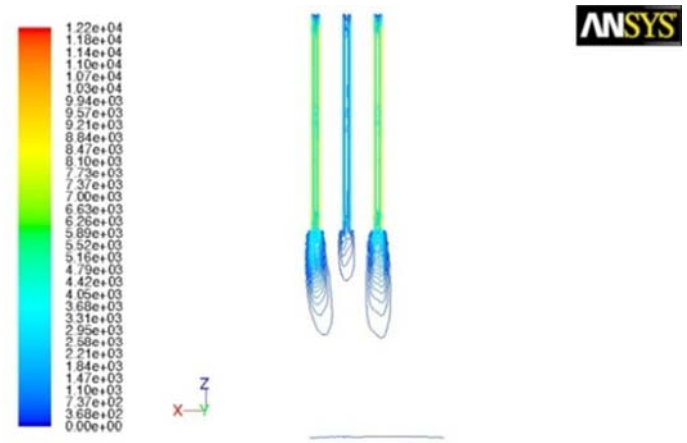

Contours of Turbulent Dissipation Rate (Epsilon) (m2/s3)

Oct 02, 2009
ANSYS FLUENT 12.0 (3d, dp, dbns exp, rke)

d)

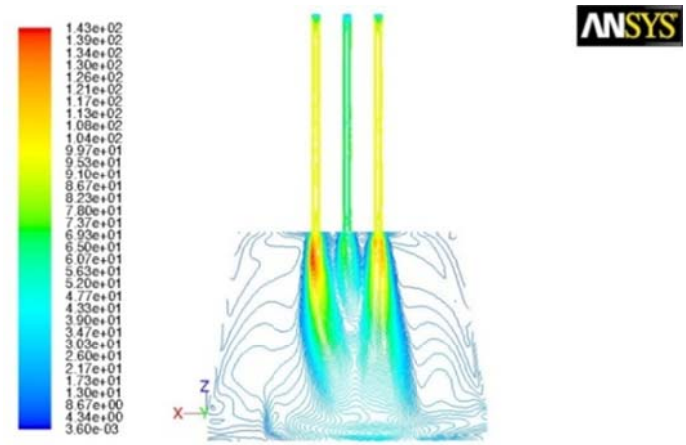

Contours of Turbulent Intensity (%)

Oct 02, 2009
ANSYS FLUENT 12.0 (3d, dp, dbns exp, rke)

e)

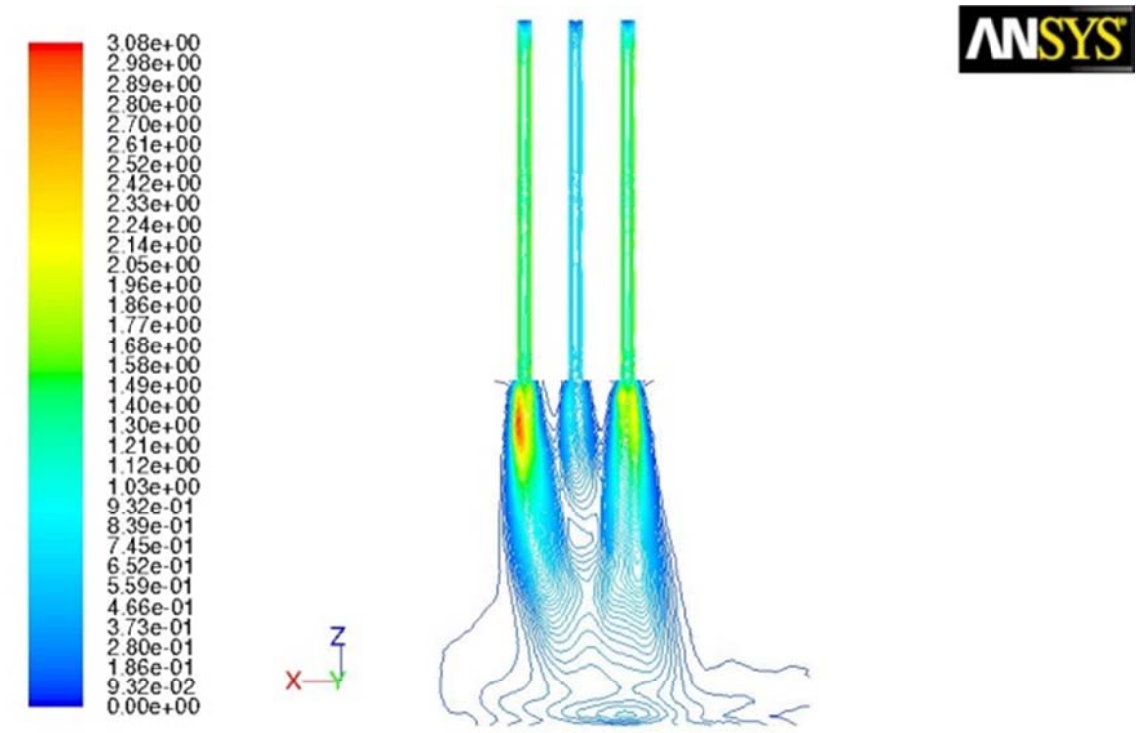
3.08e+00
2.98e+00
2.89e+00
2.80e+00
2.70e+00
2.61e+00
2.52e+00
2.42e+00
2.33e+00
2.24e+00
2.14e+00
2.05e+00
1.96e+00
1.86e+00
1.77e+00
1.68e+00
1.58e+00
1.49e+00
1.40e+00
1.30e+00
1.21e+00
1.12e+00
1.03e+00
9.32e-01
8.39e-01
7.45e-01
6.52e-01
5.59e-01
4.66e-01
3.73e-01
2.80e-01
1.86e-01
9.32e-02
0.00e+00
Z
X
Y
ANSYS
Contours of Turbulent Kinetic Energy (k) (m2/s2)
Oct 02, 2009
ANSYS FLUENT 12.0 (3d, dp, dbns exp, rke)

f)

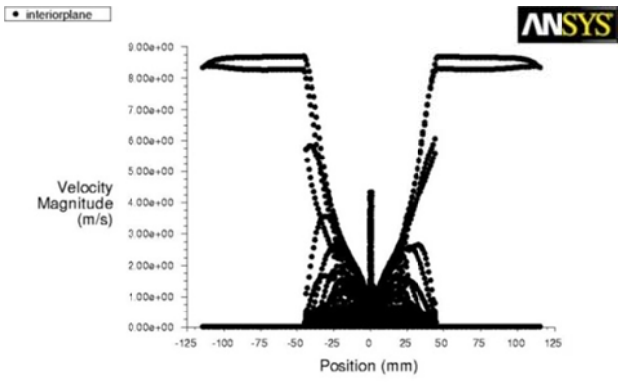
interiorplane
ANSYS
Velocity Magnitude (m/s)
9.00e+00
8.00e+00
7.00e+00
6.00e+00
5.00e+00
4.00e+00
3.00e+00
2.00e+00
1.00e+00
0.00e+00
-125 -100 -75 -50 -25 0 25 50 75 100 125
Position (mm)
Velocity Magnitude
Oct 08, 2009
ANSYS FLUENT 12.0 (3d, dp, pbns, rke)

g)

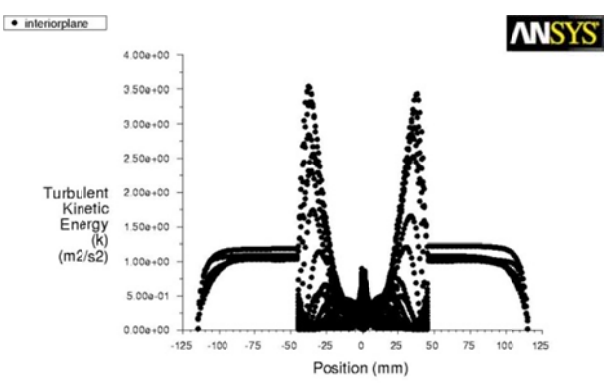
interiorplane
ANSYS
Turbulent Kinetic Energy (k) (m2/s2)
4.00e+00
3.50e+00
3.00e+00
2.50e+00
2.00e+00
1.50e+00
1.00e+00
5.00e-01
0.00e+00
-125 -100 -75 -50 -25 0 25 50 75 100 125
Position (mm)
Turbulent Kinetic Energy (k)
Oct 08, 2009
ANSYS FLUENT 12.0 (3d, dp, pbns, rke)